Controlling cell division and manipulating the cell cycle:
From RhoA regulation to photopharmacological tools

Dissertation
zur Erlangung des Doktorgrades der Naturwissenschaften
der Fakultät für Biologie
der Ludwig-Maximilians-Universität München

Friederike Eleonore Wolff

München, 2025

Diese Dissertation wurde angefertigt unter der Leitung von Prof. Dr. Esther Zanin im Bereich der Zell- und Entwicklungsbiologie an der Ludwig-Maximilians-Universität München und der Friedrich-Alexander-Universität Erlangen-Nürnberg.

Erstgutacherin: Prof. Dr. Esther Zanin

Zweitgutacher: Prof. Dr. Christof Osman

Tag der Abgabe: 16.05.2025

Tag der mündlichen Verteidigung: 08.08.2025

Eidesstaatliche Erklärung:

Ich versichere hiermit an Eides statt, dass meine Dissertation selbstständig und ohne unerlaubte Hilfsmittel angefertigt worden ist. Weiterhin wurden alle Teile der Arbeit, die mit Hilfe von Werkzeugen der künstlichen Intelligenz de novo generiert wurden, durch Fußnote/Anmerkung an den entsprechenden Stellen kenntlich gemacht und die verwendeten Werkzeuge der künstlichen Intelligenz gelistet. Die genutzten Prompts befinden sich im Anhang. Diese Erklärung gilt für alle in der Arbeit enthaltenen Texte, Graphiken, Zeichnungen, Kartenskizzen und bildliche Darstellungen.

München, d. 16.05.2025

Friederike Wolff

Erklärung:

Hiermit erkläre ich, dass die vorliegende Dissertation weder ganz, noch teilweise bei einer Prüfungskommission vorgelegt worden ist und, dass ich mich nicht anderweitig einer Doktorprüfung ohne Erfolg unterzogen habe.

München, d. 16.05.2025

Friederike Wolff

List of publications

Schneid, S.*, **Wolff, F.**, Buchner, K., Bertram, N., Baygün, S., Barbosa, P., Mangal, S., & Zanin, E. (2021). The BRCT domains of ECT2 have distinct functions during cytokinesis. *Cell reports*, *34*(9), 108805. https://doi.org/10.1016/j.celrep.2021.108805

Wolff F., Srinivasan S., Nöcker M., Mangal S., Mikeladze-Dvali T., Zanin E. (2023). Spatially distinct inputs modulate the amount of active Mitotic-phase GAP to locally restrict RhoA signaling for successful cell division. *bioRxiv* Preprint. https://doi.org/10.1101/2023.08.08.552464

Uhl, E.*, **Wolff, F.**, Mangal, S., Dube, H., & Zanin, E. (2021). Light-Controlled Cell-Cycle Arrest and Apoptosis. *Angewandte Chemie (International ed. in English)*, *60*(3), 1187–1196. https://doi.org/10.1002/anie.202008267

Köttner, L.*, **Wolff, F.**, Mayer, P., Zanin, E., & Dube, H. (2024). Rhodanine-Based Chromophores: Fast Access to Capable Photoswitches and Application in Light-Induced Apoptosis. *Journal of the American Chemical Society*, *146*(3), 1894-1903. https://doi.org/10.1021/jacs.3c07710

* contributed equally

Declaration of contribution as a co-author

Chapter I has been published in *Cell reports*. Chapter II is an published non-peer-reviewed manuscript. Chapter III has been published in *Angewandte Chemie (Internation Edition)* and Chapter IV has been published in *Journal of the American Chemical Society*. I am holding co-first authorship in Chapter I, III and IV and my contributions to these publications are listed for each of the chapter separately below.

<u>Chapter I</u>:

Schneid, S., **Wolff, F.**, Buchner, K., Bertram, N., Baygün, S., Barbosa, P., Mangal, S., & Zanin, E. (2021). The BRCT domains of ECT2 have distinct functions during cytokinesis. *Cell Reports*

Experimental design was conducted by EZ (Esther Zanin), SS (Sandra Schneid) and FW (Friederike Wolff). Experimental work and data analysis has been mainly performed by SS and FW: SS performed experiments and data analysis for Fig. 1 E-H, Fig. 3 B-G, Fig. 5 B-D, Fig. 6 F, Fig. S2-S3, Fig. S6 C-F, Fig. S7 A-D, H-K. FW performed experiments and data analysis for Fig. 4 A-F, Fig 5. E-F, Fig. 6 A-D, Fig 7. A-D, Fig. S4, Fig. S5 B-C, Fig. S6 A-B, Fig. 7S E-G. SS and FW contributed together to experiments and data analysis of Fig 1. B-D, Fig 3. A, Fig. 5A, Fig. S1 B-H. EZ and SS contributed together to experiments and data analysis of Fig. 1G, Fig. 6E. Nils Bertram (NB) supported in experimental work and data analysis for Fig. 2A-F and Kristina Buchner (KB) contributed to experimental work and analysis for Fig. 1D, Fig. 3A, Fig. 5A.

Chapter III:

Uhl, E., **Wolff, F.**, Mangal, S., Dube, H., & Zanin, E. (2021). Light-Controlled Cell-Cycle Arrest and Apoptosis. *Angewandte Chemie (International Edition)*

Experimental design was conducted by EZ (Esther Zanin), HD (Henry Dube), EU (Edgar Uhl) and FW (Friederike Wolff). Experimental work and data analysis has been performed by EU and FW: EU synthesized all chemical compounds and performed experiments and data analysis for Fig 2 A-B. FW performed experiments and data analysis for Fig 3 C-D, 4 C-F, 5 A-C. EU performed experiments and data analysis for Fig S1-S16. FW performed experiments and data analysis for Fig S17B, S18-S22.

Chapter IV:

Köttner, L., **Wolff, F.**, Mayer, P., Zanin, E., & Dube, H. (2024). Rhodanine-Based Chromophores: Fast Access to Capable Photoswitches and Application in Light-Induced Apoptosis. *Journal of the American Chemical Society*

Experimental design was conducted by EZ (Esther Zanin), HD (Henry Dube), LK (Laura Köttner) and FW (Friederike Wolff). Experimental work and data analysis has been performed by LK and FW: LK synthesized all chemical compounds and performed experiments and data analysis for Fig. 2 A-B, Fig. 3 A-C, Fig 4. A-C, Fig. S1-S94. FW performed experiments and data analysis for Fig. 5 B-F, Fig. S94-S98.

Acknowledgments

An erster Stelle möchte ich mich bei Prof. Dr. Esther Zanin bedanken, die mir die Möglichkeit gegeben hat in ihrer Arbeitsgruppe zu promovieren. Esther, ich danke dir für deine kontinuierliche Unterstützung, deine fachliche Begleitung und dein großes Vertrauen, das du mir über all die Jahre entgegengebracht hast.

Mein Dank gilt auch den Mitgliedern meines Thesis Advisory Committees, PD Dr. Annette Müller-Taubenberger und Prof. Dr. Christof Osman. Ich danke euch für die anregenden Diskussionen zu meinen Projekten und eure Unterstützung, diese immer weiter voranzutreiben. Besonders dankbar bin ich euch auch dafür, dass ihr mir stets das Gefühl gegeben habt, mit jedem Anliegen zu euch kommen zu können.

Ein großer Dank geht an meine Kollegin Dr. Sandra Schneid. Sandra, wo soll ich anfangen – du warst nicht nur die beste Kollegin und Projektpartnerin, die ich mir hätte wünschen können, sondern auch eine unglaublich große persönliche Unterstützung während dieser Zeit. Mit dir waren selbst die schwierigsten Phasen leicht und voller Lachen. Ich bin mir sicher: Ohne dich wäre diese Arbeit – und damit meine ich nicht nur das Ect2-Projekt – nicht entstanden.

Ebenso danke ich meinen beiden Kollaborationspartnern Dr. Laura Köttner und Dr. Edgar Uhl. Laura, dank deiner unermüdlich positiven Art und deines beeindruckenden Engagements (wie kann man so schnell Stoffe synthetisieren?) war die Zusammenarbeit mit dir vom ersten bis zum letzten Tag eine Freude. Ich werde nie vergessen, wie wir lachend und voller Elan die Fenster im Labor mit Alufolie abdunkelten. Ed, auch dir danke ich für deine harte Arbeit und deine Motivation. Unvergessen bleibt für mich, wie wir stundenlang im abgedunkelten Raum Zellen bestrahlt haben – dank dir war selbst das ein Vergnügen.

Mein aufrichtiger Dank gilt auch der gesamten Arbeitsgruppe von PD Dr. Tamara Mikeladze-Dvali. Tamara, du hast mich mehr als einmal mit offenen Armen in deiner Gruppe willkommen geheißen. Du hast mir stets das Gefühl gegeben Teil deines Teams zu sein und ich bin dir für deine fachliche wie auch persönliche Unterstützung zutiefst dankbar. In diesem Zusammenhang möchte ich auch meinen „Fast-Kolleginnen" Alina Schreiner und Zakiah Talib danken. Ihr wart mir in jeder Hinsicht eine große Unterstützung, und ich bin sehr dankbar für die Freundschaft, die sich aus

Abstract

Cell division is the fundamental process that underlies all life on earth. During the final stage of cell division, known as cytokinesis, the mother cell physically splits into two daughter cells and its genetic material and other cellular contents are distributed to the two new daughter cells. In animal cells, this is achieved by the formation and constriction of an actin-myosin ring between the segregating chromosomes underneath the plasma membrane. Contractile ring assembly is orchestrated by the small GTPase RhoA, which acts as a molecular switch, cycling between an active GTP-bound and an inactive GDP-bound state. RhoA activity in animal cells is controlled by the mitotic spindle from which stimulatory and inhibitory signals emanate. The spindle midzone consists of a network of overlapping microtubules and harbours the centralspindlin complex (MKLP1 and RacGAP1), the Polo-like kinase 1 and the guanine nucleotide exchange factor (GEF) Ect2. The midzone-centered stimulatory signals activate Ect2, which in turn facilitates the exchange from GDP to GTP, thereby activating RhoA. The inhibitory signals are based on astral microtubules and prevent RhoA activation at outer polar regions of the cell. Despite extensive research, the precise regulation of RhoA activity during cytokinesis remains incompletely understood due to a lack of understanding of the stimulatory signals in regard of Ect2 regulation and inhibitory signals due to their unknown molecular nature.

The first project focused on the stimulatory signals by investigating regulation of Ect2 during cytokinesis. Ect2 consists of three N-terminal BRCT domains, a DH GEF domain harbouring the catalytic GEF activity and a PH domain for membrane binding. At the beginning of this work, it was assumed that Ect2 activity is regulated by an autoinhibitory interaction of its three BRCT domains with its DH-GEF domain. Using a variety of microscopy techniques and biochemical assays, this work has shown that each BRCT domain of Ect2 has distinct functions during cytokinesis in human cells. The BRCT1 domain is essential for Ect2 activation and therefore cytokinesis. In contrast, the BRCT0 domain is not essential for successful cell division but assists in the release of Ect2 autoinhibition and correct timing of cytokinesis. The BRCT2 domain is essential for Ect2 regulation since it inhibits its GEF activity. Deletion of the BRCT2 domain leads to hyperactive RhoA and increased cytokinetic failure. It was also shown that all BRCT domains bind to the central spindle component RacGAP1 and the Polo-

like kinase 1. Furthermore, phosphorylation of the BRCT0 domain by Plk1 was shown. Overall, this study gives detailed insights into the regulation of Ect2 by its BRCT domains and interaction partners to ensure proper cell division.

The second project focused on the inhibitory signals by investigating its molecular nature. Previous work in *Caenorhabditis elegans* suggested that the spindle pole-localized kinase Aurora A inhibits contractility during cytokinesis at the poles. However, whether Aurora A function is conserved in human cells and what its phosphorylation target is was unknown. This thesis revealed that spindle pole-localized Aurora A kinase restricts contractility to the equator by phosphorylating and activating the GAP MP-GAP, which limits RhoA activity. Thereby, this work showed that Aurora A is part of the spindle-pole derived signal and identified its phosphorylation target. Three Aurora A phosphorylation sites were identified in MP-GAP and shown to be essential for the function of MP-GAP in limiting RhoA activity. The region of MP-GAP harbouring these three sites binds to its catalytic GAP domain suggesting an autoinhibitory conformation, which is released upon phosphorylation by Aurora A. It was shown that interaction of Aurora A kinase and MP-GAP takes place mainly at the polar regions of the cell and that phosphorylated MP-GAP is targeted by F-actin to the cell equator, where it accelerates the RhoA flux through the GTPase cycle, thereby preventing the spread of active RhoA. In addition, it was shown that simultaneous up-regulation of Ect2 activity and down-regulation of MP-GAP activity by inhibition of Aurora A kinase leads to strong cytokinetic failure, suggesting redundant mechanisms to spatially pattern RhoA activity. In conclusion, this work identifies for the first time a spindle pole-located signal that spatially regulates RhoA activity to ensure successful cell division in human cells.

Finally, in two last projects this thesis endeavoured to gain control over the cell cycle and an oncogenic kinase as a putative therapeutic tool through an innovative photopharmacological approach. The proteasome inhibitor MG-132 and Pim-kinase inhibitors were converted into light-responsive tools that can be switched on and/or off by light. When irradiated in living cells, MG-132 was activated and led to the arrest of human HeLa cells in metaphase and induction of apoptosis over time. Irradiation of an inactive version of the Pim kinase inhibitor Smi16a in living cells turned on their activity and induced apoptosis in several human cancer cell types. In conclusion, this work has developed highly innovative tools that enable cell cycle manipulation as a strategy for putative biomedical applications in the future.

Zusammenfassung

Die Zellteilung ist der grundlegende Prozess allen Lebens. In der letzten Phase, der Zytokinese, teilt sich die Mutterzelle und das genetische Material sowie andere zelluläre Inhalte werden auf die beiden neuen Tochterzellen verteilt. In tierischen Zellen geschieht dies durch die Bildung und das Zusammenschnüren eines Aktin-Myosin-Rings unterhalb der Plasmamembran zwischen den sich trennenden Chromosomen. Der Aufbau dieses kontraktilen Rings wird von der kleinen GTPase RhoA gesteuert, die als molekularer Schalter zwischen einem aktiven (GTP-gebundenen) und einem inaktiven (GDP-gebundenen) Zustand wechselt. In tierischen Zellen wird RhoA durch die mitotische Spindel reguliert von welcher sowohl stimulierende als auch inhibierende Signale ausgehen. Die mitotische Spindel besteht aus einem Netzwerk überlappender Mikrotubuli, dem Zentralspindel-Komplex (MKLP1 und RacGAP1), der Polo-like Kinase 1 (Plk1) und dem Guanin-Nukleotid-Austauschfaktor Ect2. Die in der Spindel zentrierten Signale aktivieren Ect2, welches daraufhin den Austausch von GDP zu GTP fördert und somit RhoA aktiviert. Die hemmenden Signale hingegen gehen von astralen Mikrotubuli aus und inhibieren die RhoA-Aktivierung an den äußeren Zellpolen. Trotz umfangreicher Forschung ist die Regulation der RhoA-Aktivität noch nicht vollständig verstanden, da sowohl die Ect2-vermittelten stimulierenden Signale als auch die molekulare Natur der inhibitorischen Signale nur teilweise aufgeklärt sind.

Das erste Projekt dieser Arbeit widmete sich den stimulierenden Signalen, indem die Regulation von Ect2 während der Zytokinese untersucht wurde. Ect2 besteht aus drei N-terminalen BRCT-Domänen, einer katalytischen DH-GEF-Domäne und einer PH-Domäne für die Membranbindung. Zu Beginn dieser Arbeit wurde angenommen, dass Ect2 durch eine autoinhibitorische Interaktion seiner BRCT-Domänen mit der GEF-Domäne reguliert wird. Durch bildgebende Verfahren und biochemische Analysen konnte gezeigt werden, dass jede einzelne BRCT-Domäne von Ect2 eine spezifische Rolle während der Zytokinese erfüllt. Die BRCT1-Domäne ist essenziell für die Aktivierung von Ect2. Die BRCT0-Domäne ist dagegen zwar nicht zwingend notwendig für die Zellteilung, unterstützt aber die Aufhebung der Autoinhibition von Ect2 und das korrekte Timing der Zytokinese. Die BRCT2-Domäne hemmt die GEF-Aktivität von Ect2, und Entfernung dieser Domäne führt zu hyperaktivem RhoA und Fehlern in der Zytokinese. Alle BRCT-Domänen binden an die zentrale

Spindelkomponente RacGAP1 und an Plk1. Zudem wurde eine Phosphorylierung der BRCT0-Domäne von Plk1 nachgewiesen. Zusammenfassend liefert dieses Projekt neue Einblicke in die Regulation von Ect2 mittels seiner BRCT-Domänen sowie dessen Interaktionspartner, um eine erfolgreiche Zellteilung zu gewährleisten.

Das zweite Projekt untersuchte den molekularen Ursprung der inhibitorischen Signale. Frühere Studien in *C. elegans* deuteten darauf hin, dass die am Spindelpol lokalisierte Kinase Aurora A die Kontraktilität an den Zellpolen während der Zytokinese inhibiert. Es war jedoch unklar, ob dies auch für menschliche Zellen gilt und was das Zielprotein der Phosphorylierung ist. Diese Arbeit hat gezeigt, dass die am Spindelpol lokalisierte Aurora-A-Kinase die Kontraktilität auf den Äquator beschränkt, indem sie MP-GAP (GAP von RhoA) phosphoryliert und aktiviert. Daher wurde in dieser Arbeit Aurora A als Teil des polaren Signals und MP-GAP als dessen Phosphorylierungsziel identifiziert. Drei essenzielle Aurora A Phosphorylierungsstellen wurden innerhalb eines Bereichs von MP-GAP, der an die katalytische GAP-Domäne bindet, gefunden. Dies deutet auf eine autoinhibitorische Konformation hin, die durch die Phosphorylierung von Aurora A aufgehoben wird. Die Interaktion zwischen Aurora A und MP-GAP tritt vor allem an den Zellpolen auf und aktiviertes MP-GAP wird von F-Aktin zum Äquator transportiert, wo es den RhoA-GTPase-Zyklus beschleunigt und so die Ausbreitung von aktivem RhoA begrenzt. Eine simultane Hochregulation von Ect2 und Herunterregulation von MP-GAP führt zu Zytokinese-Fehlern und weist auf redundante Mechanismen bezüglich der Regulation von RhoA-Aktivität hin. Insgesamt wurde hier erstmals ein Spindelpol-spezifisches Signal identifiziert, welches die lokale RhoA-Regulation in menschlichen Zellen ermöglicht.

In zwei weiteren Projekten wurde ein innovativer pharmakologischer Ansatz zur Kontrolle des Zellzyklus und zur gezielten Hemmung einer onkogenen Kinase verfolgt und entwickelt. Der Proteasom-Inhibitor MG-132 und Pim-Kinase-Inhibitoren wurden in lichtabhängige Werkzeuge umgewandelt, die durch Bestrahlung in lebenden Zellen aktiviert und/oder inaktiviert werden können. Aktiviertes MG-132 führte zu Arrest in Metaphase und Apoptose in Krebszellen. Eine inaktive Version des Pim-Kinase-Inhibitors Smi16a konnte durch Licht aktiviert werden und induzierte den Zelltod in mehreren karzinogenen Zelllinien. Damit wurden neue Werkzeuge geschaffen, die eine präzise, lichtgesteuerte Manipulation des Zellzyklus für potenzielle biomedizinische Anwendungen ermöglichen.

Table of contents

XIV

List of figures

Abbreviations

General abbreviations

AA	Aminoacid
AHD	anillin homology domain
APC/C	Anaphase promoting complex
BRCT	BRCA-1 C-terminal
C. elegans	*Caenorhabditis elegans*
CPC	chromosomal passenger complex
c-terminus	carboxy terminus
D. melanogaster	*Drosophila melanogaster*
DH	Dbl homology
DNA	deoxyribonucleic acid
Ect2	epithelial cell transforming 2
ESCRT III	Endosomal Sorting Complex Required for Transport III
FDA	Food and Drug Administration
FRAP	Fluorescence Recovery After Photobleaching
F-actin	filamentous actin
GAP	GTPase activating protein
GDI	guanosin dissociation inhibitor
GDP	guanosin diphosphate
GEF	guanine nucleotide exchange factor
GTP	guanosine triphosphate
H. sapiens	*Homo sapiens*
HTI	Hemithioindigo
M. musculus	*Mus musculus*
MT(s)	microtubule(s)
N-terminus	amino terminus
NMR	Nuclear Magnetic Resonance
PBD	Polo-box domain
PBS	polybasic sequence
PH	pleckstrin homology

RNAi	RNA interference
ROS	Reactive oxygen species
SAC	spindle assembly checkpoint
UPP	Ubiquitin proteasome pathway
UPR	Unfolded protein response
WT	wild-type
X. laevis	*Xenopus laevis*

Gene and protein abbreviations

Gene symbols	Gene name	Species
AURKA	Aurora A kinase	*H. sapiens*
AURKB	Aurora B kinase	*H. sapiens*
BAX	Bcl-2-like protein 4	*H. sapiens*
BRCA1	Breast cancer type 1 susceptibility protein	*H. sapiens*
CDK1	Cycline dependent kinase 1	*H. sapiens*
CENPE	Centromere protein E	*H. sapiens*
ECT2	Epithelial cell transforming protein 2	*H. sapiens*
FOXM1	Forkhead box protein M1	*M. musculus*
GRAF3	GTPase Regulator Associated with FAK3	*H. sapiens*
IkB	Ikappa B kinase	*H. sapiens*
INCENP	Inner centromere protein	*H. sapiens*
KIF4	Kinesin family member 4	*H. sapiens*
MCAK	Mitotic centromere-associated kinesin	*H. sapiens*
MDC1	Mediator of DNA damage checkpoint 1	*H. sapiens*
MDM2	Murine double minute 2	*H. sapiens*
MKLP1	Mitotic kinesin-like protein 1	*H. sapiens*
MKLP2	Mitotic kinesin-like protein 2	*H. sapiens*
MLCP	Myosin light chain phosphatase	*H. sapiens*
MP-GAP	Mitotic phase GTPase activating protein	*H. sapiens*
NF-kB	Nuclear factor kappa B	*H. sapiens*

PLK1	Polo-like kinase 1	*H. sapiens*
PRC1	Protein regulator of cytokinesis 1	*H. sapiens*
PUMA	P53 Upregulated Modulator of Apoptosis	*H. sapiens*
RACGAP1	Rac GTPase activating protein 1	*H. sapiens*
RAD9	DNA repair protein Rad9	*H. sapiens*
RHOA	Ras homology family member A	*H. sapiens*
ROCK	Rho associated kinase	*H. sapiens*
TOPBP1	DNA topoisomerase 2-binding protein 1	*H. sapiens*
TPX2	Targeting Protein for Xenopus Kinase-like protein 2	*H. sapiens*

1 Introduction

1.1 Overview of the cell cycle

Cell division is the essential process of life. It does not only allow the development but also the maintenance of living organisms. The cell cycle encompasses the whole life of a single cell from its birth to its division into daughter cells. The cell cycle is broken down into two main phases: The interphase and the mitotic phase (M-phase). The S-phase is part of interphase during which the DNA is replicated. The S-phase is linked to two gap phases: G1 and G2. After cell division, cells enter the G1 phase, where they can either go into a next round of division or exit the cell cycle by entering the G0 resting phase. During G1 phase, cells grow in size until a point where they can enter S-phase. After DNA synthesis and replication, cells enter G2 phase. Here the cells prepare for the mitotic phase through additional growth, synthesis of proteins and organelles, and reorganisation of their cellular contents. Therefore, the G1, G2, and S-phase are the three subphases of interphase where the cells prepare for mitosis (Alberts et al., 2002; 2015; Lodish, 2000; Morgan, 2006) (Figure 1A).

The mitotic phase is a multistep process in which the contents of the nucleus (mitosis) and the cytoplasm (cytokinesis) must be divided (Figure 1B). Mitosis starts with the prophase and prometaphase, where the nuclear envelope breaks down into small vesicles, and the DNA complex in the nucleus condenses, resulting in the formation of chromosomes. To form compact chromosomes, the sister chromatids are tightly held together by a cohesion complex, which forms a ring structure encircling the sister chromatids. Furthermore, a structure called the mitotic spindle starts to assemble, later separating the sister chromatids into two cells. The mitotic spindle is made by microtubules forming at the opposite cell poles emanating from the centrosomes and binding to the kinetochores on the sister chromatids. In metaphase, the chromosomes align in the center of the dividing cell forming the so-called metaphase plate. At anaphase onset, the kinetochore microtubules shorten and pull at the sister chromatids. The cohesion ring structures between the sister chromatids dissolve by proteolytic degradation, which leads to the movement of the sister chromatids to the two opposite ends of the cell. Moreover, a cytokinetic furrow forms and ingresses at

the cell equator between the segregating chromosomes, finally dividing the mother cell into two daughter cells (Alberts et al., 2002; 2015; Lodish, 2000; Morgan, 2006).
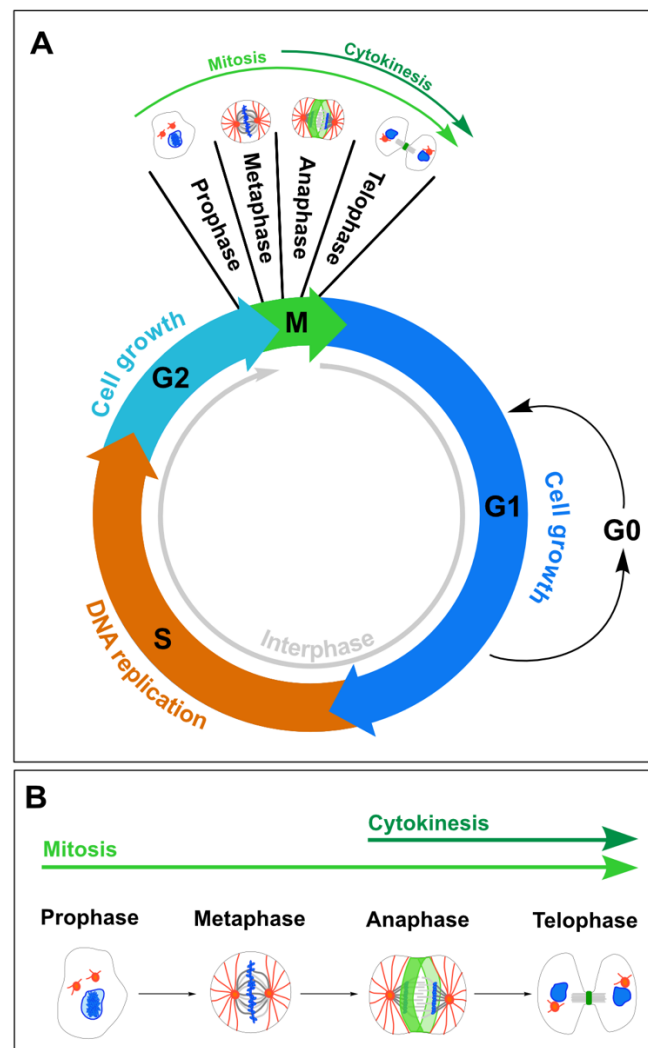
Figure 1: Illustrative representation of the cell cycle in animal cells.
A) The cell cycle encompasses two main phases: the interphase and the mitotic (M-) phase. The interphase consists of the G1, S- and G2 phase. During S-phase, G1, and G2 the cell prepares for cell division by duplicating its genetic material and cell growth. During M-phase cells first undergo genomic division and afterwards cytoplasmic division. Cells can exist the cell cycle by entering the G0 resting phase. B) The M-phase is subdivided into four stages: prophase, metaphase, anaphase and telophase – the last two depict cytokinesis. (Figure adapted from Wang, 2021)

As the cell cycle and thereby cell division is a fundamental process for life, it must be tightly regulated. There are several checkpoints along the cell cycle which are surveillance mechanisms that keep track of the order and the integrity of the different

cell cycle steps. In these several steps, three major checkpoints take place:

The first one is the G1 checkpoint, also called the start or restriction checkpoint since the cell becomes committed to entering the cell cycle. The decision to start into the cell cycle depends on activated cyclin-CDK transcription, which promotes the entry into S-phase by regulating expression of cyclins and cyclin-dependent kinases (CDKs), which are key drivers in cell cycle progression. On the other hand, DNA damages are the main indication for the cell to restrict in G1 phase and not to enter S-phase. Therefore, this checkpoint is the crucial mechanism for a cell to proceed into the cell cycle (Hartwell & Weinert, 1989).

The second checkpoint is the DNA damage checkpoint in S-phase. Problems with DNA replication initiate a signalling cascade that puts the phase on hold, thereby preventing DNA duplication errors (Barnum & O'Connell, 2014).

The third checkpoint is the spindle assembly checkpoint (SAC). It takes place at the metaphase-to-anaphase transition and maintains genome stability by guaranteeing accurate chromosome segregation. All sister chromosomes have to be properly attached to the microtubules spindle apparatus via their kinetochores. This silences the SAC and the Anaphase-Promoting Complex/Cyclosome (APC/C) triggers the degradation of securing and cyclin B1 via the 26S proteasome, which is essential to enable mitotic exit (Musacchio & Salmon, 2007).

1.2 Cytokinesis in animal cells

Cytokinesis is the last phase of mitosis in which the contents of the mother cell get partitioned between the two daughter cells (D'Avino et al., 2015). This final step of cell division starts with the formation of a contractile ring consisting of filamentous actin and non-muscle myosin II which assembles underneath the plasma membrane between the segregating chromosomes. The ingression of this contractile ring generates the force to bend the cell membrane and forms the cleavage furrow (Basant & Glotzer, 2018). After full ingression, the two daughter cells are still connected by a thin intercellular bridge, which then gets cleaved during the last step of cytokinesis, called abscission (D'Avino et al., 2015) (Figure 2).
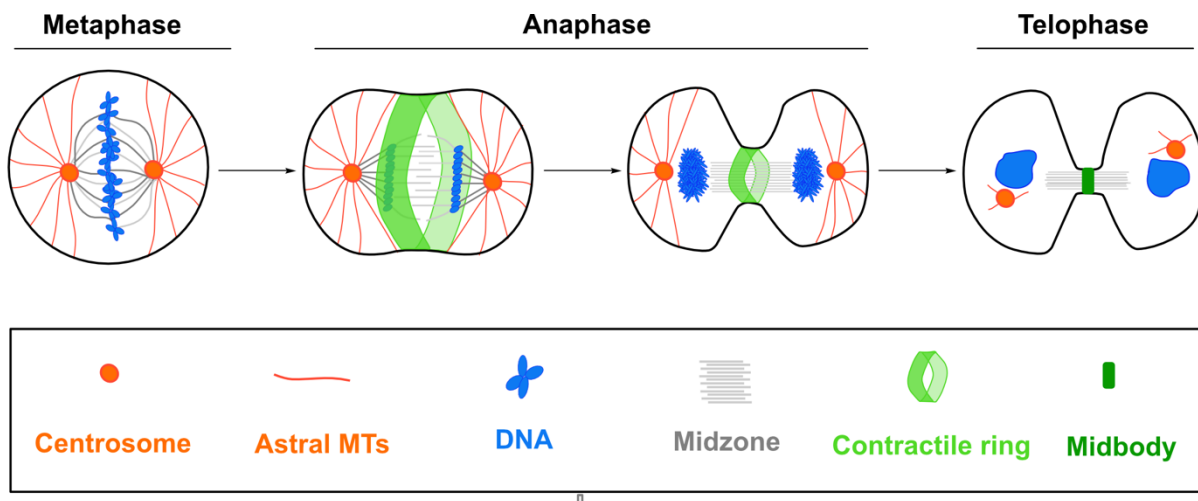
Figure 2: Illustrative representation of cytokinesis in animal cells.
The first step of cytokinesis is the formation of the spindle midzone during anaphase onset followed by the assembly of a contractile ring underneath the equatorial plasma membrane between the segregating chromosomes. Subsequently, the contractile ring constricts leading to the formation of a cleavage furrow. The two formed cells remain linked by an intercellular bridge, which is cleaved during the process of abscission.

Failure in contractile ring assembly and constriction gives rise to tetraploid cells, which are genomically unstable and can trigger tumor formation (Lacroix & Maddox, 2012; Lens & Medema, 2019). Given this important role of contractile ring formation, it is not surprising that multiple signals are involved in its temporal and spatial regulation. To ensure correct formation and ingression of the contractile ring, there is a continuous active signaling between the mitotic anaphase spindle and the cell cortex.

1.3 The mitotic spindle

The mitotic spindle is a microtubule-based machinery that has several essential roles during cell division. During metaphase, it mediates the accurate alignment of the chromosomes on the metaphase plate and during anaphase it segregates chromosomes and positions the cleavage furrow (Walcazk & Heald, 2008). Assembly of the mitotic spindle is dependent on the nucleation of three major classes of microtubules which are named according to their localization and function: kinetochore microtubules, which bind the kinetochore, astral microtubules, which grow from the spindle pole towards the cell cortex, and non-kinetochore microtubules, which

extend from both sites on the opposite spindle halves and overlap in the midplane. The arrays of these overlapping microtubules form the so-called spindle midzone between the segregating chromosomes during anaphase (Gadde & Heald, 2004; Pavin & Tolić, 2016; Prosser & Pelletier, 2017). The midzone is generated and recognized by several microtubule-associated proteins that contribute to its formation and function. One major player here is the microtubule binding and bundling protein, the protein regulator of cytokinesis 1 (PRC1), which is a Cdk substrate and essential for cell cleavage (Glotzer, 2009; Green et al., 2012). A second major player is centralspindlin, which is a complex composed of two proteins. First the mitotic kinesin-like protein 1 (MKLP1), and second, the GTPase activating protein (GAP) Rac GTPase-activating protein (RacGAP1) (Mishima et al., 2002; White & Glotzer, 2012). These two subunits are arranged in a heteromeric complex, forming the centralspindlin complex. During anaphase, centralspindlin is targeted to a narrow region at the overlapping microtubules after chromosome segregation and initiates assembly of the central spindle. PRC1 acts as a crosslinker by binding to microtubules and organizing them into a bundled structure in the middle of the spindle. Additionally, the kinase Plk1 promotes the formation of the mitotic spindle by phosphorylating centralspindlin, which is further required for furrow formation (Petronczki et al., 2008). The chromosomal passenger complex (CPC), consisting of Aurora B kinase, INCENP, Surivivin, and Borealin, translocates from the centromeres to the spindle midzone and prevents premature midzone disassembly by bundling of antiparallel microtubules and subsequent stabilization the spindle midzone (Carmena et al., 2012).

1.4 The mitotic spindle positions the contractile ring

It is of major importance that the contractile ring is precisely positioned at the equator between the segregating chromosomes to ensure an equal distribution of the cellular content of the mother cell to the two daughter cells. Therefore, the positioning of the contractile ring is regulated by multiple molecular signals between the spindle and the cell cortex. Already a pioneer study from 1985 demonstrated that changing the position of the mitotic spindle in echinoderm eggs induced regression of an already formed cleavage furrow and formation of a new cleavage furrow at the site of displacement

(Rappaport, 1985). Later studies have shown that the mitotic spindle induces the activation of the small GTPase RhoA in a narrow equatorial zone, which leads to activation of downstream effectors and thereby to formation of the contractile ring (Bement et al., 2006; Fededa & Gerlich, 2012; Yüce et al., 2005). However, there are still different models proposed how cleavage site specification is orchestrated (Figure 3). Even though it is widely accepted that signals emanating from the spindle midzone specify cleavage furrow formation, more studies arose proposing that there are inhibitory signals arising from astral microtubules which prevent RhoA activation and thereby contractility at the polar cortex (Bement et al., 2005; 2006; Chen et al., 2008; Mangal et al., 2018; van Osstende Triplet et al., 2014, von Dassow, 2009).

The midzone stimulation model is based on several studies which have shown that there are active signals emanating from the spindle midzone that promote contractility (Figure 3A). It was observed that one of the most important factors for the active signal is Ect2 (Epithelial cell transforming protein 2), a RhoA Guanine Nucleotide Exchange Factor (GEF) (Su et al., 2011; Tatsumoto et al., 1999; Yüce et al., 2005; Zhang & Glotzer, 2015). During beginning of cytokinesis, Ect2 gets enriched at the spindle midzone via RacGAP1 interaction, which induces a conformational change of Ect2 and thereby stimulates its GEF activity. Ect2 then transitions from the midzone to the equatorial plasma membrane where it activates RhoA and thereby induces the signaling cascade for contractile ring formation and contractility (Somers & Saint, 2003; Yüce et al., 2005; Zhao & Fang, 2005). However, it has also been shown that disrupting the interaction of Ect2 and RacGAP1 strongly reduced Ect2 spindle midzone localization but did not abolish furrow formation and ingression (Kotýnková et al., 2016). This gave rise for the hypothesis that another signaling pathway activates Ect2 and induces furrowing at the equatorial region of the cell.

In the stimulation by stable astral microtubules model it is proposed that a subset of stable microtubules extend from the asters reaching the equatorial cortex (Figure 3B). These microtubules carry stimulatory signals which promote contractility at the equator of the cell (Rappaport, 1961; Rieder et al., 1997; Verma & Maresca, 2019). This hypothesis was postulated after the finding that asters of independent spindles can induce furrow formation without a spindle midzone (Rappaport, 1961; Rieder et al., 1997). This hypothesis was then extended by the finding of stimulatory signals localized on the microtubule asters that could induce contractility (Verma & Maresca,

6

2019).

Additionally, more and more studies were arising postulating that astral microtubules limit contractility to the equatorial region of a cell and preventing it from the polar regions (Bement et al., 2006, Chen et al., 2008; Murthy & Wadsworth, 2008; Werner et al., 2007; von Dassow, 2009) (Figure 3C). However, the molecular nature of these inhibitory signals was poorly understood for a long time. A study of Mangal et al., 2018 was the first in gaining deeper insights into the principles of these signals: the researchers have shown that there is an active process of clearance of contractile ring components at the cell poles in *C. elegans*, which depends on activation of the kinase Aurora A by its aster-based activator TPXL-1 (TPX-2 in humans). Aurora A is a serine/threonine kinase and belongs to the Aurora kinase family. It plays major roles during cytokinesis in centrosome maturation, assembly of the mitotic spindle and chromosome segregation. During cytokinesis, Aurora A is primarily localizing to the centrosomes, where it regulates its maturation and separation, and thereby also ensures the proper assembly of the mitotic spindle (Barr & Gergely, 2007; Carmena & Earnshaw, 2003; Dutertre et al., 2002; Magnaghi-Jaulin et al., 2019; Nikonova et al., 2013). Furthermore, Aurora A has several phosphorylation targets involved in mitotic progression and microtubule dynamics (Barr & Gergely, 2007; DeLuca et al., 2018; Ong et al., 2020). Due to these named roles of Aurora A kinase, a dysregulation of its expression has been implicated in various cancers hallmarked by chromosomal instability and aberrant mitotic spindle formation (Lens & Voest, 2010). Localization and activation of Aurora A is dependent on binding to its activator TPX2 (Targeting Protein for Xenopus Kinesin-like protein 2). TPX2 translocates Aurora A to the centrosomes, stabilizes its active confirmation and interacts with its activation loop, promoting autophosphorylation of Aurora A at Thr288, which is essential for full kinase activity (Bayliss et al., 2003; Eyers et al., 2003).

If this clearing mechanism based on TPXL-1 and Aurora A kinase is conserved in human cells has to be clarified, however, there is evidence for an aster-based mechanism in human cells, which leads to a reduction of cortical stiffness at the polar regions of cells (Chen et al., 2021).
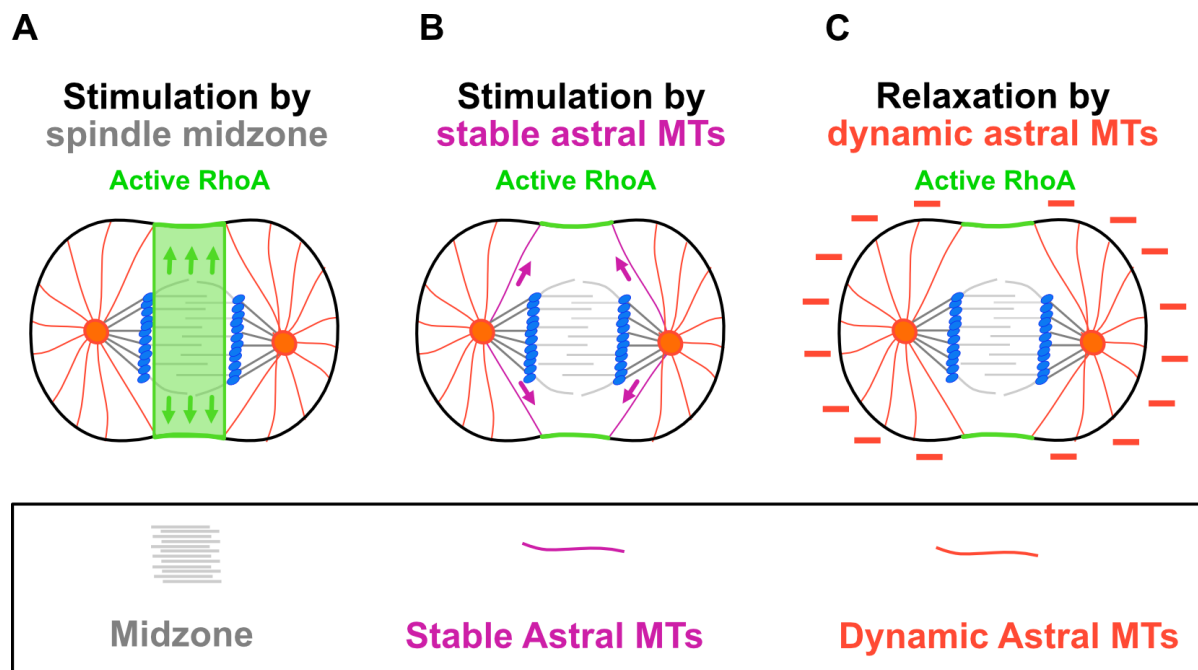
Figure 3: The mitotic spindle positions the contractile ring during cytokinesis.
A) Model of equatorial stimulation by the spindle midzone: Signals from the spindle midzone promote accumulation of active RhoA at the equatorial membrane. B) Model of equatorial stimulation by stable astral microtubules: Stimulatory signals emanating from stable astral microtubules promote active RhoA accumulation at the equatorial membrane. C) Model of polar relaxation by dynamic astral microtubules: Inhibitory signals emanating from astral microtubules prevent accumulation of active RhoA at polar regions of the cell and thereby prevent contractility and contractile ring formation besides the equatorial membrane. (Figure adapted from Mishima, 2016)

The mechanisms of how the contractile ring is precisely positioned are still not completely understood. However, since the disruption of one of these proposed models does not completely abolish furrow formation and cytokinesis, it is very likely that these different proposed mechanisms are not mutually exclusive but rather co-exist to ensure successful cell division. And indeed, it has been shown in *C. elegans* that asters and midzone separated from each other by laser ablation were independently of each other able to induce contractility (Bringman & Hymann, 2005). In general, it would be not surprising if several partially redundant mechanisms are contributing to this crucial step of cell divison to ensure its robustness against perturbations.

1.5 The small GTPase RhoA triggers contractile ring assembly

The crucial step of ring assembly is the activation of the small GTPase RhoA (Bement et al., 2006; Piekny et al., 2005). RhoA belongs together with Rac1 and Cdc42 to the small Rho GTPase family. Rho GTPases are key regulators of the actin cytoskeleton and are taking roles in various processes regarding cell motility, cell shape, adhesion and cytokinesis (D'Avino, 2015; Jordan & Canman, 2012). They are molecular switches cycling between an inactive GDP-bound and an active GTP-bound state. The activating switch is dependent on guanine nucleotide exchange factors, which catalyze the exchange of GDP to GTP. The inactivating switch is accomplished by GTPase activating proteins (GAPs), which catalyze the GTP hydrolysis. Ín humans, the major GEF for RhoA is Ect2, and the major GAP is Arhgap11a (Mitotic-phase GAP (MP-GAP)) (Tatsumoto et al., 1999; Zanin et al., 2013). Furthermore, there exist Guanine nucleotide dissociation inhibitors (GDIs) which stabilize inactive GDP-bound RhoA (Bement et al., 2006), regulate its access to GEFs and keep it cytoplasmic (Garcia-Mata et al., 2011).

During anaphase onset, RhoA gets activated by its GEF Ect2 and accumulates at the membrane of the future division site. There it activates and recruits downstream effectors, which are essential for contractility (Piekny et al., 2005). It activates the formina Dia (diaphanous member of formin-homolgy proteins), which together with profilin, mediates polymerization and assembly of actin filaments (Castrillon & Wasserman, 1994; Evangelista et al., 2002; Severson et al., 2002). Additionally, active RhoA activates the Rho-associated kinase (ROCK), which promotes Myosin II activity. Myosin II is a hexamer consisting of myosin heavy chains, light chains and light regulatory chains (rMLC). Activation of ROCK leads to phosphorylation of rMLC, which promotes myosin activity, and simultaneously prevents dephosphorylation of myosin II by binding the rMLC phosphatase, what additionally increases myosin II activity (Chihara et al., 1997; Kimura et al., 1996). To build a structural framework for the contractile ring, RhoA also activates the scaffolding protein anillin, which functions as a crosslinker. Anillin binds active RhoA, F-actin, myosin, Ect2 and septins (D'Avino et al., 2015; Field et al., 2005; Frenette et al., 2012; Oegema et al., 2000; Piekny & Glotzer, 2008; Straight et al., 2005; Sun et al., 2015). Thereby it acts as a crosslinker that links the contractile ring components to the plasma membrane and thereby

stabilizes the ingression furrow (Piekny & Glotzer, 2008; Straight et al., 2005; Zhao & Fang, 2005). It has been shown in *Drosophila melanogaster* that linking anillin to the plasma membrane is essential for cytokinesis (Kechad et al., 2012; Sun et al., 2015), hence, anillin is a major component for contractile ring formation and stability. Furthermore, the contractile ring is stabilized by septins, which are filament forming GTPases that crosslink F-actin into tightly packed arrays and thereby act as a scaffold for the contractile ring (Mavrakis et al., 2014; Menon et al., 2014) (Figure 4). Additionally, it has been shown in *C. elegans* that cortical flows compress the cortex along the axis perpendicular to the ring. This compression increases during constriction of the ring and correlates with an accumulation of myosin and anillin, which suggests that cortical flows contribute to delivery and accumulation of these contractile ring components (Khaliullin et al., 2018).
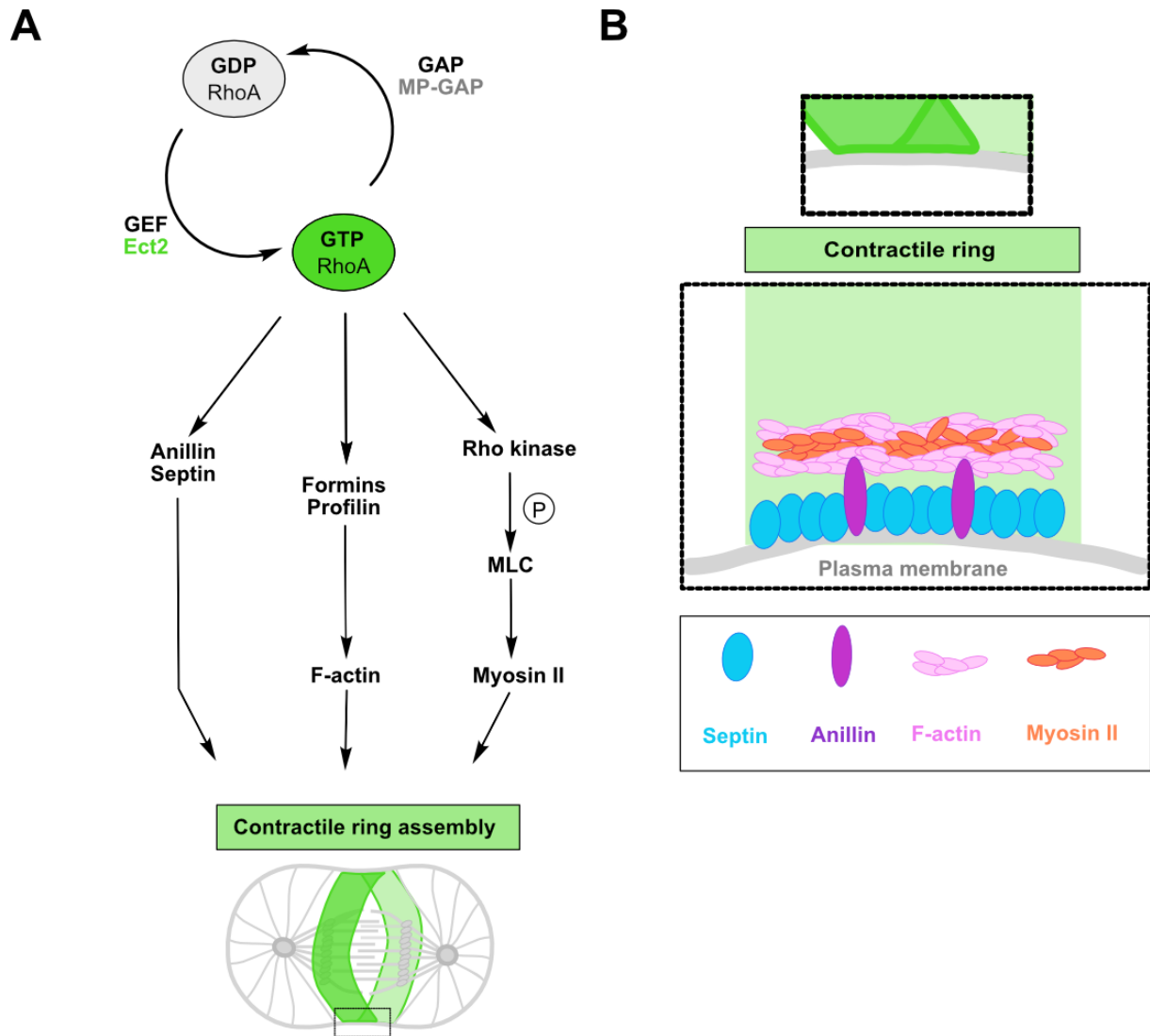
Figure 4*:* RhoA signaling pathway during cytokinesis in human cells and structural composition of the contractile ring.
A) The GTPase RhoA acts as a molecular switch cycling between an inactive GDP-bound and an active GTP-bound state. The GEF Ect2 catalyzes the exchange of GDP to GTP and thereby activates RhoA. The GAP MP-GAP facilitates the intrinsic hydrolysis from GTP to GDP leading to inactivation of RhoA. Upon activation, RhoA activates several downstream effectors: It induces polymerization of filamentous actin (F-actin) via formins and profilins, and activates myosin II via the Rho kinase. Furthermore, active RhoA recruits anillin and septins, which act as crosslinkers for the contractile ring. B) The contractile ring is primarily composed of actin filaments and myosin II, which are circumferentially arranged beneath the plasma membrane. Myosin II interacts with F-actin to facilitate contractile activity. Septins spatially stabilize the F-actin and myosin II filaments within the ring-like structure, and anillin anchors the actin filaments to the plasma membrane. (Figure adapted from Basant & Glotzer, 2018)

1.6 Cleavage furrow ingression and abscission

Successful cytokinesis does not only require the formation of a contractile ring, but also its ingression. To physically constrict a ring, an initiating force is required. How this constrictive force is generated is still actively debated. The key players to generate force for constriction are F-actin and myosin. It has been shown that actin filaments align in linear bundles at the equator, which raised the hypothesis that the required force is generated by sliding of actin filaments by myosin filaments, a similar mechanism as found in muscles (Biron et al., 2005; Maupin & Pollard, 1968; Schroeder, 1968; 1972). However, electron micrographs of different model systems did not observe the sarcomere-like arrays of myosin and actin as in muscles, which hints against this theory (Green et al., 2012). Furthermore, the capability of myosin II to cross-link and slide actin filaments was highlighted as a central mechanism for contractility, however, a study in *C. elegans* has shown that the motor activity of myosin is rather essential for force generation (Osório et al., 2019). Nevertheless, ring constriction independent of myosin motor activity has also been discussed, which relies on actin polymerization, depolymerization and cross-linking by actin-binding proteins. Actin dynamics as polymerization and depolymerization can generate forces if end-tracking crosslinkers are present, which remain bound to the depolymerizing filament ends. Also, myosin pulling on F-actin networks which are cross-linked by actin-binding proteins generates tension, which allows a network of filaments to deform (Carvalho et al., 2009; Leite et al., 2019; Zumdieck et al., 2007). The continuous polymerization and depolymerization of F-actin has also been shown to be required to keep the contractile ring dynamic and adaptable to tensions when it tightens (Pinto et al., 2012). Additional to increase contractility at the equator, decreased polar tension is required to allow efficient furrow ingression. It has been shown that contractile ring components are actively removed from the polar cortex to induce polar relaxation. Ramkumar et al., 2021 have shown that F-actin is removed from the polar cortex in human cells in an Aurora B kinase dependent manner what decreases cortical stiffness. Furthermore, Mangal et al., 2018 have shown that there is a clearance of anillin and F-actin from the polar cortex in an Aurora A kinase dependent manner in *C. elegans* what decreases contractility.

During ring constriction, the overlapping microtubules of the central spindle get tightly

compressed what leads to a point where the furrow cannot further constrict, leaving the two daughter cells connected by an intercellular bridge containing the so called midbody. The midbody is an electron-dense material consisting of microtubules, which plays a pivotal role for the final step of cytokinesis, called abscission, during which the two daughter cells get completely physically separated from each other (Elia et al., 2011). Since the midbody originates from the central spindle, the spindle proteins are re-localized to different regions of the assembling midbody. The kinesin family member 4 (KIF4) and the microtubule bundling protein PRC1 stay in the central part of the spindle and form the midbody core (Hu et al., 2012). The core is surrounded by a ring, where the former contractile ring components Ect2, centralspindlin, RhoA and anillin localize (Gai et al., 2012; Kechad et al., 2012). The midbody ring is flanked by two arms, where the motor proteins CENP-E (centromere protein E) and MKLP2 (mitotic kinesin-like protein 2) as well as the kinase Aurora B translocate (Gruneberg et al., 2004; Hu et al., 2012). The midbody arms serve as the cleavage sites for the endosomal sorting complex required for transport III (ESCRT-III), which is also involved in other membrane scission processes like multivesicular bodies (Elia et al., 2011; Schmidt & Teis, 2012). After degradation of PLK1 and Aurora B kinase, the ESCRT-III leads to the final constriction of the intercellular bridge and the separation of the two daughter cells (Vietri et al., 2020).

1.7 Temporal and spatial regulation of RhoA activity during cytokinesis

Successful cell division depends on the formation and constriction of a contractile ring. Activation of RhoA is the key step for assembly of the contractile ring, however, the activation step is not sufficient on its own for proper ring formation and constriction. It has to be activated in a well-defined amount precisely at the cell equator since this defines the location of the contractile ring. It has been shown that increased RhoA activity leads to formation of large ectopic protrusion, a hallmark for high intracellular pressure, and impairs furrow ingression dynamics (Miller & Bement, 2009; Zanin et al., 2013). On the other hand, decreased RhoA activity be depleting its GEF Ect2, leads to cytokinesis failure (Kim et al., 2005; Tatsumoto et al., 1999; Yüce et al., 2005).

These findings demonstrate the importance of a tight regulation of RhoA activity for proper cell division. After activation by its GEF Ect2, RhoA binds to the plasma membrane via two lipid anchors (Michaelson et al., 2001) and is assumed to move freely within the membrane. This assumption opens the idea that RhoA could diffuse away from the site of activation over time (Bement et al., 2006). Therefore, two theories have developed how active RhoA is maintained in a narrow region at the cell equator. The first one argues that this maintenance requires a defined balance between active and inactive RhoA, which is described in the so called RhoA flux model. It postulates that spreading of active RhoA within the membrane is prevented by inactivation through its GAP MP-GAP (Arghap11a), suggesting kind of a shut-off mechanism (Bement et al., 2006, Zanin et al., 2013). However, depletion of MP-GAP in human HeLa cells indeed led to strong membrane protrusions, but did not lead to a broadened equatorial RhoA zone, what contradicts this idea and suggests that this cannot be the only mechanism to maintain a defined narrow RhoA zone. During the last years of research, astral microtubules gained enormous attention and how they restrict RhoA activity to a precise location. It has been shown that elimination of astral microtubules by addition of low doses of the microtubule depolymerizing agent nocodazole, led to a broader equatorial RhoA zone (Bement et al., 2005; van Oostende Triplet et al., 2014; von Dassow et al., 2009; Zanin et al., 2013). Conversely, increasing the number of astral microtubules by depleting the kinesis mitotic centromere-associated kinesin (MCAK), narrowed the equatorial RhoA zone (van Oostende Triplet et al., 2014; Zanin et al., 2013). Although these findings emphasize a major role of astral microtubules in restricting RhoA to a precise location, it must not be forgotten that even in the absence of astral microtubules a RhoA zone still formed, which implies that this is not an exclusive mechanism in restricting RhoA zone dimensions. Since a broadened RhoA zone can completely abolish furrow ingression and induce cytokinesis failure (Bement et al., 2005) it is of major importance to understand the molecular principles of how a narrow zone of active RhoA is formed and maintained at the cell equator during cell division.

1.8 The GEF Ect2

The formation and ingression of the contractile ring depends on the activation of the GTPase RhoA, which in turn is dependent on Ect2. As mentioned before, Ect2 is a guanine nucleotide exchange factor and belongs to the Dbl family, which are GEFs that specifically activate Rho GTPases (Zheng, 2001). Ect2 is highly conserved and has orthologues in many species such as *Homo sapiens* (Ect2), *D. melanogaster* (Pebble) and *C. elegans* (ECT-2). Ect2 was originally described as a proto-oncogene in a screen for mitogenic transducers (Miki et al., 1991). However, later on its high homology to Rho GTPases regulators was reported and it was shown that Ect2 is a GEF for RhoA, Rac1 and Cdc42 (Miki et al., 1991; Tatsumoto et al., 1999). Ect2 is essential for cleavage furrow formation during cytokinesis in human cells, *D. melanogaster* and *C. elegans* and loss of its function leads to cell division failure (Kim et al., 2005; Tatsumoto et al., 1999; Yüce et al., 2005). Despite its role in cleavage furrow formation during cytokinesis, Ect2 is also involved in many other processes as DNA damage response (He et al., 2016) and cell rounding during metaphase (Matthews et al., 2012).

Ect2 consists of an N-terminal and a C-terminal part, which are connected by a linker called S-loop (Figure 5A). At its C-term Ect2 has the GEF characteristic DH- type GEF domain, which harbours the catalytic activity to exchange GDP to GTP (Tatsumoto et al., 1999). Additionally, at its C-term Ect2 has a pleckstrin homology (PH) domain. PH domains can mediate protein-protein interactions and recruit proteins to the plasma membrane via phosphoinositides interaction (Lemmon, 2007, 2008; Lenoir et al., 2015). However, for Ect2 it was shown that the PH domain together with a poly-basic sequence (PBS) domain is required for plasma membrane targeting (Su et al., 2011). However, for *C. elegans* ECT-2 a PBS has not been identified yet, but the C-terminus is also required for localizing Ect2 to the membrane (Chan & Nance, 2013; Su et al., 2011). A recent study revealed a potential further role of the PH domain in addition to membrane targeting: it was shown via crystal structure analysis of Ect2 that the PH domain directly interacts with the catalytic GEF domain, and that this interaction is required to restrict Ect2 GEF activity (Chen et al., 2020). This strongly indicates a role of the PH domain in negatively regulating Ect2 activity. However, the molecular

mechanism how this interaction hampers Ect2 GEF activity remains unclear. At its N-terminus Ect2 harbours three BRCA1 C-terminal (BRCT) domains: BRCT0, BRCT1, and BRCT2 (Zou et al., 2014). BRCT domains are phosphopeptide binding motifs, which can interact with binding partners upon phosphorylation (Gerloff et al., 2012; Leung & Glover, 2011). Most BRCT domains occur in tandem repeats of two, whereby it was assumed for a long time that this is also the case for Ect2 only featuring BRCT1 and BRCT2 (Kim et al., 2005; Tatsumoto et al., 1999). Zou et al. (2014) solved the crystal structure of Ect2 and demonstrated the existence of a third BRCT domain (BRCT0), which is located at the very N-terminal part of Ect2 and is the least conserved one through the animal kingdom. This unusual triple BRCT domain organization is only found in the DNA topoisomerase 2-binding protein 1 (TopBP1), which acts among other things as a scaffold in DNA repair and replication (Bagge et al., 2021; Zou et al., 2014). Even though the triple BRCT domains array of Ect2 and TopBP1 share high similarity, structural analyses revealed differences in orientation and spatial conformation (Zou et al., 2014). Therefore, the mode of function could be very different between these BRCT arrays.

In *D. melanogaster* and *C. elegans*, the Ect2 orthologues, Pebble and ECT-2, are localizing exclusively to the plasma membrane (Jenkins et al., 2006; Motegi et al., 2006). This is different to human cells, where Ect2 is located at the spindle midzone and the equatorial plasma membrane during anaphase (Tatsumoto et al., 1999) (Figure 5B). It is assumed that the spindle midzone localization of Ect2 in human cells is an important spatial cue for the formation of the active RhoA zone at the cell equator (Kotýnková et al., 2016; Su et al., 2011). This indicates that Ect2 regulation by the spindle differs between humans and other species.
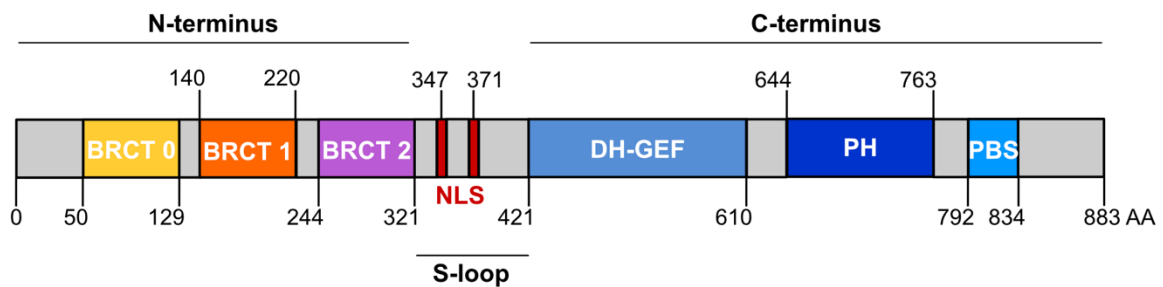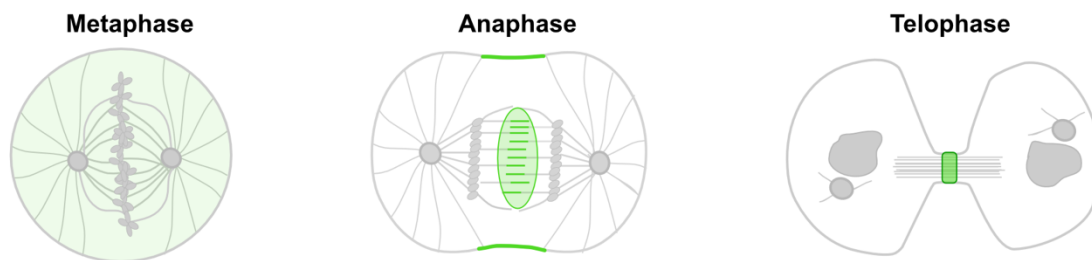
Figure 5: Structure and localization of the GEF Ect2 in human cells.
A) Ect2 harbours three N-terminal BRCT domains - BRCT0, BRCT1 and BRCT2. At its C-terminus, Ect2 harbours a DH-GEF domain containing the catalytic GEF activity, and a PH and PBS domain for membrane binding. Furthermore, Ect2 contains two NLS sequences. The N- and C-term of Ect2 are separated by the so-called S-loop. B) Ect2 is cytoplasmic during metaphase. During anaphase, human Ect2 is localizing to the spindle midzone and the equatorial plasma membrane. During telophase, Ect2 is localizing to the midbody and during interphase Ect2 is present in the nucleus.

1.8.1 Regulation of Ect2 GEF activity

Ect2 is a major player for successful cell division and therefore its activity must be precisely regulated during the cell cycle. Several studies have analyzed the behaviour of Ect2 and found that its expression is tightly coordinated during cell cycle progression (Su et al., 2011; Tatsumoto et al., 1999; Yüce et al., 2005; Zhao et al., 2006). It was shown that Ect2 levels fluctuate during the cell cycle: first, Ect2 expression gets induced in S-phase, which depends on late signals associated with S-phase entry; second, Ect2 expression reaches its maximum during mitosis, which displays its major role for RhoA activation; third, Ect2 levels drop at mitotic exit due to its degradation by the APC/C since its activity is no longer required (Liot et al., 2011; Seguin et al., 2009).

Therefore, Ect2 levels and activity are precisely regulated in time and space throughout the cell cycle.

1.8.2 Ect2 autoinhibition

Via *in vitro* binding studies and crystal structure analysis it has been shown that the BRCT domains of Ect2 bind the catalytically active C-terminal part, which inhibits its GEF activity (Chen et al., 2020; Kim et al., 2005; Saito et al., 2004). This intramolecular negative regulation of the DH-GEF domain by the N-terminus is a common regulatory mode among GEF proteins (Rossman et al., 2005). N-terminal truncation of many Rho GEFs resulted in their constitutive activation, which has also been shown for Ect2 by artificial targeting of an N-terminal truncation to the membrane, which induced increased contractility in human cells (Kotýnková et al., 2016). Furthermore, it has been shown that deletion of all BRCT domains of Ect2 led to increased GEF activity *in vitro* (Chen et al., 2020). However, not only deletion of all BRCT domains simultaneously is needed to perturb regulation of Ect2 activity. It has been shown that exchanging a highly conserved amino acid in the BRCT2 domain is sufficient to disrupt its binding to the DH-GEF domain, what highly increased its GEF activity *in vitro* (Kim et al., 2005; Saito et al., 2004; Yüce et al., 2005). This rises the question if and how each BRCT domain might contribute separately to Ect2 autoinhibition, however, this has not been addressed so far.

During the course of my study, a study shed light on a possible role of the PH domain in Ect2 autoinhibition. Using crystal structure analysis, Chen et al. (2020) have shown that the PH domain located in the C-terminus of Ect2 physically blocks the RhoA-binding site in the DH-GEF domain, which contributes to Ect2 autoinhibition. The researchers proved this observation by mutating specific sites in the PH domain required for blocking of the RhoA-binding site and found increased Ect2 GEF activity *in vitro*. This strongly hints towards a role of the PH domain in negatively regulating Ect2 activity additionally to its role in Ect2 membrane targeting.

1.8.3 Release of Ect2 autoinhibition

As mentioned before, centralspindlin recruits Ect2 to the spindle mizdone via binding of RacGAP1 to Ect2 BRCT domains (Nishimura & Yonemura, 2006; Yüce et al., 2005; Zhao & Fang, 2005). Several studies have shown that the interaction of RacGAP1 is essential for cleavage furrow formation and cytokinesis (Burkard et al., 2009; Petronczki et al., 2007; Wolfe et al., 2009; Yüce et al., 2005). Due to these findings, the current canonical model of Ect2 activation predicts that midzone-based RacGAP1 gets phosphorylated by Polo like kinase 1 (Plk1), which triggers the binding of RacGAP1 to Ect2 BRCT domains. This interaction interrupts the binding of the BRCT domains to the GEF domain, which releases autoinhibition of Ect2 and thereby activates its GEF activity. Activated Ect2 gets recruited to the adjacent equatorial plasma membrane where it in turn activates the RhoA signaling pathway. However, how Ect2 is translocated from the spindle midzone to the plasma membrane is not completely understood.

This canonical model of Ect2 activation was questioned by a study of Kotýnková et al. (2016) in which the interaction of RacGAP1 and Ect2 was abrogated by mutating two residues in the BRCT1 domain, which have been shown to be essential for RacGAP1 binding *in vitro*, what led to strong reduction of Ect2 midzone recruitment, but successful cytokinesis was still maintained. However, a study published during this thesis, questioned the findings of Kotýnková et al. and identified another surface patch in the BRCT1 domain, which is required for RacGAP1 binding and proper cytokinesis (Gomez-Cavazos et al., 2020). However, this mode of Ect2 activation is doubted since Ect2 orthologues in *D. melanogaster* (Pebble) and *C. elegans* (ECT-2) do not localize to the spindle midzone (Motegi et al., 2006; Prokopenko et al., 1999). It was recently shown that ECT-2 and the worm orthologue of RacGAP1 (Cyk-4) can interact at the spindle midzone and that the before mentioned identified surface patch in the BRCT1 domain is also conserved in worm ECT-2, what brings back the role of RacGAP1 in Ect2 activation also in *C. elegans* (Gomez-Cavazos et al., 2020). While the BRCT1 is clearly associated with Ect2 activation due to its interaction with RacGAP1, putative roles of the BRCT0 and BRCT2 in releasing Ect2 autoinhibition remain elusive. Do these two BRCT domains also contribute to release of Ect2 GEF activity?

During the course of my study, it was shown that the PH domain of Ect2 binds RhoA-binding sites in the catalytic DH-GEF domain and thereby inhibits GEF activity, a role in release of autoinhibition was also proposed for the PH domain. It is assumed that active GTP-bound RhoA binds the PH domain what initiates its unbinding from the DH-GEF domain and thereby releases Ect2 autoinhibition. This would imply an autocatalytic mechanism of RhoA self-activation in which active RhoA induces activation of more RhoA by releasing autoinhibition of Ect2 and subsequent nucleotide exchange of RhoA by Ect2 (Chen et al., 2020). This indicates a two-step mechanism of Ect2 activation: First, BRCT-mediated autoinhibition gets released at the spindle midzone by binding of phosphorylated RacGAP1 to the BRCT1 domain. Second, PH-mediated inhibition gets released at the plasma membrane due to binding to GTP-bound RhoA, which accelerates further activation of RhoA (Figure 6).
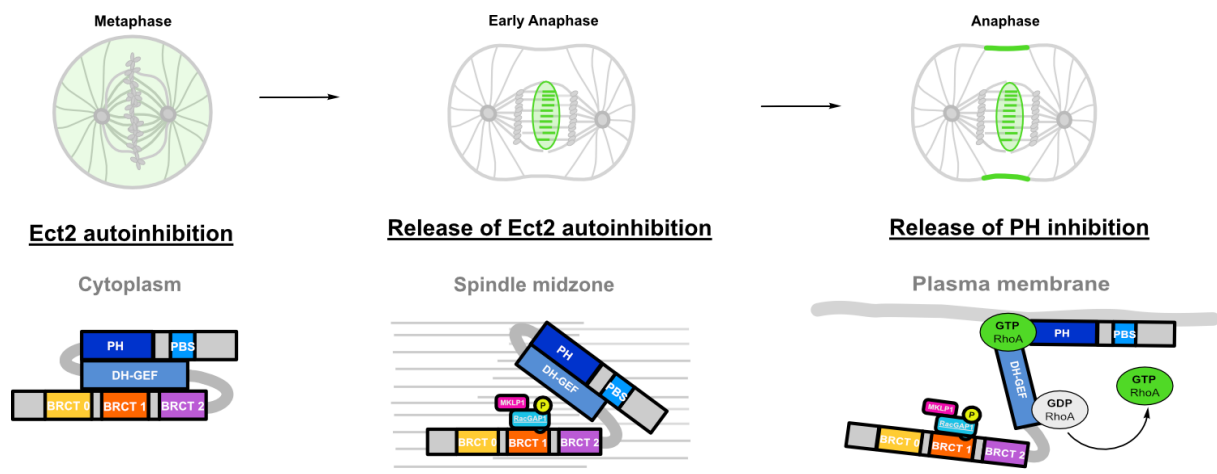
Figure 6: Two step mechanism of Ect2 activation during anaphase.
During metaphase, Ect2 is inactive due to the inhibitory interaction of its BRCT-domains and PH domain with the catalytic DH-GEF domain. Upon anaphase onset, autoinhibition of Ect2 is released at the spindle midzone by phosphorylation of RacGAP1 by Plk1 and its subsequent interaction with BRCT1 domain of Ect2 – the PH-mediated inhibition persists. During anaphase, Ect2 translocates from the spindle midzone to the plasma membrane. Binding of GTP-RhoA to the PH domain triggers its unbinding from the DH-GEF domain, which fully activates Ect2.

1.8.4 Ect2 regulation by mitotic kinases

Activity and functionality of proteins are often regulated by reversible phosphorylation. Since Ect2 is highly phosphorylated during mitosis (Kimura et al., 2002; Niiya et al.,

2005; 2006), it is assumed that phosphorylation also takes a role in regulating Ect2 activity. It has been shown that Plk1 and CDK1 phosphorylate Ect2 *in vitro* and *in vivo*, suggesting that these two kinases play a major role in controlling Ect2 activity throughout the cell cycle (Niiya et al., 2006; Suzuki et al., 2015; Wolfe et al., 2009).

Plk1 is a highly conserved serine/threonine kinase throughout the animal kingdom. It contains a polo-box domain (PBD), which is a phoshopeptide binding domain that recognizes serine/threonine consensus sites and thereby binds the target (Elia, 2003; 2003). Plk1 has several major functions during the cell cycle as metaphase to anaphase transition and centrosome maturation and separation (Lane & Nigg, 1997). As mentioned before, it is assumed that Plk1 phosphorylates RacGAP1 which is inducing the Ect2-RhoA signaling pathway. This function of Plk1 is tightly linked to its localization: During cytokinesis, Plk1 is localizing to the spindle midzone where it facilitates RhoA signaling and to the midobody to regulate abscission process (Combes et al., 2017; Petronczki et al., 2008).

CDK1 is also a highly conserved serine/threonine kinase, however, it is proline-directed. Activation of CDK1 depends on interaction with cyclins, during mitosis this is cyclin B. First, CDK1 gets activated during prophase and forms a complex with cyclin B, which regulates several mitotic processes such as nuclear envelope breakdown, centrosome separation and spindle assembly (Rhind & Russell, 2012; Suzuki et al., 2015).

It was shown that Ect2 localization and activity is dependent on Plk1 and CDK1 phosphorylation. It was demonstrated that phosphorylation of a specific residue in the S-loop of Ect2 (T342) by CDK1 is required for Ect2 interaction with RacGAP1 and therefore for its localization to the midzone (Yüce et al., 2005). On the other hand, preceding phosphorylation of RacGAP1 by PLK1 is required for this interaction as well. However, already earlier during mitosis phosphorylation regulates Ect2 localization. Ect2 comprises two nuclear localization signals (NLS). These NLS are located in the S-loop (Figure 5A) and lead to nuclear Ect2 localization during interphase (Matthews et al., 2012; Tatsumoto et al., 1999). It is proposed that Ect2 is localizing to the nucleus in interphase to prevent cytoplasmic RhoA activation before mitosis. During prophase, CDK1 phosphorylates two sites close to the NLS which promotes Ect2 export from the nucleus. A prematurely phosphorylation of Ect2 by CDK1 prevents nuclear localization of Ect2 causing strong transforming activity of Ect2 (Saito et al., 2004). Furthermore, it was shown that Ect2 membrane localization during anaphase is blocked by CDK1

21

phosphorylation of a specific residue (T815) in the PBS membrane. Expression of a phosphorylation deficient T815 mutant targets Ect2 to the plasma membrane already in metaphase (Su et al., 2011). Besides CDK1 role in regulating Ect2 localization, it also primes Ect2 for subsequent phosphorylation by Plk1. A residue in the S-loop (T412) was found to be phosphorylated by CDK1, which enables interaction of Ect2 and Plk1. Prevention of this phosphorylation (T412A) strongly reduced Ect2 association with Plk1 and overexpression of phosphomimetic T412D led to membrane blebbing suggesting increased activity (Niiya et al., 2006). However, it has not been investigated yet how phosphorylation of Ect2 by Plk1 contributes to RhoA zone formation and furrow ingression.

Therefore, it has been proposed that both kinases play a major role for correct temporal and spatial activation of Ect2, whereby CDK1 regulates localization and primes Ect2 for subsequent phosphorylation by Plk1 to regulate its function.

1.9 The GAP MP-GAP

Active RhoA specifically localizes in a narrow zone at the cell equator to assemble the contractile ring and induce contractility. The GEF Ect2 leads to activation and formation of this narrow RhoA zone, however, how is this zone maintained? It is assumed that a balance between activation and inactivation of RhoA is required to maintain this precise zone and avoid diffusion of active RhoA through the membrane to outer regions of the cell (Bement et al., 2006). This idea is postulated in the RhoA flux model which proposes that specification of narrow equatorial zone of active RhoA involves constitutive global inactivation by GAP activity (Bement, 2006; Miller & Bement, 2009). Since RhoA itself has a very low rate of intrinsic GAP activity, the existence of a RhoA GAP was assumed but remained elusive for years (Jaffe & Hall, 2005). In *Xenopus*, the GAP domain of CYK-4 (RacGAP1 in humans) was proposed to inactivate RhoA since expression of a GAP-deficient CYK-4 broadened RhoA zone dimensions. However, several studies in *C. elegans* contradicted this idea by showing that the GAP domain of CYK-4 rather promotes RhoA activation and inhibits Rac, one of the primary *in vitro* targets of CYK-4, instead of suppressing RhoA activation (Bastos et al., 2012; Canman et al., 2008; Jantsch-Plunger et al., 2000; Miller &

Bement, 2009). However, in 2013, researchers finally identified the primary GAP counteracting RhoA activation in human cells: MP-GAP (ArhGap11A) (Zanin et al., 2013). MP-GAP belongs to an ancient metazoan RhoA GAP family and depletion of MP-GAP by RNAi in human cells leads to excessive ectopic membrane protrusions, a hallmark of unconstrained RhoA activity. Similar observations were found for the distantly related orthologs of MP-GAP in *C. elegans,* RGA-3 and RGA-4 (RGA3/4). However, it was also shown that depletion of MP-GAP did not broaden the narrow equatorial zone of RhoA in human cells (Zanin et al., 2013). This contradicts the before mentioned RhoA flux model where reducing GAP-mediated inactivation of RhoA predicts broadening of RhoA zone dimensions due to enhanced RhoA activity. However, this model includes another mechanism: suppression of cortical contractility by microtubule asters (D'Avino et al., 2005; Green et al., 2012). It has been shown in different organisms that elimination of astral microtubules increased the equatorial zone width of RhoA (Bement et al.,2005; Murthy and Wadsworth, 2008). Interestingly, simultaneous downregulation of MP-GAP in human cells even enhanced this effect (Zanin et al., 2013). This indicates that MP-GAP limits RhoA activity to keep cortical contractility low and in the absence of astral microtubules also restricts RhoA zone dimension. This strengthens the idea of the RhoA flux model which predicts that these two mechanisms, GAP-mediated inactivation of RhoA and contractility suppression by asters, are coupled mechanisms (Figure 7). However, what are the molecular mechanisms of these two signals? This question has not been answered so far.
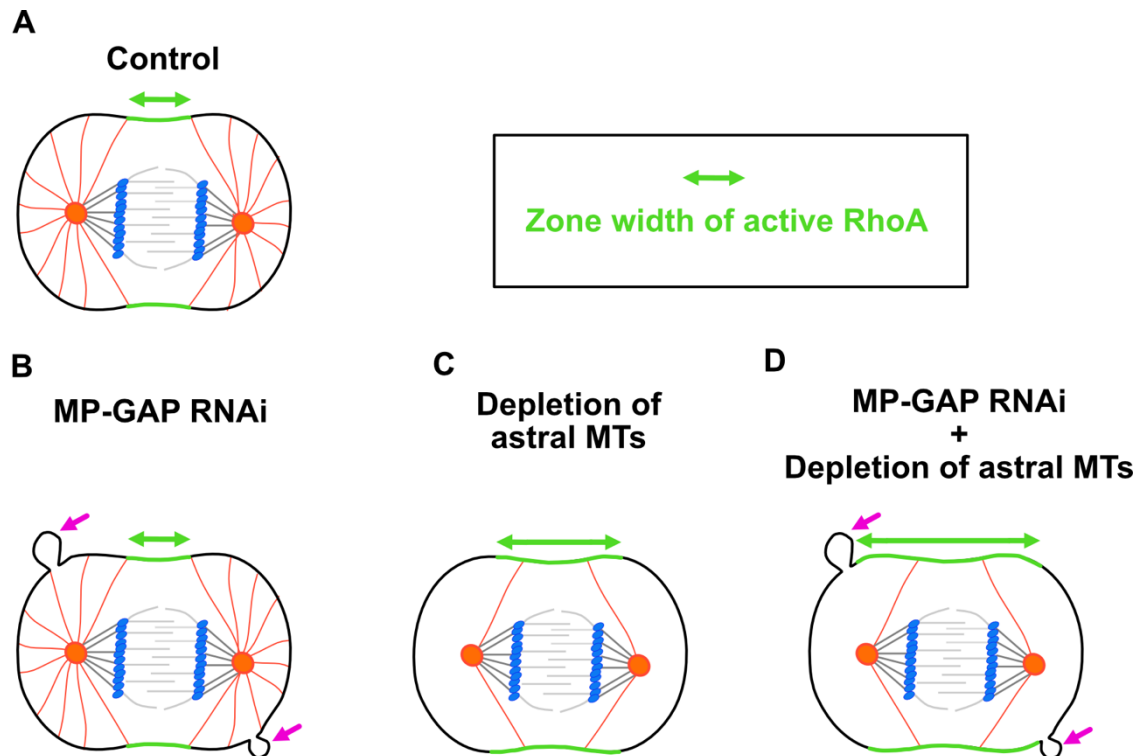
Figure 7: Cycle of the GTPase MP-GAP is crucial for RhoA patterning during cytokinesis.
A) RhoA localizes to a narrow equatorial zone during anaphase in control cells. B) RhoA activation is counteracted by the GTPase MP-GAP. Depletion of MP-GAP via RNAi leads to formation of membrane protrusions (magenta arrows), a hallmark for hyperactive RhoA. C) Depolymerization of astral microtubules leads an increase of RhoA zone width. D) Simultaneous depletion of the GTPase MP-GAP and depolymerization of astral microtubules leads to strong broadening of the equatorial RhoA zone and membrane protrusion formation (magenta arrows). (Figure based on Zanin et al., 2013)

1.10 The cell cycle as a therapeutic target

One hallmark of cancer is high and uncontrolled cell proliferation (Hanahan & Weinberg, 2011). The cell cycle gained increasing interest as an anti-cancer target since the high proliferative index of cancer cells compared to healthy tissue is due to loss of cell cycle control. For example, CDK4/6 inhibitors are clinically approved anti-cancer drugs, especially for certain types of breast cancer. Inhibiting CDK4/6 stops the cell cycle in G1 phase and thereby successfully prevents tumour cell proliferation (Finn et al., 2016; Hortobagyi et al., 2016; Sledge et al., 2017).

As mentioned in section 1.1, several checkpoints are anchored in the cell cycle which

keep track of the integrity of the different cell cycle steps. The first one during G1 phase depends on cyclin-dependent-kinase (CDK) activity, which promotes DNA replication and initiates the transition from G1 to S-phase. Targeting this checkpoint has been considered for cancer therapy because loss of this checkpoint is a common feature of cancer cells: many cancer types carry a mutation of tumor suppressor protein p53, which leads to increased CDK expression and therefore unimpeded progression of cancer cells through G1 phase. Therefore, targeting CDKs was seen as a critical strategy for cancer treatment and inhibition of expression of CDKs effectively suppressed oncogenic cell function in several cancer types (Wang et al., 2023). Even though this sounds like a promising and effective strategy for cancer treatment, it harbours several side effects and disadvantages: The untamed activity of CDK inhibitors does not only affect cancerous but also healthy tissue leading to high levels of cytotoxicity. This leads in most of the cases to neutropenia and leukopenia, a clinical picture describing low number of white blood cells resulting in a weakened immune system of the patient and high vulnerability to infections (Hortobagyi et al., 2016; Spring et al., 2017).

Another regulatory part of the cell cycle that gained increased interest during the last years of research regarding putative cancer therapies is the ubiquitin proteasome pathway (UPP). The UPP is a highly conserved pathway, which ubiquitinates dysfunctional or misfolded proteins and destines them for degradation by the 26S proteasome to regulate cellular processes (Fhu & Ali, 2021; Li et al., 2022). It has been shown that cancerous tissue is more sensitive to dysregulation of the proteasome due to several reasons. Cancer cells show higher levels of proteasome activity to facilitate their rapid proliferation. Subsequently, these cells often have a perturbed balance between proliferation and programmed cell-death, and defects in apoptotic pathways allowing them to survive but make them also more reliant on proteasomal degradation (Adams, 2003; Arlt et al., 2009; Delic et al., 1998; LeBlanc et al., 2002). This increased sensitivity of cancer cells to proteasomal activity in comparison to healthy cells raised the idea to use proteasome inhibition as a therapeutic treatment against cancer.

1.10.1 The 26S proteasome

The 26S proteasome is a multi-catalytic ATP-dependent protease complex, which is found in both the cytoplasm and the nucleus (Arrigo et al., 1988; Peters, 1994). It consists of two distinct sub-complexes, the 20S core particle and the 19S regulatory particle (Figure 8A). The 20S core forms a barrel-shaped complex consisting of four stacked protein rings (Groll et al., 1997). The two outer rings contain seven alpha subunits each, which serve as gateways for protein entry. The two inner rings contain seven beta subunits each, which contain the proteolytic active sites for protein degradation activity (Löwe et al., 1995). Thereby, the 20S subunit forms kind of a central chamber in which targeted proteins are degraded. In contrast, the 19S particle is responsible for recognition and translocation of the proteins into this narrow chamber. Therefore, it consists of a base and a lid subcomplex (Glickman et al., 1998). The base is composed of six ATPase proteins (Rpt1-6) and four non-ATPase subunits (Rpn1,2,10, and 13). The lid contains non-ATPase proteins (Rpn3, 5-9, 11,12 and 15). The base acts in recognizing and unfolding of ubiquitinated targets, while the lid mainly regulates the entry into the 20S chamber (Bedford et al., 2010; Glickman et al., 1998; Soave et al., 2017; Tomko et al., 2013).

The UPP consists of five major steps (Figure 8B): The first step is ubiquitination of target proteins, where the small protein ubiquitin is attached to the protein. This is carried out by several enzymes: The ubiquitin-activating enzyme E1 activates ubiquitin, which is then transferred to the ubiquitin-conjugating enzyme E2, which covalently attaches the ubiquitin to the target protein. The transfer is facilitated by the ubiquitin ligase enzyme E3. Several cycles of ubiquitin activation lead to polyubiquitinated proteins, that are now in the second step recoginized by the 19S particle (Chaugule & Walden, 2016; Hänzelmann et al., 2012; Hershko et al., 1998). The 19S recognises the ubiquitin chains on the protein, assists in its unfolding and translocates it into the 20S chamber. In the third step, the protein gets degraded by the proteolytic activity of the beta subunits in the two inner rings of the 20S core particle. After degradation, in the fourth step, recycling of ubiquitin molecules takes place. Therefore, the ubiquitin is released from the degraded protein by deubiquitinating enzymes and can be reused in subsequent ubiquitination of other proteins. In the last fifth step, the remnants of degraded proteins are released from the

26S proteasome complex and are further degraded into amino acids by cytosolic proteases (DeMartino & Gillette, 2007; Kisselev et al., 1999; Soave et al., 2017).

A
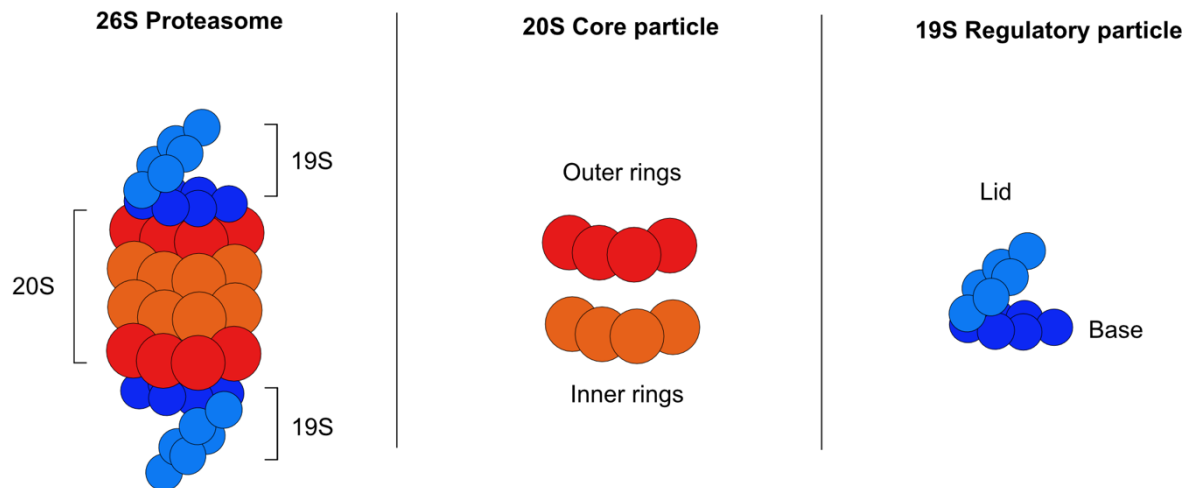
B
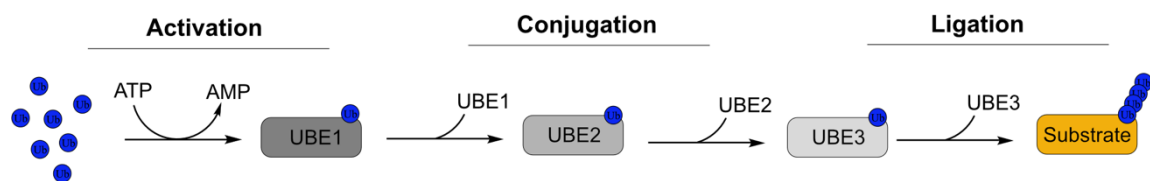
Figure 8: The ubiquitin proteasome pathway.
A) Illustrative representation of the 26S proteasome in human cells. The proteasome comprises a 20S core particle with two flanking 19S regulatory particles. The core particle consists of four rings forming a tube-like structure harbouring the catalytical sites. The access for target proteins is controlled by the 19S regulatory particle consisting of a base and lid, which plays a crucial role in substrate recognition, unfolding and translocation into the core tube. B) The ubiquitin proteasome pathway consists of enzymatic reactions for degradation of target proteins. First step is the ATP-dependent activation of ubiquitin (blue dot) by ubiquitin-activating enzyme 1 (UBE1). Second step is conjugation of activated ubiquitin via the ubiquitin-conjugating enzyme 2 (UBE2). Last step is ligation of activated ubiquitin via the ubiquitin ligase 3 (UBE3), which transfers it to the target protein. These ubiquitination steps are repeated several times, leading to targeting of multiple ubiquitin molecules to the target protein, resulting in a polyubiquitin chain, which is later on recognized by the 19S regulatory particle of the 26S proteasome. (Figure adapted from Soave et al., 2017)

The 26S proteasome pathways plays several critical roles in cell cycle regulation and progression. On the one hand, it degrades cell cycle regulators as cyclins and cyclin-dependent kinase inhibitors once their function is no longer required. Furthermore, the proteasome is involved in cell cycle checkpoints since it's degrading proteins, such as p53, which are involved in checkpoint signaling (do Patrocinio et al., 2022). After entering mitosis, the proteasome also plays a role in further progression of cell division. The APC/C targets proteins such as securin and cyclin B for proteasomal degradation to ensure progression during mitosis. Furthermore, transcription factors, e.g. members of the E2F family, which regulate gene expression for DNA replication, are targets of proteasomal degradation (Hateboer et al., 1996; Seeger et al., 2003). In summary, the proteasome is coordinating several essential processes for progression of the cell cycle by controlling protein levels. The 26S proteasome particularly takes a key role in the transition from metaphase to anaphase. During metaphase, chromosomes align at the metaphase plate. The SAC monitors if all kinetochores are correctly attached to the microtubules of the opposite spindle and prevents progression to anaphase before completion by inhibiting the APC/C (Pines, 2011). If all kinetochores are properly attached, the SAC becomes inactivated, which allows the APC/C to ubiquitinate the proteins securin and cyclin B. Ubiquitinated securin and cyclin B are degraded by the 26S proteasome, which enables anaphase onset. Degradation of securin leads to activation of separase, which cleaves the cohesion subunit Scc1 and allows chromatid separation. Degradation of cyclin B leads to inactivation of CDK1, which promotes mitotic exit. Therefore, degradation of securin and cyclin B by the 26S proteasome drive the cells from metaphase to anaphase (Musacchio, 2015; Pines, 2011; Sullivan & Morgan, 2007). The other way around, inhibition of the 26S proteasome leads to mitotic arrest since sister chromatids do not separate and CDK1 activity remains high (Clute & Pines, 1999; Genschik et al., 1998; Glotzer et al., 1991; Mailhes et al., 2002; Zeng et al., 2010).

The first anti-cancer drug based on proteasome inhibition approved for clinical use is Bortezomib (originally termed MG-341 in year 1995) (Kane et al., 2003; 2007). It is primarily used in the treatment of multiple myeloma, cancer of plasma cells and mantle cell lymphoma, a rare form of non-Hodgkin lymphoma. It works by binding reversibly to the beta subunits of the 20S core, thereby inhibiting its proteolytic activity. Therefore, cancer cells arrest in G2/M-phase and apoptosis is induced (Chen et al., 2011). Even though Bortezomib showed promising results as an anticancer agent, it

also carries severe disadvantages. Similar as CDK inhibition, it also leads to neutropenia and leukopenia due to off-target effects. Even if proteasome inhibition is more specific to cancerous cells, it shows cytotoxic effects on healthy tissues, which highly limits dose and duration of the drug treatment (Mikhael et al., 2009).

1.10.2 Pim kinases as potential therapeutic target

Another therapeutic idea for cancer treatment is the inhibition of Pim kinases. Pim kinases are a family of serine/threonine kinases involved in cell proliferation, survival and apoptosis. The family consists of Pim1, Pim2, and Pim3 which share high structural similarity, however, cancer research mostly focused on Pim1 due to its role in tumorgenesis (Saurabh et al., 2014). Pim1 is mainly localized in the cytoplasm of human cells and gets activated by various pathways including the IL7R (JKAT/STAT) signaling pathway (De Smedt et al., 2020). Upon activation it phosphorylates a wide range of substrates including transcriptional factors and other kinases. Additionally, it also phosphorylates the apoptotic regulator Bad, a pro-apoptotic protein, which subsequently binds and thereby inactivates anti-apoptotic proteins such as Bcl-2, which normally promote apoptosis (Kumar et al., 2011). Therefore, Pim1 phosphorylation of Bad prevents pro-apoptotic activity and promotes cell survival. Furthermore, Pim1 also regulates activity of the NF-kB pathway. The NF-kB pathway regulates the expression of anti-apoptotic genes, which gets enhanced by Pim1, leading to increased anti-apoptotic activity and suppression of apoptosis (Nihira et al., 2010).

Pim1 is overexpressed in various types of cancer tissues and supports their survival by increasing their resistance to apoptosis. High levels of Pim1 have been associated with rapid tumor formation, growth, metastasis and an extraordinary high resistance to chemotherapy due to their increased anti-apoptotic activity (Mou et al., 2016; Peltola et al., 2009; Wang et al., 2017; Zhu et al., 2014). All these attributes have emerged a role of Pim1 as a potential therapeutic target for cancer treatment. And indeed, usage of a small molecule inhibitor for Pim1 (AZD1208) has already shown promising results in preclinical studies, however, further research on cytotoxicity and off-target effects are needed (Kirschner et al., 2015).

1.10.3 Photopharmacology – an innovative approach

What almost all anti-cancer drugs have in common is that although they are effective, their mostly toxic side effects pose a high risk for the patient. These side effects are mostly due to their untamed reactivity, both spatially and temporally, which still limits their usage in therapy (Figure 9A). At this point the research field of photopharmacology steps in. This field involves the development of photosensitive molecules that can be activated or deactivated by light – so called photocages (Figure 9B) or photoswitches (Figure 9C). The key principle behind this innovative approach is to gain control over biological molecules to selectively activate or inhibit biological processes with high spatial and temporal resolution (Fuchter, 2020; Hull et al., 2018). Photocaging describes a strategy where the active compound of a drug is masked by protecting group ("cage"), which gets cleaved upon light irradiation and releases compound activity. Photocaging is a one-way-strategy meaning is the cage cleaved once, the molecule remains active. In contrast, photoswitching is a reversible strategy. Photoswitches are molecules that can change its shape and function upon light irradiation. Thereby, compound activity can be masked by a photoswitch and released by irradiation with light. Functionality wise, the main difference to photocages is that this release of compound activity is reversible. Upon irradiation with light of a different wavelength, the photoswitch can change back to its previous shape and again mask compound activity. This reversible on/off switching offers great advantages in biomedical applications where a specific local drug activity is required since it can be turned off at undesired locations (Hull et al., 2018; Thapalya et al., 2021).
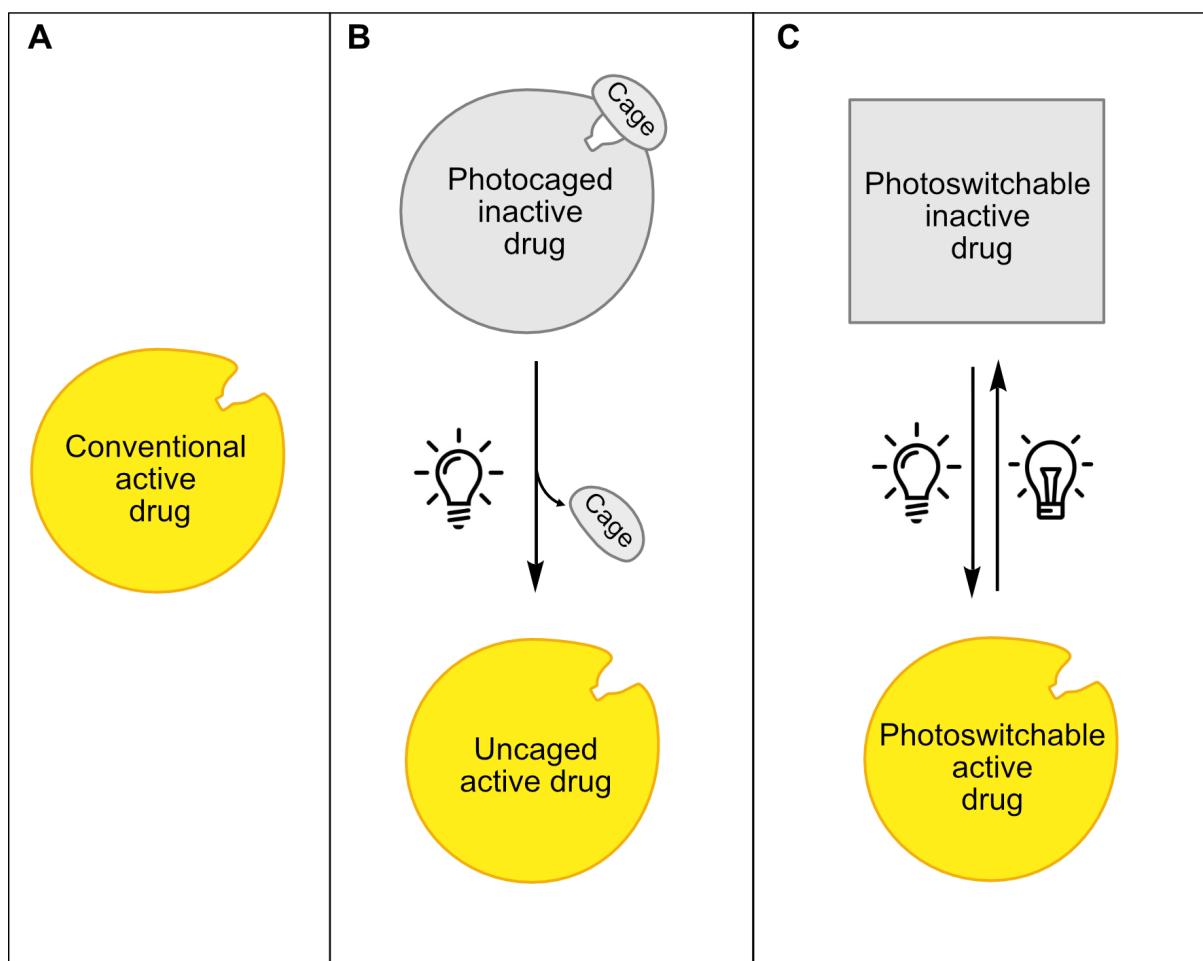
Figure 9: Illustration of drug activity controlled by photocages or photoswichtes.
A) Conventional drug: A conventional drug is constitutively active. B) Photocaged drug: A drug is rendered into an inactive drug by covalent attachment of a protecting group ("cage"), which can be removed upon light exposure, thereby releasing the active compound. C) Photoswitchable drug: A drug whose activity can be reversibly controlled by light exposure of different wavelengths.

Since this provides big advantages over drugs that lack such specificity, photopharmacology holds significant promise for biomedical research including the improvement of already existing drugs as well as developing new therapeutic strategies. It has already been shown that the idea of controlling cellular processes by light is not chasing rainbows. Borowiak et al., 2015 introduced photostatins, which are small light-responsive molecules that interfere with microtubule dynamics. They achieved the control over mitosis in living organisms within subseconds and single-cell spatial precision. Furthermore, the enzyme Caspase-3, which induces apoptosis, was converted into a photoresponsive version allowing intracellular activation and

thereby spatiotemporal induction of apoptosis in cells (Hentzen et al., 2020). However, what both described studies have in common is that UV-light (100-400nm) is used for photoconversion. Since UV-light is harmful to tissue, it is highly desirable to use non-damaging visible light in biological applications. Therefore, fundamental research in the development of such photocages and photoswitches is ongoing with high potential in disease treatment.

1.11 Aims of my thesis

Cell division is the source of all life on earth and even despite decades of research we still lack important insights to fully understand this process. In particular cytokinesis, probably one of the most important steps where the genetic material as well as other contents gets equivalently divided between cells, is still unclear in many respects. The core of cytokinesis relies on the precise activation of the small GTPase RhoA within a narrow equatorial zone at the membrane during anaphase, which subsequently triggers the formation of a contractile ring to physically divide the cell into two. Given its critical role, this whole process demands precise regulation, which is mainly on the GEF Ect2. Unfortunately, even though Ect2 has this immense role for life, its functioning und regulation is just barely understood.

Therefore, the first aim of my thesis was to fill this lack of knowledge by investigating the regulation of Ect2 during cytokinesis in human cells.

It is widely assumed that the BRCT domains of Ect2 act together in regulating its GEF activity on the one hand by keeping it in an autoinhibited state due to their binding to the catalytic GEF domain but on the other hand also in releasing its GEF activity by binding to RacGAP1. However, this whole regulation model is based on the assumption that the BRCT domains act together as a canonical tandem BRCT repeat. Since Ect2 contains three domains, which is already unusual for a canonical BRCT tandem repeat, the idea arose that each BRCT domain might act in a different way and function. For now, only the role of the BRCT1 domain regarding its GEF activity enhancing interaction with RacGAP1 has been identified. What about BRCT0 and BRCT2? What are the roles of each BRCT domain of Ect2 and how do they singly contribute to cytokinesis in human cells?

To answer these questions, the approach was to use a previously established genetic replacement system for Ect2 in HeLa cells, which enables us to either delete entire domains or to introduce specific mutations. We analysed the dynamics of cell division via live-cell imaging and the spatial patterning of RhoA via immunofluorescence staining. Furthermore, biochemical studies were performed to identify self-interaction of Ect2 as well as interaction with binding and phosphorylation partners. Results of this aim can be found in section 2 - Chapter I.

Despite Ect2 activating RhoA in a narrow equatorial zone, the question remains how

activated RhoA is kept at this location and restricted from diffusing to the more polar regions of the cell. A previous study of our lab has shown that there is an Aurora A kinase dependent clearing mechanism of contractile ring components from the poles in *C. elegans.*

Therefore, the second aim of my thesis was to investigate a putative role of Aurora A in restricting cortical patterning of contractile ring components in human cells. Does such a role for Aurora A kinase exist in human cells? If yes, what are the molecular mechanisms behind this? Due to its role in mitotic progression, depletion of Aurora A kinase via RNAi leads to mitotic arrest in human cells. Therefore, the strategy was to inhibit Aurora A kinase specifically at beginning of cytokinesis using a small molecule inhibitor. The dynamics of cell division were analysed via live-cell imaging and the cortical patterning of RhoA via immunofluorescence staining. Biochemical assays as *in vitro* kinase assays were used to identify putative phosphorylation targets of Aurora A kinase to further elucidate the molecular mechanisms. Results of this aim can be found in section 3 - Chapter II.

The major goal of our research is to understand the molecular mechanisms in our body and thereby ensure a long and healthy life. To achieve this, the development of therapies against diseases is a major milestone. One of the most harmful diseases is cancer, which curation despite decades of research is still highly challenging. Although there are effective treatments for cancer, the biggest problem lies in their untamed reactivity and the subsequent side effects. This is where the field of photopharmacology has made a huge leap forward by achieving the ability to manipulate molecules with spatiotemporal precision using light as an external stimulus while minimizing side effects. However, since photopharmacology represents a new and innovative approach, its research and application are still very limited.

Therefore, the third aim of my thesis was to convert the commercially available proteasome inhibitor MG-132 into a non-effective agent, which triggers full functionality upon light irradiation in human HeLa cells. The success of this strategy was analysed by live-cell imaging and immunofluorescence stainings. This project was fulfilled in collaboration with the research group of Prof. Dr. Henry Dube und his PhD student Dr. Edgar Uhl (Ludwig-Maximilians University Munich, Germany). Prof. Dr. Henry Dube and Dr. Edgar Uhl designed and synthesized a light-responsive version of MG-132 and our group investigated functionality in a biological context. Results of this aim can be found in section 4 - Chapter III.

The conversion of already existing drugs into a photoactivatable version is a very promising option. Of course, it is just as important to find new targets that are switchable with light in order to implement them in a potential application for medical therapy. Pim kinases gained great potential for use in cancer therapy, as their inhibition induces cell death.

Therefore, the fourth aim of my thesis was to convert PIM-1 kinase inhibitors into light-controlled biomolecular tools, that are active/inactive after irradiation with light. The success of this project was analysed by live-cell imaging and immunofluorescence staining of human HeLa, HCT-116 and RPE-1 cells. This project was fulfilled in collaboration with the research group of Prof. Dr. Henry Dube und his PhD student Dr. Laura Köttner (Friedrich-Alexander-University Erlangen-Nürnberg, Germany). Prof. Dr. Dube and Dr. Köttner designed and synthesized light-controllable PIM-1 kinase inhibitors and our group investigated their functionality in a biological context. Results of this aim can be found in section 5 - Chapter IV.

2 Chapter I - The BRCT domains of Ect2 have distinct functions during cytokinesis

Schneid, S.*, **Wolff, F.***, Buchner, K., Bertram, N., Baygün, S., Barbosa, P., Mangal, S., & Zanin, E. (2021). The BRCT domains of ECT2 have distinct functions during cytokinesis. *Cell Reports*, 34, 108805.

* contributed equally

The BRCT domains of ECT2 have distinct functions during cytokinesis

Graphical Abstract
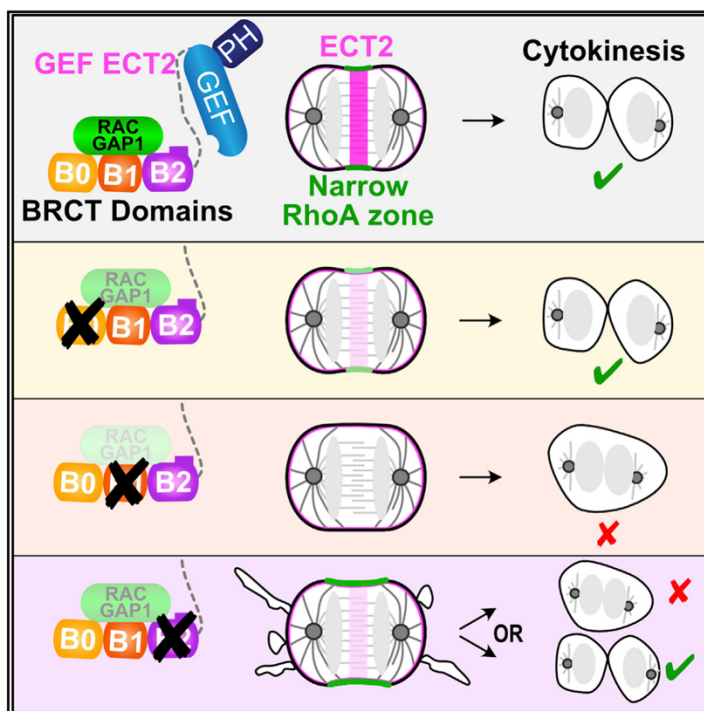
Authors

Sandra Schneid, Friederike Wolff, Kristina Buchner, ..., Pedro Barbosa, Sriyash Mangal, Esther Zanin

Correspondence

zanin@bio.lmu.de

In brief

Schneid et al. show that the three BRCT domains of ECT2 make distinct contributions to RhoA zone formation and cytokinesis. BRCT0 and BRCT1 bind RACGAP1 and promote ECT2 activation. In contrast, BRCT2 inhibits GEF activity and BRCT2 binding to RACGAP1 limits ECT2 activity spatially to the cell equator.

Highlights

- BRCT0 and BRCT1 promote ECT2 activation during cytokinesis

- BRCT2 limits ECT2 GEF activity during metaphase and anaphase

- BRCT2 binding to the GEF domain and RACGAP1 facilitates a narrow RhoA zone formation

- Polo-like kinase 1 (Plk1) phosphorylates BRCT0 and binds each BRCT domain

CellPress

37

Cell Reports

Article

The BRCT domains of ECT2 have distinct functions during cytokinesis

Sandra Schneid,[1,2] Friederike Wolff,[1,2] Kristina Buchner,[1] Nils Bertram,[1] Seren Baygün,[1] Pedro Barbosa,[1] Sriyash Mangal,[1] and Esther Zanin[1,3,*]
[1]Department Biology II, Ludwig-Maximilians University, Planegg-Martinsried, Munich 82152, Germany
[2]These authors contributed equally
[3]Lead contact
*Correspondence: zanin@bio.lmu.de
https://doi.org/10.1016/j.celrep.2021.108805

SUMMARY

During cell division, the guanine nucleotide exchange factor (GEF) ECT2 activates RhoA in a narrow zone at the cell equator in anaphase. ECT2 consists of three BRCT domains (BRCT0, 1, and 2), a catalytic GEF, and a pleckstrin homology (PH) domain. How the conserved BRCT domains spatially and temporally control ECT2 activity remains unclear. We reveal that each BRCT domain makes distinct contributions to the ECT2 function. We find that BRCT0 contributes to, and BRCT1 is essential for, ECT2 activation in anaphase. BRCT2 integrates two functions: GEF inhibition and RACGAP1 binding, which together limit ECT2 activity to a narrow zone at the cell equator. BRCT2-dependent control of active RhoA zone dimension functions in addition to the inhibitory signal of the astral microtubules. Our analysis provides detailed mechanistic insights into how ECT2 activity is regulated and how that regulation ensures, together with other signaling pathways, successful cell division.

INTRODUCTION

During cell division in animal cells, a contractile ring assembles and constricts between the segregating chromosome masses to form the two daughter cells. Contractile ring formation has to be precisely controlled in time and space to ensure that it assembles only after anaphase onset and only at the cell equator (D'Avino et al., 2015; Mishima, 2016). Failure in the contractile ring assembly or constriction results in tetraploid cells, which can cause developmental defects and malignant transformations (Lens and Medema, 2019). Ring assembly is induced by the GTPase RhoA, which is activated by the guanine nucleotide exchange factor (GEF) epithelial cell transforming 2 (ECT2) during anaphase (Basant and Glotzer, 2018). Once assembled, the contractile ring constricts and pulls behind the plasma membrane of the mother cell, and as a last step, the ESCRT complex abscises the daughter cells from each other (Mierzwa and Gerlich, 2014; Pollard and O'Shaughnessy, 2019).

Formation of the contractile ring is temporally and spatially controlled by multiple signals. During metaphase, the contractile ring assembly is blocked by high CDK1 activity (Holder et al., 2019). With the decline in CDK1 activity during anaphase, the cortical contractility increases and is spatially patterned by two signals from the mitotic spindle. A stimulatory signal at the cell equator promotes local RhoA activation, and an inhibitory signal at the cell poles prevents contractility. The stimulatory and inhibitory signals together ensure that RhoA is active in a narrow region at the cell equator. The inhibitory signal depends on the dynamic astral microtubules (von Dassow, 2009). Activation

of Aurora A kinase on astral microtubules promotes clearing of the contractile ring components from the cell poles in *Caenorhabditis elegans* (Mangal et al., 2018). The stimulatory signal originates from the spindle midzone, which consists of antiparallel microtubules forming between the segregating chromosomes. A key component of the stimulatory signal is the GEF ECT2, which activates RhoA at the equatorial membrane.

ECT2 is essential for RhoA activation and furrow formation in animal cells (Dechant and Glotzer, 2003; Prokopenko et al., 1999; Tatsumoto et al., 1999; Yüce et al., 2005). In vertebrate cells, ECT2 is enriched at the spindle midzone and equatorial plasma membrane during anaphase (Chalamalasetty et al., 2006; Su et al., 2011; Zhao and Fang, 2005). ECT2 consists of three N-terminal BRCT (BRCA1 C-terminal) domains (BRCT0, BRCT1, and BRCT2), a central GEF, and two membrane-binding domains: a pleckstrin homology (PH) domain and a poly-basic sequence (PBS). With the PH domain, ECT2 also binds the contractile ring component anillin (Frenette et al., 2012). Overexpression of ECT2 mutant proteins in cells and interaction studies suggest that the BRCT domains bind the GEF domain and thereby inhibit GEF activity (Bement et al., 2015; Chan and Nance, 2013; Chen et al., 2020; Hara et al., 2006; Kim et al., 2005; Saito et al., 2004; Su et al., 2014). ECT2 autoinhibition is released by the binding of the BRCT domains to RACGAP1 (also named Cyk4 or MgcRacGAP) (Burkard et al., 2007; Somers and Saint, 2003; Wolfe et al., 2009; Yüce et al., 2005). RACGAP1 and its binding partner, the kinesin MKLP1, form the centralspindlin complex (Mishima et al., 2002), which targets ECT2 to the spindle midzone and the equatorial membrane (Su et al., 2011;

Yüce et al., 2005; Zhao and Fang, 2005). In addition, ECT2 binds RACGAP1 via the GEF-PH domains, which was speculated to stimulate GEF activity (Zhang and Glotzer, 2015). During anaphase, RACGAP1 is phosphorylated by Polo-like kinase 1 (Plk1) at the spindle midzone, which generates a binding site for the BRCT domains of ECT2 (Burkard et al., 2009; Wolfe et al., 2009; Yüce et al., 2005). Initially, it was suggested that the BRCT1 and BRCT2 domains represent a canonical tandem BRCT repeat, and binding assays showed that RACGAP1 binding to ECT2 depends on T153 and K195 in the BRCT1 domain (Wolfe et al., 2009; Zou et al., 2014). Surprisingly, when T153 and K195 were mutated, RhoA activation was normal and cytokinesis was successful (Kotýnková et al., 2016). A recent study contradicts that report by showing that T153 and K195 are not required for RACGAP1 binding and identifies a different RAC-GAP1 interaction surface on BRCT1 (Gómez-Cavazos et al., 2020). The third BRCT domain, named BRCT0, was identified by bioinformatics, and its presence was confirmed by structural studies (Sheng et al., 2011; Zou et al., 2014). The structural analysis revealed that the linkers between the three BRCT domains are shorter than in canonical tandem BRCT repeats, resulting in a perpendicular orientation of BRCT1 relative to BRCT2, in contrast to the parallel orientation typically found in canonical tandem BRCT repeats (Zou et al., 2014). Therefore, the three BRCT domains of ECT2 display a novel BRCT domain configuration. If BRCT1 is the main RACGAP1 interaction site, the question remains: what are the functions of BRCT0 and BRCT2 in ECT2 activation during cytokinesis? Further, how autoinhibition by the BRCT domains spatially and temporally controls ECT2 activity and contributes to RhoA zone formation and ring ingression has, to our knowledge, not been addressed. Here, we employed a genetic replacement system in HeLa cells to elucidate the individual and combined functions of the BRCT domains in ECT2 activation and autoinhibition during cell division.

RESULTS

The BRCT domains inhibit GEF activity and are required for cytokinesis

To investigate the functions of the BRCT domains of ECT2 during cytokinesis, we determined whether removal of all three BRCT domains increases ECT2 activity during mitosis. Previous GEF assays, ECT2 interaction studies, and structural data suggest that the BRCT domains bind the GEF domain and thereby inhibit GEF activity (Chen et al., 2020; Kim et al., 2005; Saito et al., 2004; Zou et al., 2014). Autoinhibition by the BRCT domains is also supported by artificial membrane targeting of the GEF domain and transient overexpression of a C-terminal fragment (Bement et al., 2015; Chan and Nance, 2013; Kim et al., 2005; Kotýnková et al., 2016; Matthews et al., 2012; Saito et al., 2004; Su et al., 2011, 2014). In addition, overexpression of a C-terminal ECT2 fragment does not support cytokinesis if the endogenous ECT2 is depleted (Matthews et al., 2012). In all these experiments, mutant forms of ECT2 were either overexpressed, which might sequester ECT2 interaction partners, or an artificial membrane tether was used, which could cause synergistic effects with the deletion of the BRCT domains. To analyze the function of the BRCT domains during cytokinesis, we established a genetic replacement system for ECT2. We stably

integrated a NeonGreen-tagged (NG-tagged) ECT2 wild-type (ECT2^{WT}) transgene into HeLa cells. After ECT2 RNAi, endogenous ECT2 was undetectable even after long exposure of the immunoblot (Figures 1A and 1B), and ECT2^{WT} showed similar expression levels to endogenous ECT2 (Figure S1A). To determine whether the BRCT domains inhibit GEF activity, we deleted all three BRCT domains (ECT2$^{\Delta B0-2}$; Figure 1A). We confirmed that ECT2$^{\Delta B0-2}$ was expressed similarly to endogenous ECT2 and ECT2^{WT} (Figures S1A and S1B). ECT2 depletion in the host cell line resulted in high percentages of bi- and multinucleated cells and expression of ECT2^{WT}, but not ECT2$^{\Delta B0-2}$, rescued the phenotype (Figures 1C and 1D). This demonstrates that the three BRCT domains are essential for cytokinesis.

During cytokinesis, small membrane blebs form at the cell poles in anaphase (Hickson et al., 2006; Sedzinski et al., 2011; Tokumitsu and Maramorosch, 1967; Figure 1E). Increased RhoA activity results in the formation of large blebs, which are typically much larger than the normally occurring anaphase blebs (Zanin et al., 2013). Therefore, large bleb formation represents a good readout for increased ECT2 activity. To analyze whether deletion of the BRCT domains results in increased GEF activity, we acquired bright-field transmission videos during mitosis. A high percentage of ECT2$^{\Delta B0-2}$ cells formed large blebs (>6 μm) in comparison to the control and ECT2^{WT} cells (Figures 1E and 1F). We also counted the number of large blebs per cell and observed that the percentage of cells with more than five large blebs was greater during anaphase than it was during metaphase. If large blebs form in ECT2$^{\Delta B0-2}$ cells because of increased RhoA activation, the addition of the RhoA inhibitor C3 exoenzyme should suppress large bleb formation. Indeed, the addition of C3 exoenzyme to ECT2$^{\Delta B0-2}$ cells reduced large bleb formation (Figures 1G and 1H), indicating that the deletion of the three BRCT domains results in increased RhoA activation.

In accordance with prior transient overexpression studies (Bement et al., 2015; Chan and Nance, 2013; Matthews et al., 2012; Saito et al., 2004; Su et al., 2014), we find that expression of ECT2 without the three BRCT domains causes the formation of large blebs during mitosis, indicating that ECT2 activity is increased. Further, our data demonstrate that expression of ECT2 lacking the three BRCT domains at native levels is insufficient to support cytokinesis.

Each BRCT domain contributes to midzone targeting and interacts with RACGAP1

Because we found that the three BRCT domains together are required for cytokinesis and to inhibit GEF activity, we dissected their individual functions during cytokinesis. We generated cell lines with transgenes in which the BRCT0 (ECT2$^{\Delta B0}$), BRCT1 (ECT2$^{\Delta B1}$), or BRCT2 (ECT2$^{\Delta B2}$) domain was deleted (Figure S1C). We also included the T153A, K195M (ECT2^{TK}) (Kotýnková et al., 2016), and W307 (ECT2^{W307A}) mutations. The W307 residue in the BRCT2 domains is in direct contact with the GEF domain, and its mutation to alanine, similar to the removal of all BRCT domains, increased GEF activity in vitro (Chen et al., 2020). Expression levels of all ECT2 mutant proteins were similar to that of endogenous ECT2 and ECT2^{WT} after ECT2 RNAi (Figures S1A–S1H). We performed time-lapse imaging to determine the localization of the ECT2 mutants. As published, ECT2^{WT} is
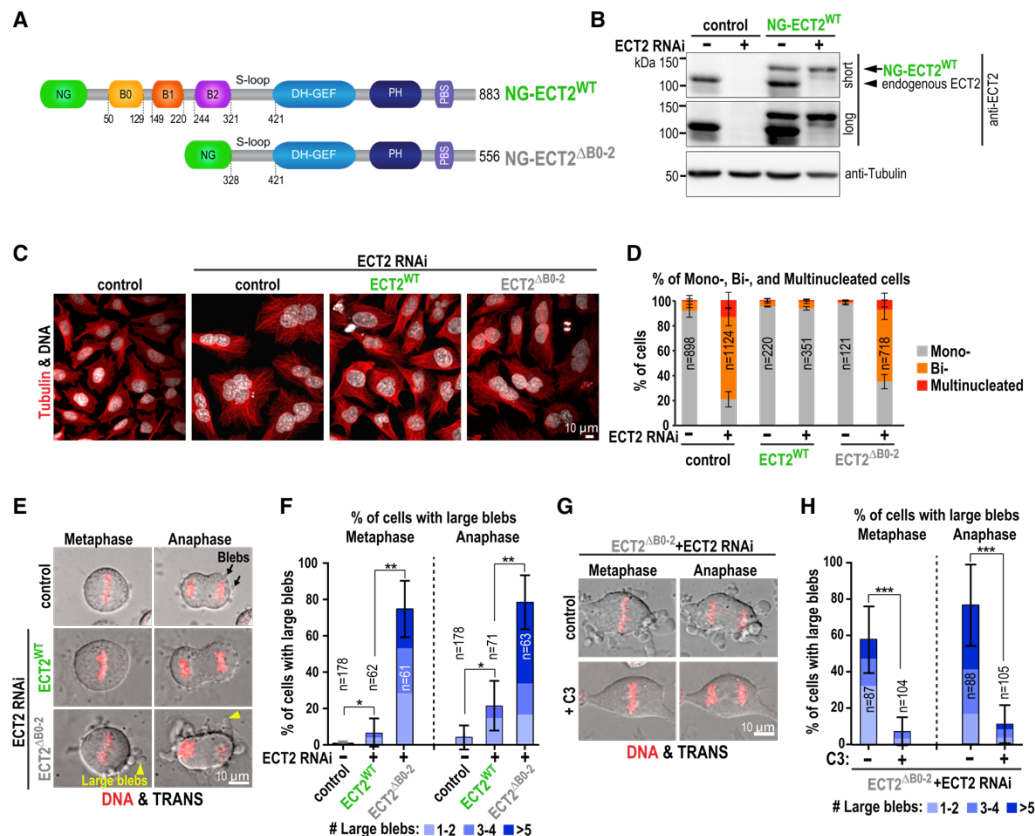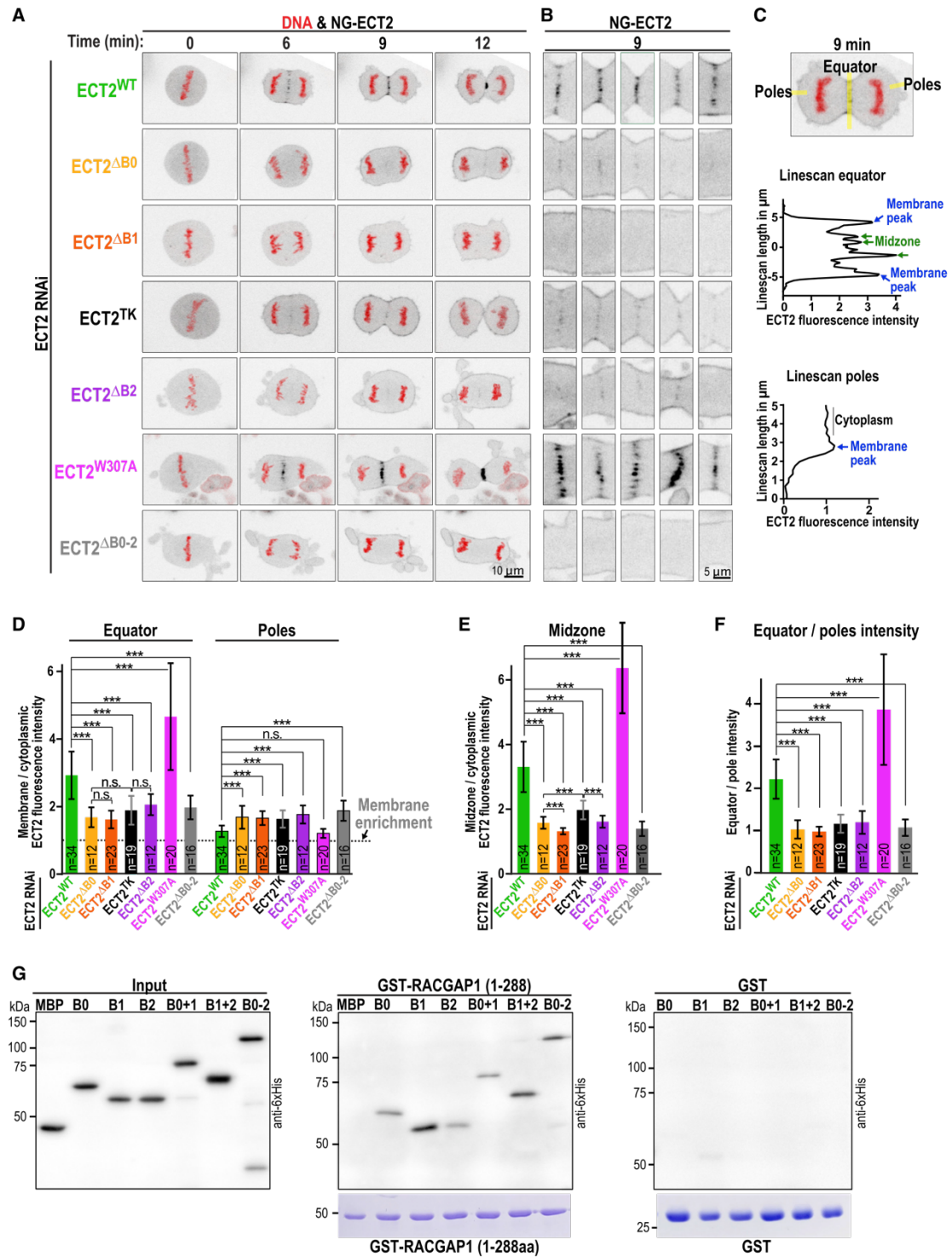
Figure 1. The BRCT domains inhibit ECT2 GEF activity and are required during cytokinesis

(A) Schematic representation of human NG-tagged ECT2[WT] and ECT2[ΔB0-2] proteins.

(B) Immunoblot of control (without transgene) and NG-tagged ECT2[WT] cells for the indicated RNAi conditions probed with anti-ECT2 and anti-α-tubulin antibody. The two blots on top are the same with short and long exposure times.

(C) Fluorescent images of control, ECT2[WT], and ECT2[ΔB0-2] cells for the indicated RNAi treatments stained for DNA (white) and α-tubulin (red).

(D) Mean percentages of mono-, bi-, and multinucleated cells are displayed for the indicated conditions.

(E) Merged live-cell transmission and DNA (red) images of control, ECT2[WT], and ECT2[ΔB0-2] cell lines for the indicated RNAi conditions. Normal blebs are highlighted by black arrows and large blebs by yellow arrowheads.

(F) Mean percentages of cells with 1–2, 3–4, and ≥ 5 large blebs are plotted. p Values were determined by Kruskal-Wallis test for control and ECT2[WT] and by the Student's t test for ECT2[WT] and ECT2[B0-2].

(G) Merged transmission and DNA (red) images of ECT2[ΔB0-2] cells treated with and without the Rho inhibitor C3 exoenzyme.

(H) Mean percentages of cells with large blebs are displayed. p Values were determined by Tukey's test.

For all ≥ 2 independent experiments, n = number of cells, and error bars denote SD. For all figures: p values are represented by n.s., p > 0.05; *p < 0.05; **p < 0.01; ***p < 0.001.

cytoplasmic during metaphase and is enriched at the spindle midzone and the equatorial plasma membrane during anaphase (Figures 2A and 2B; Chalamalasetty et al., 2006; Su et al., 2011; Zhao and Fang, 2005). To quantitatively compare the localization of the different ECT2 variants, we measured their fluorescence intensities (Figure 2C). ECT2[WT] was ~2-fold enriched at the cell equator in comparison to the cell poles (Figures 2D–2F; Kotýnková et al., 2016). All ECT2 mutant proteins were still enriched at the membrane, consistent with the fact that the two membrane-binding motifs are still present (Su et al., 2011). However, deletion of single BRCT domains resulted in a decrease at the

equatorial, and an increase at the polar, membranes (Figures 2D–2F). This change in localization was similar to the previously reported ECT2[TK] mutation (Kotýnková et al., 2016). When comparing the spindle midzone localization, we observed that all BRCT deletion mutants were strongly reduced on the midzone in comparison to ECT2[WT]. The midzone signals of the ECT2[ΔB0-2] and ECT2[ΔB1] were completely absent (Figure 2E), possibly because binding to RACGAP1 was lost. Interestingly, midzone localization of ECT2[ΔB2] and ECT2[ΔB0] was strongly reduced in comparison with that of ECT2[WT] but was increased in comparison with ECT2[ΔB1]. Midzone and equatorial membrane, but not

A

DNA & NG-ECT2

Time (min): 0   6   9   12

ECT2 RNAi

ECT2^WT
ECT2^ΔB0
ECT2^ΔB1
ECT2^TK
ECT2^ΔB2
ECT2^W307A
ECT2^ΔB0-2

10 μm

B NG-ECT2

9

5 μm

C

9 min

Equator
Poles   Poles

Linescan equator

Membrane peak
Midzone
Membrane peak

ECT2 fluorescence intensity

Linescan poles

Cytoplasm
Membrane peak

ECT2 fluorescence intensity

D

Equator   Poles

Membrane / cytoplasmic ECT2 fluorescence intensity

Membrane enrichment

ECT2 RNAi

E Midzone

Midzone / cytoplasmic ECT2 fluorescence intensity

ECT2 RNAi

F Equator / poles intensity

Equator / pole intensity

ECT2 RNAi

G

Input

kDa MBP B0 B1 B2 B0+1 B1+2 B0-2

anti-6xHis

GST-RACGAP1 (1-288)

kDa MBP B0 B1 B2 B0+1 B1+2 B0-2

anti-6xHis

GST-RACGAP1 (1-288aa)

GST

kDa B0 B1 B2 B0+1 B1+2 B0-2

anti-6xHis

GST

(legend on next page)

the polar membrane, localization of ECT2^{W307A} was enhanced (Figures 2A–2F), suggesting that ECT2^{W307A} binds more strongly to RACGAP1 than ECT2^{WT}.

ECT2 is targeted to the spindle midzone by binding to the centralspindlin component RACGAP1. Previous studies have demonstrated that all BRCT domains together and the BRCT1 domain alone are sufficient to pull down RACGAP1 from mitotic extracts (Burkard et al., 2009; Wolfe et al., 2009; Yüce et al., 2005). Because we observed a strong reduction in midzone localization in BRCT0 and BRCT2 deletion mutants, we determined whether the BRCT0 and BRCT2 domains also bind RACGAP1. Purified single (B0, B1, and B2), double (B0–1 and B1–2), and triple (B0–2) BRCT domains were used, together with a RACGAP1 fragment, in pull-down assays. Consistent with previous studies, the triple and double BRCT domains were pulled down by RACGAP1. When testing the single BRCT domains, we found that B1 bound most efficiently to RACGAP1; however, B0 and B2 also interacted (Figure 2G).

In summary, our data show that the BRCT1 domain is absolutely essential for midzone localization and binds strongly to RACGAP1. The recent identification of a conserved RACGAP1-binding patch on the BRCT1 domain (Gómez-Cavazos et al., 2020) complements our observations. Our work expands that finding by showing that, in addition to BRCT1, BRCT0 and BRCT2 also bind RACGAP1 and contribute to midzone targeting and equatorial membrane enrichment of ECT2 during anaphase.

BRCT2 has a dual function during cytokinesis

We found that the BRCT2 domain interacts with RACGAP1 and W307 inhibits GEF activity *in vitro* (Chen et al., 2020). To investigate whether the BRCT2 domain inhibits GEF activity during mitosis, we analyzed the phenotype of ECT2$^{\Delta B2}$ and ECT2^{W307A} cells. After ECT2 RNAi, the number of mononucleated cells was decreased in ECT2$^{\Delta B2}$ and was similar to that of control cells in ECT2^{W307A} (Figure 3A), indicating that ECT2$^{\Delta B2}$ is partially, and ECT2^{W307A} is fully functional during cytokinesis. To determine whether GEF activity is increased, we filmed ECT2$^{\Delta B2}$ and ECT2^{W307A} cells during mitosis. We found that the percentages of ECT2$^{\Delta B2}$ and ECT2^{W307A} cells with large blebs were similar to ECT2$^{\Delta B0–2}$ and were increased in comparison to that of ECT2^{WT} cells (Figures 1F, 3B, and 3G). Addition of RhoA inhibitor to ECT2$^{\Delta B2}$ cells reduced the percentage of cells with large blebs (Figure S2A). More than 60% of the large blebs were located at the poles, whereas the remaining ones were at the side or at the equator of the cell (Figures 3C and S2B). To compare the dynamics of the large blebs in ECT2$^{\Delta B2}$ and ECT2$^{\Delta B0–2}$ cells with blebs normally occurring during anaphase, we measured bleb

duration and maximum length during mitosis. The maximum bleb length in ECT2$^{\Delta B2}$ and ECT2$^{\Delta B0–2}$ cells was strongly increased in comparison with control or ECT2^{WT} cells (Figures 3D and S2C). When we compared the duration of the blebs, we found that large blebs took much longer to retract in metaphase than they did in anaphase (Figure 3E), suggesting that the retraction machinery works more efficiently in anaphase (Taneja and Burnette, 2019). Together, these findings reveal that the deletion of the BRCT2 domain or the mutation of W307 results in increased GEF and, thus, RhoA activity during mitosis.

During anaphase, ECT2 is active at the cell equator to generate a narrow zone of active RhoA. In the ECT2$^{\Delta B0–2}$, ECT2$^{\Delta B2}$, and ECT2^{W307A} mutants, large blebs formed, suggesting that ECT2 activity increased. To analyze whether a cleavage furrow still formed, we filmed those cells during anaphase (Videos S1, S2, S3, and S4). To compare the timing of ring ingression, we measured the equatorial cell width at 12 min after anaphase onset, the time at which the contractile ring was already fully ingressed in control cells. Cell width in ECT2^{WT} cells was indistinguishable from that of control cells, demonstrating that ECT2^{WT} fully rescued the furrow ingression defect (Figures 3F and 3G). In ECT2$^{\Delta B2}$ and ECT2$^{\Delta B0–2}$ cells, the equatorial cell width was narrower in comparison with that of ECT2 RNAi but was wider than that of ECT2^{WT} cells. Cells expressing ECT2^{W307A} exhibited even better furrow ingression than ECT2$^{\Delta B2}$ did but were still delayed in comparison with ECT2^{WT} cells. More than 12% of the ECT2$^{\Delta B2}$, ECT2$^{\Delta B0–2}$, and ECT2^{W307A}, but not ECT2^{WT} (1.3%, n = 78) cells displayed shape oscillations during anaphase (Figure S3A). Such shape oscillations are typically observed when cellular tension is imbalanced between the forming daughter cells (Sedzinski et al., 2011) and are another indication that ECT2 activity is increased in those mutants.

Furrow ingression in ECT2$^{\Delta B2}$ cells might be compromised because of excessive formation of large blebs. To test that, we added the RhoA kinase inhibitor Y27632, which prevents bleb formation caused by increased RhoA activity (Zanin et al., 2013) but does not prevent furrow ingression (Kosako et al., 2000). As expected, addition of Y27632 to ECT2$^{\Delta B2}$ cells suppressed bleb formation (Figures S3B–S3D), but cell width was still larger than that of Y27632-treated control cells. This suggests that large bleb formation is not the primary cause for slow contractile ring ingression in ECT2$^{\Delta B2}$ cells.

In summary, the BRCT2 domain is required for ECT2 autoinhibition and efficient furrow ingression and contributes to successful cytokinesis. Because the percentages of ECT2$^{\Delta B0–2}$, ECT2$^{\Delta B2}$, and ECT2^{W307A} cells with large blebs are comparable, we conclude that the loss of GEF inhibition is similar in those

---

Figure 2. Each BRCT domain contributes to midzone targeting and binds RACGAP1

(A) Merged time-lapse images of the NG-tagged ECT2 mutants and DNA (red). Time is displayed in minutes after anaphase onset.

(B) Magnification of the equatorial region, 9 min after anaphase onset.

(C) ECT2 fluorescence intensity was measured by an equatorial and two polar line scans. Middle and bottom panels show equator and polar line scans, respectively, for an ECT2^{WT} cell. Regions used for the quantification are marked.

(D–F) Plotted are the normalized mean fluorescence intensities at the equatorial and polar membrane (D), the mean peak intensities at the midzone (E), and the ratio of equatorial to polar membrane (F). Data from ≥2 independent experiments, n = number of cells, error bars denote SD, and p values were calculated with the Kruskal-Wallis or Student's t tests.

(G) Immunoblots incubated with anti-6xHis antibody and Coomassie gels of a pull-down assay with purified MBP/6xHis-tagged ECT2 fragments and GST-RACGAP1.
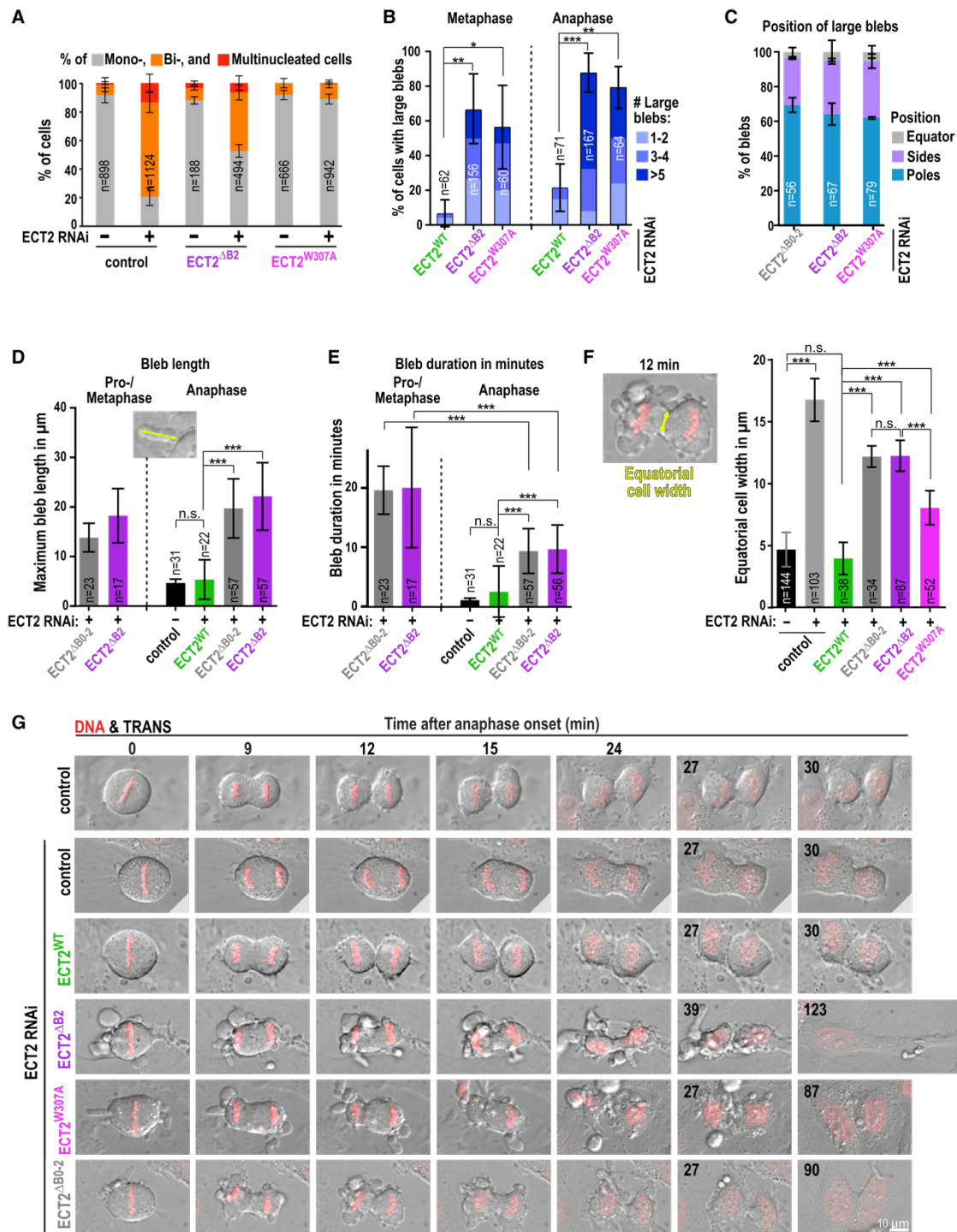
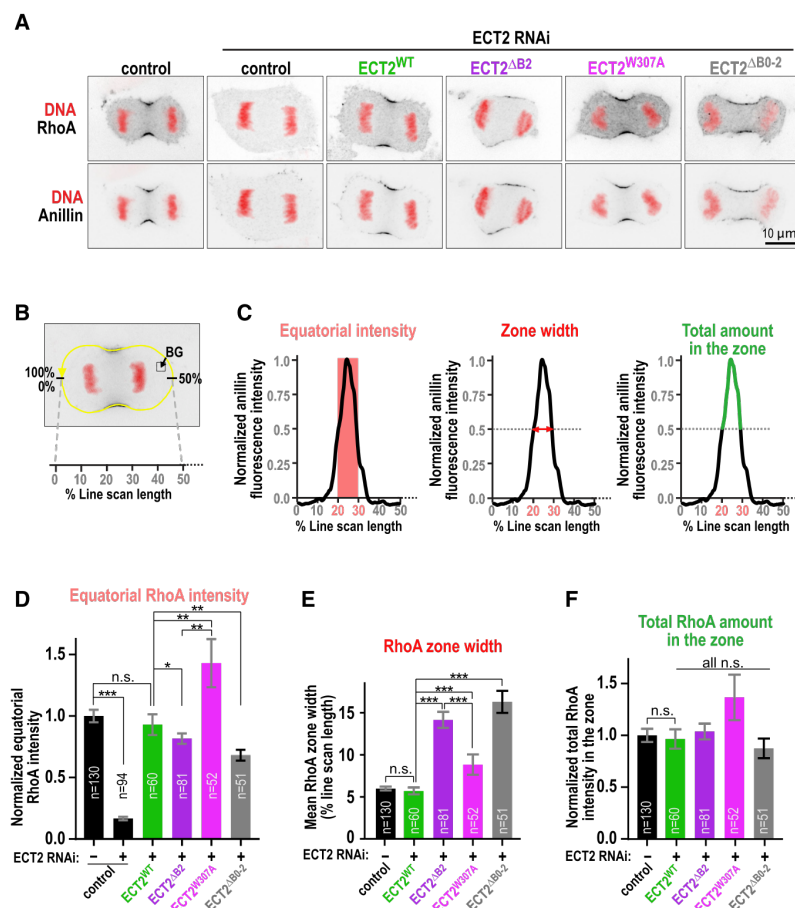**Figure 4. BRCT2 is required for the formation of a narrow RhoA zone**

(A) Immunofluorescence images for the indicated conditions. Cells were stained for DNA (red), RhoA (top row, black), and anillin (bottom row, black).

(B) A line scan was drawn around the cell periphery, starting at one cell pole to quantify RhoA and anillin fluorescence intensity along the cortex.

(C) The normalized anillin fluorescence intensity from 0%–50% line scan length is shown for a control cell. The mean equatorial anillin intensity was calculated for 20%–30% and 70%–80% line scan length (left), the anillin zone width was determined at the half maximum fluorescence intensity for each side of the cell (middle), and the total amount of anillin within the zone was summed up as indicated (right).

(D–F) The mean equatorial RhoA intensity (D), RhoA zone width (E), and total RhoA amount in the zone (F) are plotted for the indicated conditions. For all n = number of cells, and ≥ 3 independent experiments were performed for each condition. Error bars are SEM, and p values were calculated with the Kruskal-Wallis test.

mutants. Together with the observations that midzone targeting is decreased for ECT2$^{\Delta B2}$, but increased for ECT2^{W307A}, our findings show that the BRCT2 domain integrates two key functions: RACGAP1 binding and GEF inhibition.

BRCT2 binding to the GEF domain restricts ECT2 activity to a narrow zone

Our observations reveal that BRCT2 is the primarily responsible BRCT domain for GEF inhibition. Releasing BRCT2-mediated inhibition could result in the activation of RhoA all around the cell periphery, or alternatively, RhoA could still be active in a zone at the cell equator. To determine the spatial patterning of RhoA activity, we stained cells for RhoA and anillin, which binds active RhoA and mimics active RhoA localization (Piekny and Glotzer, 2008; Sun et al., 2015). In control, but not ECT2 RNAi anaphase cells, RhoA and anillin were enriched in a zone at the cell equator (Figure 4A). Surprisingly, RhoA and anillin still localized to an equatorial zone in ECT2$^{\Delta B2}$ and ECT2$^{\Delta B0-2}$ cells; however, the zone appeared to be broader than that in control cells. To quantitatively compare RhoA and anillin localization, we measured their fluorescence intensity around the cell cortex by drawing a line starting at one pole of the cell (Figure 4B). To quantify the RhoA and anillin levels

---

Figure 3. BRCT2 inhibits GEF activity and is partially required for cytokinesis

(A) Mean percentages of mono-, bi-, and multinucleated cells for the indicated conditions are displayed. Control is from Figure 1D.

(B) Shown are the mean percentages of cells with large blebs for the indicated conditions. p Values were determined by the Student's t test; ECT2^{WT} is from Figure 1F.

(C) Displayed are the mean percentages of large blebs positioned at the poles, sides, or equator.

(D and E) Maximum bleb length (D) and mean bleb duration (E) are displayed for the indicated conditions and time. p Values were determined with Tukey's test.

(F) Mean equatorial cell width is shown for the indicated conditions. p Values were determined with Tukey's test.

(G) Merged time-lapse transmission and DNA (red) images for the indicated conditions.

For all ≥ 2 independent experiments: n = number of cells in (A), (B), and (F) and n = number of blebs (C–E). Error bars are SD.

at the equatorial region, we calculated the mean equatorial fluorescence intensity from 20%–30% and 70%–80% line scan length for each cell because those length ranges include the RhoA and anillin zone in control cells (Figure 4C). As expected, expression of ECT2^{WT} restored equatorial RhoA and anillin levels back to control levels (Figures 4A, 4D, and S4A). In ECT2$^{\Delta B2}$ and ECT2$^{\Delta B0-2}$ cells, the mean equatorial RhoA and anillin levels were reduced in comparison to that of ECT2^{WT} cells (Figures 4D and S4A). In control cells, RhoA and anillin localized to a narrow equatorial zone, and we calculated the width of that zone at the half maximum fluorescence intensity for each cell. Although expression of ECT2^{WT} resulted in a RhoA and anillin zone width indistinguishable from that in control cells, the RhoA and anillin zone width was ~2-fold broader in ECT2$^{\Delta B0-2}$ and ECT2$^{\Delta B2}$ cells (Figures 4E and S4A). We found that BRCT2 binds RACGAP1 and inhibits GEF activity, thus, the complete deletion of BRCT2 affects both functions. To reveal whether the loss of GEF inhibition alone also results in a broader RhoA zone, we analyzed ECT2^{W307A} cells. In ECT2^{W307A} cells, the RhoA and anillin zones were smaller than they were in ECT2$^{\Delta B2}$ but still larger than they were in control cells (Figures 4E and S4A). This suggests that BRCT2 binding to the GEF domain is required for the formation of a narrow RhoA zone. Furthermore, the mean equatorial RhoA and anillin levels were increased in ECT2^{W307A} cells (Figures 4D and S4A). Thus, maintaining RACGAP1-BRCT2 interaction when autoinhibition is lost tethers active ECT2 to the cell equator. To estimate the total amount of RhoA and anillin within the respective zone, we summed up the fluorescence intensity within the zones for each cell (Figure 4C). We found that this was similar in ECT2$^{\Delta B0-2}$, ECT2$^{\Delta B2}$, and ECT2^{W307A} cells, in comparison to ECT2^{WT} cells (Figures 4F and S4A). Thus, the total amount of ECT2 activated within the zone is similar, and BRCT2 inhibition of GEF activity and RACGAP1 binding spatially restrict ECT2 activity.

Because ECT2$^{\Delta B0-2}$, ECT2$^{\Delta B2}$, and ECT2^{W307A} cells exhibited excessive bleb formation, we reasoned that this could be a mechanism to remove cortical regions with high ECT2 or RhoA activity from the cell body, which might facilitate RhoA and anillin zone formation. To investigate that possibility, we analyzed RhoA and anillin localization in the presence of the Rho kinase inhibitor Y27632, which suppressed bleb formation (Figure S3D). In ECT2$^{\Delta B0-2}$, ECT2$^{\Delta B2}$, and ECT2^{W307A} Y27632-treated cells, RhoA and anillin still localized to an equatorial zone that was ~2-fold broader in comparison with control cells (Figures S4B–S4E). This demonstrates that large bleb formation is not a prerequisite for RhoA zone formation in ECT2$^{\Delta B0-2}$, ECT2$^{\Delta B2}$, and ECT2^{W307A} cells.

ECT2$^{\Delta B0-2}$ and ECT2$^{\Delta B2}$ cells showed similar localization of RhoA (Figure 4) and equatorial cell width 12 min after anaphase onset (Figure 3F), yet ECT2$^{\Delta B2}$ partially rescued cytokinesis failure whereas ECT2$^{\Delta B0-2}$ did not. ECT2 localizes to the midbody during abscission (Hu et al., 2012; Simon et al., 2008); however, it is not known whether the membrane- or midzone-bound ECT2 pool or both contribute to midbody localization. Because ECT2$^{\Delta B0-2}$ localized to the plasma membrane, but not to the spindle midzone, during anaphase, we speculated that ECT2$^{\Delta B0-2}$ was absent from the midbody. We observed in fixed cells that ECT2$^{\Delta B2}$ was absent from the midbody region in 37% of the cells and was weaker in the remaining ones (Figure S5A),

consistent with the observation that midzone localization is strongly reduced but not absent in ECT2$^{\Delta B2}$. In contrast, ECT2$^{\Delta B0-2}$ was never observed at the midbody region, suggesting that ECT2 membrane binding is not sufficient to target ECT2 to the midbody. Midbody localization of ECT2$^{\Delta B2}$ is most likely facilitated by binding of BRCT0 and/or BRCT1 to RACGAP1. Because ECT2$^{\Delta B2}$, but not ECT2$^{\Delta B0-2}$, partially rescued the cytokinesis failure phenotype, our observations point toward a role of ECT2 at the midbody.

In summary, deletion of the BRCT2 domain results in a strong broadening of the RhoA zone during anaphase. The broader RhoA zone is partially rescued in the ECT2 W307A mutation, which restores RACGAP1 binding but still lacks GEF inhibition. Together, this suggests that binding of BRCT2 to the GEF domain and RACGAP1 both contribute to restrict ECT2 activity to a narrow zone at the cell equator in anaphase.

BRCT1 is essential, and BRCT0 facilitates equatorial RhoA recruitment

We observed that BRCT2 inhibits GEF activity. Therefore, we investigated whether BRCT0 and BRCT1 have similar functions during cytokinesis. We found that ECT2$^{\Delta B0}$ cells treated with ECT2 RNAi displayed a comparable number of bi- and multinucleated cells to that of control cells (Figure 5A), suggesting that BRCT0 is not essential for cytokinesis. Filming ECT2$^{\Delta B0}$ cells during mitosis revealed that the percentage of cells with large blebs was not significantly increased in ECT2$^{\Delta B0}$ in comparison to ECT2^{WT} cells, but furrow ingression was delayed (Figures 5B–5D; Video S5). Furthermore, shape oscillations were not observed in ECT2$^{\Delta B0}$ cells (n = 85) during anaphase. This is consistent with in vitro GEF assays showing that BRCT0 deletion does not elevate GEF activity (Chen et al., 2020). To determine whether slower contractile ring ingression in ECT2$^{\Delta B0}$ cells was due to RhoA activation being reduced, we stained cells for RhoA and anillin. In ECT2$^{\Delta B0}$ anaphase cells, the equatorial RhoA and anillin levels were decreased; however, the width of the zone was not affected (Figures 5E, 5F, and S5B). Furthermore, the total amount of RhoA and anillin within the zone was reduced, suggesting that ECT2 is less active when lacking the BRCT0 domain. Together, the BRCT0 domain is not essential for cytokinesis and does not inhibit GEF activity during mitosis. However, the BRCT0 domain facilitates RhoA activation at the cell equator and furrow ingression, possibly by assisting the release of ECT2 autoinhibition.

The function of the BRCT1 domain has been controversial because ECT2^{TK} did not immunoprecipitate RACGAP1, but cytokinesis was normal (Kotýnková et al., 2016; Wolfe et al., 2009). A recent study challenged those observations by showing that bacterial-purified ECT2^{TK} still interacts with RACGAP1. In addition, a conserved surface patch, distinct from the TK residues, was identified and was demonstrated to be essential for RACGAP1 binding, furrow ingression, and cytokinesis (Gómez-Cavazos et al., 2020). To clarify whether the BRCT1 domain is essential for the release of autoinhibition and/or inhibits GEF activity, we analyzed cytokinesis in ECT2^{TK} and ECT2$^{\Delta B1}$ cells. The ECT2^{TK} mutant fully rescued all cytokinesis defects, confirming previous observations (Kotýnková et al., 2016; Figures 5A–5F, S5B, and S5C). No increase in the formation of large blebs was observed in ECT2^{TK}
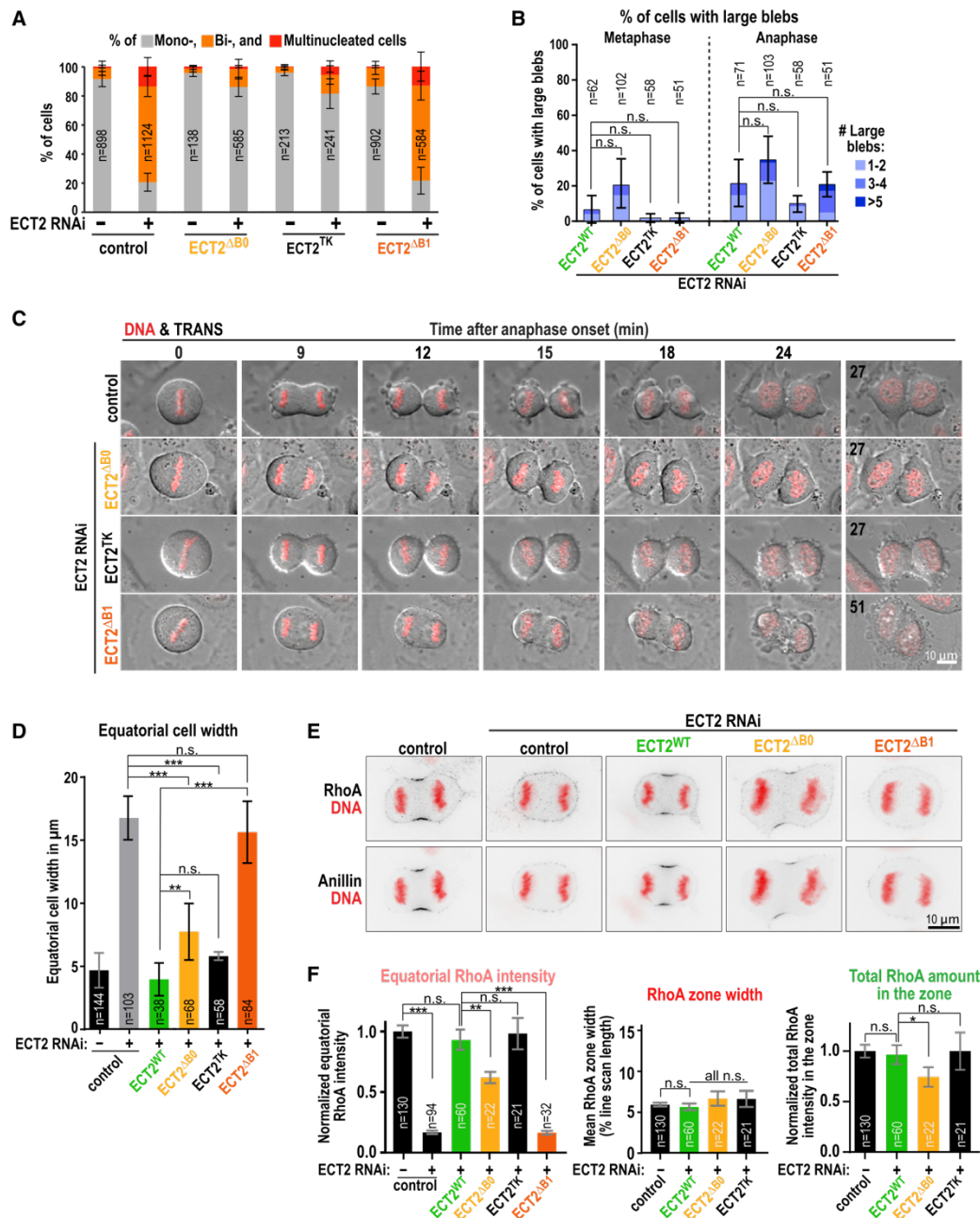
Figure 5. BRCT0 facilitates and BRCT1 is essential for equatorial RhoA zone formation

(A) Shown are mean percentages of mono-, bi-, and multinucleated cells (±SD) for the indicated conditions. Control is from Figure 1D.

(B) Mean percentages of cells (±SD) with large blebs for the indicated conditions are displayed. p Values were determined with the Student's t and Kruskal-Wallis tests; ECT2[WT] is from Figure 1F.

(C) Merged transmission and DNA (red) live-cell images for the indicated conditions.

(D) Graph displays the mean equatorial cell width (±SD) for the indicated conditions. p Values were determined with Tukey's test. Control and ECT2[WT] were from Figure 3F.

(E) Immunofluorescence images of cells for the indicated conditions stained for DNA (red), RhoA (top, black), and anillin (bottom, black).

(F) Plotted are the mean equatorial RhoA intensity (left), the mean RhoA zone width (middle), and the mean total amount of RhoA in the zone (right) for the indicated conditions. Control and ECT2[WT] are from Figures 4D–4F. Error bars are SEM, and p values were calculated with the Kruskal-Wallis test.

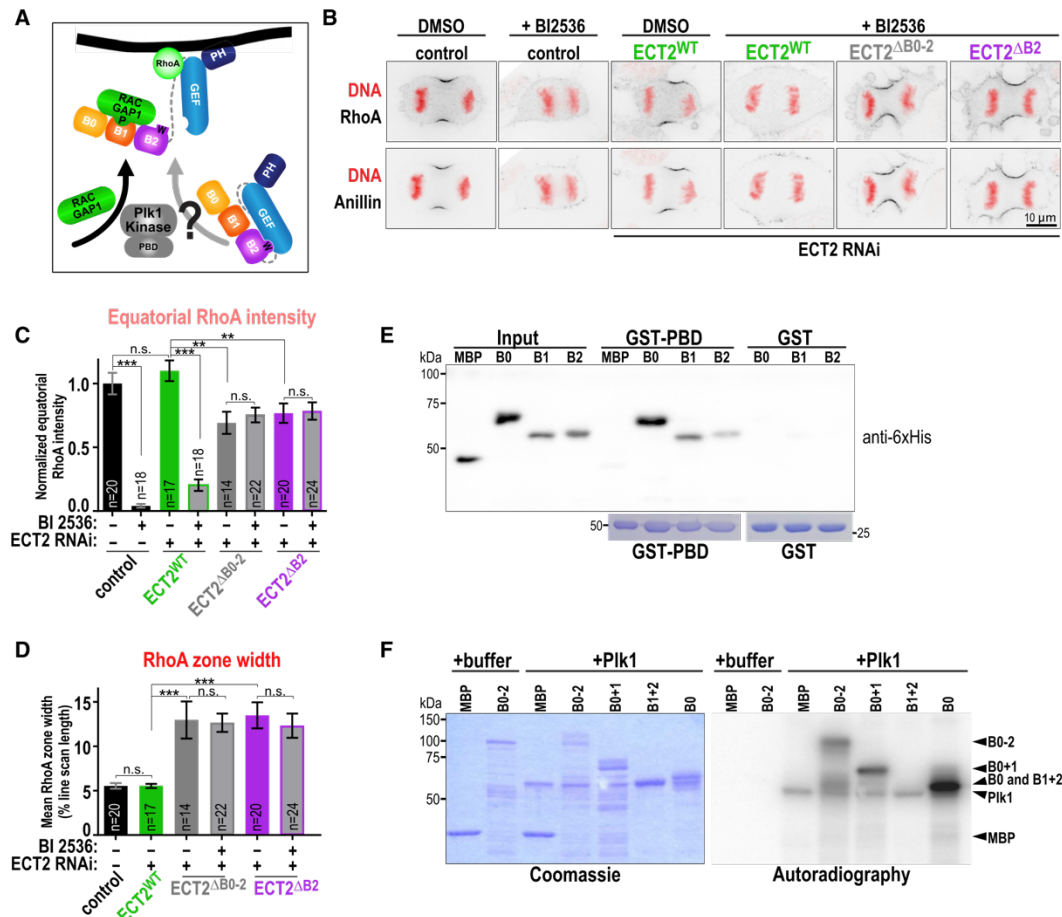For all, ≥2 independent experiments were performed; n = number of cells.

Figure 6. Plk1 acts upstream of BRCT2-GEF inhibition, binds the BRCT domains, and phosphorylates BRCT0

(A) Plk1 could promote RACGAP1-ECT2 complex formation independent of RACGAP1 phosphorylation (Wolfe et al., 2009).

(B) Immunofluorescence images of cells for the indicated conditions stained for DNA (red), RhoA (black, top), and anillin (bottom, black) are shown.

(C and D) Mean equatorial RhoA intensity (C) and mean RhoA zone width (D) are plotted for the indicated conditions. Error bars are SEM. p Values were calculated with the Kruskal-Wallis test. For all, ≥2 independent experiments were performed; n = number of cells.

(E) Shown is an immunoblot treated with anti-6xHis antibody and Coomassie gels of a pull-down experiment with the indicated MBP/6xHis-tagged BRCT domains and GST-PBD.

(F) Coomassie gel and autoradiography of a Plk1 kinase assay with the indicated MBP/6xHis-tagged ECT2 fragments are displayed.

cells (Figure 5B), demonstrating that T153 and K195 are not involved in ECT2 autoinhibition. ECT2$^{\Delta B1}$ did not support furrow ingression and cytokinesis in the absence of endogenous ECT2 (Figures 5A, 5C, and 5D). Although deletion of the BRCT2 domain resulted in large bleb formation, deletion of the BRCT1 domain did not (Figures 5B and 5C; Video S6). Furthermore, shape oscillations were never observed in ECT2$^{\Delta B1}$ cells (n = 45), and the equatorial cell width was similar for ECT2$^{\Delta B1}$ and ECT2 RNAi cells (Figure 5D). Finally, the mean RhoA and anillin fluorescence intensity at the equatorial cortex in ECT2$^{\Delta B1}$ anaphase cells was strongly reduced in comparison to that of ECT2^{WT} cells and was indistinguishable from ECT2 RNAi cells (Figures 5E, 5F, and S5B). In summary, we find that the BRCT1 domain is absolutely essential for RhoA zone formation and ECT2 function during cytokinesis,

which is consistent with the presence of a conserved RACGAP1 binding patch in the BRCT1 domain (Gómez-Cavazos et al., 2020). Our data also demonstrate that BRCT1, in contrast to BRCT2, does not inhibit GEF activity.

Plk1 acts upstream of BRCT2-mediated inhibition, and PBD binds each BRCT domain

During anaphase, Plk1 is required for RhoA zone and furrow formation (Brennan et al., 2007; Petronczki et al., 2007; Santamaria et al., 2007). It phosphorylates RACGAP1 and thereby induces binding of RACGAP1 to ECT2 (Burkard et al., 2009; Wolfe et al., 2009; Yüce et al., 2005). Exchanging the Plk1 phosphosites in RACGAP1 to phosphomimetic residues rescues RACGAP1 depletion but does not bypass the requirement of Plk1
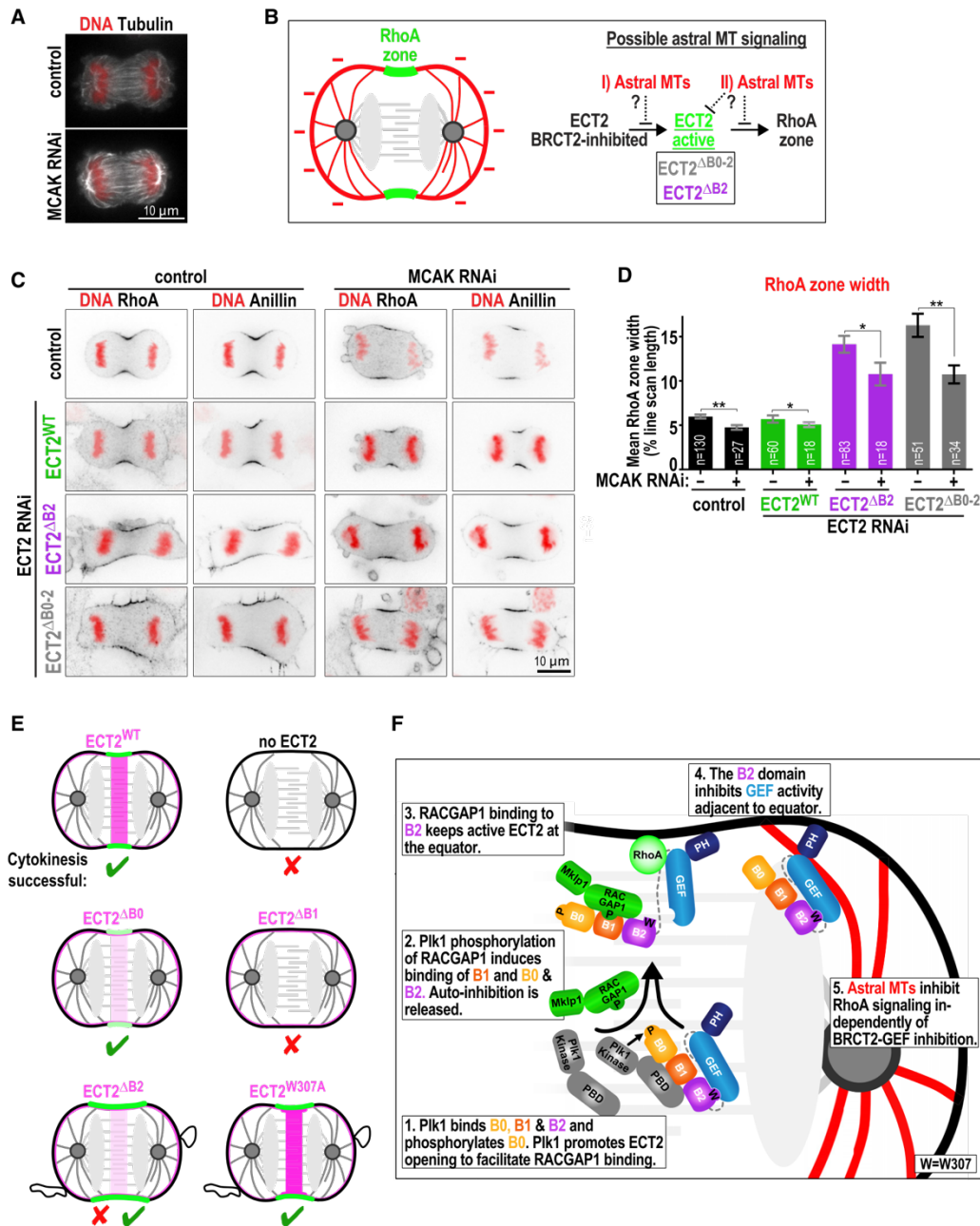
Figure 7. Astral microtubules facilitate the formation of a narrow RhoA zone independent of BRCT2-mediated ECT2 inhibition

(A) Immunofluorescence images of a control and MCAK RNAi cell stained for α-tubulin (white) and DNA (red) are shown.

(B) Astral microtubules could contribute to the formation of a narrow RhoA zone upstream (I) or downstream (II) of BRCT2-mediated GEF inhibition.

(C) Immunofluorescence images of cells stained for DNA (red), RhoA (black), and anillin (black) for the indicated conditions are shown.

(D) Mean RhoA zone width (±SEM) is plotted for the indicated conditions. p Values were calculated with the Kruskal-Wallis test; two independent experiments for each condition.

(E) Schematic overview of the localization and phenotype of ECT2^{WT}, and the different ECT2 mutant proteins are analyzed.

(legend continued on next page)

for cytokinesis (Wolfe et al., 2009). Furthermore, in the absence of Plk1 activity, phosphomimetic RACGAP1 only recruits the N terminus, but not full-length, ECT2 to the spindle midzone. This suggests that Plk1 facilitates the release of ECT2 autoinhibition independently from RACGAP1 phosphorylation (Figure 6A). We found that ECT2$^{\Delta B2}$ and ECT2$^{\Delta B0-2}$ are active in anaphase and result in the formation of a broader RhoA zone and large blebs. Therefore, these ECT2 mutants constitute an ideal tool to test whether Plk1 acts up- and/or downstream of BRCT2-mediated inhibition. To test that, we treated cells with the Plk1 inhibitor BI2536. As expected, inhibition of Plk1 resulted in a strong reduction of mean RhoA and anillin intensity at the cell equator in control and ECT2^{WT} cells (Figures 6B–6D, S6A, and S6B). In contrast, the mean RhoA and anillin fluorescence intensities at the cell equator and the width of their zones did not change after adding BI2536 to ECT2$^{\Delta B2}$ or ECT2$^{\Delta B0-2}$ cells. Further, the percentage of ECT2$^{\Delta B2}$ cells with large blebs in anaphase was not altered after the inhibition of Plk1 (Figures S6C and S6D). Together, our data show that RhoA zone formation in the absence of BRCT2 is independent of Plk1, consistent with a function of Plk1 upstream of BRCT2-mediated autoinhibition.

Full-length ECT2 binds the polo-box domain (PBD) of Plk1, and an N-terminal ECT2 fragment that includes the S-loop is phosphorylated by Plk1 (Niiya et al., 2006). To analyze to which ECT2 region the PBD binds, we purified the BRCT domains with the S-loop (B0-S-loop), B0, B0+1, and B1+2 and performed pull-down assays. We found that B0, B0+1, B1+2, and B0-S loop were all pulled down by GST-PBD but not by GST alone (Figure S6E). Because Plk1 bound the B0 and B1+2 fragments, we tested whether PBD also binds B1 and B2 alone. PBD interacted strongly with B0 and weakly with B1 and B2 (Figure 6E). Next, we dissected which domains of ECT2 are phosphorylated by Plk1. N-terminal ECT2 fragments, with or without the S-loop, were both efficiently phosphorylated (Figure S6F), suggesting that the S-loop is not the main phosphorylation site for Plk1. To determine which BRCT domain is phosphorylated by Plk1, we incubated B0, B0+1, and B1+2 domains with Plk1. The B0 and B0+1, but not the B1+2, domains were phosphorylated by Plk1 (Figure 6F). This shows that the main Plk1 phosphorylation site(s) are in the BRCT0 domain of ECT2.

We conclude that Plk1 is not required for RhoA zone formation when the BRCT2 domain is missing, indicating that it acts upstream of BRCT2 inhibition, which is consistent with its role in RACGAP1 phosphorylation. We also found that the PBD of Plk1 binds efficiently to the BRCT0 and weakly to the BRCT1 and BRCT2 domain and that Plk1 phosphorylates the BRCT0 domain.

Astral microtubules inhibit RhoA signaling independently of BRCT2-mediated ECT2 inhibition

The dynamic microtubules emanating from the centrosomes are an important determinant in controlling the spatial patterning of RhoA activity during cytokinesis. In human cells, removal of the astral microtubules results in the broadening of the RhoA zone (Murthy and Wadsworth, 2008; van Oostende Triplet et al., 2014; Zanin et al., 2013). Elongating astral microtubules by removing the microtubule depolymerizing kinesin MCAK (Desai et al., 1999; Hedrick et al., 2008; Rankin and Wordeman, 2010; Figure 7A) results in a narrower RhoA zone (van Oostende Triplet et al., 2014; Zanin et al., 2013). Ectopic activation of RhoA at the cell poles or the cell equator with optogenetics results in a similar extent of cleavage furrow ingression at both locations. This suggests that astral microtubules inhibit RhoA signaling upstream of RhoA activation (Wagner and Glotzer, 2016). One possibility is that astral microtubules promote ECT2 inactivation by stimulating the binding of BRCT2 to the GEF domain. To test that, we depleted MCAK in ECT2$^{\Delta B2}$ and ECT2$^{\Delta B0-2}$ cells. If the astral microtubules stimulate binding of BRCT2 to the GEF domain, increasing microtubule length in those cells should not affect the width of the RhoA zone. However, if astral microtubules inhibit RhoA signaling independently of BRCT2-mediated inhibition, the width of the RhoA zone should decrease (Figure 7B). As published, MCAK-depleted cells formed medium-sized blebs because of the pushing of the elongated astral microtubules against the membrane (Rankin and Wordeman, 2010; Figures S7A–S7C). MCAK depletion did not induce large blebs (Figure S7D), which were typically observed after the loss of ECT2 autoinhibition. MCAK RNAi reduced the width of the RhoA and anillin zones in control and ECT2^{WT} cells in anaphase but did not affect furrow ingression or cytokinesis completion (Figures 7C, 7D, and S7E–S7G), which is similar to previous observations (van Oostende Triplet et al., 2014; Zanin et al., 2013). Upon depletion of MCAK in ECT2$^{\Delta B2}$ and ECT2$^{\Delta B0-2}$ cells, the width of the RhoA and anillin zones was reduced (Figures 7D and S7G). Increasing astral microtubule length by MCAK RNAi could narrow RhoA zone width by facilitating ECT2$^{\Delta B2}$ and ECT2$^{\Delta B0-2}$ enrichment at the equatorial membrane. We observed that ECT2^{WT}, ECT2$^{\Delta B0-2}$, and ECT2$^{\Delta B2}$ still localized to the membrane, and importantly, their enrichment at the cell equator was not increased upon MCAK depletion (Figures S7H–S7K). Thus, increasing astral microtubule length does not promote ECT2 enrichment at the cell equator. In summary, we found that astral microtubules can narrow the width of the RhoA zone, even when autoinhibition of ECT2 by the BRCT2 domain is lost. This indicates that astral microtubules promote the formation of a narrow RhoA zone downstream of BRCT2-mediated ECT2 autoinhibition.

DISCUSSION

The GEF ECT2 regulates numerous cellular processes, including cell polarity, cell division, and gene expression. During cell division, ECT2 activates RhoA at the cell equator, and precise regulation of ECT2 activity is important for error-free mitosis. Our

---

(F) Model: (1) At the spindle midzone, Plk1 binds the BRCT domains and phosphorylates BRCT0, which favors an open conformation of ECT2. (2) Plk1 also phosphorylates RACGAP1, which induces binding of the BRCT1 domain to RACGAP1. RACGAP1 also binds BRCT0 and BRCT2, and BRCT2 is released from the GEF domain. (3) After the release of autoinhibition, RACGAP1 remains bound to ECT2 and tethers active ECT2 to the cell equator. (4) Active ECT2 that escapes from the cell equator is shut off by binding of the BRCT2 to the GEF domain. (5) Astral microtubules inhibit RhoA signaling independent of BRCT2-GEF binding or ECT2 membrane targeting.

work reveals how the conserved BRCT domains temporally and spatially regulate ECT2 activity during cell division. We discover that deletion of each BRCT domain results in a unique phenotype (Figure 7E), suggesting that the BRCT domains make distinct contributions to cytokinesis. Based on our and previous findings, we propose the following model (Figure 7F): during metaphase, ECT2 activity is low because of the intramolecular binding of W307 of the BRCT2 to the GEF domain (Chen et al., 2020). During anaphase, Plk1 phosphorylates RACGAP1 (Burkard et al., 2007; Wolfe et al., 2009) and the BRCT0 domain of ECT2, and Plk1 binds with its PBD to the BRCT domains. The BRCT-PBD interaction and BRCT0 phosphorylation could partially open ECT2 and facilitates the interaction with phosphorylated RAC-GAP1. It could also keep Plk1 in close proximity to its phosphorylation target RACGAP1 and, thereby, facilitate the RACGAP1-ECT2 complex formation. Phosphorylated RACGAP1 binds BRCT1 (Gómez-Cavazos et al., 2020), but also the BRCT0 and BRCT2, domains, and this induces unbinding of BRCT2 from the GEF domain. Importantly, RACGAP1 binding not only releases autoinhibition but also maintains active ECT2 at the equatorial zone. In cases in which active ECT2 escapes the equatorial zone, the BRCT2 domain binds the GEF domain again, and ECT2 activity is shut off. We propose that GEF and RACGAP1 binding of the BRCT2 domain represents two safeguard mechanisms to avoid spreading of active ECT2 away from the cell equator. Therefore, our work reveals that the BRCT2-mediated spatial control of ECT2 activity is a novel, astral-microtubule-independent mechanism that contributes to the formation of a narrow, active RhoA zone.

Previous work suggested that the entire N terminus inhibits GEF activity, but whether each BRCT domain is required for autoinhibition and the role of autoinhibition in the spatial and temporal control of ECT2 activity were unknown. We find that ECT2 lacking BRCT2, but not BRCT0 or BRCT1, domain causes the formation of large blebs. During furrow formation, cells release cortical tension and stabilize cell shape by the formation of small blebs at the poles (Sedzinski et al., 2011). Elevated RhoA activity increases cellular tension and blebs grow larger (Tinevez et al., 2009). We used the formation of large blebs as a readout for increased ECT2, and thus RhoA, activity. Although bleb formation represents only an indirect measurement for GEF activity, our data are supported by the observations that deletion of all BRCT domains, but not BRCT0 or BRCT0+1, increased GEF activity in vitro (Chen et al., 2020). Normally, blebs buffer tension differences, but if they grow too big, they can also generate tension imbalances and thereby cause shape instabilities and oscillations (Tinevez et al., 2009). More than 12% of the cells with disrupted ECT2 autoinhibition exhibited shape oscillations, suggesting that either compensation of tension differences failed or large blebs introduced tension differences.

Our binding studies showed that the BRCT2 domain binds RACGAP1; therefore, we propose that the BRCT2 domain integrates two key functions of ECT2: RACGAP1 binding and GEF inhibition. Surprisingly, without the BRCT2 domain, an equatorial zone of active RhoA still forms, but RhoA is distributed over a larger region. Restoring only RACGAP1 binding, but not GEF inhibition, in the W307A mutation resulted in a narrower RhoA zone again. Thus, when autoinhibition is absent, RACGAP1 binding to

BRCT2 prevents the spreading of active ECT2 over the membrane. This shows that RACGAP1 is not only essential to activate ECT2 but also simultaneously keeps ECT2 restricted to the equator. We propose that RACGAP1 binding to ECT2, after its release from autoinhibition, represents a safeguard mechanism to keep active ECT2 at the equatorial zone. RACGAP1 is tethered to midzone microtubules via MKLP1 (Mishima et al., 2002), and together, they form clusters at the equatorial membrane (Basant et al., 2015). Therefore, midzone-tethered RACGAP1 could limit the spreading of active ECT2.

We observed that the ECT2 midzone recruitment is strongly increased when the contact between the BRCT2 and the GEF domain is lost in the W307A mutation. This implies that releasing W307-mediated autoinhibition increases the pool of open ECT2 to which phosphorylated RACGAP1 can bind. Thus, in WT cells, a significant pool of ECT2 remains autoinhibited in anaphase, and autoinhibition represents an essential regulatory tool to control the activity of ECT2.

It was proposed that ECT2 activity is inhibited by the PH domain and that the interaction of RhoA with the PH domain upon membrane binding, releases the PH-mediated inhibition (Chen et al., 2020). The BRCT0 deletion and the TK mutant displayed increased membrane localization at the cell poles, yet they did not exhibit increased ECT2 activity. This indicates that ECT2$^{\Delta B0}$ and ECT2^{TK} remain inactive at the poles by BRCT2-mediated GEF inhibition. We also found that ECT2 without the BRCT1 domain is inactive. Therefore, the release of the PH-mediated inhibition must depend on the BRCT1 function. In previous studies, an increase in GEF activity was not observed after removal of the PH domain (Solski et al., 2004; Su et al., 2011), and thus, future work will be needed to address the function of PH-mediated GEF inhibition during cell division.

Without all BRCT domains or the BRCT2 domain, an equatorial RhoA zone still forms. Where does the spatial clue for RhoA zone formation come from in the absence of the three BRCT domains? We observed that astral microtubules limit RhoA signaling independent of BRCT2-mediated inhibition. Therefore, the astral microtubules keep RhoA activity low at the cell poles in WT cells; however, they cannot fully compensate for an increase in GEF activity in ECT2$^{\Delta B0-2}$ cells, and thus, the RhoA zone broadens. In addition to astral microtubules, inactivation of RhoA by MP-GAP or chromosome-dependent signal(s) might contribute to the spatial pattern of RhoA activity (Rodrigues et al., 2015; Zanin et al., 2013). These inhibitory signals at the cell poles might promote RhoA zone formation in ECT2$^{\Delta B0-2}$ cells together with positive feedback loops at the cell equator. For example, RACGAP1 and anillin have been shown to bind the GEF and PH domain, respectively (Frenette et al., 2012; Zhang and Glotzer, 2015). Both interactions were proposed to facilitate ECT2 activity at the cell equator independently of the BRCT domains. Therefore, RACGAP1 and anillin might contribute to the formation of the equatorial RhoA zone in the absence of the BRCT domains.

The role of the BRCT1 domain in activating ECT2 has been controversial because abolishing the BRCT1-RACGAP1 interaction did not prevent cytokinesis (Kotýnková et al., 2016; Wolfe et al., 2009). Our analysis of the BRCT1 deletion is consistent with the recent identification of a conserved RACGAP1-binding patch on BRCT1, suggesting that BRCT1 binding to RACGAP1

releases autoinhibition (Burkard et al., 2009; Gómez-Cavazos et al., 2020; Wolfe et al., 2009; Yüce et al., 2005). In ECT2$^{\Delta B1}$ cells, formation of large blebs was not elevated, and no RhoA accumulated at the cell equator. This demonstrates that BRCT1 is not involved in GEF inhibition. We further found that the BRCT1 bound strongly to RACGAP1; however, BRCT0 and BRCT2 also interacted and contributed to midzone targeting. Because no midzone localization of the BRCT1-deletion mutation was observed, BRCT0 and BRCT2 binding to RACGAP1 is not sufficient to bring ECT2 to the spindle midzone and release BRCT2-mediated autoinhibition. We speculate that binding of RACGAP1 to the BRCT domains has to occur in a sequential manner, so that first, BRCT1 binds, which in turn, enables binding of BRCT0 and BRCT2.

The last identified BRCT domain was the BRCT0 domain. Without the BRCT0 domain, ECT2 displays strongly reduced midzone localization, indicating that even when RACGAP1 binding is severely compromised, cytokinesis can be successful. We are convinced that the reduction in RhoA levels and the delay in furrow ingression in the BRCT0 mutation is not due to its reduced equatorial membrane enrichment because the ECT2^{TK} mutant showed a similar reduction at the equatorial membrane, but the RhoA zone was normal. Therefore, our data suggest that the BRCT0 domain directly contributes to the release of BRCT2-mediated inhibition. The BRCT0 could assist the BRCT1 domain, and/or phosphorylation of BRCT0 by Plk1 might weaken the interaction between the BRCT2 and GEF domain.

We found that Plk1 activity is not required for RhoA zone formation when BRCT2-mediated GEF inhibition is absent. This suggests that Plk1 acts upstream of the release of ECT2 autoinhibition, which is consistent with Plk1 phosphorylating RACGAP1 and thereby enhancing ECT2 binding (Burkard et al., 2009; Gómez-Cavazos et al., 2020; Wolfe et al., 2009; Yüce et al., 2005). We observed that the BRCT0 domain, and to a lesser extent the BRCT1 and BRCT2 domains, efficiently bound to the PBD of Plk1. The BRCT0 domain, but not the BRCT1 or BRCT2 domains, was also phosphorylated by Plk1. Based on that, we propose that Plk1 binding to the BRCT domains facilitates phosphorylation of RACGAP1 in close proximity to its binding partner ECT2 and thereby enhances complex formation. In addition, Plk1 binding to the BRCT domains, and in particular phosphorylation of BRCT0, could partially open up ECT2 to promote RACGAP1 binding. That BRCT0 takes part in releasing autoinhibition is also supported by our observation that, in BRCT0 mutants, equatorial RhoA levels are reduced. Partial release of ECT2 autoinhibition by Plk1 binding and/or phosphorylation could explain the fact that phosphomimetic RACGAP1 recruits only the N terminus of, but not the full length of, ECT2 to the midzone when Plk1 activity is inhibited (Wolfe et al., 2009).

In summary, our work provides mechanistic insights into how ECT2 activity is spatially and temporally regulated by the three N-terminal BRCT domains during cell division. Future studies will need to address how RACGAP1 binding to the BRCT domains releases the BRCT2-GEF interaction at the cell equator. ECT2 is an oncogene, and changes in ECT2 activity have been linked tightly to cancer development (Fields and Justilien, 2010); thus, understanding how ECT2 activity is controlled might pave the way for new therapeutic treatments.

STAR★METHODS

Detailed methods are provided in the online version of this paper and include the following:

- KEY RESOURCES TABLE
- RESOURCE AVAILABILITY
  - Lead contact
  - Materials availability
  - Data and code availability
- EXPERIMENTAL MODEL AND SUBJECT DETAILS
- METHOD DETAILS
  - Cloning of NG-ECT2 transgenes and protein expression constructs
  - siRNA transfections
  - Anillin antibody production
  - Immunostaining
  - Immunoblotting
  - Inhibition of Plk1 (BI2536), Rho (C3 exoenzyme), and RhoA kinase (Y27632)
  - MBP/6xHis-ECT2 fragments, GST-RACGAP1 and GST-PBD expression and purification
  - MBP/6xHis-ECT2 pulldown assays with GST-RACGAP1 or GST-PBD
  - Plk1 kinase assays
  - Microscopy and image acquisition
  - Microscopy image analyses and quantifications
- QUANTIFICATION AND STATISTICAL ANALYSIS

Cell Reports
Article

REFERENCES

Basant, A., and Glotzer, M. (2018). Spatiotemporal regulation of RhoA during cytokinesis. Curr. Biol. *28*, R570–R580.

Basant, A., Lekomtsev, S., Tse, Y.C., Zhang, D., Longhini, K.M., Petronczki, M., and Glotzer, M. (2015). Aurora B kinase promotes cytokinesis by inducing centralspindlin oligomers that associate with the plasma membrane. Dev. Cell *33*, 204–215.

Bement, W.M., Leda, M., Moe, A.M., Kita, A.M., Larson, M.E., Golding, A.E., Pfeuti, C., Su, K.-C., Miller, A.L., Goryachev, A.B., and von Dassow, G. (2015). Activator-inhibitor coupling between Rho signalling and actin assembly makes the cell cortex an excitable medium. Nat. Cell Biol. *17*, 1471–1483.

Brennan, I.M., Peters, U., Kapoor, T.M., and Straight, A.F. (2007). Polo-like kinase controls vertebrate spindle elongation and cytokinesis. PLoS ONE *2*, e409.

Bretz, F., Hothorn, T., and Westfall, P. (2010). Multiple Comparisons Using R, First Edition (CRC Press).

Burkard, M.E., Randall, C.L., Larochelle, S., Zhang, C., Shokat, K.M., Fisher, R.P., and Jallepalli, P.V. (2007). Chemical genetics reveals the requirement for Polo-like kinase 1 activity in positioning RhoA and triggering cytokinesis in human cells. Proc. Natl. Acad. Sci. USA *104*, 4383–4388.

Burkard, M.E., Maciejowski, J., Rodriguez-Bravo, V., Repka, M., Lowery, D.M., Clauser, K.R., Zhang, C., Shokat, K.M., Carr, S.A., Yaffe, M.B., and Jallepalli, P.V. (2009). Plk1 self-organization and priming phosphorylation of HsCYK-4 at the spindle midzone regulate the onset of division in human cells. PLoS Biol. *7*, e1000111–e1000116.

Chalamalasetty, R.B., Hümmer, S., Nigg, E.A., and Silljé, H.H.W. (2006). Influence of human Ect2 depletion and overexpression on cleavage furrow formation and abscission. J. Cell Sci. *119*, 3008–3019.

Chan, E., and Nance, J. (2013). Mechanisms of CDC-42 activation during contact-induced cell polarization. J. Cell Sci. *126*, 1692–1702.

Cheeseman, I.M., and Desai, A. (2005). A combined approach for the localization and tandem affinity purification of protein complexes from metazoans. Sci. STKE *2005*, pl1.

Chen, M., Pan, H., Sun, L., Shi, P., Zhang, Y., Li, L., Huang, Y., Chen, J., Jiang, P., Fang, X., et al. (2020). Structure and regulation of human epithelial cell transforming 2 protein. Proc. Natl. Acad. Sci. USA *117*, 1027–1035.

D'Avino, P.P., Giansanti, M.G., and Petronczki, M. (2015). Cytokinesis in animal cells. Cold Spring Harb. Perspect. Biol. *7*, a015834.

Dechant, R., and Glotzer, M. (2003). Centrosome separation and central spindle assembly act in redundant pathways that regulate microtubule density and trigger cleavage furrow formation. Dev. Cell *4*, 333–344.

Desai, A., Verma, S., Mitchison, T.J., and Walczak, C.E. (1999). Kin I kinesins are microtubule-destabilizing enzymes. Cell *96*, 69–78.

Fields, A.P., and Justilien, V. (2010). The guanine nucleotide exchange factor (GEF) Ect2 is an oncogene in human cancer. Adv. Enzyme Regul. *50*, 190–200.

Frenette, P., Haines, E., Loloyan, M., Kinal, M., Pakarian, P., and Piekny, A. (2012). An anillin-Ect2 complex stabilizes central spindle microtubules at the cortex during cytokinesis. PLoS ONE *7*, e0034888.

Gassmann, R., Holland, A.J., Varma, D., Wan, X., Civril, F., Cleveland, D.W., Oegema, K., Salmon, E.D., and Desai, A. (2010). Removal of spindly from microtubule-attached kinetochores controls spindle checkpoint silencing in human cells. Genes Dev. *24*, 957–971.

Gómez-Cavazos, J.S., Lee, K.-Y., Lara-González, P., Li, Y., Desai, A., Shiau, A.K., and Oegema, K. (2020). A non-canonical BRCT-phosphopeptide recognition mechanism underlies RhoA activation in cytokinesis. Curr. Biol. *30*, 3101–3115.e11.

Hara, T., Abe, M., Inoue, H., Yu, L.-R., Veenstra, T.D., Kang, Y.H., Lee, K.S., and Miki, T. (2006). Cytokinesis regulator ECT2 changes its conformation through phosphorylation at Thr-341 in G2/M phase. Oncogene *25*, 566–578.

Hedrick, D.G., Stout, J.R., and Walczak, C.E. (2008). Effects of anti-microtubule agents on microtubule organization in cells lacking the kinesin-13 MCAK. Cell Cycle *7*, 2146–2156.

Hickson, G.R.X., Echard, A., and O'Farrell, P.H. (2006). Rho-kinase controls cell shape changes during cytokinesis. Curr. Biol. *16*, 359–370.

Hofweber, M., Hutten, S., Bourgeois, B., Spreitzer, E., Niedner-Boblenz, A., Schifferer, M., Ruepp, M.-D., Simons, M., Niessing, D., Madl, T., and Dormann, D. (2018). Phase separation of FUS is suppressed by its nuclear import receptor and arginine methylation. Cell *173*, 706–719.e13.

Holder, J., Poser, E., and Barr, F.A. (2019). Getting out of mitosis: spatial and temporal control of mitotic exit and cytokinesis by PP1 and PP2A. FEBS Lett. *593*, 2908–2924.

Hothorn, T., Bretz, F., and Westfall, P. (2008). Simultaneous inference in general parametric models. Biom. J. *50*, 346–363.

Hu, C.-K., Coughlin, M., and Mitchison, T.J. (2012). Midbody assembly and its regulation during cytokinesis. Mol. Biol. Cell *23*, 1024–1034.

Kim, J.-E., Billadeau, D.D., and Chen, J. (2005). The tandem BRCT domains of Ect2 are required for both negative and positive regulation of Ect2 in cytokinesis. J. Biol. Chem. *280*, 5733–5739.

Kosako, H., Yoshida, T., Matsumura, F., Ishizaki, T., Narumiya, S., and Inagaki, M. (2000). Rho-kinase/ROCK is involved in cytokinesis through the phosphorylation of myosin light chain and not ezrin/radixin/moesin proteins at the cleavage furrow. Oncogene *19*, 6059–6064.

Kotýnková, K., Su, K.-C., West, S.C., and Petronczki, M. (2016). Plasma membrane association but not midzone recruitment of rhoGEF ECT2 is essential for cytokinesis. Cell Rep. *17*, 2672–2686.

Lens, S.M.A., and Medema, R.H. (2019). Cytokinesis defects and cancer. Nat. Rev. Cancer *19*, 32–45.

Mangal, S., Sacher, J., Kim, T., Osório, D.S., Motegi, F., Carvalho, A.X., Oegema, K., and Zanin, E. (2018). TPXL-1 activates Aurora A to clear contractile ring components from the polar cortex during cytokinesis. J. Cell Biol. *217*, 837–848.

Martino, L., Morchoisne-Bolhy, S., Cheerambathur, D.K., Van Hove, L., Dumont, J., Joly, N., Desai, A., Doye, V., and Pintard, L. (2017). Channel nucleoporins recruit PLK-1 to nuclear pore complexes to direct nuclear envelope breakdown in *C. elegans*. Dev. Cell *43*, 157–171.e7.

Matthews, H.K., Delabre, U., Rohn, J.L., Guck, J., Kunda, P., and Baum, B. (2012). Changes in Ect2 localization couple actomyosin-dependent cell shape changes to mitotic progression. Dev. Cell *23*, 371–383.

Mierzwa, B., and Gerlich, D.W. (2014). Cytokinetic abscission: molecular mechanisms and temporal control. Dev. Cell *31*, 525–538.

Mishima, M. (2016). Centralspindlin in Rappaport's cleavage signaling. Semin. Cell Dev. Biol. *53*, 45–56.

Mishima, M., Kaitna, S., and Glotzer, M. (2002). Central spindle assembly and cytokinesis require a kinesin-like protein/RhoGAP complex with microtubule bundling activity. Dev. Cell *2*, 41–54.

Murthy, K., and Wadsworth, P. (2008). Dual role for microtubules in regulating cortical contractility during cytokinesis. J. Cell Sci. *121*, 2350–2359.

Niiya, F., Tatsumoto, T., Lee, K.S., and Miki, T. (2006). Phosphorylation of the cytokinesis regulator ECT2 at G2/M phase stimulates association of the mitotic kinase Plk1 and accumulation of GTP-bound RhoA. Oncogene *25*, 827–837.

Petronczki, M., Glotzer, M., Kraut, N., and Peters, J.-M. (2007). Polo-like kinase 1 triggers the initiation of cytokinesis in human cells by promoting recruitment of the RhoGEF Ect2 to the central spindle. Dev. Cell *12*, 713–725.

Piekny, A.J., and Glotzer, M. (2008). Anillin is a scaffold protein that links RhoA, actin, and myosin during cytokinesis. Curr. Biol. *18*, 30–36.

Pollard, T.D., and O'Shaughnessy, B. (2019). Molecular mechanism of cytokinesis. Annu. Rev. Biochem. *88*, 661–689.

Prokopenko, S.N., Brumby, A., O'Keefe, L., Prior, L., He, Y., Saint, R., and Bellen, H.J. (1999). A putative exchange factor for Rho1 GTPase is required for initiation of cytokinesis in *Drosophila*. Genes Dev. *13*, 2301–2314.

Rankin, K.E., and Wordeman, L. (2010). Long astral microtubules uncouple mitotic spindles from the cytokinetic furrow. J. Cell Biol. *190*, 35–43.

R Development Core Team. (2015). R: A Language and Environment for Statistical Computing. (R Foundation for Statistical Computing).

Rodrigues, N.T.L., Lekomtsev, S., Jananji, S., Kriston-Vizi, J., Hickson, G.R.X., and Baum, B. (2015). Kinetochore-localized PP1-Sds22 couples chromosome segregation to polar relaxation. Nature *524*, 489–492.

Saito, S., Liu, X.-F., Kamijo, K., Raziuddin, R., Tatsumoto, T., Okamoto, I., Chen, X., Lee, C.-C., Lorenzi, M.V., Ohara, N., and Miki, T. (2004). Deregulation and mislocalization of the cytokinesis regulator ECT2 activate the Rho signaling pathways leading to malignant transformation. J. Biol. Chem. *279*, 7169–7179.

Santamaria, A., Neef, R., Eberspächer, U., Eis, K., Husemann, M., Mumberg, D., Prechtl, S., Schulze, V., Siemeister, G., Wortmann, L., et al. (2007). Use of the novel Plk1 inhibitor ZK-thiazolidinone to elucidate functions of Plk1 in early and late stages of mitosis. Mol. Biol. Cell *18*, 4024–4036.

Schindelin, J., Arganda-Carreras, I., Frise, E., Kaynig, V., Longair, M., Pietzsch, T., Preibisch, S., Rueden, C., Saalfeld, S., Schmid, B., et al. (2012). Fiji: an open-source platform for biological-image analysis. Nat. Methods *9*, 676–682.

Sedzinski, J., Biro, M., Oswald, A., Tinevez, J.-Y., Salbreux, G., and Paluch, E. (2011). Polar actomyosin contractility destabilizes the position of the cytokinetic furrow. Nature *476*, 462–466.

Sheng, Z.-Z., Zhao, Y.-Q., and Huang, J.-F. (2011). Functional evolution of BRCT domains from binding DNA to protein. Evol. Bioinform. Online *7*, 87–97.

Simon, G.C., Schonteich, E., Wu, C.C., Piekny, A., Ekiert, D., Yu, X., Gould, G.W., Glotzer, M., and Prekeris, R. (2008). Sequential Cyk-4 binding to ECT2 and FIP3 regulates cleavage furrow ingression and abscission during cytokinesis. EMBO J. *27*, 1791–1803.

Solski, P.A., Wilder, R.S., Rossman, K.L., Sondek, J., Cox, A.D., Campbell, S.L., and Der, C.J. (2004). Requirement for C-terminal sequences in regulation of Ect2 guanine nucleotide exchange specificity and transformation. J. Biol. Chem. *279*, 25226–25233.

Somers, W.G., and Saint, R. (2003). A RhoGEF and Rho family GTPase-activating protein complex links the contractile ring to cortical microtubules at the onset of cytokinesis. Dev. Cell *4*, 29–39.

Su, K.-C., Takaki, T., and Petronczki, M. (2011). Targeting of the RhoGEF Ect2 to the equatorial membrane controls cleavage furrow formation during cytokinesis. Dev. Cell *21*, 1104–1115.

Su, K.-C., Bement, W.M., Petronczki, M., and von Dassow, G. (2014). An astral simulacrum of the central spindle accounts for normal, spindle-less, and anucleate cytokinesis in echinoderm embryos. Mol. Biol. Cell *25*, 4049–4062.

Sun, L., Guan, R., Lee, I.-J., Liu, Y., Chen, M., Wang, J., Wu, J.-Q., and Chen, Z. (2015). Mechanistic insights into the anchorage of the contractile ring by anillin and Mid1. Dev. Cell *33*, 413–426.

Taneja, N., and Burnette, D.T. (2019). Myosin IIA drives membrane bleb retraction. Mol. Biol. Cell *30*, 1051–1059.

Tatsumoto, T., Xie, X., Blumenthal, R., Okamoto, I., and Miki, T. (1999). Human ECT2 is an exchange factor for Rho GTPases, phosphorylated in G2/M phases, and involved in cytokinesis. J. Cell Biol. *147*, 921–928.

Tighe, A., Johnson, V.L., and Taylor, S.S. (2004). Truncating APC mutations have dominant effects on proliferation, spindle checkpoint control, survival and chromosome stability. J. Cell Sci. *117*, 6339–6353.

Tinevez, J.Y., Schulze, U., Salbreux, G., Roensch, J., Joanny, J.F., and Paluch, E. (2009). Role of cortical tension in bleb growth. Proc. Natl. Acad. Sci. USA *106*, 18581–18586.

Tokumitsu, T., and Maramorosch, K. (1967). Cytoplasmic protrusions in insect cells during mitosis in vitro. J. Cell Biol. *34*, 677–683.

van Oostende Triplet, C., Jaramillo Garcia, M., Haji Bik, H., Beaudet, D., and Piekny, A. (2014). Anillin interacts with microtubules and is part of the astral pathway that defines cortical domains. J. Cell Sci. *127*, 3699–3710.

von Dassow, G. (2009). Concurrent cues for cytokinetic furrow induction in animal cells. Trends Cell Biol. *19*, 165–173.

Wagner, E., and Glotzer, M. (2016). Local RhoA activation induces cytokinetic furrows independent of spindle position and cell cycle stage. J. Cell Biol. *213*, 641–649.

Wolfe, B.A., Takaki, T., Petronczki, M., and Glotzer, M. (2009). Polo-like kinase 1 directs assembly of the HsCyk-4 RhoGAP/Ect2 RhoGEF complex to initiate cleavage furrow formation. PLoS Biol. *7*, e1000110–e1000115.

Yonemura, S., Hirao-Minakuchi, K., and Nishimura, Y. (2004). Rho localization in cells and tissues. Exp. Cell Res. *295*, 300–314.

Yüce, O., Piekny, A., and Glotzer, M. (2005). An ECT2-centralspindlin complex regulates the localization and function of RhoA. J. Cell Biol. *170*, 571–582.

Zanin, E., Desai, A., Poser, I., Toyoda, Y., Andree, C., Moebius, C., Bickle, M., Conradt, B., Piekny, A., and Oegema, K. (2013). A conserved RhoGAP limits M phase contractility and coordinates with microtubule asters to confine RhoA during cytokinesis. Dev. Cell *26*, 496–510.

Zhang, D., and Glotzer, M. (2015). The RhoGAP activity of CYK-4/MgcRacGAP functions non-canonically by promoting RhoA activation during cytokinesis. eLife *4*, e08898.

Zhao, W.-M., and Fang, G. (2005). MgcRacGAP controls the assembly of the contractile ring and the initiation of cytokinesis. Proc. Natl. Acad. Sci. USA *102*, 13158–13163.

Zou, Y., Shao, Z., Peng, J., Li, F., Gong, D., Wang, C., Zuo, X., Zhang, Z., Wu, J., Shi, Y., and Gong, Q. (2014). Crystal structure of triple-BRCT-domain of ECT2 and insights into the binding characteristics to CYK-4. FEBS Lett. *588*, 2911–2920.

STAR★METHODS

KEY RESOURCES TABLE

REAGENT or RESOURCE	SOURCE	IDENTIFIER
Antibodies		
Rabbit polyclonal anti-Anillin	This study	N/A
Mouse monoclonal anti-Tubulin (clone DM1A)	Sigma-Aldrich	Cat# T6199, RRID:AB_477583
Mouse monoclonal anti-RhoA (26C4)	Santa Cruz Biotechnology	Cat# sc-418, RRID:AB_628218
Mouse monoclonal anti-ECT2 (G4)	Santa Cruz Biotechnology	Cat# Sc-514750
Mouse monoclonal anti 6x-His	Thermo Scientific	Cat# MA1-135, RRID:AB_2536841
Goat Anti-Mouse IgG (HL)-HRP Conjugate antibody	Bio-Rad	Cat# 170-6516, RRID:AB_11125547
Alexa Fluor^{TM} 635 goat anti-mouse	Life Technologies	Cat# A31574, RRID:AB_1500640
Alexa Fluor^{TM} 568 donkey anti-rabbit	Life Technologies	Cat# A10042, RRID:AB_2534017
Bacterial and virus strains		
DH5α	Thermo Scientific	Cat # 18265017
BL21(DE3)	N/A	N/A
Chemicals and recombinant proteins		
BI2536 PLK1-Inhibitor	Selleckchem	Cat# S1109
Y27632 ROCK-Inhibitor	VWR	Cat# CAYM10005583-1
C3 coenzyme	tebu-bio	Cat# CT04-A
PLK1 Recombinant Human Protein	Thermo Scientific	Cat# PV3501
[gamma-P32]ATP, 800 Ci/mmol,10mCi/ml	Hartmann Analytic	Cat# SRP-801
X-tremeGene9	Sigma-Aldrich	Cat# 8079398949
Lipofectamine^{TM} RNAiMAX	Thermo Fischer	Cat# 13778075
SuperSignal^{TM} West Femto Maximum Sensitivity	Thermo Scientific	Cat# 34094
ECL^{TM} Western Blotting Reagents	GE Healthcare	Cat# RPN2106
ECL^{TM} Prime Western Blotting	GE Healthcare	Cat# RPN22236
cOmplete Protease inihibitor cocktail	Roche	Cat# 11836153001
Glutathione Sepharose	Sigma	Cat# GE17-0756-01
PMSF	Sigma	Cat# P7626-1G
Amylose resin	NEB	Cat# E8021S
Experimental models: cell lines		
Host cell line: HeLa Flp-In T-Rex	Tighe et al., 2004	N/A
NG-ECT2^{WT}	This study	EZ69
NG-ECT2$^{\Delta BRCT0}$ (ΔAA 1-138)	This study	EZ70
NG-ECT2$^{\Delta BRCT0-2}$ (ΔAA 1-327)	This study	EZ72
NG-ECT2$^{\Delta BRCT2}$ (ΔAA 238-327)	This study	EZ74
NG-ECT2$^{\Delta BRCT1}$ (ΔAA 139-237)	This study	EZ76
NG-ECT2$^{T153A/K195M}$	This study	EZ80
NG-ECT2$^{\Delta BRCT1}$ FACS EZ76: clone C8	This study	EZ104
NG-ECT2$^{\Delta BRCT1}$ FACS EZ76: clone B10	This study	EZ107
NG-ECT2^{W307A}	This study	EZ119

Continued

REAGENT or RESOURCE	SOURCE	IDENTIFIER
Oligonucleotides		
siRNA targeting sequence ECT2 GGCGGAAUGAACAGGAUUU	Dharmacon	N/A
siRNA targeting sequence MCAK GCAGGCUAGCAGACAAAUAUU	Dharmacon	N/A
ON-TARGET *plus* Non-targeting siRNA #1	Dharmacon	D-001810-01-20
Recombinant DNA		
pcDNA5/FRT/TO, CMV promoter	Cheeseman and Desai, 2005	N/A
NG-ECT2^{WT}	This study	pEZ197
NG-ECT2$^{\Delta BRCT0}$	This study	pEZ227
NG-ECT2$^{\Delta BRCT0-2}$	This study	pEZ204
NG-ECT2$^{\Delta BRCT2}$	This study	pEZ232
NG-ECT2$^{\Delta BRCT1}$	This study	pEZ242
NG-ECT2$^{T153A/K195M}$	This study	pEZ247
NG-ECT2^{W307A}	This study	pEZ313
mNeonGreen	Allele Biotechnologie	N/A
pGEX-4T	GE Healthcare	Cat#GE28-9545-49
pGST-4T-RACGAP1 (AA 1-288)	This study	pEZ336
pGST-4T-anillin (AA 417-687)	This study	pEZ154
pGEX-6P-1 PBD	Martino et al., 2017	N/A
MBP/6xHis	Hofweber et al., 2018	N/A
pMBP/6xHis-B0-S-loop (AA 1-421)	This study	pEZ330
MBP/6xHis-B0-2 (AA 1-324)	This study	pEZ335
MBP/6xHis-B0 (AA 1-136)	This study	pEZ340
MBP/6xHis-B2 (AA 238-324)	This study	pEZ334
MBP/6xHis-B1+2 (AA 137-324)	This study	pEZ331
MBP/6xHis-B1 (AA 137-237)	This study	pEZ332
MBP/6xHis-B0+1 (AA 1-237)	This study	pEZ338
Software and algorithms		
ImageJ	NIH	https://imagej.nih.gov
Prism	GraphPad	https://www.graphpad.com
R Development Core Team, 2015	R studio	https://www.rstudio.com
Image Lab v. 5.2.1. build 11	Bio-Rad	https://www.bio-rad.com
Knime 4.2.1.	N/A	https://www.knime.com

RESOURCE AVAILABILITY

Lead contact
Further information and requests for resources and reagents should be directed to and will be fulfilled by the Lead Contact, Esther Zanin (zanin@bio.lmu.de).

Materials availability
New plasmids and cell lines generated in this study are available upon request via the lead contact.

Data and code availability
Primary data associated with the paper is available upon reasonable request.

EXPERIMENTAL MODEL AND SUBJECT DETAILS

HeLa Flp-In T-Rex cells were grown at 37°C in 5% CO_2 in Dulbecco's growth medium (DMEM, Thermo Scientific, 61965059), with 10% FBS (Thermo Scientific, 10270106), and with 1% penicillin/streptomycin (PS, Merck, A2213). Isogenic cell lines harboring stable

integrations of RNAi resistant NG-tagged ECT2 transgenes were obtained by FRT/Flp-mediated recombination (Gassmann et al., 2010; Tighe et al., 2004). This system allows us to express at native levels specifically engineered RNAi-resistant NG-tagged ECT2 mutants controlled by an inducible promoter, after depleting endogenous ECT2 by RNAi. To generate stable cell lines, the vectors pOG44 and pcDNA5/FRT/TO (Invitrogen) (Cheeseman and Desai, 2005; Gassmann et al., 2010) containing different ECT2 transgenes tagged with NeonGreen at the N terminus were transfected in the Flp-In T-Rex host cell line using X-tremeGene9 (Sigma Aldrich, 8079398949). Transfected cells were cultured in DMEM containing 10% FBS, 1% PS, 0.2 mg/ml hygromycin for 2-3 weeks and colonies were pooled together. Throughout all experiments 0.2 µg/ml tetracycline was present to induce ECT2 trans-gene expression. Two independent integrations of ECT2$^{\Delta B1}$ showed reduced expression levels (not shown). Therefore, two clones were identified by fluorescence activated cell sorting (FACS) that expressed ECT2$^{\Delta B1}$ similarly to endogenous ECT2. In all experiments the two ECT2$^{\Delta B1}$ FACS clones gave similar results and therefore their data were pooled in the figures.

METHOD DETAILS

Cloning of NG-ECT2 transgenes and protein expression constructs

The cDNA of human ECT2 (NP_001245245.1) was amplified from a human cDNA library and cloned together with mNeonGreen (Allele Biotechnology) into the pcDNA5/FRT/TO vector with Gibson assembly (NEB, E2611). ECT2 was rendered RNAi resistant by introducing 4 silent mutations (GG<u>A</u>GGAAC<u>C</u>GAGCA<u>A</u>GAT) in the siRNA recognition site by side-directed mutagenesis. All ECT2 deletion mutant variants were cloned by Gibson assembly and point mutations (T153A/K195M, W307A) were introduced by side-directed mutagenesis.

For the pulldown and kinase assays PCR amplified human ECT2 fragments were cloned with XhoI into the pMal-Tev-Flag-Tev-6xHis (MBP/6xHis, Hofweber et al., 2018). The human N-terminal RACGAP1 (AA 1-288) and anillin (AA 417-687) fragments were amplified by PCR and cloned into pGEX-4T with Gibson assembly.

siRNA transfections

The phenotype of ECT2^{WT} and the various ECT2 mutant proteins was determined after depleting endogenous ECT2 by RNAi unless indicated otherwise. One day prior to siRNA transfection cells were plated in 12 well plates with DMEM (10%FBS, 0.2 µg/ml tetracycline) at approximately 30% confluency. For immunofluorescence, cells were seeded on 18 mm poly-L-lysine (Y1251-100G, Sigma) coated glass coverslips (P233.1, Menzel). Next day, cells were transfected with a final concentration of 30 nM ECT2 siRNA oligo (GGCGGAAUGAA CAGGAUUU, Dharmacon, (Yüce et al., 2005)) using Lipofectamine RNAiMAX (13778075, Thermo Fischer). For depletion of MCAK, cells were transfected with a final concentration of 30 nM MCAK (GCAGG-CUAGCAGACAAAUAUU, Dharmacon (Rankin and Wordeman, 2010)) and 30 nM control siRNA oligos 3 hr before the transfection with ECT2 siRNA oligo. As a control 30 nM non-targeting siRNA (D-001810-01-20, Dharmacon) was used. 18-20 hr after siRNA transfection fresh medium containing 0.5 mM thymidine (T1895, Sigma) and 0.2 µg/ml tetracycline was added to synchronize the cell cycle. For live-cell imaging cells were simultaneously passaged into ibidiTreat chambers (80426, Ibidi). After 22-24 hr incubation, cells were released from the thymidine block by washing 3x for 5 min with DMEM (10% FBS, 0.2 µg/ml tetracycline). 8-9 hr after the thymidine release live-cell imaging was started or cells were fixed for immunofluorescence of anaphase cells. To count the number of mono-, bi- and multinucleated cells, cells were fixed and stained for α-tubulin and Hoechst 23-25 hr after the thymidine release.

Anillin antibody production

Polyclonal antibodies against human anillin were generated against the GST-tagged anillin fragment (AA 417-687; Piekny and Glotzer, 2008). GST-Anillin was expressed in BL21(DE3) *E. coli* for 4 hr at 37°C, purified over a glutathione-Sepharose column and used to immunize rabbits (Davids Biotechnology GmbH). After depleting GST antibodies from the obtained serum, the anillin antibodies were purified with GST-Anillin-coupled SulfoLink resin. Antibodies that were bound to the SulfoLink resin were eluted in 0.2 M glycine pH 2.5 and immediately neutralized by 1 M TrisHCl pH 8.5. The obtained antibodies were concentrated and the buffer was exchanged to 1x Phosphate Buffered Saline (PBS) using Pierce Protein Concentrator (10K MWCO; Life Technologies, 88527). Specificity of the anillin antibody was verified by the absence of immunostaining after anillin depletion with RNAi.

Immunostaining

For anillin and RhoA stainings cells were fixed in ice-cold 10% TCA (Merck, 1008070100) for 15 min on ice (Yonemura et al., 2004). After fixation cells were washed in 1x PBS and incubated with blocking solution (1x PBS, 4% BSA, 0.1% Triton) for 1 hr at room temperature (RT). As primary antibodies anti-anillin (1:3000, self-made) and anti-RhoA (1:25, 26C4, Santa Cruz) were diluted in blocking solution and incubated for 2 hr at RT. Coverslips were washed 3x 5 min in 1x PBS (0.1% Triton) and incubated with Alexa Fluor^{TM} 568 donkey anti-rabbit (1:500, A10042, Life Technologies) and Alexa Fluor^{TM} 635 goat anti-mouse (1:500, A31574, Life Technologies), and Hoechst 33258 (861405; Sigma-Aldrich) in blocking solution for 1 hr at RT. Coverslips were washed 3x 5 min in 1x PBS (0.1% Triton) and covered with mounting medium (1x PBS, 4% n-Propyl-Gallate, 90% Glycerol).

For α-tubulin stainings (Figure S5A) coverslips were washed once with 1x PBS, fixed in ice-cold methanol for 5 min and incubated in blocking solution for 1 hr at RT. The anti α-tubulin (1:500, T6199, Sigma) antibody was incubated for 2 hr at RT in blocking solution.

After primary antibody incubation, coverslips were treated as described above and subsequently incubated with Alexa Fluor[TM] 635 goat anti-mouse and Hoechst 33258.

For MCAK depletion α-tubulin stainings (Figure 7A) were performed by washing coverslips once with 1x PBS and fixing in 1x PBS containing 0.5% glutaraldehyde (340855, Sigma), 0.5% Triton for 10 min at RT. After fixation coverslips were washed 3x 10 min with freshly made 1x PBS containing 0.1% NaBH$_4$ (806373, Merck) at RT. Cells were washed once with 1x PBS, blocked and stained for α-tubulin and DNA as described above.

Immunoblotting

For immunoblotting cell lines were seeded in 6-well plates, transfected with ECT2 siRNA, and synchronized with single thymidine block as described above. Cells were collected 8-9 hr after thymidine release. Samples were heated at 95°C for 5 min and sonicated in a water bath for 20 min. As primary antibodies mouse anti α-tubulin (1:10 000, T6199, Sigma) and mouse anti-ECT2 (1:250, sc-514750, Santa Cruz) were used; and as secondary antibody HRP-conjugated mouse (1:3000 for ECT2, 1:20 000 for α-tubulin, 170-6516; Bio-Rad). For immunoblotting pulldown experiments membranes were incubated with anti-6xHis (1:10 000, MA1-135, Thermo Scientific) at 4°C over night. After washing, membranes were incubated with HRP-conjugated mouse (1:10 000, 170-6516; Bio-Rad) for 1 hr at RT. Membranes were developed with SuperSignal[TM] West Femto (34094, Thermo Scientific) for the anti-ECT2 antibody, ECL[TM] Western Blotting (GE Healthcare, RPN2106) for the anti-α-tubulin, and ECL[TM] Prime Western Blotting (GE Healthcare, RPN22236) for the anti-6xHis antibody.

Expression levels of the endogenous and different NG-tagged ECT2 proteins were quantified by measuring the intensities of the ECT2 and α-tubulin bands using the Image Lab software (v.5.2.1. build 11, Bio-Rad). NG-tagged and endogenous ECT2 levels were first normalized to α-tubulin levels and subsequently the levels of NG-tagged ECT2 variants relative to endogenous ECT2 were calculated.

Inhibition of Plk1 (BI2536), Rho (C3 exoenzyme), and RhoA kinase (Y27632)

Stock solutions for Plk1 inhibitor BI2536 (Selleckchem, S1109) and Y27632 (VWR, CAYM10005583-1) were made in DMSO and C3 transferase (CT04-A, Tebu Bio) in H$_2$O. BI2536 was used at a final concentration of 100 nM. For immunostaining cells were synchronized with a single thymidine block and 8 hr after release they were treated for 40-50 min with 100 nM BI2536. For live-cell imaging, image acquisition of metaphase and early anaphase cell was started ∼15 min after adding BI2536. To inhibit RhoA, cells were treated for 6 hr with DMEM (without FBS) containing 0.5 μg/ml C3 transferase. For control cells medium was exchanged to DMEM without FBS. For inhibition of RhoA kinase, cells were incubated with full medium supplemented with 10 μM Y27632 for 1 hr.

MBP/6xHis-ECT2 fragments, GST-RACGAP1 and GST-PBD expression and purification

All GST-tagged and MBP/6xHis-tagged proteins were expressed in 1 L BL21(DE3) cultures. Protein expression was induced at an OD$_{600}$ of 0.4-0.8. for either 3 hr at 37°C with 1 mM IPTG (pGEX-4T, pGEX-6P-1 PBD) (Martino et al., 2017), 5 hr at 25°C with 0.1 mM IPTG (pGST-RACGAP1) (Gómez-Cavazos et al., 2020), or 3 hr at 25°C with 0.3 mM IPTG (pMBP/6xHis, pMBP/6xHis-ECT2 fragments). After harvesting, bacterial pellets were washed once with cold 1x PBS and snap frozen in liquid N$_2$. Pellets were resuspended in lysis buffer (10 mM Tris pH 8, 150 mM NaCl, 1 mM EDTA, 0.05% NP-40), that was supplemented with 5 mM DTT (Roth, 6908,3), 1 mM PMSF (Sigma, P7626-1G) and cOmplete protease inhibitor cocktail (Roche, 11836153001). Bacteria were lysed by sonification and cleared lysates were incubated with glutathione Sepharose (Sigma, GE17-0756-01) for 1.5 h at 4°C. The glutathione Sepharose was washed 3x with ∼30x bed volumes lysis buffer containing 5 mM DTT and 1 mM PMSF and stored at 4°C.

MBP/6xHis-ECT2 bacteria pellets were washed once and resuspended in MBP buffer (20 mM Tris pH 7.4, 200 mM NaCl, 1 mM EDTA), snap frozen in liquid N$_2$ and stored at −80°C. During thawing bacterial solutions were supplemented with 1 mM DTT, 1 mM PMSF, and cOmplete protease inhibitor cocktail. After sonification, 1% Triton X-100 was added and the lysates were rotated for 20 min at 4°C. The cleared lysates were added to packed amylose resin (NEB, E8021S) columns and incubated for 15 min at 4°C. The amylose resin was washed with ∼5 bed volumes washing buffer (20 mM Tris pH 7.4, 800 mM NaCl, 1 mM EDTA), proteins were eluted with ∼5 bed volumes elution buffer (20 mM Tris pH 7.4, 200 mM NaCl, 1 mM EDTA, 20 mM Maltose), flash frozen in liquid N$_2$ and stored at −80°C.

MBP/6xHis-ECT2 pulldown assays with GST-RACGAP1 or GST-PBD

For pulldown assays purified GST-RACGAP1 or GST-PBD beads were mixed with purified MBP/6xHis-ECT2 fragments in a total volume of 300 μl binding buffer (20 mM HEPES pH 7.2, 150 mM NaCl, 5 mM MgCl2, 0.1% Triton X-100, 1 mM DTT) and with ∼2 μM final concentration for each protein. Samples were rotated at 4°C for 1 hr. Beads were washed 3x 5 min in binding buffer and resuspended in 2x sample buffer (0.1 M Tris, 4% SDS, 1.4% β-mercaptoethanol, 20% glycerol, 1% Bromophenol blue). Samples were run on a SDS-PAGE and either stained with Coomassie or detected by immunoblotting with anti-6xHis antibody in cases where the MBP/6xHis-ECT2 fragments had a similar molecular weight as GST-RACGAP1 or GST-PBD.

Plk1 kinase assays

PLK1 kinase assays were performed in kinase buffer (25 mM HEPES pH 7.5, 50 mM NaCl, 10 mM MgCl$_2$, 0.1% Triton X-100 and 1 mM DTT [Gómez-Cavazos et al., 2020]) containing ∼300 ng MBP/6xHis-tagged ECT2 fragments or MBP/6xHis protein and

~200 ng recombinant human PLK1 kinase (Thermo Scientific, PV3501), 1µCi of [gamma-P32]ATP (Hartmann Analytic, SRP-801) and 0.2 mM rATP (N10015, Metabion) with a final volume of 20 µl. The kinase reaction was incubated at 30°C for 30 min and it was terminated by the addition of 2x sample buffer. Samples were heated to 95°C for 5 min and then separated by a SDS-PAGE. The SDS-Gel was stained with Coomassie blue (B0149, Sigma) and dried prior to autoradiography.

Microscopy and image acquisition

For live-cell imaging cells were plated in ibidiTreat chambers one day before filming and incubated in medium containing 100 nM SiR-DNA (251SC007, Tebu Bio) for 60-90 min prior to image acquisition. Imaging was performed at 37°C in a heated-chamber and cells were maintained in CO_2-independent medium (18045054, Thermo Fischer) complemented with: 10% FBS, 1% P/S, 0.2 µg/ml tetracycline, 2 mM L-Glutamine. Fixed interphase cells (Figure 1C), transmission, SiR-DNA, and NG-ECT2 live-cell images were acquired on a Nikon eclipse Ti spinning disk confocal microscope. The Nikon was controlled by NIS Elements 4.51 and was equipped with a 60x Apo TIRF oil immersion DIC N2, a 40x Apo LWD WI λS DIC N2 objective, a 405-, a 488-, a 640-nm laser line, and an Andor DU-888 X-11056 camera (1,024 × 1,024 pixels). All other immunofluorescence images were acquired on an UltraVIEW VoX spinning disk confocal microscope (PerkinElmer), which was controlled by Volocity 6.1.1. software (PerkinElmer) and mounted on an Axio Observer D1 stand (Zeiss). The UltraVIEW VoX was equipped with a 63x and 100x 1.4-NA Plan-Apochromat oil immersion objective (Zeiss), EMCCD C9100-50 camera (Hamamatsu) and 405-, 488-, 561-, and 640-nm lasers.

Microscopy image analyses and quantifications

To determine the number of blebs per cell during mitosis, measure equatorial cell width, and determine NG-ECT2 localization during anaphase, images were acquired every 3 min in 5 z-planes. Cell width at the cell equator was measured on transmission or NG-ECT2 images 12 min after anaphase onset. Using the time-lapse movies blebs were manually grouped into two categories based on their maximum bleb length: medium sized blebs were ~2 – 6 µm (Figure S7B) and large blebs were > 6 µm (e.g., Figures 1F and 1H) in length. To measure the maximum length and duration of the blebs, transmission images were acquired every 30 s in 15 z-planes (Figures 3D, 3E, and S2C). For these measurements blebs were chosen, which were clearly visible during their entire lifetime and irrespective of their size. The length and width of the blebs were measured at the time of their maximal extension. Bleb duration was defined as the time between their first emergence from the cell body till their complete absorption. The positions of the large blebs around the cell (Figures 3C and S2B) were determined on z stacks of RhoA stained anaphase cells.

All fluorescence intensity measurements were performed on raw images in Fiji (Schindelin et al., 2012). To measure RhoA or anillin fluorescence intensity a 6 pixel wide line was drawn around the cell periphery starting at one pole of anaphase cells. From the cortical RhoA or anillin fluorescence intensity the corresponding cytoplasmic fluorescence intensity, which was measured in a small box adjacent to the cell pole, was subtracted. Fluorescence intensity files of each cell were imported into KNIME (https://www.knime.com) and the mean equatorial intensity, the zone width, and total amount of anillin were calculated for each cell. The equatorial fluorescence intensity represents the mean equatorial RhoA or anillin fluorescence intensity at 20%–30% and 70%–80% of line scan length. To measure the width of the RhoA or anillin zone the running averages were calculated to smooth the curve. Zone widths were calculated at the half maximum fluorescence intensity for each zone at the cell equator. The total amount of RhoA or anillin in their zones were calculated by summing up the fluorescence intensity within the respective zone.

NG-ECT2 fluorescence intensity was measured 9 min after anaphase onset by drawing a line scan centered at the cell equator (Figure 2C). With this line scan the midzone and equatorial membrane peaks of ECT2 could be clearly assigned. In addition, two line scans were drawn across the poles of the cells avoiding blebs and their mean intensity was calculated. From each fluorescence intensity value the mean background intensity, which was measured in a small box outside the cell, was subtracted. The mean NG-ECT2 cytoplasmic intensity was calculated 4 pixels away from the polar membrane peak. The normalized equator and polar membrane fluorescence intensities (Figure 2D) were calculated by dividing the peak polar and equator membrane intensities by the mean cytoplasmic intensity for each cell. For the equator / pole ratio (Figure 2F) the normalized equator intensities were divided by the normalized polar membrane intensities. To calculate the midzone fluorescence intensity (Figure 2E) the mean intensity of the ten brightest midzone pixels was calculated and normalized to the cytoplasmic intensity for each cell.

QUANTIFICATION AND STATISTICAL ANALYSIS

The statistical analyses were performed using the software R (R Development Core Team, 2015) and the package multcomp (Hothorn et al., 2008). Data were tested for normal distribution using the Shapiro-Wilk test. Datasets with two conditions with normal distribution were analyzed by Student's t test and non-normally distributed data with Kruskal Wallis Rank sum test. For data with multiple conditions and non-normal distribution generalized linear models (GLM) were fitted and an ANOVA was performed. Subsequently, p values were calculated by multiple comparison tests after Tukey according to the method by Westfall (Bretz et al., 2010). Which statistical test was used is indicated in the figure legends.

Supplemental information

The BRCT domains of ECT2 have

distinct functions during cytokinesis

Sandra Schneid, Friederike Wolff, Kristina Buchner, Nils Bertram, Seren Baygün, Pedro Barbosa, Sriyash Mangal, and Esther Zanin
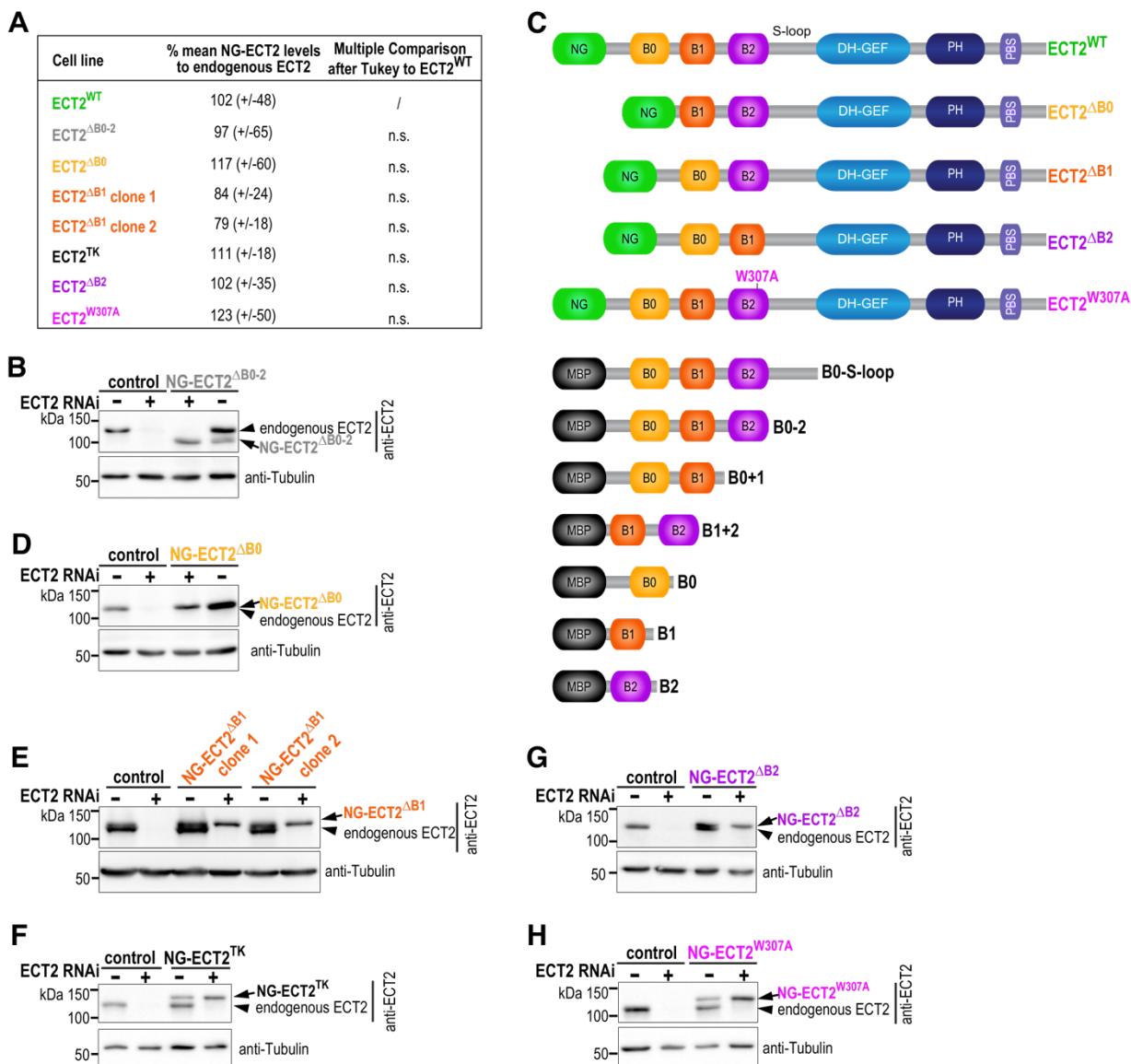
Figure S1, related to Figures 1-2: Characterization of stable ECT2 cell lines
A) Summary of the expression level quantifications of different cell lines by immunoblotting. The mean NG-ECT2 levels (+/- Stdev) after ECT2 RNAi relative to endogenous ECT2 in control cells (no transgene) were calculated for 2-4 independent cell extracts. No difference in the expression levels of ECT2^{WT} in comparison to the various ECT2 mutants was observed (n.s. p>0.05). **B)** Immunoblot of the control and NG-tagged ECT2$^{\Delta B0-2}$ expressing cell line for the indicated RNAi conditions probed with anti-ECT2 and anti-α-tubulin as a loading control. **C)** Schematic representation of the different NG-tagged and MBP-/6xHis-tagged ECT2 mutant proteins used in this study. **D-H**) Immunoblots of the control and ECT2$^{\Delta B0}$ (D), ECT2$^{\Delta B1}$ (E), ECT2^{TK} (F), ECT2$^{\Delta B2}$ (G), and ECT2^{W307A} (H) expressing cell lines for the indicated RNAi conditions probed with anti-ECT2 and anti-α-tubulin. For the ECT2$^{\Delta B1}$ mutant two independent FACS clones are shown.
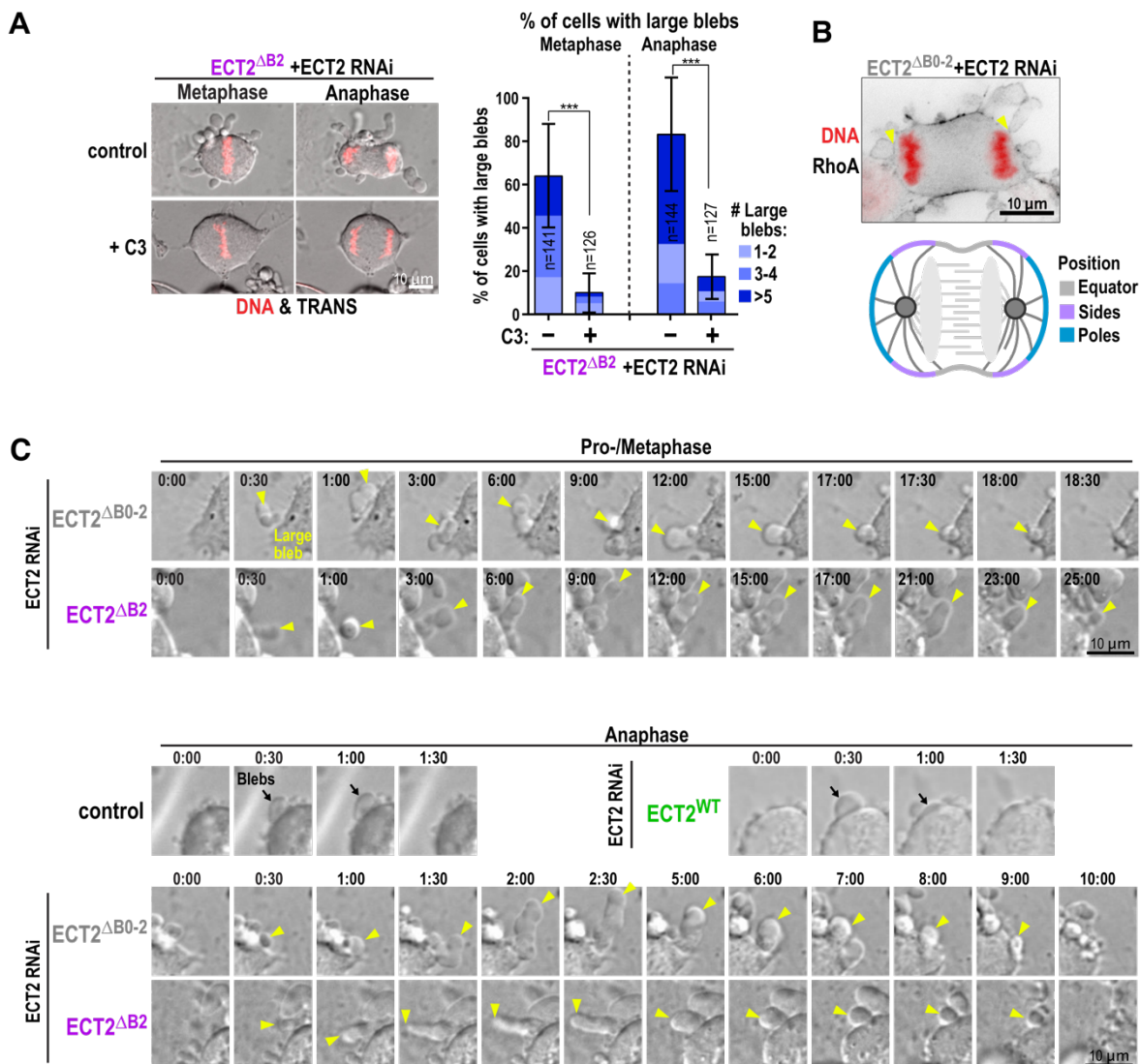
Figure S2, related to Figure 3: Large bleb formation in ECT2$^{\Delta B2}$ expressing cells depends on active RhoA
A) Live-cell merged transmission and DNA (red, SiR-DNA) images of ECT2$^{\Delta B2}$ cells treated with ECT2 RNAi and with or without C3 exoenzyme in metaphase and anaphase (left). Mean percentages of cells with 1-2, 3-4 and >5 large blebs for the indicated conditions (3 independent experiments). Error bars are Stdev, P-values were calculated using Tukey's test, n=number of cells. **B)** ECT2$^{\Delta B0-2}$ cell treated with ECT2 RNAi and stained for RhoA (black) and DNA (red). The emergence of the large blebs from the cell body was manually determined on z-stack images and assigned to the poles, side or equator of the cell (bottom). **C)** Transmission images of control (no transgene), ECT2^{WT}, ECT2$^{\Delta B2}$, and ECT2$^{\Delta B0-2}$ cells for the indicated RNAi conditions. Images were acquired every 30 seconds to analyze bleb duration and bleb size during pro-/metaphase and anaphase (Fig. 3D, E). Normal anaphase blebs observed in control and ECT2^{WT} cells are marked with black arrows and large blebs in ECT2$^{\Delta B2}$ and ECT2$^{\Delta B0-2}$ cells with yellow arrowheads.

61
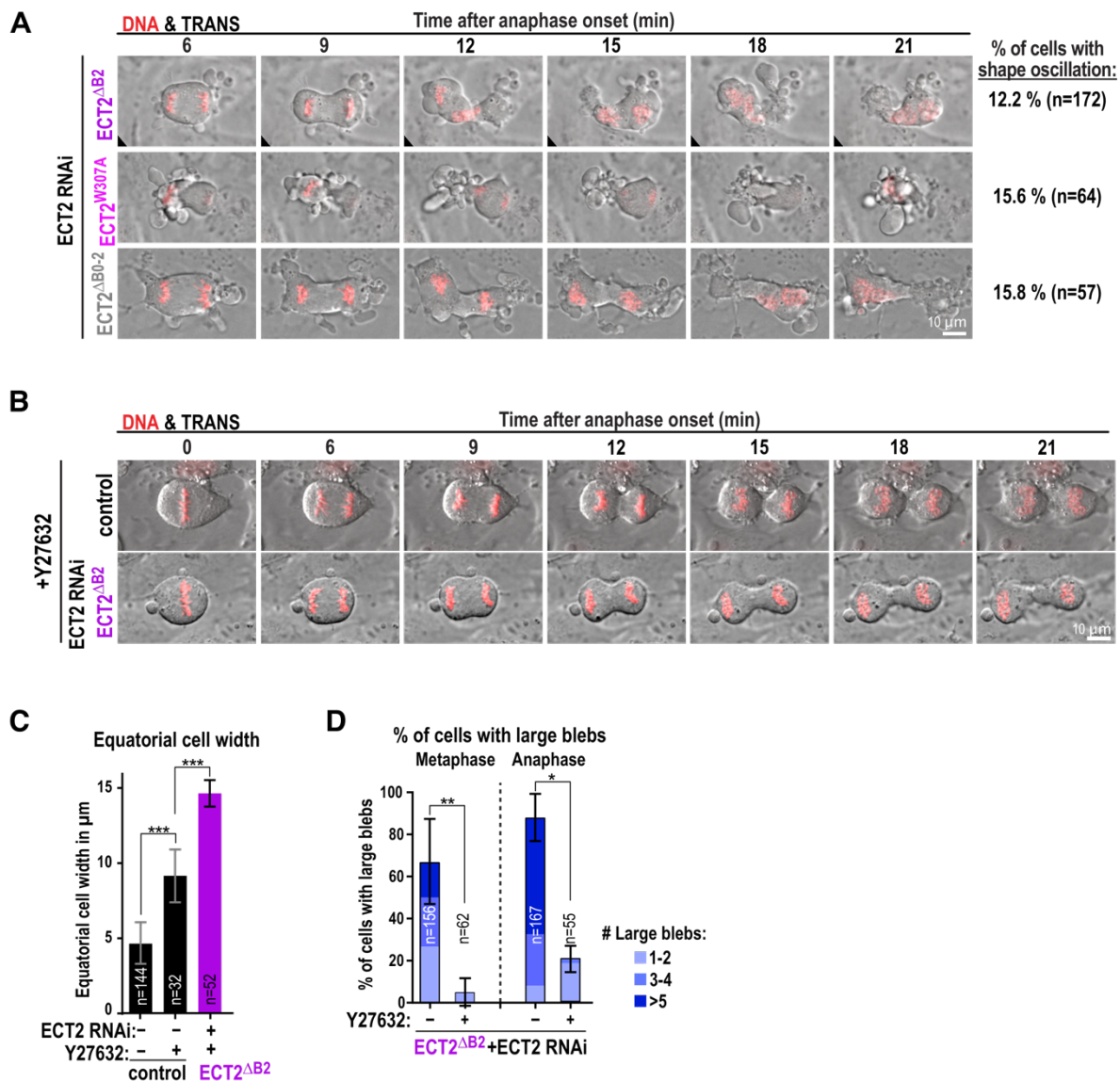
Figure S3, related to Figure 3: Loss of ECT2 autoinhibition results in shape oscillations during anaphase
A) Merged transmission and DNA (red, SiR-DNA) images of ECT2$^{\Delta B2}$, ECT2^{W307A}, and ECT2$^{\Delta B0-2}$ cells treated with ECT2 RNAi that display shape oscillations during anaphase and fail cytokinesis. **B)** Merged transmission and DNA (red, SiR-DNA) live-cell images of a control (no transgene) and an ECT2$^{\Delta B2}$ cell both treated with the RhoA kinase inhibitor Y27632. **C)** Displayed is the mean equatorial cell width at 12 min after anaphase onset for the indicated conditions. P-values were determined with Tukey's test, control is reproduced from Fig. 3F. **D)** The mean percentages of cells with 1-2, 3-4 and >5 large blebs during metaphase and anaphase for the indicated treatments. P-values for metaphase were calculated using student's t-test and for anaphase Kruskal Wallis test. ECT2$^{\Delta B2}$+ECT2 RNAi graphs are reproduced from Fig. 3B. For all of ≥2 independent experiments, error bars are Stdev, and all n=number of cells and *p<0.05, ***p<0.001.
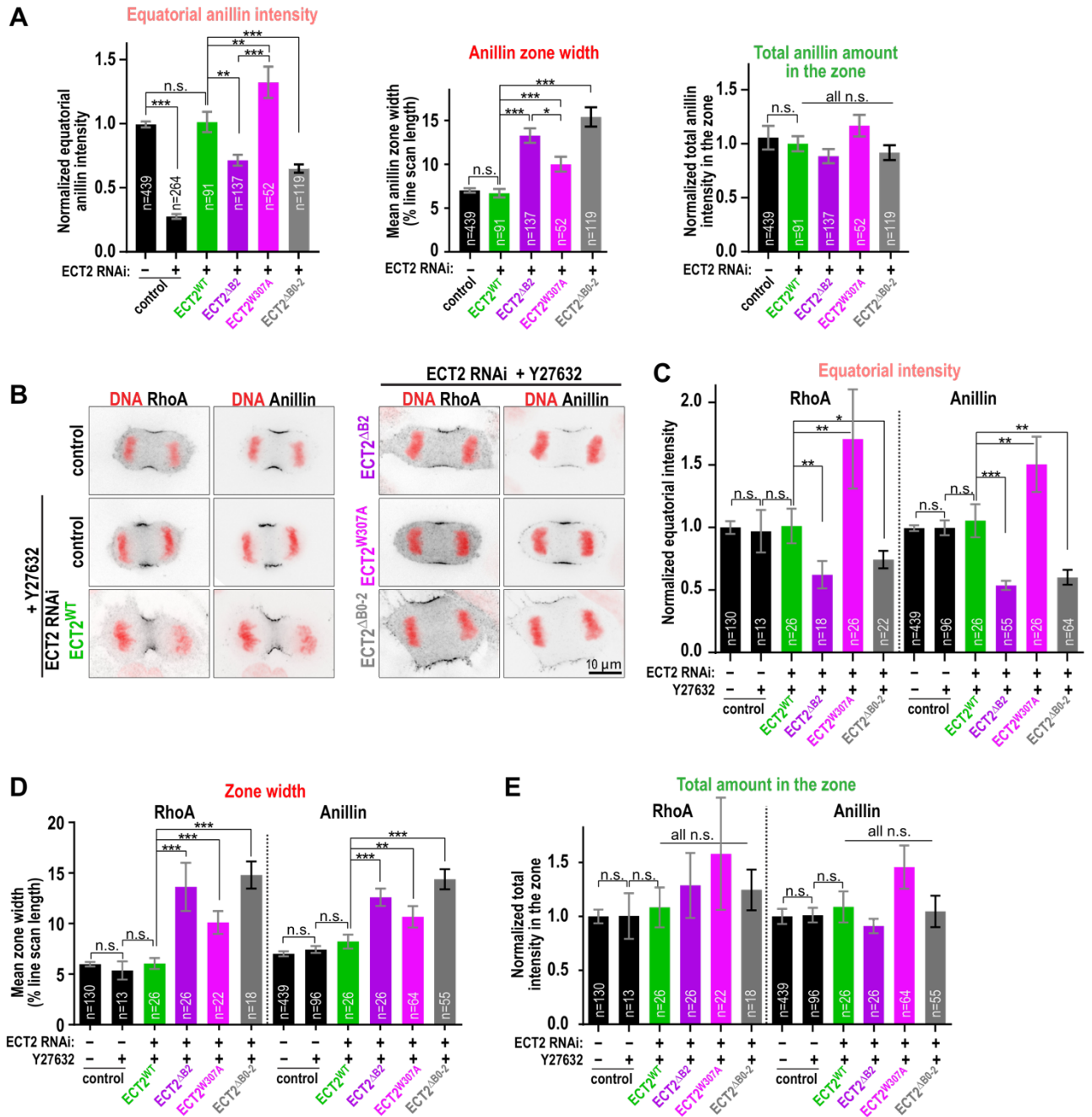
Figure S4, related to Figure 4: Loss of autoinhibition by BRCT2 results in a broader RhoA and anillin zone even when bleb formation is suppressed

A) The mean equatorial anillin intensity (left), anillin zone width (middle) and total anillin amount in the zone (right) are plotted for the indicated cell lines and RNAi conditions (≥3 independent experiments). Sample images for this quantification are shown in Fig. 4A. **B)** Confocal immunofluorescence images of anaphase cells stained for DNA (red), RhoA (left, black) and anillin (right, black) of the indicated conditions. **C-E)** The mean RhoA and anillin equatorial intensity (C), the mean RhoA and anillin zone width (D), and mean total RhoA or anillin amount in the respective zone (E) are shown for each condition (≥2 independent experiments). Control graphs without Y27632 are reproduced from Fig. 4D-F, S4A.

For all error bars are SEM, P-values were calculated using Kruskal Wallis test, n=number of cells and n.s. $p>0.05$; *$p<0.05$; **$p<0.01$; ***$p<0.001$.

A ECT2 RNAi

ECT2^{WT} ECT2$^{\Delta B2}$ ECT2$^{\Delta B0\text{-}2}$

NG-ECT2
Tubulin

10 μm

Midbody Localization: 97% (n=48)   63% (n=65)   0% (n=48)

B

Equatorial anillin intensity

Anillin zone width

Total anillin amount
in the zone

C   control   ECT2^{TK}

DNA
RhoA

DNA
Anillin

10 μm

ECT2 RNAi
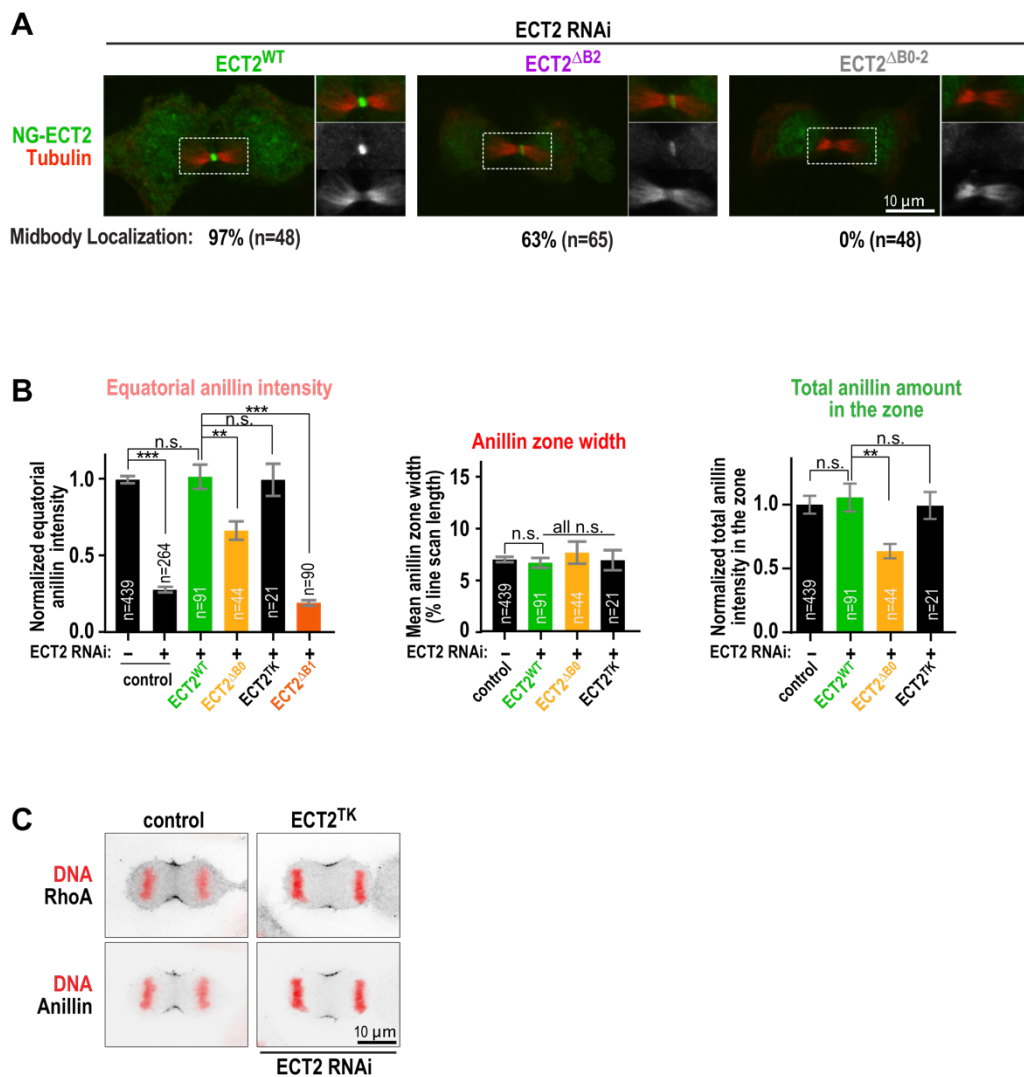
Figure S5, related to Figures 4-5: The BRCT domains are required for midbody localization
A) Confocal immunofluorescence images of late telophase cells expressing NG-tagged ECT2^{WT}, ECT2$^{\Delta B2}$, or ECT2$^{\Delta B0\text{-}2}$ after depleting endogenous ECT2 by RNAi. Cells were stained for α-tubulin (red) and the localization of ECT2^{WT}, ECT2$^{\Delta B2}$, or ECT2$^{\Delta B0\text{-}2}$ (green) to the midbody region was quantified. Shown are the percentages of cells with NG-ECT2 midbody localization (2 independent experiments). **B)** The mean equatorial anillin intensity (left), anillin zone width (middle) and total anillin amount in the zone (right) are plotted for the indicated cell lines and RNAi conditions (≥2 independent experiments). Sample images for this quantification are shown in Fig. 5E, S5C. P-values were calculated using Kruskal Wallis test and n.s. p>0.05; **p<0.01; ***p<0.001. **C)** Confocal immunofluorescence images of anaphase cells stained for DNA (red), RhoA (top, black) and anillin (bottom, black) for the indicated conditions.
All n=number of analyzed cells.
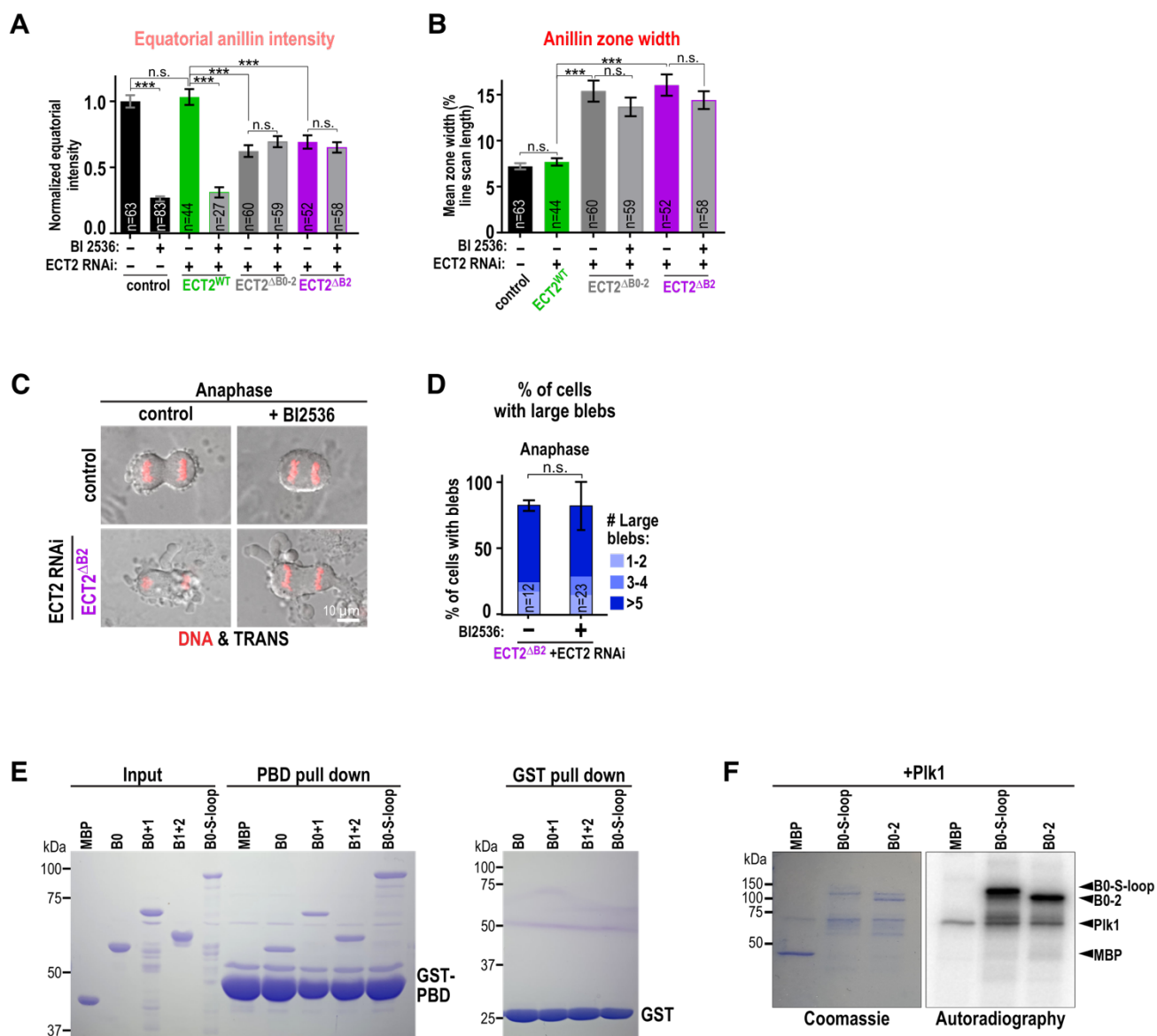
Figure S6, related to Figure 6: The PBD binds the BRCT domains and the main Plk1 phosphorylation site(s) are not in the S-loop

A, B) The mean equatorial anillin intensity (A) and anillin zone width (B) (+/-SEM) are plotted for the indicated cell lines and treatments (≥3 independent experiments). Sample images for this quantification are shown in Fig. 6B. P-values were calculated using Kruskal Wallis test. **C)** Merged transmission and DNA (red, SiR-DNA) time-lapse images of anaphase cells for the indicated conditions. **D)** Mean percentages of ECT2$^{\Delta B2}$ anaphase cells with 1-2, 3-4, >5 large blebs (+/-Stdev) for the indicated conditions are displayed (≥2 independent experiments). P-values were calculated using Tukey's test. **E)** Coomassie-stained gels of a GST-PBD pulldown assay using indicated N-terminal ECT2 fragments tagged with MBP/6xHis. **F)** Coomassie-stained gel and autoradiography of a Plk1 kinase assay using N-terminal ECT2 fragments with (B0-S-loop) and without (B0-2) the S-loop.

For all n.s. p>0.05; ***p<0.001 and n=number cells.
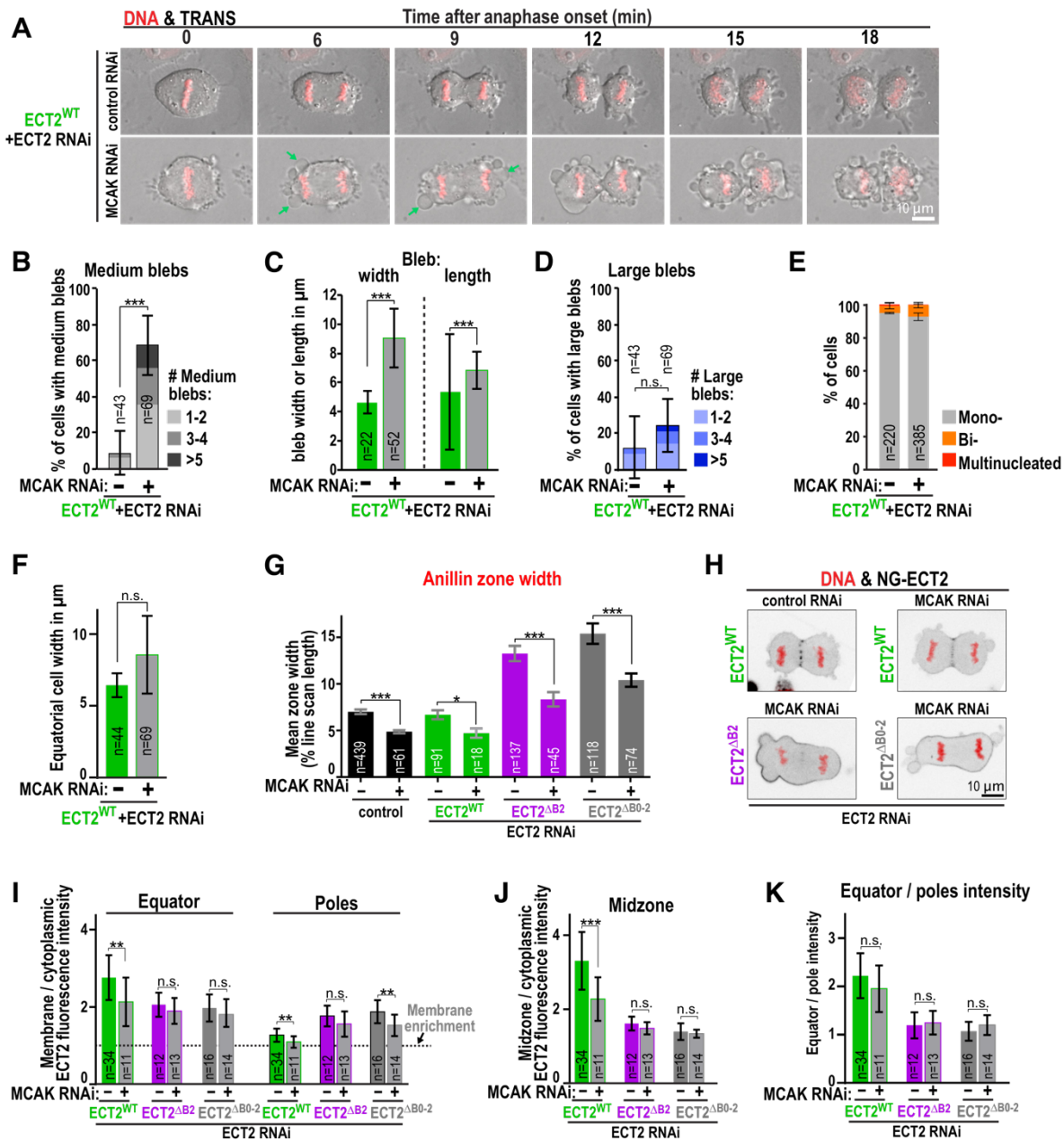
Figure S7, related to Figure 7: MCAK depletion does not enrich ECT2 at the equatorial membrane

A) Merged transmission and DNA (red, SiR-DNA) time-lapse images for the indicated conditions. Green arrows mark medium sized blebs. **B)** The mean percentage of anaphase cells with medium sized blebs is displayed for the indicated conditions. P-values were calculated using student's t-test. **C)** The mean maximum bleb width and length measured in anaphase are displayed. P-values were calculated using Kruskal Wallis test. **D)** The mean percentage of anaphase cells with large blebs. P-values were calculated using student's t-test. **E)** Mean percentages of mono-, bi-, and multinucleated cells are displayed (ECT2[WT] without MCAK RNAi from Fig. 1D). **F)** Mean equatorial cell width measured 12 min after anaphase onset is plotted. P-values were calculated using student's t-test. **G)** The mean anillin zone width is plotted. Sample images are shown in Fig. 7C. P-values were calculated using Kruskal Wallis test. **H-K)** Confocal images of ECT2[WT], ECT2[ΔB2], and ECT2[ΔB0-2] 9 min after anaphase onset for the indicated RNAi conditions (H). Fluorescence intensity was quantified as in Fig. 2C. Normalized mean equatorial and polar membrane signal (I), mean midzone signal (J) and the ratio of Equator/Polar membrane intensity (K) are shown for the different conditions. P-values were calculated using student`s t-/Kruskal Wallis test according to normality.

For all ≥2 independent experiments, error bars are Stdev, n.s. $p>0.05$; *$p<0.05$; **$p<0.01$; ***$p<0.001$. For (D-K) n=number of cells and (C) n=number of blebs.

3 Chapter II - Spatially distinct inputs modulate the amount of active Mitotic-phase GAP to locally restrict RhoA signaling for successful cell division

Wolff, F., Srinivasan S., Nöcker M.C., Mangal S., Mikeladze-Dvali T., Zanin E.

Spatially distinct inputs modulate the amount of active Mitotic-phase GAP to locally restrict RhoA signaling for successful cell division

Friederike Wolff[1], Swathi Srinivasan[1], Marie Christin Nöcker[1], Sriyash Mangal[2], Tamara Mikeladze-Dvali[2], Esther Zanin[1, 2] *

[1]Department Biologie, Friedrich-Alexander-Universität Erlangen-Nürnberg, 91058 Erlangen

[2]Department Biology, Ludwig-Maximilians University, Munich, 82152 Planegg-Martinsried, Germany

*Corresponding author and lead contact: Esther Zanin (esther.zanin@fau.de)

1

Abstract

At the end of mitosis a contractile ring consisting of filamentous actin (F-actin) assembles at the cell equator and ring constriction equally partitions the cellular content. Inhibitory and stimulatory signaling cascades spatially limit RhoA activity to a narrow central zone to promote F-actin polymerization only at the cell equator. While the stimulatory signal is well-characterized, the mechanisms by which inhibitory signals restrict active RhoA to a narrow equatorial zone and prevent improper RhoA activity at the cell poles are not known. Here, we identify two regulatory inputs that control the activation and cortical targeting of the Mitotic-phase GTPase activating protein (MP-GAP) for RhoA which limits RhoA activity both at the cell poles and at the cell equator. We show that at cell poles, MP-GAP is a direct phosphorylation target of spindle-pole associated Aurora A kinase. We identify three Aurora A target residues in a region of MP-GAP that binds directly to its catalytic GAP domain suggesting the Aurora A phosphorylation releases MP-GAP autoinhibition. We show that phosphorylation of these sites is required to keep RhoA activity low at the cell poles. At the cell equator, F-actin facilitates MP-GAP enrichment, which opposes RhoA GEF activity and thereby accelerates RhoA flux through the GTPase cycle for the formation of a narrow equatorial zone of active RhoA. Thus, the amount of active MP-GAP is modulated by two distinct regulatory inputs that function in spatially restricted locations: Aurora A phosphorylation relieves MP-GAP autoinhibition to limit RhoA activity at the cell poles, while F-actin polymerization promotes MP-GAP targeting to prevent distribution of active RhoA in a broad zone at the cell equator. By determining the mechanism of spatially confining RhoA activity at the equator and the cell poles during cytokinesis, our work has broad implications to how Rho activity zones are formed and maintained during cytokinesis and how defects in their formation impact animal development and disease.

2

Introduction

During the last step of cell division, called cytokinesis, the content of the mother cell is segregated between the two daughter cells. A contractile ring consisting of filamentous actin (F-actin) and non-muscle myosin II assembles at the cell equator during anaphase and ring constriction forms the two daughter cells (Basant and Glotzer, 2018; Mishima, 2016; Pollard and O'Shaughnessy, 2019). Contractile ring formation is induced by the small GTPase RhoA, which is active in a narrow zone at the cell equator. Opposing stimulatory and inhibitory signals from spindle-associated proteins restrict RhoA activity to a narrow equatorial zone and thereby tightly link chromosome segregation with cleavage plane specification. The well characterized stimulatory signal derives from the spindle midzone, which consists of overlapping antiparallel microtubule bundles forming between the segregating chromosomes. The stimulatory signal releases autoinhibition of the RhoA GEF Ect2 and thereby promotes RhoA activation at the cell equator (Burkard et al., 2009; Chen et al., 2019; Dechant and Glotzer, 2003; Gomez-Cavazos et al., 2020; Prokopenko et al., 1999; Schneid et al., 2021; Somers and Saint, 2003; Tatsumoto et al., 1999; Wolfe et al., 2009; Yüce et al., 2005). Whereas the molecular mechanisms of the stimulatory signal are known, how the inhibitory signals restrict RhoA activity to a narrow zone at the cell equator and limit RhoA activity at the cell poles are less understood.

It has been demonstrated decades ago that the spindle poles can induce furrowing without being connected by a spindle in a seminal paper by Rappaport (Rappaport, 1961). Based on those observations it was postulated that the spindle poles are the source of an inhibitory signal that induces relaxation of the cell poles (White and Borisy, 1983; Wolpert, 1960). Since then, numerous studies in different organisms have confirmed the presence of a spindle pole-based inhibitory signal. For example, ablation of the centrosome or selective removal of astral microtubules broadens the zone of active RhoA at the cell equator (Bement et al., 2005; Foe and von Dassow, 2008; Murthy and Wadsworth, 2008; van Oostende Triplet et al., 2014; von Dassow et al., 2009; Zanin et al., 2013). Shifting the position of the spindle poles by genetic or mechanical manipulation to one site causes an accumulation of contractile ring proteins at the opposite site (Chen et al., 2008; Werner et al., 2007). Similarly, altering spindle pole position by laser microsurgery causes the furrow site to shift in position (Bringmann and Hyman, 2005; von Dassow et al., 2009). In contrast, increasing the number of astral microtubules by depleting the microtubules depolymerizing kinesin MCAK narrows the RhoA zone (van Oostende Triplet et al., 2014; Zanin et al., 2013). The reduction in cortical contractility at the cell poles was proposed to induce equatorial directed flows which cause equatorial compression of the cortex and consequently a positive feedback loop that mediates ring ingression (Khaliullin et al., 2018; Murthy and Wadsworth, 2005; Reymann et al., 2016; Zhou and Wang, 2008).

3

70

We found that the Aurora A kinase activator, TPXL-1 (TPX2 in humans), promotes clearing of contractile ring components from the cell poles in the *C. elegans* one-cell embryo (Mangal et al., 2018). TPXL-1/TPX2 binds astral microtubules where it activates Aurora A via its N-terminus (Bayliss et al., 2003; Kufer et al., 2002). Aurora A is a major mitotic kinase involved in mitotic entry, centrosome maturation and spindle assembly (Tavernier et al., 2021). Aurora A localizes to astral microtubules and centrosomes and is active in a gradient around monopolar spindles (Kufer et al., 2002; Portier et al., 2007; Stenoien et al., 2003; Sugimoto et al., 2002; Ye et al., 2015). Thus, active Aurora A could diffuse from the spindle poles to the overlaying cell cortex where it inhibits RhoA signaling. In the *C. elegans* zygote, a recent report proposes that Aurora A phosphorylation of Ect2 in its membrane binding PH domain removes Ect2 from the posterior pole during anaphase causing an accumulation of Ect2 at the opposite anterior membrane (Longhini and Glotzer, 2022). How Ect2 activity is shut off at the anterior membrane to avoid polar RhoA activity remains unclear. Additionally, astral microtubules serve as tracks for dynein dependent myosin II removal from the cell poles in *C. elegans* (Chapa-y-Lazo et al., 2020).

Besides spindle pole derived signals, other mechanisms were also shown to inhibit polar contractility. The kinetochore localized phosphatase PP1 inactivates ezrin/radixin/moesin at the cell poles and thereby softens the polar cortex (Rodrigues et al., 2015). Another chromatin localized signal comprises the GTPase Ran, which blocks binding of contractile ring components to the polar regions (Beaudet et al., 2017; Beaudet et al., 2020; Kiyomitsu and Cheeseman, 2013; Ozugergin et al., 2021; Ozugergin et al., 2022).

The key negative regulator of RhoA activity during mitosis, which increases the low intrinsic GTP hydrolysis rate of RhoA, is MP-GAP (also named ArhGAP11a). MP-GAP is conserved from *C. elegans* to human and localizes to the cell periphery in metaphase and enriches at the cell equator during anaphase (Michaud et al., 2022; Zanin et al., 2013). *C. elegans* has two MP-GAP homologues called RGA-3 and RGA-4 (RGA-3/4) which limit the accumulation of contractile ring proteins to the cell cortex during mitosis and thereby redundantly contribute to successful cytokinesis (Bell et al., 2020; Schmutz et al., 2007; Schonegg et al., 2007; Zanin et al., 2013). RGA-3/4 localization to the cell periphery requires an intact F-actin cortex and RGA-3/4 terminate RhoA activity pulses during polarization in *C. elegans* and in frog and starfish oocytes during mitosis (Michaud et al., 2022; Michaux et al., 2018). In human cells, MP-GAP limits cortical contractility and in case the spindle pole-based inhibitory signal is reduced, MP-GAP restricts RhoA zone dimension during cytokinesis (Zanin et al., 2013).

Thus, the molecular mechanisms of how inhibitory signals spatially confine RhoA activity during mitosis remain sparse. Here we reveal that Aurora A kinase is part of a spindle-pole localized inhibitory signal in human cells and blocks RhoA signaling at the cell poles. Using microscopy and biochemistry-based assays we demonstrate that Aurora A limits RhoA

4

71

signaling at the cell poles by phosphorylating MP-GAP in a region adjacent to its catalytic GAP domain. Binding studies show that this region of MP-GAP binds to its catalytic GAP domain suggesting that MP-GAP adopts an autoinhibitory conformation, which is released by Aurora A kinase phosphorylation. Furthermore, our data also demonstrate that MP-GAP not only functions at the cell poles but also at the cell equator. MP-GAP is targeted to the cell equator by F-actin, and due to high activation of RhoA by Ect2 in this region, equatorial MP-GAP accelerates RhoA flux through the GTPase cycle and thereby narrows the width of the zone of active RhoA. In summary, we discover that MP-GAP is regulated by two spatially distinct regulatory inputs: spindle-pole dependent activation by Aurora A and equatorial recruitment by F-actin. Together these two inputs spatially fine tune the amount of active MP-GAP and thereby contribute to the formation of a narrow RhoA zone at the cell equator and low RhoA activity at the cell poles.

5

Results

Aurora A kinase restricts anillin accumulation at the cell poles and to a narrow equatorial zone during anaphase in human cells

The Aurora A kinase activator TXPL-1 promotes clearing of contractile ring components from the cell poles in *C. elegans* (Mangal et al., 2018). To test whether the function of Aurora A is conserved in human cells (Fig. 1A), we treated HCT-116 cells, a colon cancer cell line expressing endogenously NeonGreen-tagged anillin (Husser et al., 2022) with the highly specific Aurora A inhibitor MK-5108 (de Groot et al., 2015). Since anillin binds active RhoA it represents an excellent readout for active RhoA localization (Budnar et al., 2019; Piekny and Glotzer, 2008; Sun et al., 2015). To exclude that the observed phenotype arises from the inhibition of highly similar Aurora B kinase by MK-5108, we also inhibited Aurora B for comparison. For Aurora B inhibition we chose AZD1152-HQPA (AZD), which was shown to be highly selective for Aurora B (de Groot et al., 2015). MK-5108 and AZD were added during live-cell imaging before anaphase onset and as expected Aurora A but not Aurora B inhibition reduced spindle midzone length during anaphase confirming previous findings (Fig. S1A, (Reboutier et al., 2013)). Furthermore, cytokinesis failure was only observed after AZD but not after MK-5108 treatment (Fig. S1B, (Carmena et al., 2012)). Since MK-5108 and AZD treatment resulted in distinct and previously published phenotypes, we are confident that our treatment conditions are highly specific for each kinase and thus we continued to analyze anillin localization. In control anaphase cells treated with DMSO, anillin is strongly enriched in a narrow equatorial zone and weakly present at the cell poles (Fig. 1B, C). After Aurora A, but not Aurora B, inhibition the equatorial anillin zone appeared broader and more anillin accumulated at the cell poles. To quantitatively compare anillin distribution, we measured anillin fluorescence intensity around the cell periphery (Fig. 1B) and confirmed that polar anillin levels were increased and the equatorial anillin zone was broader after Aurora A, but not Aurora B inhibition (Fig. 1C). Equatorial levels of anillin were not increased after Aurora A or Aurora B inhibition (Fig. 1C). A broader spindle midzone results in a broader equatorial anillin zone (Hu et al., 2011), however after Aurora A inhibition the spindle midzone length was shorter and thus cannot explain the broadened anillin zone. To ensure that Aurora A inhibition does not indirectly alter anillin localization by reducing the number of astral microtubules, we stained anaphase cells for α-tubulin. In MK-5108-treated HCT-116 cells the spindle midzone was disorganized (Reboutier et al., 2013) but the astral microtubules were still present and did not exhibit any difference to astral microtubules in control cells (Fig. S1C). Aurora A is present on spindle microtubules and centrosomes already during metaphase (Kufer et al., 2002; Sugimoto et al., 2002) and therefore we asked whether Aurora A inhibition during metaphase also increases cortical anillin levels. HCT-116 cells expressing NG-tagged anillin were treated during live-cell imaging with each inhibitor during prometaphase and cortical anillin levels at

6

metaphase were analyzed. Indeed, cortical anillin levels were also increased in metaphase cells after Aurora A, but not Aurora B inhibition (Fig. S1D).

Finally, we investigated whether Aurora A limits anillin accumulation during mitosis also in human cervical cancer HeLa cells. Like in HCT-116 cells, Aurora A inhibition resulted in a shorter spindle midzone length and Aurora B inhibition caused cytokinesis failure (Fig. S1E, F). Immunostaining of endogenous anillin revealed that after Aurora A inhibition polar anillin levels were increased, the width of the anillin zone was widened, and equatorial anillin levels were decreased in comparison to control anaphase cells (Fig. 1D). Similar to HCT-116 cells, cortical anillin levels were also elevated at metaphase after Aurora A inhibition (Fig. S1G). Although Aurora B inhibited cells frequently failed in cytokinesis, they did not show any alteration in anillin localization during mitosis (Fig. 1D, S1G).

In summary, Aurora A limits the cortical anillin accumulation at the cell poles and maintains anillin in a narrow equatorial zone during anaphase, suggesting that the inhibitory role of Aurora A at the cell poles is conserved in human cells.

Aurora A kinase phosphorylates S285, S304, S345 of MP-GAP

Next, we aimed to identify the phosphorylation target of Aurora A kinase that limits RhoA signaling at the cell poles. We hypothesized that Aurora A promotes RhoA inactivation by activating the negative RhoA regulator MP-GAP (Fig. 2A). To test if Aurora A phosphorylates MP-GAP, we split MP-GAP into three fragments comprising the catalytic GAP domain (GST-GAP: 1-253 AA), the F1 (GST-F1: 254-640 AA), or F2 (GST-F2: 640-1021 AA, Fig. 2B) region. Each fragment was incubated with Aurora A kinase and their phosphorylation was tested by *in vitro* kinase assays. We found that GST-F1, but not GST-GAP or GST-F2 was phosphorylated by Aurora A kinase (Fig. 2C). To narrow down which amino acids are phosphorylated, we used the group-based prediction system (GPS 5.0) program and identified seven conserved Aurora kinase consensus phosphorylation sites in F1 region (Fig. 2D). To test which sites are phosphorylated we grouped them into two clusters and generated phosphodeficient cluster 1 (C1: S285A, S304A, S345A) and cluster 2 (C2: S403A, S434A, S500A, T508A) GST-F1 variants (Fig. 2B). After incubation of the GST-F1-C1, but not GST-F1-C2 mutant with Aurora A, we observed a strong reduction in the amount of phosphorylation (Fig. 2E). We finally tested whether any single-site-mutation to alanine in C1 reduced Aurora A kinase phosphorylation. Indeed, we observed that each single-site-mutation in C1 (S285A, S304A, or S345A) reduced Aurora A kinase phosphorylation (Fig. 2F), suggesting that each site is phosphorylated. In sum, Aurora A kinase phosphorylates S285, S304, and S345 in the F1 region of MP-GAP *in vitro*.

7

MP-GAP phosphorylation at S285, S304, and S345 limits anillin accumulation at the cell poles and to a narrow equatorial zone

After Aurora A inhibition cortical anillin levels were increased at the cell poles and its equatorial zone was broadened. Since Aurora A phosphorylates MP-GAP *in vitro*, we asked whether MP-GAP depletion mimics the Aurora A inhibition phenotype. After MP-GAP depletion cortical anillin levels were increased during metaphase (Fig. 3A). Similarly, during anaphase the cortical levels of anillin at the cell poles were also elevated and the equatorial zone width was increased, however the equatorial anillin levels were unchanged (Fig. 3B, C). To test if Aurora A phosphorylation of S285, S304, and S345 is required for MP-GAP function, we made use of a genetic replacement system, which consists of a stably integrated RNAi-resistant GFP-tagged MP-GAP wild-type (MP-GAP^WT) transgene in HeLa cells (Fig. S2A, B, (Zanin et al., 2013)). Additionally, we generated a cell line expressing a full length phosphodeficient MP-GAP mutant transgene in which S285, S304, and S345 of MP-GAP were mutated to alanine (MP-GAP^S3A, Fig. S2A). By performing western blotting, we confirmed that after MP-GAP RNAi, endogenous MP-GAP was strongly reduced and MP-GAP^WT and MP-GAP^S3A were expressed at similar levels as endogenous MP-GAP (Fig. S2B). Finally, we analyzed cortical anillin localization during mitosis: we observed that after MP-GAP RNAi expression of MP-GAP^WT, but not MP-GAP^S3A, reduced cortical anillin levels in metaphase (Fig. 3A). Similarly, during anaphase MP-GAP^WT but not MP-GAP^S3A expressing cells treated with MP-GAP RNAi had lower cortical anillin levels at the cell poles and a control-like anillin zone at the cell equator (Fig. 3B, C).

Lastly, we tested whether MP-GAP depletion has any effect on furrow ingression. We filmed HeLa cells after MP-GAP depletion and measured the equatorial and pole-to-pole cell width from anaphase onset until the contractile ring was fully ingressed. In control cells, the equatorial cell width decreased and the pole-to-pole cell width increased after anaphase onset (Fig. 3D, E, S2C). Both, the decrease in equatorial cell width and the increase in pole-to-pole cell width was strongly delayed in cells depleted of MP-GAP by RNAi, but eventually most cells completed cytokinesis (Fig. 3D-F, S2C). Expression of MP-GAP^WT, but not MP-GAP^S3A rescued the delay in furrow formation and ingression and pole-to-pole cell elongation.

Altogether, after MP-GAP depletion cortical anillin levels at the cell poles increased and the equatorial anillin zone widened, which resulted in delayed cell elongation and furrow ingression. Expression of wild-type MP-GAP, but not the Aurora A kinase phosphodeficient mutant, rescues the MP-GAP depletion phenotype suggesting that phosphorylation of MP-GAP by Aurora A kinase promotes MP-GAP activity.

F-actin, but not Aurora A phosphorylation, targets MP-GAP to the cell periphery

8

75

Aurora A kinase localizes to the centrosomes and astral microtubules (Kufer et al., 2002; Portier et al., 2007; Stenoien et al., 2003; Sugimoto et al., 2002; Ye et al., 2015) and MP-GAP to the cell periphery (Zanin et al., 2013). Therefore, phosphorylation of MP-GAP by Aurora A could occur around the spindle poles and/or at the cell periphery. To analyze whether and where MP-GAP and Aurora A are in close proximity within the cell we performed in situ proximity ligation assays (PLA). Cells were incubated either with anti-Aurora A and anti-MP-GAP primary antibodies or only with one primary antibody as a negative control. If both epitopes are less than 10 nm apart bright PLA foci are expected. Indeed, we observed numerous PLA foci when cells were incubated with both primary antibodies but not in the negative control (Fig. 4A). This suggests that Aurora A and MP-GAP are in close proximity and might interact with each other. To analyze the subcellular distribution of the PLA foci within the cell, we split the cell into three regions: periphery, middle and center and counted the number of foci in each region. PLA foci were strongly enriched at the cell periphery in comparison to the middle or center in metaphase and anaphase (Fig. 4B). Lastly, we determined whether PLA foci were equally present at the cell equator and poles in anaphase cells. We found more foci enriched at the polar in comparison to the central area (Fig. 4C).

MP-GAP localizes to the cell periphery in metaphase and anaphase (Zanin et al., 2013) and in *C. elegans* the MP-GAP homologue requires F-actin polymerization for cortical targeting (Michaux et al., 2018). Thus, we asked whether cortical localization of human MP-GAP also depends on the presence of F-actin. Inhibition of F-actin polymerization by Latrunculin A treatment caused a strong reduction of cortical F-actin and MP-GAP during metaphase and anaphase (Fig. 4D, E). To quantitatively measure changes in MP-GAP localization, we drew linescans across the polar and equatorial regions of the cells and determined the enrichment of MP-GAP at the cell periphery (Fig. 4F). In control metaphase cells MP-GAP is ~1.5 fold enriched at the cortex in comparison to the cytoplasm. During anaphase MP-GAP exhibits ~2 fold enrichment at the cell equator and a ~1.5 enrichment at the cell poles. After F-actin depolymerization by Latrunculin A addition, MP-GAP enrichment at the entire cortex is lost and equals cytoplasmic levels (Fig. 4G).

Since Aurora A preferentially phosphorylates MP-GAP at the cell periphery we asked whether Aurora A phosphorylation of MP-GAP is required for MP-GAP targeting to the cell periphery. After Aurora A inhibition cortical MP-GAP enrichment was not reduced in comparison to DMSO treated control cells (Fig. 4G, H). This observation was supported by quantitatively measuring cortical localization of MP-GAP[WT] and MP-GAP[S3A] after the depletion of endogenous MP-GAP. MP-GAP[WT] and MP-GAP[S3A] enriched to a similar extent at the cell cortex in metaphase and anaphase (Fig. 4I, J).

Concluding, MP-GAP localization to the cell cortex requires F-actin polymerization. Although, Aurora A phosphorylates MP-GAP preferentially at the cell periphery in mitotic cells and

particularly at the polar area in anaphase cells, Aurora A is not involved in targeting MP-GAP to the actin cortex.

The F1 region of MP-GAP binds the catalytic GAP domain

MP-GAP consists of the N-terminal localized catalytic GAP domain and a large C-terminal region of unknown function. To check whether MP-GAP could adopt an autoinhibitory conformation, we tested binding of the F1 or F2 region of MP-GAP to the catalytic GAP domain. We immobilized purified GST-tagged GAP, F1 or F2 MP-GAP fragments on beads and incubated them with His-tagged GAP domain. We observed that GST-tagged F1, but not F2 or the GAP domain itself, bound to the His-tagged GAP domain (Fig. 5A). This points toward the possibility that the binding of F1 to the GAP domain inhibits GAP activity. Since Aurora A phosphorylates the F1 region, this could regulate binding of F1 to the GAP domain. If the phosphorylation sites are in the binding surface, interaction between F1 and the GAP is expected to be abolished. If the phosphorylation sites are in the hinge region connecting the catalytic GAP domain with the binding surface in F1, binding should still occur. To test this, we generated a phosphomimetic F1 ($F1^{S3D}$) region and tested for GAP binding. The phosphomimetic $F1^{S3D}$ fragment still bound the GAP domain (Fig. 5B), indicating that the Aurora A target sites are in the hinge region that connects the GAP domain with the F1 fragment. Together, the F1 region binds the GAP domain suggesting that MP-GAP adopts an autoinhibitory conformation.

Aurora A-dependent signaling and Ect2 autoinhibition protect the cell against cytokinesis failure

Aurora A inhibition did not cause cytokinesis failure although more anillin accumulated at the cell poles and the equatorial anillin zone was broader. We asked whether Aurora A inhibited cells succeed in cytokinesis since RhoA activation hardly occurs outside the cell equator due to the autoinhibition of Ect2 (Fig. 6A). Ect2 autoinhibition by the BRCT2 domain is only released at the cell equator which results in local RhoA activation (Chen et al., 2019; Schneid et al., 2021) (Fig. 6A). Mutating W307 of the BRCT2 domain to alanine abolished Ect2 autoinhibition and increased RhoA signaling but did not cause cytokinesis failure (Chen et al., 2019; Schneid et al., 2021), most likely, since Aurora A activity still promotes RhoA inactivation at the cell poles. To test whether simultaneous inhibition of Aurora A and absence of Ect2 autoinhibition cause cytokinesis failure, we employed a previously established genetic replacement system for Ect2, in which RNAi resistant $Ect2^{WT}$ and $Ect2^{W307A}$ are expressed in HeLa cells (Schneid et al., 2021). We inhibited Aurora A kinase during live-cell imaging before anaphase onset in $Ect2^{WT}$ and $Ect2^{W307A}$-expressing cells after the depletion of endogenous Ect2 (Fig. 6B). Similar to HCT-116 cells, Aurora A inhibition in $Ect2^{WT}$ HeLa control cells did not elevate cytokinesis

failure rate (Fig. 6B-D). In contrast, Aurora A inhibition in Ect2^{W307A}-expressing cells strongly increased cytokinesis failure rate and the percentage of cells with shape oscillation (Fig. 6B-D, S3A, B).

In summary, polar inhibition of RhoA activity mediated by Aurora A signaling and Ect2 autoinhibition are redundant mechanisms to spatially pattern RhoA activity and protect against cytokinesis failure.

11

Discussion

During cytokinesis stimulatory and inhibitory signals spatially control RhoA activity and thereby induce contractile ring formation and cleavage furrow formation at the right location. Here we reveal that the activity and localization of the negative regulator of RhoA, MP-GAP, is controlled by two distinct regulatory inputs which together spatially limit RhoA signaling during cytokinesis. Based on our data we suggest the following model: MP-GAP activity could be suppressed by the binding of the F1 region to the catalytic GAP domain. This autoinhibition is released by the phosphorylation of three amino acid residues by Aurora A kinase in the hinge region between the F1 region and the GAP domain. Since Aurora A is active in a gradient around spindle-poles this results in a preferential increase of MP-GAP activity at the overlaying polar cortex and consequently RhoA inactivation at the polar membrane (Fig. 6E). Our findings identify a long-searched spindle pole-located inhibitory signal suppressing RhoA activity at the cell poles. However, MP-GAP restricts RhoA activity not only at the cell poles but also at the cell equator. MP-GAP requires an intact F-actin cortex to enrich at the cell periphery and since F-actin levels are high at the equator, total cortical MP-GAP levels are also higher at the equator compared to the poles of the cell. At the equator RhoA is continuously activated by Ect2 and together with MP-GAP-mediated RhoA inactivation this results in a high RhoA flux through the GTPase cycle and thereby restricts active RhoA to a narrow equatorial zone. Collectively, MP-GAP activity integrates two regulatory inputs: targeting to the cell periphery by F-actin and elevation of MP-GAP activity by Aurora A phosphorylation (Fig. 6E). Together both inputs allow independent fine tuning of the amounts and activity of MP-GAP: if RhoA activity is high, F-actin polymerization is induced and MP-GAP is recruited and increases RhoA flux to form a narrow active RhoA zone. At the cell poles where F-actin levels and subsequently MP-GAP levels are low, MP-GAP activity is boosted by Aurora A phosphorylation to shut RhoA off.

Aurora A turns over rapidly (Portier et al., 2007; Stenoien et al., 2003) and is active in a gradient around monopolar spindles (Ye et al., 2015). Our data show, that Aurora A preferentially interacts with MP-GAP at the polar cell periphery and not at the spindle poles, suggesting that active Aurora A diffuses from the spindle poles to the overlying cortex where it phosphorylates F-actin-bound MP-GAP. Using pull down assays we demonstrate that the F1 region of MP-GAP binds the catalytic GAP domain which points toward the possibility that MP-GAP adopts an autoinhibitory conformation. Intriguingly, the three identified Aurora A target sites are located in the F1 fragment suggesting that phosphorylation of those sites regulates F1 binding to the GAP domain. Exchanging Aurora A phosphorylation sites to phosphomimetic residues did not block binding of F1 to the GAP domain and therefore, we speculate that the Aurora A target sites are located in the hinge between the binding surface of the F1 region and the GAP

12

79

domain. Phosphorylation of the hinge region by Aurora A might promote opening and increase GAP activity.

Aurora A inhibition or MP-GAP depletion increases cortical anillin levels not only during anaphase but also in metaphase. Thus, Aurora A elevates MP-GAP activity already in metaphase. In metaphase the cell is round and the spindle poles are closely together and therefore a uniform Aurora A activity throughout the cell is expected. The metaphase signaling of Aurora A ensures, together with CDK1 phosphorylation of Ect2 (Su et al., 2011), that RhoA activity remains low prior to anaphase onset. Elevated RhoA activity levels during metaphase cause spindle positioning and chromosome segregation defects and might be responsible for the protumorigenic activity of RhoA (Limzerwala et al., 2020).

During anaphase the cell elongates and the distance between the two spindle poles increases. Due to its centrosome-centered localization, Aurora A activity is expected to be graded, high at the cell poles and low at the cell equator. Thereby MP-GAP activation at the cortex is particularly enforced at the cell poles. However, MP-GAP is not only present at the polar cortex but also enriches at the equatorial cortex. MP-GAP requires F-actin to localize to the cell cortex demonstrating that MP-GAP F-actin binding or F-actin associated protein binding is conserved from worms to humans (Michaud et al., 2022; Michaux et al., 2018). Since active RhoA and consequently F-actin levels are high at the cell equator, MP-GAP enriches there and has some basal GAP activity. Active RhoA is tethered to the plasma membrane with its lipid moiety and is highly dynamic (Budnar et al., 2019). Therefore, active RhoA is predicted to diffuse away from the site of activation and distribute over the plasma membrane. However, this is not observed in cells and therefore, it was suggested that inactivation of RhoA and accelerating RhoA flux through the GTPase cycle by the RhoA GAP is prerequisite for the formation of a narrow active RhoA zone at the cell equator (Bement et al., 2006). Indeed MP-GAP depletion causes a broader anillin zone, which suggests that equatorial MP-GAP-accelerated RhoA flux restricts RhoA zone dimensions. In the presented study, the efficiency of MP-GAP depletion was improved in comparison to our previous publication (Zanin et al., 2013), which explains the stronger phenotypes. A phosphodeficient MP-GAP mutant or Aurora A inhibition also broadened the anillin zone suggesting that Aurora A phosphorylation, to some extent, also activates MP-GAP at the cell equator. Consistently, we also observed some MP-GAP-Aurora A PLA foci at the equatorial cortex, although their number was reduced in comparison to the cell poles. Spatially altering RhoA activity during anaphase by MP-GAP depletion or abolishing Aurora A phosphorylation of MP-GAP strongly delayed pole-to-pole elongation and furrow ingression demonstrating that spatially limiting RhoA activity is needed for the overall cell shape changes during cytokinesis.

Abolishing Aurora A signaling and Ect2 autoinhibition together resulted in high frequency of cytokinesis failure suggesting that limiting RhoA activity by one mechanism is sufficient

13

however if both are absent cytokinesis fails. After the disruption of Aurora A signaling (this work) or Ect2 autoinhibition (Schneid et al., 2021) a wider anillin zone still forms. This is possible since both pathways use spatial landmarks of the mitotic spindle to pattern RhoA activity: Aurora A signaling is high above the spindle poles where it shuts off RhoA activity and Ect2 adopts an autoinhibitory conformation, which is only released at the spindle midzone. In the absence of Aurora A signaling, Ect2 autoinhibition is still preferentially released above the midzone and therefore the RhoA zone still forms at the cell equator although it is broader. In case Ect2 autoinhibition is lost, Aurora A provides a spatial clue for RhoA inactivation at the cell poles. Together these two complementary mechanisms of controlling RhoA activity are the foundation for the enormous robustness of cytokinesis.

Recent studies revealed two mechanistically distinct pathways that limit the accumulation of myosin II and F-actin on the poles in an astral microtubule-dependent manner. In *C. elegans* polar myosin II is removed by dynein (Chapa-y-Lazo et al., 2020) and in human tissue culture cells polar y-actin nucleation is blocked by the inhibition of formin (Chen et al., 2020). Both mechanisms do not block RhoA activity directly and thus might become essential when MP-GAP-mediated RhoA inactivation at the cell poles is compromised. In addition, several spindle-pole independent signals emanating from the spindle-midzone, the kinetochores and the chromatin (Beaudet et al., 2017; Beaudet et al., 2020; Kiyomitsu and Cheeseman, 2013; Ramkumar et al., 2021; Rodrigues et al., 2015) control the dynamics of contractile ring components at the cell poles. For example, spindle midzone enriched Aurora B promotes F-actin removal from the cell poles (Ramkumar et al., 2021). We did not observe an increase of anillin at the poles or a wider zone after Aurora B inhibition, similar to previous observations (Adriaans et al., 2019). This suggests that Aurora B has a more direct role in blocking F-actin nucleation at the polar cortex maybe by regulating F-actin nucleators or stabilizers. Future investigations will need to study whether those pathways work redundantly with Aurora A signaling and whether specific cell types rely on selected pathways. A recent study suggests that AIR-1, the Aurora A homologue in *C. elegans*, prevents ECT-2 membrane binding by phosphorylating the PH domain (Longhini and Glotzer, 2022). Whether Aurora A controls Ect2 localization and/or activity in addition to MP-GAP in human cells must be studied in the future. In summary, our work provides mechanistic insights into how the regulation of MP-GAP activity and localization by Aurora A and F-actin patterns RhoA activity during mitosis. Spatially and temporally restricted small GTPases activity zones are frequently observed during many cellular processes including cell migration, cell polarization or wound healing (Bement and von Dassow, 2014). Thus, the modulation of GAP localization and activity by distinct spatial clues might also shape GTPase activity zones in other cellular contexts. Furthermore, Aurora A kinase also inhibits contractility during other cellular processes such as cell polarization (Kapoor and Kotak, 2019; Klinkert et al., 2019; Zhao et al., 2019) where the same pathway

14

81

might act as well. Aurora A kinase is also an oncogene and overexpression has been reported in a broad range of human malignancies (Du et al., 2021), thus, a better understanding of Aurora A's role in cell division might be crucial for the development of new therapeutic treatments.

15

Material and Methods

Cell culture

Human HCT-116 and HeLa Flp-In T-Rex cells were grown at 37°C in 5% CO_2 in McCoy 5A growth media (for HCT-116, Thermo Scientific, 16600082) and Dulbecco's growth medium (for HeLa, DMEM, Thermo Scientific, 61965059) supplemented with 10% FBS (Thermo Scientific, 10270106) and 1% penicillin/streptomycin (PS, Merck, A2213). CRISPR-tagged Neongreen-Anillin HCT-116 cell line was a gift from Alisa Piekny (Husser et al., 2022). Isogenic HeLa cell line harboring stable integration of RNAi resistant GFP-tagged wild-type MP-GAP was used from a previous study (Zanin et al., 2013). GFP-tagged MP-GAP[S3A] (S285A, S304A, and S345A) phosphodeficient transgene was obtained by FRT/Flp-mediated recombination. HeLa Flp-In host cell was transfected with pOG44 and GFP-MP-GAP[S3A] using X-tremeGene 9 (Sigma Aldrich, 8079398949). After transfection, cells were cultured in DMEM (10% FBS, 1% PS) supplemented with hygromycin (0.2 mg/ml) to select for transgene integration. After 2.5 weeks the clones were pooled. In all MP-GAP[WT] and MP-GAP[S3A] experiments, transgene expression was induced with 0.2 µg/ml tetracycline.

Cloning of MP-GAP variants

The MP-GAP fragments used for pulldown (GST-GAP: AA2-253 (pEZ365); GST-F1 AA255-641 (pEZ359); GST-F2 AA641-1023 (pEZ360)), or antibody generation (GST-MP-GAP[AA560-801] (pEZ229)) were cloned into the pGEX-4T using Gibson assembly. The phosphodeficient mutants (GST-F1-C1: S285A, S304A, and S345A (pEZ371)) and single site mutations (S304A (pEZ366), S345A (pEZ367), S345A (pEZ368)) of F1 were obtained by side-directed mutagenesis. The GST-F1-C2 mutant (S403A, S434A, S500A and T508A (pEZ377)) was synthesized by Eurofins and subcloned into the pGEX-4T vector with Gibson assembly. The phosphomimetic F1 fragment (GST-F1-S3D, S285D, S304D, and S345D (pEZ426)) was generated by site-directed mutagenesis and cloned into pGEX-4T. RNAi resistant MP-GAP[S3A] (S285A, S304A, and S345A, pEZ378) was cloned into the pcDNA5/FRT/TO vector containing a GFP-tag using Gibson assembly. All plasmids generated for the study are listed in Table 1.

siRNA transfection

The phenotype of MP-GAP[WT] and MP-GAP[S3A] was determined after depleting endogenous MP-GAP by RNAi. One day prior to siRNA transfection cells were plated in 12 well plates with DMEM (10%FBS, 0.2 mg/ml tetracycline) at approximately 30% confluency. For immunofluorescence, cells were seeded on 18 mm poly-L-lysine (P1524-100G, Sigma) coated glass coverslips (P233.1, Menzel) and for live-cell imaging cells were seeded into ibidiTreat chambers (80426, Ibidi). Next day, cells were transfected with a final concentration of 40 nM

16

MP-GAP siRNA oligo (ATTACAGGCTGCAGTAGTA, J-021122-05-0020, Dharmacon, (Zanin et al., 2013)) using Interferin (Polyplus-transfection, 101000028). 18-20 hr after siRNA transfection 0.5 mM thymidine (T1895, Sigma) was added to synchronize the cell cycle. After 22-24 hr incubation, cells were released from the thymidine block by washing 3x for 5 min with DMEM (10% FBS, 0.2 mg/ml tetracycline). 8-9 hr after the thymidine release live-cell imaging was started or cells were fixed for immunofluorescence of mitotic cells.

Same procedure was followed for depletion of endogenous Ect2 (Fig. 6), however, cells were transfected with a final concentration of 30 nM Ect2 siRNA oligo (GGCGGAAUGAA CAGGAUUU, Dharmacon, (Yüce et al., 2005)) using Lipofectamine RNAiMAX (13778075, Thermo Fischer).

MP-GAP antibody production

Polyclonal antibodies against purified GST-tagged MP-GAP$^{AA\,560-801}$ were generated in rabbits. GST-MP-GAP$^{AA560-801}$ expression was induced in BL21(DE3) *E. coli* for 4 hr at 37°C with 0.5 mM IPTG and purified over a glutathione-Sepharose column. After depleting GST antibodies from the obtained rabbit serum, the MP-GAP antibodies were purified with GST-MP-GAP$^{AA\,560-801}$-coupled SulfoLink resin. Antibodies bound to the SulfoLink resin were eluted in 0.2 M glycine pH 2.5 and neutralized by 1 M TrisHCl pH 8.5. Antibodies were concentrated and the buffer was exchanged to 1x Phosphate Buffered Saline (PBS) using Pierce Protein Concentrator (10K MWCO; Life Technologies, 88527). Specificity of the MP-GAP antibody was verified by the absence of immunostaining after MP-GAP depletion by RNAi.

Immunostaining

For anillin stainings cells were fixed in ice-cold 10% TCA (Merck, 1008070100) or 100% ice-cold methanol for 15 min on ice. For MP-GAP stainings cells were fixed in 100% ice-cold methanol. After fixation cells were washed in 1x PBS and incubated with blocking solution (1x PBS, 4% BSA, 0.1% Triton) for 1 hr at room temperature (RT). As primary antibodies anti-anillin (1:3000, self-made), or MP-GAP (1:250, self-made) were diluted in blocking solution and incubated for 2 hr at RT. Coverslips were washed 3x 5 min in 1x PBS/0.1% Triton and incubated with Alexa FluorTM 568 donkey anti-rabbit (1:500, A10042, Life Technologies) and Alexa FluorTM 635 goat anti-mouse (1:500, A31574, Life Technologies), and Hoechst 33258 (861405; Sigma-Aldrich) in blocking solution for 1 hr at RT.

For visualizing astral microtubules after MK-5108 treatment in HCT-116 cells, α-tubulin (1:10 000, T6199, Sigma) stainings were performed by washing coverslips once with 1x PBS and fixing in 1x PBS containing 0.5% glutaraldehyde (340855, Sigma), 0.5% Triton for 10 min at RT. After fixation coverslips were washed 3x 10 min with freshly made 1x PBS containing 0.1% NaBH4 (806373, Merck) at RT. Cells were washed once with 1x PBS, blocked and

17

84

stained for α-tubulin and DNA as described above. For F-actin staining after Latrunculin A treatment, cells were fixed in 4% cold PFA. Following fixation, slides were washed in 1x PBS and incubated with blocking solution (1x PBS, 4% BSA, 0.1% Triton) for 1 hr at RT. After blocking, slides were incubated with Alexa Fluor™ 568 Phalloidin (1:500, Life Technologies, A12380) and Hoechst 33258 (861405; Sigma) in blocking solution for 1 hr at RT. For all stainings: at the end coverslips were washed 3x 5 min in 1x PBS/0.1% Triton and covered with mounting medium (1x PBS, 4% n-Propyl-Gallate, 90% Glycerol) and stored at -20°C.

Immunoblotting

For immunoblotting cell lines were seeded in 6-well plates, transfected with MP-GAP siRNA, and synchronized with single thymidine block as described above. Cells were collected 8-9 hr after thymidine release. Samples were heated at 95°C for 5 min and sonicated in a water bath for 20 min. As primary antibodies rabbit anti a-actin (1:3000, A-1978, Sigma) and rabbit anti-MP-GAP (1:100, self-made) were used; and as secondary antibody HRP-conjugated anti-rabbit or anti-mouse (both 1:10 000; anti-rabbit (1706515; Bio-Rad); anti-mouse (170-6516; Bio-Rad) were used. Membranes were developed with ECL™ Prime Western Blotting (Sigma, Cytiva RPN2236). Expression levels of the endogenous and the GFP-tagged MP-GAP proteins were quantified by measuring the intensities of the MP-GAP and a-actin bands using the ImageJ software. GFP-tagged and endogenous MP-GAP levels were first normalized to a-actin levels and subsequently the levels of GFP-tagged MP-GAP variants relative to endogenous MP-GAP were calculated.

Inhibitor treatments with MK-5108, AZD1152-HQPA and Latrunculin A

Stock solutions MK-5108 (Selleckchem, S2770, 10 mM), AZD1152-HQPA (Sigma, SML0268-10MG, 10 mM) and Latrunculin A (Enzo, BML-T119-0100, 10 mM) were made in DMSO and stored at -20°C. Inhibitors were diluted in complete cell culture medium and used at the following final concentrations: 10 µM for MK-5108, 200 nM for AZD and 2.5 µM for Latrunculin A. For immunostaining cells were synchronized with a single thymidine block and 8 hr after release they were treated for 10-24 min with 10 µM MK-5108 and 200 nM AZD, or for 20 min with 2.5 µM Latrunculin A. For live-cell imaging, MK-5108 and AZD were present on the cells for maximum 26 min and 14 min, respectively.

Aurora A kinase assays

Aurora A kinase assays were performed in kinase buffer (25 mM HEPES pH 7.5, 50 mM NaCl, 10 mM MgCl2, 0.1% Triton X-100 and 1 mM DTT (Gomez-Cavazos et al., 2020) containing 300 ng GST-tagged MP-GAP fragments and 200 ng recombinant human Aurora A kinase (Merck, 14-511), 1mCi of [gamma-P32]ATP (Hartmann Analytic, SRP-801) and 0.2 mM dATP

(mi-N1010L, Metabion) with a final volume of 20 µl. The kinase reaction was incubated at 30°C for 30 min and it was terminated by the addition of 2x sample buffer (120 mM Tris pH 6.8, 4% SDS, 20% Glycerol, 0.02% bromphenol blue, 5% β-mercaptoethanol). Samples were heated to 95°C for 5 min and then separated by SDS-PAGE. The SDS-Gel was stained with Coomassie blue (B0149, Sigma) and dried prior to autoradiography on Whatman filter paper. Phosphor imaging was performed with a Typhoon Variable Mode Imager (Amersham Biosciences) connected to Amersham™ Typhoon™ scanner control software.

Proximity ligation assay

Proximity ligation assays with Aurora A kinase and MP-GAP were performed in HeLa cells using mouse anti-Aurora A Kinase antibody (1:500, A1231 Merck), rabbit anti-MP-GAP antibody (1:250, self-made), Duolink *In Situ* PLA Probe Anti-Mouse MINUS (DUO92004, Sigma-Aldrich), Duolink *In Situ* PLA Probe Anti-Rabbit PLUS (DUO92002, Sigma-Aldrich), and Duolink *In Situ* Detection Reagents Orange (DUO92007, Sigma-Aldrich). Cells were seeded on 12 mm poly-L-lysine (Y1251-100G, Sigma) coated glass coverslips (P231.1, Carl Roth), synchronized with 0.5 mM thymidine (T1895, Sigma) for 24h, released and fixed 8-9 h later with 100% ice-cold methanol. Cells were blocked with provided blocking solution, incubated with primary antibodies against Aurora A and MP-GAP for 2 h at RT and washed with Wash Buffer (0.01 M Tris, 0.15 M NaCl and 0.05% Tween20, pH 7.4.) The two PLA probes were added and incubated for 1 h at 37°C. The probes were ligated together by adding ligation solution for 30 min at 37°C. Amplification buffer and polymerase were added to amplify positive signal for 1.5 h at 37°C, cells were washed with two wash buffers (Buffer A pH 7.4: 0.01M Tris, 0.15M NaCl, 0.05% Tween-29; Buffer B pH 7.5: 0.2M Tris, 0.1M NaCl), and co-stained with Hoechst 33258 (861405; Sigma-Aldrich). As a negative control same protocol was followed, however just one primary antibody against Aurora A or MP-GAP was used.

Microscopy and image acquisition

For live-cell imaging cells were plated in ibidiTreat chambers on day one and incubated in medium containing 100 nM SiR-DNA (251SC007, Tebu Bio) for 60 min prior to image acquisition. Imaging was performed at 37°C in a heated chamber and cells were maintained in CO_2-independent medium (18045054, Thermo Fischer) complemented with 10% FBS, 1% P/S, 0.2 mg/ml tetracycline, 2 mM L-Glutamine. MK-5108 and AZD treatments in HCT-116 during live-cell images were acquired on a Nikon eclipse Ti spinning disk confocal microscope. The Nikon was controlled by NIS Elements 4.51 and was equipped with a 100x 1.45-NA Plan-Apochromat oil immersion objective, a 488-, a 640-nm laser line, and an Andor DU-888 X-11056 camera (1,024 x 1,024 pixels). Other live-cell images (Fig. 6) were acquired on confocal DIVE-FALCON laser scanning confocal microscope (Leica Microsystems) controlled by the

19

Leica LAS X Life Science software using the HCX PL APO CS 63.0×/1.30 NA glycerol immersion objective and 488 nm and 633 nm lasers. Immunofluorescence images were acquired on a Zeiss AxioImager.Z1 ApoTome microscope, which was controlled by AxioRel 4.6 software. The Zeiss AxioImager.Z1 was equipped with a 63x 1.4-NA Plan-Apochromat oil immersion objective (Zeiss) and AxioCamMR camera.

Microscopy image analyses and quantifications

All fluorescence intensity measurements were performed using Fiji (ImageJ, Version 1.5) software. For anillin fluorescence intensity measurements a 6 pixel-wide linescan was drawn around the cell periphery from pole to pole (Fig. 1B). Additionally, a box adjacent to the cell pole was drawn to measure the cytoplasmic fluorescence intensity (CI). The fluorescence intensity profiles and mean cytoplasmic values were imported into KNIME (https://www.knime.com) for each cell and further processed. From all peripheral fluorescence intensity values the mean cytoplasmic values were subtracted. For metaphase cells, the mean fluorescence intensity over the whole cortex for each cell was calculated. For anaphase cells the mean polar intensity (0-10%, 40-60% and 90-100%) and equatorial intensity (20-30%, 70-80%) of total linescan length were calculated. To calculate the mean equatorial zone width running averages were calculated to smooth the fluorescence intensity curve and the zone width was calculated at half maximum fluorescence intensity for each zone of each cell at the cell equator.

MP-GAP cortical fluorescence intensity was measured by drawing two perpendicular 10 pixel-wide linescans across the cell periphery. One linescan was positioned at the cell equator and one from pole-to-pole (Fig. 4F). After plotting the fluorescence intensity data, the cortex peaks of MP-GAP could be assigned. The cytoplasmic MP-GAP intensities were calculated for each cell 5 pixel away from the two polar cortex peaks by averaging the measured intensities of the following 4 pixels. To normalize fluorescence intensities the measured cortex peak intensities were divided by the mean cytoplasmic intensity of each cell. For metaphase cells, the MP-GAP cortex factor was calculated by averaging the normalized intensities of the equatorial and polar linescan.

Spindle midzone length MK-5108 and AZD treatment was determined by measuring the distance between the two segregating chromosome masses at 6 min after anaphase onset in living HCT-116 cells (Fig. S1A) or during anaphase in fixed HeLa cells (Fig. S1E).

Cell elongation was quantified by measuring the pole-to-pole distance for each cell during anaphase over time (Fig. S2C). The measured distance of each timepoint was normalized to the distance at anaphase onset of the specific cell. Similarly, furrow ingression was analyzed by measuring the equatorial cell width for each cell during anaphase over time until complete

20

87

furrow ingression (Fig. 3E). The measured equatorial cell width of each timepoint was normalized to the distance of the specific cell at anaphase onset.

6xHis-GAP and GST-MP-GAP fragments expression and purification

All 6xHis-tagged and GST-tagged proteins were expressed in 1L *E. coli* BL21(DE3) cultures. Protein expression was induced at an OD_{600} of 0.6-0.8 for 14h at 18°C with 0.1mM IPTG. Cells were harvested, bacterial pellets were washed once with cold 1x PBS and snap frozen in liquid N_2. For the purification of 6xHis-tagged GAP domain (pEZ72 (Zanin et al., 2013)), bacterial pellets were thawn on ice and resuspended in lysis buffer (20 mM Tris-HCL pH 7.4, 500 mM NaCl, 0.2% Triton-X-100, 1 mM DTT (Roth, 6908.3), 1 mM PMSF (Sigma, p7626-1G), cOmplete protease inhibitor cocktail (Roche, 11836153001). Cells were lysed by sonification and clear lysates were incubated with Ni-NTA agarose beads (Qiagen, 30210) in binding buffer (50mM Tris-HCL, 500mM NaCl, 50mM Imidazol (Roth, 3899.1), 10% Glycerol) at 4°C for 1.5 hr. Lysates and beads were transferred into purification column, washed 3x 5min with 5x volumes binding buffer and proteins were eluted with elution buffer (50 mM Tris-HCL pH 7.4, 500 mM NaCl, 500 mM Imidazol, 10% Glycerol). Purified 6xHis-tagged proteins were dialysed at 4°C over-night with exchange buffer (10 mM Tris pH 8.0, 150 mM NaCl, 1 mM EDTA) using Slide-A-Lyzer™ Dialysis Casette (ThermoFischer, 66380) following the manufactures instructions.

For purification of GST-tagged proteins, bacterial pellets were thawn on ice and resuspended in lysis buffer (10 mM Tris pH 8.0, 150 mM NaCl, 1 mM EDTA, 0.05% NP-40, 5 mM DTT, 1 mM PMSF, cOmplete protease inhibitor cocktail). Cells were lysed by sonification and clear lysates were incubated with glutathione Sepharose beads (Sigma, GE17-0756-01) at 4°C for 1.5 hr. Afterwards, beads were washed 3x 10min with lysis buffer and stored at 4°C.

Pull down assay

For pull down assays 1 μg purified 6xHis-GAP domain was mixed with 2 μg purified Sepharose beads-bound GST-MP-GAP fragments in a total of 300 ml binding buffer (10 mM Tris pH 8.0, 150 mM NaCl, 1 mM EDTA, 10 mM Imidazol, 4 mM β-mercaptoethanol). Samples were rotated at 4°C for 1hr. Beads were washed 3x10min in binding buffer and resuspended in equal volumes of 2x sample buffer (0.1 M Tris, 4% SDS, 1.4% β-mercaptoethanol, 20% glycerol, 1% Bromphenol blue). Samples were cooked at 95°C for 5 min, run on a SDS-Page and stained with Coomassie and immunoblotted with anti-6xHis antibody (Invitrogene, MA1-135) to detect the bound 6xHis-GAP domain.

Quantification and statistical analysis

21

88

The software R was used for statistical analyses (R Development Core Team, 2015) including the add-in package multcomp (Hothorn et al., 2008). First, data were examined for normal distribution using Shapiro-Wilk test. Datasets with two conditions with normal distributed data were analyzed by Student's t-test and non-normally distributed data with Kruskal-Wallis Rank sum test. Datasets containing multiple conditions (>2) with non-equal distribution were analyzed by Kruskal-Wallis Rank sum test followed by multiple comparison post-hoc test. The corresponding statistical tests are indicated in the figure legends.

22

Table 1 Plasmids generated for the study

Plasmid number	Content
pEZ229	GST-MP-GAP AA560-801
pEZ359	GST-F1 MP-GAP AA255-641
pEZ360	GST-F2 MP-GAP AA641-1023
pEZ365	GST-GAP MP-GAP AA2-253
pEZ366	GST-F1 MP-GAP AA255-641 (S285A)
pEZ367	GST-F1 MP-GAP AA255-641 (S304A)
pEZ368	GST-F1 MP-GAP AA255-641 (S345A)
pEZ371	GST-F1-C1 MP-GAP AA255-641 (S285A, S304A, S345A)
pEZ377	GST-F1-C2 MP-GAP AA255-641 (S403A, S434A, S500A and T508A)
pEZ378	DNA5/FRT/TO GFP-MP-GAP^{S3A} (S285A, S304A, S345A)
pEZ426	GST-F1 MP-GAP AA255-641 (S285D, S304D, S345D)

Figure Legends

Figure 1 Aurora A kinase limits anillin accumulation at the cell poles and to a narrow equatorial zone in human cells

A) Scheme of the stimulatory and inhibitory spindle-derived signals that spatially pattern RhoA activity during cytokinesis.

B) A linescan was drawn around the cell periphery, starting at one cell pole to quantify anillin, fluorescence intensity along the cortex. Anillin cytoplasmic intensity (CI) was measured in a box in the cytoplasm. The normalized anillin fluorescence intensity from 0%–100% line scan length is shown for a control HCT-116 cell. The polar anillin intensity was the mean intensity from 0%-10%, 40-60% and 90-100% line scan length, the equatorial intensity the mean from 40-50% and 70-80%, and the anillin zone width was determined at the half maximum fluorescence intensity.

C) Shown are time-lapse fluorescent images of HCT-116 cells expressing NG-Anillin (pseudocolour) labeled for DNA (SiR-DNA, grey) 6 min after anaphase onset. HCT-116 cells were treated with MK-5108, AZD, or DMSO (control). Insets show a magnification of the poles. Plotted is the mean normalized fluorescence intensity of anillin at the cell poles, the equator and the width of the equatorial anillin zone in % linescan length 6 min after anaphase onset.

D) Immunofluorescent images of anaphase HeLa cells labeled for endogenous anillin (pseudocolor) and DNA (grey) treated with MK-5108, AZD, or DMSO (control). Insets show a magnification of the poles. Intensity scalings are increased for the magnifications to better visualize polar anillin accumulation. Plotted is the mean normalized fluorescence intensity of anillin at the cell poles, the cell equator and the width of the equatorial anillin zone.

For all n = number of cells, and ≥3 independent experiments were performed for each condition. Error bars are SEM, and p values were calculated with the Kruskal-Wallis test. Scale bars are 5 μm.

Figure S1 Addition of MK-5108 but not AZD increases cortical anillin levels in HCT-116 and HeLa cells during metaphase

A) Spindle midzone length was measured 6 min after anaphase onset in NG-Anillin expressing HCT-116 cells treated with DMSO (control), MK-5108 or AZD.

B) Percentage of cytokinesis failure in NG-Anillin HCT-116 cells determined by live-cell imaging after treatment with the indicated inhibitors.

C) Immunofluorescent images of HCT-116 cells treated with DMSO (control) or MK-5108 stained for α-tubulin (grey) and DNA (red).

D) Shown are time-lapse fluorescent images of HCT-116 cells expressing NG-Anillin (pseudocolour) labeled for DNA (SiR-DNA, grey) in metaphase. HCT-116 cells were treated

24

with the MK-5108, AZD, or DMSO (control). Insets show a magnification of the poles. Plotted is the mean normalized fluorescence intensity of anillin at the cortex during metaphase.

E) Spindle midzone length of fixed HeLa cells in anaphase treated with DMSO, MK-5108 or AZD.

F) Percentage of cytokinesis failure of HeLa cells determined by live-cell imaging after treatment with or without AZD.

For all n = number of cells, and ≥2 independent experiments were performed for each condition. Error bars are SEM and p values were calculated with the Kruskal-Wallis test. Scale bars are 5 µm.

Figure 2 Aurora A kinase phosphorylates S285, S304 and S345 of MP-GAP

A) Aurora A kinase could facilitate RhoA inactivation by activating the RhoA GAP MP-GAP.

B) Schematic of MP-GAP domain organization highlighting the three fragments and putative phosphosites tested in the kinase assays.

C) Coomassie gel and autoradiography images of Aurora A kinase assays with GST-tagged GAP domain and F1 and F2 region of MP-GAP. Different lanes of the same gel are shown.

D) Sequence alignment of the F1 region of MP-GAP. The conserved putative Aurora A phosphosites are highlighted in red.

E, F) Coomassie gel and autoradiography images of Aurora A kinase assays with the myelin basic protein (MBP, positive control), GST (negative control), GST-tagged F1-WT, F1-C1 (S285A, S304A, S345A) and F1-C2 (S403A, S434A, S500A, T508A) (E) or F1-S285A, F1-S304A, and F1-S345A (F) of MP-GAP.

Figure 3 Aurora A kinase phosphorylation of MP-GAP limits anillin accumulation to a narrow equatorial zone and at the poles of the cell

A) Shown are immunofluorescence images of anillin (pseudocolour) and DNA (grey) stained metaphase HeLa cells. Control cells (no transgene), GFP-MP-GAP^{WT} and GFP-MP-GAP^{S3A} expressing cells were treated with or without MP-GAP siRNA as indicated. Magnifications of the polar cortex are shown (left). Mean cortical anillin fluorescence intensity for indicated conditions (right).

B) Shown are immunofluorescence images of anillin (pseudocolour) and DNA (grey) stained anaphase HeLa cells for the indicated conditions. Magnifications of the polar cortex are shown. Intensity scalings are increased for the magnifications to better visualize polar anillin accumulation.

C) Plotted is the mean anillin fluorescence intensity the cell poles, at the cell equator and the zone width in anaphase for the indicated cell lines and RNAi conditions.

D) Merged time-lapse transmission and DNA (SiR-DNA, red) images of HeLa cells expressing no transgene (control), MP-GAP^{WT} or MP-GAP^{S3A} for the indicated RNAi conditions.

E) Plotted is the mean equatorial cell width over time for the indicated conditions.

F) Plotted is the % of cytokinesis failure during live-cell imaging for the indicated conditions.

For all n = number of cells, and ≥2 independent experiments were performed for each condition. Error bars are SEM, and p values were calculated with the Kruskal-Wallis test. Scale bars are 5 μm.

Figure S2 MP-GAP is required for cell elongation during anaphase

A) Scheme of the GFP-tagged RNAi resistant MP-GAP transgenes used.

B) Immunoblot of control (without transgene) and GFP-tagged MP-GAP^{WT} and MP-GAP^{S3A} expressing HeLa cells for the indicated RNAi conditions probed with anti-MP-GAP and anti-actin antibody. Mean levels of endogenous MP-GAP, GFP-MP-GAP^{WT} or GFP-MP-GAP^{S3A} after MP-GAP RNAi relative to endogenous MP-GAP after control RNAi are shown for 3 independent extracts.

C) Plotted is the mean pole-to-pole cell length over time for the indicated conditions.

Figure 4 MP-GAP is targeted to the actin cortex independently of Aurora A activity

A) Merged immunofluorescent images showing PLA foci (white) and DNA (red) for metaphase and anaphase HeLa cell. Staining was performed either with the anti-Aurora A and anti-MP-GAP together (positive) or only with one antibody (negative).

B) Distribution of the PLA foci in % at the cell periphery, middle or center during metaphase and anaphase.

C) The number of PLA foci per 100 μm^2 is plotted for the central or polar area of the cell.

D) Immunofluorescence images of F-actin (white) and DNA (red) stained HeLa cells treated with DMSO or 2.5 μM Latrunculin A (LatA).

E) Immunofluorescence images of MP-GAP (white) and DNA (red) stained HeLa cells treated with DMSO or 2.5 μM Latrunculin A.

F) MP-GAP fluorescence intensity is plotted for an equatorial linescan. Examples of an equatorial and polar linescan are shown for illustration.

G) Quantification of the mean cortical MP-GAP intensity as depicted in (F) for the entire cell cortex in metaphase and for the poles and equator in anaphase cells for indicated treatments. Values above the dotted line represent cortical MP-GAP enrichment.

H) Shown are immunofluorescence images of metaphase and anaphase HeLa cells treated with DMSO or MK-5108. Cells were stained for MP-GAP (white) and DNA (red).

26

93

I) Shown are immunofluorescence images of metaphase and anaphase HeLa cells expressing GFP-MP-GAP^{WT} or GFP-MP-GAP^{S3A} and treated with MP-GAP siRNA. Cells were stained for MP-GAP (white) and DNA (red).

J) Quantification of the mean cortical MP-GAP intensity as depicted in (F) for the entire cell cortex in metaphase and for the poles and equator in anaphase cells for indicated treatments. For all n = number of cells, and ≥2 independent experiments were performed for each condition. Error bars are SEM, and p values were calculated with the Kruskal-Wallis test. Scale bars are 5 μm.

Figure 5 The F1 region binds the catalytic GAP domain of MP-GAP

A) Scheme of the possible autoinhibitory conformation of MP-GAP (left). Coomassie gel and anti-His probed immunoblot of pull down assays incubating immobilized GST-tagged MP-GAP fragments (F1, F2 and GAP) with soluble 6xHis-tagged GAP domain (right).

B) Scheme of the putative position of the Aurora A phosphorylation sites in either the hinge region (left) or on the binding surface (right) of F1. Coomassie gel and anti-His probed immunoblot of pull down assays incubating immobilized GST-tagged F1 wild type or F1^{S3D} with soluble 6xHis-tagged GAP domain (right).

Figure 6 Autoinhibition of Ect2 and Aurora A kinase-signaling protect the cell against cytokinesis failure

A) In normal cells Aurora A signal is high at the poles and Ect2 autoinhibition is locally released at the cell equator (top). Abolishing Ect2 autoinhibition by the W307A mutation, results in active Ect2 throughout the cell (middle). Without Aurora A signaling, Ect2 autoinhibition is still locally released at the equator (bottom). In all conditions cytokinesis succeeds.

B) Merged time-lapse transmission and DNA (SiR-DNA, red) images of HeLa cells expressing Ect2^{WT} or Ect2^{W307A}. Cells were treated during live-cell imaging around anaphase onset with DMSO or MK-5108 as indicated.

C, D) Percentage of cytokinesis failure (C) and equatorial cell width (D) of the conditions filmed in (B).

E) Two spatially distinct regulatory inputs control MP-GAP function at the cell equator and the cell poles during anaphase. At the cell poles F-actin levels are low, but Aurora A kinase activity is high. Aurora A phosphorylates the hinge region between the GAP domain and the F1 region resulting in opening and activation of MP-GAP and RhoA inactivation. At the cell equator Ect2 autoinhibition is released, RhoA is activated and promotes F-actin polymerization. Due to high F-actin levels MP-GAP enriches at the equator and increases the GTP hydrolysis rate of RhoA resulting in high RhoA flux and narrowing of the active RhoA zone.

27

For all n = number of cells, and ≥2 independent experiments were performed for each condition. Scale bars are 5 µm.

Figure S3

A) Merged transmission and DNA (SiR-DNA, red) time-lapse images of HeLa cell expressing Ect2^{W307A} and treated with MK-5108 around anaphase onset. Scale bar is 5 µm.

B) Graph displays the percentage of HeLa cells with shape oscillation for the different treatment conditions. For all n = number of cells.

28

Acknowledgments

29

References

Adriaans, I.E., A. Basant, B. Ponsioen, M. Glotzer, and S.M.A. Lens. 2019. PLK1 plays dual roles in centralspindlin regulation during cytokinesis. *The Journal of Cell Biology*. 218:1250-1264.

Basant, A., and M. Glotzer. 2018. Spatiotemporal Regulation of RhoA during Cytokinesis. *Current Biology*. 28:R570-R580.

Bayliss, R., T. Sardon, I. Vernos, and E. Conti. 2003. Structural basis of Aurora-A activation by TPX2 at the mitotic spindle. *Molecular Cell*. 12:851-862.

Beaudet, D., T. Akhshi, J. Phillipp, C. Law, and A. Piekny. 2017. Active Ran regulates anillin function during cytokinesis. *Molecular biology of the cell*:mbc.E17-04-0253.

Beaudet, D., N. Pham, N. Skaik, and A. Piekny. 2020. Importin binding mediates the intramolecular regulation of anillin during cytokinesis. *Molecular biology of the cell*. 31:1124-1139.

Bell, K.R., M.E. Werner, A. Doshi, D.B. Cortes, A. Sattler, T. Vuong-Brender, M. Labouesse, and A.S. Maddox. 2020. Novel cytokinetic ring components drive negative feedback in cortical contractility. *Molecular biology of the cell*. 31:1623-1636.

Bement, W.M., H.A. Benink, and G. von Dassow. 2005. A microtubule-dependent zone of active RhoA during cleavage plane specification. *The Journal of Cell Biology*. 170:91-101.

Bement, W.M., A.L. Miller, and G. von Dassow. 2006. Rho GTPase activity zones and transient contractile arrays. *BioEssays*. 28:983-993.

Bement, W.M., and G. von Dassow. 2014. Single cell pattern formation and transient cytoskeletal arrays. *Current Opinion in Cell Biology*. 26:51-59.

Bringmann, H., and A.A. Hyman. 2005. A cytokinesis furrow is positioned by two consecutive signals. *Nature*. 436:731-734.

Budnar, S., K.B. Husain, G.A. Gomez, M. Naghibosadat, A. Varma, S. Verma, N.A. Hamilton, R.G. Morris, and A.S. Yap. 2019. Anillin Promotes Cell Contractility by Cyclic Resetting of RhoA Residence Kinetics. *Developmental Cell*. 49:894-906.e812.

Burkard, M.E., J. Maciejowski, V. Rodriguez-Bravo, M. Repka, D.M. Lowery, K.R. Clauser, C. Zhang, K.M. Shokat, S.A. Carr, M.B. Yaffe, and P.V. Jallepalli. 2009. Plk1 Self-Organization and Priming Phosphorylation of HsCYK-4 at the Spindle Midzone Regulate the Onset of Division in Human Cells. *PLoS Biology*. 7:e1000111-1000116.

Carmena, M., M. Wheelock, H. Funabiki, and W.C. Earnshaw. 2012. The chromosomal passenger complex (CPC): from easy rider to the godfather of mitosis. *Nature Publishing Group*. 13:789-803.

Chapa-y-Lazo, B., M. Hamanaka, A. Wray, M.K. Balasubramanian, and M. Mishima. 2020. Polar relaxation by dynein-mediated removal of cortical myosin II. *The Journal of Cell Biology*. 219:1250-1225.

Chen, A., P.D. Arora, C.C. Lai, J.W. Copeland, T.F. Moraes, C.A. McCulloch, B.D. Lavoie, and A. Wilde. 2020. The scaffold-protein IQGAP1 enhances and spatially restricts the actin-nucleating activity of Diaphanous-related formin 1 (DIAPH1). *Journal of Biological Chemistry*. 295:3134-3147.

Chen, M., H. Pan, L. Sun, P. Shi, Y. Zhang, L. Li, Y. Huang, J. Chen, P. Jiang, X. Fang, C. Wu, and Z. Chen. 2019. Structure and regulation of human epithelial cell transforming 2 protein. *Proceedings of the National Academy of Sciences of the United States of America*. 16:201913054.

Chen, W., M. Foss, K.-F. Tseng, and D. Zhang. 2008. Redundant mechanisms recruit actin into the contractile ring in silkworm spermatocytes. *PLoS Biology*. 6:e209.

de Groot, C.O., J.E. Hsia, J.V. Anzola, A. Motamedi, M. Yoon, Y.L. Wong, D. Jenkins, H.J. Lee, M.B. Martinez, R.L. Davis, T.C. Gahman, A. Desai, and A.K. Shiau. 2015. A Cell Biologist's Field Guide to Aurora Kinase Inhibitors. *Frontiers in Oncology*. 5:285.

Dechant, R., and M. Glotzer. 2003. Centrosome separation and central spindle assembly act in redundant pathways that regulate microtubule density and trigger cleavage furrow formation. *Developmental Cell*. 4:333-344.

Du, R., C. Huang, K. Liu, X. Li, and Z. Dong. 2021. Targeting AURKA in Cancer: molecular mechanisms and opportunities for Cancer therapy. *Mol Cancer*. 20:15.

Foe, V.E., and G. von Dassow. 2008. Stable and dynamic microtubules coordinately shape the myosin activation zone during cytokinetic furrow formation. *The Journal of Cell Biology*. 183:457-470.

Gomez-Cavazos, J.S., K.-Y. Lee, P. Lara-Gonzalez, Y. Li, A. Desai, A.K. Shiau, and K. Oegema. 2020. A Non-canonical BRCT-Phosphopeptide Recognition Mechanism Underlies RhoA Activation in Cytokinesis. *Current Biology*:1-27.

Hothorn, T., F. Bretz, and P. Westfall. 2008. Simultaneous inference in general parametric models. *Biom J*. 50:346-363.

Hu, C.-K., M. Coughlin, C.M. Field, and T.J. Mitchison. 2011. KIF4 Regulates Midzone Length during Cytokinesis. *Current Biology*. 21:815-824.

Husser, M.C., I. Ozugergin, T. Resta, V.J.J. Martin, and A.J. Piekny. 2022. Cytokinetic diversity in mammalian cells is revealed by the characterization of endogenous anillin, Ect2 and RhoA. *Open Biol*. 12:220247.

Kapoor, S., and S. Kotak. 2019. Centrosome Aurora A regulates RhoGEF ECT-2 localisation and ensures a single PAR-2 polarity axis in C. elegans embryos. *Development*. 146.

Khaliullin, R.N., R.A. Green, L.Z. Shi, J.S. Gomez-Cavazos, M.W. Berns, A. Desai, and K. Oegema. 2018. A positive-feedback-based mechanism for constriction rate acceleration during cytokinesis in Caenorhabditis elegans. *eLife*. 7:91.

Kiyomitsu, T., and I.M. Cheeseman. 2013. Cortical dynein and asymmetric membrane elongation coordinately position the spindle in anaphase. *Cell*. 154:391-402.

Klinkert, K., N. Levernier, P. Gross, C. Gentili, L. von Tobel, M. Pierron, C. Busso, S. Herrman, S.W. Grill, K. Kruse, and P. Gönczy. 2019. Aurora A depletion reveals centrosome-independent polarization mechanism in Caenorhabditis elegans. *eLife*. 8:316.

Kufer, T.A., H.H.W. Silljé, R. Körner, O.J. Gruss, P. Meraldi, and E.A. Nigg. 2002. Human TPX2 is required for targeting Aurora-A kinase to the spindle. *The Journal of Cell Biology*. 158:617-623.

Limzerwala, J.F., K.B. Jeganathan, J.A. Kloeber, B.A. Davies, C. Zhang, I. Sturmlechner, J. Zhong, R.F. Velasco, A.P. Fields, Y. Yuan, D.J. Baker, D. Zhou, H. Li, D.J. Katzmann, and J.M. van Deursen. 2020. FoxM1 insufficiency hyperactivates Ect2–RhoA– mDia1 signaling to drive cancer. *Nature Cancer*:1-34.

Longhini, K.M., and M. Glotzer. 2022. Aurora A and cortical flows promote polarization and cytokinesis by inducing asymmetric ECT-2 accumulation. *Elife*. 11.

Mangal, S., J. Sacher, T. Kim, D.S. Osório, F. Motegi, A.X. Carvalho, K. Oegema, and E. Zanin. 2018. TPXL-1 activates Aurora A to clear contractile ring components from the polar cortex during cytokinesis. *The Journal of Cell Biology*. 217:837-848.

Michaud, A., M. Leda, Z.T. Swider, S. Kim, J. He, J. Landino, J.R. Valley, J. Huisken, A.B. Goryachev, G. von Dassow, and W.M. Bement. 2022. A versatile cortical pattern-

31

forming circuit based on Rho, F-actin, Ect2, and RGA-3/4. *The Journal of Cell Biology*. 221.

Michaux, J.B., F.B. Robin, W.M. McFadden, and E.M. Munro. 2018. Excitable RhoA dynamics drive pulsed contractions in the early C. elegans embryo. *The Journal of Cell Biology*. 115:jcb.201806161-201806130.

Mishima, M. 2016. Centralspindlin in Rappaport's cleavage signaling. *Seminars in Cell and Developmental Biology*. 53:45-56.

Murthy, K., and P. Wadsworth. 2005. Myosin-II-Dependent Localization and Dynamics of F-Actin during Cytokinesis. *Current Biology*. 15:724-731.

Murthy, K., and P. Wadsworth. 2008. Dual role for microtubules in regulating cortical contractility during cytokinesis. *Journal of Cell Science*. 121:2350-2359.

Ozugergin, I., K. Mastronardi, C. Law, and A. Piekny. 2021. The Ran pathway uniquely regulates cytokinesis in cells with different fates in the early C. elegansembryo. 31:1124-1142.

Ozugergin, I., K. Mastronardi, C. Law, and A. Piekny. 2022. Diverse mechanisms regulate contractile ring assembly for cytokinesis in the two-cell Caenorhabditis elegans embryo. *Journal of Cell Science*. 135.

Piekny, A.J., and M. Glotzer. 2008. Anillin is a scaffold protein that links RhoA, actin, and myosin during cytokinesis. *Current Biology*. 18:30-36.

Pollard, T.D., and B. O'Shaughnessy. 2019. Molecular Mechanism of Cytokinesis. *Annual Review of Biochemistry*. 88:661-689.

Portier, N., A. Audhya, P.S. Maddox, R.A. Green, A. Dammermann, A. Desai, and K. Oegema. 2007. A Microtubule-Independent Role for Centrosomes and Aurora A in Nuclear Envelope Breakdown. *Developmental Cell*. 12:515-529.

Prokopenko, S.N., A. Brumby, L. O'Keefe, L. Prior, Y. He, R. Saint, and H.J. Bellen. 1999. A putative exchange factor for Rho1 GTPase is required for initiation of cytokinesis in Drosophila. *Genes & Development*. 13:2301-2314.

Ramkumar, N., J.V. Patel, J. Anstatt, and B. Baum. 2021. Aurora B-dependent polarization of the cortical actomyosin network during mitotic exit. *EMBO reports*:e52387.

Rappaport, R. 1961. Experiments concerning the cleavage stimulus in sand dollar eggs. *The Journal of experimental zoology*. 148:81-89.

Reboutier, D., M.-B. Troadec, J.-Y. Cremet, L. Chauvin, V. Guen, P. Salaun, and C. Prigent. 2013. Aurora A is involved in central spindle assembly through phosphorylation of Ser 19 in P150Glued. *The Journal of Cell Biology*. 201:65-79.

Reymann, A.-C., F. Staniscia, A. Erzberger, G. Salbreux, and S.W. Grill. 2016. Cortical flow aligns actin filaments to form a furrow. *eLife*. 5:883.

Rodrigues, N.T.L., S. Lekomtsev, S. Jananji, J. Kriston-Vizi, G.R.X. Hickson, and B. Baum. 2015. Kinetochore-localized PP1-Sds22 couples chromosome segregation to polar relaxation. *Nature*. 524:489-492.

Schmutz, C., J. Stevens, and A. Spang. 2007. Functions of the novel RhoGAP proteins RGA-3 and RGA-4 in the germ line and in the early embryo of C. elegans. *Development*. 134:3495-3505.

Schneid, S., F. Wolff, K. Buchner, N. Bertram, S. Baygün, P. Barbosa, S. Mangal, and E. Zanin. 2021. The BRCT domains of ECT2 have distinct functions during cytokinesis. *CellReports*. 34:108805.

Schonegg, S., A.T. Constantinescu, C. Hoege, and A.A. Hyman. 2007. The Rho GTPase-activating proteins RGA-3 and RGA-4 are required to set the initial size of PAR domains in Caenorhabditis elegans one-cell embryos. *Proceedings of the National Academy of Sciences*. 104:14976-14981.

Somers, W.G., and R. Saint. 2003. A RhoGEF and Rho family GTPase-activating protein complex links the contractile ring to cortical microtubules at the onset of cytokinesis. *Developmental Cell*. 4:29-39.

Stenoien, D.L., S. Sen, M.A. Mancini, and B.R. Brinkley. 2003. Dynamic association of a tumor amplified kinase, Aurora-A, with the centrosome and mitotic spindle. *Cell motility and the cytoskeleton*. 55:134-146.

Su, K.-C., T. Takaki, and M. Petronczki. 2011. Targeting of the RhoGEF Ect2 to the equatorial membrane controls cleavage furrow formation during cytokinesis. *Developmental Cell*. 21:1104-1115.

Sugimoto, K., T. Urano, H. Zushi, K. Inoue, H. Tasaka, M. Tachibana, and M. Dotsu. 2002. Molecular dynamics of Aurora-A kinase in living mitotic cells simultaneously visualized with histone H3 and nuclear membrane protein importinalpha. *Cell Struct Funct*. 27:457-467.

Sun, L., R. Guan, I.-J. Lee, Y. Liu, M. Chen, J. Wang, J.-Q. Wu, and Z. Chen. 2015. Mechanistic Insights into the Anchorage of the Contractile Ring by Anillin and Mid1. *Developmental Cell*. 33:413-426.

Tatsumoto, T., X. Xie, R. Blumenthal, I. Okamoto, and T. Miki. 1999. Human ECT2 is an exchange factor for Rho GTPases, phosphorylated in G2/M phases, and involved in cytokinesis. *The Journal of Cell Biology*. 147:921-928.

Tavernier, N., F. Sicheri, and L. Pintard. 2021. Aurora A kinase activation: Different means to different ends. *The Journal of Cell Biology*. 220.

van Oostende Triplet, C., M. Jaramillo Garcia, H. Haji Bik, D. Beaudet, and A. Piekny. 2014. Anillin interacts with microtubules and is part of the astral pathway that defines cortical domains. *Journal of Cell Science*. 127:3699-3710.

von Dassow, G., K.J.C. Verbrugghe, A.L. Miller, J.R. Sider, and W.M. Bement. 2009. Action at a distance during cytokinesis. *The Journal of Cell Biology*. 187:831-845.

Werner, M., E. Munro, and M. Glotzer. 2007. Astral Signals Spatially Bias Cortical Myosin Recruitment to Break Symmetry and Promote Cytokinesis. *Current Biology*. 17:1286-1297.

White, J.G., and G.G. Borisy. 1983. On the mechanisms of cytokinesis in animal cells. *J Theor Biol*. 101:289-316.

Wolfe, B.A., T. Takaki, M. Petronczki, and M. Glotzer. 2009. Polo-Like Kinase 1 Directs Assembly of the HsCyk-4 RhoGAP/Ect2 RhoGEF Complex to Initiate Cleavage Furrow Formation. *PLoS Biology*. 7:e1000110-1000115.

Wolpert, L. 1960. The mechanics and mechanism of cleavage. *International Review of Cytology*. 10:163-216.

Ye, A.A., J. Deretic, C.M. Hoel, A.W. Hinman, D. Cimini, J.P. Welburn, and T.J. Maresca. 2015. Aurora A Kinase Contributes to a Pole-Based Error Correction Pathway. *Current Biology*. 25:1842-1851.

Yüce, O., A. Piekny, and M. Glotzer. 2005. An ECT2-centralspindlin complex regulates the localization and function of RhoA. *The Journal of Cell Biology*. 170:571-582.

Zanin, E., A. Desai, I. Poser, Y. Toyoda, C. Andree, C. Moebius, M. Bickle, B. Conradt, A. Piekny, and K. Oegema. 2013. A conserved RhoGAP limits M phase contractility and coordinates with microtubule asters to confine RhoA during cytokinesis. *Developmental Cell*. 26:496-510.

Zhao, P., X. Teng, S.N. Tantirimudalige, M. Nishikawa, T. Wohland, Y. Toyama, and F. Motegi. 2019. Aurora-A Breaks Symmetry in Contractile Actomyosin Networks Independently of Its Role in Centrosome Maturation. *Developmental Cell*. 48:631-645.e636.

33

Zhou, M., and Y.-l. Wang. 2008. Distinct pathways for the early recruitment of myosin II and actin to the cytokinetic furrow. *Molecular biology of the cell*. 19:318-326.
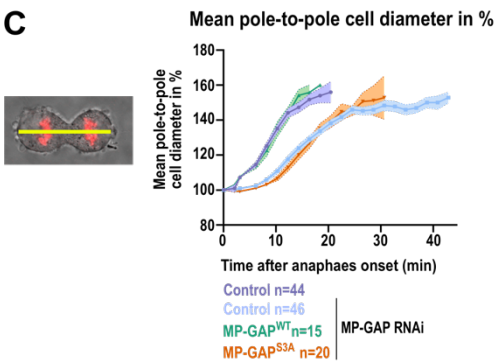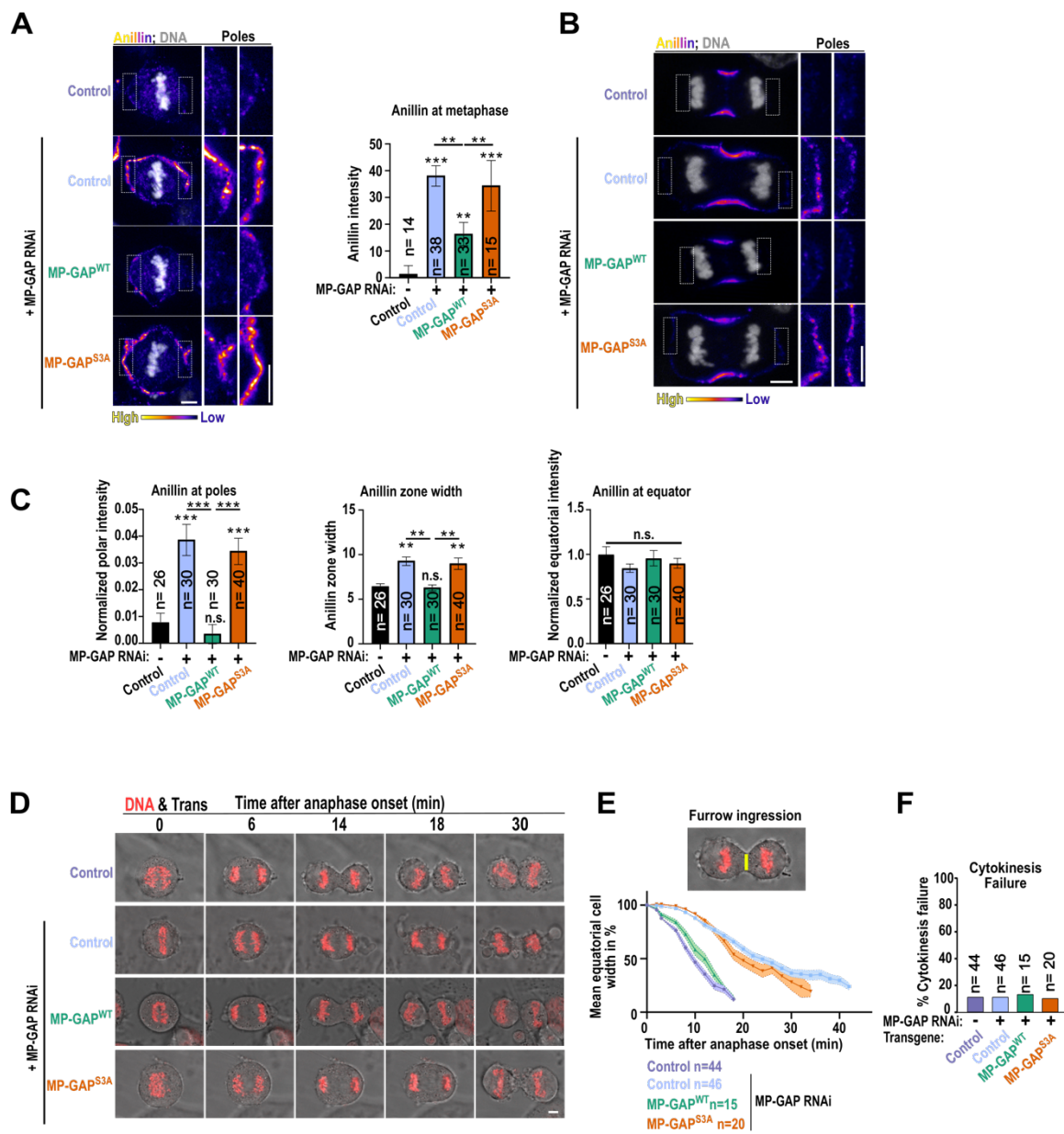
34

Figure 1

Figure S1

Figure 2

Figure S2

A

B

C

Mean pole-to-pole cell diameter in %

Control n=44
Control n=46 ⎫ MP-GAP RNAi
MP-GAP^WT n=15 ⎬
MP-GAP^S3A n=20 ⎭

105

Figure 3

Figure S3

A

B

Figure 4

Figure 5

A

Self interaction of MP-GAP

Coomassie

anti-His

B

Aurora A target sites:

in the hinge   OR   on binding surface

binding: ✔   ✘

Coomassie

anti-His

109

Figure 6

110

4 Chapter III - Light-Controlled Cell-Cycle Arrest and Apoptosis

Uhl, E.*, **Wolff, F.***, Mangal, S., Dube, H., & Zanin, E. (2021). Light-Controlled Cell-Cycle Arrest and Apoptosis. *Angewandte Chemie (International ed. in English)*, 60(3), 1187–1196.

* contributed equally

Chemical Biology

Light-Controlled Cell-Cycle Arrest and Apoptosis

Edgar Uhl[+]*, Friederike Wolff*[+]*, Sriyash Mangal, Henry Dube, and Esther Zanin**

In memory of François Diederich

Abstract: *Cell-cycle interference by small molecules has widely been used to study fundamental biological mechanisms and to treat a great variety of diseases, most notably cancer. However, at present only limited possibilities exist for spatio-temporal control of the cell cycle. Here we report on a photo-caging strategy to reversibly arrest the cell cycle at metaphase or induce apoptosis using blue-light irradiation. The versatile proteasome inhibitor MG132 is photocaged directly at the reactive aldehyde function effectively masking its biological activity. Upon irradiation reversible cell-cycle arrest in the metaphase is demonstrated to take place in vivo. Similarly, apoptosis can efficiently be induced by irradiation of human cancer cells. With the developed photopharmacological approach spatio-temporal control of the cell cycle is thus enabled with very high modulation, as caged MG132 shows no effect on proliferation in the dark. In addition, full compatibility of photo-controlled uncaging with dynamic microscopy techniques in vivo is demonstrated. This visible-light responsive tool should be of great value for biological as well as medicinal approaches in need of high-precision targeting of the proteasome and thereby the cell cycle and apoptosis.*

Introduction

The development of versatile molecular tools enabling elucidation of fundamental bio-chemical processes, detailed mechanistic understanding of diseases, sensitive and selective

[*] E. Uhl,[+] Prof. Dr. H. Dube
Ludwig-Maximilians-Universität München, Department of Chemistry and Center for Integrated Protein Science CIPSM
Butenandtstr. 5–13, 81377 München (Germany)

F. Wolff,[+] S. Mangal, Dr. E. Zanin
Ludwig-Maximilians-Universität München, Center for Integrated Protein Science CIPSM, Department Biology II
Planegg-Martinsried, 82152 München (Germany)
E-mail: zanin@biologie.uni-muenchen.de

Prof. Dr. H. Dube
Current address: Friedrich-Alexander-Universität Erlangen-Nürnberg, Department of Chemistry and Pharmacy
Nikolaus-Fiebiger-Str. 10, 91058 Erlangen (Germany)

[+] These authors contributed equally to this work.

Supporting information and the ORCID identification number(s) for the author(s) of this article can be found under:
https://doi.org/10.1002/anie.202008267.

diagnostics, or efficient treatment of medical conditions is a central goal of chemical biology today. Towards this goal, significant progress has been made with the introduction of photo-pharmacological concepts introducing spatio-temporal control to the bioactivity of molecular agents.[1] Such an approach is not only valuable in the context of disease treatment to reduce side-effects and dosage but also shows high potential in enhancing diagnostics and in fundamental research in biology, medicine, or pharmaceutical sciences. A great variety of bioactive components are currently altered into light-responsive versions either by introducing photo-switch motives[1d,2] or by photolabile protecting groups[1f,3] that cage the crucial bioactive function. In general, photo-switchable variants offer intrinsically greater spatial resolution due to the possibility of turning off their activity at places where it is not wanted. Photocaging approaches however, possess the advantage of very high ON/OFF modulation of activity as residual activity of the caged forms is typically extremely small. In biological applications it is further highly desirable to use nondamaging visible or even near infrared light for photocontrol. Consequentially fundamental research developing such photoswitches and cages is currently a very active area in itself (for recent developments see selected ref. [4] for photoswitches and ref. [5] for cages).

Using photoresponsive tools for the photoinduction of cell death in a selective fashion is of particular interest not least for drug development. Different strategies are followed that include photoswitching and photocaging,[1b,2a,b,3d,6] or optogenetics,[7] as well as classic photodynamic therapy approaches (for selected references see[8]). Photoinduction of apoptosis has been achieved either by controlling cellular uptake of proapoptotic peptides[8a,9] or caspase 3,[10] optogenetically modified caspases,[7,11] or photoswitchable BH3 peptides.[12] Light control of the cell cycle has been accomplished by the development of photoswitchable microtubule inhibitors[13] or by optogenetic methods.[14] Despite these efforts, examples for precise control of the cell cycle are very scarce at the moment stressing the need for effective photopharmacological tools in this area. Light-controlled targeting of specifically the proteasome—a key player in cell cycle regulation—is currently only possible with photoswitchable Bortezomib© variants[15] enabling up to five-fold modulation of activity.[15a]

MG132 is a well-established proteasome inhibitor that is used as a versatile biochemical tool to study various cellular processes including the cell-cycle, apoptosis,[16] proteostasis, or virus life cycle[17] (Figure 1). It consists of a simple tri-peptide structure that mainly targets the chymotrypsin-type catalytic centers at the beta-subunits of the proteasome—a multi-component enzyme, which is responsible for protein degradation. At higher concentrations MG132 also inhibits

the protease calpain.[18] MG132 forms a covalent hemi-acetal adduct with the catalytically active threonine in the active site of the proteasome efficiently inhibiting its proteolytic activity.[19] Proteasome inhibition severely alters protein turnover of the cell. Of special importance in this regard is inhibition of the proteasomes role in cell-cycle control leading to cell-cycle arrest in metaphase.[20] Prolonged inhibition of the proteasome ultimately induces apoptosis, preferentially so in cancer cells as compared to healthy ones.[21] Therefore, MG132 also represents an interesting candidate for cancer research and antidotes although its untamed reactivity and rather fast metabolism currently hampers development into a medical drug.[22] Taken together MG132 can be regarded as a multi-faceted, versatile, and easily applicable biochemical agent, however control of MG132 activity in time or place is currently not possible. We envisioned that especially a light-responsive MG132 version would thus represent a highly valuable tool for a plethora of different applications. In general, such tool would enable studying fundamental and highly dynamic biological processes directly linked to proteasome function with precise spatial and temporal resolution. For example, dynamic modulation of the proteasome-dependent protein turnover would become possible during cell cycle progression, cellular signaling, or immune responses. The dynamic nature and resolution advantage would be even more critical in the context of tissues or organisms to instill local and timed effects—for example, in applications for local cancer treatment, tissue targeting, or apoptosis studies in developing animals, to name a few exciting possibilities. Furthermore, caging could prevent fast metabolism of MG132 during its distribution in an organism and thus would potentially alleviate some of the challenges encountered in its drug development.

In this work we present a photocaging strategy allowing us to convert MG132 into a noneffective agent in its protected MG132-Cage (**1**) form but trigger full functionality upon irradiation with blue light (Figure 1). For this purpose the covalent binding moiety, that is the aldehyde function of MG132, is protected as mixed acetal of the photolabile 4,5-dimethoxy-2-nitrobenzyl (DMNB) cage,[23] which fully blocks binding to the proteasome. This caging approach therefore is highly effective as it targets the main reactivity of MG132 directly, while also removing potential toxicity of the aldehyde, that is, side effects and unselective reactions with nucleophiles within a cell, before uncaging. Blue-light irradiation at 405 nm enables full recovery of the MG132 structure at a given time and place and thus allows to instill spatio-temporal control of the inhibitor function in living cells. The high potential of this new light-responsive proteasome inhibitor for biological as well as pharmacological research is showcased by light-induced cell-cycle arrest as well as apoptosis induction in living human tissue culture cells.

Results and Discussion

Synthesis and Photochemical Assessment

To be able to effectively mask the biological activity of MG132, the main functionality responsible for covalent binding to the proteasome, that is, the aldehyde function, was targeted for protection with a photolabile group. To regain the aldehyde upon irradiation, the oxidation state of its carbon atom should not be altered during uncaging and thus protection as acetal was deemed the most straight-forward approach. To the best of our knowledge such an aldehyde
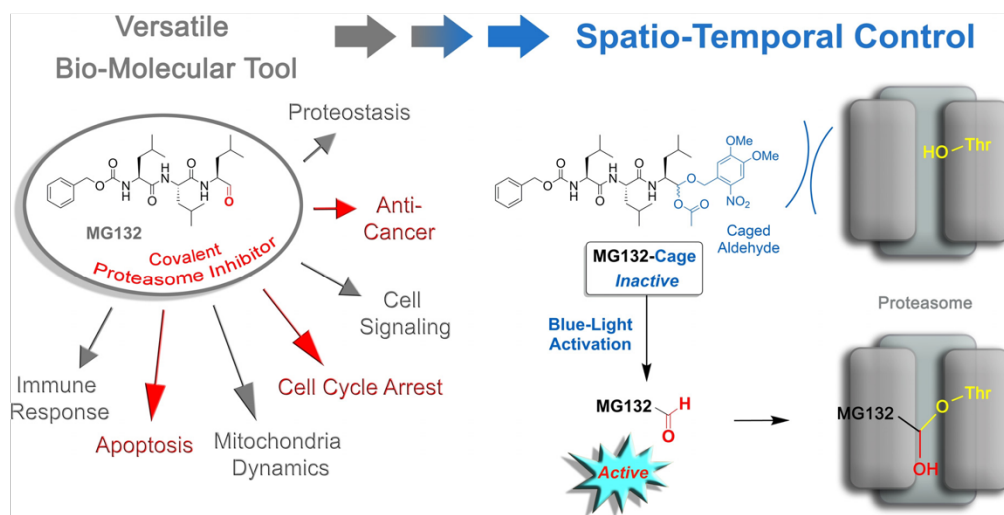
Figure 1. Transformation of the versatile covalent proteasome inhibitor MG132 into a blue-light-controlled biomolecular tool MG132-Cage (**1**) enabling spatio-temporal control of various fundamental biological phenomena. The reactive aldehyde anchorpoint of MG132 is caged by a photolabile protecting group in the form of an acetal rendering the resulting compound MG132-Cage (**1**) fully inactive. Upon blue-light irradiation the aldehyde function is restored and covalent proteasome binding and inhibition is triggered.

113
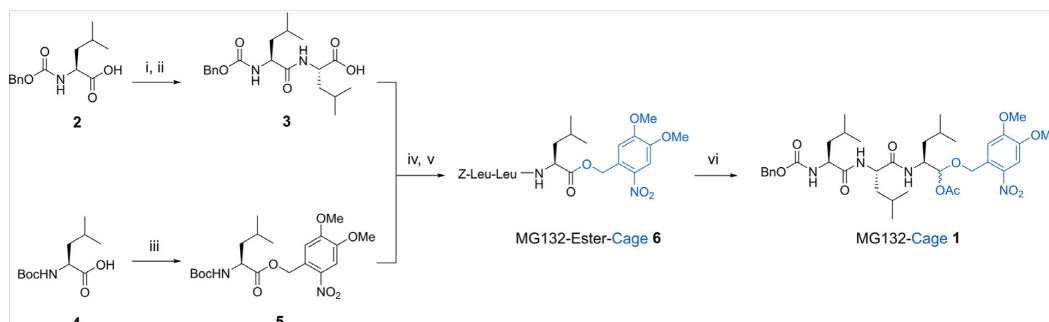
Scheme 1. Synthesis of photocaged MG132-Cage (**1**). The synthetic precursor MG132-Ester-Cage (**6**) is used as control compound in the biological experiments. The caging group DMNB is introduced via an ester link early in the synthesis. After successive peptide couplings a final reductive step yields MG132-Cage with the aldehyde protected as acetal. Conditions: i) Leucine methyl ester x HCl, PyBOP, DIPEA; ii) NaOH 57% yield over two steps; iii) DMNB-alcohol, DCC, DMAP, 69% yield; iv) **5**, TFA; v) **3**, DIPEA, DCC, HOBt, 77% yield over two steps; vi) DIBAL-H, acetic anhydride, 17% yield.

caging/uncaging method—albeit recently introduced for simple organic aldehydes[24]—has not been used for bioactive compounds or in a biological setting so far. The DMNB photolabile group was chosen for its well established photo-caging properties and particularly because of its blue-light responsiveness, which is favorable for biological applications.[23] MG132-Cage (**1**) was synthesized in a convergent and iterative peptide-coupling sequence as shown in Scheme 1 (for full details see Supporting Information, Scheme S1–S4, and Figure S1–S8). Carboxybenzyl (*Z*)-protected leucine **2** was first coupled with leucine methyl ester and after subsequent ester hydrolysis dipeptide **3** was obtained in 57% yield. The DMNB photolabile protecting group was introduced to another *tert*-butyloxycarbonyl (Boc)-protected leucine (**4**) via an ester linkage to give the Boc-protected amine **5** in 69% yield. After Boc-deprotection of **5** using trifluoroacetic acid (TFA) the corresponding free amine **7** was joined with **3** to the tripeptide **6** using standard peptide coupling conditions in 77% yield over the two steps. A final one-pot ester reduction and mixed acetal formation sequence gave the desired MG132-Cage (**1**) in acceptable 17%. Additionally, the DMNB cage was introduced to propionic acid to obtain the control compound Propionic Acid-Cage (**8**, for details see the Supporting Information).

Photodeprotection efficiency of **1** was tested using UV/Vis and especially ^{1}H NMR spectroscopy as quantitative tool (Figure 2a and Figure S13 and S15). Irradiation with various wavelengths showed 405 nm to be the longest wavelength at which full photodeprotection proceeded in reasonable time scales, that is, within several minutes at high NMR concentrations (approximately 2–5 mM in DMSO solution). Concomitant with the decreasing signals of **1**, the known signals of MG132 with the indicative aldehyde signal at 9.5 ppm increased. The responsiveness of the MG132-Cage towards 405 nm is attributed to its absorption profile, which tails out but does not yet reach zero at this wavelength. Irradiation at UV/Vis concentrations (typically 10^{-5} M in DMSO solution) with 405 nm light shows the typical spectral changes expected for deprotection of a DMNB group (Figure 2b). Likewise, photodeprotection of the two control compounds MG132-

Ester-Cage (**6**) and Propionic Acid-Cage (**8**) in DMSO solution leads to the analogous absorption spectral changes (see Figure S11 and S12, respectively) proving effective uncaging also in these cases. Quantum yield measurements were conducted for the MG132-Cage in DMSO solution due to solubility issues in buffer media. Consistent with a previous literature report for the same DMNB photocaging group and photorelease of alcohols,[25] we measured a quantum yield of 1.0% for 405 nm irradiation (for details see Supporting Information and Figure S14–S16). This quantum yield is high enough to warrant effective photodeprotection within minutes under the biological experimental conditions. In a typical biological setup (see below) 1 mL of 5 or 10 μM solutions of caged compound are used (5 or 10 nmol), which are irradiated with a 105 mW 405 nm LED or a 375 mW 405 nm LED positioned in ca. 2 cm distance from the sample solutions.

Light-Induced Metaphase Arrest in HeLa Cells

After demonstrating a proper photochemical response of the MG132-Cage, we moved to *in vivo* studies to showcase its functionality in biological context. For this purpose, light-induced cell-cycle control was evidenced using a quantitative imaging assay in HeLa cells (Figure 3a,b and Figure S17). The cell cycle consists of interphase, during which the cell content including the DNA is duplicated, and the mitotic phase during which the content of the mother cell is distributed to the two daughter cells. The mitotic phase starts with the prometa-phase, followed by the metaphase, anaphase, and telophase. During prometaphase the DNA condenses and at metaphase the chromosomes align at the metaphase plate. After chromosome alignment on the metaphase plate the cell proceeds into anaphase and distributes the chromosomes to the two daughter cells. Finally, the mother cell is split into two daughter cells during telophase. During cell division the cell needs to ensure that it only proceeds into anaphase after all chromosomes are correctly attached to the mitotic spindle and aligned at the metaphase plate. Chromosome alignment
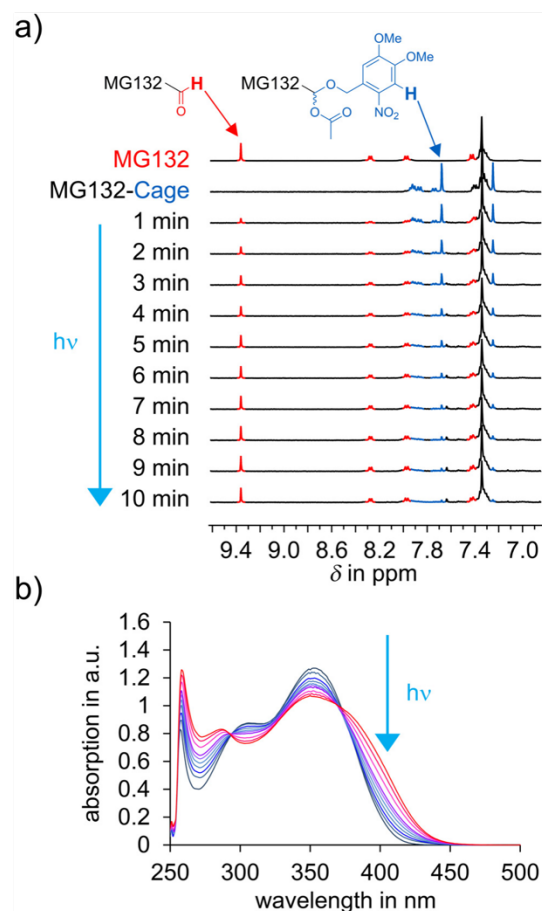
a)

b)

Figure 2. Blue-light irradiation of MG132-Cage (**1**) leads to release of MG132 and restoration of its covalently binding aldehyde function. a) ¹H NMR monitoring of the uncaging process shows almost complete photodeprotection, while at the same time the signal of the aldehyde proton of MG132 increases. The spectrum of pure MG132 is shown at the top, and the spectrum of pure MG132-Cage directly below. Spectra recorded in 1 min intervals during irradiation of a [D₆]DMSO solution of MG132-Cage with a 405 nm LED are shown starting with the third spectrum from the top. b) Changes of the UV/ Vis absorption recorded in intervals during 405 nm irradiation of MG132-Cage in DMSO (blue starting point to red final spectrum).

is monitored by the spindle assembly checkpoint (SAC).[26] In case not all chromosomes are aligned properly at the metaphase plate the SAC keeps the cell in metaphase. To allow metaphase to anaphase transition the proteasome needs to be active to degrade key cell-cycle regulators for example cyclin B[20] and securin.[27] Our first aim was to arrest cells with light in metaphase by using MG132-Cage. HeLa cells were synchronized to enrich for mitotic cells. Cells were then incubated with 5 or 10 μM DMSO solutions of MG132-Cage and either exposed to low power 405 nm LED light for 5 or 10 min or maintained in the dark. After light exposure, cells were incubated for 2 h after which they were fixed and stained

for α-tubulin, filamentous actin (F-actin), and DNA to determine the cell-cycle stage by confocal microscopy (Figure 3b). Over >95% of the mitotic cells were arrested in metaphase when cells were exposed to 10 min light irradiation (Figure 3c,d and Figure S17). Similar metaphase arrest was observed when cells were treated directly with MG132 in 5 μM and 10 μM concentrations with and without 10 min LED light irradiation (Figure 3b and Figure S17b). As a control MG132-Cage-treated cells were maintained in the dark for the same time period. We observed that 58% of those cells were in ana-/telophase, which was indistinguishable from untreated cells or cells treated with DMSO (Figure 3d and Figure S17b). Since mitotic cells spend the same amount of time in metaphase as in ana- and telophase combined (Figure 3b, top) a 1:1 ratio of metaphase to ana-/telophase is expected for non-disturbing conditions. The control experiments thus confirm that uncaging of MG132-Cage in the absence of light is neglectable *in vivo*. To exclude that 405 nm light treatment used for uncaging results in an unspecific metaphase arrest, we also exposed DMSO-treated and untreated cells to irradiation. We found that DMSO-treated and untreated cells that were exposed to 405 nm light for 10 min behaved indistinguishably from control cells kept in the dark. In both cases the cells proceeded readily to ana-/telophase (Figure 3d and Figure S17b). This demonstrated that 405 nm irradiation does not induce cell-cycle arrest at metaphase. To test whether the light-induced arrest in metaphase was reversible, an inhibitor-washout protocol was applied 2 h after light exposure of MG132-Cage treated cells (Figure 3b). After another 2 h waiting time the typical 51% of the mitotic cells were in ana-/telophase evidencing light-induced metaphase arrest can be fully reversed and cells proceed normally into anaphase.

During photodeprotection MG132-Cage is split into MG132 and a nitrosobenzaldehyde. To exclude that the nitrosobenzaldehyde induces metaphase arrest we used the synthetic precursor MG132-Ester-Cage (compound **6**) as well as propionic acid, which was caged with the same photolabile DMNB cage. Upon photoirradiation MG132-Ester-Cage as well as Propionic-Acid-Cage release the corresponding carboxylic acids (the simple tripeptide Z-Leu-Leu-Leu and propionic acid), which are nontoxic to cells and do not inhibit the proteasome. Both caged control compounds also release the very same nitrosobenzaldehyde. Cells that were incubated with 10 μM MG132-Ester-Cage or Propionic-Acid-Cage and irradiated for 10 min did not arrest in metaphase (Figure 3d and Figure S17b). Therefore, light exposed MG132-Cage-treated cells arrest in metaphase due to the release of MG132 and not due to the presence of released nitrosobenzaldehyde. Finally, we addressed whether uncaging of MG132-Cage changes its diffusion across the plasma membrane. To test if uncaging of MG132-Cage promotes its cellular uptake we incubated cells for 1 h with MG132-Cage in the dark and subsequently exchanged the MG132-Cage containing medium with fresh medium without MG132-Cage just before irradiation with 405 nm light. We found 100% of the cells were arrested in metaphase after another 2 h incubation in the dark (Figure 3d, prewash condition). This result was similar to the one from the analogous experiment lacking
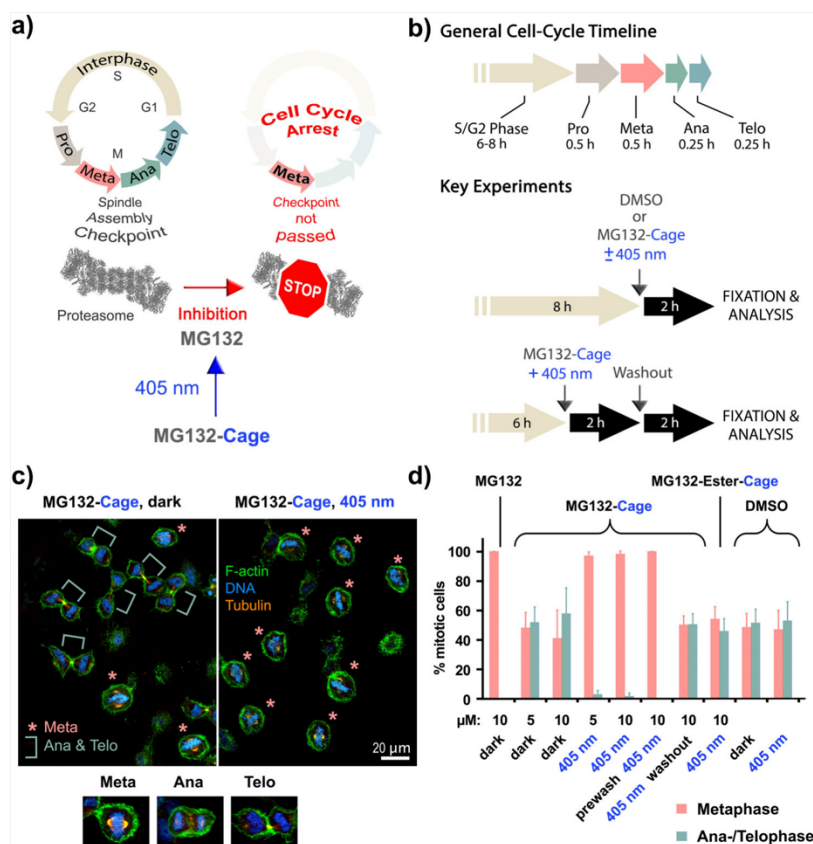
115

Figure 3. Cell-cycle control with blue light. a) General mechanism of cell-cycle arrest induced by photoactivated MG132-Cage. Blue-light irradiation releases MG132, which inhibits the proteasome leading to arrest in metaphase. For depiction of the human proteasome crystallographic data (PDB code 5GJR) from Ref. [28] were used. b) Key experimental setups to quantify blue-light-induced metaphase arrest. c) Confocal microscopy images of HeLa cells incubated with MG132-Cage and either maintained in the dark (left) or exposed for 10 min to 405 nm light (right). Cells were stained for DNA (blue), F-actin (green), and α-tubulin (orange). Metaphase cells are marked with an asterisk and ana-/telophase cells with a green bar. Representative confocal images of a metaphase, anaphase, and telophase cell stained for DNA, F-actin, and α-tubulin are shown at the bottom. d) Mean percentages of mitotic cells in metaphase and ana-/telophase for the indicated conditions. The mean of 3–7 independent experiments is shown and error bars represent standard deviations. For the different conditions a minimum of 110 and maximum of 476 cells were analyzed individually.

a prewash step. It shows that MG132-Cage is taken up by the cells and is present in the cytoplasm prior photoactivation. Light-induced metaphase arrest is thus due to the release of the active compound MG132 and not due to allowing cellular uptake of released MG132.

Light-Induced Apoptosis in HeLa Cells

Proteasome inhibitors induce apoptosis in many cell types including cancer cells. Inhibition of the proteasome results in an increase of proapoptotic factors such as p53 and caspases.[29] For this reason proteasome inhibitors are promising candidates in cancer therapies, bortezomib© for example is used to treat multiple myeloma.[30] Our next goal was to induce apoptosis with blue light in HeLa cells using MG132-

Cage (Figure 4a). HeLa cells were incubated with DMSO or MG132-Cage and either exposed to 405 nm light for 10 min or kept in the dark. To monitor cell viability over time the number of healthy cells was counted using fixed samples 0 h, 12 h, 18 h, and 24 h after light exposure (Figure 4b). In the negative control experiments the number of cells doubled within 24 h (200%). However, for cells incubated with MG132-Cage and exposed to light for 10 min the cell number was reduced to 41% after 18 h and 2% after 24 h (Figure 4c,d). This decrease in cell number over time was comparable to cells treated with 10 μм MG132 (Figure S18a) suggesting that MG132-Cage is very effectively uncaged *in vivo*. Cells incubated with MG132-Cage but kept in the dark continued to proliferate similar to DMSO-treated cells (Figure 4d). This suggests that MG132-Cage is not uncaged in the absence of light even over prolonged incubation time of

116
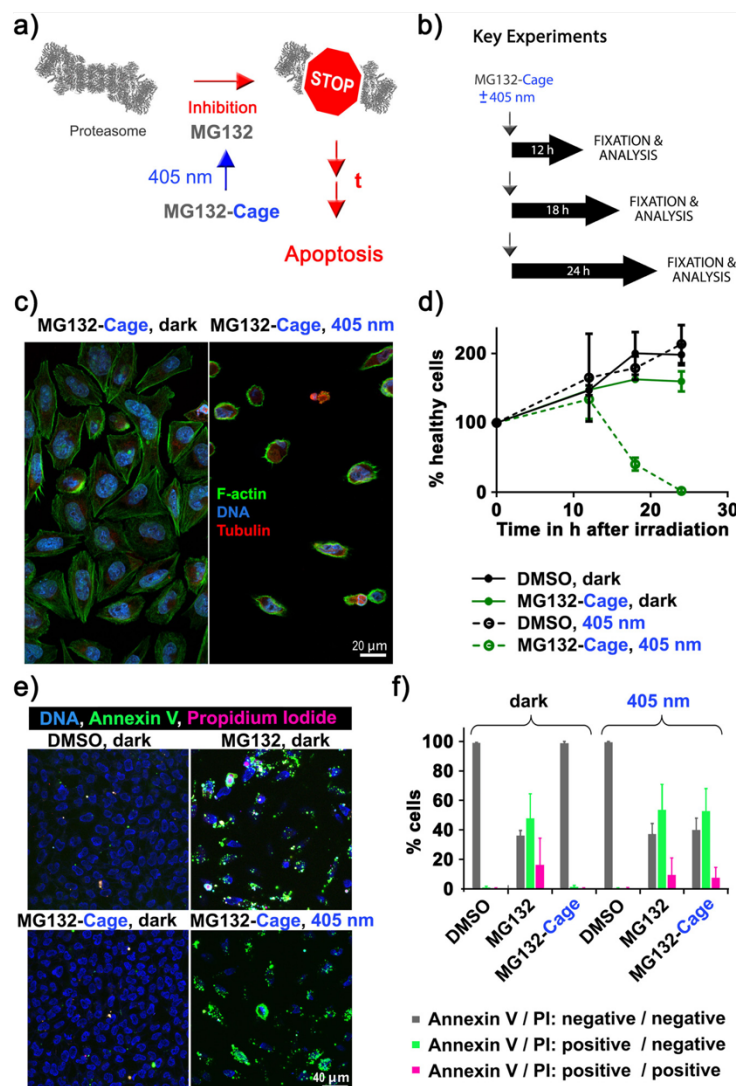
Figure 4. Induction of apoptosis in HeLa cells with blue light. a) Simplified mechanism of apoptosis induction by photoactivated MG132-Cage. Blue-light irradiation triggers MG132 release, which inhibits the proteasome leading to apoptosis of the respective cell after prolonged (t) exposure. b) Experimental setups to quantify blue-light-induced cell death over time. c) Confocal microscopy images of HeLa cells incubated with 10 μM MG132-Cage and either maintained in the dark for 24 h (left) or exposed to 405 nm light for 10 min and then cultured for 24 h (right, the few remaining cells display hallmarks of apoptosis such as cell shrinkage and DNA condensation). d) Mean percentages of healthy cells at different time points under the indicated conditions. Photodeprotection of 10 μM MG132-Cage results in complete cell death 24 hours after irradiation. Mean of two independent experiments is shown and error bars represent standard deviation. e) Maximum z-projections of five images of HeLa cells stained with Hoechst dye to label all nuclei (DNA, blue), annexin V (green), and PI (red). HeLa cells were treated with 0.1% DMSO or 10 μM MG132 and maintained in the dark, or treated with 10 μM MG132-Cage and either exposed to 405 nm light for 10 min or kept in the dark. The 20 h time point was chosen to monitor annexin and PI labeling while cells are dying. f) Percentages of cells that were labeled by annexin V and/or PI for the indicated conditions. The mean of three independent experiments is shown and error bars represent standard deviation. For the different conditions a minimum of 123 and maximum of 409 cells were analyzed individually.

several hours. After irradiating control cells with 405 nm light for 10 min we found that light exposure had no effect on cell number suggesting that the amount of light used to uncage MG132-Cage is not toxic. We also performed an inhibitor-washout experiment to determine whether the effects of 2 h

exposure to uncaged MG132-Cage can be reversed. Cells treated with MG132-Cage, DMSO, or MG132 were exposed to 405 nm light for 10 min and incubated for 2 h followed by inhibitor washout. When we counted cell numbers 24 h later we found that MG132-Cage, DMSO, or MG132 treated cells

117

that had undergone washout displayed similar cell numbers like DMSO-treated control cells without applied washout (Figure S18b). To exclude that the co-released nitrosobenzaldehyde reduces cell viability we incubated cells with 10 μM MG132-Ester-Cage as well as with 10 μM Propionic Acid-Cage and exposed them to 405 nm light for 10 min. After 24 h the healthy cell number in these two control experiments were comparable to the ones observed for DMSO-treated cells indicating that the co-released nitrosobenzaldehyde does not negatively affect cellular growth (Figure S18b). To corroborate these findings we quantified cell viability using a resazurin-based assay. In living cells resazurin is reduced to strongly fluorescent resorufin.[31] When we plotted fluorescence intensity for MG132-Cage (with and without 405 nm light), MG132-Ester-Cage (with 405 nm light), Propionic Acid-Cage (with 405 nm light), MG132 (dark) treated cells against DMSO-treated control cells similar results were obtained as for the single-cell fixed analysis (Figure S19).

To evaluate whether uncaging of MG132-Cage kills cells with the same efficiency as MG132 we performed dose-response experiments. Cells were incubated with different concentrations of MG132 (dark) or MG132-Cage (irradiated with 405 nm light). After 24 h cells were fixed and stained and the number of healthy cells was counted and plotted relative to DMSO-treated cells (Figure S20). For both conditions the cell number started to increase at ≈1.5 μM and reached control levels at ≈0.1 μM concentrations. Our dose-response experiments are in very good agreement with a previous literature report of the dose response of MG132 induced cell death.[32] These experiments confirm that blue-light irradiation of MG132-Cage kills cells in a dose-dependent manner.

To determine whether cells are dying indeed via the apoptosis pathway we also analyzed the cleavage of poly(ADP-ribose) polymerase-1 (PARP). In healthy cells PARP mediates DNA damage repair and with the induction of apoptosis PARP is cleaved by caspases. PARP is a 114 kDa protein and upon caspase activation it is cleaved into a 89 and a 24 kDa fragment.[33] PARP cleavage was analyzed by immunoblots and cells that were incubated with MG132-Cage and exposed to 405 nm light for 10 min showed a reduction in the 114 kDa band and an increase in the 89 kDa fragment, which was similar to cells treated with MG132 (Figure S21). DMSO-treated cells and MG132-Cage treated cells that were maintained in the dark showed a prominent band at 114 kDa and were indistinguishable from each other.

During apoptosis phosphatidylserine translocates from the inner to the outer leaflet of the plasma membrane to generate an "eat me" signal for macrophages.[34] To further confirm that MG132-Cage treated and irradiated cells die by apoptosis, cells were stained with annexin V, which strongly binds to phosphatidylserine.[35] The cells were additionally incubated with propidium iodide (PI), which is a membrane impermeable dye that only labels dead cells. More than 99% of the DMSO-treated cells that were either incubated in the dark or irradiated with 405 nm light for 10 min were negative for annexin V and PI (Figure 4e,f). Treatment of cells with MG132-Cage and subsequent exposure to 405 nm light for 10 min resulted in 53% annexin V positive and PI negative

cells indicating that these cells were still alive but initiated apoptosis. In addition, 7% of the cells were positive for both annexin V and PI showing that these cells were dead. Importantly cells incubated with MG132-Cage but maintained in the dark were indistinguishable from DMSO-treated control cells. Together with the dose-response results these experiments confirm that release of MG132 upon blue-light irradiation induces apoptosis in a dose-dependent manner.

To dynamically follow the light-induced cell-cycle arrest as well as execution of apoptosis upon uncaging of MG132-Cage, a live-cell imaging approach was chosen. Transmission and confocal images of mitotic HeLa cells expressing fluorescently labeled α-tubulin (mKate-α-tubulin) were acquired. For transmission images a 470 nm cut-off filter was placed in the light path to exclude the blue parts of the imaging light and thus to prevent uncaging by image acquisition. Cells were treated with 10 μM MG132-Cage and either exposed to 405 nm LED light for 5 min or maintained in the dark. After light exposure imaging was resumed and continued for 20 h. As expected from our analysis of fixed cells, we found that 405 nm light exposure resulted in efficient cell cycle arrest at metaphase for several hours (Figure 5a, see Movie 1 in the Supporting Information). Following 405 nm light exposed cells for longer time revealed that after ≈12 h cells started to shrink and display strong plasma membrane blebbing, which are both hallmarks of apoptosis (Figure 5b, Movie 2 in the Supporting Information). 20 h post light exposure the majority of cells were undergoing apoptosis. In contrast, cells treated with MG132-Cage but not exposed to 405 nm LED light continued to proliferate and did not show any signs of apoptosis. To dynamically follow reversibility of blue-light-induced metaphase arrest an additional washout experiment was performed using live-cell imaging. MG132-Cage treated cells were exposed to 405 nm LED light, which resulted in metaphase arrest (Figure 5c, Figure S22, and Movie 3 in the Supporting Information). After 2 h cells were washed and imaging was continued. We observed that metaphase cells entered anaphase after the washout and completed cell division. Furthermore, long-term imaging revealed that the cells continued to proliferate and did not display signs of apoptosis. These results demonstrate that uncaging of MG132-Cage can easily be combined with live-cell imaging techniques allowing the investigation of dynamic proteasome-dependent processes in living cells or organisms at high spatial and temporal resolution.

Conclusion

In summary, we present an efficient approach for establishing spatio-temporal control over the cell-cycle stage as well as apoptosis of human cancer cells by blue-light irradiation. To this end a photocaging strategy is used, which effectively masks the reactive and covalently binding aldehyde function of the versatile proteasome inhibitor MG132. In the presence of MG132-Cage without light, cell viability and proliferation remained unperturbed *in vivo*. However, after 5–10 min blue-light irradiation prometaphase cells treated with MG132-Cage are arrested in metaphase for
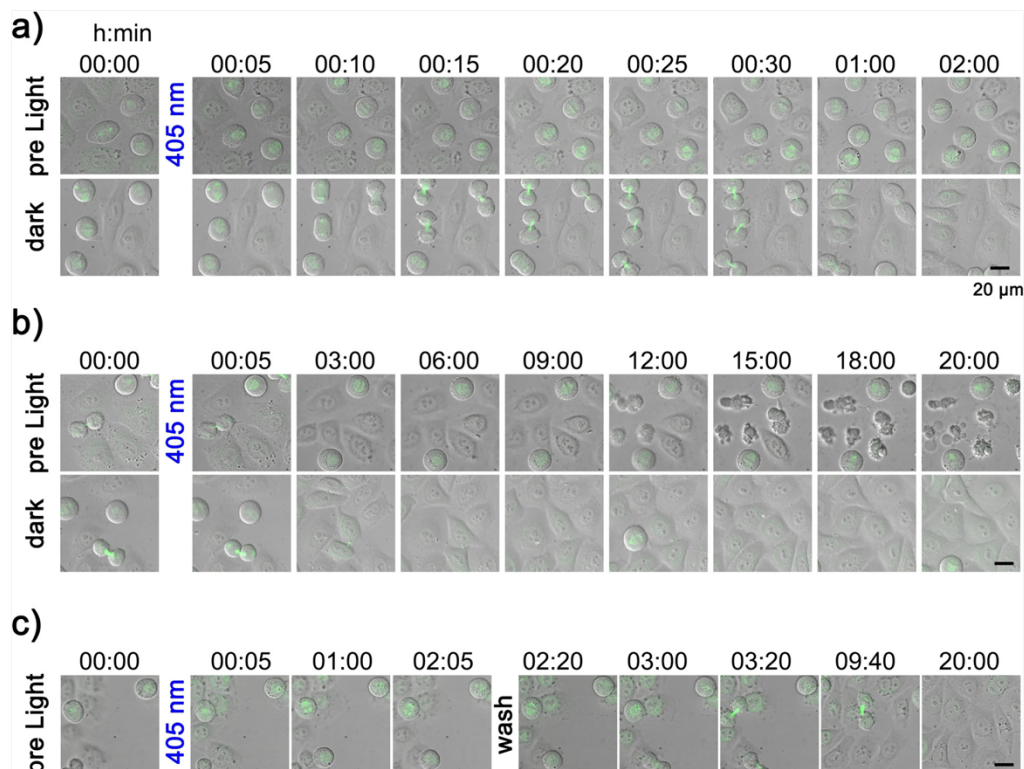
Figure 5. Live-cell imaging of blue-light-induced metaphase arrest and apoptosis in HeLa cells. Cells treated with 10 μM MG132-Cage were either exposed to 405 nm LED light for 5 min (top row) or maintained in the dark (bottom row). Merged transmission and confocal mKate-α-tubulin (maximum z-projection shown in green) images for indicated time points are shown. Scale bars represent 20 μm. a) Prometaphase cells exposed to 405 nm light arrested in metaphase (top row). Control cells in the dark entered anaphase and completed cell division (bottom row). Selected time frames are taken from Movie 1 (see Supporting Information). b) First apoptotic cells were observed ≈12 h after 405 nm light exposure (top row). Cells maintained in the dark continued proliferation without undergoing apoptosis (bottom row). Selected time frames are taken from Movie 2 (see Supporting Information). c) Prometaphase cells exposed to 405 nm light arrested in metaphase for 2 h. After washing the cells proliferation continues establishing reversibility of the arrest. After 20 h no signs of apoptosis are seen. Selected time frames are taken from Movie 3 (see Supporting Information).

several hours. This metaphase arrest can be alleviated by applying a washing protocol. If cells are irradiated in the presence of MG132-Cage and subsequently cultured for prolonged time in the dark almost quantitative apoptosis is induced. Both metaphase arrest as well as apoptosis were followed dynamically with a fluorescent live-cell imaging approach proving full compatibility of photo-controlled uncaging with dynamic microscopy techniques *in vivo*. With this approach a highly promising photopharmacological tool for full spatio-temporal control of cell cycle, apoptosis, and cancer treatment via simple non-toxic blue-light irradiation is presented. We believe that MG132-Cage will be of great interest for a broad variety of biologically and medically oriented research. Our future efforts are directed at establishing full spatial control over proteasome activity in tissues and organisms as well as studying highly dynamic processes related to the biochemistry of the proteasome.

119

[1] a) W. A. Velema, W. Szymanski, B. L. Feringa, *J. Am. Chem. Soc.* **2014**, *136*, 2178–2191; b) K. Hüll, J. Morstein, D. Trauner, *Chem. Rev.* **2018**, *118*, 10710–10747; c) T. Fehrentz, M. Schonberger, D. Trauner, *Angew. Chem. Int. Ed.* **2011**, *50*, 12156–12182; *Angew. Chem.* **2011**, *123*, 12362–12390; d) J. Broichhagen, J. A. Frank, D. Trauner, *Acc. Chem. Res.* **2015**, *48*, 1947–1960; e) J. Morstein, D. Trauner, *Curr. Opin. Chem. Biol.* **2019**, *50*, 145–151; f) C. Brieke, F. Rohrbach, A. Gottschalk, G. Mayer, A. Heckel, *Angew. Chem. Int. Ed.* **2012**, *51*, 8446–8476; *Angew. Chem.* **2012**, *124*, 8572–8604.

[2] a) W. Szymański, J. M. Beierle, H. A. Kistemaker, W. A. Velema, B. L. Feringa, *Chem. Rev.* **2013**, *113*, 6114–6178; b) L. Albert, O. Vazquez, *Chem. Commun.* **2019**, *55*, 10192–10213; c) V. Peddie, A. D. Abell, *J. Photochem. Photobiol. C* **2019**, *40*, 1–20; d) S. Kitzig, M. Thilemann, T. Cordes, K. Rück-Braun, *ChemPhysChem* **2016**, *17*, 1252–1263; e) R. J. Mart, R. K. Allemann, *Chem. Commun.* **2016**, *52*, 12262–12277.

[3] a) J. B. Hansen, W. A. Velema, M. M. Lerch, W. Szymanski, B. L. Feringa, *Chem. Soc. Rev.* **2015**, *44*, 3358–3377; b) A. Bardhan, A. Deiters, *Curr. Opin. Struct. Biol.* **2019**, *57*, 164–175; c) A. Deiters, *ChemBioChem* **2010**, *11*, 47–53; d) N. Ankenbruck, T. Courtney, Y. Naro, A. Deiters, *Angew. Chem. Int. Ed.* **2018**, *57*, 2768–2798; *Angew. Chem.* **2018**, *130*, 2816–2848.

[4] a) P. Lentes, E. Stadler, F. Rohricht, A. Brahms, J. Grobner, F. D. Sonnichsen, G. Gescheidt, R. Herges, *J. Am. Chem. Soc.* **2019**, *141*, 13592–13600; b) K. Klaue, Y. Garmshausen, S. Hecht, *Angew. Chem. Int. Ed.* **2018**, *57*, 1414–1417; *Angew. Chem.* **2018**, *130*, 1429–1432; c) J. Moreno, M. Gerecke, L. Grubert, S. A. Kovalenko, S. Hecht, *Angew. Chem. Int. Ed.* **2016**, *55*, 1544–1547; *Angew. Chem.* **2016**, *128*, 1569–1573; d) M. Dong, A. Babalhavaeji, C. V. Collins, K. Jarrah, O. Sadovski, Q. Dai, G. A. Woolley, *J. Am. Chem. Soc.* **2017**, *139*, 13483–13486; e) M. Dong, A. Babalhavaeji, S. Samanta, A. A. Beharry, G. A. Woolley, *Acc. Chem. Res.* **2015**, *48*, 2662–2670; f) D. Bléger, J. Schwarz, A. M. Brouwer, S. Hecht, *J. Am. Chem. Soc.* **2012**, *134*, 20597–20600; g) S. Samanta, A. A. Beharry, O. Sadovski, T. M. McCormick, A. Babalhavaeji, V. Tropepe, G. A. Woolley, *J. Am. Chem. Soc.* **2013**, *135*, 9777–9784; h) L. N. Lameijer, S. Budzak, N. A. Simeth, M. J. Hansen, B. L. Feringa, D. Jacquemin, W. Szymanski, *Angew. Chem. Int. Ed.* **2020**, *59*, 21663–21670; *Angew. Chem.* **2020**, *132*, 21847–21854; i) D. B. Konrad, G. Savasci, L. Allmendinger, D. Trauner, C. Ochsenfeld, A. M. Ali, *J. Am. Chem. Soc.* **2020**, *142*, 6538–6547; j) F. Kink, M. P. Collado, S. Wiedbrauk, P. Mayer, H. Dube, *Chem. Eur. J.* **2017**, *23*, 6237–6243; k) C. Petermayer, S. Thumser, F. Kink, P. Mayer, H. Dube, *J. Am. Chem. Soc.* **2017**, *139*, 15060–15067.

[5] a) M. A. Fichte, X. M. Weyel, S. Junek, F. Schafer, C. Herbivo, M. Goeldner, A. Specht, J. Wachtveitl, A. Heckel, *Angew. Chem. Int. Ed.* **2016**, *55*, 8948–8952; *Angew. Chem.* **2016**, *128*, 9094–9098; b) Y. Becker, E. Unger, M. A. H. Fichte, D. A. Gacek, A. Dreuw, J. Wachtveitl, P. J. Walla, A. Heckel, *Chem. Sci.* **2018**, *9*, 2797–2802; c) J. A. Peterson, C. Wijesooriya, E. J. Gehrmann, K. M. Mahoney, P. P. Goswami, T. R. Albright, A. Syed, A. S. Dutton, E. A. Smith, A. H. Winter, *J. Am. Chem. Soc.* **2018**, *140*, 7343–7346; d) P. Shrestha, K. C. Dissanayake, E. J. Gehrmann, C. S. Wijesooriya, A. Mukhopadhyay, E. A. Smith, A. H. Winter, *J. Am. Chem. Soc.* **2020**, *142*, 15505–15512; e) J. P. Olson, M. R. Banghart, B. L. Sabatini, G. C. Ellis-Davies, *J. Am. Chem. Soc.* **2013**, *135*, 15948–15954; f) M. Bojtár, K. Németh, F. Domahidy,

G. Knorr, A. Verkman, M. Kállay, P. Kele, *J. Am. Chem. Soc.* **2020**, *142*, 15164–15171; g) D. P. Walton, D. A. Dougherty, *J. Am. Chem. Soc.* **2017**, *139*, 4655–4658; h) T. A. Shell, J. R. Shell, Z. L. Rodgers, D. S. Lawrence, *Angew. Chem. Int. Ed.* **2014**, *53*, 875–878; *Angew. Chem.* **2014**, *126*, 894–897.

[6] M. M. Lerch, M. J. Hansen, G. M. van Dam, W. Szymanski, B. L. Feringa, *Angew. Chem. Int. Ed.* **2016**, *55*, 10978–10999; *Angew. Chem.* **2016**, *128*, 11140–11163.

[7] Y. Nihongaki, H. Suzuki, F. Kawano, M. Sato, *ACS Chem. Biol.* **2014**, *9*, 617–621.

[8] a) B. O. Engesaeter, A. Bonsted, T. Lillehammer, O. Engebraaten, K. Berg, G. M. Maelandsmo, *Cancer Biol. Ther.* **2006**, *5*, 1511–1520; b) D. E. J. G. J. Dolmans, D. Fukumura, R. K. Jain, *Nat. Rev. Cancer* **2003**, *3*, 380–387; c) Z. Zhang, R. Dai, *BioMetals* **2017**, *30*, 37–42; d) N. L. Oleinick, R. L. Morris, I. Belichenko, *Photochem. Photobiol. Sci.* **2002**, *1*, 1–21.

[9] Y. Shamay, L. Adar, G. Ashkenasy, A. David, *Biomaterials* **2011**, *32*, 1377–1386.

[10] N. B. Hentzen, R. Mogaki, S. Otake, K. Okuro, T. Aida, *J. Am. Chem. Soc.* **2020**, *142*, 8080–8084.

[11] E. Mills, X. Chen, E. Pham, S. Wong, K. Truong, *ACS Synth. Biol.* **2012**, *1*, 75–82.

[12] a) P. Wysoczanski, R. J. Mart, E. J. Loveridge, C. Williams, S. B. Whittaker, M. P. Crump, R. K. Allemann, *J. Am. Chem. Soc.* **2012**, *134*, 7644–7647; b) R. J. Mart, R. J. Errington, C. L. Watkins, S. C. Chappell, M. Wiltshire, A. T. Jones, P. J. Smith, R. K. Allemann, *Mol. BioSyst.* **2013**, *9*, 2597–2603.

[13] a) M. Borowiak, W. Nahaboo, M. Reynders, K. Nekolla, P. Jalinot, J. Hasserodt, M. Rehberg, M. Delattre, S. Zahler, A. Vollmar, D. Trauner, O. Thorn-Seshold, *Cell* **2015**, *162*, 403–411; b) A. Sailer, F. Ermer, Y. Kraus, F. H. Lutter, C. Donau, M. Bremerich, J. Ahlfeld, O. Thorn-Seshold, *ChemBioChem* **2019**, *20*, 1305–1314.

[14] a) Y. Goto, K. Aoki, *bioRxiv* **2020**, https://doi.org/10.1101/2020.06.22.166264; b) H. Zhang, C. Aonbangkhen, E. V. Tarasovetc, E. R. Ballister, D. M. Chenoweth, M. A. Lampson, *Nat. Chem. Biol.* **2017**, *13*, 1096–1101.

[15] a) B. Blanco, K. A. Palasis, A. Adwal, D. F. Callen, A. D. Abell, *Bioorg. Med. Chem.* **2017**, *25*, 5050–5054; b) M. J. Hansen, W. A. Velema, G. de Bruin, H. S. Overkleeft, W. Szymanski, B. L. Feringa, *ChemBioChem* **2014**, *15*, 2053–2057.

[16] N. Guo, Z. Peng, *Asia Pac. J. Clin. Oncol.* **2013**, *9*, 6–11.

[17] Q. Tang, P. Wu, H. Chen, G. Li, *Life Sci.* **2018**, *207*, 350–354.

[18] S. Tsubuki, Y. Saito, M. Tomioka, H. Ito, S. Kawashima, *J. Biochem.* **1996**, *119*, 572–576.

[19] M. L. Stein, H. Cui, P. Beck, C. Dubiella, C. Voss, A. Krüger, B. Schmidt, M. Groll, *Angew. Chem. Int. Ed.* **2014**, *53*, 1679–1683; *Angew. Chem.* **2014**, *126*, 1705–1709.

[20] P. Clute, J. Pines, *Nat. Cell Biol.* **1999**, *1*, 82–87.

[21] Q. P. Dou, J. A. Zonder, *Curr. Cancer Drug Targets* **2014**, *14*, 517–536.

[22] a) Z. X. Du, Y. Yan, H. Y. Zhang, B. Q. Liu, Y. Y. Gao, X. F. Niu, Y. Guan, X. Meng, H. Q. Wang, *Endocr.-Relat. Cancer* **2010**, *17*, 553–560; b) C. M. Lee, V. Kumar, R. I. Riley, E. T. Morgan, *Drug Metab. Dispos.* **2010**, *38*, 2166–2172.

[23] H. Görner, *Photochem. Photobiol. Sci.* **2005**, *4*, 822–828.

[24] J. Lage Robles, C. G. Bochet, *Org. Lett.* **2005**, *7*, 3545–3547.

[25] G. A. Krafft, W. R. Sutton, R. T. Cummings, *J. Am. Chem. Soc.* **1988**, *110*, 301–303.

[26] D. Hayward, T. Alfonso-Perez, U. Gruneberg, *FEBS Lett.* **2019**, *593*, 2889–2907.

[27] R. Ciosk, W. Zachariae, C. Michaelis, A. Shevchenko, M. Mann, K. Nasmyth, *Cell* **1998**, *93*, 1067–1076.

[28] X. Huang, B. Luan, J. Wu, Y. Shi, *Nat. Struct. Mol. Biol.* **2016**, *23*, 778–785.

[29] S. R. Vlahakis, A. D. Badley, *Curr. Opin. Clin. Nutr.* **2006**, *9*, 42–47.

120

[30] P. Moreau, P. G. Richardson, M. Cavo, R. Z. Orlowski, J. F. San Miguel, A. Palumbo, J. L. Harousseau, *Blood* **2012**, *120*, 947–959.

[31] J. O'Brien, I. Wilson, T. Orton, F. Pognan, *Eur. J. Biochem.* **2000**, *267*, 5421–5426.

[32] Y. H. Han, H. J. Moon, B. R. You, W. H. Park, *Oncol. Rep.* **2009**, *22*, 215–221.

[33] G. V. Chaitanya, A. J. Steven, P. P. Babu, *Cell Commun. Signaling* **2010**, *8*, 31.

[34] S. Nagata, *Annu. Rev. Immunol.* **2018**, *36*, 489–517.

[35] M. van Engeland, L. J. W. Nieland, F. C. S. Ramaekers, B. Schutte, C. P. M. Reutelingsperger, *Cytometry* **1998**, *31*, 1–9.

121

Supporting Information

Light-Controlled Cell-Cycle Arrest and Apoptosis

Edgar Uhl[+], Friederike Wolff[+], Sriyash Mangal, Henry Dube, and Esther Zanin*

anie_202008267_sm_miscellaneous_information.pdf
anie_202008267_sm_Movie_1.avi
anie_202008267_sm_Movie_2.avi
anie_202008267_sm_Movie_3.avi

Supporting Information

Table of Contents

1

Materials and Methods

Chemistry

General

Reagents and solvents were obtained from *abcr*, *Merck*, *Sigma-Aldrich* or *TCI* in the qualities *puriss*., *p.a*., or *purum* and used as received. Technical solvents were distilled prior to use for column chromatography and extraction on a rotary evaporator (*Heidolph Laborota* 4000 and 4001). Reactions were monitored on *Merck* Silica 60 F254 TLC plates and detection was done by irradiation with UV light (254 nm or 366 nm).

Column chromatography was performed on silica gel (*Merck*, particle size 0.040 - 0.063 mm or *ACROS*, 0.035 – 0.070 mm) using distilled technical solvents.

High Performance Liquid Chromatography (HPLC) was performed on a *Shimadzu* HPLC system consisting of a LC-20AP solvent delivery module, a CTO-20A column oven, a SPD-M20A photodiode array UV/Vis detector, and a CBM-20A system controller using a preparative Silica column from Diacel and HPLC grade solvents (EtOAc and *n*-heptane) from *Sigma-Aldrich* and *ROTH*.

^{1}H NMR and ^{13}C NMR spectra were measured on a JEOL ECX 400 (400 MHz), Bruker AVANCE III HD 400 (400 MHz), Varian VNMRS 400 (400 MHz), Varian VNMRS 600 (600 MHz), or Bruker AVANCE III HD 800 (800 MHz) NMR spectrometer. Deuterated solvents were obtained from *Cambridge Isotope Laboratories* and used without further purification. Chemical shifts (δ) are given relative to tetramethylsilane as external standard. Residual solvent signals in the ^{1}H and ^{13}C NMR spectra were used as internal reference. CDCl$_3$: δ_H = 7.260 ppm, δ_C = 77.160 ppm; CD$_2$Cl$_2$: δ_H = 5.320 ppm, δ_C = 54.000 ppm. Resonance multiplicity is indicated as s (singlet), d (doublet), t (triplet), q (quartet), and m (multiplet). Chemical shifts are given in parts per million (ppm) on the delta scale (δ) and the coupling constant values (J) are in hertz (Hz). Signal assignments are given in the experimental part with the arbitrary numbering indicated.

Electrospray ionisation (ESI) mass spectra were measured on a *Thermo Finnigan LTQ-FT* mass spectrometer.

Infrared spectra were recorded on a *Perkin Elmer Spectrum BX-FT-IR* instrument equipped with a *Smith DuraSamplIR II* ATR-device. Transmittance values are qualitatively described by wavenumber (cm^{-1}) as very strong (vs), strong (s), medium (m), and weak (w).

2

Synthesis

Precursor **3** was prepared according to a published procedure.[1]
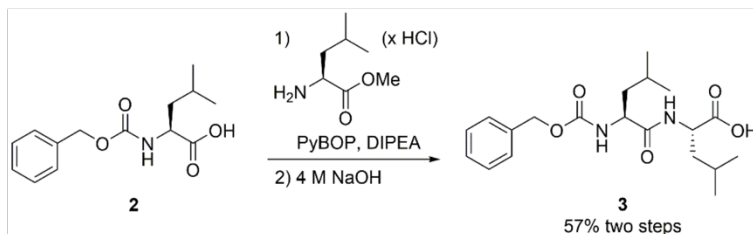
Scheme S1 Synthesis of dipeptide **3**.[1] Conditions: 1) Leu-OMe · HCl (1.0 eq), PyBOP (1.0 eq), DIPEA (2.0 eq), CH$_2$Cl$_2$, 4 h, 23 °C, 74%. 2) 4 M NaOH (1.3 eq), 1,4-dioxane:MeOH (3:1), 4 h, 23 °C, 77%; 57% over two steps.
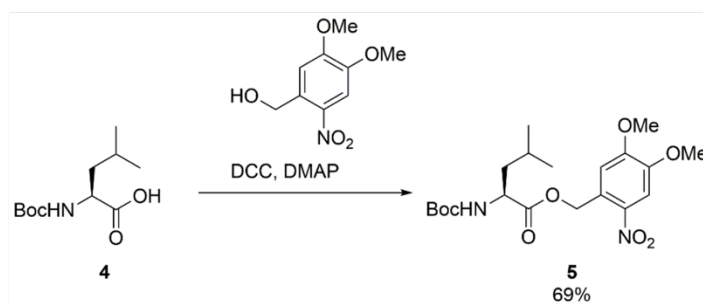
**Scheme S2** Synthesis of photocaged leucine **5**. Conditions: 1) 4,5-Dimethoxy-2-nitrobenzyl alcohol (1.0 eq), DCC (1.1 eq), DMAP (0.1 eq), CH$_2$Cl$_2$, 20 h, 23 °C, 69%.
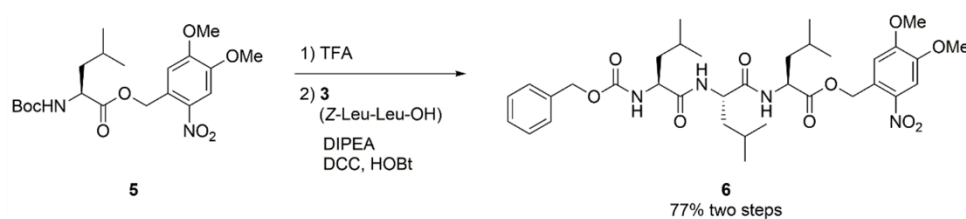
Scheme S3 Synthesis of photocaged tripeptide **6**. Conditions: 1) TFA, CH$_2$Cl$_2$, 0 °C – 23 °C, 2 h; 2) Z-Leu-Leu-OH (**3**, 1.0 eq), HOBt (1.1 eq), DCC (1.1 eq), DIPEA (2.0 eq), THF, 0 °C to 23 °C, 16 h, 77% over two steps.

3
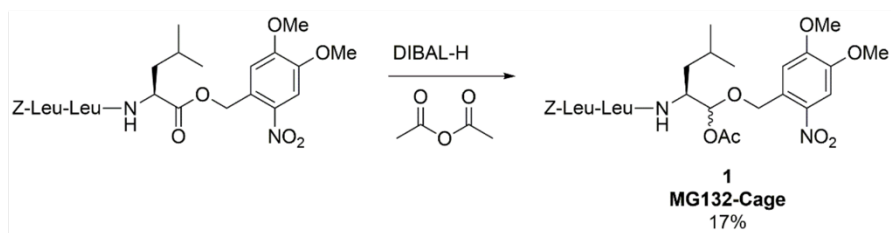
Scheme S4 Synthesis of photocaged MG132 (**1**). Conditions: DIBAL-H (1 M in hexanes, 2.0 eq), CH₂Cl₂, −78 °C, 45 min then pyridine (3.0 eq), DMAP (0.7 eq), acetic anhydride (6.0 eq), 20 h, 17%.

4

((Benzyloxy)carbonyl)-L-leucyl-L-leucine (3)
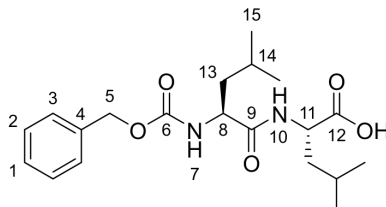
[378.469]

$C_{20}H_{30}N_2O_5$

A solution of Z-Leu-OH (2.80 g, 10.8 mmol, 1.0 eq) and Leu-OMe · HCl (1.96 g, 10.8 mmol, 1.0 eq) in CH_2Cl_2 (40 mL) was treated with PyBOP (5.60 g, 10.8 mmol, 1.0 eq) and DIPEA (3.65 mL, 21.5 mmol, 2.0 eq) and stirred for 4 h at 23 °C. The reaction mixture was extracted with aqueous 1 M HCl, saturated $NaHCO_3$ solution and brine. The organic phase was dried over Na_2SO_4, filtered and the solvent was evaporated *in vacuo*. After flash column chromatography (SiO_2, CH_2Cl_2/methanol 97:3, R_f = 0.16 and SiO_2, *i*-Hex/EtOAc 7:3, R_f = 0.50) Z-Leu-Leu-OMe **3** (3.14 g, 8.00 mmol, 74%) was obtained as a colorless oil that was used directly in next step.

To a solution of Z-Leu-Leu-OMe (3.12 g, 7.95 mmol, 1.0 eq) in 1,4-dioxane (30 mL) and methanol (10 mL) was added sodium hydroxide (420 mg, 10.5 mmol, 1.32 eq) as aqueous 4 M solution. After stirring for 4 h at 23 °C the reaction mixture was acidified to pH 2 using aqueous 1 M HCl and concentrated *in vacuo*. The residue was taken up in EtOAc. The organic phase was extracted with water and brine, dried over Na_2SO_4, filtered and the solvent was evaporated *in vacuo*. After recrystallization from *i*-Hex/EtOAc compound **3** (2.32 g, 6.12 mmol, 77%) was obtained as a colorless solid.

^{1}H NMR (599 MHz, $CDCl_3$, 27 °C) δ = 7.36 – 7.28 (m, 5H, H-C(1), H-C(2) and H-C(3)), 6.86 (d, *J* = 8.2 Hz, 1H, H-N(10)), 5.73 (d, *J* = 8.7 Hz, 1H, H-N(7)), 5.09 (s, 2H, H-C(5)), 4.59 (td, *J* = 8.6, 4.6 Hz, 1H, H-C(11)), 4.32 – 4.26 (m, 1H, H-C(8)), 1.73 – 1.47 (m, 6H, H-C(13) and H-C(14)), 0.94 – 0.85 (m, 12H, H-C(15)).

^{13}C NMR (151 MHz, $CDCl_3$, 27 °C) δ = 176.00 (C-12), 172.88 (C-9), 156.63 (C-6), 136.21 (C-4), 128.66 (C-2), 128.33 (C-1), 128.07 (C-3), 67.29 (C-5), 53.54 (C-8), 50.96 (C-11), 41.27 (C-13), 24.94 (C-14), 24.70 (C-14), 22.92 (C-15), 22.23 (C-15), 21.96 (C-15).

5

IR: $\tilde{v}$ = 3298 (w), 2957 (m), 2871 (w), 1700 (vs), 1637 (vs), 1536 (s), 1232 (s), 1211 (s), 1151 (m), 1042 (s), 1028 (m), 736 (m), 695 (s).

HR-MS (ESI$^+$), [M+H]$^+$ calc. for [$C_{20}H_{31}N_2O_5$]: 379.2227, found: 379.2229.

4,5-Dimethoxy-2-nitrobenzyl (*tert*-butoxycarbonyl)-L-leucinate (5)
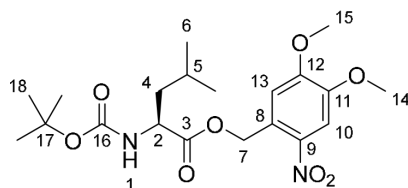
[426.466]

$C_{20}H_{30}N_2O_8$

Boc-Leu-OH (1.00 g, 4.32 mmol, 1.0 eq), 4,5-dimethoxy-2-nitrobenzyl alcohol (992 mg, 4.32 mmol, 1.0 eq), DCC (981 mg, 4.76 mmol, 1.1 eq) and DMAP (52.8 mg, 4.76 mmol, 0.1 eq) in CH_2Cl_2 (30 mL) were stirred for 20 h at 23 °C in the dark. The reaction mixture was filtered and partitioned between EtOAc and 10% citric acid and the aqueous phase was extracted with EtOAc. The combined organic phases were washed with saturated NaHCO$_3$ solution and brine, dried over Na$_2$SO$_4$, filtered and the solvent was evaporated *in vacuo*. After flash column chromatography (SiO$_2$, *i*-Hex/EtOAc 8:2, R_f = 0.26) compound **5** (1.28 g, 3.00 mmol, 69%) was obtained as a yellow solid that crystallized under high vacuum.

^{1}H NMR (599 MHz, CDCl$_3$, 27 °C) δ = 7.73 (s, 1H, H-C(10)), 7.08 (s, 1H, H-C(13)), 5.66 (d, *J* = 15.3 Hz, 1H, H-C(7)), 5.52 (d, *J* = 15.0 Hz, 1H, H-C(7)), 4.87 (d, *J* = 8.5 Hz, 1H, H-N(1)), 4.40 (td, *J* = 9.1, 5.5 Hz, 1H, H-C(2)), 4.03 (s, 3H, H-C(15)), 3.96 (s, 3H, H-C(14)), 1.78 − 1.71 (m, 1H, H-C(5)), 1.66 (ddd, *J* = 13.7, 8.2, 5.5 Hz, 1H, H-C(4)), 1.61 − 1.51 (m, 1H, H-C(4)), 1.42 (d, *J* = 1.6 Hz, 9H, H-C(18)), 0.97 (m, 6H, H-C(6)).

^{13}C NMR (151 MHz, CDCl$_3$, 27 °C) δ = 173.38 (C-3), 155.70 (C-16), 154.01 (C-12), 148.27 (C-11), 139.66 (C-8), 127.47 (C-9), 109.99 (C-13), 108.28 (C-10), 80.20 (C-17), 63.96 (C-7), 56.79 (C-14), 56.56 (C-15), 52.49 (C-2), 41.59 (C-4), 28.45 (C-18), 25.04 (C-5), 23.00 (C-6), 22.00 (C-6).

6

IR: $\tilde{v}$ = 3450 (w), 2963 (w), 1747 (m), 1706 (s), 1522 (m), 1502 (s), 1325 (m), 1277 (m), 1226 (s), 1156 (vs), 1067 (m), 1051 (m), 987 (m), 887 (m), 853 (m), 796 (m), 757 (m).

HR-MS (ESI$^+$), [M+NH$_4$]$^+$ calc. for [C$_{20}$H$_{34}$N$_3$O$_8$]: 444.2340, found: 444.2349.

4,5-Dimethoxy-2-nitrobenzyl ((benzyloxy)carbonyl)-L-leucyl-L-leucyl-L-leucinate (6)
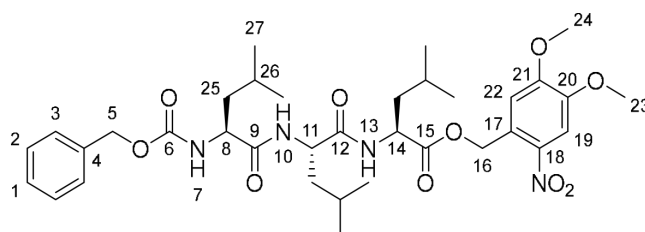
[686.803]

C$_{35}$H$_{50}$N$_4$O$_{10}$

Trifluoroacetic acid (1.0 mL) was added to a stirring solution of compound **5** (500 mg, 1.17 mmol, 1.0 eq) in CH$_2$Cl$_2$ (4.0 mL) at 0 °C. The solution was stirred for 2 h at 23 °C and the solvent was evaporated *in vacuo* to give the deprotected TFA-Leu-NVOC (**7**). The amount of residual trifluoroacetic acid was calculated from the difference to 100% yield and neutralized in the following step with additional DIPEA (1:1).

TFA-Leu-NVOC (**7**) (1.17 mmol, 1.0 eq), Cbz-Leu-Leu (**3**) (433 mg, 1.17 mmol, 1.0 eq), HOBt · H$_2$O (197 mg, 1.29 mmol, 1.1 eq) and DCC (266 mg, 1.29 mmol, 1.1 eq) in THF (5.0 mL) were cooled to 0 °C. DIPEA (408 mL, 303 mg, 2.34 mmol, 2.0 eq) was added and the reaction mixture was stirred at 23 °C for 16 h. The mixture was partitioned between EtOAc and 10% citric acid and the aqueous phase was extracted with EtOAc. The combined organic phases were washed with saturated NaHCO$_3$ solution and brine, dried over Na$_2$SO$_4$, filtered and the solvent was evaporated *in vacuo*. After flash column chromatography (SiO$_2$, CH$_2$Cl$_2$:MeOH 97:3, R_f = 0.33) compound **6** (620 mg, 903 µmol, 77%) was obtained as a colorless solid.

^{1}H NMR (599 MHz, CDCl$_3$, 27 °C) δ = 7.71 (s, 1H, H-C(19)), 7.37 − 7.27 (m, 5H, H-C(1) to H-C(3)), 7.03 (s, 1H, H-C(22)), 6.87 (d, *J* = 7.8 Hz, 1H, H-N(13)), 6.63 (d, *J* =

7

7.9 Hz, 1H, H-N(10)), 5.60 – 5.51 (m, 2H, H-C(16)), 5.38 (d, *J* = 8.1 Hz, 1H, H-N(7)), 5.12 – 5.05 (m, 2H, H-C(5)), 4.66 – 4.59 (m, 1H, H-C(14)), 4.50 – 4.43 (m, 1H, H-C(11)), 4.22 – 4.16 (m, 1H, H-C(8)), 4.01 (s, 3H, H-C(24)), 3.94 (s, 3H, H-C(23)), 1.72 – 1.54 (m, 7H, H-C(25) and H-C(26)), 1.52 – 1.44 (m, 2H, H-C(25)), 0.94 – 0.81 (m, 18H, H-C(27)).

^{13}C NMR (151 MHz, CDCl$_3$, 27 °C) δ = 172.43 (C-9), 172.35 (C-15), 171.89 (C-12), 156.43 (C-6), 153.91 (C-21), 148.33 (C-20), 139.74 (C-18), 136.15 (C-4), 128.67 (C-2), 128.37 (C-1), 128.09 (C-3), 127.08 (C-17), 110.27 (C-22), 108.28 (C-19), 67.26 (C-5), 64.10 (C-16), 56.78 (C-24), 56.52 (C-23), 53.66 (C-8), 51.72 (C-11), 51.10 (C-14), 41.33 (C-25), 41.02 (C-25), 40.57 (C-25), 24.95 (C-26), 24.80 (C-26), 22.98 (C-27), 22.83 (C-27), 22.22 (C-27), 22.12 (C-27), 21.84 (C-27).

IR: $\tilde{v}$ = 3324 (m), 2927 (s), 2850 (m), 1704 (w), 1645 (m), 1625 (vs), 1572 (s), 1523 (vs), 1436 (m), 1311 (m), 1273 (s), 1242 (s), 1221 (s), 1185 (m), 1156 (m), 1087 (m), 1067 (s), 1045 (m), 983 (w), 891 (m), 870 (w), 796 (w), 733 (w).

HR-MS (ESI$^+$), [M+NH$_4$]$^+$ calc. for [C$_{35}$H$_{54}$N$_5$O$_{10}$]: 704.3865, found: 704.3876.

8

(5*S*,8*S*,11*S*)-14-(4,5-dimethoxy-2-nitrophenyl)-5,8,11-triisobutyl-3,6,9-trioxo-1-phenyl-2,13-dioxa-4,7,10-triazatetradecan-12-yl acetate – MG132-Cage (1)
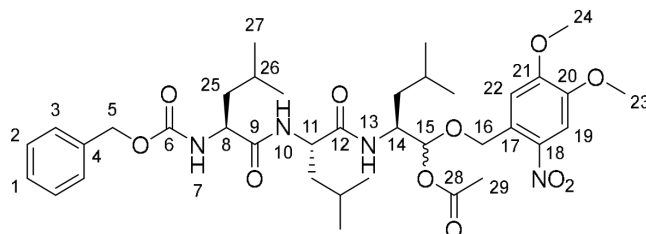
[730.856]

$C_{37}H_{54}N_4O_{11}$

Compound **6** (222 mg, 323 mmol, 1.0 eq) in CH_2Cl_2 (2 mL) was cooled to −78 °C and DIBAL-H (1 M in hexanes, 646 µL, 646 µmol, 2.0 eq) was added dropwise. 45 min after complete addition pyridine (76.7 mg, 970 µmol, 3.0 eq), DMAP solution (26.0 mg, 213 µmol, 0.66 eq in 1 mL CH_2Cl_2) and acetic anhydride (198 mg, 1.94 mmol, 6.0 eq) were added. The reaction mixture was stirred for another 20 h at −78 °C before it was warmed to 0 °C. After another 35 min the reaction was stopped by addition of saturated ammonium chloride solution and saturated Rochelle salt solution. The mixture was stirred for 50 min at 22 °C and then extracted with CH_2Cl_2. The combined organic phases were washed with ice cold 1 M potassium bisulfate solution, saturated sodium bicarbonate solution and brine. The organic phase was dried over Na_2SO_4, filtered and the solvent was evaporated *in vacuo*. After flash column chromatography (SiO_2, *i*-Hex/EtOac 3:1, R_f = 0.14) **MG132-Cage** (**1**) (mixture of diastereomers (6:4), 40 mg, 54.7 µmol, 17%) was obtained as an off-white solid.

^{1}H NMR (800 MHz, CD_2Cl_2, 27 °C) δ = 7.68 (s, 1H, H-C(19)), 7.38 – 7.31 (m, 5H, H-C(1) to H-C(3)), 7.27 (s, 1H, H-C(22)), 7.21 (s, 1H, H-C(22)), 6.32 – 6.25 (m, 2H, H-N(10) and H-N(13)), 5.90 (d, *J* = 3.6 Hz, 1H, H-C(15)), 5.87 (d, *J* = 3.2 Hz, 1H, H-C(15)), 5.15 – 4.98 (m, 5H, H-C(5), H-N(7) and H-C(16)), 4.36 – 4.29 (m, 2H, H-C(11) and H-C(14)), 4.10 – 4.03 (m, 1H, H-C(8)), 3.99 (s, 3H, H-C(24)), 3.91 (s, 2H, H-C(23)), 3.90 (s, 1H, H-C(24)), 2.09 (s, 1H, H-C(29)), 2.05 (s, 2H, H-C(29)), 1.73 – 1.40 (m, 9H, H-C(25) and H-C(26)), 0.95 – 0.83 (m, 18H, H-C(27)).

^{13}C NMR (201 MHz, CD_2Cl_2, 27 °C) δ = 172.52 (C-9), 171.97 (C-12), 171.15 (C-28), 154.52 (C-21), 154.39 (C-21), 148.63 (C-20), 139.94 (C-18), 136.88 (C-4), 129.49 (C-9

17), 129.09 (C-2), 128.80 (C-1), 128.53 (C-3), 128.50 (C-3), 110.75 (C-22), 110.68 (C-22), 108.60 (C-19), 108.49 (C-19), 97.93 (C-15), 97.82 (C-15), 69.38 (C-16), 69.14 (C-16), 67.67 (C-5), 57.02 (C-24), 56.94 (C-24), 56.84 (C-23), 56.81 (C-23), 52.59 (C-11 or C-14), 52.48 (C-11 or C-14), 50.37 (C-11 or C-14), 50.12 (C-11 or C-14), 41.66 (C-25), 41.06 (C-25), 40.93 (C-25), 39.06 (C-25), 39.01 (C-25), 25.32 (C-26), 25.28 (C-26), 25.11 (C-26), 25.01 (C-26), 23.87 (C-27), 23.76 (C-27), 23.26 (C-27), 23.23 (C-27), 23.11 (C-27), 22.26 (C-27), 22.13 (C-27), 22.09 (C-27), 22.00 (C-27), 21.91 (C-27), 21.38 (C-29).

HR-MS (ESI$^+$), [M+NH$_4$]$^+$ calc. for [C$_{35}$H$_{58}$N$_5$O$_{11}$]: 748.4127 found: 748.4133.

4,5-dimethoxy-2-nitrobenzyl propionate (Propionic acid-Cage 8)
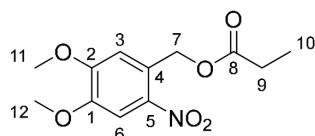
[269.253]

C$_{12}$H$_{15}$NO$_6$

TEA (405 mg, 4.00 mmol, 2.0 eq) and propionyl chloride (204 mg, 2.20 mmol, 1.1 eq) were added to a stirring solution of 6-nitroveratryl alcohol (426 mg, 2.00 mmol, 1.0 eq) and DMAP (24.4 mg, 0.20 mmol, 0.1 eq) in CH$_2$Cl$_2$ (20.0 mL). The solution was stirred for 3 d at 23 °C before it was transferred to a separatory funnel charged with aqueous 2 M HCl solution. The aqueous phase was extracted with CH$_2$Cl$_2$ and the combined organic phases were washed with saturated NaHCO$_3$ solution and brine, dried over Na$_2$SO$_4$, filtered, and the solvent was evaporated *in vacuo*. After flash column chromatography (SiO$_2$, *i*-Hex:EtOAc 3:2) compound **8** (398 mg, 1.48 mmol, 74%) was obtained as a pale yellow solid.

^{1}H NMR (599 MHz, CDCl$_3$, 27 °C) δ = 7.72 (s, 1H, H-C(6)), 7.00 (s, 1H, H-C(3)), 5.51 (s, 2H, H-C(7)), 3.98 (s, 3H, H-C(11)), 3.96 (s, 3H, H-C(12)), 2.48 – 2.42 (m, 2H, H-C(9)), 1.22 – 1.19 (m, 3H, H-C(10)).

10

^{13}C NMR (151 MHz, CDCl$_3$, 27 °C) δ = 173.86 (C-8), 153.58 (C-2), 148.37 (C-1), 140.18 (C-5), 127.33 (C-4), 110.56 (C-3), 108.41 (C-6), 63.24 (C-7), 56.57 (C-11), 56.51 (C-12), 27.75 (C-9), 9.32 (C-10).

HR-MS (ESI$^+$), [M+NH$_4$]$^+$ calc. for [C$_{12}$H$_{19}$N$_2$O$_6$]: 287.1243, found: 287.1239.

11

NMR Spectra

Compound 3
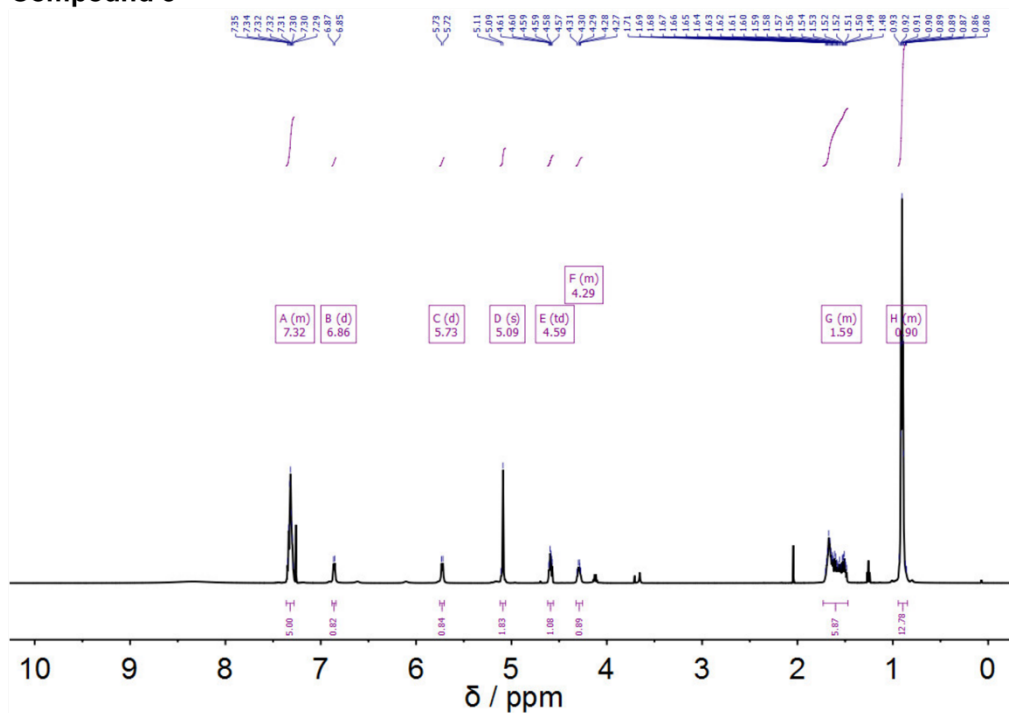
Figure S1 ¹H NMR spectrum (599 MHz, CDCl₃, 27 °C) of compound **3**.
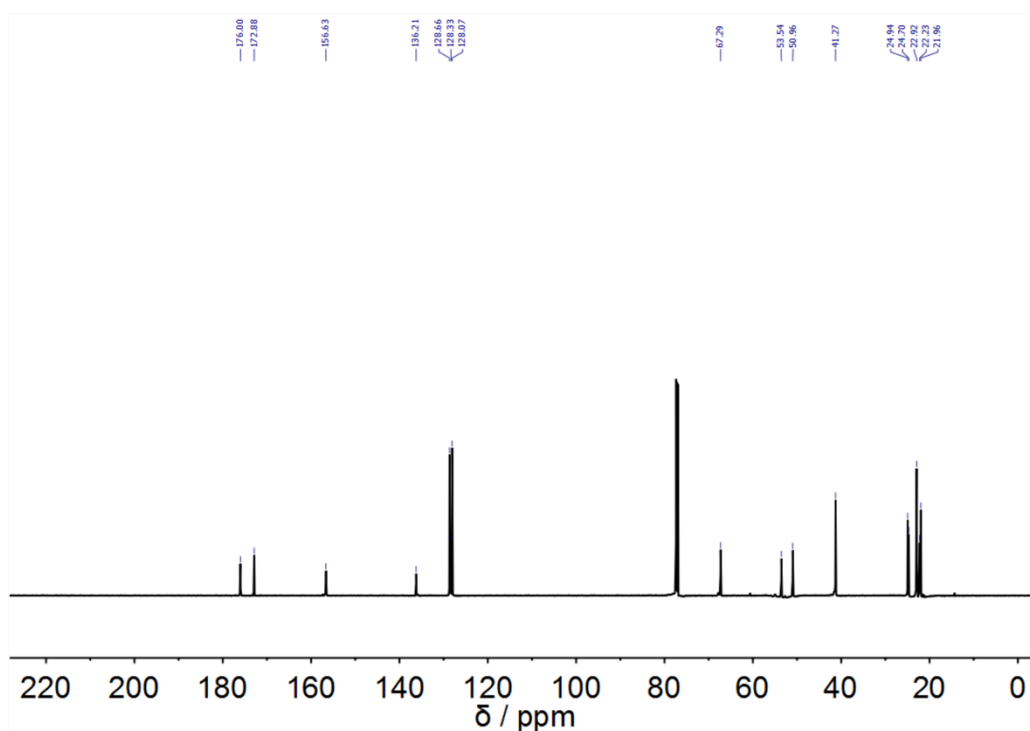
Figure S2 ¹³C NMR spectrum (151 MHz, CDCl₃, 27 °C) of compound **3**.

12

Compound 5

Figure S3 ^{1}H NMR spectrum (599 MHz, CDCl₃, 27 °C) of compound **5**.

Figure S4 ^{13}C NMR spectrum (151 MHz, CDCl₃, 27 °C) of compound **5**.

13

135
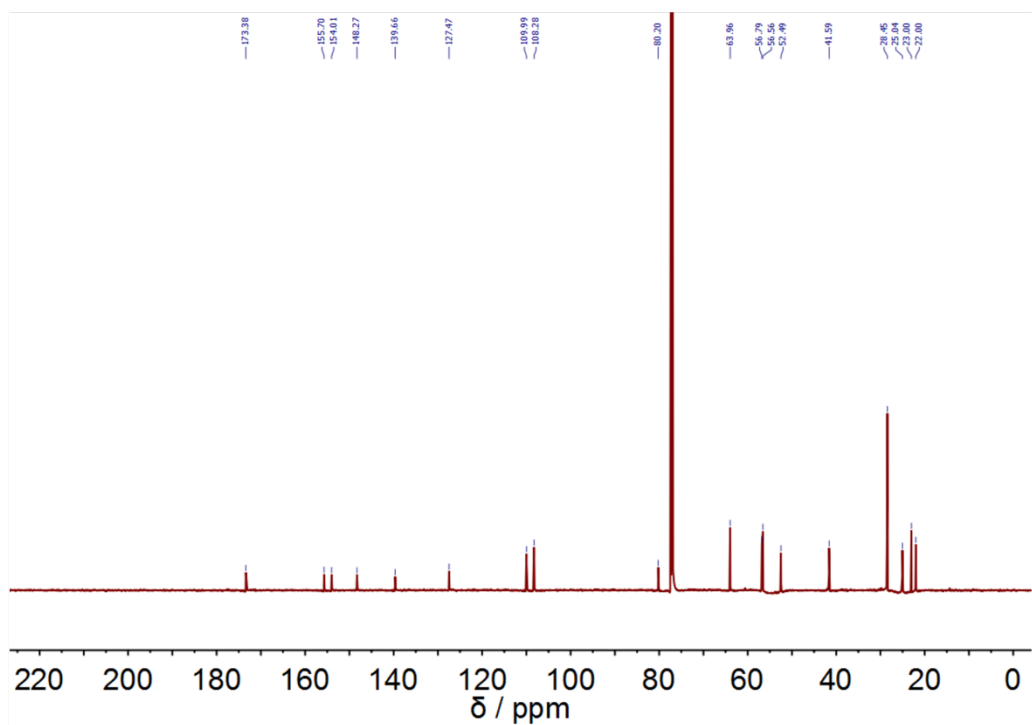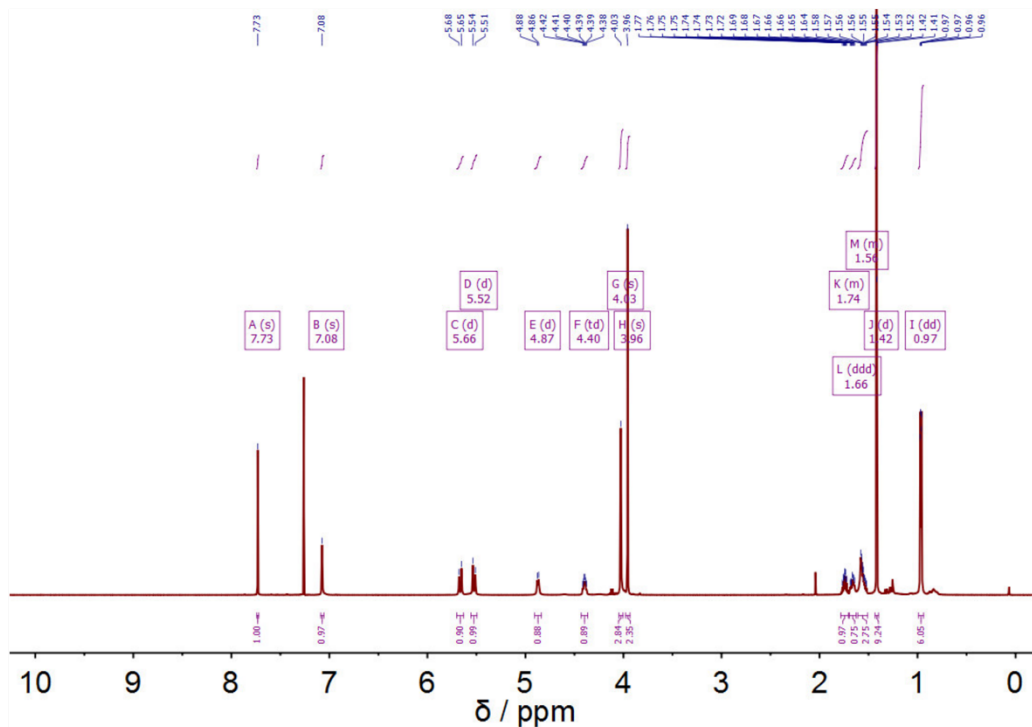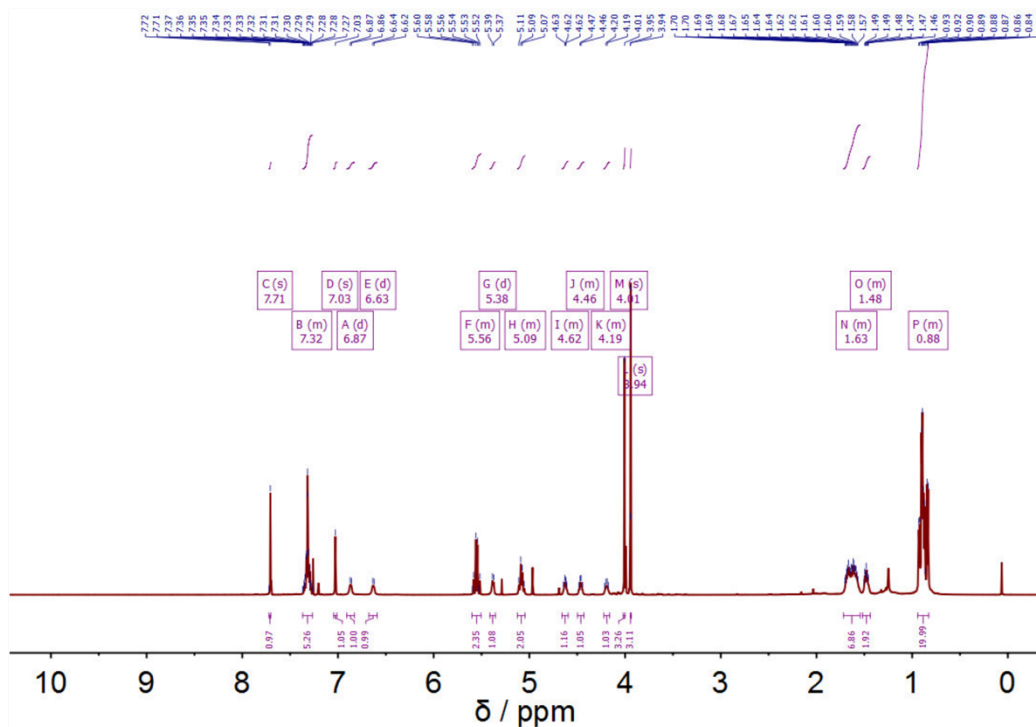
Compound 6

Figure S5 ^{1}H NMR spectrum (599 MHz, CDCl$_3$, 27 °C) of compound **6**.
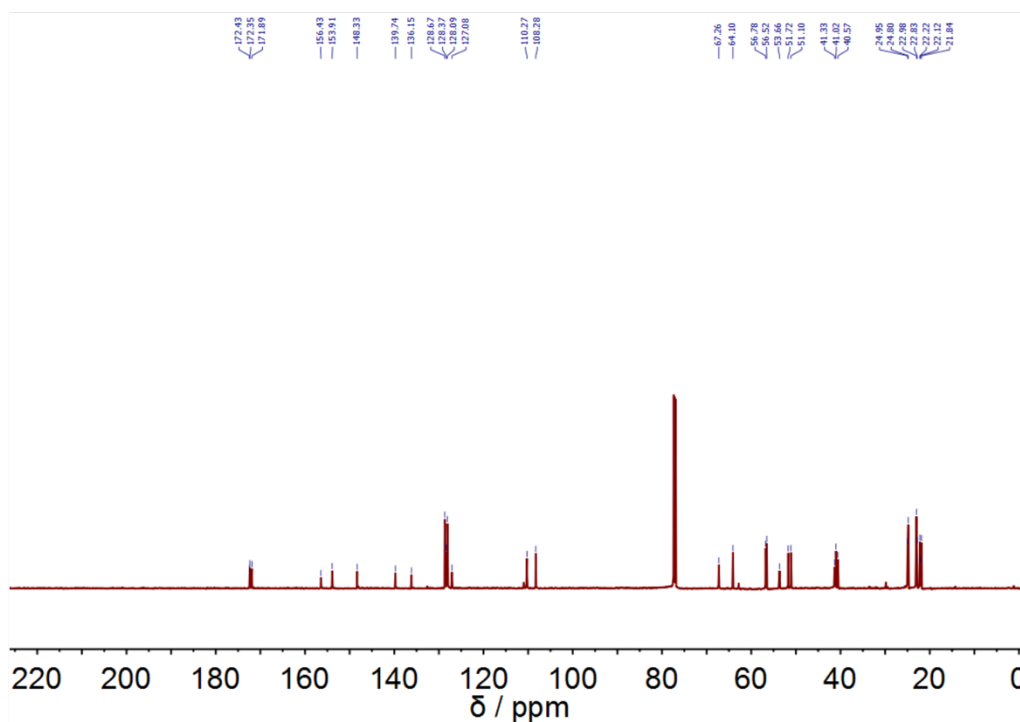
Figure S6 ^{13}C NMR spectrum (151 MHz, CDCl$_3$, 27 °C) of compound **6**.

14

136

Compound 1

Figure S7 ^{1}H NMR spectrum (800 MHz, CD$_2$Cl$_2$, 27 °C) of compound **1**.

Figure S8 ^{13}C NMR spectrum (201 MHz, CD$_2$Cl$_2$, 27 °C) of compound **1**.

15
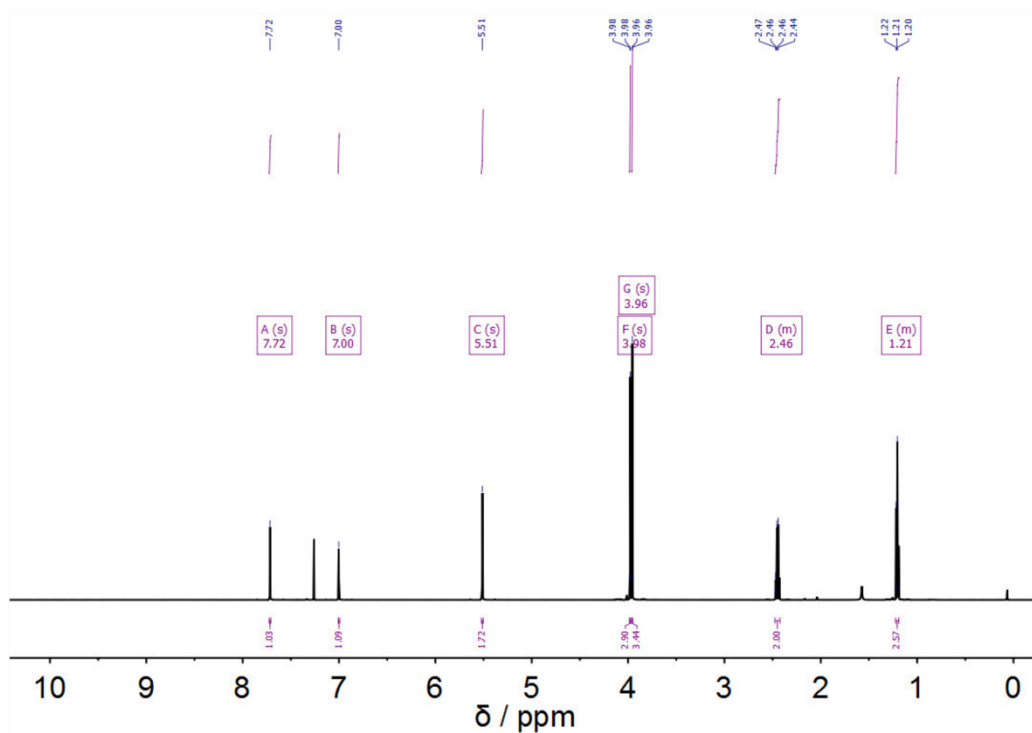
Figure S9 ¹H NMR spectrum (599 MHz, CDCl₃, 27 °C) of compound **8**.
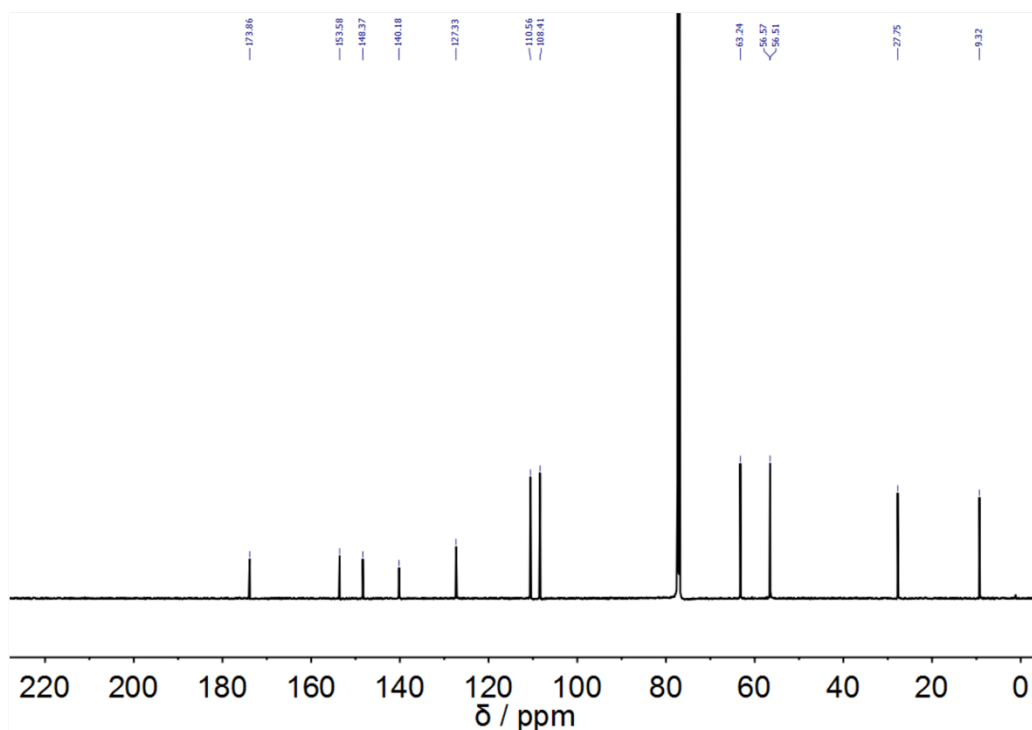
Figure S10 ¹³C NMR spectrum (151 MHz, CDCl₃, 27 °C) of compound **8**.

16

138

Photodeprotection of Propionic Acid-Cage, MG132-Ester-Cage, and MG132-Cage upon irradiation with 405 nm light
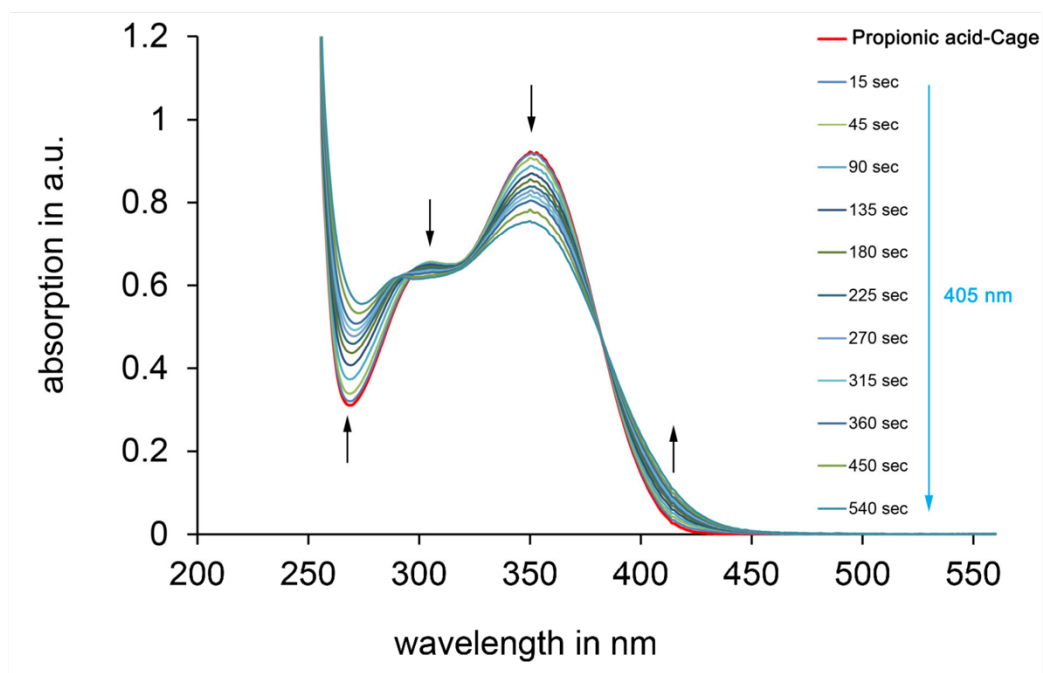
Figure S11   Changes of the UV/Vis absorption recorded in intervals during 405 nm irradiation of Propionic-Acid-Cage in DMSO solution at 20 °C.

17
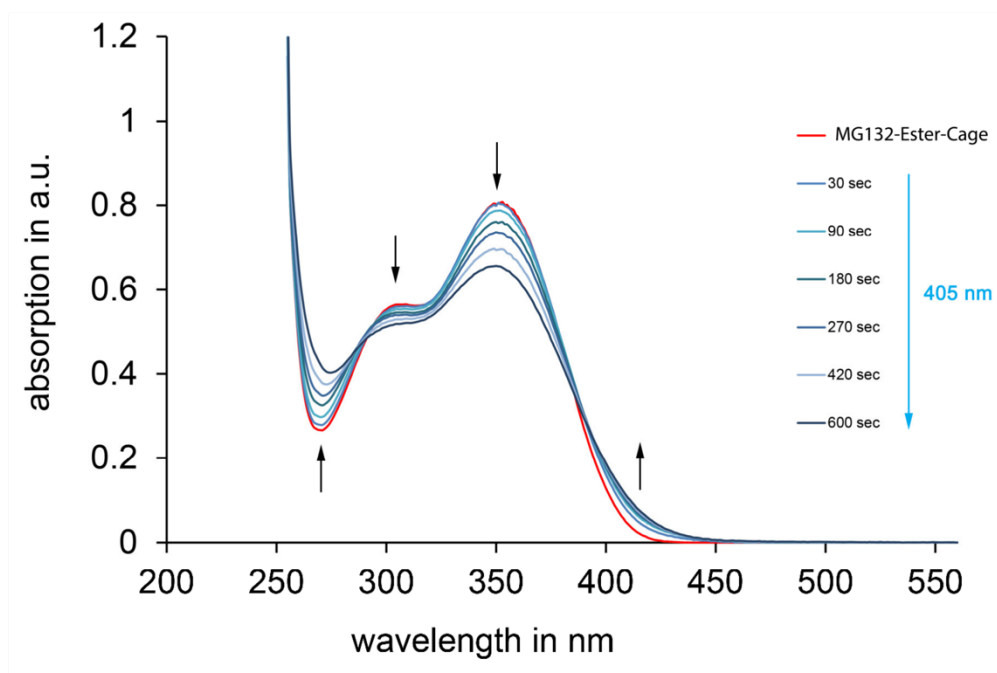
Figure S12 Changes of the UV/Vis absorption recorded in intervals during 405 nm irradiation of MG132-Ester-Cage in DMSO solution at 20 °C.
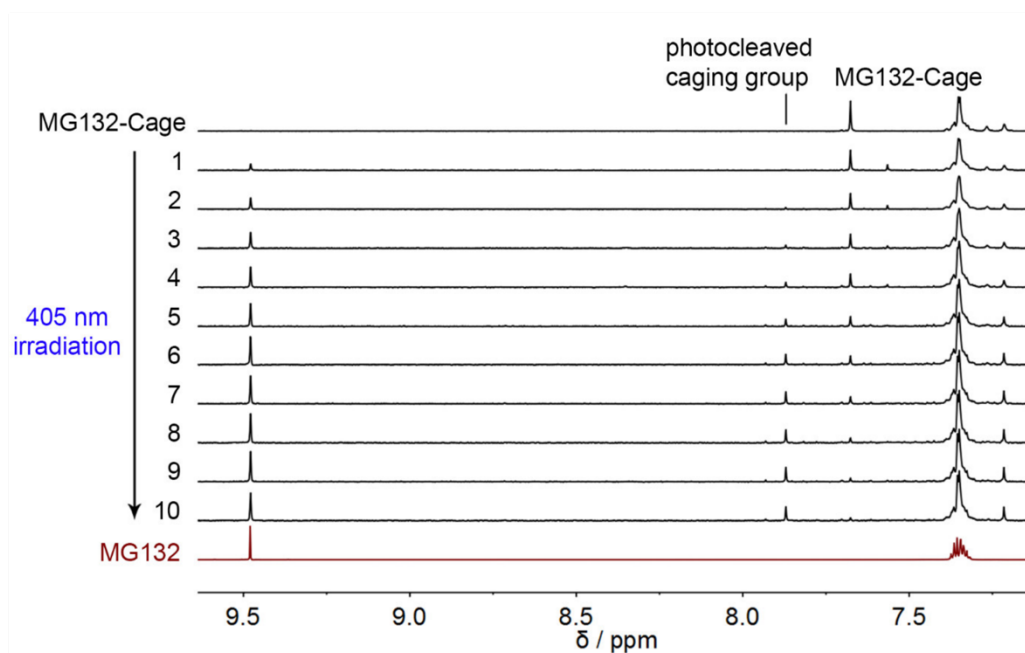
Figure S13 Aromatic part of the ^{1}H NMR spectra of a solution of MG132-Cage (400 MHz, CD_2Cl_2, 22 °C) before (top) and during (spectra 1-10) irradiation with 405 nm light. Spectra were taken in intervals of 1 min. A spectrum of pure MG132 (bottom) is shown for comparison.

19

Quantum yield measurement

Quantum yield measurements were conducted in DMSO solution because of the limited solubility of MG132-Cage in buffered solutions.

For the quantum yield measurement the molar absorption coefficients have to be determined first in order to relate spectral changes to photoreaction turnover in a quantitative way. The molar absorption coefficients for MG132-Cage are depicted in Figure S14.
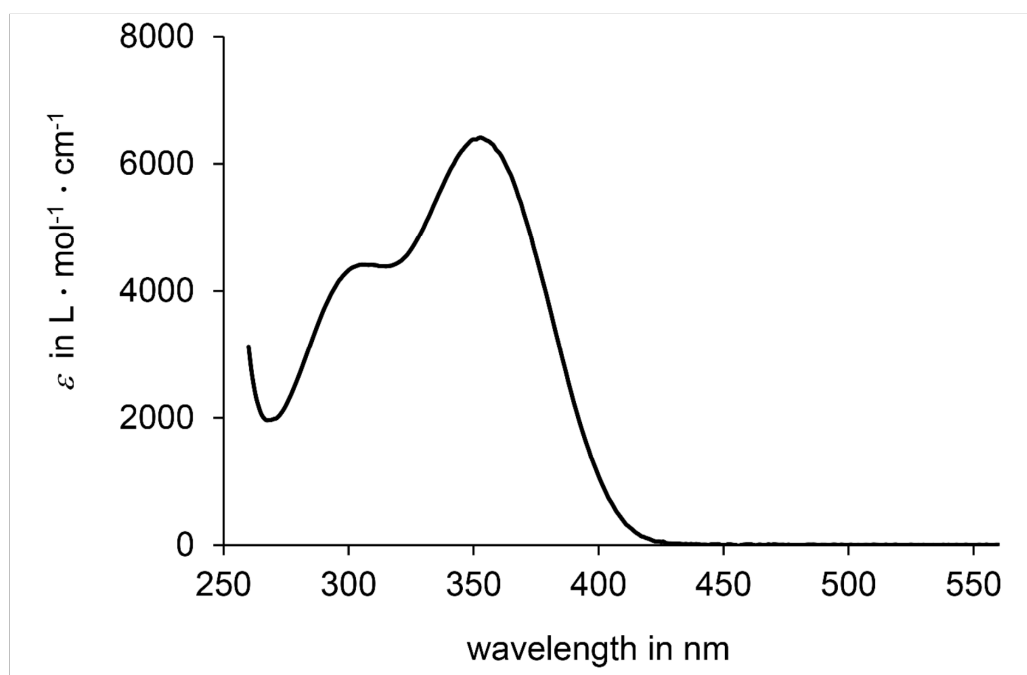
Figure S14   Molar absorption coefficients of MG132-Cage in DMSO solution.

To obtain the molar absorption coefficients of the photoreaction product a solution of MG132-Cage was prepared in DMSO-d_6 and irradiated for a short time period resulting in exactly 20% conversion as determined by ^{1}H NMR spectroscopy. A sample of this resulting NMR solution was diluted in DMSO and the corresponding UV/Vis spectrum was recorded. Normalization of this UV/Vis spectrum to the known isosbestic points

20

(see Figure 2b in the manuscript) allowed to relate absorption changes occurring during irradiation quantitatively to molecular conversion (Figure S15).
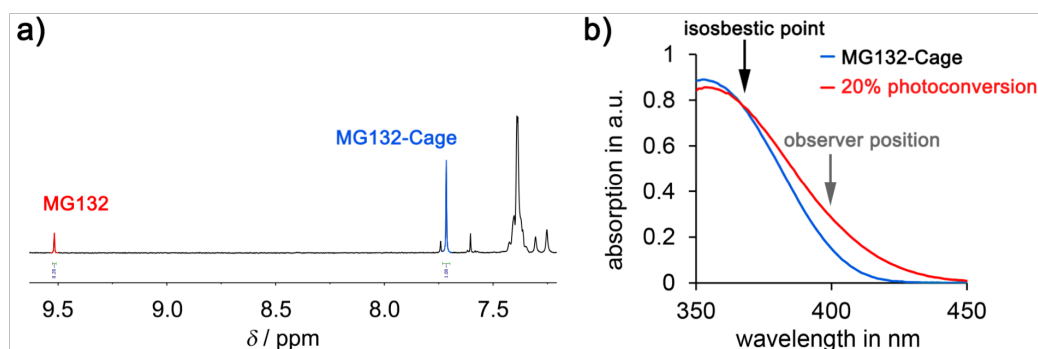
Figure S15   a) ^{1}H NMR spectrum (400 MHz, DMSO-d_6, 27 °C) of MG132-Cage obtained after short irradiation with 405 nm light. 20% of MG132-Cage are photodeprotected as judged by integration of the indicated signals. b) Corresponding UV/Vis spectrum of a diluted sample of the same NMR solution obtained after short irradiation with 405 nm light with known ration between MG132-Cage and released MG132 (red). The 20% conversion spectrum was normalized to the isosbestic point at 368 nm (black arrow) occurring during photodeprotection of MG132-Cage to obtain absolute molar absorptions. The spectrum of pure MG132-Cage in DMSO solution is shown for comparison (blue) with the observer position at 400 nm indicated (grey arrow).

The photochemical quantum yield of the photoconversion reactions was calculated as the ratio between the numbers of isomerized molecules and the number of absorbed photons according to eq. 1.

$$\Phi = \frac{n(isomerized\ molecules)}{n(absorbed\ photons)} \qquad (eq.\ 1)$$

To determine the quantum yield Φ, a solution of pure MG132-Cage in DMSO, with known concentration and volume, was irradiated within a cuvette with a focused light beam of a 405 nm LED within the published instrumental setup from the group of *E. Riedle*.[2] To determine the number of photo-uncaged molecules UV-Vis absorption spectra were taken after different irradiation periods as shown in Figure S16. Using the

21

known molar absorption coefficients (see above) the change in concentration of MG132-Cage and therefore the number of uncaged molecules could be determined for each irradiation step.

The number of absorbed photons over time was measured directly at the thermal photometer according to eq. 2.

$$n(h\upsilon) = \frac{\Delta P \; \cdot \; \lambda_{\text{ex}} \cdot t}{c \; \cdot \; h}$$

(eq. 2)

Where c is the speed of light ($2.99792.10^{8}$ m·s^{-1}), h is the Planck's constant ($6.62607 \cdot 10^{-34}$ J·s), λ_{ex} is the excitation wavelength in m, t is the elapsed time during irradiation, and ΔP is the difference in power readouts at the thermal photometer between a cuvette filled with solvent (P_0) and a cuvette containing the sample solution (P_t) during the initial period in Watt (eq. 3). The power read out during the irradiation period did not change substantially (~4%) and was averaged over the sixteen steps that were used for the calculations.

$$\Delta P = P_{\text{t}} - P_0$$

(eq. 3)

At the start of the experiment only the pure MG132-Cage is converted resulting in a linear behavior. Therefore the first sixteen steps of the measurement were used to determine the quantum yield Φ (Figure S12).

22
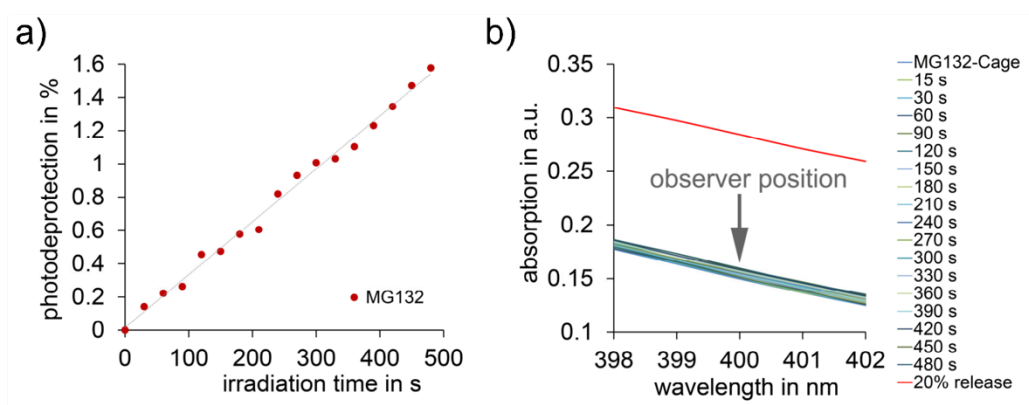
Figure S16　　Quantum yield measurement for photodeprotection of MG132-Cage. a) Quantification of the concentration changes of MG132-Cage induced by irradiation with 405 nm light. Concentrations were calculated after different time intervals of irradiation from UV-Vis spectra at 400 nm spectral position using the molar absorption coefficients. The first sixteen data points were used for the quantum yield determination. b) Absorption increase occurring during the quantum yield measurements around the observer position at 400 nm (grey arrow, bottom spectra) and corresponding spectrum recorded after 20% deprotection (red).

The determined quantum yield is 1.0% for 405 nm irradiation, which is in very good agreement with the previously reported quantum yield of 1.0% (350 nm irradiation) for the photodeprotection of an alcohol bearing the same DMNB photocage.[3]

23

Biology

Cell culture and cell line generation

HeLa cells were grown at 37 °C in 5% CO_2 in Dulbecco's growth medium (DMEM, Life Technologies, 2172747) supplemented with 10% FCS (Merck, 2017-103299) and 1% penicillin/streptomycin (Merck, A2213). The HeLa cell lines EZ56, which expressed mKate2-α-tubulin and anillin-GFP, and Flp-In T-Rex[4] were used. The Flp-In T-Rex HeLa cell line was used for the annexin V and propidium iodide (PI) staining and the EZ56 HeLa cell line for all other experiments. For the EZ56 cell line mKate2-α-tubulin was cloned in the pcDNA6 mammalian expression vector and integrated in the HeLa cell line stably expressing anillin-GFP.[5] Sequences encoding mKate,[6] α-tubulin,[7] and the pcDNA6 plasmid backbone including blasticidin[8] resistance were amplified by polymerase chain reaction (PCR) and assembled together by Gibson cloning (NEB, E2611). The generated plasmid encoding mKate-α-tubulin was transfected into anillin-GFP expressing HeLa cells using X-tremeGENE 9 (06365779001, Roche). After selection with blasticidin (InvivoGen, ant-bl-1) stable clones co-expressing anillin-GFP and mKate-α-tubulin were isolated by fluorescence-activated cell sorting (FACS).

Experimental setup for compound treatment and 405 nm light exposure

Stock solutions for proteasome-inhibitor MG132 (Calbiochem, 474790) and MG132-Cage were prepared in DMSO (Sigma, D8418) with a concentration of 10 mM. To analyze cell cycle arrest, cells were synchronized with a double thymidine block. Cells were seeded at 50% confluency in 12-well plates (Greiner, 665180) containing 18 mm poly-L-lysine (Sigma, Y1251-100G) coated glass coverslips (Menzel, P233.1) for immunostainings; in 6-well plates (Greiner, 657160) for live-cell imaging; and in 8-well ibidiTreat chambers (Ibidi, 80826) for the prewash experiments. After cell attachment fresh medium containing 0.5 mM thymidine (Sigma, T1895) was added and cells were incubated for 15 h. Cells were released from the first thymidine block by washing 3x for 5 min with 1 mL DMEM/10%FCS medium. 8-10 h after the release, a second thymidine block was performed by adding fresh medium containing 0.5 mM thymidine.

24

After 15 h incubation, cells were released from the second thymidine block by washing 3x for 5 min with 1 mL DMEM/10%FCS medium.

8 h after release from the second thymidine block the DMEM/10%FCS medium was removed and fresh DMEM medium (Biochrom, F0475) supplemented with 10% FCS, 2 mM L-Glutamine (Life Technologies, 25030149) and containing 5 or 10 µM MG132-Cage, 5 or 10 µM MG132, 0.1% DMSO, or no additive was added. Immediately after addition of the different compounds 12-well plates were irradiated for 5 or 10 min using two 405 nm LEDs (Roithner H2A1-H405 405 nm, 105 mW; and Thorlabs M405D2 405 nm run at ca. 375 mW, FWHM = 12 nm) in a self-made dark chamber at room temperature. For irradiation two LED lights were placed approximately 2 cm above the wells of the plates. Control cells without irradiation were protected from light during the experiment until fixation. For inhibitor-washout experiments, cells were treated with MG132-Cage, MG132, or 0.1% DMSO 6 h after the release from the second thymidine block, exposed to 10 min 405 nm light, incubated for 2 h, washed 3x with 1 mL DMEM/10%FCS/2mM L-Glutamine medium and fixed after another 2 h incubation.

For prewash experiments cells were seeded in 8-well ibidiTreat chambers (Ibidi, 80826) and the cell cycle was synchronized with a double thymidine block as described above. 8 h after the release from the second thymidine block the medium was removed and 80 µL prewarmed DMEM medium (Biochrom, F0475) supplemented with 10% FCS, 2 mM L-Glutamine (Life Technologies, 25030149) and containing 10 µM MG132-Cage, or 10 µM MG132 was added and cells were incubated for 1 h in the dark. Prior to 10 min 405 nm LED irradiation, the MG132-Cage- or MG132-containing medium was removed and 80 µL prewarmed DMEM medium without MG132-Cage or MG132 was added. After another 2 h incubation cells were fixed and stained for F-actin and Hoechst in the chambers.

To determine the number of healthy cells HeLa cells were seeded in DMEM/10%FCS on 18 mm poly-L-lysine coated coverslips. One day later the culture medium was exchanged for fresh DMEM (Biochrom, F0475) supplemented with 10% FCS/2 mM L-Glutamine and containing 10 µM MG132-Cage, 10 µM MG132, 0.1% DMSO, or no additive. Plates were exposed to 405 nm LED light for 10 min or maintained in the dark as described above. Subsequently cells were fixed and stained 0 h, 12 h, 18 h, and 24 h after 405 nm light exposure.

25

For annexin V and propidium iodide (PI) labeling cells were seeded in 8-well ibidiTreat chambers (Ibidi, 80826) and one day later incubated with 10 µM MG132-Cage, 10 µM MG132, or 0.1% DMSO and exposed for 10 min to 405 nm LED light or maintained in the dark. After 20 h incubation cells were labeled for annexin V, PI and Hoechst in the chambers.

Immunostaining

For immunostaining, coverslips or ibidiTreat chambers were washed once with 1xPBS (Phosphate buffered saline), fixed in 4% PFA/1x PBS (formaldehyde, 28908 Thermo Scientific) for 15 min on ice and blocked with 4% BSA/1x PBS/0.1% Triton™ X-100 at 4 °C over night. The primary anti α-tubulin (1:500, T6199, Sigma) antibody was incubated for 2 h at room temperature (RT) in 4% BSA/1x PBS/0.1% Triton™ X-100. Afterwards, coverslips were washed 3x for 5 min with 1x PBS/0.1% Triton™ X-100. Subsequently, the secondary antibodies Alexa Fluor™ 635 goat anti-mouse (1:500, Life Technologies, A31574), Alexa Fluor™ phalloidin 568 (1:500, Life Technologies, A12380) and Hoechst 33258 (1:1,000, Sigma-Aldrich, 86140) in 4% BSA/1x PBS/0.1% Triton™ X-100 were incubated for 1 h at 22 °C. After incubation, coverslips were washed 3x for 5 min in 1x PBS/0.1% Triton™ X-100, placed on glass slides, covered with mounting medium (1x PBS/4% n-Propyl-Gallate, 90% Glycerol) and stored at -20 °C until imaging.

For annexin V and PI labeling (ab14085, Abcam) the medium was removed 20 h after light exposure and 100 µL 1x Binding Buffer containing 1 µL FITC-annexin V, 1 µL PI and 1 µL Hoechst (1:1,000) was added and incubated for 10 min at 22 °C in the dark. Subsequently, cells were fixed with 4% PFA/1x Binding Buffer for 15 minutes on ice and washed once with 1x Binding buffer. Images were acquired by confocal microscopy within 36 h.

Immunoblotting

Cells were seeded in 6-well plates at 40% confluence and one day later 10 µM MG132-Cage, 10 µM MG132, or 0.1% DMSO were added. Plates were irradiated for 10 min with 405 nm LED or maintained in the dark. Cells were collected 14 h after light irradiation in ice-cold PBS, washed 3x with 1x PBS and incubated in RIPA buffer (50

26

mM Tris-HCl pH=7.5, 150 mM NaCl, 0.5% Na-deoxycholate, 1% Triton X 100, 1% SDS, 1% protease inhibitor cocktail) rotating for 30 min at 4 °C. 2x Sample buffer (0.1M Tris, 4% SDS, 1.4% ß-mercaptoethanol, 20% glycerol, 1% Bromophenol blue) was added, samples were sonicated in a water bath for 20 min, heated at 95 °C for 5 min and resolved on a 10% SDS-page. As primary antibodies mouse anti-actin (1:10,000, #A5316, Sigma) and mouse anti-PARP (1:1,000, #9542, Cell Signaling) were used; and as secondary antibodies HRP-conjugated mouse (1:10,000 for actin, 1:3,000 for PARP, 170-6516; Bio-Rad). Antibody-probed membranes were developed using ECL™ Prime Western Blotting (GE Healthcare, RPN22236) for PARP and ECL™ Western Blotting (GE Healthcare, RPN2106) for actin. Membranes were imaged on a Molecular Imager ChemiDoc™ XRS+ (Bio-Rad).

Resazurin-based cell viability measurements

To measure cell viability 15,000 cells per well were seeded into black 96-well plates (655090, Greiner). One day later medium was removed and 100 µL medium containing no additive, 0.1% DMSO, 10 µM MG132-Cage, 10 µM MG132, 10 µM Propionic Acid-Cage, or 10 µM MG132-Ester-Cage were added in triplicates. To correct for background fluorescence medium was added to empty wells. Plates with MG132-Cage, Propionic Acid-Cage, or MG132-Ester-Cage were exposed to 405 nm LED light for 10 min. 28 h after addition of MG132 or light exposure, 10 µL of CellTiter Blue® reagent containing resazurin (G8080, Promega) was added to each well. Plates were shaken for 2 min and centrifuged at 1,000 rpm for 1 min. Fluorescence intensity (excitation 560 nm/emission 590 nm) was measured every 30 min using a Tecan Infinite Pro2000 (bottom reading) until saturation of the signal.[9] For each well the mean background fluorescence intensity for wells without cells was subtracted and for each condition the mean fluorescence intensity for each triplicate was calculated. All values were normalized to the mean fluorescence intensity of control cells.

27

Microscopy and image analysis

Immunofluorescence images (Figure 3, 4) were acquired on a Leica laser scanning confocal TCS SP5 microscope which was controlled by the Leica Application Suite Software 2.7.2, and equipped with a 63x 1.4-NA Plan-Apochromat oil immersion objective and 405-, 594- and 635-nm lasers. Live-cell movies (Figure 5, S22) and dose-response images (Figure S20a) were acquired on a Nikon eclipse Ti spinning disk confocal microscope.

For live-cell imaging cells were seeded in 6-well plates and the cell cycle was synchronized with a double thymidine block as described above. Cells were transferred into 2-well ibidiTreat chambers (Ibidi, 80286) at the start of the second thymidine block one day before filming. During live-cell imaging cells were maintained at 37 °C in CO_2-independent medium (18045054, Thermo Fischer) containing 10% FCS/1% penicillin/streptomycin/2mM L-Glutamine. Transmission and mKate-α-tubulin live-cell movies were acquired on a Nikon eclipse Ti spinning disk confocal microscopy, which was controlled by the NIS Elements 4.51 software. For transmission images a 470 nm cut-off filter was placed in the light path to exclude the blue parts of the imaging light. The Nikon eclipse was outfitted with a 60x Apo TIRF oil immersion DIC N2 and an Apo LWD 40x WI Lambda S DIC N2 objective and an Andor DU-888 X-11056 camera. Exposure to 405 nm LED light for 5 min was performed on the microscope stage using one LED (either Roithner H2A1-H405 or Thorlabs M405D2) without removing the imaging chamber.

To analyze the mitotic stage and the cell number of the fixed cells, images were randomly acquired on each coverslip. For analyzing the immunofluorescence images and live-cell movies, the open-source software Fiji[10] was used. For all live-cell mKate-α-tubulin images a maximum z-projection of three z-planes 4 μm apart is shown. To quantify the intensities of the PARP and cleaved PARP bands on western blot the Biorad Image Lab[TM] software (Version 5.2.1) was used. Figures were assembled in Affinity Designer or Photoshop and graphs were plotted with Prism (Graphpad) or Excel (Microsoft).
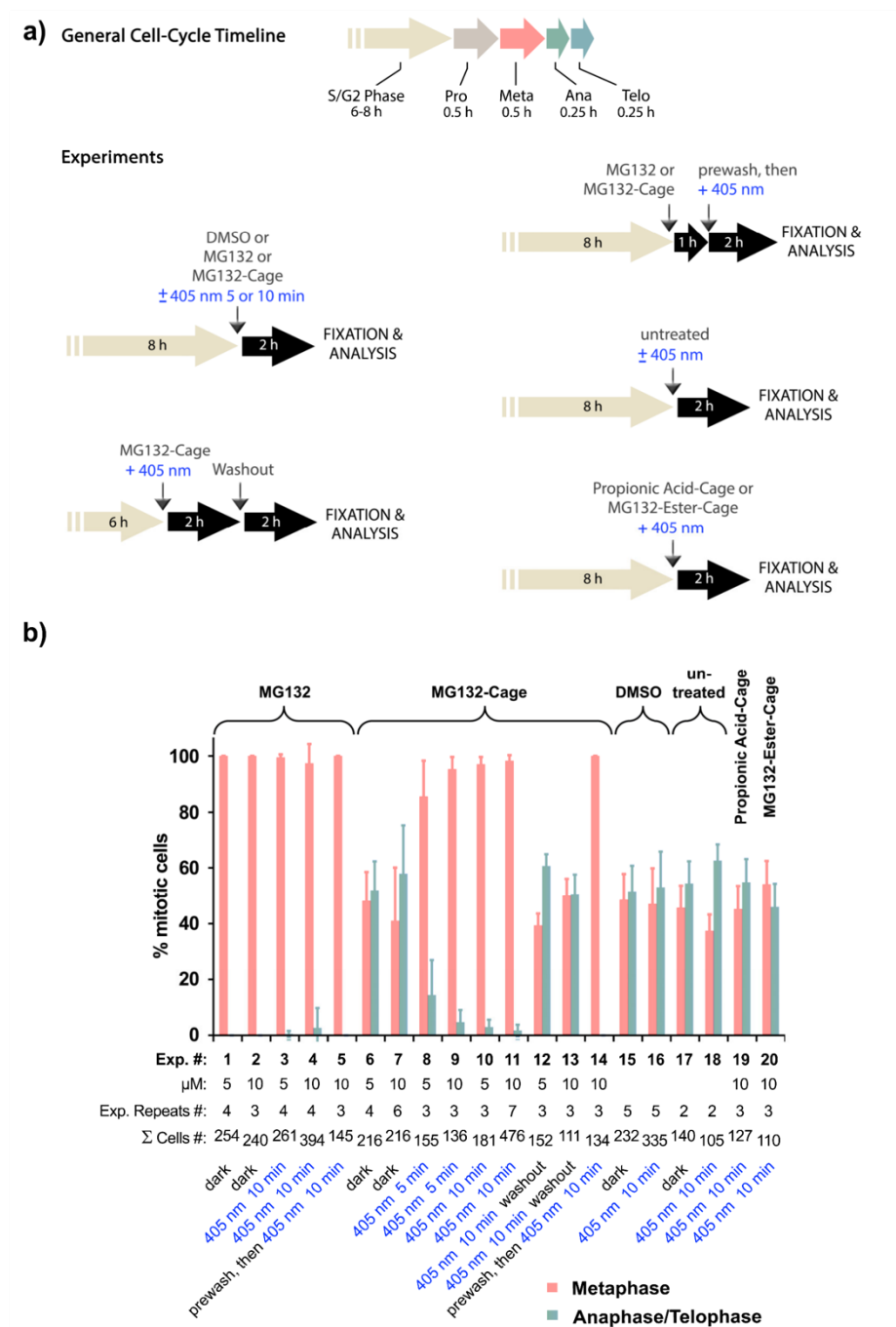
28

Figure S17 Cell-cycle control with blue light including control experiments. a) Experimental setups to quantify blue-light induced metaphase arrest and control experiments using MG132-Cage, MG132, Propionic Acid-Cage, MG132-Ester-Cage, DMSO, or no additive. b) Mean percentages of mitotic cells in metaphase and ana-/telophase for the indicated conditions. Mean number of independent experiments and the total number of cells analyzed is shown. Error bars represent standard deviation. Experiments # 2, 6, 7, 10, 11, 13, 15, 16, 20 are reproduced from Figure 3d in the main manuscript.
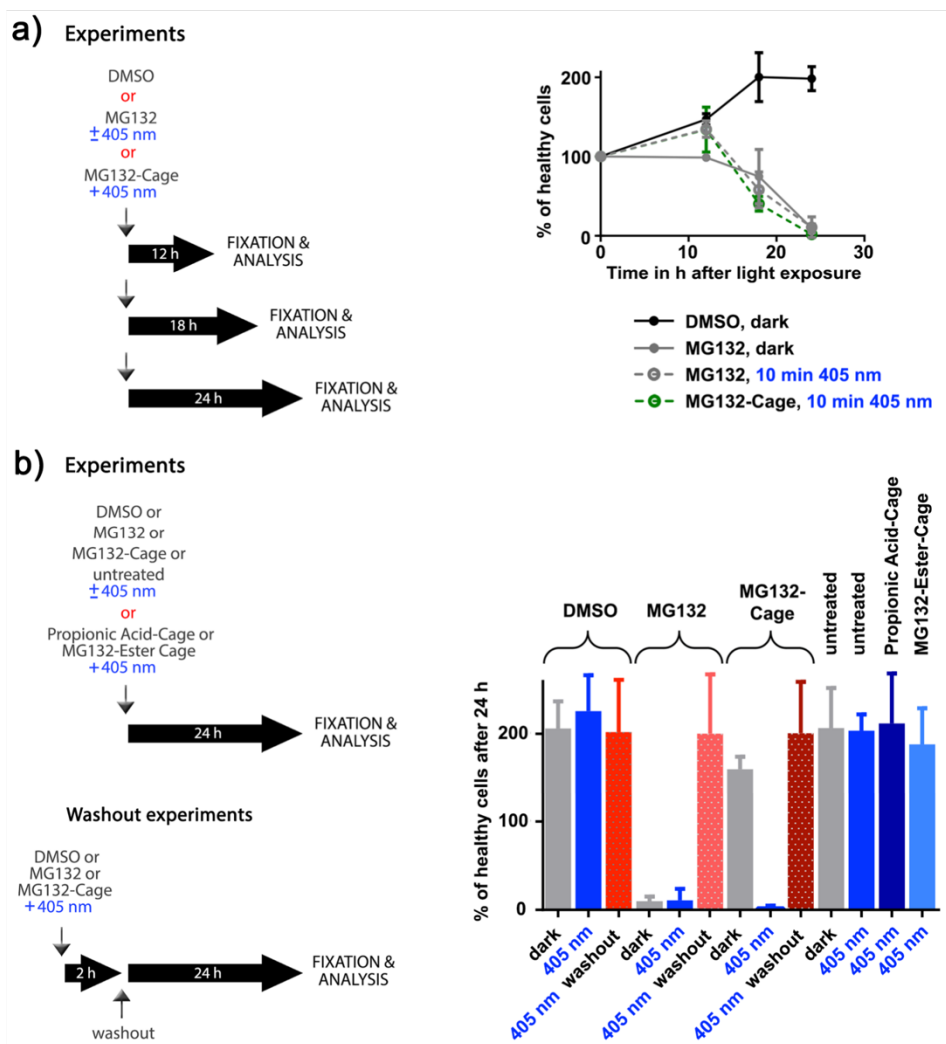
Figure S18   Induction of cell death in HeLa cells with blue light. a) Experimental setups to quantify blue-light induced cell death over time (left). Mean percentages of healthy cells relative to 0 h DMSO-treated cells for the indicated conditions (right). Uncaging of MG132-Cage results in complete cell death 24 hours after irradiation similar to addition of MG132 with or without irradiation. Data of the DMSO control and MG132-Cage with 405 nm are replica taken from Figure 4d in the main manuscript. Mean of 2 independent experiments is shown and error bars represent the standard deviation. b) Quantitative comparison of the % of healthy cells obtained under the indicated experimental conditions after 24 h. An additional washout experiment is included for DMSO, MG132, and MG132-Cage cells in which the washout was performed 2 h after light irradiation. After 24 h the cell number is the same as in the DMSO control showing reversibility of the effect of MG132-Cage unmasking by blue light. Cells were also incubated without any additive in the dark and with 405 nm 10 min light exposure and with 10 μM MG132-Ester-Cage and 10 μM Propionic-Acid-Cage with 405 nm 10 min light exposure. The means of 2-5 independent experiments are shown and between 104 and 782 cell were analyzed for each condition. Error bars represent standard deviation.
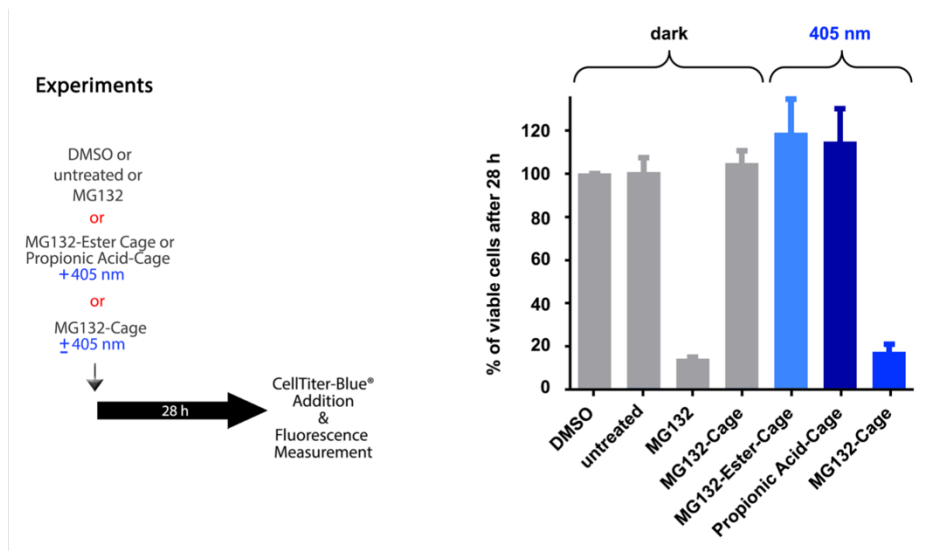
Figure S19 Blue light induced cellular toxicity. Cells were treated with 10 µM solutions of the different compounds as shown on the left, exposed to 405 nm light for 10 min or maintained in the dark, and cultured for 28 h in 96-well plates. After the addition of CellTiter Blue® (resazurin) the fluorescence intensity at 590 nm was measured in triplicate. For each condition the fluorescence intensity was normalized to 0.1% DMSO-treated cells maintained in the dark. Means of 2 independent experiments are shown and error bars represent standard deviation.

31
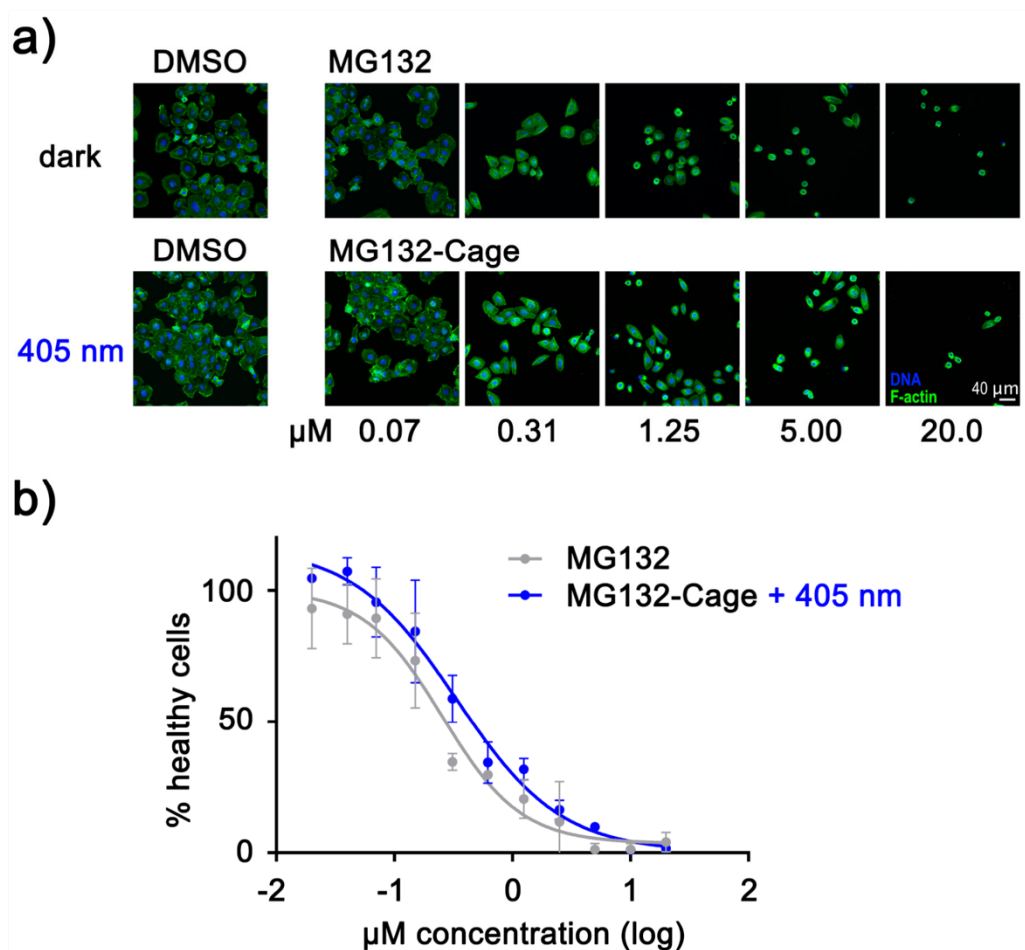
Figure S20 Dose-dependent induction of cell death in MG132-Cage treated cells exposed to 405 nm light for 10 min. a) HeLa cells were incubated in 0.1% DMSO and serial dilutions of MG132 (dark) or MG132-Cage (405 nm 10 min LED light). After 24 h cells were fixed and stained for F-actin (green) and DNA (blue) and the number of healthy cells was determined. Shown are maximum z-projections of confocal images. Scale bar represents 40 µm. b) The % of healthy cells relative to control cells is plotted for the indicated conditions. The means for 3 independent experiments are shown and error bars represent standard deviation.

32
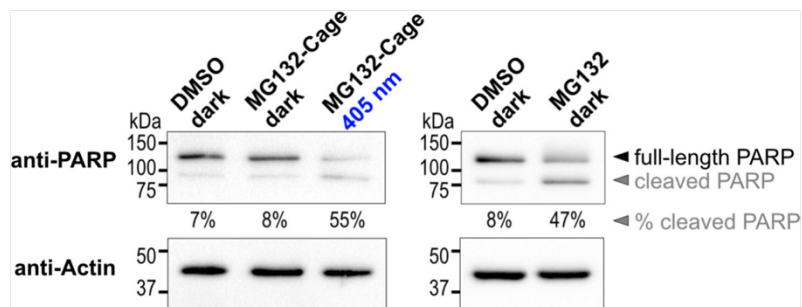
Figure S21   Cells were incubated with 0.1% DMSO, 10 μM MG132-Cage (with and without 405 nm light for 10 min), or 10 μM MG132 for 14 h**.** Immunoblots were probed with anti-actin as a loading control and anti-PARP antibodies. The percentage of cleaved PARP relative to uncleaved PARP is shown for each condition.
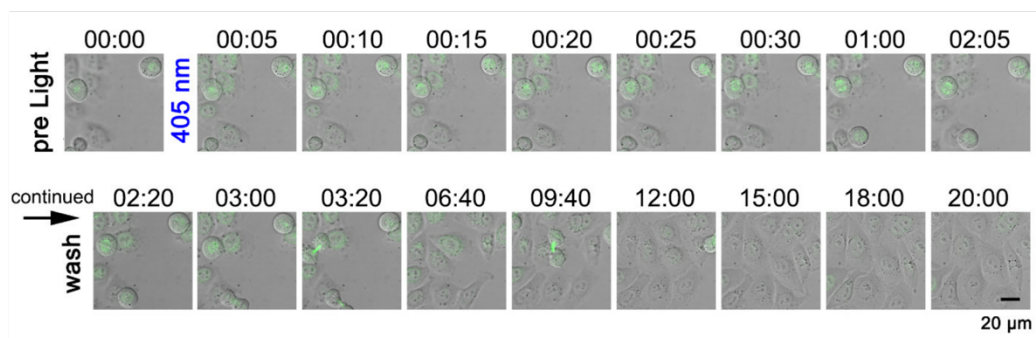
Figure S22   Live-cell imaging of reversible blue light induced metaphase arrest in HeLa cells with greater time resolution as compared to Figure 5c in the main manuscript. Selected time frames are taken from Suppl. Movie 3. Merged transmission and confocal mKate-α-tubulin (maximum z-projection shown in green) images for indicated time points are shown. Prometaphase cells exposed to 405 nm light arrested in metaphase. After 2 h inhibitor washout was performed and the cells continued to proliferate, thus establishing reversibility of the arrest. After 20 h no signs of apoptosis are seen. Scale bar represents 20 μm.

33

Supplementary Movie figure legends

Supplementary Movie 1   Merged transmission and confocal mKate-α-tubulin (maximum z-projection shown in green) images of HeLa cells incubated with 10 µM MG132-Cage and either exposed to 405 nm light for 5 min (left) or maintained in the dark (right). Images were acquired every 5 min with a 60x 1.45-NA Plan-Apochromat oil immersion objective on Nikon eclipse spinning disc confocal microscope.

Supplementary Movie 2   Merged transmission and confocal mKate-α-tubulin (maximum z-projection shown in green) images of HeLa cells incubated with 10 µM MG132-Cage and either exposed to 405 nm light for 5 min (left) or maintained in the dark (right). Images were acquired every 5 min for 20 h, as described for Suppl. Movie 1. After 1 h displayed time-intervals are increased to every 20 min.

Supplementary Movie 3   Merged transmission and confocal mKate-α-tubulin (maximum z-projection shown in green) images of HeLa cells incubated with 10 µM MG132-Cage and exposed to 405 nm light for 5 min. 2 h after light exposure the inhibitor was washed out and imaging was continued for 20 h. Images were acquired every 5 min for 20:20 (h:min) as described for Suppl. Movie 1. After 5 h displayed time-intervals are increased to every 20 min.

References

[1]   M. Verdoes, B. I. Florea, W. A. van der Linden, D. Renou, A. M. van den Nieuwendijk, G. A. van der Marel, H. S. Overkleeft, *Org. Biomol. Chem.* **2007**, *5*, 1416-1426.

[2]   U. Megerle, R. Lechner, B. König, E. Riedle, *Photochem. Photobiol. Sci.* **2010**, *9*, 1400-1406.

[3]   G. A. Krafft, W. R. Sutton, R. T. Cummings, *J. Am. Chem. Soc.* **1988**, *110*, 301-303.

[4]   A. Tighe, V. L. Johnson, S. S. Taylor, *J. Cell Sci.* **2004**, *117*, 6339-6353.

[5]   E. Zanin, A. Desai, I. Poser, Y. Toyoda, C. Andree, C. Moebius, M. Bickle, B. Conradt, A. Piekny, K. Oegema, *Dev. Cell* **2013**, *26*, 496-510.

[6]   D. M. Shcherbakova, M. A. Hink, L. Joosen, T. W. Gadella, V. V. Verkhusha, *J. Am. Chem. Soc.* **2012**, *134*, 7913-7923.

[7]   F. V. Subach, G. H. Patterson, S. Manley, J. M. Gillette, J. Lippincott-Schwartz, V. V. Verkhusha, *Nat. Methods* **2009**, *6*, 153-159.

[8]   M. Shuda, H. J. Kwun, H. Feng, Y. Chang, P. S. Moore, *J. Clin. Invest.* **2011**, *121*, 3623-3634.

[9]   G. Linden, L. Zhang, F. Pieck, U. Linne, D. Kosenkov, R. Tonner, O. Vazquez, *Angew. Chem. Int. Ed.* **2019**, *58*, 12868-12873.

[10]   J. Schindelin, I. Arganda-Carreras, E. Frise, V. Kaynig, M. Longair, T. Pietzsch, S. Preibisch, C. Rueden, S. Saalfeld, B. Schmid, J. Y. Tinevez, D. J. White, V. Hartenstein, K. Eliceiri, P. Tomancak, A. Cardona, *Nat. Methods* **2012**, *9*, 676-682.

35

5   Chapter IV - Rhodanine-Based Chromophores –Fast Access to Capable Photoswitches and Application in Light Induced Apoptosis

* contributed equally

Article

Rhodanine-Based Chromophores: Fast Access to Capable Photoswitches and Application in Light-Induced Apoptosis

Laura Köttner, Friederike Wolff, Peter Mayer, Esther Zanin,* and Henry Dube*

Read Online

ACCESS | 📊 Metrics & More | 📖 Article Recommendations | ⓢ Supporting Information

ABSTRACT: Molecular photoswitches are highly desirable in all chemistry-related areas of research. They provide effective outside control over geometric and electronic changes at the nanoscale using an easy to apply, waste-free stimulus. However, simple and effective access to such molecular tools is typically not granted, and elaborate syntheses and substitution schemes are needed in order to obtain efficient photoswitching properties. Here we present a series of rhodanine-based photoswitches that can be prepared in one simple synthetic step without requiring elaborate purification. Photoswitching is induced by UV and visible light in both switching directions, and thermal stabilities of the metastable states as well as quantum yields are very high. An additional benefit is the hydrogen-bonding capacity of the rhodanine fragment, which

enables applications in supramolecular or medicinal chemistry. We further show that the known rhodanine-based inhibitor SMI-16a is a photoswitchable apoptosis inducer. The biological activity of SMI-16a can effectively be switched ON or OFF by reversible photoisomerization between the inactive *E* and the active *Z* isomer. Rhodanine-based photoswitches therefore represent an easy to access and highly valuable molecular toolbox for implementing light responsiveness to the breadth of functional molecular systems.
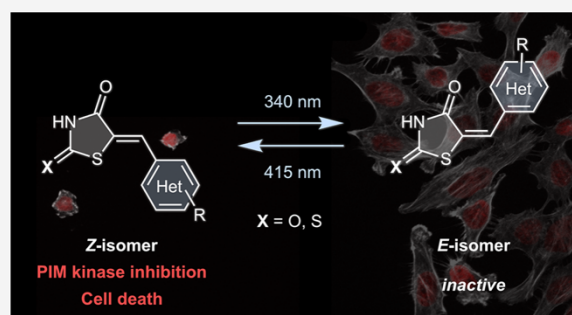
■ INTRODUCTION

Molecular photoswitches[1,2] are versatile tools to control the behavior of matter at the nanoscale by light stimuli. Applications cover vast areas of research from molecular machines[3,4] to smart materials,[5−7] catalysis,[8,9] or photopharmacology.[10−12] Key to this success is oftentimes the precise control of photoswitch geometry, and double-bond isomerizing systems are frequently employed for this purpose. Stilbene[13,14] and azobenzene[15,16] based photoswitches represent probably the best-known examples, but more recently other molecular core structures[17] such as Stenhouse adducts,[18,19] hydrazones,[20−23] imidazole-biradicals,[24,25] or hemipiperazine[26] have emerged. Indigoid chromophores[27−30] represent another different option for double-bond isomerizing photoswitches. They undergo predictable changes in their geometry and can use visible light of different colors for both *Z* to *E* and *E* to *Z* photoisomerizations. The favorable photochemistry and synthetic versatility of indigoid chromophores have allowed their application in many different functional areas, giving rise to unique light-controlled molecular machines,[31−37] chiroptical switches,[38] supramolecular systems,[39,40] or biological[41−44] and photopharmacology tools,[45,46] to name just a few examples. A recent survey has further emphasized the potential of hemiindigoid chromophores as photopharmacological tools that still lies dormant.[47]

In this work we present a new class of related, yet distinctive photoswitches with distinct potential for applications especially in a biomedical context. Rhodanine-based[48,49] photoswitches inherit parts of the hemithioindigo (HTI) motif,[50] but the benzannulated thioindigo fragment is replaced with a rhodanine or oxo-rhodanine unit to which the stilbene fragment is connected (Figure 1a). A simple one-step condensation of rhodanine and an aldehyde[51] provides access to a large number of derivatives, which usually do not require column chromatography for purification. The thus-obtained structures are well established motifs in different areas of research such as fluorophore design,[52] ion sensing,[53] solar-cell dyes,[54−58] and medicinal and biological chemistry.[59−61] For example, a number of widely used kinase inhibitors such as SMI-16a[62,63] or SMI-4a[62,64] with activity against PIM (Provirus Integration site for Moloney leukemia virus) kinases[64−66] are based on this structural motif. Despite this great versatility, only the related dicyanorhodanine structure in conjunction with thiophenes[67,68] and related solar cell dye structures[69,70] were shown to undergo photoisomerization so far. A distinct, light-induced singlet-oxygen sensitization of the
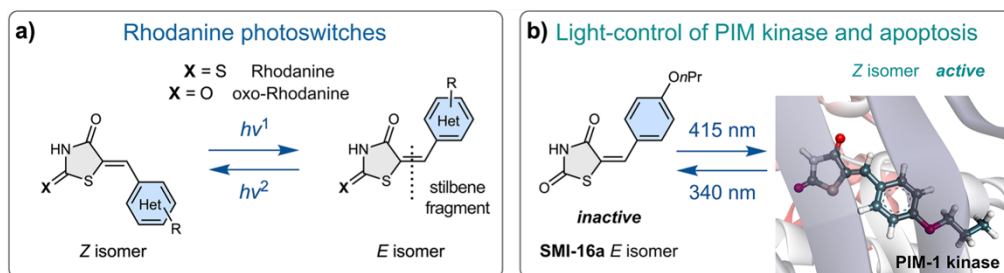
Figure 1. Rhodanine and oxo-rhodanine-based chromophores for visible light responsive photoswitching. (a) Rhodanine-based photoswitches. (b) Application of rhodanines as a photopharmacological tool allowing light control of apoptosis via isomer selective PIM kinase inhibition. The image on the right side schematically shows the Z isomer of SMI-16a in the active site of PIM-1 kinase.
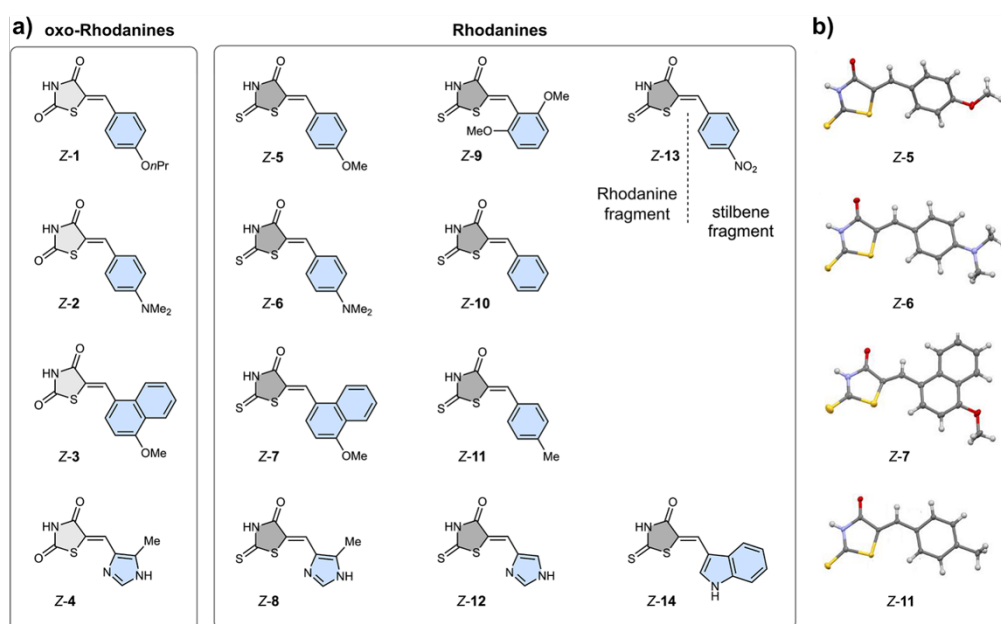

Figure 2. Molecular structures of oxo-rhodanine- and rhodanine-based chromophores **1−14** investigated in this study. (a) The thermodynamically most stable Z isomers are shown schematically. (b) Structures of derivatives **5−7** and **11** in their Z-isomeric configuration in the crystalline state.

rhodanine optovin was used for photoactivation of transient receptor potential cation channel subfamily A member 1 (TRPA1).[71] To the best of our knowledge, the capacity for photoswitching in the core-chromophore class of rhodanine structures itself has not been investigated yet.

Here we show that rhodanine chromophores are capable photoswitches with high quantum yields and strongly tunable property profiles allowing tailoring of them for particular applications (Figure 1). Thermal stability of metastable states can be precisely modulated by simply changing from the highly bistable oxo-rhodanine structures to the sulfur-substituted rhodanines. At the same time a significant red-shift of the absorption is observed for the latter. By introducing further heterocyclic structures, which have recently been shown effective in enhancing photoswitching of HTI chromophores,[72] strongly improved switching properties of rhodanines are obtained. These include enhanced photochromism, near-quantitative switching, and elevated thermal bistability. The additional benefits of increased hydrogen-bonding capacities are of interest not only for biomedical applications but also for supramolecular interactions, implementation into materials, or

molecular sensing and recognition purposes. Finally, we demonstrate their application as chemical biology tools for rhodanine-based photoswitches acting as inhibitors of PIM kinases. PIM kinases are promising drug targets for cancer therapy and play a central role in multiple cell cycle and apoptotic pathways.[73,74] They are overexpressed in different types of cancer cells, such as pancreatic cancer or acute myeloid leukemia. We show here that the known PIM kinase inhibitor SMI-16a (derivative **1**) is in itself a capable photopharmacology tool, which allows reversible photocontrol over apoptosis in cancer cells. A related rhodanine variant (derivative **5**) possesses a pronounced red-shifted absorption and is also biologically active in its Z-isomeric form. Our findings thus open up a facile avenue to a plethora of capable light-responsive tools enabling the manipulation of molecular phenomena and biological functions by light.

■ RESULTS AND DISCUSSION

In this study, we investigated 14 different rhodanine chromophores for their photoswitching capacity (Figure 2). These include four derivatives (**1−4**) bearing an oxo-

Table 1. Photochemical and Photophysical Properties of (Oxo)-Rhodanine-Based Photoswitches Measured in the Indicated Solvents and at the Indicated Temperatures

(oxo)-rhodanine	λ_{max}; ε of Z/E isomers most red-shifted abs./ nm; L mol⁻¹ cm⁻¹ in THF-d_8 or *in 1% DMSO/PBS buffer	isomer yield in pss/% (nominal LED) in THF-d_8 or *in 1% DMSO/PBS buffer	$\Phi_{Z\to E}$ & $\Phi_{E\to Z}$ in THF	ΔG/kcal mol⁻¹ (solvent)	$t_{1/2}$/h (T, solvent)
1	344; 26,700	57% E (340 nm)	36% & 33%	≥2.1 (dioxane-d_8)	114 (85 °C, dioxane-d_8)
	361; 22,000	99% Z (405 nm)			
	*347; 26,000	*61% E (340 nm)		≥2.4 (DMSO-d_6)	0.6 (130 °C DMSO-d_6)
	*358; 16,600	*93% Z (405 nm)			
2	401; 36,200	53% E (405 nm)	36% & 34%	≥0.6 (dioxane-d_8)	138 (85 °C, dioxane-d_8)
	419; 32,300	98% Z (470 nm)		≥2.4 (DMSO-d_6)	0.2 (130 °C DMSO-d_6)
3	374; 19,200	68% E (365 nm)	28% & 28%	≥0.3 (dioxane-d_8)	≥480 (85 °C, dioxane-d_8)
	392; 12,700	97% Z (450 nm)		≥2.4 (DMSO-d_6)	3.4 (130 °C DMSO-d_6)
4	344; 29,900	85% E (365 nm)	34% & 11%	no isomerization	no isomerization (85 °C, dioxane-d_8)
	378; 21,800	100% Z (405 nm)		≥2.4 (DMSO-d_6)	3.0 (140 °C DMSO-d_6)
5	392; 36,100	52% E (385 nm)	36% & 38%	≥1.9 (THF-d_8)	30 (55 °C, THF-d_8)
	397; 35,000	86% Z (420 nm)			
	*396; 33,900	*65% E (385 nm)		≥2.1 (DMSO-d_6)	3.6 (90 °C DMSO-d_6)
	*404; 27,500	*86% Z (470 nm)			
6	455; 45,300	52% E (420 nm)	26% & 27%	≥1.9 (THF-d_8)	7 (55 °C, THF-d_8)
	474; 51,500	89% Z (505 nm)		≥2.1 (DMSO-d_6)	4.7 (90 °C DMSO-d_6)
7	414; 25,900	62% E (385 nm)	37% & 25%	≥1.9 (THF-d_8)	143 (55 °C, THF-d_8)
	428; 21,200	90% Z (470 nm)		≥2.1 (DMSO-d_6)	10.9 (90 °C DMSO-d_6)
8	401; 37,800	81% E (385 nm)	40% & 21%	≥1.7 (dioxane-d_8)	95 (85 °C, dioxane-d_8)
	435; 31,300	100% Z (470 nm)		≥2.1 (DMSO-d_6)	0.6 (80 °C DMSO-d_6)
	*404; 33,600	*75% E (385 nm)		≥1.9 (MeOH-d_4)	6 (50 °C MeOH-d_4)
	*419; 32,300	*89% Z (470 nm)			
9	384; 29,500	68% E (385 nm)	39% & 39%	≥1.7 (dioxane-d_8)	101(85 °C, dioxane-d_8)
	373; 17,900	44% Z (340 nm)		≥2.4 (DMSO-d_6)	3.9 (130 °C DMSO-d_6)
10	344; 26,700	49% E (365 nm)	29% & 37%	≥2.1 (dioxane-d_8)	85 (85 °C, dioxane-d_8)
	375, 32,800	88% Z (420 nm)			
11	382; 38,400	53% E (365 nm)	32% & 38%	≥1.9 (THF-d_8)	19 (55 °C, THF-d_8)
	382; 35,400	91% Z (420 nm)		≥2.1 (DMSO-d_6)	2.2 (90 °C DMSO-d_6)
12	388; 37,300	70% E (365 nm)	37% & 36%	≥2.1 (dioxane-d_8)	110 (85 °C, dioxane-d_8)
	408; 33,800	94% Z (415 nm)		≥1.9 (DMSO-d_6)	3.1 (60 °C DMSO-d_6)
13	377; 34,500	45% E (385 nm)	22% & 50%	≥1.9 (THF-d_8)	82 (55 °C, THF-d_8)
	387; 30,500	85% Z (420 nm)		≥1.9 (DMSO-d_6)	0.4 (60 °C DMSO-d_6)
14	433; 32,900	67% E (410 nm)	35% & 19%	≥1.6 (dioxane-d_8)	12 (85 °C, dioxane-d_8)
	447; 39,00	92% Z (470 nm)			

rhodanine fragment and 10 derivatives (**5**−**14**) bearing a rhodanine fragment. Variations at the stilbene fragment include electron-neutral, electron-rich, and electron-deficient benzenes as well as different imidazole and indole heterocycles, which have recently been shown to enable superior photoswitch properties in HTIs.[72] For direct comparison of the effect of variation at the X-position (oxygen in oxo-rhodanines and sulfur in rhodanines), derivatives **1**−**4** were matched with **5**−**8**.

Synthesis of rhodanine-based chromophores proceeds in one step from commercially available starting materials, i.e., oxo-rhodanine or rhodanine and different aromatic aldehydes. The reaction can be conducted neat at higher temperatures (typically 110 °C) using urea to facilitate the reaction as described previously.[51] In case the mixture is not liquefying under the reaction conditions, which prevents proper mixing, the reaction can also be done in methanol solution at 60 °C. After short heating times, the reaction mixtures turn colorful, and, depending on the aldehyde used, yellow to purple colors are observed, signifying product formation. Typically, good to very good yields are obtained for the different products, which can be isolated in pure form by a simple filtration and washing/recrystallization procedure omitting workup, extraction, and

chromatography (for details see the Supporting Information). In this way, the 14 different rhodanine-based photoswitches **1**−**14** (Figure 2a) were prepared in up to 98% yield. After crystallization, the structures of pure Z isomers of compounds **5**, **6**, **7**, and **11** could be obtained by single-crystal X-ray diffraction (Figure 2b), evidencing the expected constitutions. The crystal structures of Z isomeric **5**,[75] **6**,[76] and **11**[77] have also been published before. Pure E isomers of derivatives **1**, **5**, and **8** were isolated after high-performance liquid chromatography separation.

The thermal properties of rhodanine-based photoswitches **1**−**14** were scrutinized first to establish stabilities of the metastable states in different solvents in the dark (for a summary of measured half-lives at various temperatures and Gibbs energies of activation see Table 1). Both oxo- and rhodanine-based photoswitches seem not to thermally interconvert via simple first-order reactions but rather more complex processes in ether solutions. Therefore, no Gibbs energies of activation were calculated in these solvents, and only half-life times were taken into consideration when comparing thermal stabilities. Thermal isomerization experiments were additionally conducted for derivatives **4** and **8** in
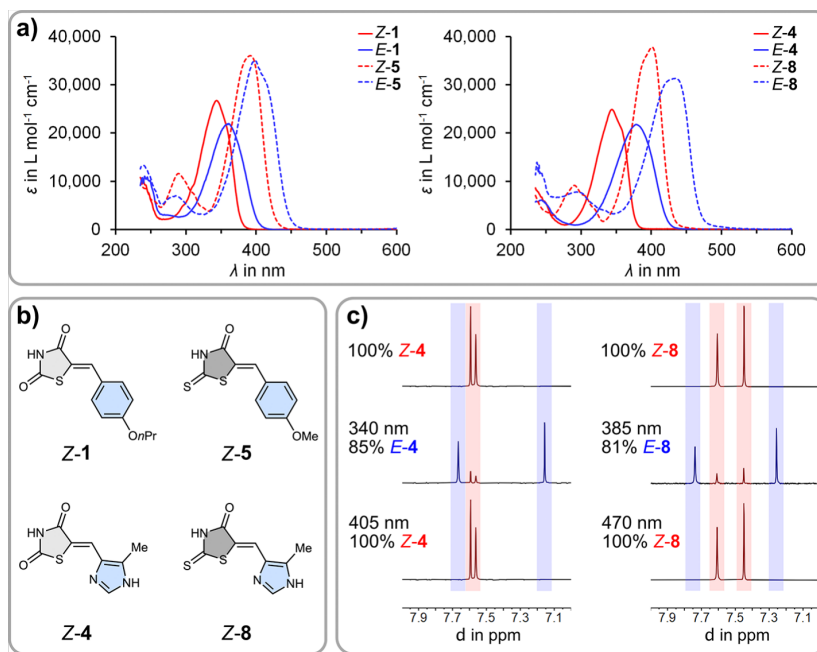
Figure 3. Photoswitching properties of selected rhodanine-based chromophores. (a) Absorption comparison of oxo-rhodanine with rhodanine photoswitches. Molar absorption coefficients are shown for both Z and E isomers of derivatives **1** and **5** as well as for **4** and **8** in THF solution. (b) Schematic representation of rhodanine-based chromophores **1**, **4**, **5**, and **8**. (c) Partial ^{1}H NMR spectra (400 MHz, THF-d_8, 23 °C) showing light-induced isomer interconversions from top to bottom for **4** and **8**.

MeOD-d_4 solution and for derivatives **1**−**9** and **11**−**13** in DMSO-d_6 solution. Clean first-order kinetics were observed in these solvents. In MeOD-d_4 kinetics are faster than in DMSO-d_6; however the corresponding half-life times are sufficiently high for general applicability (Table 1). At present the origin of the behavior in ether solutions is not known, but it seems to involve hydrogen-bonding-induced aggregation and will be investigated in more detail in the future. So far it is established that hydrogen-bond-donating solvents are very effective in disrupting it (no aggregation in H-bond-donating/accepting MeOD-d_4 and DMSO-d_6 but observable effects in medium polar and weakly H-bond-accepting ethers). Further clear trends are observed upon thermal isomerization. In all cases the Z isomer is the thermodynamically most stable, rendering the E isomer metastable, which is similar to the behavior of related HTI photoswitches.[72,78,79] Typically, complete thermal conversion to the Z isomer occurs upon heating. Thermal E to Z isomerization proceeds slowly for all photoswitches with half-lives ranging from hours to days at 55 °C (THF-d_8 solution) for photoswitches **5**, **6**, **7**, **11**, and **13** and at 85 °C (dioxane-d_8 solution) for the remaining derivatives, depending on the particular substitution. In 1% DMSO/PBS buffer solution, thermal stability is diminished, but still thermal half-lives in the range of minutes to several hours at 37 °C are retained (see Figure 4a and the Supporting Information for details). A consistent trend is observed when comparing oxo-rhodanines **1**−**4** with the corresponding rhodanines **5**−**8**, in which the former exhibit significantly higher thermal stabilities of the metastable E isomers. With these thermal stabilities, (oxo)-rhodanine-based chromophores are competitive with other capable photoswitches such as azobenzenes or HTIs.

With high thermal bistabilities established, the photophysical and photochemical properties were quantified next (Table 1).

Measured molar absorption coefficients reveal narrow absorption bands in the UV and/or visible part of the electromagnetic spectrum for all rhodanine-based photoswitches **1** to **14**. The rhodanine chromophores show a significant bathochromic shift of their absorptions (reaching up to 57 nm) when compared to the corresponding oxo-rhodanine-based derivatives (see Figure 3a and b for examples and also the Supporting Information). Further bathochromic shifts can be achieved by introducing electron-donating substituents at the stilbene fragments or by heterocycle substitution. With the exception of derivative **9** all rhodanine-based photoswitches **1** to **14** exhibit positive photochromism with a bathochromic shift of the absorption for the metastable E isomer. The absolute difference in absorption between E and Z isomers is not very large for benzene-substituted derivatives but is much more pronounced for heterocyclic derivatives **4**, **8**, **12**, and **14**. Consequently, photoswitching for the former is not complete in the Z to E isomerization direction, and a maximum of 68% of E isomer can be accumulated in the photostationary state (pss). For many applications, such performance is still effective, especially if threshold effects or bulk responses are intended. However, photoisomerization of heterocyclic derivatives **4** and **8** yields significantly higher yields of the E isomer beyond 80% (Figure 3c). For all derivatives except **9** the corresponding E to Z photoisomerizations are more pronounced, yielding the Z isomer in >85% in the pss. For heterocyclic derivatives **4** and **8** even quantitative conversion is achieved (Figure 3c). In the case of derivatives **2** and **6**−**14** photoswitching in both switching directions can be conducted using visible light instead of UV light, which adds another advantage to this class of chromophores. To test the influence of the solvent, THF with intermediate polarity and nonprotic nature as well as
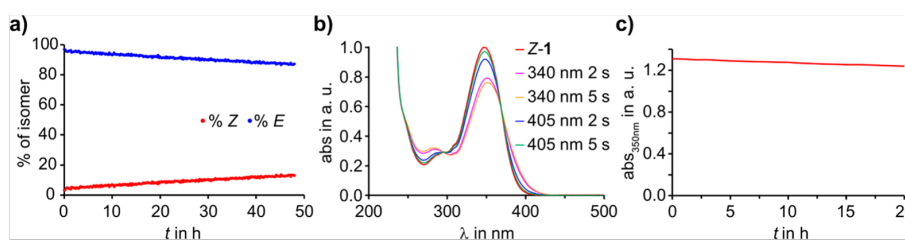
Figure 4. (a) Thermal stability of *E*-**1** and *Z*-**1** in 1% DMSO/PBS buffer solution at 37 °C in the dark. (b) Photoswitching of **1** in 1% DMSO/PBS buffer solution at 23 °C. (c) Stability of *Z*-**1** against reduced glutathione in a MeOH/PBS buffer (1:1) solution at 23 °C with 50 μM *Z*-**1** and 10 mM reduced glutathione.

methanol with high polarity and protic nature were chosen (see Supporting Information for all conditions tested). For the known inhibitor SMI-16a, i.e., derivative **1**, as well as **5** and **8** also photoswitching experiments in buffer solution and cell media were performed (see Figure 4b and Supporting Information). For benzene-substituted derivatives the effects of solvent changes on the photoswitching capacity are very small, and also buffer and cell media environments do not lead to deterioration of performance. In the case of heterocyclic derivatives, a somewhat diminished completeness for the *Z* to *E* photoisomerization direction in protic media is seen for **8**.

Quantum yield measurements revealed very good performance of (oxo)-rhodanines and unusually high values, typically for both *Z* to *E* and also *E* to *Z* photoisomerizations (see Table 1 for all determined values). Clear trends in the quantum yields are not observed, neither when comparing oxo-rhodanines with rhodanines nor with respect to the particular electronic character of the substituted benzene rings. However, heterocyclic derivatives **4**, **8**, and **14** show diminished quantum yields for the *E* to *Z* photoisomerization. The latter effect might be caused by a significant hydrogen-bonding interaction, stabilizing the *E* configuration and hampering efficient photoisomerization.

Taken together, these results showcase that both oxo-rhodanine and rhodanine-based chromophores represent capable photoswitches, the properties of which can be tuned in a wide range by different substitutions at the rhodanine or the stilbene fragment. Best performances are given by imidazole and indole incorporating **4**, **8**, **12**, and **14**. These derivatives combine high isomer enrichment in the photostationary state, pronounced photochromism, visible light responsiveness at least for one switching direction, good quantum yields, and high thermal stabilities of metastable states.

To further showcase the potential of rhodanine-based photoswitches, we investigated the capacity for biological applications using the structure of known PIM kinase inhibitor SMI-16a, i.e., oxo-rhodanine *Z*-**1**, as inspiration. PIM kinases are oncogenes, and they belong to the class of constitutively active kinases. They phosphorylate several proliferation promoting and antiapoptotic master regulators such as c-myc and BAD (BCL-2 antagonist of cell death). The architecture of ATP binding sites of PIM kinases is unique in comparison to other kinases, which enables highly selective inhibition of PIM. For these reasons, PIM kinases are gaining increasing attention as promising pharmacological targets for specific cancer therapy.[73,74,80] The *Z* isomer of oxo-rhodanine **1** has been shown to selectively and strongly inhibit PIM-1 kinase.[62] Upon PIM-1 inhibition, the nonphosphorylated target protein BAD inhibits the pro-survival protein BCLXL1 and apoptosis is

induced.[74,80] Additionally, inhibition of the related PIM-2 kinase by oxo-rhodanine *Z*-**1** has also been demonstrated, which furthers its impact as an anticancer agent.[66] In this biological context, we scrutinized the biological activity of rhodanine-based photoswitches **5** and **8**. Derivative **5** was chosen for its close structural relation to **1** (bearing a sulfur instead of the oxygen at position X and a shorter alkyl residue at the stilbene oxygen atom, i.e., methyl instead of *n*-propyl) but offering a significantly red-shifted absorption. Derivative **8** was chosen for its outstanding photoswitching properties, retaining the rhodanine fragment as an important PIM kinase binding motif.[81]

First, the stability against glutathione was tested for derivatives **1**, **5**, and **8**. Over the course of 20 h, no significant change of absorption could be observed for 50 μm in 1:1 MeOH/PBS buffer solutions in the presence of 10 mM glutathione (see Figure 4c and Supporting Information for further details and experiments also in DMSO/PBS buffer mixture). Thus, despite the presence of a Michael-acceptor system, (oxo)-rhodanine photoswitches possess high stability against glutathione addition and are not expected to be quickly eliminated via such a mechanism within the cell.

The thermodynamically stable *Z* isomers of **5** and **8** were then tested in human cervix carcinoma HeLa cells by incubating the cells with 150 μM of the respective photoswitch. After 19 h of incubation, cells were fixed and stained for DNA and F-actin, and the total number of cells was determined. In these experiments, it was revealed that *Z*-**5** shows biological activity and kills cancer cells with similar effectiveness to *Z*-**1** at 50 and 150 μM concentration (Figure 5a−c and Supporting Information; see below for further details on *Z*-**1** activity). Derivative *Z*-**8** however did not show promising biological activity and thus was not further scrutinized. With *Z*-**5** as a biologically active agent we then set out to test the activity of its corresponding *E* isomer. However, the low thermal stability of *E*-**5** in buffer media did not allow us to examine its potency in the biological context (see Supporting Information for details). Despite the more favorable absorption properties of **5** in the visible region of the spectrum, its poor photochromism also prevented a continuous irradiation approach to permanently enrich the *E* isomer upon bulk photoisomerization of the *Z* isomer. Therefore, an effective photopharmacological application of **5** as a light-controlled anticancer agent was hampered; however, its potency as prospective inhibitor of PIM kinases could be demonstrated for the *Z* isomer.

As discussed above, oxo-rhodanine **1** (SMI-16a) itself can be photoisomerized reversibly. In buffer solution photoswitching capacity is retained between the thermodynamically stable *Z* isomer (up to 93% under blue light irradiation of, for example,
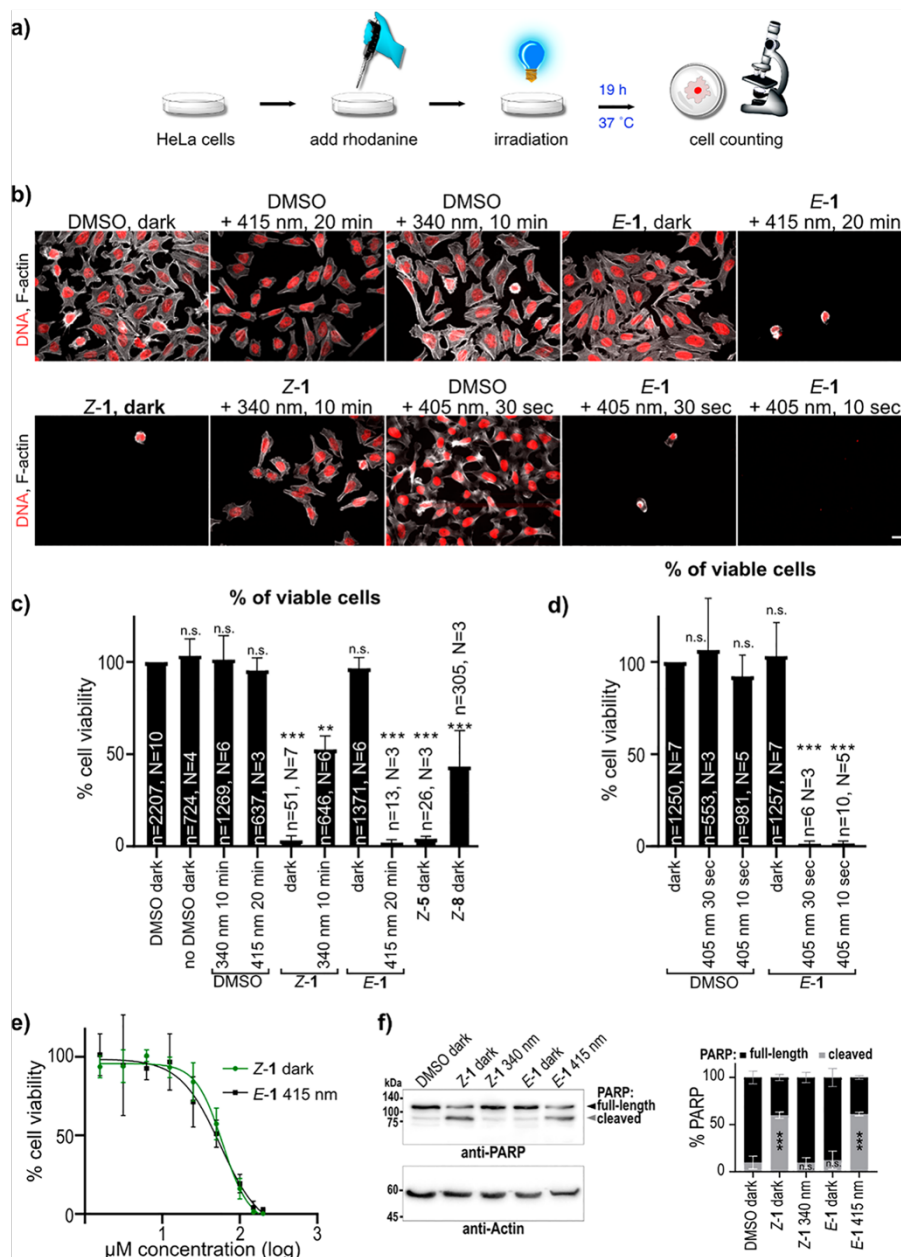
Figure 5. Biological experiments with (oxo)-rhodanine-based photoswitches. (a) Schematic representation of the experimental setup testing for biological activity. Human cervix carcinoma cells (HeLa) were treated with the different isomers of (oxo)-rhodanine-based photoswitches **1**, **5**, and **8** and either kept in the dark or irradiated with light of different wavelengths for different times. After 19 h of incubation, the cell number was determined. (b) Confocal microscopy images of HeLa cells stained for DNA (red) and F-actin (white) for the indicated conditions. Cells were incubated with medium containing 1.5% DMSO, 150 μM *E*-**1**, or 150 μM *Z*-**1** and either kept in the dark or irradiated with light. *Z*-**1**-treated cells were irradiated with 340 nm light for 10 min. *E*-**1**-treated cells were irradiated with 415 nm for 20 min or with 405 nm light for 10 or 30 s. Scale bar is 20 μm. (c, d) Mean percentage (%) of viable HeLa cells for the indicated treatments. All *E*/*Z* isomers were used at 150 μM concentration, and wavelength and time of irradiation are indicated. The total number of experiments (*N*) and cells (*n*) analyzed are shown. (e) Mean percentage (%) of cell viability for different concentrations of *Z*-**1** (dark) or *E*-**1** illuminated with 415 nm light for 20 min. The mean of 3 independent experiments is shown. (f) HeLa cells were incubated with either 1.5% DMSO (dark), 150 μM *Z*-**1** (dark or 340 nm light for 10 min), or 150 μM *E*-**1** (dark or 415 nm light for 20 min) and immunoblotted after 10 h with anti-PARP and anti-actin antibodies, as a loading control. Upon entry into apoptosis full-length PARP (black arrowhead) is cleaved (gray arrowhead, left). The mean percentages of full-length and cleaved PARP for four independent immunoblots of two different extracts were calculated (right). All error bars are standard deviation, and *p*-values were calculated using either Student's *t* test or Kruskal–Wallis multiple comparison and represent n.s. $p > 0.05$, **$p < 0.01$, ***$p < 0.001$ in comparison to DMSO-treated cells (dark).

165

405 nm and also 415 nm wavelengths; for biological experiments both wavelengths were used) and the metastable *E* isomer (up to 61% under UV light irradiation of 340 nm) without disturbance by thermal *E* to *Z* isomerization (Figure 4a and b). Although the *Z* isomer is a known and commercially available inhibitor of PIM kinases,[62,64] the corresponding *E* isomer has not been scrutinized for its biological activity to the best of our knowledge. If the *E* isomer of **1** is, in fact, biologically inactive, an opportunity for light-induced activation by blue light would present itself. The intrinsically very high thermal stability of the *E* isomer would, for example, allow a global administration and timed local activation scheme.

We have tested this hypothesis in HeLa cells by incubating them with 150 μM pure SMI-16a *Z*-**1** or *E*-**1** isomer. Again, after 19 h of incubation, cells were fixed and stained for DNA and F-actin and the total number of cells was determined. As expected, incubation with the *Z*-**1** isomer strongly reduced cell number to only 3% living cells (Figure 5a, b, and c) due to induction of apoptosis.[66] The cytotoxic effect of the *Z*-**1** isomer was also tested in DLD-1, HCT116, and RPE1 cell lines and showed the same efficiency as in HeLa cells (see Supporting Information for details). Next, we analyzed the corresponding *E*-**1** isomer, and to our delight, incubation with *E*-**1** resulted in 96% living cells and thus did not induce apoptosis, suggesting the *E*-**1** isomer is inactive (Figure 5b and c). To confirm those observations, we used an independent cell viability assay, which measures the level of oxidation of resazurin in the mitochondria of healthy cells. Incubation of cells with the *Z*-**1** isomer results in high cytotoxicity, whereas treatment with the corresponding *E*-**1** isomer had no effect on cell viability (see also Supporting Information). The strong difference in activity of the *E* and *Z* isomers thus served as the foundation for light control of PIM kinase activity. To induce *E* to *Z* photoisomerization, the *E*-**1** isomer was irradiated with blue 415 nm light for 10 min in a cell culture medium prior to adding it to the cells. As a result, after 19 h, the cell number was strongly reduced (see the Supporting Information). Next, the *E*-**1** isomer or DMSO was added to the cell culture medium and irradiated with blue 415 nm light for 20 min directly on the cells. In the presence of **1**, but not DMSO alone, the cell number was strongly reduced with only 2% of living cells left after the irradiation (Figure 5a, b, and c), which was similar to the effect of the pure *Z*-**1** isomer addition. High cytotoxicity of **1** irradiated with 415 nm light on cells could be confirmed with the resazurin-based viability assay (see Supporting Information for details). For biomedical applications short illumination times are desirable, and therefore we repeated the experiment using a high-power 405 nm LED. Illumination of *E*-**1**-treated cells with intense 405 nm light for 10 or 30 s resulted in only 2% of viable cells (Figure 5b and d). DMSO-treated cells did not show any effect with the same high-power illumination. This shows that irradiation of the *E*-**1** isomer even at the time scale of seconds results in highly efficient photoisomerization into the *Z*-**1** isomer and subsequent inhibition of PIM kinase and cell death.

To quantitatively compare the ON switching of the *E*-**1** isomer with that of the pure *Z*-**1** isomer, we further conducted dose−response experiments. Cells were treated with various concentrations of *Z*-**1** and *E*-**1** and either kept in the dark or treated with 415 nm light, respectively. The quantification of the percentage of viable cells revealed that cells were killed with the same efficiency when treated with *Z*-**1** (dark) or with

E-**1** and illuminated with 415 nm light (Figure 5e; see the Supporting Information for more details).

Thus, a light-controlled ON switching and induction of apoptosis could be established with the oxo-rhodanine-based photoswitch **1**, showcasing its very high potential as a molecular tool for medicinal chemistry. Also, the reverse behavior can be elicited by irradiating the *Z*-**1** isomer with 340 nm light in cell culture medium followed by the addition of the medium to the cells (Supporting Information) or by directly irradiating cells treated with *Z*-**1** (Figure 5b and c, Supporting Information). The irradiation of the *Z*-**1** isomer with 340 nm light leads to a significant recovery of cell viability with 54% viable cells, which indicates the photogeneration of the inactive *E* isomer. The percentage of living cells is fully consistent with the maximum possible light-induced enrichment of the *E*-**1** isomer in solution (61%) when using 340 nm light.

Finally, we confirmed that the *Z*-**1** isomer and photoswitching of the *E*-**1** isomer both result in the activation of specifically the apoptosis pathway by immunoblotting against poly-[ADP-ribose]-polymerase (PARP), which is cleaved by caspases after the onset of apoptosis.[82] As expected DMSO-, *E*-**1** (dark)- and *Z*-**1** (340 nm)-treated cells contained less than 13% of cleaved PARP, evidencing that these cells were healthy and apoptosis was not induced. In contrast, cells treated with either *Z*-**1** in the dark or *E*-**1** illuminated with 415 nm light showed more than 60% cleaved PARP, demonstrating the activation of the apoptosis pathway (Figure 5f).

Taken together, the biological effect perfectly correlates with the amount of active *Z* isomer or inactive *E* isomer produced in solution by the photoreaction. Therefore, the deliberate and reversible control of the biological PIM kinase function and induction of apoptosis was established using an oxo-rhodanine-based photoswitch (Figure 5a−f).

■ CONCLUSION

In conclusion, we demonstrate that oxo-rhodanine and rhodanine chromophores are highly capable photoswitching motifs for light-induced double-bond isomerization reactions. Their simple synthesis delivers fast access to a variety of different structures and thus allows tuning of thermal and photochemical/photophysical properties in a wide range. Introduction of heterocyclic residues deliver outstanding performance with very efficient photoisomerizations, strong photochromism, high thermal stabilities of the metastable *E* isomers, and very good quantum yields for both isomerization directions. Absorptions can be shifted up to 57 nm to the red by replacing one oxygen in oxo-rhodanines by sulfur. Thermal stability of the *E* isomers is lowered by this substitution, making this property highly tunable by a simple one-atom replacement. The biological application of rhodanine-based photoswitch *Z*-**5** demonstrated induction of apoptosis with similar effectiveness to *Z*-**1**, i.e., the known PIM kinase inhibitor SMI-16a. Derivative *Z*-**1** itself was further shown to exhibit very pronounced photomodulation of its biological activity, enabling light-induced apoptosis induction with high efficiency at short time scales. (Oxo)-rhodanine chromophores are thus shown to be highly promising photocontrollable molecular tools with especially potent applicability in biological and medicinal context.

■ ASSOCIATED CONTENT

Ⓢ Supporting Information

The Supporting Information is available free of charge at https://pubs.acs.org/doi/10.1021/jacs.3c07710.

> Details of synthesis, structural analyses, photochemical, photophysical, and thermal behavior, and biological experiments (PDF)

Accession Codes

CCDC 2233273−2233276 contain the supplementary crystallographic data for this paper. These data can be obtained free of charge via www.ccdc.cam.ac.uk/data_request/cif, or by emailing data_request@ccdc.cam.ac.uk, or by contacting The Cambridge Crystallographic Data Centre, 12 Union Road, Cambridge CB2 1EZ, UK; fax: +44 1223 336033.

■ AUTHOR INFORMATION

Corresponding Authors

Esther Zanin − *Department of Biology, Friedrich-Alexander-Universität Erlangen-Nürnberg, 91058 Erlangen, Germany*; Email: esther.zanin@fau.de

Henry Dube − *Department of Chemistry and Pharmacy, Friedrich-Alexander-Universität Erlangen-Nürnberg, 91058 Erlangen, Germany*; ⓞ orcid.org/0000-0002-5055-9924; Email: henry.dube@fau.de

Authors

Laura Köttner − *Department of Chemistry and Pharmacy, Friedrich-Alexander-Universität Erlangen-Nürnberg, 91058 Erlangen, Germany*

Friederike Wolff − *Department of Biology, Friedrich-Alexander-Universität Erlangen-Nürnberg, 91058 Erlangen, Germany*

Peter Mayer − *Department of Chemistry and Munich Center for Integrated Protein Science CIPSM, Ludwig-Maximilians-Universität München, D-81377 Munich, Germany*

Complete contact information is available at:
https://pubs.acs.org/10.1021/jacs.3c07710

Author Contributions

L.K. and F.W. contributed equally to this work.

Notes

The authors declare no competing financial interest.

■ REFERENCES

(1) *Molecular Photoswitches. Chemistry, Properties, and Applications*; Wiley-VCH: Weinheim, 2022; p 1152.

(2) *Molecular Switches*; Wiley-VCH: Weinheim, 2011; Vol. *1*, p 792.

(3) Kassem, S.; van Leeuwen, T.; Lubbe, A. S.; Wilson, M. R.; Feringa, B. L.; Leigh, D. A. Artificial molecular motors. *Chem. Soc. Rev.* **2017**, *46* (9), 2592−2621.

(4) Erbas-Cakmak, S.; Leigh, D. A.; McTernan, C. T.; Nussbaumer, A. L. Artificial Molecular Machines. *Chem. Rev.* **2015**, *115* (18), 10081−10206.

(5) Boelke, J.; Hecht, S. Designing Molecular Photoswitches for Soft Materials Applications. *Adv. Optical Mater.* **2019**, *7* (16), No. 1900404.

(6) Goulet-Hanssens, A.; Eisenreich, F.; Hecht, S. Enlightening Materials with Photoswitches. *Adv. Mater.* **2020**, *32* (20), No. e1905966.

(7) Danowski, W.; van Leeuwen, T.; Browne, W. R.; Feringa, B. L. Photoresponsive porous materials. *Nanoscale Advances* **2021**, *3* (1), 24−40.

(8) Göstl, R.; Senf, A.; Hecht, S. Remote-controlling chemical reactions by light: Towards chemistry with high spatio-temporal resolution. *Chem. Soc. Rev.* **2014**, *43* (6), 1982−1996.

(9) Dorel, R.; Feringa, B. L. Photoswitchable catalysis based on the isomerisation of double bonds. *Chem. Commun.* **2019**, *55* (46), 6477−6486.

(10) Morstein, J.; Trauner, D. New players in phototherapy: photopharmacology and bio-integrated optoelectronics. *Curr. Opin. Chem. Biol.* **2019**, *50*, 145−151.

(11) Hull, K.; Morstein, J.; Trauner, D. In Vivo Photopharmacology. *Chem. Rev.* **2018**, *118* (21), 10710−10747.

(12) Lerch, M. M.; Hansen, M. J.; van Dam, G. M.; Szymanski, W.; Feringa, B. L. Emerging Targets in Photopharmacology. *Angew. Chem., Int. Ed.* **2016**, *55* (37), 10978−10999.

(13) Waldeck, D. H. Photoisomerization Dynamics of Stilbenes. *Chem. Rev.* **1991**, *91* (3), 415−436.

(14) Villaron, D.; Wezenberg, S. J. Stiff-Stilbene Photoswitches: From Fundamental Studies to Emergent Applications. *Angew. Chem., Int. Ed.* **2020**, *59* (32), 13192−13202.

(15) Bandara, H. M.; Burdette, S. C. Photoisomerization in different classes of azobenzene. *Chem. Soc. Rev.* **2012**, *41* (5), 1809−1825.

(16) Jerca, F. A.; Jerca, V. V.; Hoogenboom, R. Advances and opportunities in the exciting world of azobenzenes. *Nat. Rev. Chem.* **2022**, *6* (1), 51−69.

(17) Harris, J. D.; Moran, M. J.; Aprahamian, I. New molecular switch architectures. *Proc. Natl. Acad. Sci. U. S. A.* **2018**, *115* (38), 9414−9422.

(18) Helmy, S.; Leibfarth, F. A.; Oh, S.; Poelma, J. E.; Hawker, C. J.; Read de Alaniz, J. Photoswitching using visible light: a new class of organic photochromic molecules. *J. Am. Chem. Soc.* **2014**, *136* (23), 8169−8172.

(19) Zulfikri, H.; Koenis, M. A. J.; Lerch, M. M.; Di Donato, M.; Szymanski, W.; Filippi, C.; Feringa, B. L.; Buma, W. J. Taming the Complexity of Donor-Acceptor Stenhouse Adducts: Infrared Motion Pictures of the Complete Switching Pathway. *J. Am. Chem. Soc.* **2019**, *141* (18), 7376−7384.

(20) Yang, Y.; Hughes, R. P.; Aprahamian, I. Visible light switching of a BF2-coordinated azo compound. *J. Am. Chem. Soc.* **2012**, *134* (37), 15221−15224.

(21) Yang, Y.; Hughes, R. P.; Aprahamian, I. Near-infrared light activated azo-BF2 switches. *J. Am. Chem. Soc.* **2014**, *136* (38), 13190−13193.

(22) Shao, B.; Aprahamian, I. Hydrazones as New Molecular Tools. *Chem.* **2020**, *6* (9), 2162−2173.

(23) van Dijken, D. J.; Kovaricek, P.; Ihrig, S. P.; Hecht, S. Acylhydrazones as Widely Tunable Photoswitches. *J. Am. Chem. Soc.* **2015**, *137* (47), 14982−14991.

(24) Mutoh, K.; Nakagawa, Y.; Sakamoto, A.; Kobayashi, Y.; Abe, J. Stepwise Two-Photon-Gated Photochemical Reaction in Photochromic [2.2]Paracyclophane-Bridged Bis(imidazole dimer). *J. Am. Chem. Soc.* **2015**, *137* (17), 5674−5677.

(25) Mutoh, K.; Kobayashi, Y.; Yamane, T.; Ikezawa, T.; Abe, J. Rate-Tunable Stepwise Two-Photon-Gated Photoresponsive Systems

Employing a Synergetic Interaction between Transient Biradical Units. *J. Am. Chem. Soc.* **2017**, *139* (12), 4452−4461.

(26) Kirchner, S.; Leistner, A. L.; Godtel, P.; Seliwjorstow, A.; Weber, S.; Karcher, J.; Nieger, M.; Pianowski, Z. Hemipiperazines as peptide-derived molecular photoswitches with low-nanomolar cytotoxicity. *Nat. Commun.* **2022**, *13* (1), 6066.

(27) Bartelmann, T.; Dube, H. Indigoid Photoswitches. *Molecular Photoswitches* **2022**, 283−302.

(28) Huang, C. Y.; Bonasera, A.; Hristov, L.; Garmshausen, Y.; Schmidt, B. M.; Jacquemin, D.; Hecht, S. N,N′-Disubstituted Indigos as Readily Available Red-Light Photoswitches with Tunable Thermal Half-Lives. *J. Am. Chem. Soc.* **2017**, *139* (42), 15205−15211.

(29) Thumser, S.; Kottner, L.; Hoffmann, N.; Mayer, P.; Dube, H. All-Red-Light Photoswitching of Indirubin Controlled by Supramolecular Interactions. *J. Am. Chem. Soc.* **2021**, *143* (43), 18251−18260.

(30) Kohl, F.; Gerwien, A.; Hampel, F.; Mayer, P.; Dube, H. Hemithioindigo-Based Trioxobicyclononadiene: 3D Multiswitching of Electronic and Geometric Properties. *J. Am. Chem. Soc.* **2022**, *144* (7), 2847−2852.

(31) Guentner, M.; Schildhauer, M.; Thumser, S.; Mayer, P.; Stephenson, D.; Mayer, P. J.; Dube, H. Sunlight-powered kHz rotation of a hemithioindigo-based molecular motor. *Nat. Commun.* **2015**, *6* (1), 8406.

(32) Gerwien, A.; Mayer, P.; Dube, H. Photon-Only Molecular Motor with Reverse Temperature-Dependent Efficiency. *J. Am. Chem. Soc.* **2018**, *140* (48), 16442−16445.

(33) Gerwien, A.; Mayer, P.; Dube, H. Green light powered molecular state motor enabling eight-shaped unidirectional rotation. *Nat. Commun.* **2019**, *10* (1), 4449.

(34) Uhl, E.; Mayer, P.; Dube, H. Active and Unidirectional Acceleration of Biaryl Rotation by a Molecular Motor. *Angew. Chem.* **2020**, *59* (14), 5730−5737.

(35) Bach, N. N.; Josef, V.; Maid, H.; Dube, H. Active Mechanical Threading by a Molecular Motor. *Angew. Chem., Int. Ed.* **2022**, *61* (19), No. e202201882.

(36) Gerwien, A.; Gnannt, F.; Mayer, P.; Dube, H. Photogearing as a concept for translation of precise motions at the nanoscale. *Nat. Chem.* **2022**, *14*, 670−676.

(37) Roke, D.; Sen, M.; Danowski, W.; Wezenberg, S. J.; Feringa, B. L. Visible-Light-Driven Tunable Molecular Motors Based on Oxindole. *J. Am. Chem. Soc.* **2019**, *141* (18), 7622−7627.

(38) Petermayer, C.; Dube, H. Circular Dichroism Photoswitching with a Twist: Axially Chiral Hemiindigo. *J. Am. Chem. Soc.* **2018**, *140* (42), 13558−13561.

(39) Wiedbrauk, S.; Bartelmann, T.; Thumser, S.; Mayer, P.; Dube, H. Simultaneous complementary photoswitching of hemithioindigo tweezers for dynamic guest relocation. *Nat. Commun.* **2018**, *9* (1), 1456.

(40) Grill, K.; Dube, H. Supramolecular Relay-Control of Organocatalysis with a Hemithioindigo-Based Molecular Motor. *J. Am. Chem. Soc.* **2020**, *142* (45), 19300−19307.

(41) Lougheed, T.; Borisenko, V.; Hennig, T.; Rück-Braun, K.; Woolley, G. A. Photomodulation of ionic current through hemithioindigo-modified gramicidin channels. *Org. Biomol. Chem.* **2004**, *2* (19), 2798−2801.

(42) Herre, S.; Schadendorf, T.; Ivanov, I.; Herrberger, C.; Steinle, W.; Rück-Braun, K.; Preissner, R.; Kuhn, H. Photoactivation of an inhibitor of the 12/15-lipoxygenase pathway. *ChemBioChem.* **2006**, *7* (7), 1089−1095.

(43) Cordes, T.; Elsner, C.; Herzog, T. T.; Hoppmann, C.; Schadendorf, T.; Summerer, W.; Rück-Braun, K.; Zinth, W. Ultrafast Hemithioindigo-based peptide-switches. *Chem. Phys.* **2009**, *358* (1−2), 103−110.

(44) Regner, N.; Herzog, T. T.; Haiser, K.; Hoppmann, C.; Beyermann, M.; Sauermann, J.; Engelhard, M.; Cordes, T.; Rück-Braun, K.; Zinth, W. Light-switchable hemithioindigo-hemistilbene-containing peptides: ultrafast spectroscopy of the Z –> E isomer-

ization of the chromophore and the structural dynamics of the peptide moiety. *J. Phys. Chem. B* **2012**, *116* (14), 4181−4191.

(45) Sailer, A.; Ermer, F.; Kraus, Y.; Lutter, F. H.; Donau, C.; Bremerich, M.; Ahlfeld, J.; Thorn-Seshold, O. Hemithioindigos for Cellular Photopharmacology: Desymmetrised Molecular Switch Scaffolds Enabling Design Control over the Isomer-Dependency of Potent Antimitotic Bioactivity. *ChemBioChem.* **2019**, *20* (10), 1305−1314.

(46) Sailer, A.; Meiring, J. C. M.; Heise, C.; Pettersson, L. N.; Akhmanova, A.; Thorn-Seshold, J.; Thorn-Seshold, O. Pyrrole Hemithioindigo Antimitotics with Near-Quantitative Bidirectional Photoswitching that Photocontrol Cellular Microtubule Dynamics with Single-Cell Precision. *Angew. Chem., Int. Ed.* **2021**, *60* (44), 23695−23704.

(47) Lazinski, L. M.; Royal, G.; Robin, M.; Maresca, M.; Haudecoeur, R. Bioactive Aurones, Indanones, and Other Hemiindigoid Scaffolds: Medicinal Chemistry and Photopharmacology Perspectives. *J. Med. Chem.* **2022**, *65* (19), 12594−12625.

(48) Brown, F. C. 4-Thiazolidinones. *Chem. Rev.* **1961**, *61* (5), 463−521.

(49) Singh, S. P.; Parmar, S. S.; Raman, K.; Stenberg, V. I. Chemistry and biological activity of thiazolidinones. *Chem. Rev.* **1981**, *81* (2), 175−203.

(50) Wiedbrauk, S.; Dube, H. Hemithioindigo—an emerging photoswitch. *Tetrahedron Lett.* **2015**, *56* (29), 4266−4274.

(51) Shah, S.; Singh, B. Urea/thiourea catalyzed, solvent-free synthesis of 5-arylidenethiazolidine-2,4-diones and 5-arylidene-2-thioxothiazolidin-4-ones. *Bioorg. Med. Chem. Lett.* **2012**, *22* (17), 5388−5391.

(52) Li, Z.; Huang, B.; Wang, Y.; Yuan, W.; Wu, Y.; Yu, R.; Xing, G.; Zou, T.; Tao, Y. Design, synthesis and application in biological imaging of a novel red fluorescent dye based on a rhodanine derivative. *RSC Adv.* **2021**, *11* (1), 160−163.

(53) Christopher Leslee, D. B.; Karuppannan, S.; Karmegam, M. V.; Gandhi, S.; Subramanian, S. A Fluorescent Turn-On Carbazole-Rhodanine Based Sensor for Detection of Ag(+) Ions and Application in Ag(+) Ions Imaging in Cancer Cells. *J. Fluoresc.* **2019**, *29* (1), 75−89.

(54) Liu, H.; Li, Z. a.; Zhao, D. Rhodanine-based nonfullerene acceptors for organic solar cells. *Science China Materials* **2019**, *62* (11), 1574−1596.

(55) Moll, B.; Tichelkamp, T.; Wegner, S.; Francis, B.; Muller, T. J. J.; Janiak, C. Near-infrared (NIR) surface-enhanced Raman spectroscopy (SERS) study of novel functional phenothiazines for potential use in dye sensitized solar cells (DSSC). *RSC Adv.* **2019**, *9* (64), 37365−37375.

(56) Madrid-Usuga, D.; Melo-Luna, C. A.; Insuasty, A.; Ortiz, A.; Reina, J. H. Optical and Electronic Properties of Molecular Systems Derived from Rhodanine. *J. Phys. Chem. A* **2018**, *122* (43), 8469−8476.

(57) Meyer, T.; Ogermann, D.; Pankrath, A.; Kleinermanns, K.; Muller, T. J. Phenothiazinyl rhodanylidene merocyanines for dye-sensitized solar cells. *J. Org. Chem.* **2012**, *77* (8), 3704−3715.

(58) Morel, D. L.; Stogryn, E. L.; Ghosh, A. K.; Feng, T.; Purwin, P. E.; Shaw, R. F.; Fishman, C.; Bird, G. R.; Piechowski, A. P. Organic photovoltaic cells. Correlations between cell performance and molecular structure. *J. Phys. Chem.* **1984**, *88* (5), 923−933.

(59) Mousavi, S. M.; Zarei, M.; Hashemi, S. A.; Babapoor, A.; Amani, A. M. A conceptual review of rhodanine: current applications of antiviral drugs, anticancer and antimicrobial activities. *Artif. Cells, Nanomed. Biotechnol.* **2019**, *47* (1), 1132−1148.

(60) Tarahomi, M.; Baharfar, R.; Mohseni, M. Synthesis and antibacterial activity evaluation of novel rhodanine based amide derivatives. *Clin. Microbiol. Infect. Dis.* **2019**, *4* (2), 1−5.

(61) Moorthy, B. T.; Ravi, S.; Srivastava, M.; Chiruvella, K. K.; Hemlal, H.; Joy, O.; Raghavan, S. C. Novel rhodanine derivatives induce growth inhibition followed by apoptosis. *Bioorg. Med. Chem. Lett.* **2010**, *20* (21), 6297−6301.

168

(62) Beharry, Z.; Zemskova, M.; Mahajan, S.; Zhang, F.; Ma, J.; Xia, Z.; Lilly, M.; Smith, C. D.; Kraft, A. S. Novel benzylidene-thiazolidine-2,4-diones inhibit Pim protein kinase activity and induce cell cycle arrest in leukemia and prostate cancer cells. *Mol. Cancer Ther.* **2009**, *8* (6), 1473−1483.

(63) Hiasa, M.; Teramachi, J.; Oda, A.; Amachi, R.; Harada, T.; Nakamura, S.; Miki, H.; Fujii, S.; Kagawa, K.; Watanabe, K.; Endo, I.; Kuroda, Y.; Yoneda, T.; Tsuji, D.; Nakao, M.; Tanaka, E.; Hamada, K.; Sano, S.; Itoh, K.; Matsumoto, T.; Abe, M. Pim-2 kinase is an important target of treatment for tumor progression and bone loss in myeloma. *Leukemia* **2015**, *29* (1), 207−17.

(64) Xia, Z.; Knaak, C.; Ma, J.; Beharry, Z. M.; McInnes, C.; Wang, W.; Kraft, A. S.; Smith, C. D. Synthesis and Evaluation of Novel Inhibitors of Pim-1 and Pim-2 Protein Kinases. *J. Med. Chem.* **2009**, *52* (1), 74−86.

(65) Xu, L.; Meng, Y.-C.; Guo, P.; Li, M.; Shao, L.; Huang, J.-H. Recent Research Advances in Small-Molecule Pan-PIM Inhibitors. *Pharmaceutical Fronts* **2022**, *04* (04), e207−e222.

(66) Fujii, S.; Nakamura, S.; Oda, A.; Miki, H.; Tenshin, H.; Teramachi, J.; Hiasa, M.; Bat-Erdene, A.; Maeda, Y.; Oura, M.; Takahashi, M.; Iwasa, M.; Endo, I.; Yoshida, S.; Aihara, K. I.; Kurahashi, K.; Harada, T.; Kagawa, K.; Nakao, M.; Sano, S.; Abe, M. Unique anti-myeloma activity by thiazolidine-2,4-dione compounds with Pim inhibiting activity. *Br. J. Hamaetol.* **2018**, *180* (2), 246−258.

(67) Kornman, C. T.; Li, L.; Weldeab, A. O.; Ghiviriga, I.; Abboud, K. A.; Castellano, R. K. Photoisomerization of dicyanorhodanine-functionalized thiophenes. *Chem. Sci.* **2020**, *11* (37), 10190−10197.

(68) Camero, D. M.; Grinalds, N. J.; Kornman, C. T.; Barba, S.; Li, L.; Weldeab, A. O.; Castellano, R. K.; Xue, J. Thin-Film Morphology and Optical Properties of Photoisomerizable Donor-Acceptor Oligothiophenes. *ACS Appl. Mater. Interfaces* **2023**, *15* (21), 25134−25147.

(69) Che, Y.; Niazi, M. R.; Izquierdo, R.; Perepichka, D. F. Mechanism of the Photodegradation of A-D-A Acceptors for Organic Photovoltaics. *Angew. Chem., Int. Ed.* **2021**, *60* (47), 24833−24837.

(70) El-Zohry, A.; Orthaber, A.; Zietz, B. Isomerization and Aggregation of the Solar Cell Dye D149. *J. Phys. Chem. C* **2012**, *116* (50), 26144−26153.

(71) Kokel, D.; Cheung, C. Y.; Mills, R.; Coutinho-Budd, J.; Huang, L.; Setola, V.; Sprague, J.; Jin, S.; Jin, Y. N.; Huang, X. P.; Bruni, G.; Woolf, C. J.; Roth, B. L.; Hamblin, M. R.; Zylka, M. J.; Milan, D. J.; Peterson, R. T. Photochemical activation of TRPA1 channels in neurons and animals. *Nat. Chem. Biol.* **2013**, *9* (4), 257−263.

(72) Josef, V.; Hampel, F.; Dube, H. Heterocyclic Hemithioindigos: Highly Advantageous Properties as Molecular Photoswitches. *Angew. Chem., Int. Ed.* **2022**, *61* (43), No. e202210855.

(73) Rathi, A.; Kumar, D.; Hasan, G. M.; Haque, M. M.; Hassan, M. I. Therapeutic targeting of PIM KINASE signaling in cancer therapy: Structural and clinical prospects. *Biochim. Biophys. Acta Gen. Subj.* **2021**, *1865* (11), No. 129995.

(74) Nawijn, M. C.; Alendar, A.; Berns, A. For better or for worse: the role of Pim oncogenes in tumorigenesis. *Nat. Rev. Cancer* **2011**, *11* (1), 23−34.

(75) Okazaki, M.; Uchino, N.; Ishihara, M.; Fukunaga, H. Intermolecular Hydrogen Bonds of 5-Benzylidene-2,4-thiazolidine-dione Derivatives and Related Compounds in Crystalline State. *Bull. Chem. Soc. Jpn.* **1998**, *71* (7), 1713−1718.

(76) Guerraoui, A.; Goudjil, M.; Direm, A.; Guerraoui, A.; Şengün, İ. Y.; Parlak, C.; Djedouani, A.; Chelazzi, L.; Monti, F.; Lunedei, E.; Boumaza, A. A rhodanine derivative as a potential antibacterial and anticancer agent: Crystal structure, spectral characterization, DFT calculations, Hirshfeld surface analysis, in silico molecular docking and ADMET studies. *J. Mol. Struct.* **2023**, *1280*, No. 135025.

(77) Delgado, P.; Quiroga, J.; Cobo, J.; Low, J. N.; Glidewell, C. Supramolecular structures of four (Z)-5-arylmethylene-2-thioxothia-zolidin-4-ones: hydrogen-bonded dimers, chains of rings and sheets. *Acta Crystallogr. C* **2005**, *61*, o477−82.

(78) Maerz, B.; Wiedbrauk, S.; Oesterling, S.; Samoylova, E.; Nenov, A.; Mayer, P.; de Vivie-Riedle, R.; Zinth, W.; Dube, H. Making fast photoswitches faster–using Hammett analysis to understand the limit of donor-acceptor approaches for faster hemithioindigo photo-switches. *Chem.—Eur. J.* **2014**, *20* (43), 13984−13992.

(79) Wiedbrauk, S.; Maerz, B.; Samoylova, E.; Mayer, P.; Zinth, W.; Dube, H. Ingredients to TICT Formation in Donor Substituted Hemithioindigo. *J. Phys. Chem. Lett.* **2017**, *8* (7), 1585−1592.

(80) Luszczak, S.; Kumar, C.; Sathyadevan, V. K.; Simpson, B. S.; Gately, K. A.; Whitaker, H. C.; Heavey, S. PIM kinase inhibition: co-targeted therapeutic approaches in prostate cancer. *Signal Transduct. Target Ther.* **2020**, *5* (1), 7.

(81) Asati, V.; Bharti, S. K.; Budhwani, A. K. 3D-QSAR and virtual screening studies of thiazolidine-2,4-dione analogs: Validation of experimental inhibitory potencies towards PIM-1 kinase. *J. Mol. Struct.* **2017**, *1133*, 278−293.

(82) Chaitanya, G. V.; Alexander, J. S.; Babu, P. P. PARP-1 cleavage fragments: signatures of cell-death proteases in neurodegeneration. *Cell Commun. Signal.* **2010**, *8* (1), 31.

169

Rhodanine-Based Chromophores – Fast Access to Capable Photoswitches and Application in Light Induced Apoptosis

Laura Köttner,[a§] Friederike Wolff,[b§] Peter Mayer,[c] Esther Zanin,[b]* Henry Dube[a]*

[a] Friedrich-Alexander-Universität Erlangen-Nürnberg, Department of Chemistry and Pharmacy, Nikolaus- Fiebiger-Str. 10, 91058 Erlangen, Germany.

[b] Friedrich-Alexander-Universität Erlangen-Nürnberg, Department of Biology, Staudtstrasse 5, 91058 Erlangen, Germany.

[c] Ludwig-Maximilians-Universität München, Department für Chemie and Munich Center for Integrated Protein Science CIPSM, D-81377 Munich, Germany.

[§] both authors contributed equally to this work

Supporting Information

Table of content

2

Materials and general methods

Reagents and solvents were obtained from *BLDpharm*, *Fisher Scientific*, *Sigma-Aldrich*, or *TCI* in the qualities *puriss.*, *p.a.*, or *purum* and used as received. Reactions were monitored on *Merck* Silica 60 F254 TLC plates and detection was done by irradiation with UV light (254 nm or 366 nm).

^{1}H NMR and ^{13}C NMR spectra were measured on a *Bruker AVANCE III HD 400* (400 MHz), *Bruker Avance Neo HDX 500 MHz*, and *Bruker Avance III HD 800 MHz* NMR spectrometer. Deuterated solvents were obtained from *Deutero GmbH* or *Sigma-Aldrich* and used without further purification. The chemical shifts are given in parts per million (ppm) on the delta scale (δ) relative to tetramethylsilane as external standard. Residual solvent signals in the ^{1}H and ^{13}C NMR spectra were used as internal reference. Tetrahydrofuran-d_8: δ_H = 3.58 ppm, δ_C = 67.57 ppm; methanol-d_4: δ_H = 3.31 ppm, dimethylsulfoxide-d_8: δ_H = 2.50 ppm, δ_C = 39.52 ppm, and dioxane-d_8: δ_H = 3.53 ppm. The resonance multiplicity is indicated as *s* (singlet), *d* (doublet), *t* (triplet), *q* (quartet), *m* (multiplet). The coupling constant values (*J*) are given in hertz (Hz). Signal assignments are given in the experimental part with the arbitrary numbering indicated.

High Performance Liquid Chromatography (HPLC) was performed on a *Shimadzu* HPLC system consisting of a *LC-20AP* solvent delivery module, a *CTO-20A* column oven, a *SPD-M20A* photodiode array UV/Vis detector, and a *CBM-20A* system controller using a preparative Silica column from *Diacel* and HPLC grade solvents (EtOAc, *n*-hexane and *i*-propanol) from *Fisher Scientific* and *Sigma- Aldrich*.

Electron Impact (EI) and Atmospheric pressure photoionization (APPI) mass spectra were measured on a *Finnigan MAT95Q*, on a *Finnigan MAT90*, or a MicroTOF II instrument, respectively. The found masses from *high resolution* measurements (HR-EI-MS or HR-APPI-MS) are reported in *m/z* units with *M* as the molecular ion.

Melting points (m.p.) were determined on a *Büchi B-540 or EZ-Melt MPA 120* melting point apparatus in open capillaries.

Infrared spectra were measured on a *Perkin Elmer Spectrum BX-FT-IR* instrument equipped with a *Smith DuraSamplIR II* ATR-device or a *Thermo Scientific Nicolet iS 5 FT-IR* instrument equipped with a *iD7* ATR-device. Transmittance values are described by wavenumber (cm^{-1}) as strong (*s*), medium (*m*) and weak (*w*).

UV/vis spectra were recorded on a *Varian Cary 5000* spectrophotometer or a *Varian Cary 60* spectrophotometer with a quartz cuvette (10 mm, 5 mm). Spectral grade solvents were

3

obtained from *VWR* and *Merck*. Absorption wavelengths (λ) are given in nm and the molar absorption coefficients (ε) in L·mol^{-1}·cm^{-1}. For heating experiments a *Varian Cary Single cell Peltier Accessory* was used.

Photoisomerization experiments were conducted using LEDs from *Roithner Lasertechnik GmbH and Thorlabs Inc.* (nominal 300 nm, 340 nm, 365 nm, 375 nm, 385 nm, 395 nm, 405 nm, 415 nm, 420 nm, 430 nm, 450 nm, 470 nm, 505 nm) for illumination at 23 °C.

X-ray crystallography was performed on a *Bruker D8Venture TXS* using molybdenum-Kα-radiation or on a *SuperNova Atlas* using Cu-Kα-radiation diffractometer.

Synthesis of oxo-rhodanine and rhodanine based photoswitches

Rhodanine- and oxo-rhodanine-based photoswitches were synthesized in one-step via condensation between commercially available rhodanine or oxo-rhodanine and different aldehydes catalyzed by urea (Scheme S1). This synthesis follows a published procedure.[1] Rhodanine based photoswitch **1** is also commercially available.

X = O, S
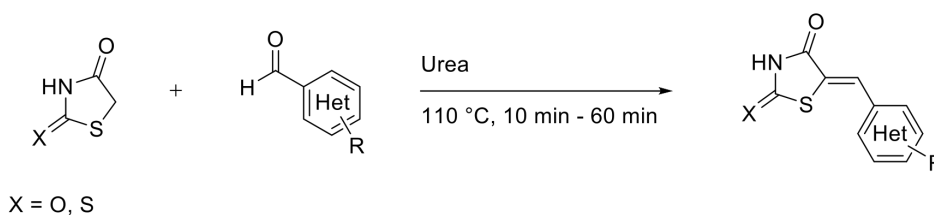
Scheme S1   General synthesis of rhodanine- and oxo-rhodanine-based photoswitches **1 – 14**.

General Procedure 1: Rhodanine or oxo-rhodanine (thiazolidine-2,4-dione) (1.0 equiv.), aldehyde (1.0 equiv.) and urea (0.1 equiv.) were heated neat to 110 °C. The reaction mixture was heated for 10 min – 60 min until the reaction was finished. After cooling 23 °C the reaction mixture was washed with water and *i*-hexanes. The crude product was recrystallized from a suitable solvent.

General Procedure 2: Rhodanine or oxo-rhodanine (thiazolidine-2,4-dione) (1.0 equiv.), aldehyde (1.0 equiv.) and urea (0.1 equiv.) were dissolved in methanol and heated to 70 °C. The reaction mixture was heated for 10 min – 60 min until the reaction was finished. After cooling to 23 °C the crude product was recrystallized from a suitable solvent.

5

14 derivatives of rhodanine- or oxo-rhodanine-based photoswitches were analyzed, see Figure S1.
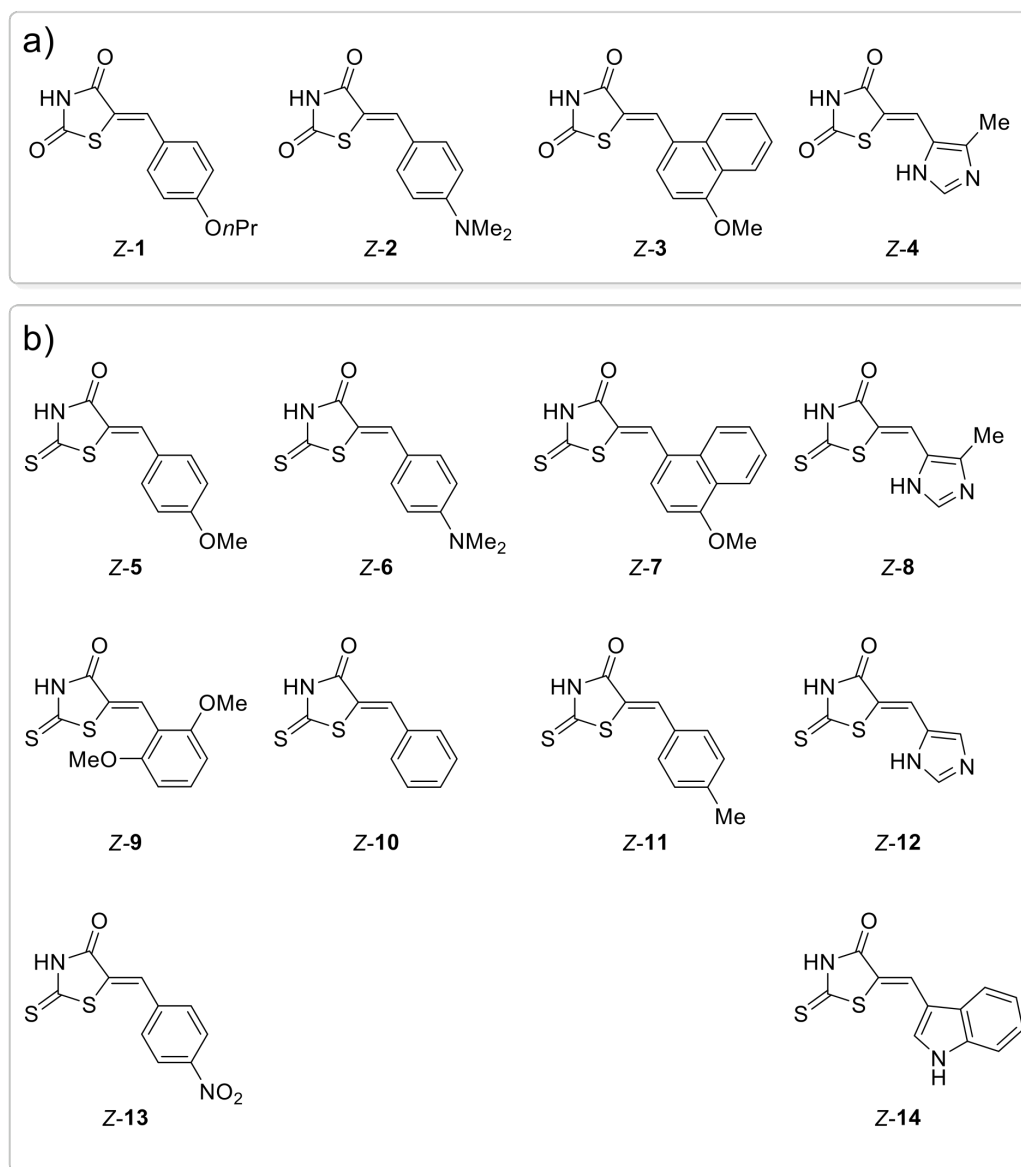
Figure S1   Overview of all synthesized and analyzed oxo- and rhodanine-based photoswitches. a) Oxo-rhodanine-based photoswitches **1** – **4** and b) rhodanine-based photoswitches **5** – **14**.
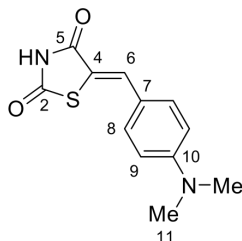
(*Z*)-5-(4-Propoxybenzylidene)thiazolidine-2,4-dione (1)
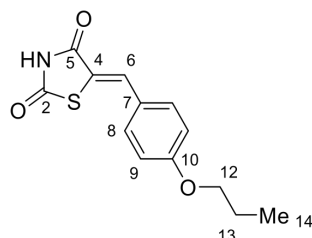
(*Z*)-5-(4-Propoxybenzylidene)thiazolidine-2,4-dione (**1**) was prepared according to **general procedure 1** from thiazolidine-2,4-dione (15.0 mmol), 4-propoxybenzaldehyde (15.0 mmol) and urea (1.50 mmol). The title compound was filtered and isolated as a light yellow solid (3.193 g, 12.1 mmol, 81%).

^{1}H NMR (400 MHz, DMSO-d_6) δ (ppm) = 12.52 (s, 1H, H-N), 7.76 (s, 1H, H-C(6)), 7.56z (d, 2H, *J* = 8.8 Hz; H-C(8)), 7.11 (d, 2H, *J* = 8.8 Hz, H-C(9)), 4.02 (t, *J* = 6.5 Hz, 2H, H$_2$-C(12)), 1.76 (h, *J* = 7.1 Hz, 2H, H$_2$-C(13)), 0.99 (t, *J* = 7.4 Hz, 3H, H$_3$-C(14)); **^{13}C NMR** (101 MHz, DMSO-d_6) δ (ppm) = 168.0 (C(2)), 167.5 (C(4)), 160.5 (C(10)), 132.1 (C(8)), 131.9 (C(6)), 125.3 (C(7)), 120.1 (C(5)), 115.3 (C(9)), 69.3 (C(12)), 21.9 (C(13)), 10.3 (C(14)); **R$_f$** = 0.45 (SiO$_2$, *i*-hexane/ ethyl acetate 8:2); **m. p.:** 189 °C; **HRMS** (APPI), [M+H]$^+$: *m/z* calc.: 264.0689 for [C$_{13}$H$_{14}$NO$_3$S]$^+$, found: 164.0690; **IR:** $\tilde{v}$ (cm^{-1}) = 2963w, 1732s, 1682m, 1587m, 1567m, 1511m, 1474m, 1428w, 1329m, 1311m, 1258s, 1179m, 1150m, 1043m, 1027w, 1012m, 905m, 825m, 766m, 729w, 717m, 688m, 638m, 605m, 528s, 492m.

7

(*Z*)-5-(4-(Dimethylamino)benzylidene)thiazolidine-2,4-dione (2)

(*Z*)-5-(4-(Dimethylamino)benzylidene)thiazolidine-2,4-dione (**2**) was prepared according to **general procedure 1** from thiazolidine-2,4-dione (15.0 mmol), 4-(dimethylamino)benzaldehyde (15.0 mmol) and urea (1.50 mmol). The title compound was isolated as red crystals (1.554 g, 6.3 mmol, 42%) after recrystallization from ethanol.

¹H NMR (500 MHz, DMSO-d_6) δ (ppm) = 12.31 (s, 1H, H-N), 7.66 (s, 1H, H-C(6)), 7.42 (d, *J* = 9.0 Hz, 2H, H-C(8)), 6.81 (d, *J* = 9.0 Hz, 2H, H-C(9)), 3.01 (s, 6H, H₃-C(11)); **¹³C NMR** (126 MHz, DMSO-d_6) δ (ppm) = 168.2 (C(2)), 167.6 (C(5)), 151.5 (C(10)), 132.9 (C(6)), 132.1 (C(8)), 119.8 (C(7)), 120.05 (C(4)), 115.7 (C(4)), 112.1 (C(9)); **R*f*** = 0.58 (SiO₂, *i*-hexane/ ethyl acetate 7:3); **m. p.:** 287 °C; **HRMS** (EI⁺), [M]⁺: *m/z* calc.: 249.0692 for [C₁₂H₁₃N₂O₂S]⁺, found: 249.0699; **IR:** $\tilde{v}$ (cm⁻¹) = 2763w, 1720m, 1677m, 1611m, 1558m, 1516m, 1435m, 1379m, 1327m, 1288m, 1232m, 1186m, 1136m, 1067m, 1029m, 944m, 900m, 803s, 738m, 687m, 645m, 629m, 596s, 512s, 494m, 478s, 464m.

8

(*Z*)-5-((4-Methoxynaphthalen-1-yl)methylene)-2-thiazolidine-2,4-dione (3)
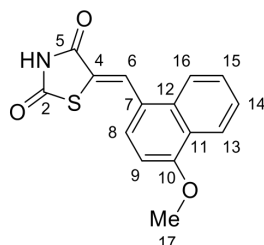
(*Z*)-5-((4-Methoxynaphthalen-1-yl)methylene)-2-thiazolidine-2,4-dione (**3**) was prepared according to **general procedure 1** from thiazolidine-2,4-dione (2.9 mmol), 4-methoxy-1-naphthaldehyde (2.9 mmol) and urea (0.29 mmol). The title compound was isolated as yellow crystals (136 mg, 0.50 mmol, 17%) after recrystallization from methanol.

^{1}H NMR (400 MHz, THF-d_8) δ (ppm) = 11.16 (s, 1H, H-N), 8.46 (s, 1H, H-C(6)), 8.31 (d, J = 8.3 Hz, 1H, H-C(13)), 8.31 (d, J = 8.1 Hz, 1H, H-C(16)), 7.68 (d, J = 8.2 Hz, 1H, H-C(8)), 7.65 – 7.58 (m, 1H, H-C(15)), 7.57 – 7.50 (m, 1H, H-C(14)), 7.06 (d, J = 8.2 Hz, 1H, H-C(9)), 4.07 (s, 3H, H$_3$-C(17)); **^{13}C NMR** (101 MHz, THF-d_8) δ (ppm) = 168.0 (C(2)), 167.7 (C(5)), 158.7 (C(10)), 134.1 (C(12)), 129.4(C(6)), 128.8 (C(8)), 128.6 (C(15)), 126.9 (C(11)), 126.8 (C(14)), 125.3 (C(4)), 124.1 (C(16)), 124.0 (C(7)), 123.6 (C(13)), 104.7 (C(9)), 56.4 (C(17)); **R**$_f$ = 0.51 (SiO$_2$, *i*-hexane/ ethyl acetate 7:3); **m. p.:** 251 °C; **HRMS** (APPI), [MH]$^+$: *m/z* calc.: 286.0532 for [C$_{15}$H$_{12}$NO$_3$S]$^+$, found: 286.0538; **IR:** $\tilde{v}$ (cm^{-1}) = 3012w, 2761w, 1739m, 1680s, 1591m, 1558s, 1511m, 1458w, 1424w, 1371m, 1336s, 1318s, 1283m, 1224s, 1153m, 1165m, 1093s, 1019m, 972m, 820m, 780w, 762m, 731m, 715m, 681s, 621m, 609s, 590s, 518m, 486m, 467s, 453m.

9

(*Z*)-5-((4-Methyl-1*H*-imidazol-5-yl)methylene)-2-thiazolidine-2,4-dione (4)
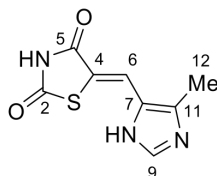
(*Z*)-5-((4-Methyl-1*H*-imidazol-5-yl)methylene)-2-thiazolidine-2,4-dione (**4**) was prepared according to **general procedure 2** from thiazolidine-2,4-dione (9.08 mmol), 4-methyl-1*H*-imidazole-5-carbaldehyde (9.08 mmol) and urea (0.908 mmol). The title compound was isolated as red crystals (906 mg, 4.33 mmol, 48%) after recrystallization from tetrahydrofuran.

^{1}H NMR (400 MHz, THF-d_8) δ (ppm) = 11.39 (s, 1H, H-N), 10.62 (s, 1H, H-N), 7.59 (s, 1H, H-C(6)), 7.56 (s, 1H, H-C(9)), 2.38 (s, 3H, H$_3$-C(12)); **^{13}C NMR** (201 MHz, THF-d_8) δ (ppm) = 171.8 (C(2)), 168.3 (C(5)), 135.6 (C(9)), 134.2 (C(11)), 132.6 (C(7)), 122.8 (C(6)), 120.9 (C(4)), 9.5 (C(12)), **decomposition:** >241 °C; **HRMS** (APPI), [MH]$^+$: *m/z* calc.: 210.0332for [C$_8$H$_8$N$_3$O$_2$S] $^+$, found: 210.0332; **IR:** $\tilde{v}$ (cm^{-1}) =3227w, 2970w, 2773w, 1703m, 1670m, 1595m, 1558m, 1432m, 1329m, 135m, 1285m, 1245m, 1168m, 1129m, 941m, 825m, 758m, 741m, 698s, 655w, 626m, 609s, 575s, 531m, 503m, 475m, 415m.

10

(*Z*)-5-(4-Methoxybenzylidene)-2-thioxothiazolidin-4-one (5)
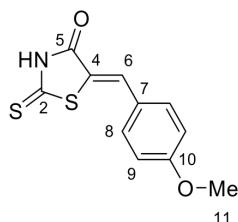
(*Z*)-5-(4-Methoxybenzylidene)-2-thioxothiazolidin-4-one (**5**) was prepared according to **general procedure 1** from rhodanine (0.75 mmol), 4-methoxybenzaldehyde (0.75 mmol) and urea (0.075 mmol). The title compound was isolated as yellow crystals (161 mg, 0.64 mmol, 85%) after recrystallization from ethanol/dimethylformamid.

¹H NMR (800 MHz, THF-d_8) δ (ppm) = 12.42 (s, 1H, H-N), 7.56 (s, 1H, H-C(6)), 7.52 (d, 2H, J = 8.9 Hz; H-C(8)), 7.05 (d, 2H, J = 8.9 Hz, H-C(9)), 3.85 (s, 3H, H₃-C(11)); **¹³C NMR** (201 MHz, THF-d_8) δ (ppm) = 196.1 (C(2)), 170.1 (C(5)), 163.7 (C(10)), 133.5 (C(8)), 132.3 (C(6)), 127.26 (C(7)), 124.2 (C(4)), 115.8 (C(9)), 56.0 (C(14)); **R$_f$** = 0.36 (SiO₂, *i*-hexane/ ethyl acetate 8:2); **m. p.:** 253 °C; **HRMS** (EI⁺), [M]⁺: *m/z* calc.: 251.0075 for [C₁₁H₉NO₂S₂]⁺, found: 251.0069; **IR:** $\tilde{v}$ (cm⁻¹) = 3133*m*, 2998*m*, 2836*m*, 2204*w*, 2048*w*, 2007*w*, 1683*s*, 1581*s*, 1562*s*, 1442*s*, 1419*m*, 1343*w*, 1307*m*, 1319*m*, 1257*s*, 1237*s*, 1197*s*, 1168*s*, 1127*m*, 1102*m*, 1069*m*, 1013*s*, 943*m*, 903*m*, 840*m*, 808*m*, 821*s*, 778*m*, 736*m*, 714*m*.
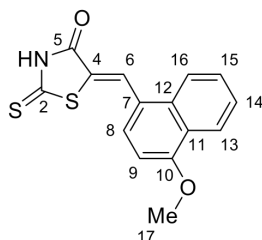
11

(*Z*)-5-(4-(Dimethylamino)benzylidene)-2-thioxothiazolidin-4-one (6)
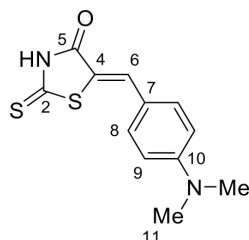
(*Z*)-5-(4-(Dimethylamino)benzylidene)-2-thioxothiazolidin-4-one (**6**) was prepared according to **general procedure 1** from rhodanine (0.75 mmol), 4-(dimethylamino)benzaldehyde (0.75 mmol) and urea (0.075 mmol). The title compound was isolated as yellow crystals (162 mg, 0.61 mmol, 82%) after recrystallization from tetrahydrofuran/water.

^{1}H NMR (400 MHz, THF-d_8) δ (ppm) = 7.49 (s, 1H, H-C(6)), 7.40 (d, J = 8.9 Hz, 2H, H-C(8), H-C(12)), 6.81 (d, J = 8.9 Hz, 2H, H-C(9), H-C(11)), 3.05 (s, 6H, H$_3$-C(14), H$_3$-C(15)); ^{13}**C NMR** (101 MHz, THF-d_8) δ (ppm) = 195.9 (C(2)), 170.2 (C(5)), 153.0 (C(10)), 133.7 (C(8)), 133.6 (C(6)), 122.1 (C(7)), 120.1 (C(4)), 113.1 (C(9)), 40.1 (C(11)); **R$_f$** = 0.30 (SiO$_2$, *i*-hexane/ ethyl acetate 8:2); **m. p.:** 272 °C; **HRMS** (EI$^+$), [M]$^+$: *m/z* calc.: 264.0391 for [C$_{12}$H$_{12}$N$_2$OS$_2$]$^+$, found: 264.0368; **IR:** $\tilde{v}$ (cm^{-1}) = 3133m, 3031m, 2904m, 2841m, 2383w, 2215w, 1985w, 1680s, 1613m, 1565s, 1520s, 1435s, 1407m, 1378m, 1339m, 1292m, 1251m, 1213s, 1167s, 1089m, 1062m, 1023m, 996w, 992m, 898m, 850m, 828m, 745m, 715m, 701w, 675s.
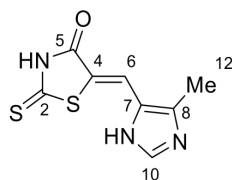
12

(*Z*)-5-((4-Methoxynaphthalen-1-yl)methylene)-2-thioxothiazolidin-4-one (7)

(*Z*)-5-((4-Methoxynaphthalen-1-yl)methylene)-2-thioxothiazolidin-4-one (**7**) was prepared according to **general procedure 1** from rhodanine (0.75 mmol), 4-methoxy-1-naphthaldehyde (0.75 mmol) and urea (0.075 mmol). The title compound was isolated as yellow crystals (75 mg, 0.25 mmol, 33%) after recrystallization from tetrahydrofuran/water.

¹H NMR (800 MHz, THF-d_8) δ (ppm) = 12.47 (s, 1H, H-N), 8.34 – 8.29 (m, 2H, H-C(6)), H-C(13)), 8.19 (d, J = 8.4 Hz, 1H, H-C(16)), 7.68 – 7.61 (m, 2H, H-C(8), H-C(15)), 7.55 (dd, J = 8.1, 1.1 Hz, 1H, H-C(14)), 7.08 (d, J = 8.1 Hz, 1H, H-C(9)), 4.08 (s, 3H, H$_3$-C(17)); **¹³C NMR** (201 MHz, THF-d_8) δ (ppm) = 196.7 (C(2)), 169.8 (C(5)), 159.1 (C(10)), 134.2 (C(12)), 129.6 (C(8)), 128.9 (C(6)), C(15)), 127.2 (C(4)), 126.9 (C(14)), 126.9 (C(7)), 124.1 (C(16)), 123.9 (C(11)), 123.7 (C(13)), 105.0 (C(9)), 56.4 (C(17)); **R**$_f$ = 0.37 (SiO$_2$, *i*-hexane/ ethyl acetate 8:2); **m. p.:** 239 °C; **HRMS** (EI$^+$), [M]$^+$: *m/z* calc.: 301.0231 for [C$_{15}$H$_{11}$NO$_2$S$_2$]$^+$, found: 301.0225; **IR:** $\tilde{v}$ (cm^{-1}) = 3133*m*, 3006*m*, 2839*m*, 2527m, 2204*w*, 2161*w*, 1987*w*, 1939*w*, 1682*s*, 1616*w*, 1589*m*, 1554*s*, 1511*m*, 1458*m*, 1438*m*, 1369*s*, 1335*m*, 1308*s*, 1282*m*, 1236*m*, 1206*s*, 1168*m*, 1153*m*, 1093*s*, 1071*m*, 1013*m* , 972*m*, 896*m*, 844*m*, 822*m*, 808*m*, 778*m*, 765*m*, 757*s*, 726*m*, 713*m*.

13

(*Z*)-5-((4-Methyl-1*H*-imidazol-5-yl)methylene)-2-thioxothiazolidin-4-one (8)

(*Z*)-5-((4-Methyl-1*H*-imidazol-5-yl)methylene)-2-thioxothiazolidin-4-one (**8**) was prepared according to **general procedure 2** from rhodanine (0.75 mmol), 4-methyl-1*H*-imidazole-5-carbaldehyde (0.75 mmol) and urea (0.075 mmol). The title compound was isolated as red crystals (130 mg, 0.58 mmol, 77%) after recrystallization from tetrahydrofuran/ethanol.

^{1}H NMR (400 MHz, THF-d_8) δ (ppm) = 11.96 (s, 1H, H-N), 11.54 (s, 1H, H-N), 7.61 (s, 1H, H-C(10)), 7.45 (s, 1H, H-C(6)), 2.40 (s, 3H, H$_3$-C(12)); **^{13}C NMR** (201 MHz, THF-d_8) δ (ppm) = 201.2 (C(2)), 170.2 (C(5)), 137.1 (C(10)), 134.4 (C(7)), 133.9 (C(4)), 123.4 (C(8)), 122.6 (C(6)), 9.6 (C(12)), **R$_f$** = 0.06 (SiO$_2$, *i*-hexane/ ethyl acetate 7:3); **m. p.:** 304 °C; **HRMS** (APPI), [MH]$^+$: *m/z* calc.: 226.0103 for [C$_8$H$_8$N$_3$OS$_2$]$^+$, found: 226.0110; **IR:** $\tilde{v}$ (cm^{-1}) = 3028*m*, 2846*m*, 1666*m*, 1598*m*, 1561*m*, 1434*m*, 1288*m*, 1189*s*, 1065*m*, 1012*m*, 942*m*, 868*m*, 810*m*, 738*m*, 723*m*, 683*m*, 627*m*, 573*s*, 542*s*, 467*m*, 434*m*, 411*m*.
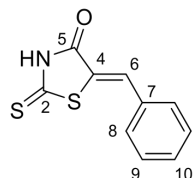
14

(*Z*)-5-(2,6-Dimethoxybenzylidene)-2-thioxothiazolidin-4-one (9)
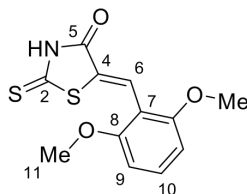
(*Z*)-5-(2,6-Dimethoxybenzylidene)-2-thioxothiazolidin-4-one (**9**) was prepared according to **general procedure 1** from rhodanine (0.75 mmol), 2,6-dimethoxybenzaldehyde (0.75 mmol) and urea (0.075 mmol). The title compound was isolated as a yellow solid (190 mg, 0.68 mmol, 91%) after recrystallization from ethanol.

^{1}H NMR (400 MHz, THF-d_8) δ (ppm) = 12.17 (s, 1H, H-N), 7.92 (s, 1H, H-C(6)), 7.37 (t, J = 8.4 Hz, 1H, H-C(10)), 6.66 (d, J = 8.5 Hz, 1H, H-C(9)), 3.89 (s, 6H, H$_3$-C(11)); **^{13}C NMR** (201 MHz, THF-d_8) δ (ppm) = 198.3 (C(2)), 170.3 (C(5)), 160.0 (C(8)), 134.0 (C(10)), 128.6 (C(4)), 126.4 (C(6)), 112.1 (C(7)), 104.7 (C9)), 56.1 (C(11)); **R$_f$** = 0.24 (SiO$_2$, *i*-hexane/ ethyl acetate 8:2); **m. p.:** 265 °C; **HRMS** (APPI), [MH]$^+$: *m/z* calc.: 282.0253 for [C$_{12}$H$_{12}$N$_2$O$_3$S$_2$]$^+$, found: 264.0368; **IR:** $\bar{v}$ (cm^{-1}) = 3055*w*, 2863*w*, 1685*s*, 1582*m*, 1565*m*, 1340*w*, 1308*w*, 1257*m*, 1230*m*, 1197*m*, 1177*m*, 1108*s*, 1076*m*, 1022*m*, 1006*m*, 956*w*, 914*m*, 807*m*, 773*s*, 734*s*, 712*m*, 688*s*, 633*m*, 615*m*, 579*s*, 550*m*, 519*s*, 444*m*, 428*m*.
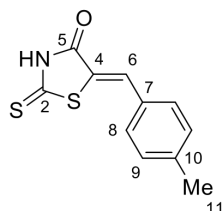
15

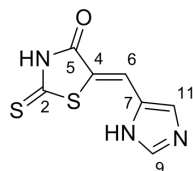**(*Z*)-5-Benzylidene-2-thioxothiazolidin-4-one (10)**

(*Z*)-5-Benzylidene-2-thioxothiazolidin-4-one (**10**) was prepared according to **general procedure 1** from rhodanine (0.75 mmol), benzaldehyde (0.75 mmol) and urea (0.075 mmol). The title compound was isolated as yellow crystals (149 mg, 0.68 mmol, 91%) after recrystallization from ethanol/dimethylformamid.

^{1}H NMR (500 MHz, THF-d_8) δ (ppm) = 12.49 (s, 1H, N-H), 7.60 (s, 1H, C-H(6)), 7.58 – 7.54 (m, 2H, C-H(8)), 7.51 – 7.47 (m, 3H, C-H(9)), 7.45 – 7.41 (m, 1H, C-H(10)); **^{13}C NMR** (126 MHz, THF-d_8) δ (ppm) = 196.2 (C(2)), 170.0 (C(5)), 134.8 (C(7)), 132.1 (C(6)), 131.5 (C(8)), 131.4 (C(10)), 130.3 (C(9)), 127.4 (C(4)); **R$_f$** = 0.49 (SiO$_2$, *i*-hexane/ ethyl acetate 8:2); **m. p.** = 202 °C; **HRMS** (APPI), [MH]$^+$: *m/z* calc.: 222.0042 for [C$_{10}$H$_8$NOS$_2$]$^+$, found: 222.0044; **IR:** $\tilde{v}$ (cm^{-1}) = 3044*w*, 2846*w*, 1697*m*, 1669*m*, 1599*m*, 1587*m*, 1568*w*, 1434*m*, 1312*w*, 1288*m*, 1232*m*, 1193*m*, 1073*m*, 1009*w*, 920*m*, 897*w*, 850*m*, 808*m*, 760*m*, 710*s*, 674*s*. 636*m*, 550*w*, 526*s*, 517*m*, 428*m*.

16

(*Z*)-5-(4-Methylbenzylidene)-2-thioxothiazolidin-4-one (11)

(*Z*)-5-(4-Methylbenzylidene)-2-thioxothiazolidin-4-one (**11**) was prepared according to **general procedure 1** from rhodanine (0.75 mmol), 4-methylbenzaldehyde (0.75 mmol) and urea (0.075 mmol). The title compound was isolated as yellow crystals (172 mg, 0.73 mmol, 98%) after recrystallization from tetrahydrofuran/water.

^{1}H NMR (400 MHz, THF-d_8) δ (ppm) = 12.44 (s, 1H, H-N), 7.57 (s, 1H, H-C(6)), 7.44 (d, J = 8.2 Hz, 2H, H-C(8)), 7.31 (d, J = 8.1 Hz, 2H, H-C(9)), 2.38 (s, 3H, H$_3$-C(11)); **^{13}C NMR** (101 MHz, THF-d_8) δ (ppm) = 196.2 (C(2)), 170.1 (C(5)), 142.2 (C(10)), 132.3 (C(6)), 132.1 (C(7)), 131.6 (C(8)), 131.0 (C(9)), 126.2 (C(4)), 21.7 (C11)); **R$_f$** =0.15 (SiO$_2$, *i*-hexane/ ethyl acetate 8:2); **m. p.** = 230 °C; **HRMS** (EI$^+$), [M]$^+$: *m/z* calc.: 235.0126 for [C$_{11}$H$_9$NOS$_2$] $^+$, found: 235.0122; **IR:** $\tilde{v}$ (cm^{-1}) = 3642*w*, 3133*w*, 3027*w*, 2843*w*, 2269*w*, 2200*w*, 2155*w*, 2081*w*, 2035*w*, 2025*w*, 1984*w*, 1963*w*, 1940*w*, 1804*w*, 1689*s*, 1589*s*, 1565*m*, 1508*m*, 1432*s*, 1334*w*, 1311*m*, 1291*m*, 1235*s*, 1224*s*, 1197*s*, 1181*s*, 1127*m*, 1102*w*, 1070*m*, 1016*m*, 964*w*, 903*w*, 818*s*, 807*s*, 780*w*, 755*w*,731*w*, 704*m*.
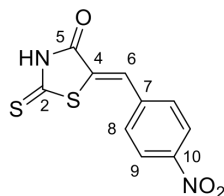
17

(*Z*)-5-((1*H*-Imidazol-5-yl)methylene)-2-thioxothiazolidin-4-one (12)

(*Z*)-5-((1*H*-Imidazol-5-yl)methylene)-2-thioxothiazolidin-4-one (**12**) was prepared according to **general procedure 2** from rhodanine (10.4 mmol), 1*H*-imidazole-5-carbaldehyde (10.4 mmol) and urea (1.04 mmol). The title compound was isolated as a yellow solid (1.805 g, 8.5 mmol, 82%) after recrystallization from tetrahydrofuran.

^{1}H NMR (400 MHz, THF-d_8) δ (ppm) = 12.03 (s, 1H, H-N), 11.70 (s, 1H, H-N), 7.74 (s, 1H, H-C(9)), 7.56 (s, 1H, H-C(11)), 7.45 (s, 1H, H-C(6)); **^{13}C NMR** (101 MHz, THF-d_8) δ (ppm) = 201.1 (C(2)), 170.2 (C(5)), 138.6 (C(9)), 138.1 (C(7)), 124.8 (C(4)), 123.6 (C(6)), 123.2 (C(11)); **decomposition:** >250 °C; **HRMS** (APPI), [MH]$^+$: *m/z* calc.: 211.9947 for [C$_7$H$_6$N$_3$OS$_2$]$^+$, found: 211.9949; **IR:** $\tilde{v}$ (cm^{-1}) = 3227m, 1677m, 1605m, 1491m, 1421m, 1329m, 1240s, 1197m, 1140m, 1111m, 1068m, 993m, 956m, 764m, 738m, 696m, 670m, 607s, 571s, 538s, 467m, 424m.

18

(*Z*)-5-(4-Nitrobenzylidene)-2-thioxothiazolidin-4-one (13)

(*Z*)-5-(4-Nitrobenzylidene)-2-thioxothiazolidin-4-one (**13**) was prepared according to **general procedure 1** from rhodanine (0.75 mmol), 4-nitrobenzaldehyde (0.75 mmol) and urea (0.075 mmol). The title compound was isolated as a yellow solid (172 mg, 0.65 mmol, 87%) after recrystallization from tetrahydrofuran/ ethanol.

^{1}H NMR (500 MHz, THF-d_8) δ (ppm) = 12.67 (s, 1H, H-N), 8.34 (d, J = 8.8 Hz, 2H, H-C(9)), 7.80 (d, J = 8.8 Hz, 2H, H-C(8)), 7.68 (s, 1H, H-C(6)); **^{13}C NMR** (126 MHz, THF-d_8) δ (ppm) = 195.5 (C(2)), 169.8 (C5)), 149.3 (C(10)), 140.7 (C7)), 132.1 (C(8)), 131.7 (C(4)), 129.0 (C(6)), 125.2 (C(9)); **R_f** = 0.15 (SiO$_2$, *i*-hexane/ ethyl acetate 8:2); **m. p.:** 252 °C; **HRMS** (APPI), [MH]$^+$: *m/z* calc.: 266.9893 for [C$_{10}$H$_7$N$_2$O$_3$S$_2$]$^+$, found: 266.9894; **IR:** $\tilde{v}$ (cm^{-1}) = 3041*m*, 2848*m*, 1714*s*, 1605*m*, 1587*m*, 1522*m*, 1442*m*, 1406*m*, 1340*m*, 1318*m*, 1300*m*, 1284*s*, 1232*m*, 1184*s*, 1108*m*, 1122*m*, 1060*s*, 1001*w*, 906*m*, 866*m*, 845*s*, 825*m*, 764*m*, 751*m*, 715*m*, 681*s*, 669*m*, 569*m*, 542*s*, 514*m*, 424*m*.

(*Z*)-5-((1*H*-Indol-3-yl)methylene) thioxothiazolidin-4-one (14)
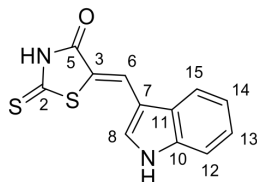
(*Z*)-5-((1*H*-Indol-3-yl)methylene)thiazolidine-2,4-dione (**14**) was prepared according to **general procedure 2** from rhodanine (0.75 mmol), indole-3-carboxaldehyde (0.75 mmol) and urea (0.075 mmol). The title compound was isolated as a red solid (158 mg, 0.61 mmol, 81%) after recrystallization from tetrahydrofuran/ethanol.

^{1}H NMR (500 MHz, THF-*d₈*) δ (ppm) = 12.19 (s, 1H, H-N), 11.27 (s, 1H, H-N), 7.96 (s, 1H, H-C(6))), 7.90 – 7.86 (m, 1H, H-C(15)), 7.65 (d, *J* = 3.0 Hz, 1H, H-C(8))), 7.45 – 7.41 (m, 1H, H-C(12))), 7.26 – 7.17 (m, 2H, H-C(13, 14)); **^{13}C NMR** (126 MHz, THF-*d₈*) δ (ppm) = 195.4 (C(2)), 169.8 (C(5)), 137.9 (C(10)), 129.7 (C(8)), 128.5 (C(11)), 124.8 (C(6)), 124.3 (C(13)), 122.4 (C(14)), 120.5 (C(4/7)), 119.4 (C(15)), 113.1 (C(4/7)), 112.93 (C(12)); **R$_f$** = 0.43 (SiO₂, *i*-hexane/ ethyl acetate 7:3); **m. p.:** 305 °C; **HRMS** (APPI), [MH]⁺: *m/z* calc.: 261.0151 for [C₁₂H₉N₂O₂S]⁺, found: 261.0144; **IR:** ṽ (cm⁻¹) = 3261*m*, 2849*m*, 1676*m*, 1588*m*, 1561*m*, 1510*m*, 1491*m*, 1451*m*, 1434*m*, 1347*m*, 1330*m*, 1292*m*, 1209*s*, 1139*s*, 1074*m*, 1011*m*, 909*w*, 770*m*, 713*m*, 701*m*, 684*m*, 629*s*, 602*m*, 550*s*, 519*s*, 466*m*, 449*s*, 418*m*.

Thermal isomerization

Z isomers are the thermodynamically most stable forms of all photoswitches **1 – 14**. At elevated temperatures in the dark metastable *E* isomers are thermally interconverting into *Z* isomers. The thermal *E* to *Z* isomerization kinetics were determined by heating samples enriched in metastable *E* isomer in an oil-bath and monitoring the conversion process by ^{1}H NMR spectroscopy at 25 °C in selected time intervals.

When the thermal decay follows a first order reaction type the Gibbs energy of activation *Δ*G‡ can be calculated by using the *Eyring* equation, see equation 1.

$$k = \frac{k\, k_B T}{h} e^{-\frac{\Delta G^{\ddagger}}{RT}}$$

eq. 1

With k_B = Bolzmann constant (1.381 · 10^{-23} J · K^{-1})

    T = temperature in K

    h = Planck constant (6.626 · 10^{-34} J · s)

    k = rate constant of the reaction

R = ideal gas constant (8.314 J · K^{-1} · mol^{-1})Eq. 1 can be rearranged and the numerical value of the rate constant can then be inserted into eq. 2:

$$\Delta G^{\ddagger}(in\, J\, mol^{-1}) = -\ln\left(\frac{k\, h}{k_B\, T}\right) R\, T$$

eq. 2

The half-life times are calculated by dividing ln (2) by the rate constant *k*, see eq. 3.

$$t_{1/2} = \frac{\ln(2)}{k}$$

eq. 3

To calculate the relative energy differences *ΔG* between the two isomeric states *Z* and *E*, the equilibrium constant *K* must be determined at a given temperature and can then be inserted into eq. 4 (with *K* = ([*Z*]/[*E*]), [*Z*] the concentration of the *Z* isomer in thermal equilibrium and [*E*] the concentration of the *E* isomer in thermal equilibrium.

$$-\Delta G = ln(K)\, R\, T$$

eq. 4

When thermal decays of the *E* isomers didn't follow typical first order reaction half-life times $t_{1/2}$ and equilibrium half-life times $t_{1/2}^{eq}$ of metastable *E* isomers were determined by fitting the change of isomeric ratio over time with a polynomial fit.

Gibbs energies of activation $\Delta G^{\ddagger}$, half-life times $t_{1/2}$ and equilibrium half-life times $t_{1/2}^{eq}$ and relative energy differences ΔG between the two isomeric states of photoswitches **1** – **14** are given in Table S1.

22

Table S1   Gibbs energy of activation $\Delta G^{\ddagger}$, half-life times $t_{1/2}$ of the E isomers of photoswitches **1** – **14** and relative energy differences ΔG between the two isomeric states at the indicated temperatures. Thermal E to Z isomerizations were measured in tetrahydrofuran-d_8, dioxane-d_8, MeOH-d_4 or DMSO-d_6 at different temperatures. Isomeric ratios $Z:E$ after thermal isomerization as well as the rates of thermal isomerizations were determined by ^{1}H NMR spectroscopy.

	solvent	T [°C]	$\Delta G^{\ddagger}$ [kcal mol⁻¹]	$t_{1/2}$ [h]	$Z:E$ [%]	ΔG [kcal mol⁻¹]
1	dioxane-d_8[a]	85	-	114	100 : 0	≥2.1
	DMSO-d_6[a]	130	30.3	0.6	100 : 0	≥2.4
2	dioxane-d_8[b]	85	-	138[c]	-	≥0.6
	DMSO-d_6[a]	130	29.4	0.2	100 : 0	≥2.4
3	dioxane-d_8[a]	85	-	≥480[c]	-	≥0.3
	DMSO-d_6[a]	130	31.7	3.4	100 : 0	≥2.4
4	dioxane-d_8	85	-	-	-	-
	MeOH-d_4	50	-	-	-	≥0.9
	DMSO-d_6	140	32.4	3	100 : 0	≥2.4
5	THF-d_8	55	-	30	100 : 0	≥1.9
	DMSO-d_6	90	28.5	3.6	100 : 0	≥2.1
6	THF-d_8	55	-	7	100 : 0	≥1.9
	DMSO-d_6	90	28.7	4.7	100 : 0	≥2.1
7	THF-d_8	55	-	143	100 : 0	≥1.9
	DMSO-d_6	90	29.3	10.9	98 : 2	≥2.1
8	dioxane-d_8	85	-	95[c]	-	≥1.7
	MeOH-d_4	50	25.6	6	100 : 0	≥1.9
	DMSO-d_6	80	26.5	0.6	100 : 0	≥2.1
9	dioxane-d_8	85	-	101[d]	92 : 8	1.7
	DMSO-d_6	130	31.8	3.9	100 : 0	≥2.4
10	dioxane-d_8	85	-	85	100 : 0	≥2.1
11	THF-d_8	55	-	19	100 : 0	≥1.9
	DMSO-d_6	90	28.1	2.2	100 : 0	≥2.1
12	dioxane-d_8	85	-	110	100 : 0	≥2.1
	DMSO-d_6	60	26.0	3.1	100 : 0	≥1.9
13	THF-d_8	55	-	82	100 : 0	≥1.9
	DMSO-d_6	60	25.7	0.4	100 : 0	≥1.9
14	dioxane-d_8	85	-	12[c]	-	≥1.6

[a]minor decomposition during heating; [b]decomposition during heating; [c]calculated half-life time $t_{1/2}$ if thermal E/Z isomerization will proceed for 100%; [d]equilibrium half-life time $t_{1/2}^{eq}$.

23

For photoswitches **2**, **3**, **8** and **14** it was assumed that thermal E/Z isomerization will proceed for 100% in dioxane-d_8. **4** did not show any thermal isomerization over 162 h in dioxane-d_8 at 85 °C and only minor thermal isomerization over 66 h in MeOH-d_4 at 50 °C. Due to overlapping signals the thermal stability of **10** and **14** were not able to determine in DMSO-d_6.

The ratio of $Z : E$ shows the final isomeric ratio between Z and E isomer.

Figure S2 – Figure S15 show the thermal isomerization of metastable E isomer to stable isomer Z isomer in the dark as followed by ^{1}H NMR spectroscopy and corresponding plots of the E/Z-conversion of isomers during heating over time.
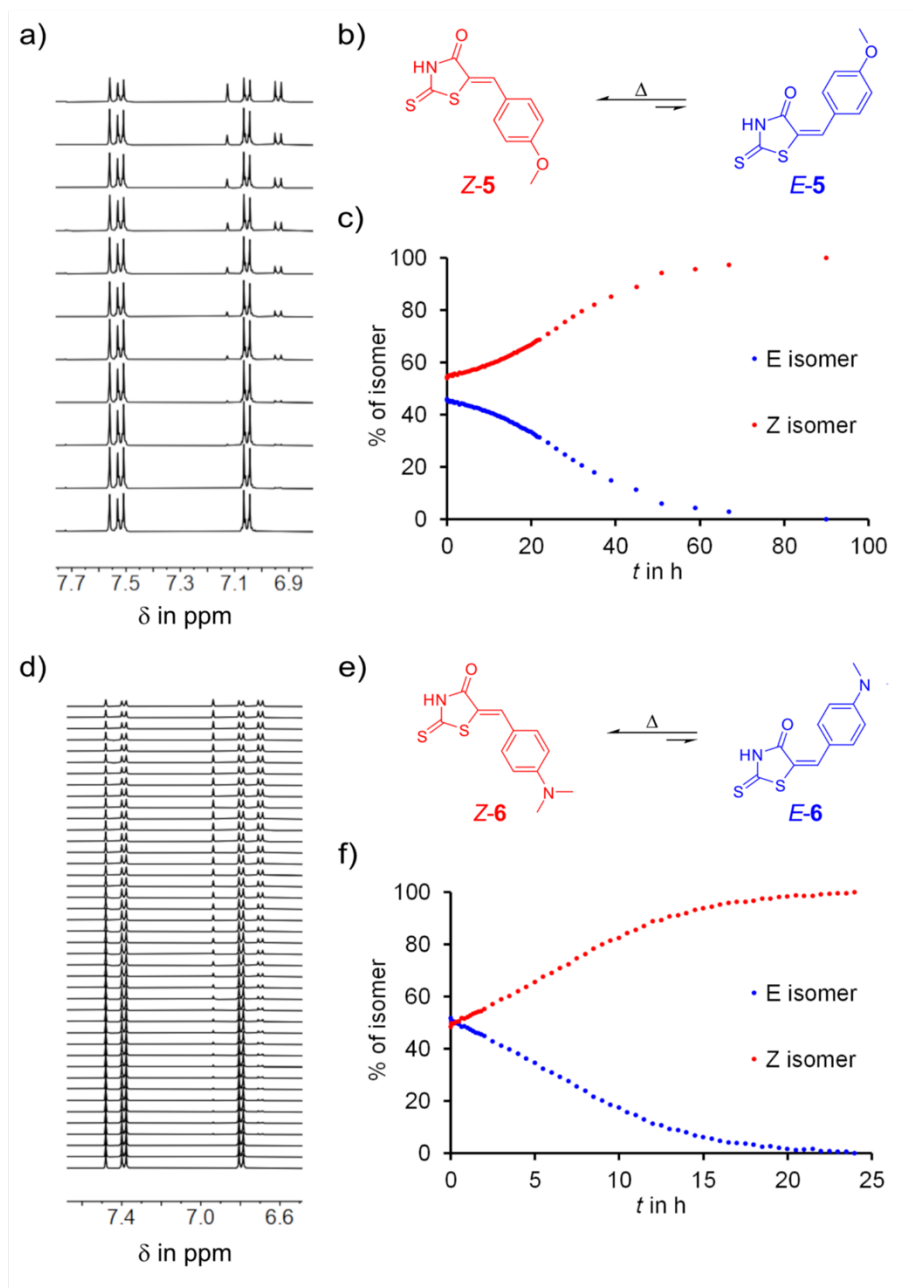
24
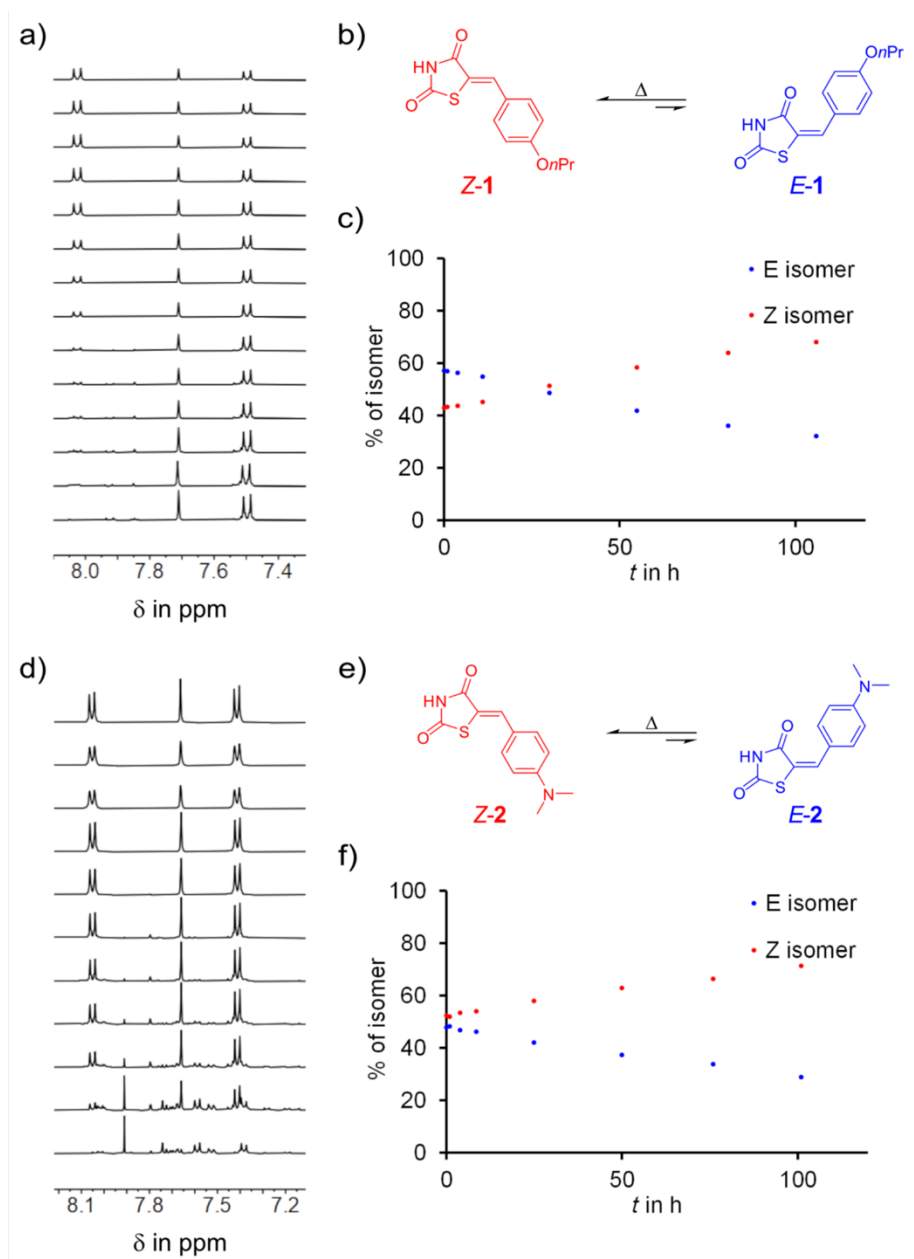
Figure S2   Thermal isomerization experiments followed by ^{1}H NMR spectroscopy in regular time intervals. a) Partial ^{1}H NMR spectra (400 MHz, dioxane-d_8, 25°C) recorded during the conversion of metastable isomer *E*-**1** to stable isomer *Z*-**1** at 85 °C. b) Schematic representation of the thermal isomerization of *E*-**1** to *Z*-**1**. c) Conversion of isomers of **1** in % at 85 °C. d) Partial ^{1}H NMR spectra (400 MHz, dioxane-d_8, 25°C) recorded during the conversion of metastable isomer *E*-**2** to stable isomer *Z*-**2** at 85 °C. e) Schematic representation of the thermal isomerization of *E*-**2** to *Z*-**2**. f) Conversion of isomers of **2** in % at 85 °C.
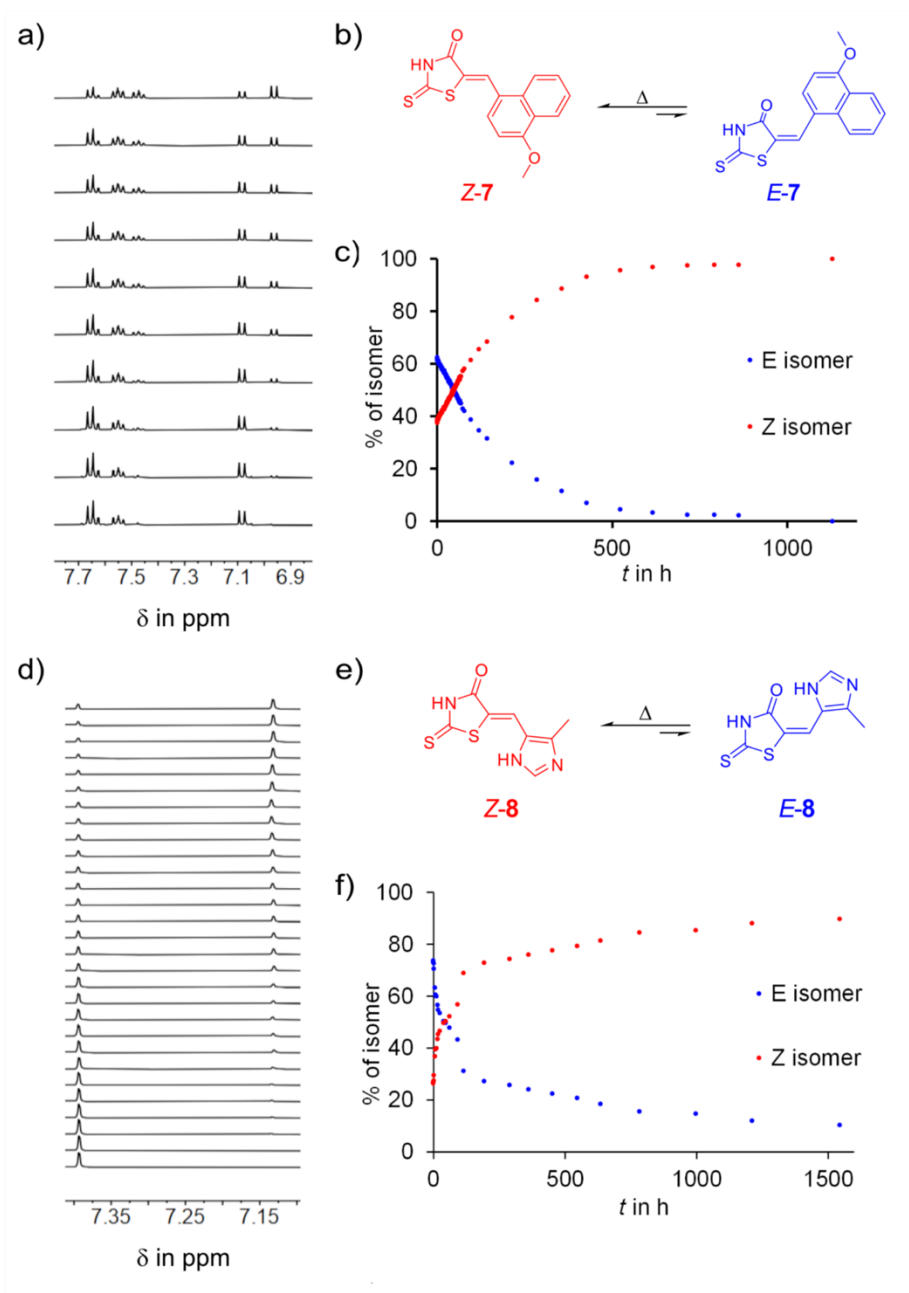
25
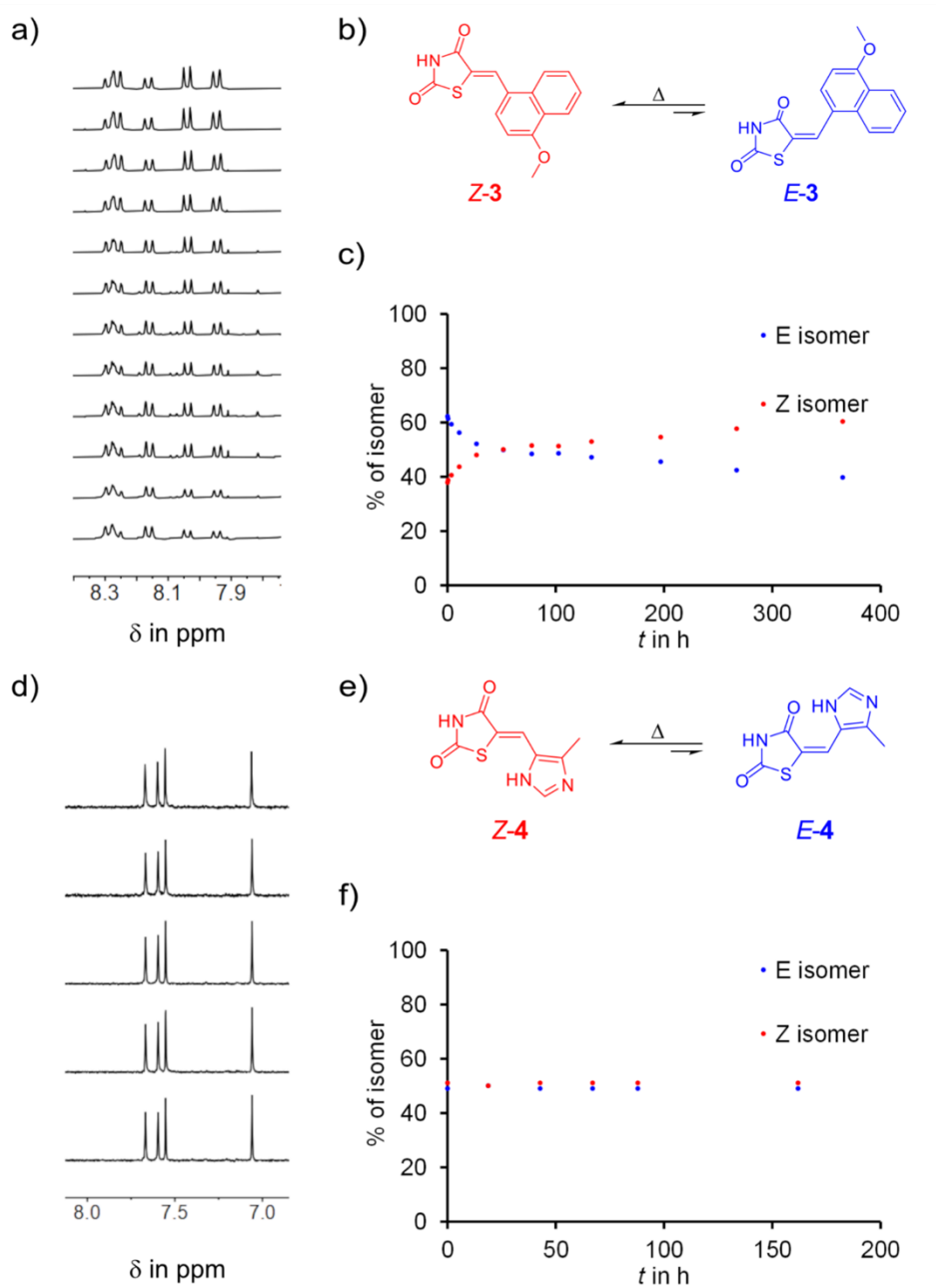
Figure S3   Thermal isomerization experiments followed by ^{1}H NMR spectroscopy in regular time intervals. a) Partial ^{1}H NMR spectra (400 MHz, dioxane-d_8, 25°C) recorded during the conversion of metastable isomer *E*-**3** to stable isomer *Z*-**3** at 85 °C. b) Schematic representation of the thermal isomerization of *E*-**3** to *Z*-**3**. c) Conversion of isomers of **3** in % at 85 °C. d) Partial ^{1}H NMR spectra (400 MHz, dioxane-d_8, 25°C) recorded during the conversion of metastable isomer *E*-**4** to stable isomer *Z*-**4** at 85 °C. e) Schematic representation of the thermal isomerization of *E*-**4** to *Z*-**4**. f) Conversion of isomers of **4** in % at 85 °C.
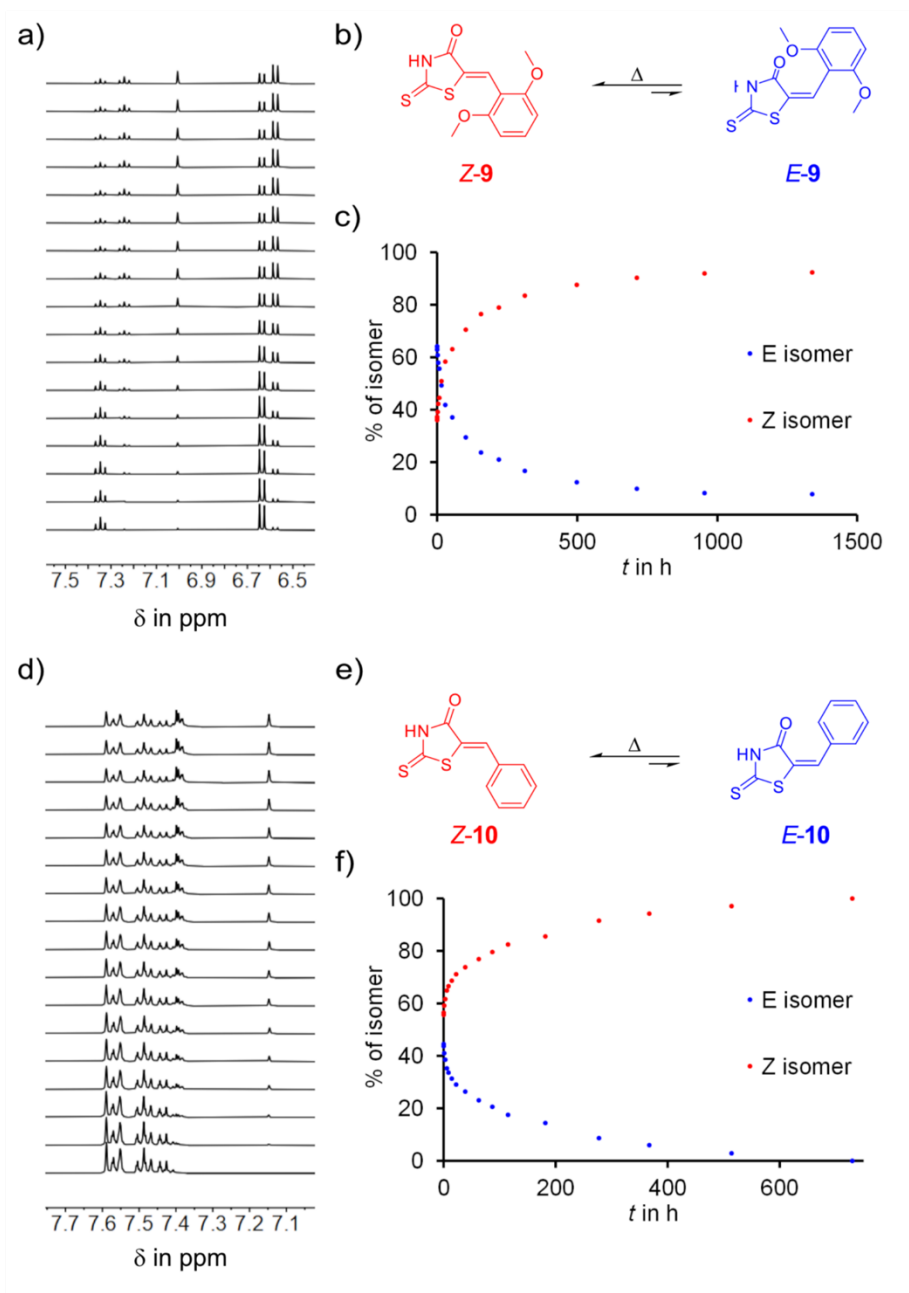
26

Figure S4   Thermal isomerization experiments followed by ^{1}H NMR spectroscopy in regular time intervals. a) Partial ^{1}H NMR spectra (400 MHz, tetrahydrofuran-d_8, 25°C) recorded during the conversion of metastable isomer *E*-**5** to stable isomer *Z*-**5** at 55 °C. b) Schematic representation of the thermal isomerization of *E*-**5** to *Z*-**5**. c) Conversion of isomers of **5** in % at 55 °C. d) Partial ^{1}H NMR spectra (400 MHz, tetrahydrofuran-d_8, 25°C) recorded during the conversion of metastable isomer *E*-**6** to stable isomer *Z*-**6** at 55 °C. e) Schematic representation of the thermal isomerization of *E*-**6** to *Z*-**6**. f) Conversion of isomers of **6** in % at 55 °C.
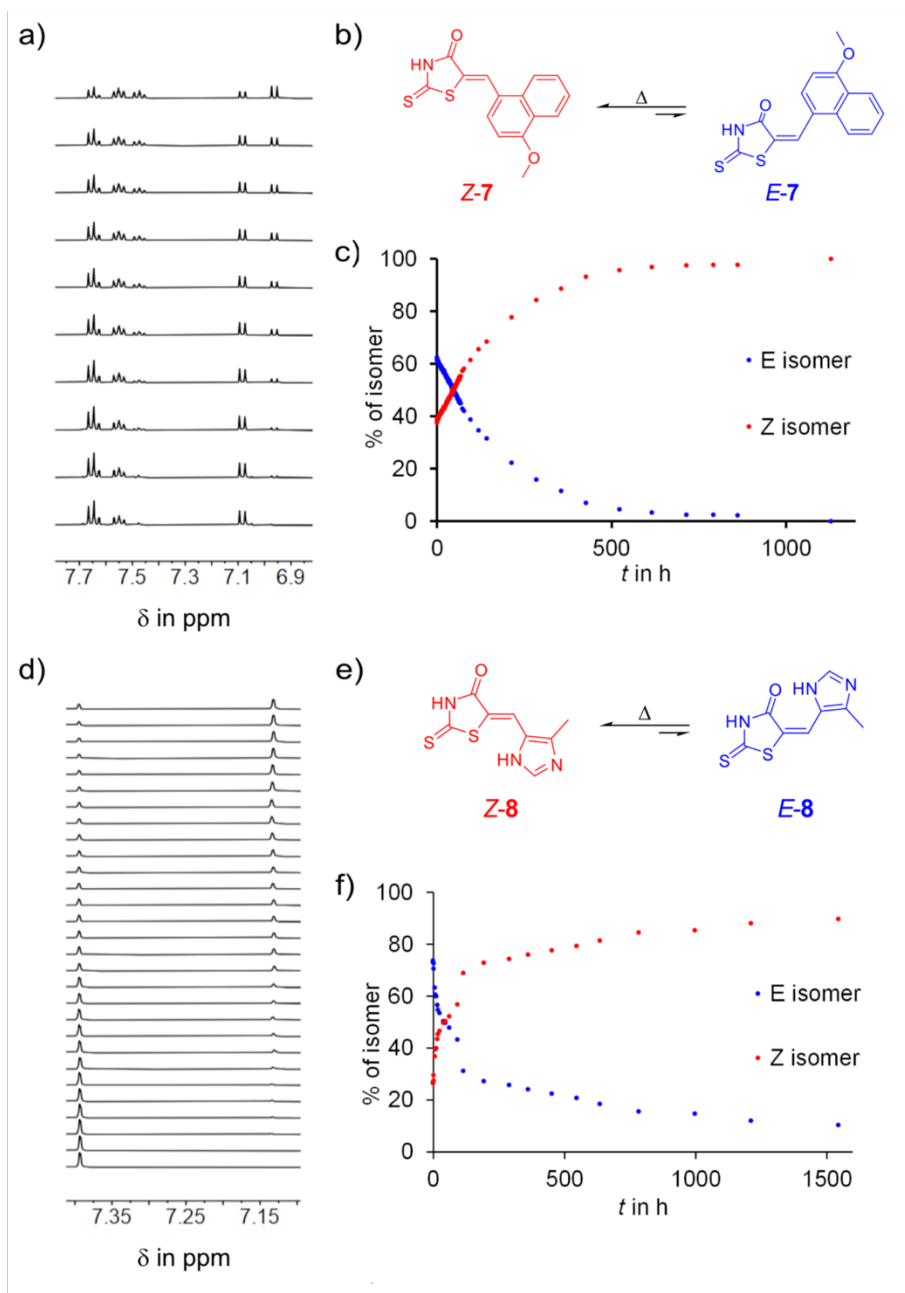
27

Figure S5   Thermal isomerization experiments followed by ^{1}H NMR spectroscopy in regular time intervals. a) Partial ^{1}H NMR spectra (400 MHz, tetrahydrofuran-d_8, 25°C) recorded during the conversion of metastable isomer *E*-**7** to stable isomer *Z*-**7** at 55 °C. b) Schematic representation of the thermal isomerization of *E*-**7** to *Z*-**7**. c) Conversion of isomers of **7** in % at 55 °C. d) Partial ^{1}H NMR spectra (400 MHz, dioxane-d_8, 25°C) recorded during the conversion of metastable isomer *E*-**8** to stable isomer *Z*-**8** at 85 °C. e) Schematic representation of the thermal isomerization of *E*-**8** to *Z*-**8**. f) Conversion of isomers of **8** in % at 85 °C.

28

Figure S6   Thermal isomerization experiments followed by ^{1}H NMR spectroscopy in regular time intervals. a) Partial ^{1}H NMR spectra (400 MHz, dioxane-d_8, 25°C) recorded during the conversion of metastable isomer *E*-**9** to stable isomer *Z*-**9** at 85 °C. b) Schematic representation of the thermal isomerization of *E*-**9** to *Z*-**9**. c) Conversion of isomers of **9** in % at 85 °C. d) Partial ^{1}H NMR spectra (400 MHz, dioxane-d_8, 25°C) recorded during the conversion of metastable isomer *E*-**10** to stable isomer *Z*-**10** at 85 °C. e) Schematic representation of the thermal isomerization of *E*-**10** to *Z*-**10**. f) Conversion of isomers of **10** in % at 85 °C.
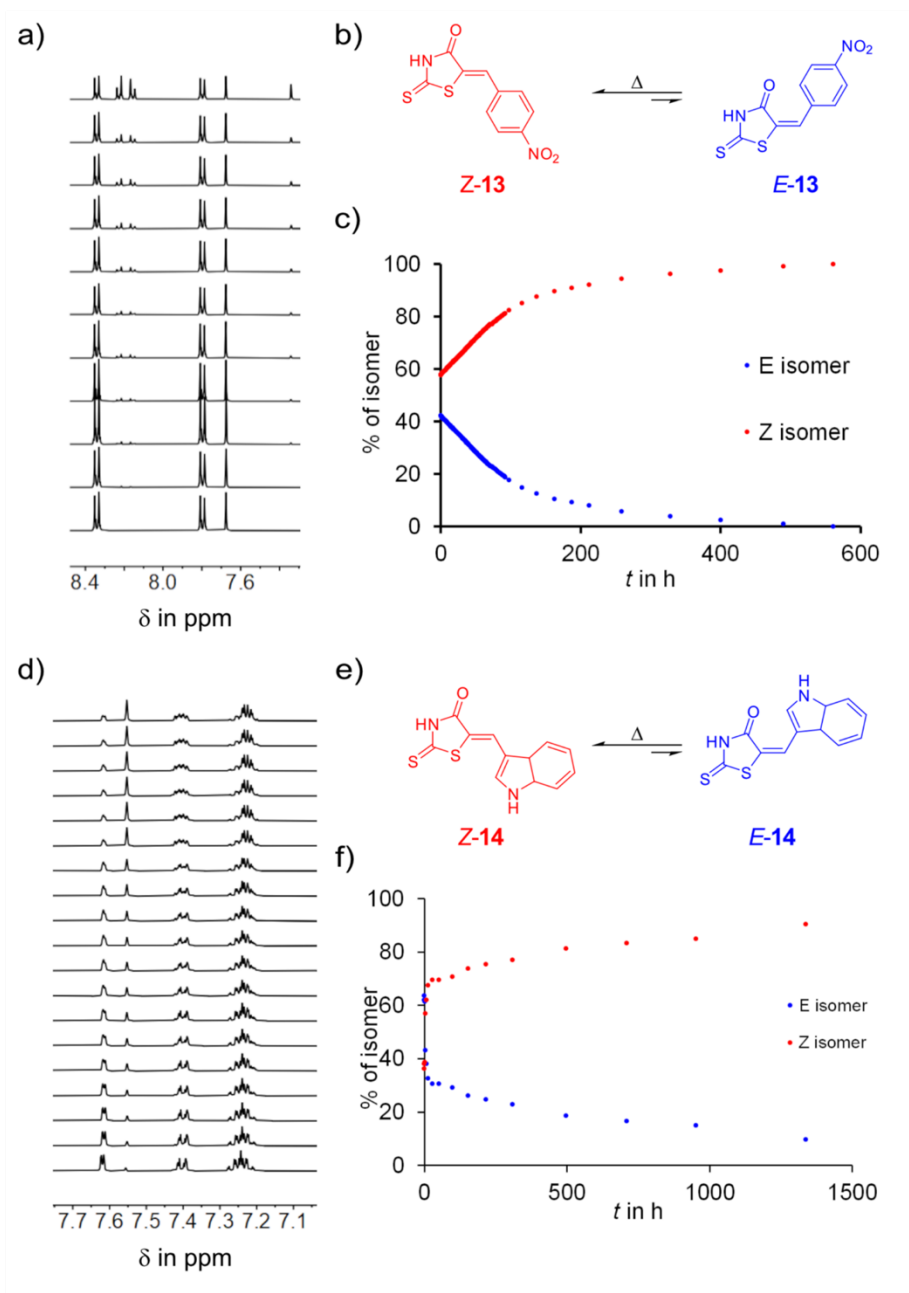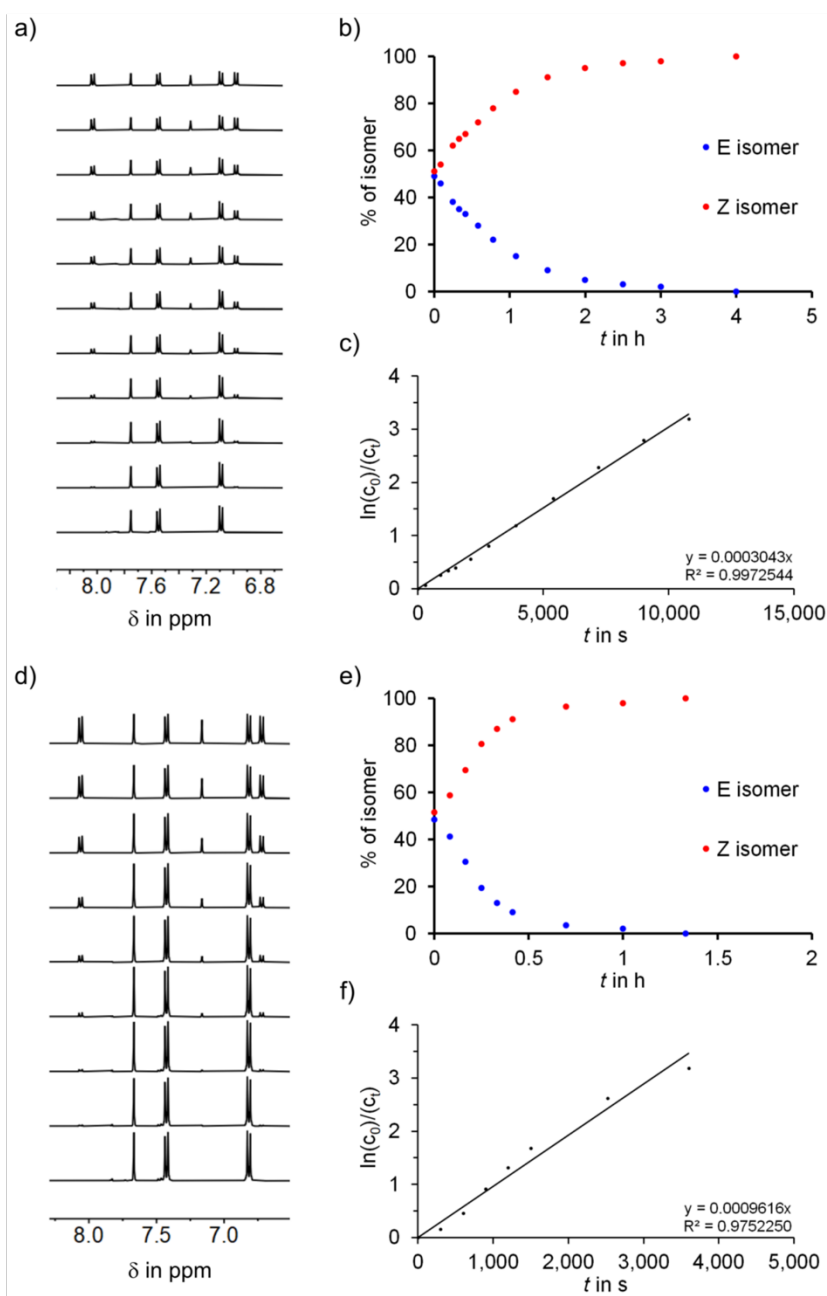
29

Figure S7   Thermal isomerization experiments followed by ^{1}H NMR spectroscopy in regular time intervals. a) Partial ^{1}H NMR spectra (400 MHz, tetrahydrofuran-d_8, 25°C) recorded during the conversion of metastable isomer *E*-**11** to stable isomer *Z*-**11** at 55 °C. b) Schematic representation of the thermal isomerization of *E*-**11** to *Z*-**11**. c) Conversion of isomers of **11** in % at 55 °C. d) Partial ^{1}H NMR spectra (400 MHz, dioxane-d_8, 25°C) recorded during the conversion of metastable isomer *E*-**12** to stable isomer *Z*-**12** at 85 °C. e) Schematic representation of the thermal isomerization of *E*-**12** to *Z*-**12**. f) Conversion of isomers of **12** in % at 85 °C.
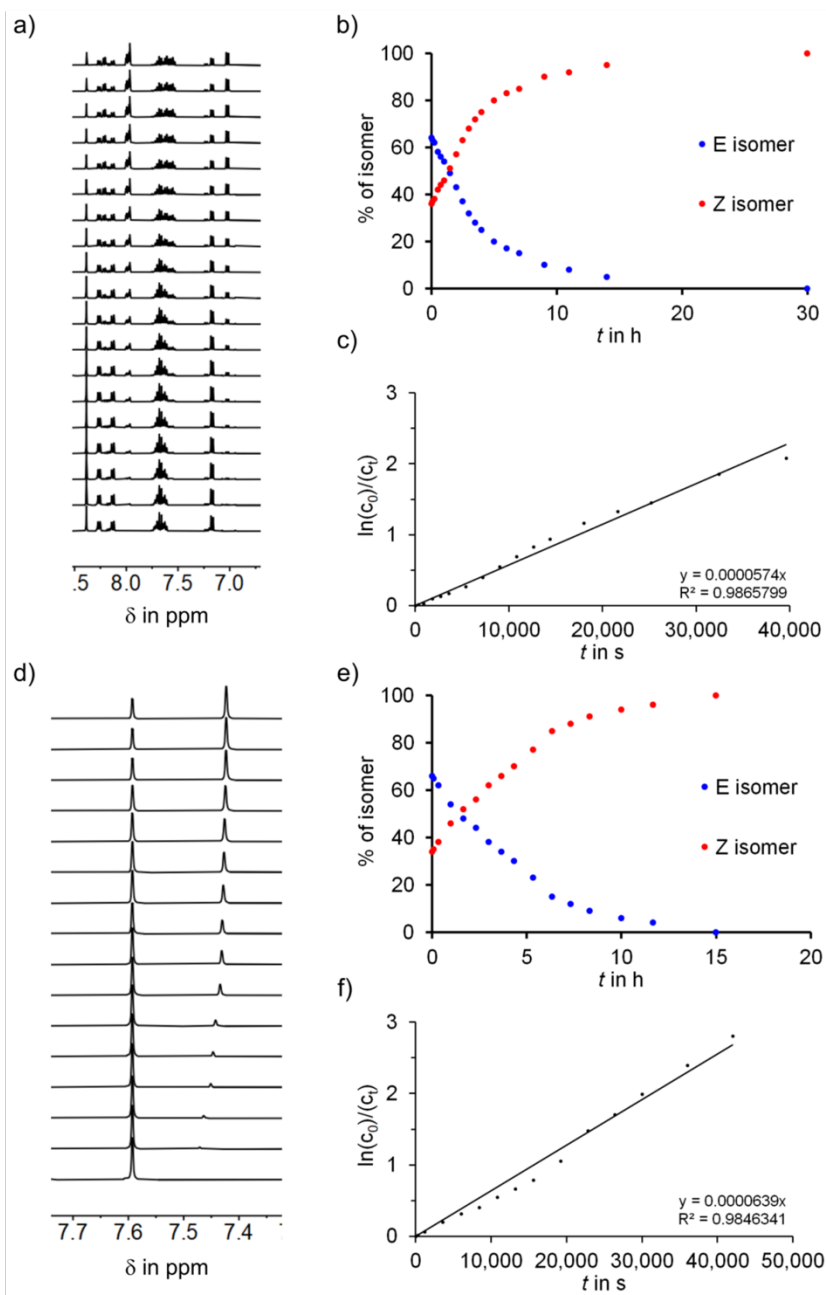
Figure S8   Thermal isomerization experiments followed by ^{1}H NMR spectroscopy in regular time intervals. a) Partial ^{1}H NMR spectra (400 MHz, tetrahydrofuran-d_8, 25°C) recorded during the conversion of metastable isomer *E*-**13** to stable isomer *Z*-**13** at 55 °C. b) Schematic representation of the thermal isomerization of *E*-**13** to *Z*-**13**. c) Conversion of isomers of **13** in %. d) Partial ^{1}H NMR spectra (400 MHz, dioxane-d_8, 25°C) recorded during the conversion of metastable isomer *E*-**14** to stable isomer *Z*-**14** at 85 °C. e) Schematic representation of the thermal isomerization of *E*-**14** to *Z*-**14**. f) Conversion of isomers of **14** in % at 85 °C.

Figure S9   Thermal isomerization experiments followed by ^{1}H NMR spectroscopy in regular time intervals. a) Partial ^{1}H NMR spectra (400 MHz, DMSO-d_6, 25°C) recorded during the conversion of metastable isomer *E*-**1** to stable isomer *Z*-**1** at 130 °C. b) Conversion of isomers of **1** in % at 130 °C. c) Linearized kinetic plot of decreasing *E*-**1** in DMSO-d_6 at 130 °C. d) Partial ^{1}H NMR spectra (400 MHz, DMSO-d_6, 25°C) recorded during the conversion of metastable isomer *E*-**2** to stable isomer *Z*-**2** at 130 °C. e) Conversion of isomers of **2** in % at 130 °C. f) Linearized kinetic plot of decreasing *E*-**2** in DMSO-d_6 at 130 °C.
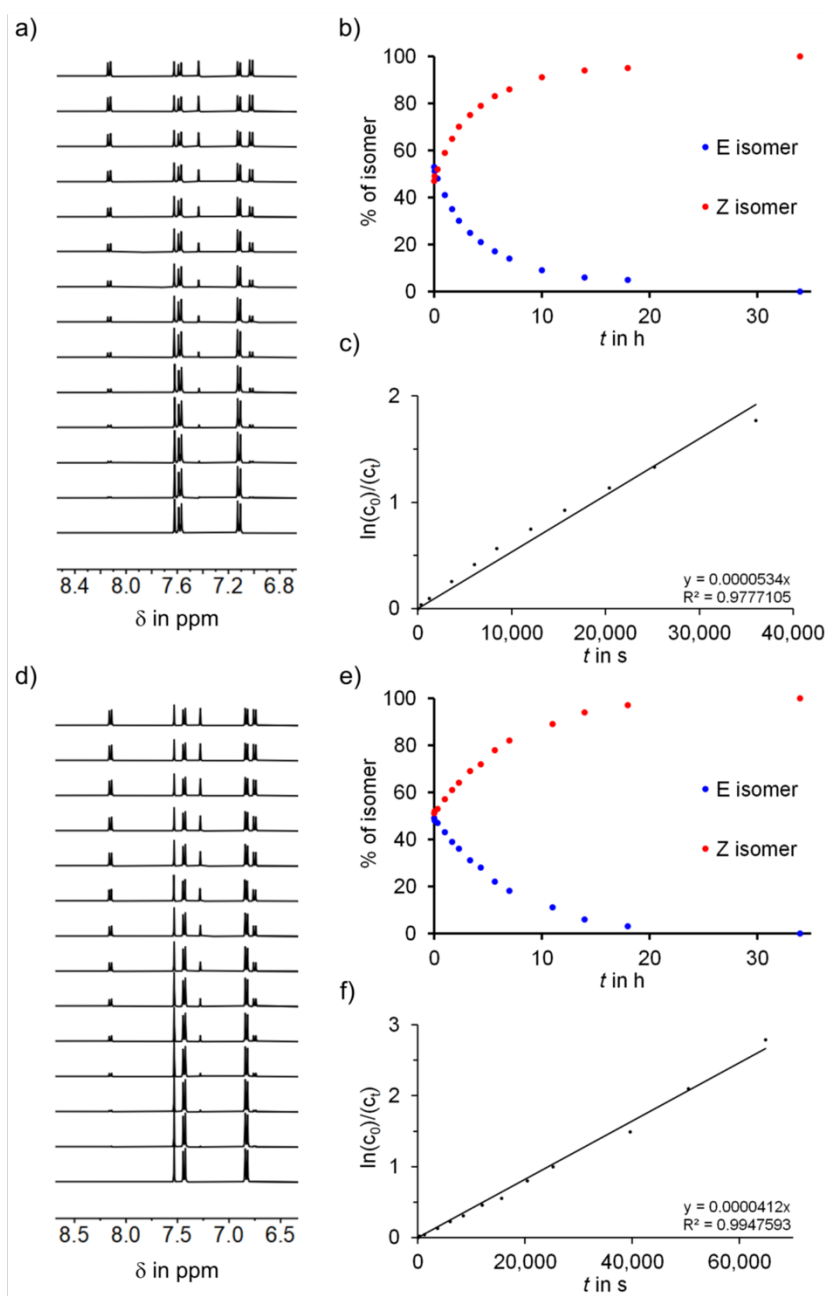
32

Figure S10   Thermal isomerization experiments followed by ^1H NMR spectroscopy in regular time intervals. a) Partial ^1H NMR spectra (400 MHz, DMSO-d_6, 25°C) recorded during the conversion of metastable isomer E-3 to stable isomer Z-3 at 130 °C. b) Conversion of isomers of 3 in % at 130 °C. c) Linearized kinetic plot of decreasing E-3 in DMSO-d_6 at 130 °C. d) Partial ^1H NMR spectra (400 MHz, DMSO-d_6, 25°C) recorded during the conversion of metastable isomer E-4 to stable isomer Z-4 at 140 °C. e) Conversion of isomers of 4 in % at 140 °C. f) Linearized kinetic plot of decreasing E-4 in DMSO-d_6 at 140 °C.
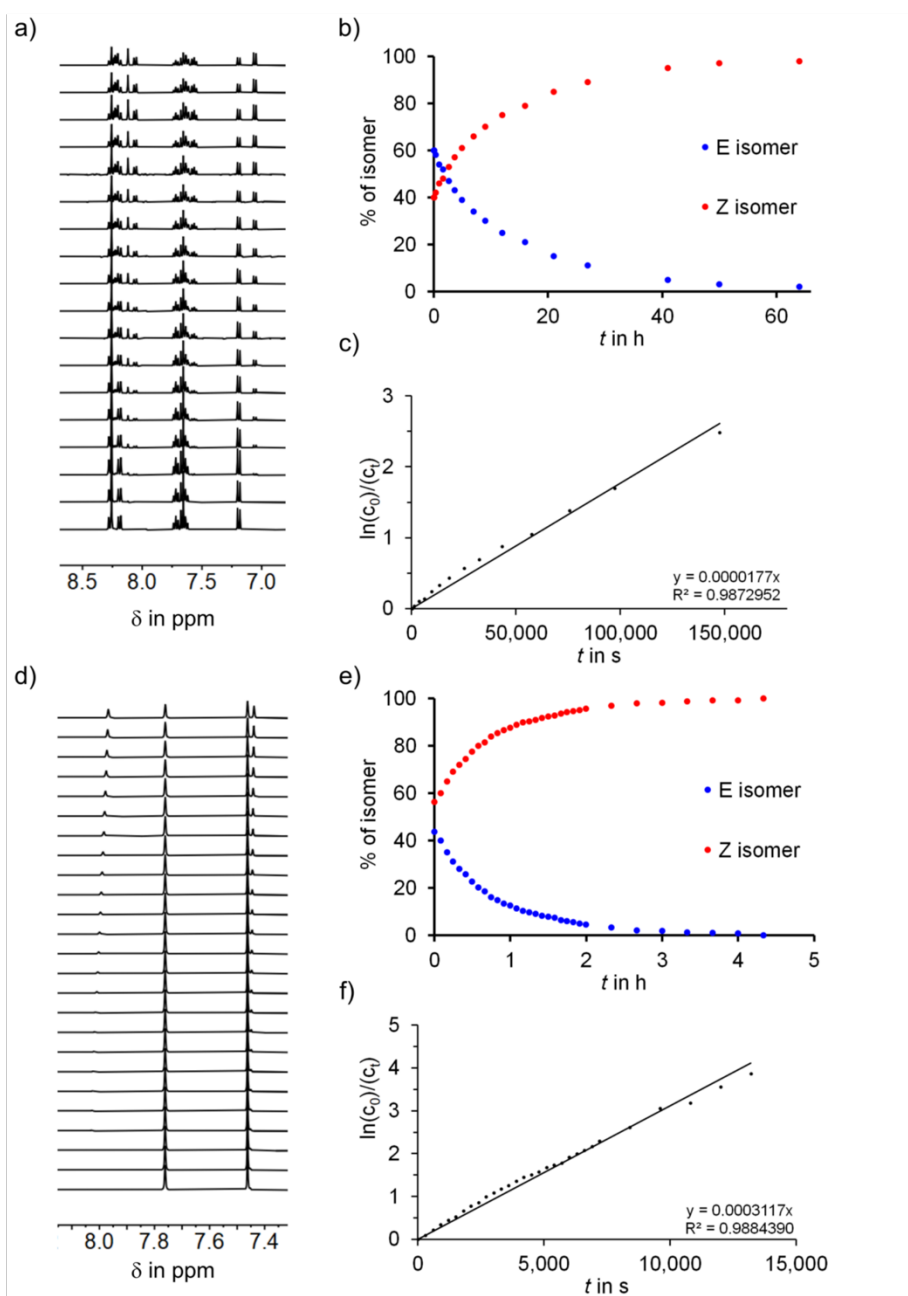
33

Figure S11   Thermal isomerization experiments followed by ^{1}H NMR spectroscopy in regular time intervals. a) Partial ^{1}H NMR spectra (400 MHz, DMSO-d_6, 25°C) recorded during the conversion of metastable isomer *E*-**5** to stable isomer *Z*-**5** at 90 °C. b) Conversion of isomers of **5** in % at 90 °C. c) Linearized kinetic plot of decreasing *E*-**5** in DMSO-d_6 at 90 °C. d) Partial ^{1}H NMR spectra (400 MHz, DMSO-d_6, 25°C) recorded during the conversion of metastable isomer *E*-**6** to stable isomer *Z*-**6** at 90 °C. e) Conversion of isomers of **6** in % at 90 °C. f) Linearized kinetic plot of decreasing *E*-**6** in DMSO-d_6 at 90 °C.
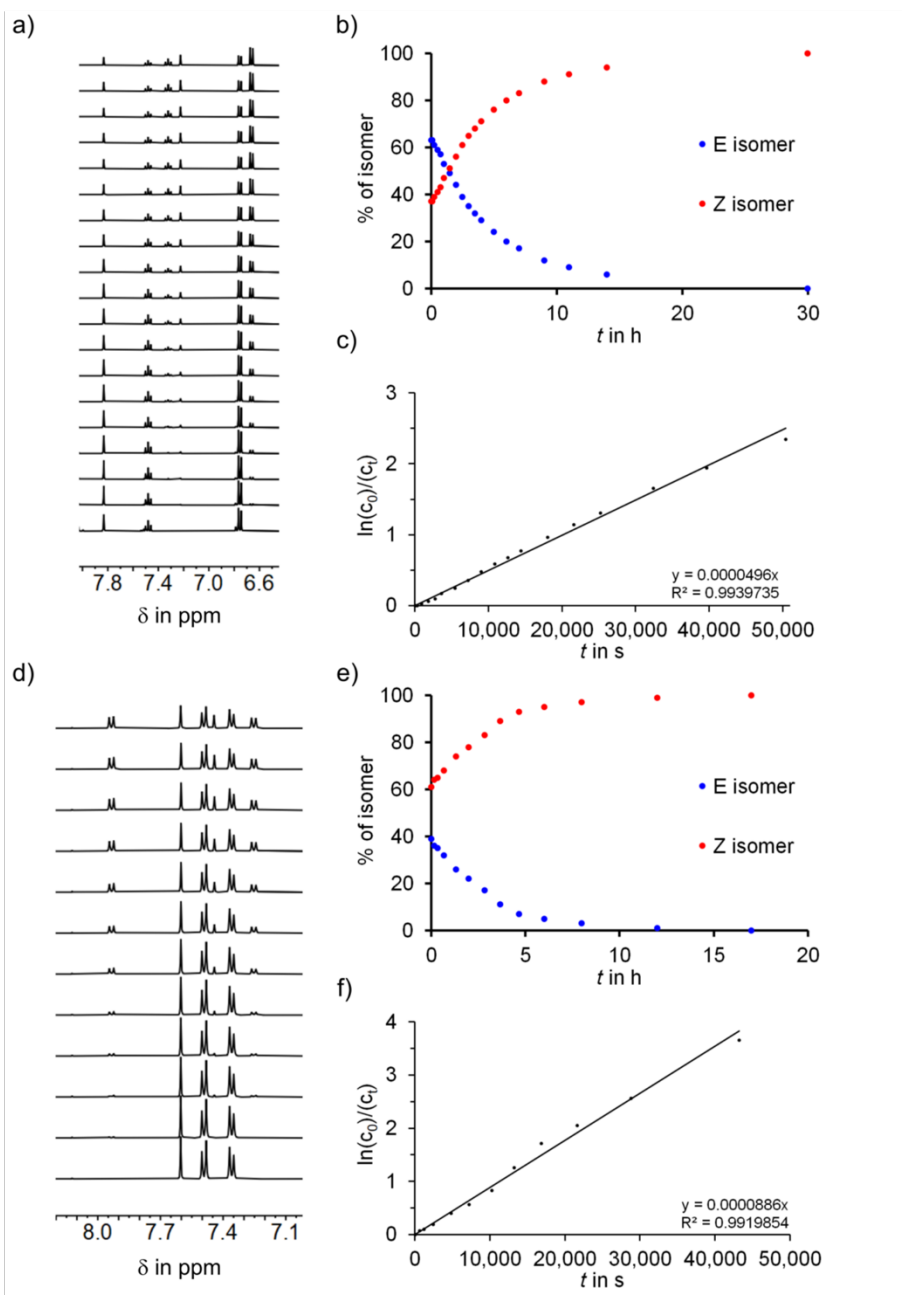
34

Figure S12   Thermal isomerization experiments followed by ^{1}H NMR spectroscopy in regular time intervals. a) Partial ^{1}H NMR spectra (400 MHz, DMSO-d_6, 25°C) recorded during the conversion of metastable isomer *E*-**7** to stable isomer *Z*-**7** at 90 °C. b) Conversion of isomers of **7** in % at 90 °C. c) Linearized kinetic plot of decreasing *E*-**7** in DMSO-d_6 at 70 °C. d) Partial ^{1}H NMR spectra (400 MHz, DMSO-d_6, 80°C) recorded during the conversion of metastable isomer *E*-**8** to stable isomer *Z*-**8** at 80 °C. e) Conversion of isomers of **8** in % at 80 °C. f) Linearized kinetic plot of decreasing *E*-**8** in DMSO-d_6 at 80 °C.
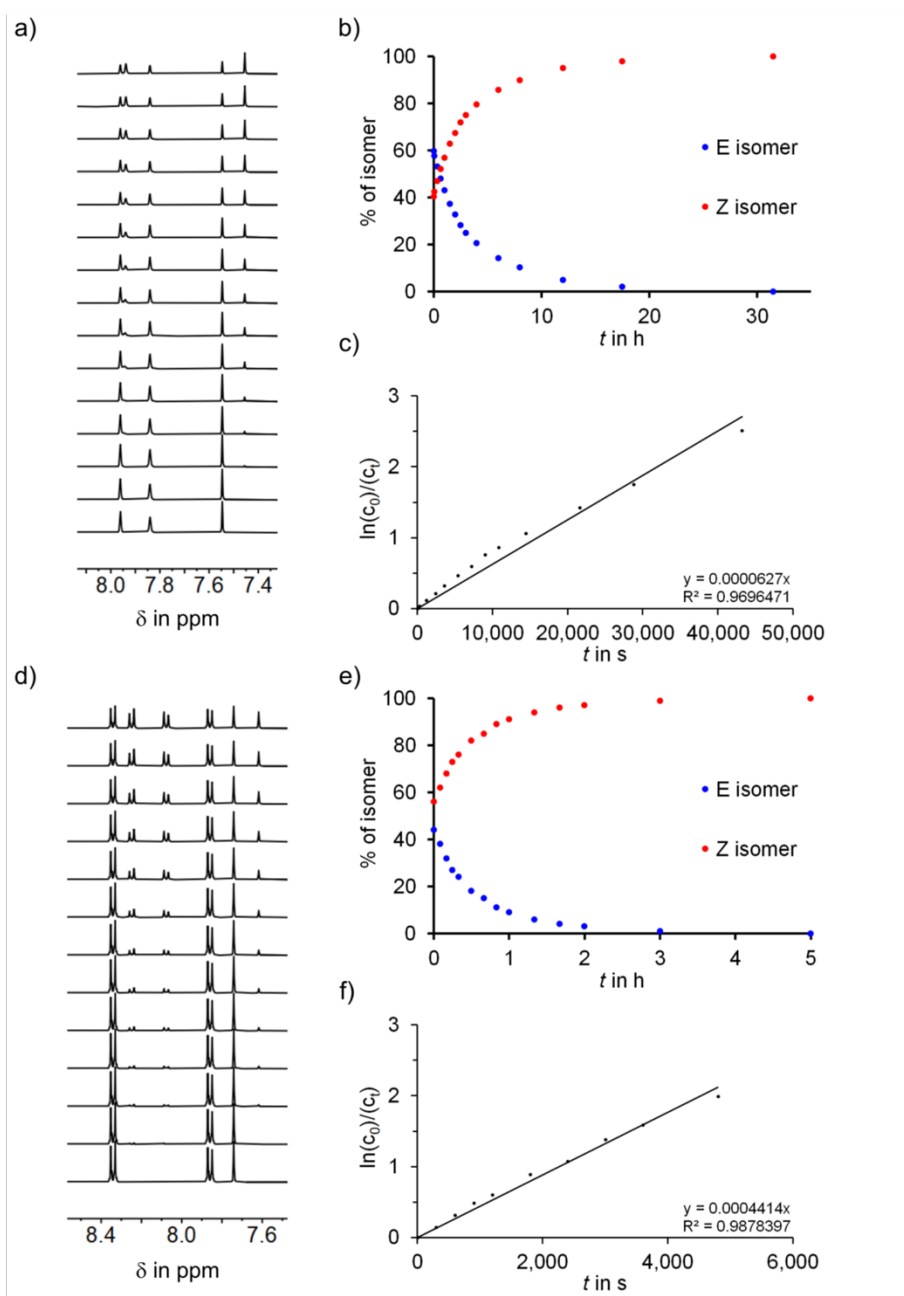
35

Figure S13   Thermal isomerization experiments followed by ^{1}H NMR spectroscopy in regular time intervals. a) Partial ^{1}H NMR spectra (400 MHz, DMSO-d_6, 25°C) recorded during the conversion of metastable isomer *E*-**9** to stable isomer *Z*-**9** at 130 °C. b) Conversion of isomers of **9** in % at 130 °C. c) Linearized kinetic plot of decreasing *E*-**9** in DMSO-d_6 at 130 °C. d) Partial ^{1}H NMR spectra (400 MHz, DMSO-d_6, 25°C) recorded during the conversion of metastable isomer *E*-**11** to stable isomer *Z*-**11** at 130 °C. e) Conversion of isomers of **11** in % at 130 °C. f) Linearized kinetic plot of decreasing *E*-**11** in DMSO-d_6 at 130 °C.
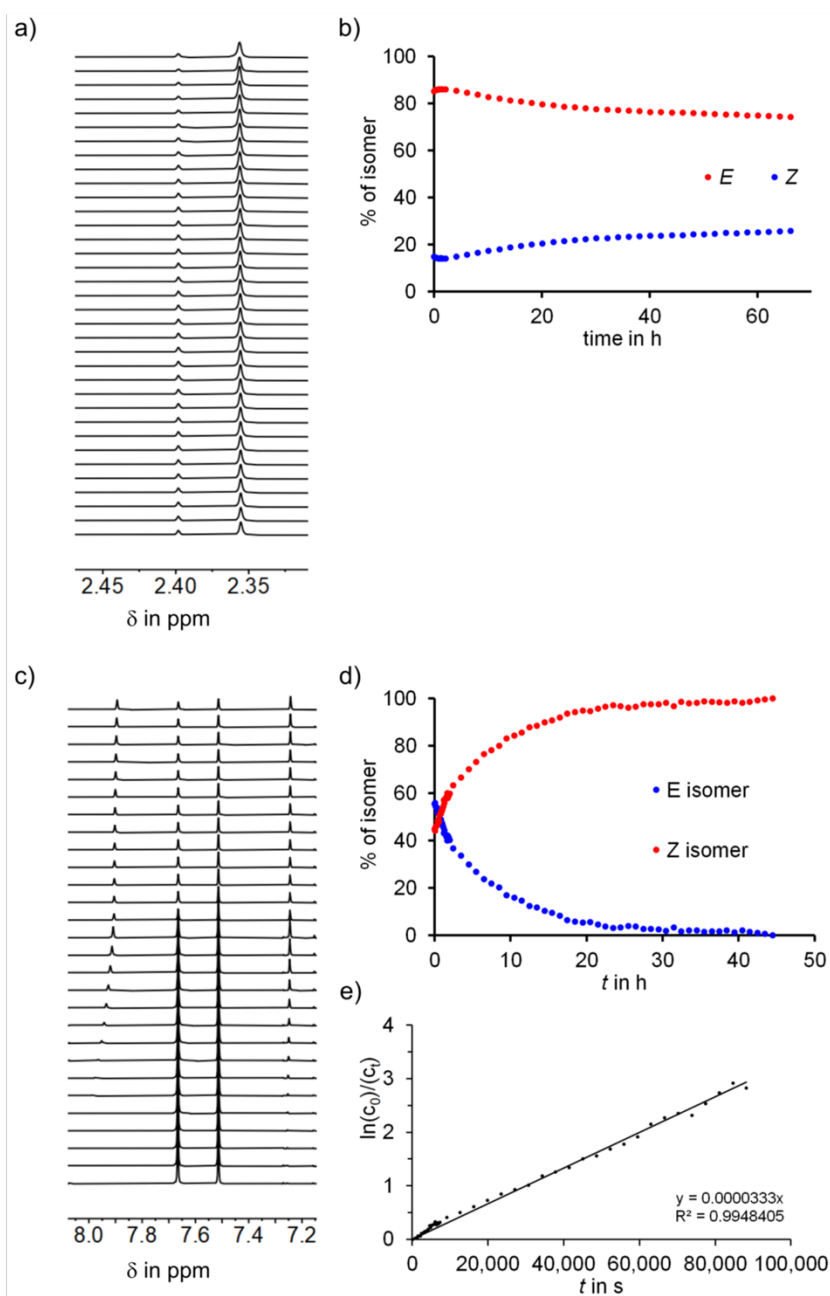
36

Figure S14   Thermal isomerization experiments followed by ^{1}H NMR spectroscopy in regular time intervals. a) Partial ^{1}H NMR spectra (400 MHz, DMSO-d_6, 25°C) recorded during the conversion of metastable isomer *E*-**12** to stable isomer *Z*-**12** at 60 °C. b) Conversion of isomers of **12** in % at 60 °C. c) Linearized kinetic plot of decreasing *E*-**12** in DMSO-d_6 at 60 °C. d) Partial ^{1}H NMR spectra (400 MHz, DMSO-d_6, 25°C) recorded during the conversion of metastable isomer *E*-**13** to stable isomer *Z*-**13** at 60 °C. e) Conversion of isomers of **13** in % at 60 °C. f) Linearized kinetic plot of decreasing *E*-**13** in DMSO-d_6 at 60 °C.

37

Figure S15   Thermal isomerization experiments followed by ^{1}H NMR spectroscopy in regular time intervals. a) Partial ^{1}H NMR spectra (400 MHz, MeOH-d_4, 50°C) recorded during the conversion of metastable isomer *E*-**4** to stable isomer *Z*-**4** at 50 °C. b) Conversion of isomers of **4** in % at 50 °C. c) Partial ^{1}H NMR spectra (400 MHz, MeOH-d_4, 50°C) recorded during the conversion of metastable isomer *E*-**8** to stable isomer *Z*-**8** at 50 °C. e) Conversion of isomers of **8** in % at 50 °C. f) Linearized kinetic plot of decreasing *E*-**5** in MeOH-d_4 at 50 °C.

38

Photophysical properties

Pss determination using ^{1}H NMR spectroscopy

Table S2 gives an overview over the isomeric ratios of rhodanine- and oxo-rhodanine-based photoswitches **1** – **14** obtained after irradiation with light of different wavelength to the respective pss in tetrahydrofuran-d_8. Ratios were determined by ^{1}H NMR spectroscopy at 23 °C.

Table S2   Isomer yields of **1** – **14** obtained after irradiation with light of different wavelengths until the respective pss was reached. Isomeric rations were determined in tetrahydrofuran-d_8 solutions at 23 °C using ^{1}H NMR spectroscopy.

	$\lambda\, Z \rightarrow E$	$Z : E$	t [min]	$\lambda\, E \rightarrow Z$	$Z : E$	t [min]
1	340 nm	43 : 57	80	405 nm	99 : 1	5
2	405 nm	47 : 53	30	470 nm	98 : 2	5
3	365 nm	32 : 68	15	450 nm	97 : 3	5
4	365 nm	15 : 85	30	405 nm	100 : 0	15
5	385 nm	48 : 52	45	420 nm	86 : 14	20
6	420 nm	48 : 52	30	505 nm	89 : 11	60
7	385 nm	38 : 62	30	470 nm	90 : 10	10
8	385 nm	19 : 81	40	470 nm	100 : 0	10
9	385 nm	32 : 68	30	340 nm	44 : 56	60
10	365 nm	51 : 49	35	420 nm	88 : 12	5
11	365 nm	47 : 53	35	420 nm	91 : 9	10
12	365 nm	30 : 70	15	415 nm	94 : 6	5
13	385 nm	55 : 45	30	420 nm	85 : 15	15
14	410 nm	33 : 67	30	470 nm	92 : 8	10

Figure S16 – Figure S22 show ^{1}H NMR spectra of (oxo)-rhodanine photoswitches **1** – **14** before and after irradiation at 25 °C in tetrahydrofuran-d_8. Starting with 100% of the stable *Z* isomer, the metastable *E* isomer can be enriched by irradiating. Using a different wavelength the reverse *E*/*Z* photoisomerisation occurs.
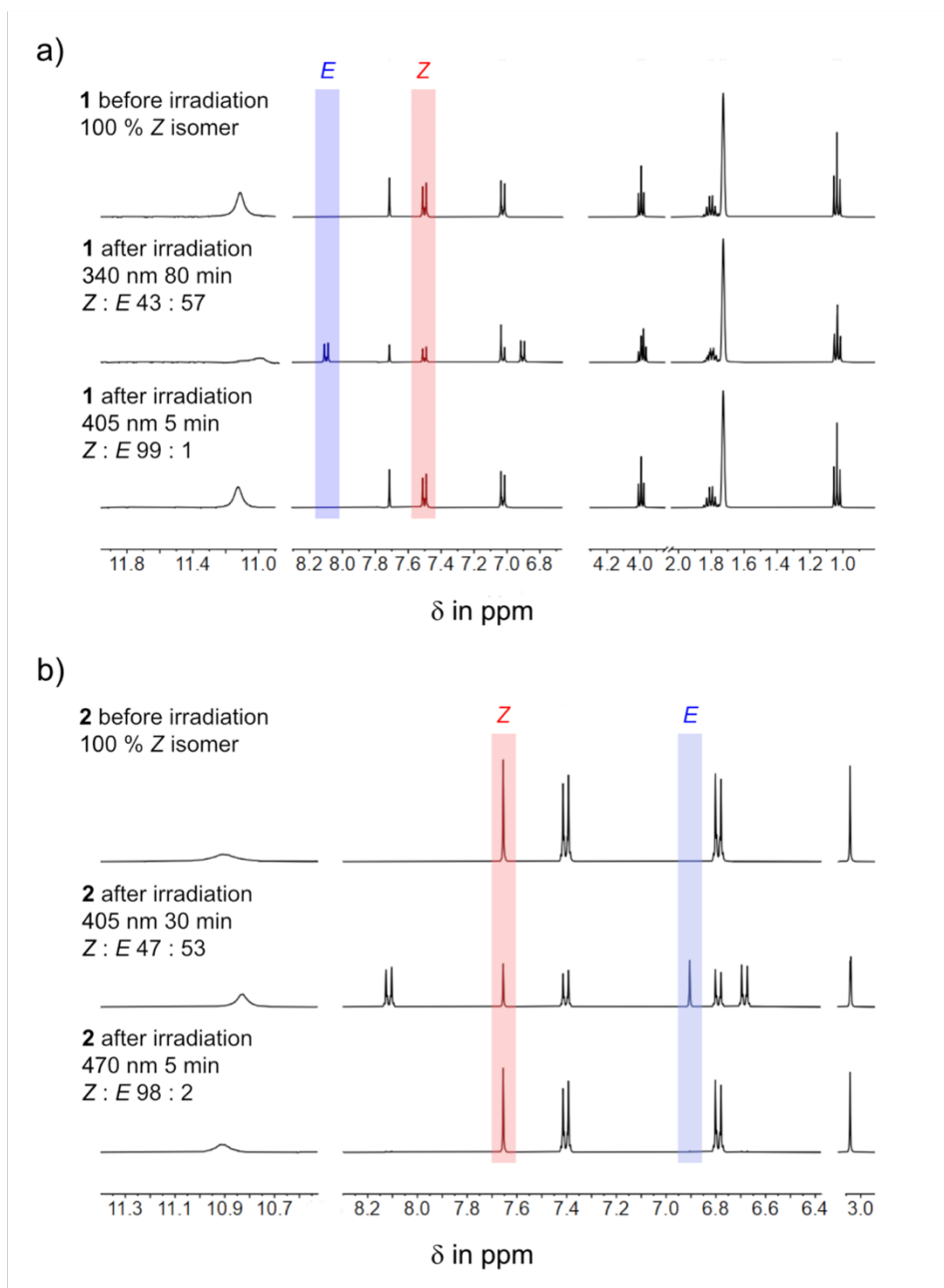
39

Figure S16   Partial ^{1}H NMR spectra (400 MHz, tetrahydrofuran-d_8, 10 mM, 25 °C) recorded before and after irradiation. Intensity magnification varies between H-N, aromatic and aliphatic regions. a) Irradiation experiment of **1**. Top to bottom: pure Z-**1** isomer was irradiated with 340 nm to enrich the E isomer, after 80 min the pss was reached with an isomeric ratio of 47 : 53 (Z : E). Irradiation with 405 nm for 5 min leads to Z enrichment with an isom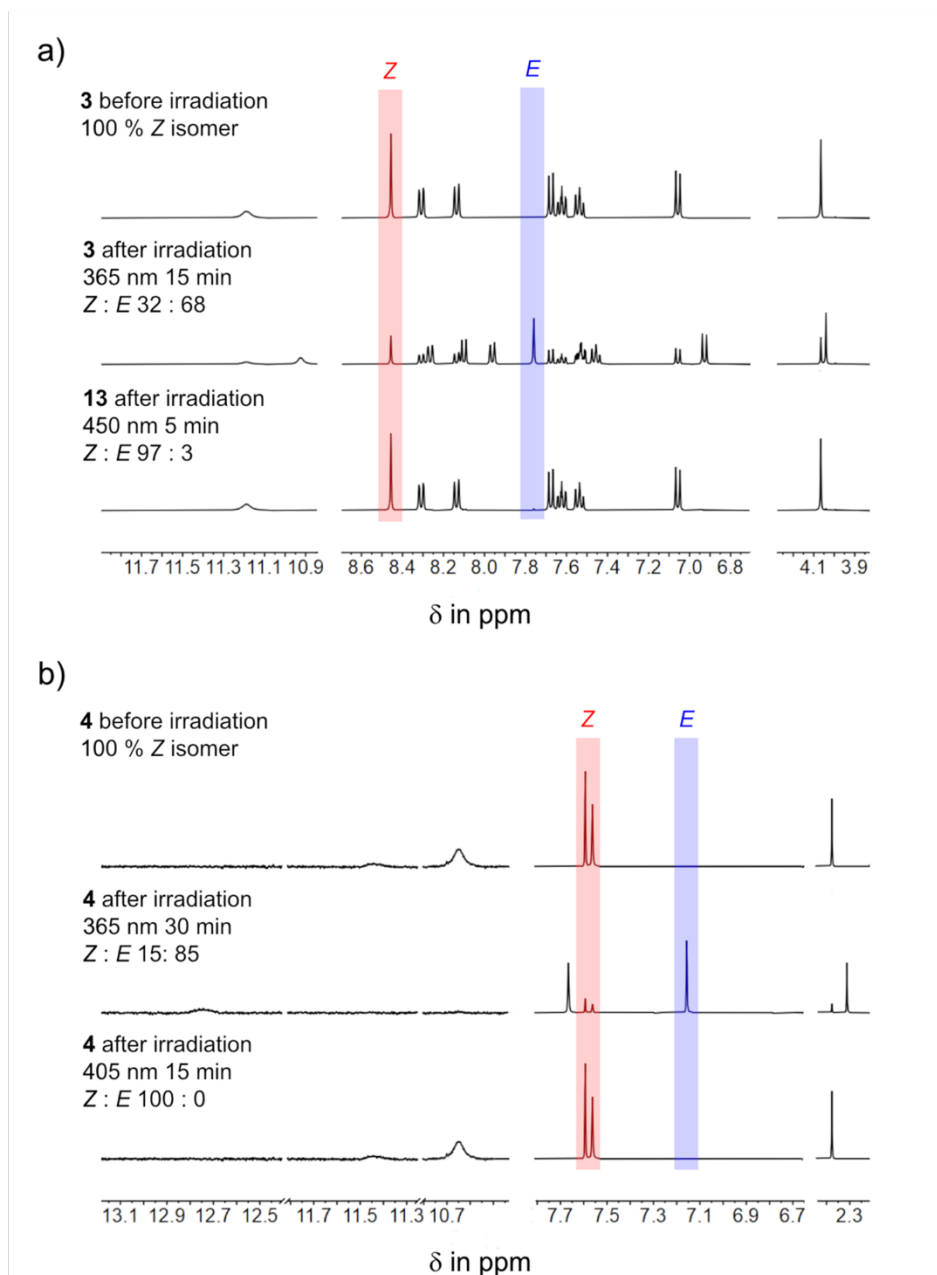eric ratio in the pss of 99 : 1 (Z : E). b) Irradiation experiment of **2**. From to bottom: pure Z-**2** isomer was irradiated with 405 nm to enrich the E isomer, after 30 min the pss was reached with an isomeric ratio of 47 : 53 (Z : E). Irradiation with 470 nm for 5 min leads to Z enrichment with a isomeric ratio in the pss of 98 : 2 (Z : E).
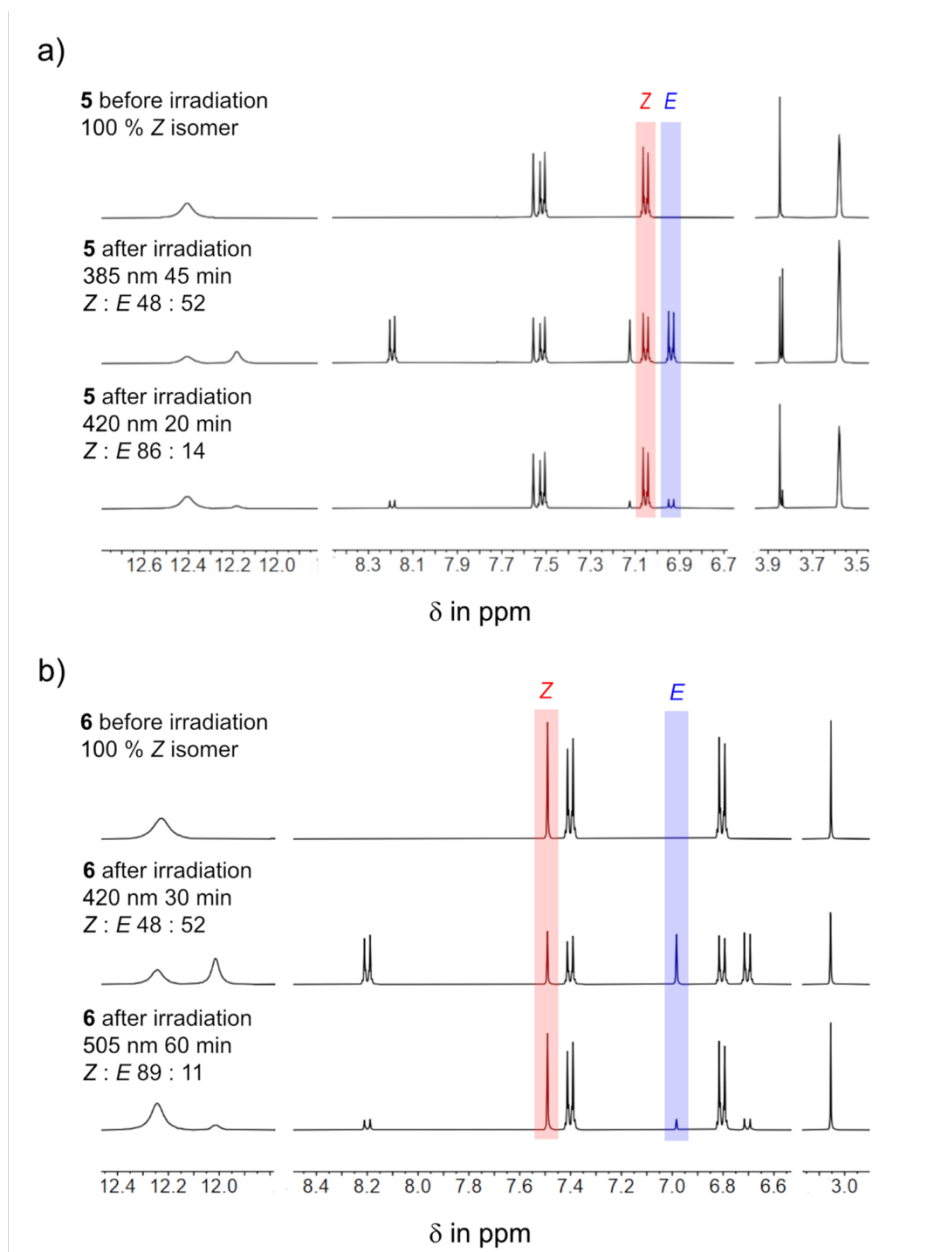
40

Figure S17   Partial ^{1}H NMR spectra (400 MHz, tetrahydrofuran-d_8, 10 mM, 25 °C) recorded before and after irradiation. Intensity magnification varies between H-N, aromatic and aliphatic regions. a) Irradiation experiment of **3**. Top to bottom: pure *Z*-**3** isomer was irradiated with 365 nm to enrich the *E* isomer, after 15 min the pss was reached with an isomeric ratio of 32 : 68 (*Z* : *E*). Irradiation with 450 nm for 5 min leads to *Z* enrichment with an isomeric ratio in the pss of 97 : 3 (*Z* : *E*). b) Irradiation experiment of **4**. From to bottom: pure *Z*-**4** isomer was irradiated with 365 nm to enrich the *E* isomer, after 30 min the pss was reached with a isomeric ratio of 15 : 85 (*Z* : *E*). Irradiation with 405 nm for 15 min leads to 100% *Z* enrichment.

41

210

Figure S18   Partial ^{1}H NMR spectra (400 MHz, tetrahydrofuran-d_8, 20 mM, 25 °C) recorded before and after irradiation. Intensity magnification varies between H-N, aromatic and aliphatic regions. a) Irradiation experiment of **5**. Top to bottom: pure Z-**5** isomer was irradiated with 385 nm to enrich the E isomer, after 45 min the pss was reached with an isomeric ratio of 48 : 52 (Z : E). Irradiation with 420 nm for 20 min leads to Z enrichment with an isome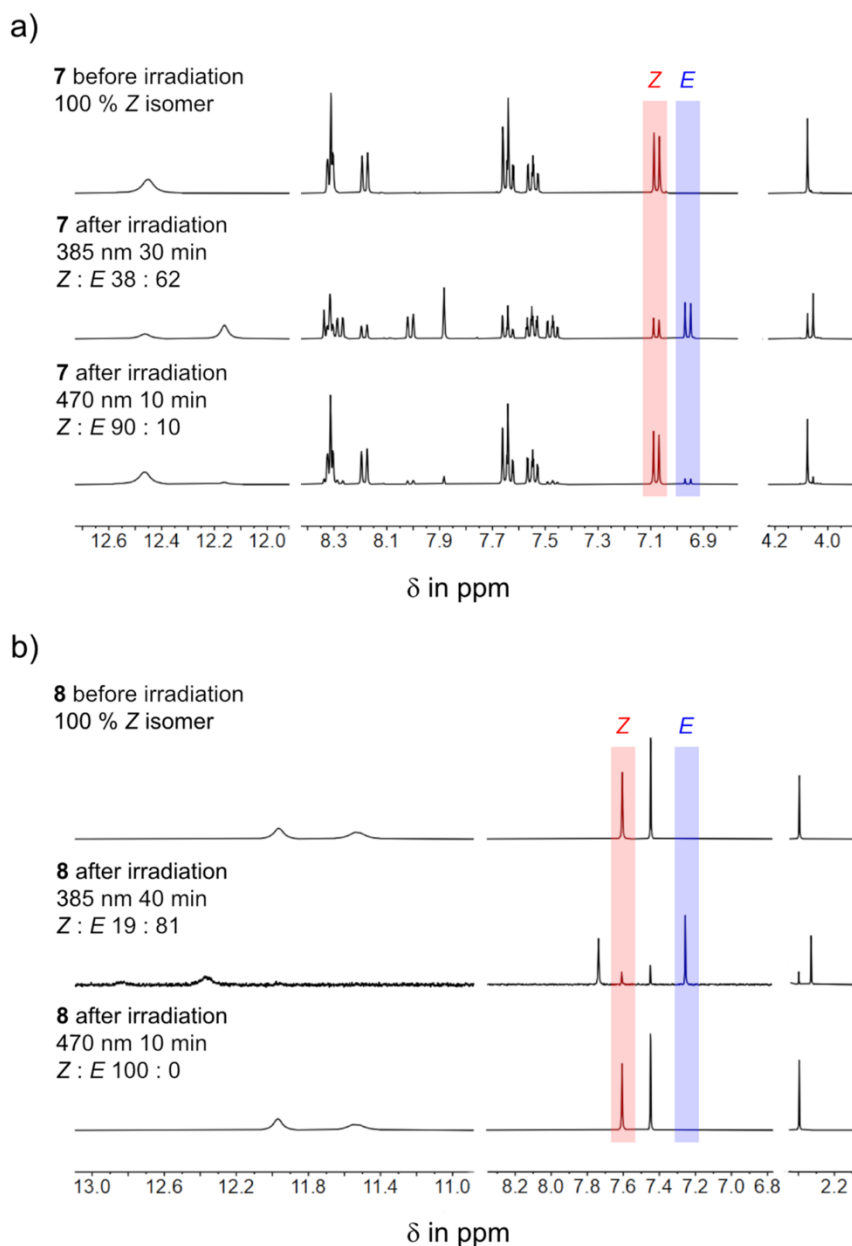ric ratio in the pss of 86 : 14 (Z : E). b) Irradiation experiment of **6**. From to bottom: pure Z-**6** isomer was irradiated with 420 nm to enrich the E isomer, after 30 min the pss was reached with an isomeric ratio of 48 : 52 (Z : E). Irradiation with 405 nm for 15 min leads to Z enrichment with a isomeric ratio in the pss of 89 : 11 (Z : E).

42

Figure S19   Partial ^{1}H NMR spectra (400 MHz, tetrahydrofuran-d_8, 10 mM, 25 °C) recorded before and after irradiation. Intensity magnification varies between H-N, aromatic and aliphatic regions. a) Irradiation experiment of **7**. Top to bottom: pure Z-**7** isomer was irradiated with 385 nm to enrich the E isomer, after 30 min the pss was reached with an isomeric ratio of 38 : 62 (Z : E). Irradiation with 470 nm for 10 min leads to Z enrichment with an isomeric ratio in the pss of 90 : 10 (Z : E). b) Irradiation experiment of **8**. From to bottom: pure Z-**8** isomer was irradiated with 385 nm to enrich the E isomer, after 40 min the pss was reached with an isomeric ratio of 19 : 81 (Z : E). Irradiation with 470 nm for 10 min leads to 100% Z enrichment.
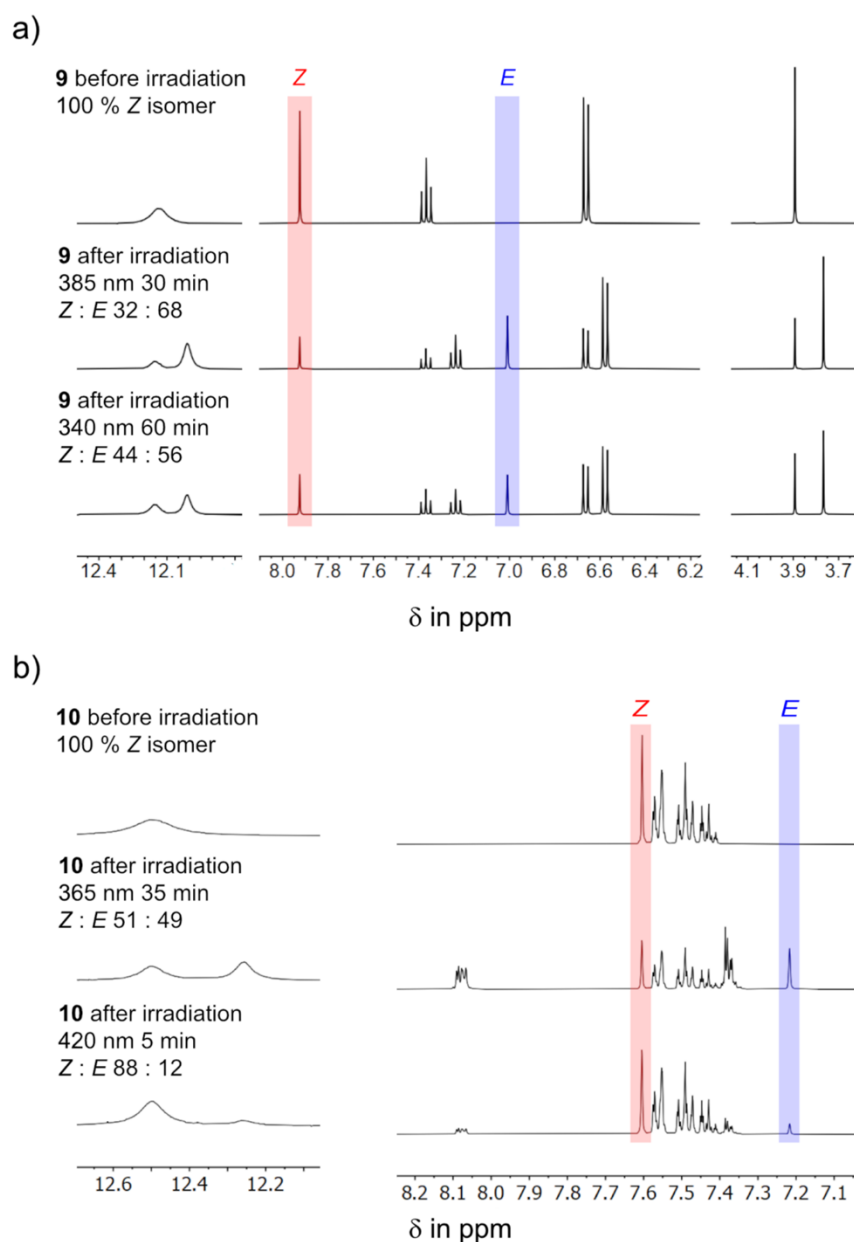
43

Figure S20   Partial ^{1}H NMR spectra (400 MHz, tetrahydrofuran-d_8, 10 mM, 25 °C) recorded before and after irradiation. Intensity magnification varies between H-N, aromatic and aliphatic regions. a) Irradiation experiment of **9**. Top to bottom: pure Z-**9** isomer was irradiated with 385 nm to enrich the E isomer, after 30 min the pss was reached with an isomeric ratio of 32 : 68 (Z : E). Irradiation with 340 nm for 60 min leads to Z enrichment with an isomeric ratio in the pss of 44 : 56 (Z : E). b) Irradiation experiment of **10**. From to bottom: pure Z-**10** isomer was irradiated with 365 nm to enrich the E isomer, after 35 min the pss was reached with an isomeric ratio of 51 : 49 (Z : E). Irradiation with 420 nm for 5 min leads to Z enrichment with a isomeric ratio in the pss of 88 : 12 (Z : E).
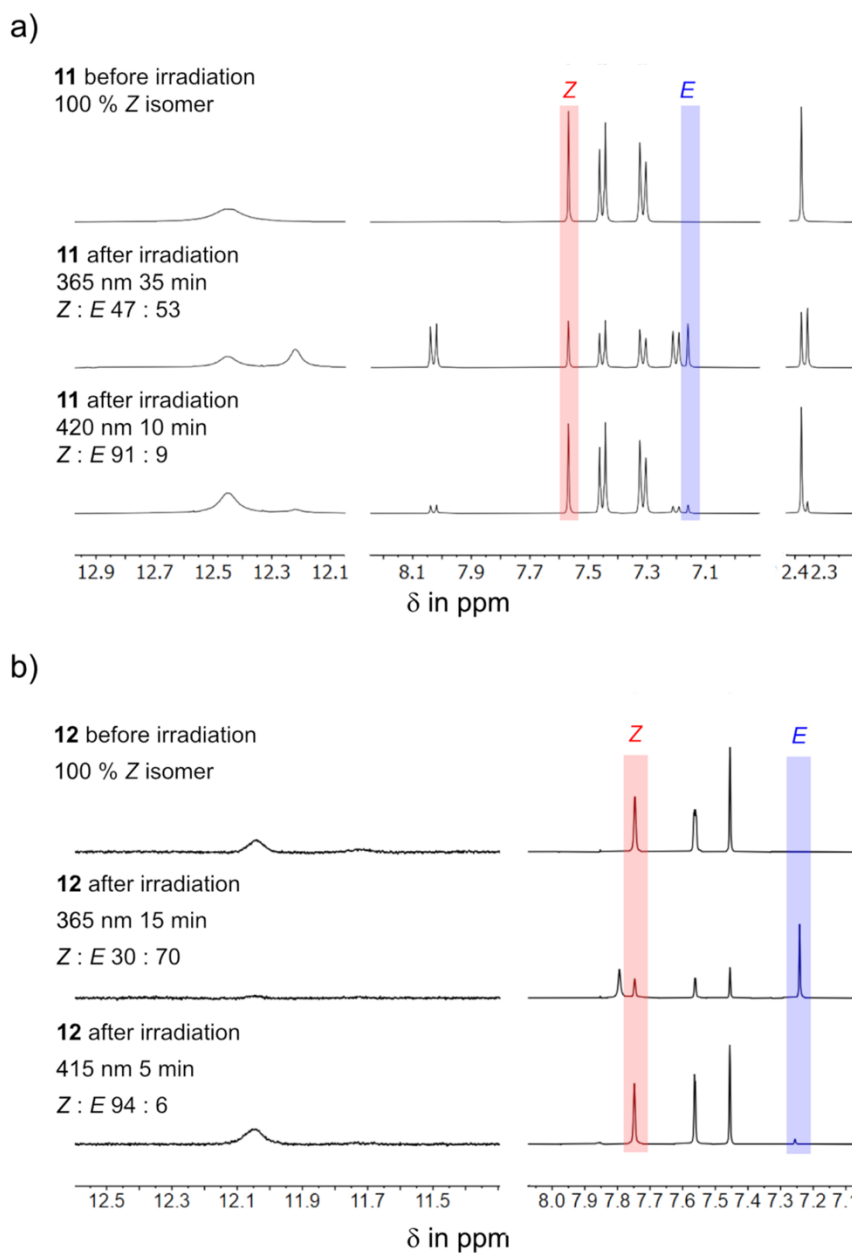
44

Figure S21   Partial ^{1}H NMR spectra (400 MHz, tetrahydrofuran-d_8, 10 mM, 25 °C) recorded before and after irradiation. Intensity magnification varies between H-N, aromatic and aliphatic regions. a) Irradiation experiment of **11**. Top to bottom: pure *Z*-**11** isomer was irradiated with 365 nm to enrich the *E* isomer, after 305min the pss was reached with an isomeric ratio of 47 : 53 (*Z* : *E*). Irradiation with 420 nm for 10 min leads to *Z* enrichment with an isomeric ratio in the pss of 91 : 9 (*Z* : *E*). b) Irradiation experiment of **12** From to bottom: pure *Z*-**12** isomer was irradiated with 365 nm to enrich the *E* isomer, after 15 min the pss was reached with an isomeric ratio of 30 : 70 (*Z* : *E*). Irradiation with 415 nm for 5 min leads to *Z* enrichment with an isomeric ratio in the pss of 94 : 6 (*Z* : *E*).
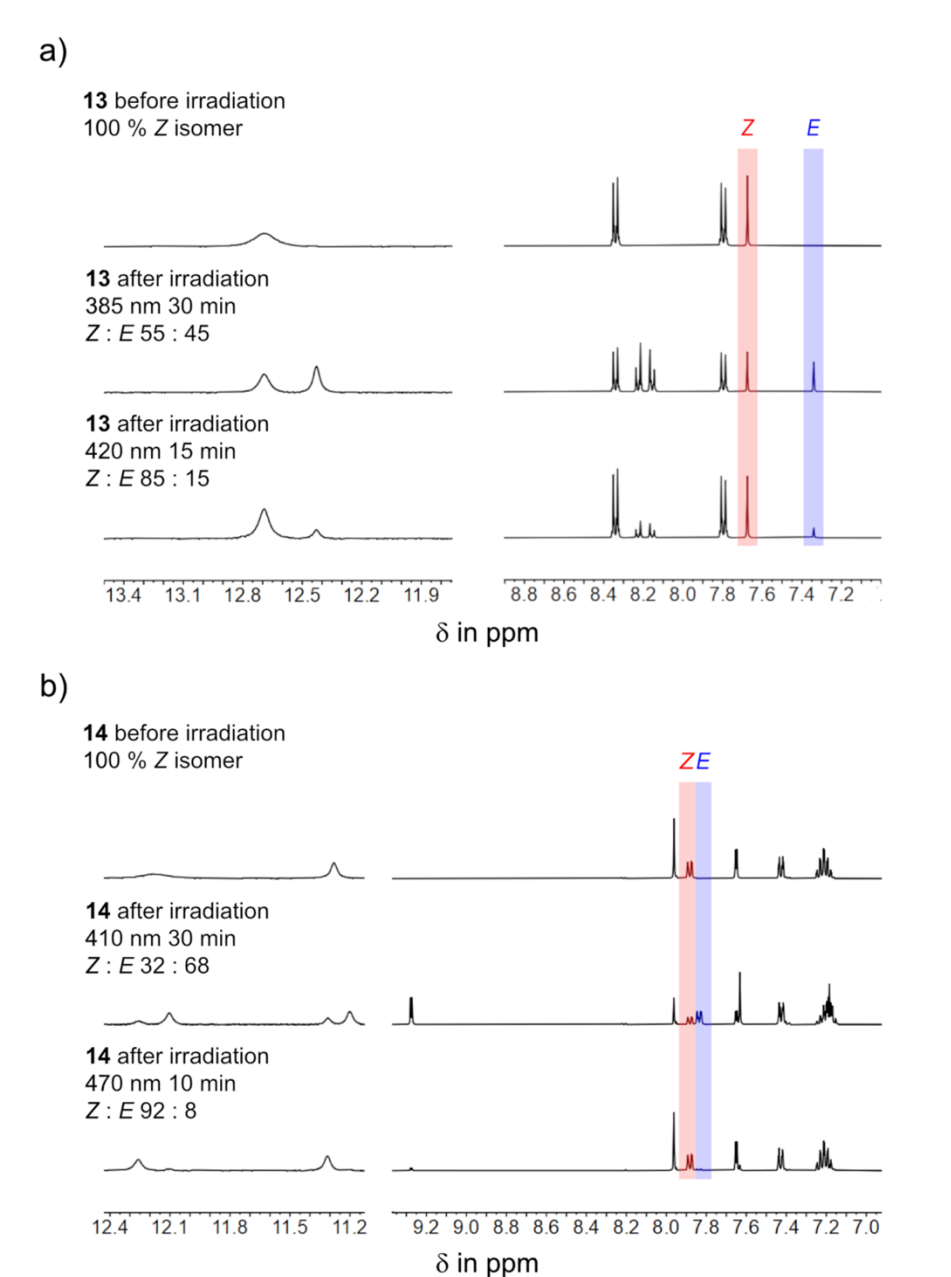
45

Figure S22   Partial ^{1}H NMR spectra (400 MHz, tetrahydrofuran-d_8, 10 mM, 25 °C) recorded before and after irradiation. Intensity magnification varies between H-N, aromatic and aliphatic regions. a) Irradiation experiment of **13**. Top to bottom: pure Z-**13** isomer was irradiated with 385 nm to enrich the E isomer, after 30 min the pss was reached with an isomeric ratio of 55 : 45 (Z : E). Irradiation with 420 nm for 15 min leads to Z enrichment with an isomeric ratio in the pss of 85 : 15 (Z : E). b) Irradiation experiment of **14** From to bottom: pure Z-**14** isomer was irradiated with 410 nm to enrich the E isomer, after 30 min the pss was reached with an isomeric ratio of 32 : 68 (Z : E). Irradiation with 470 nm for 10 min leads to Z enrichment with an isomeric ratio in the pss of 92 : 8 (Z : E).

46

Table S3 gives an overview over the isomeric ratios of (oxo)-rhodanine photoswitches **1 – 14** obtained after irradiation with light of different wavelengths to the respective pss in methanol-d_4. Ratios were determined by ^{1}H NMR spectroscopy at 23 °C.

Table S3   Isomer yields of **1 – 14** obtained after irradiation with light of different wavelengths until the respective pss was reached. Isomeric rations were determined in methanol-d_4 solutions at 23 °C using ^{1}H NMR spectroscopy.

	$\lambda\, Z \rightarrow E$	$Z : E$	t [min]	$\lambda\, E \rightarrow Z$	$Z : E$	t [min]
1	340 nm	42 : 58	80	405 nm	95 : 5	5
2	405 nm	50 : 50	50	470 nm	91 : 9	5
3	365 nm	33 :67	20	450 nm	92 : 8	10
4	340 nm	23 : 77	50	405 nm	97 : 3	15
5	385 nm	47 :53	10	430 nm	84 : 16	5
6	420 nm	47 : 53	10	505 nm	85 :15	5
7	385 nm	35 : 65	10	470 nm	74 : 26	10
8	385 nm	41 : 59	10	470 nm	94 : 6	10
9	395 nm	39 : 61	10	340 nm	47 : 53	10
10	365 nm	50 : 50	30	420 nm	87 : 13	10
11	365 nm	49 : 51	30	420 nm	89 : 11	5
12	365 nm	41 : 59	15	415 nm	90 : 10	5
13	375 nm	51 : 49	20	415 nm	73 : 27	5
14	410 nm	40 : 60	20	470 nm	83 : 17	20

Figure S23 – Figure S29 show ^{1}H NMR spectra of (oxo)-rhodanine photoswitches **1 – 14** before and after irradiation at 25 °C in methanol-d_4. Starting with 100% of the stable *Z* isomer, the metastable *E* isomer can be enriched by irradiating. Using a different wavelength the reverse *E*/*Z* photoisomerisation occurs.
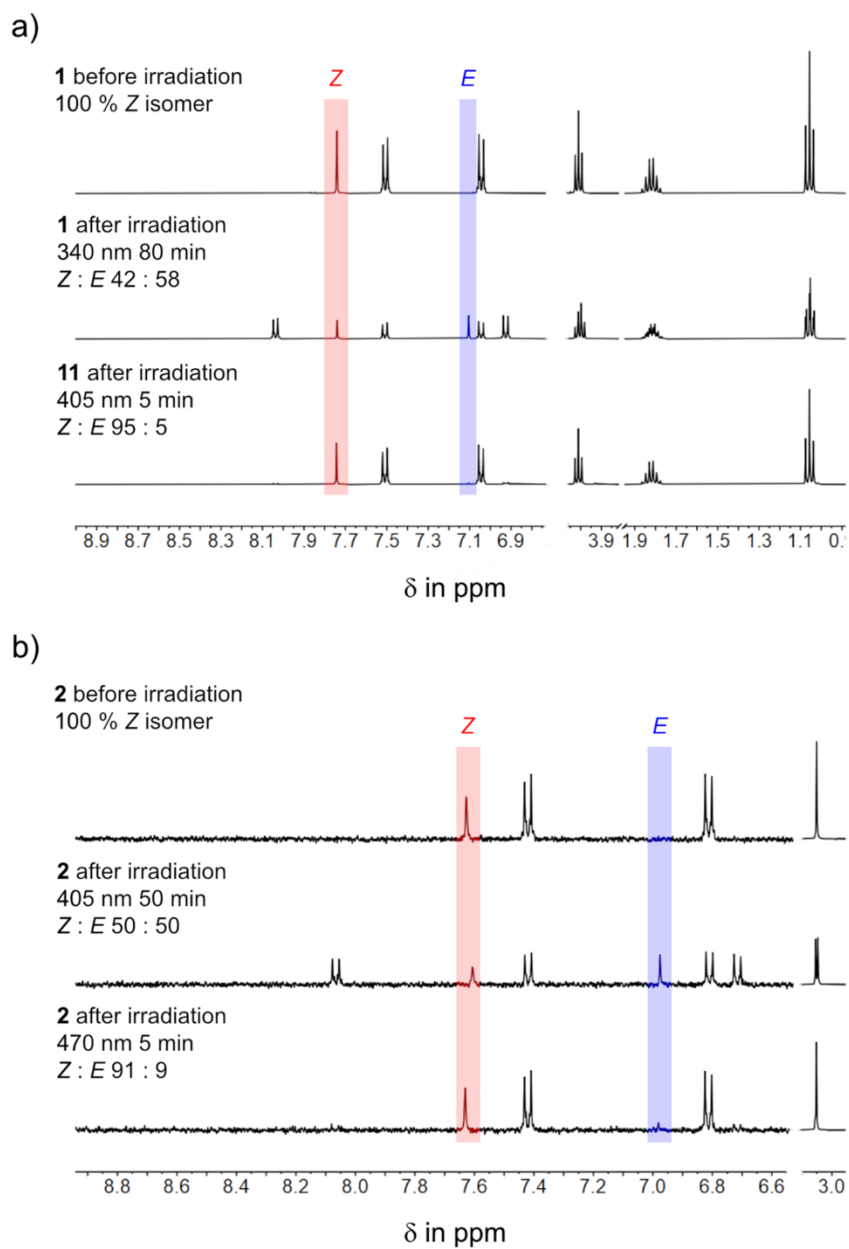
47

Figure S23   Partial ^{1}H NMR spectra (400 MHz, methanol-d_4, 5 mM, 25 °C) recorded before and after irradiation. Intensity magnification varies between H-N, aromatic and aliphatic regions. a) Irradiation experiment of **1**. Top to bottom: pure Z-**1** isomer was irradiated with 340 nm to enrich the E isomer, after 80 min the pss was reached with an isomeric ratio of 42 : 58 (Z : E). Irradiation with 405 nm for 5 min leads to Z enrichment with a isomeric ratio in the pss of 95 : 5 (Z : E). b) Irradiation experiment of **2**. From to bottom: pure Z-**2** isomer was irradiated with 405 nm to enrich the E isomer, after 50 min the pss was reached with an isomeric ratio of 50 : 50 (Z : E). Irradiation with 470 nm for 5 min leads to Z enrichment with an isomeric ratio in the pss of 91 : 9 (Z : E).
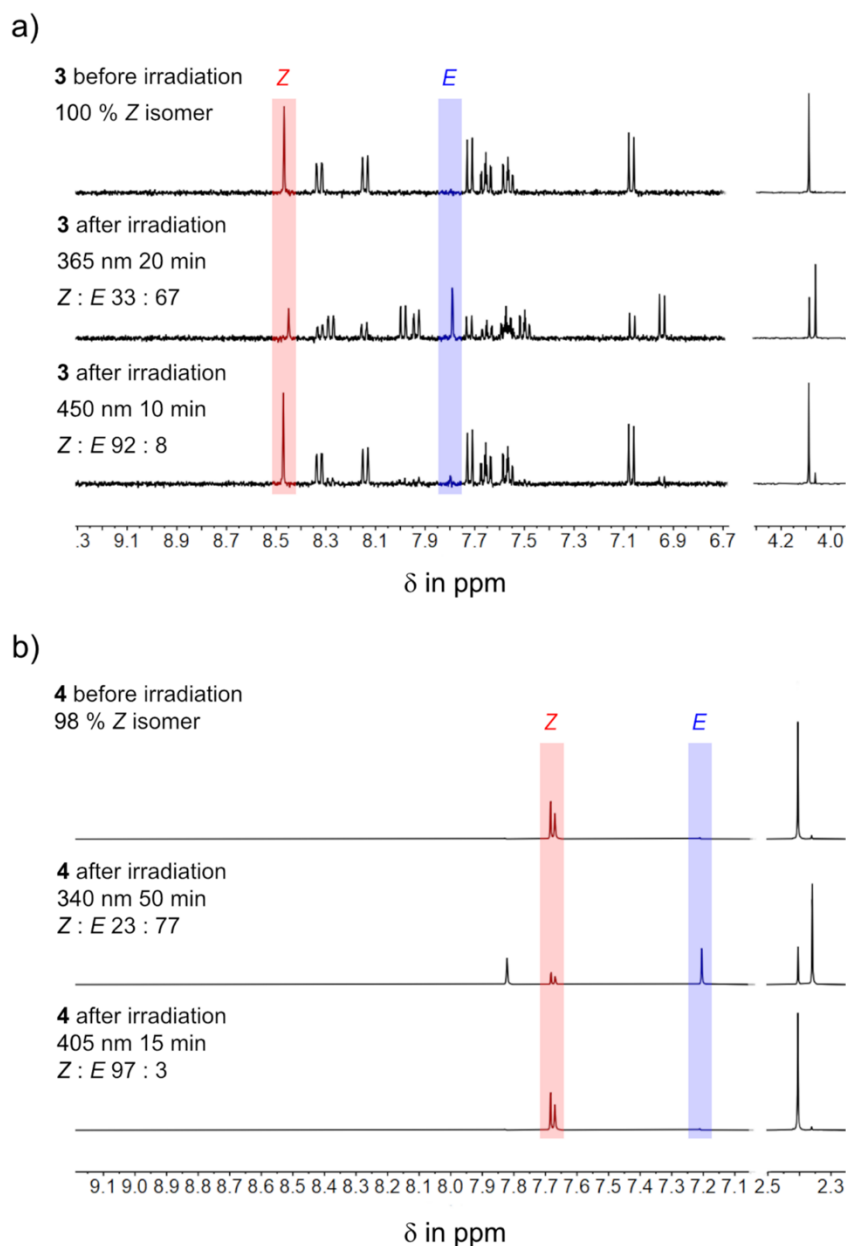
48

Figure S24　　Partial ^{1}H NMR spectra (400 MHz, methanol-d_4, 5 mM, 25 °C) recorded before and after irradiation. Intensity magnification varies between H-N, aromatic and aliphatic regions. a) Irradiation experiment of **3**. Top to bottom: pure *Z*-**3** isomer was irradiated with 365 nm to enrich the *E* isomer, after 15 min the pss was reached with an isomeric ratio of 33 : 67 (*Z* : *E*). Irradiation with 450 nm for 5 min leads to *Z* enrichment with a isomeric ratio in the pss of 90 : 10 (*Z* : *E*). b) Irradiation experiment of **4**. From to bottom: 98% *Z*-**4** isomer was irradiated with 340 nm to enrich the *E* isomer, after 50 min the pss was reached with an isomeric ratio of 23 : 77 (*Z* : *E*). Irradiation with 405 nm for 15 min leads to *Z* enrichment with an isomeric ratio in the pss of 97 : 3 (*Z* : *E*).
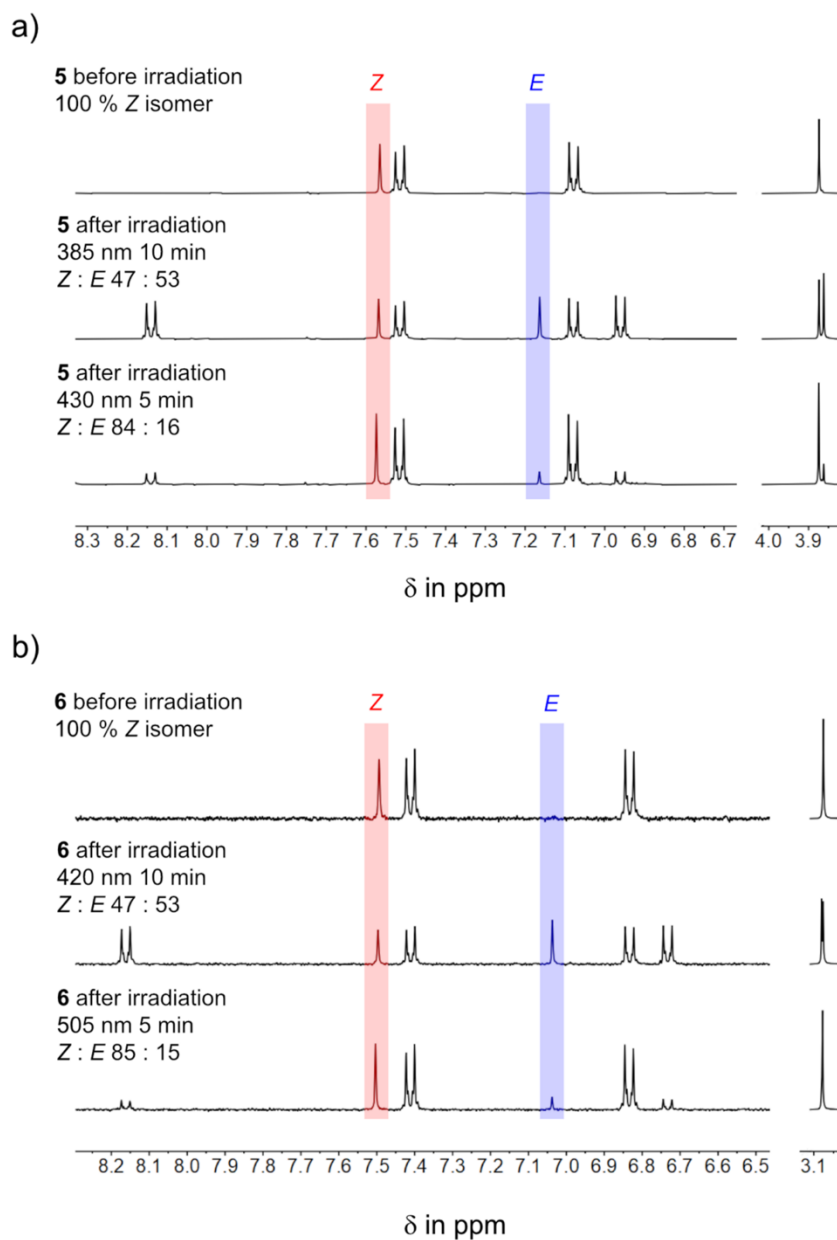
49

Figure S25   Partial ^{1}H NMR spectra (400 MHz, methanol-d_4, 5 mM, 25 °C) recorded before and after irradiation. Intensity magnification varies between H-N, aromatic and aliphatic regions. a) Irradiation experiment of **5**. Top to bottom: pure Z-**5** isomer was irradiated with 385 nm to enrich the *E* isomer, after 10 min the pss was reached with an isomeric ratio of 47 : 53 (*Z* : *E*). Irradiation with 430 nm for 5 min leads to *Z* enrichment with an isomeric ratio in the pss of 84 : 16 (*Z* : *E*). b) Irradiation experiment of **6**. From to bottom: pure Z-**6** isomer was irradiated with 420 nm to enrich the *E* isomer, after 10 min the pss was reached with an isomeric ratio of 47 : 53 (*Z* : *E*). Irradiation with 505 nm for 5 min leads to *Z* enrichment with an isomeric ratio in the pss of 85 : 15 (*Z* : *E*).
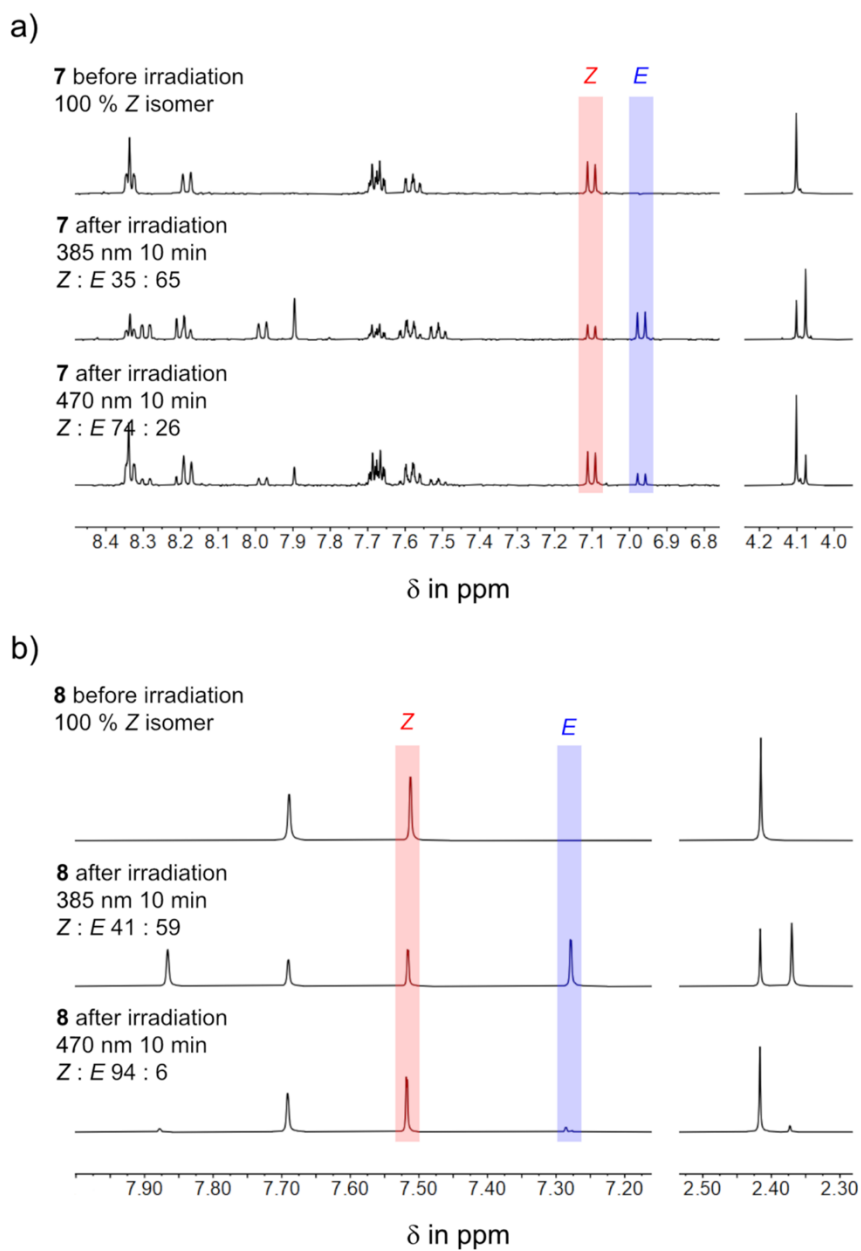
50

Figure S26   Partial ^{1}H NMR spectra (400 MHz, methanol-d_4, 5 mM, 25 °C) recorded before and after irradiation. Intensity magnification varies between H-N, aromatic and aliphatic regions. a) Irradiation experiment of **7**. Top to bottom: pure Z-**7** isomer was irradiated with 385 nm to enrich the E isomer, after 10 min the pss was reached with an isomeric ratio of 35 : 65 (Z : E). Irradiation with 470 nm for 10 min leads to Z enrichment with an isomeric ratio in the pss of 74 : 26 (Z : E). b) Irradiation experiment of **8**. From to bottom: pure Z-**8** isomer was irradiated with 385 nm to enrich the E isomer, after 10 min the pss was reached with an isomeric ratio of 41 : 59 (Z : E). Irradiation with 470 nm for 10 min leads to Z enrichment with an isomeric ratio in the pss of 94 : 6 (Z : E).
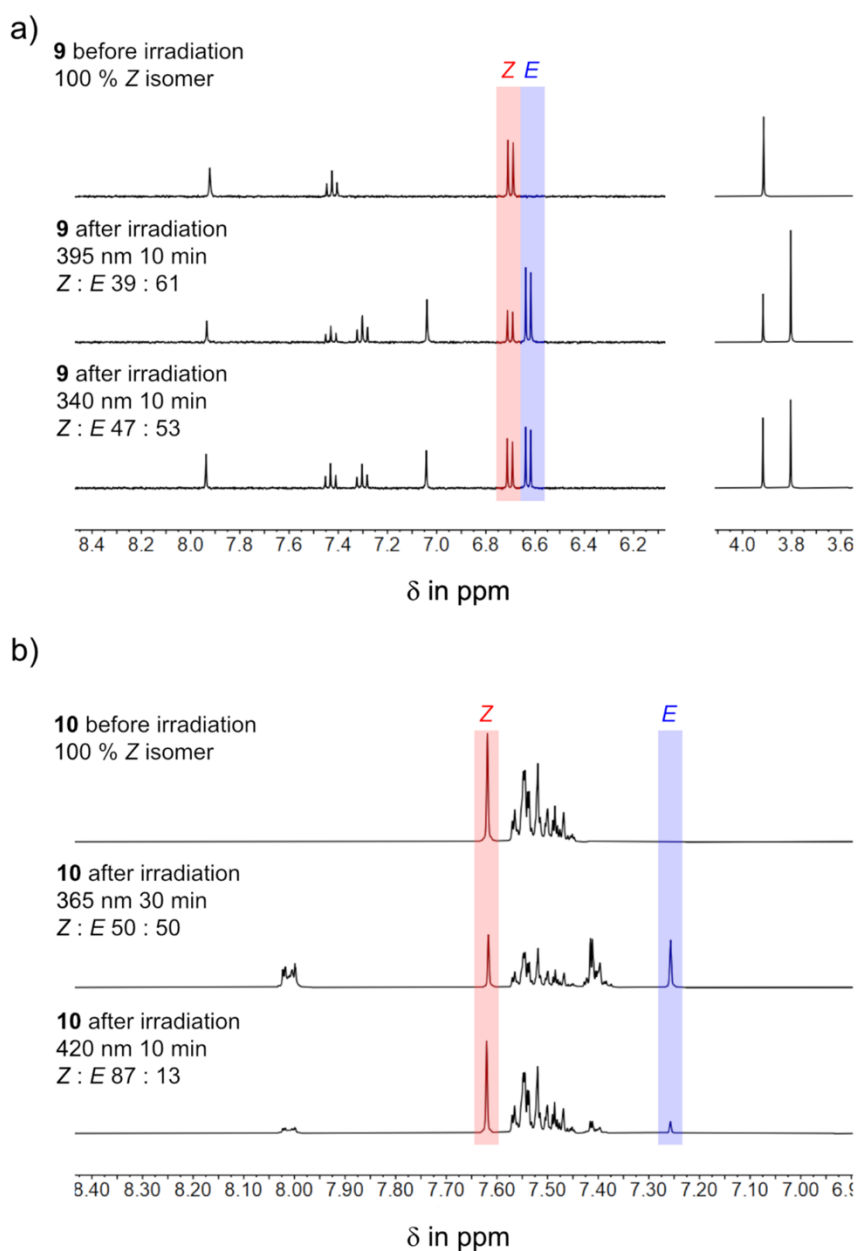
51

Figure S27   Partial ^{1}H NMR spectra (400 MHz, methanol-d_4, 5 mM, 25 °C) recorded before and after irradiation. Intensity magnification varies between H-N, aromatic and aliphatic regions. a) Irradiation experiment of **9**. Top to bottom: pure Z-**9** isomer was irradiated with 395 nm to enrich the E isomer, after 10 min the pss was reached with an isomeric ratio of 39 : 61 (Z : E). Irradiation with 340 nm for 10 min leads to Z enrichment with an isomeric ratio in the pss of 47 : 53 (Z : E). b) Irradiation experiment of **10**. From to bottom: pure Z-**10** isomer was irradiated with 365 nm to enrich the E isomer, after 30 min the pss was reached with an isomeric ratio of 50 : 50 (Z : E). Irradiation with 420 nm for 10 min leads to Z enrichment with an isomeric ratio in the pss of 87 : 13 (Z : E).
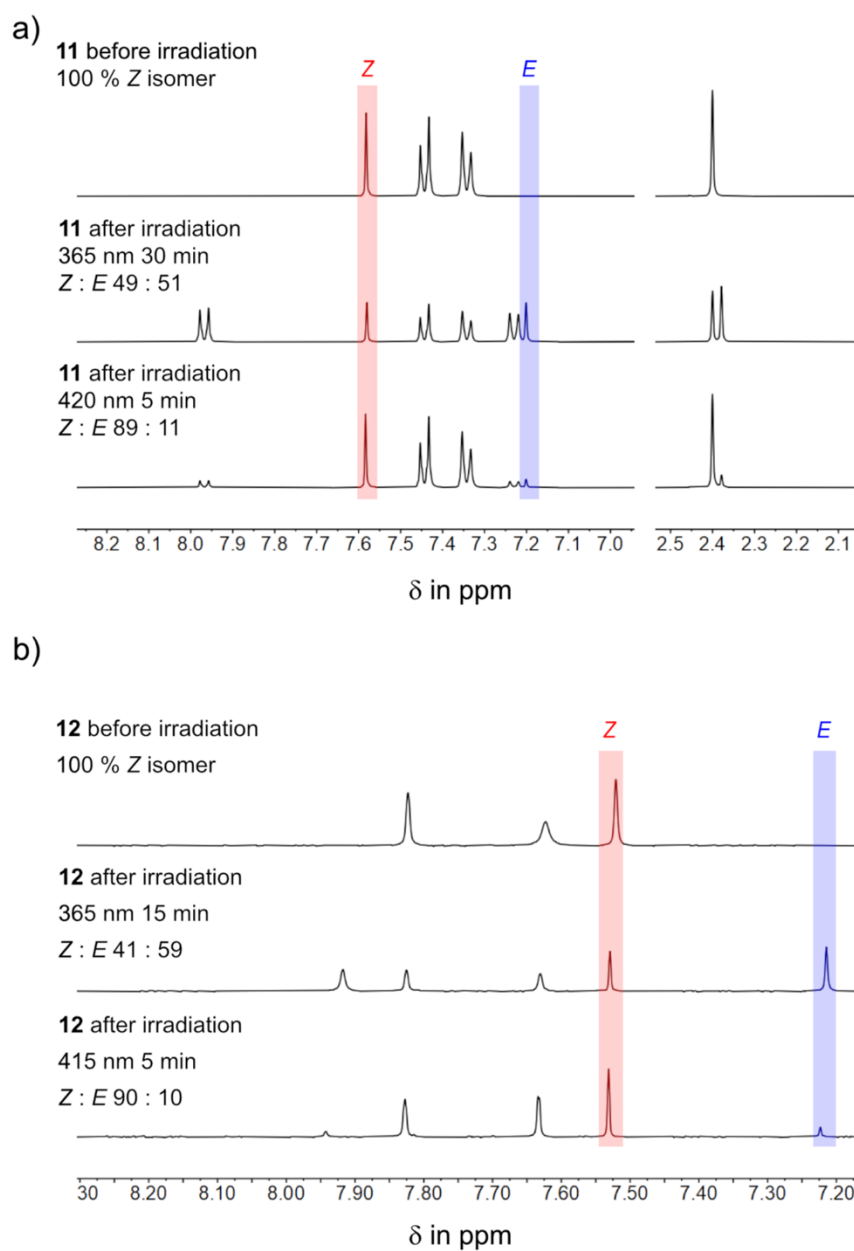
52

Figure S28   Partial ^{1}H NMR spectra (400 MHz, methanol-d_4, 5 mM, 25 °C) recorded before and after irradiation. Intensity magnification varies between H-N, aromatic and aliphatic regions. a) Irradiation experiment of **11**. Top to bottom: pure Z-**11** isomer was irradiated with 365 nm to enrich the E isomer, after 30 min the pss was reached with an isomeric ratio of 49 : 51 (Z : E). Irradiation with 420 nm for 5 min leads to Z enrichment with an isomeric ratio in the pss of 89 : 11 (Z : E). b) Irradiation experiment of **12**. From to bottom: pure Z-**12** isomer was irradiated with 365 nm to enrich the E isomer, after 15 min the pss was reached with an isomeric ratio of 41 : 59 (Z : E). Irradiation with 415 nm for 5 min leads to Z enrichment with an isomeric ratio in the pss of 90 : 10 (Z : E).
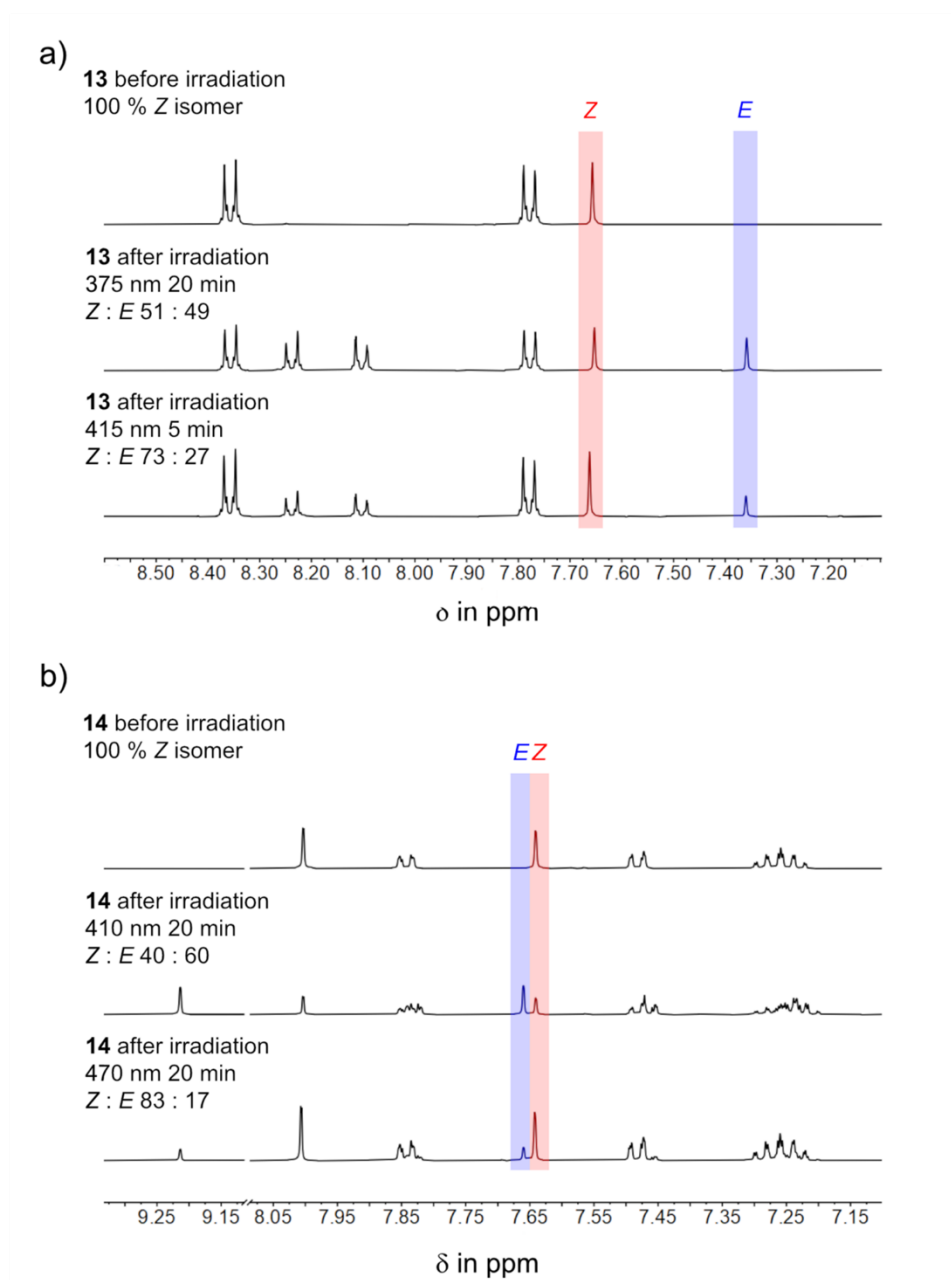
53

Figure S29   Partial ^{1}H NMR spectra (400 MHz, methanol-d_4, 5 mM, 25 °C) recorded before and after irradiation. Intensity magnification varies between H-N, aromatic and aliphatic regions. a) Irradiation experiment of **13**. Top to bottom: pure *Z*-**13** isomer was irradiated with 375 nm to enrich the *E* isomer, after 20 min the pss was reached with an isomeric ratio of 51 : 49 (*Z* : *E*). Irradiation with 415 nm for 5 min leads to *Z* enrichment with an isomeric ratio in the pss of 73 : 27 (*Z* : *E*). b) Irradiation experiment of **14**. From to bottom: pure *Z*-**14** isomer was irradiated with 410 nm to enrich the *E* isomer, after 20 min the pss was reached with an isomeric ratio of 40 : 60 (*Z* : *E*). Irradiation with 470 nm for 20 min leads to *Z* enrichment with an isomeric ratio in the pss of 83 : 17 (*Z* : *E*).

54

Irradiation followed by UV/Vis spectroscopy

Figure S30 – Figure S33 show UV/Vis spectra measured before and after irradiation of (oxo)-rhodanine photoswitches **1** – **14** at 23 °C in tetrahydrofuran or methanol solution. A stock-solution of each photoswitch was prepared in tetrahydrofuran or methanol and diluted to generate a final concentration of ~ $2 \cdot 10^{-5}$ mM in a 10 mm pathlength cuvette. Starting with 100% of the stable *Z* isomer, the metastable *E* isomer can be enriched by irradiating. Using a different wavelength the reverse *E*/*Z* photoisomerisation occurs.
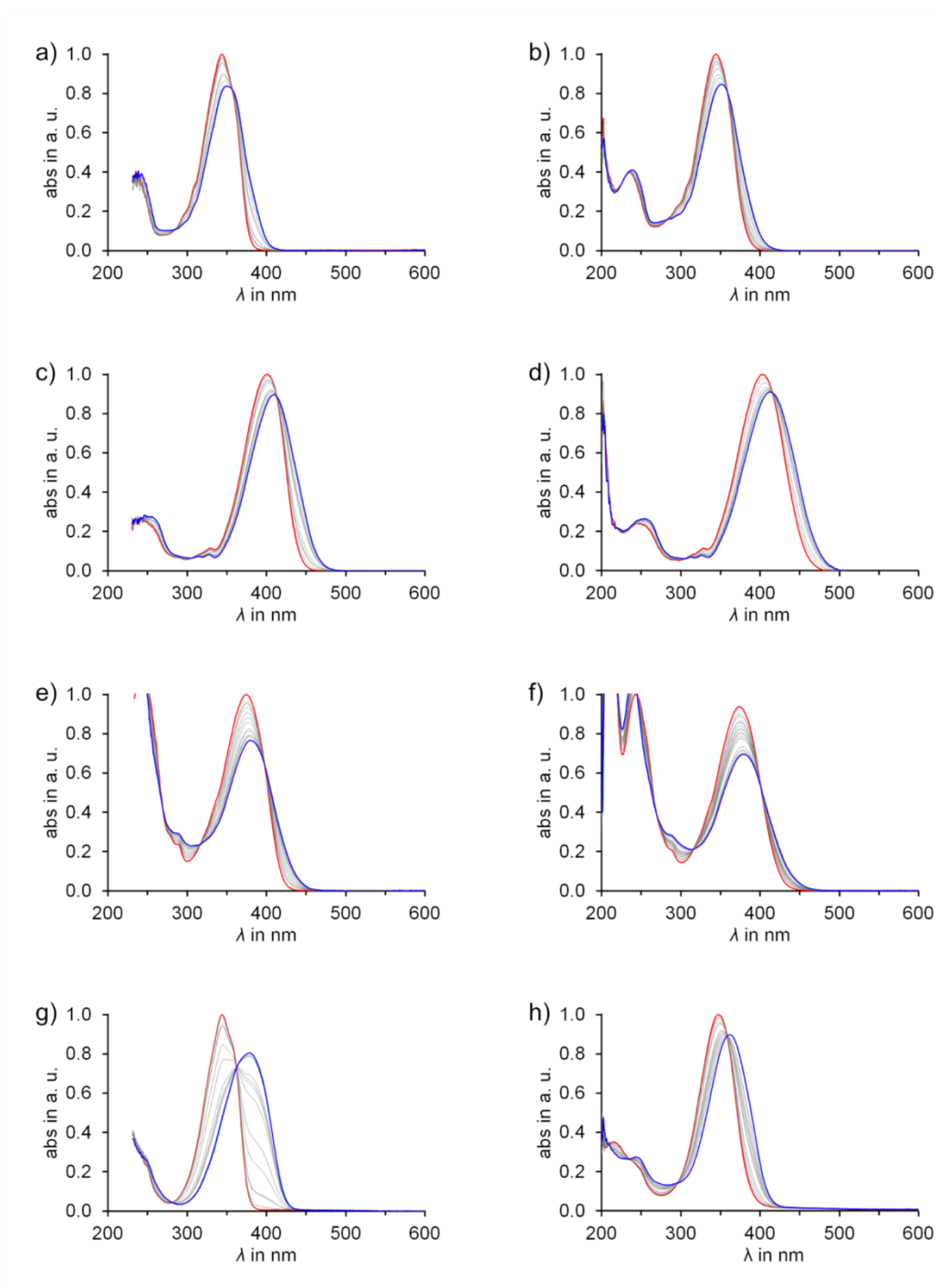
55

Figure S30   Normalized absorption spectra of photoswitches **1**-**4** recorded before and after irradiation at 23 °C. a) **1** in THF. b) **1** in MeOH. c) **2** in THF d) **2** in MeOH. e) **3** in THF. f) **3** in MeOH. g) **4** in THF. h) **4** in MeOH. Pure *Z* isomers are shown in red, irradiations in grey and the pss in blue.

56

Figure S31   Normalized absorption spectra of photoswitches **5**-**8** recorded before and after irradiation at 23 °C. a) **5** in THF. b) **5** in MeOH. c) **6** in THF d) **6** in MeOH. e) **7** in THF. f) **7** in MeOH. g) **8** in THF. h) **8** in MeOH. Pure *Z* isomers are shown in red, irradiations in grey and the pss in blue.
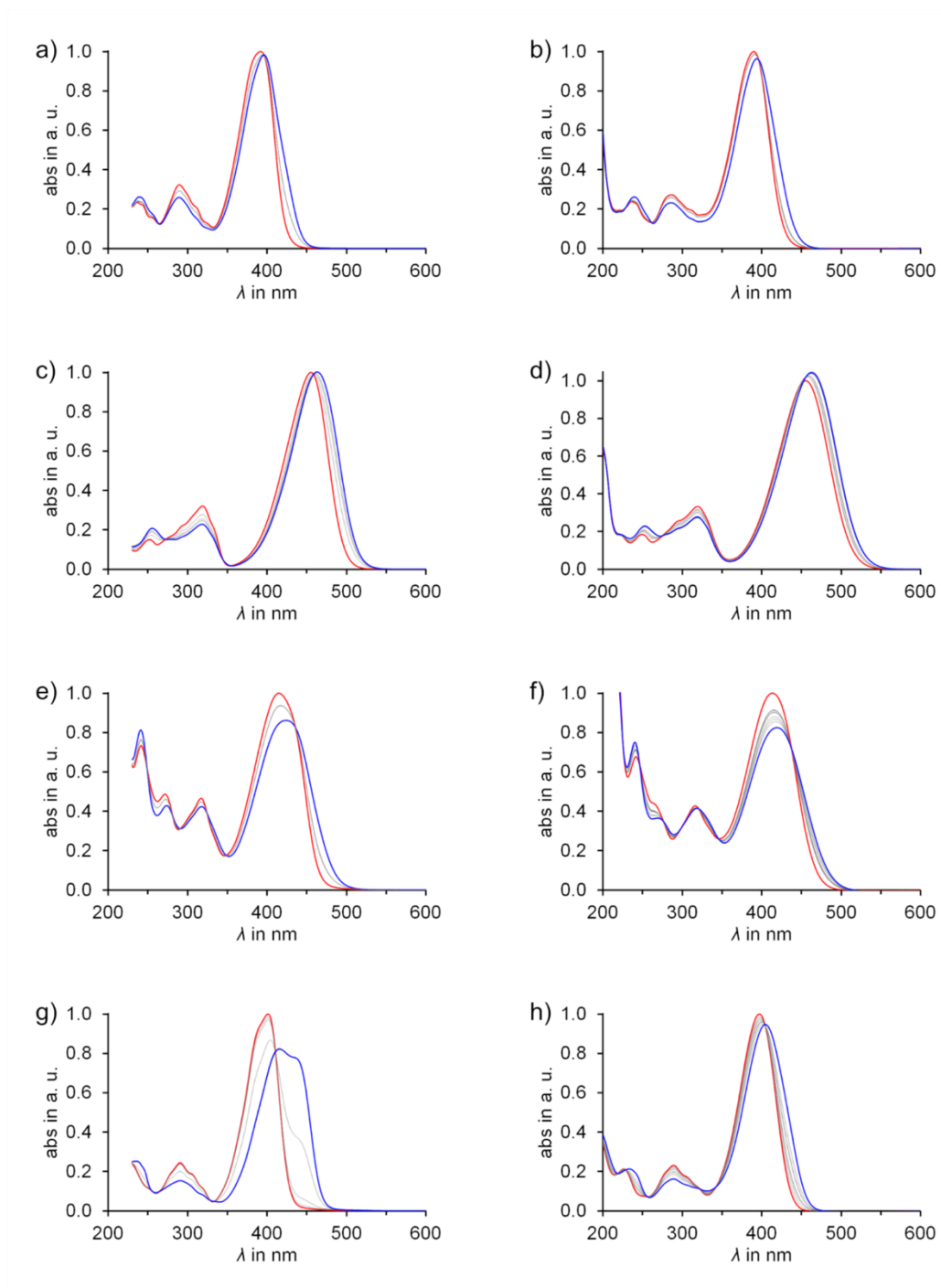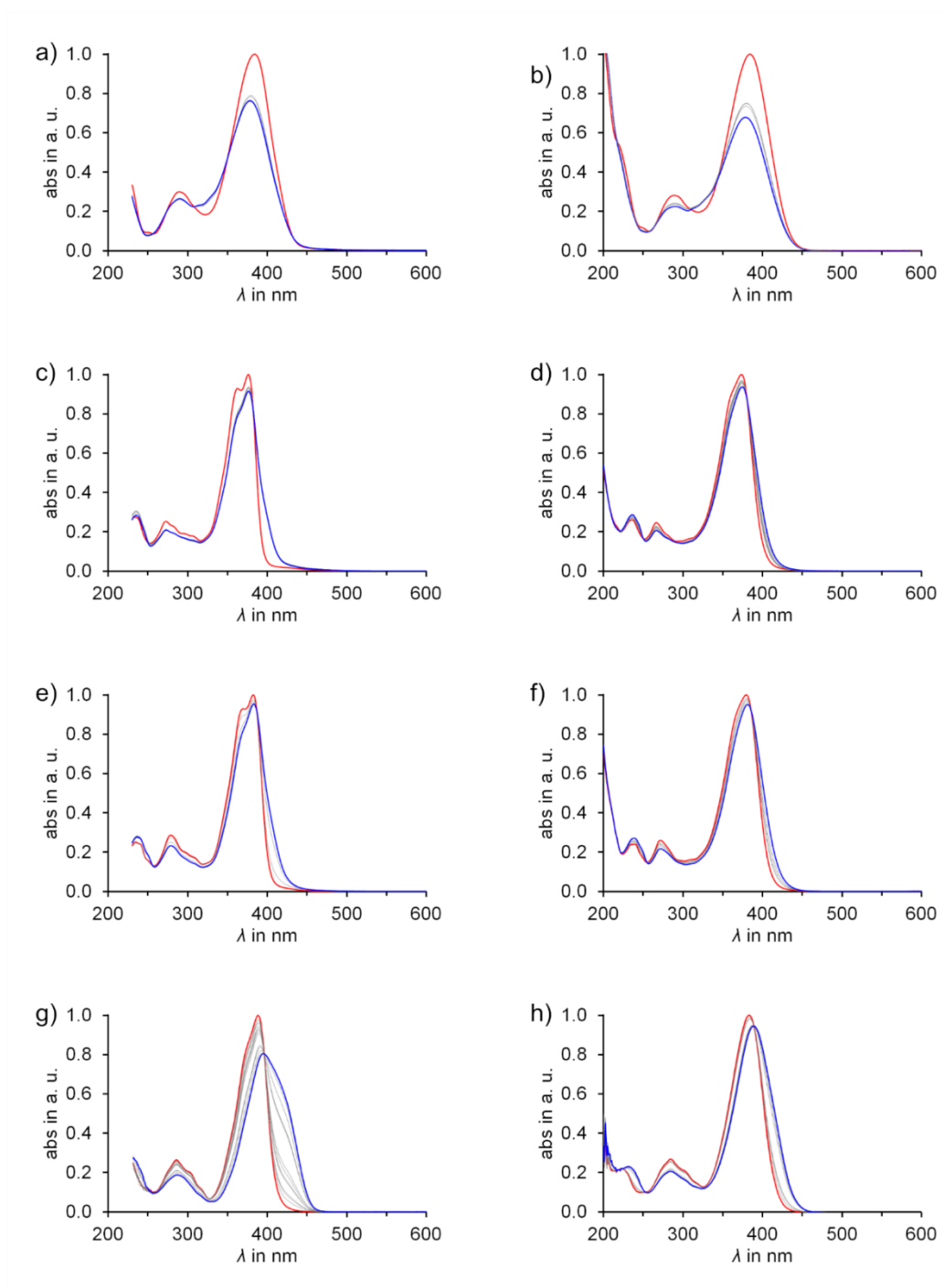
57

226

Figure S32   Normalized absorption spectra of photoswitches **9-12** recorded before and after irradiation at 23 °C. a) **9** in THF. b) **9** in MeOH. c) **10** in THF. d) **10** in MeOH. e) **11** in THF. f) **11** in MeOH. g) **12** in THF. h) **12** in MeOH. Pure *Z* isomers are shown in red, irradiations in grey and the pss in blue.
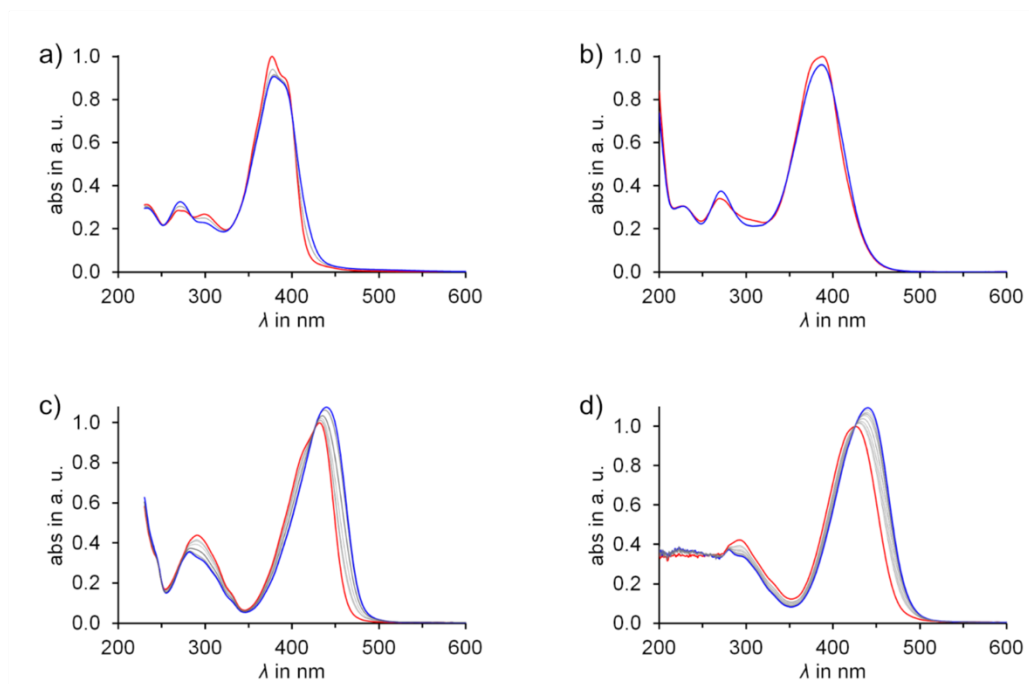
Figure S33   Normalized absorption spectra of photoswitches **13** and **14** recorded before and after irradiation at 23 °C. a) **13** in THF. b) **13** in MeOH. c) **14** in THF. d) **14** in MeOH. Pure *Z* isomers are shown in red, irradiations in grey and the pss in blue.

59

Molar absorption coefficient

The molar absorption coefficients ε of Z isomers were obtained directly from isomerically pure material using the *Lambert-Beer* law. The molar absorption coefficients of E isomers were obtained by measuring the absorption of an E enriched solution with known isomeric composition (determined by ^{1}H NMR spectroscopy) and subtracting the spectral components of remaining Z isomer. Table S4 shows the maximum wavelength and molar absorption coefficients of the most redshifted absorption in tetrahydrofuran at 23°C, as well as the difference of the maximum wavelength $\Delta\lambda_{max}$ of the most redshifted absorption band between Z and E isomers.

Table S4   Quantitative comparison of the maximum wavelength λ_{max} and molar absorption coefficients ε of most redshifted absorption of Photoswitches **1 – 14**. Absolute difference $\Delta\lambda_{max}$ between maximum wavelength of Z isomer $\lambda_{max(Z)}$ and E isomer $\lambda_{max(E)}$ of most redshifted absorption. Data were measured in tetrahydrofuran solutions at 23°C.

	Z isomer		E isomer		$\Delta\lambda_{max}$
	λ_{max} [nm]	ε [L mol^{-1} cm^{-1}]	λ_{max} [nm]	ε [L mol^{-1} cm^{-1}]	[nm]
1	344	26,700	361	22,000	17
2	401	36,200	419	32,300	18
3	374	19,200	392	12,700	18
4	344	24,900	378	21,800	34
5	392	36,100	397	35,000	5
6	455	45,300	474	51,500	19
7	414	25,900	428	21,200	14
8	401	37,800	435	31,300	34
9	384	29,500	373	17,900	11
10	376	34,700	375	32,800	1
11	382	38,400	382	35,400	0
12	388	37,300	408	33,800	20
13	377	34,500	387	30,500	10
14	433	32,900	447	39,000	14

60

Figure S34 – Figure S40 show the molar absorption coefficients ε of (oxo)-rhodanine based photoswitches **1** – **14** at 23 °C in tetrahydrofuran. *Z* isomers are shown in red, *E* isomers are displayed in blue.
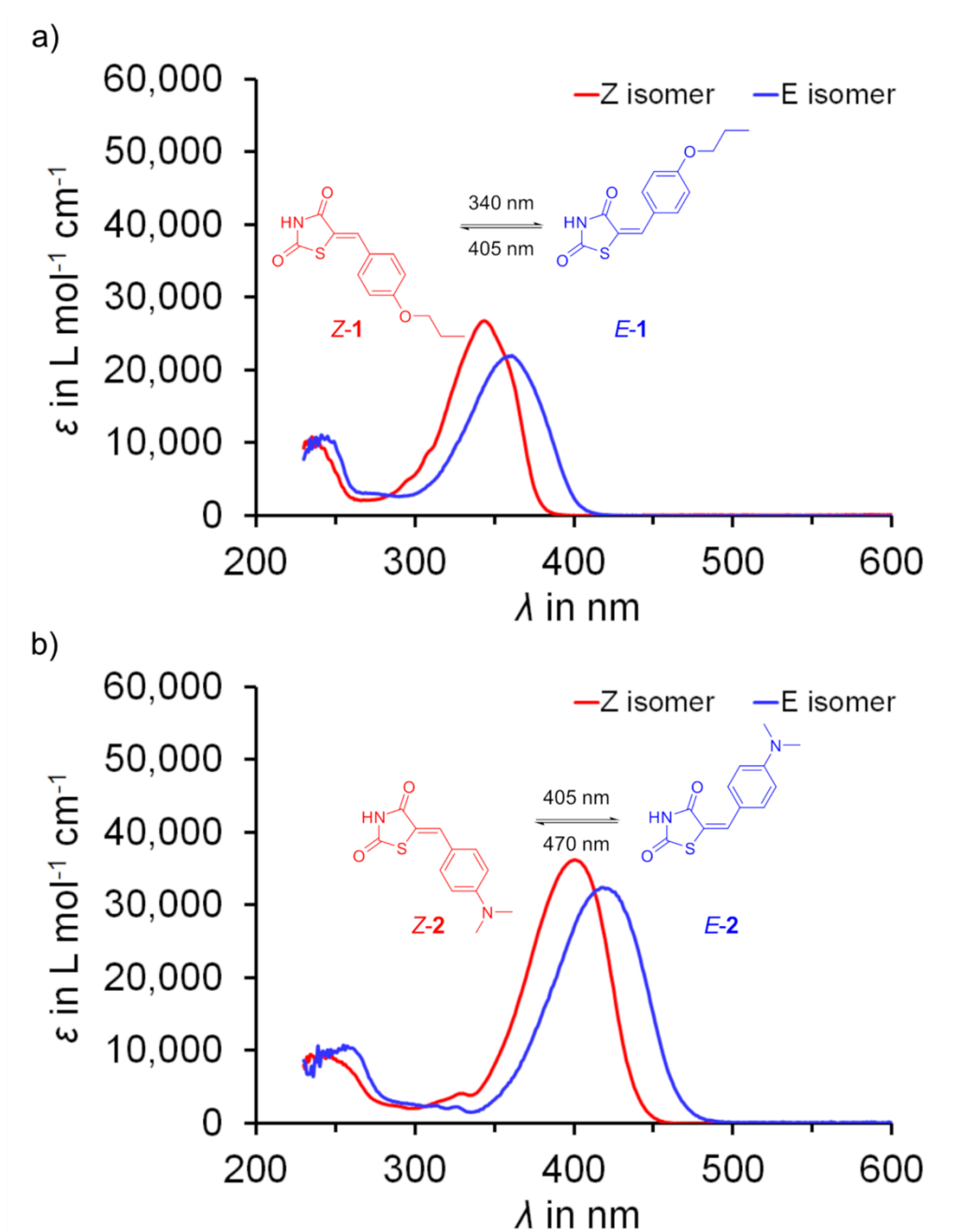

Figure S34   Molar absorption coefficients ε of a) **1**, b) **2** in tetrahydrofuran at 23 °C. *Z* isomers are displayed in red, *E* isomers are displayed in blue.

Figure S35   Molar absorption coefficients ε of a) **3**, b) **4** in tetrahydrofuran at 23 °C. *Z* isomers are displayed in red, *E* isomers are displayed in blue.

62
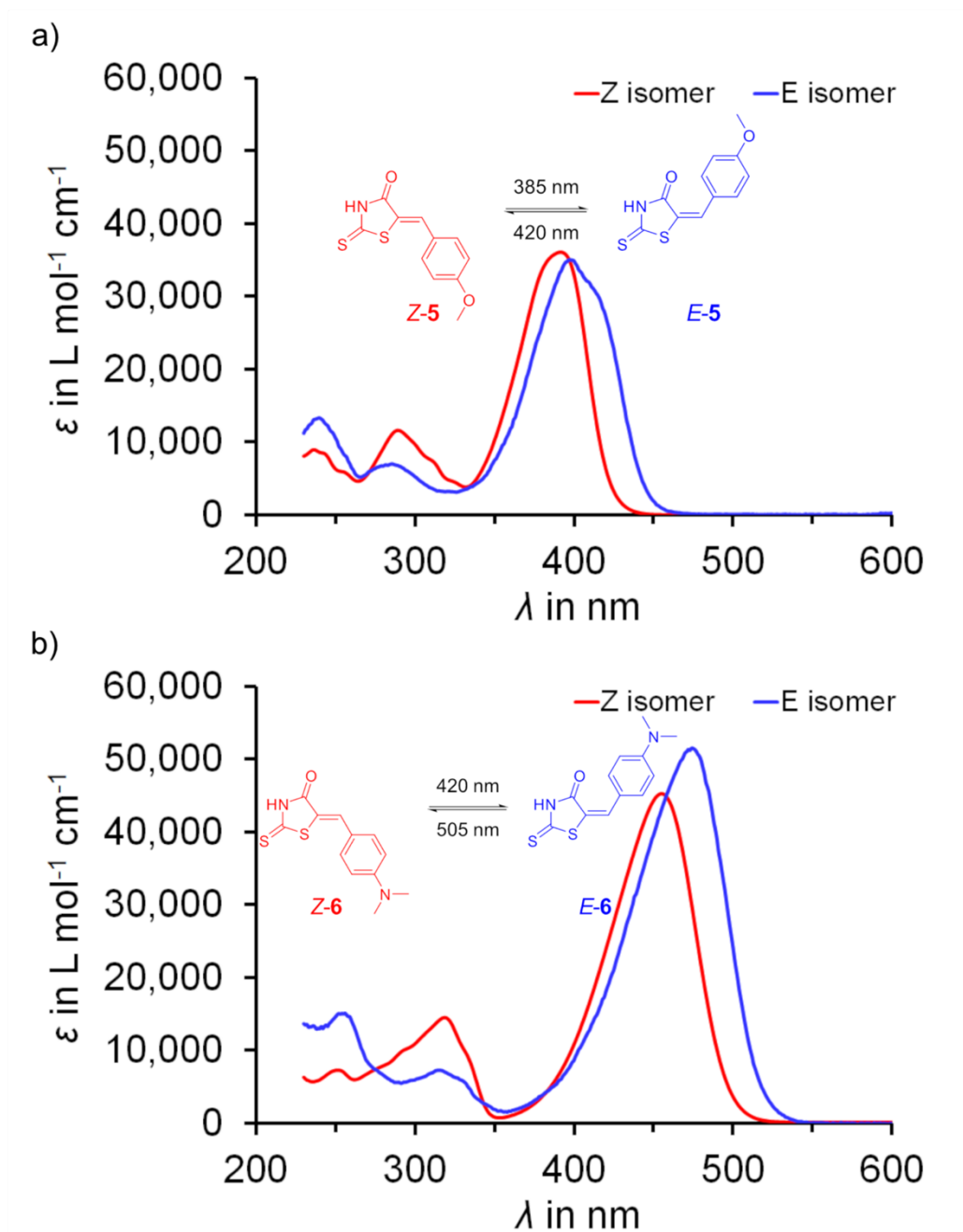
Figure S36   Molar absorption coefficients ε of a) **5**, b) **6** in tetrahydrofuran at 23 °C. *Z* isomers are displayed in red, *E* isomers are displayed in blue.

63
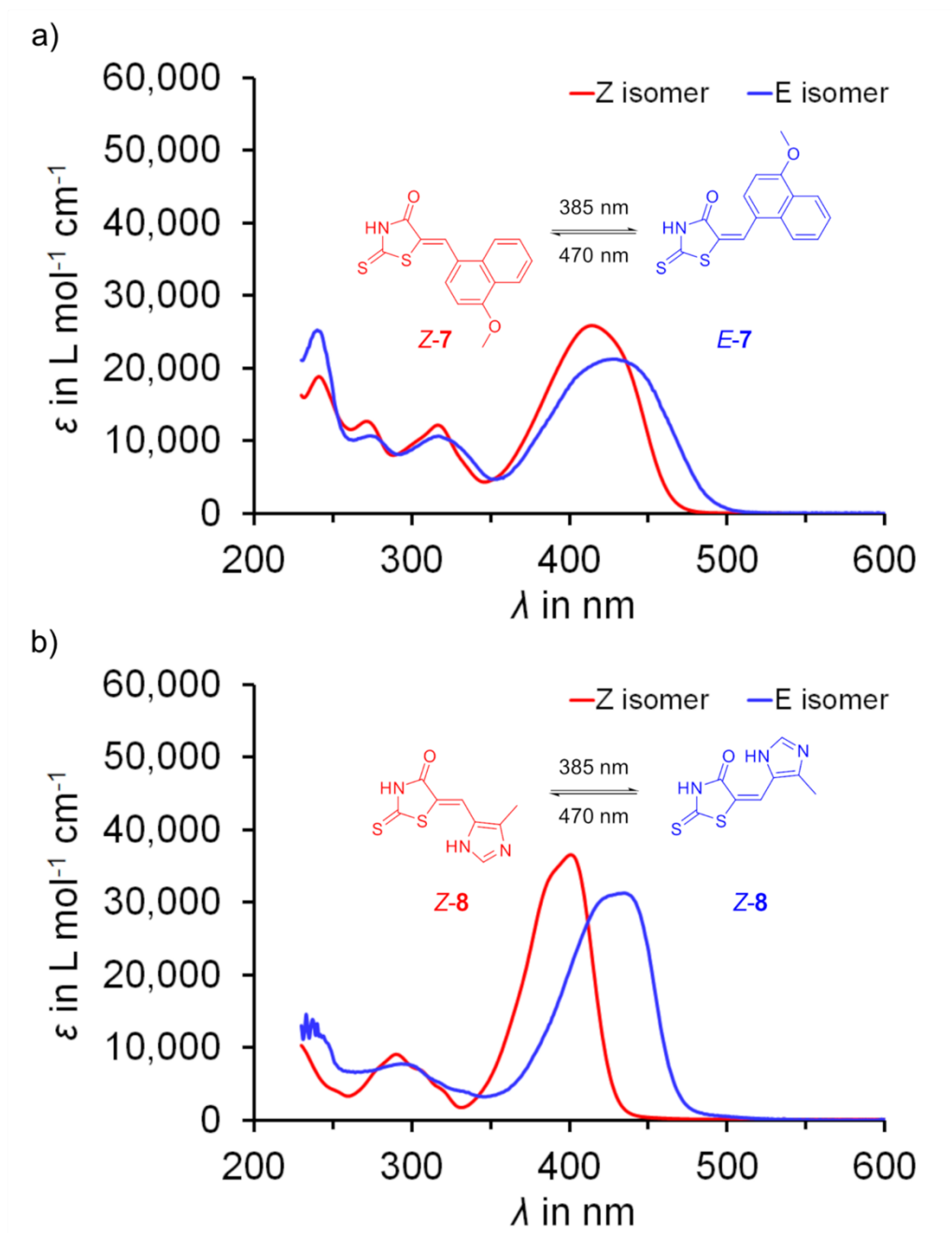
Figure S37   Molar absorption coefficients ε of a) **7**, b) **8** in tetrahydrofuran at 23 °C. *Z* isomers are displayed in red, *E* isomers are displayed in blue.
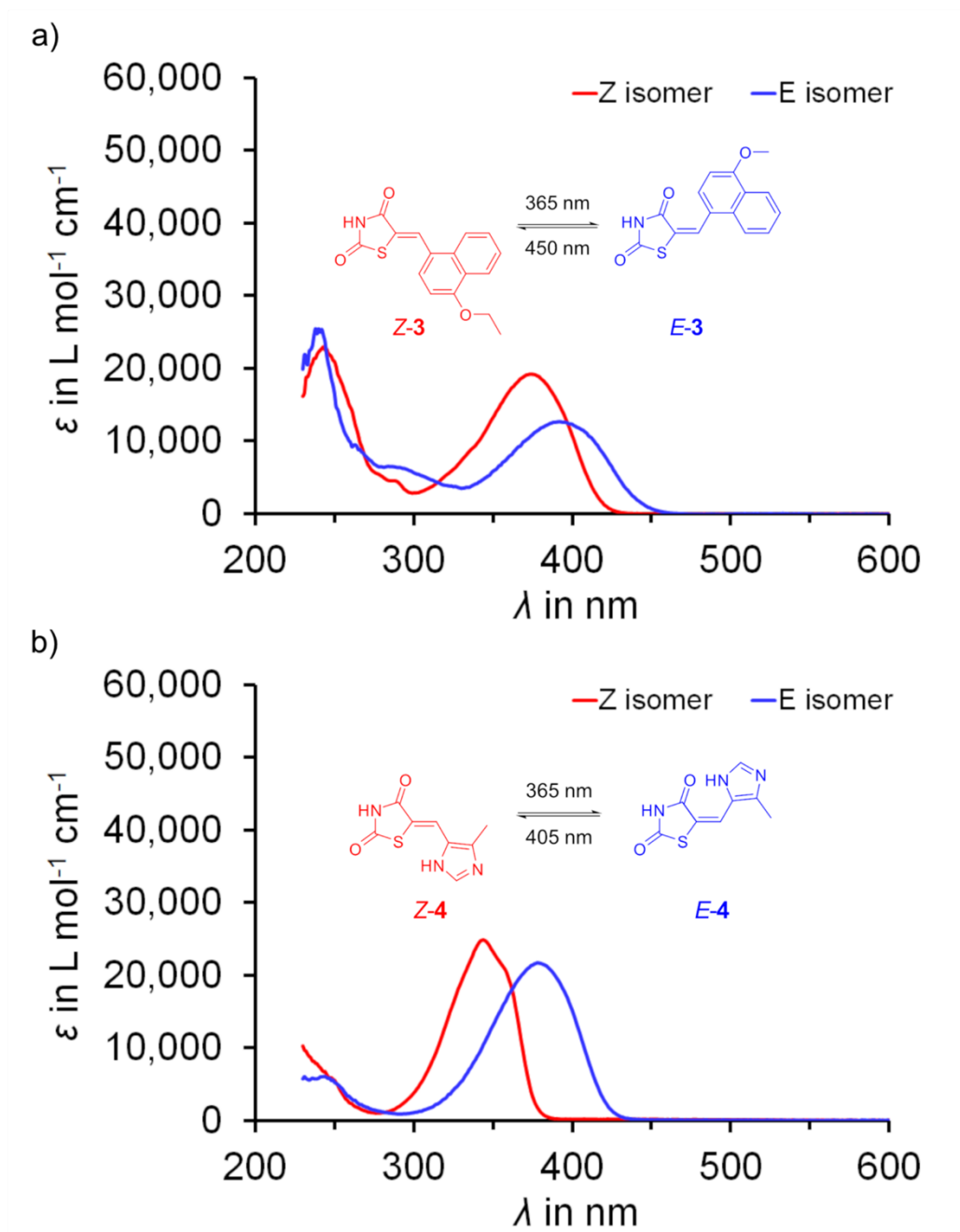
64

Figure S38   Molar absorption coefficients ε of a) **9**, b) **10** in tetrahydrofuran at 23 °C. *Z* isomers are displayed in red, *E* isomers are displayed in blue.

65

Figure S39 Molar absorption coefficients ε of a) **11**, b) **12** in tetrahydrofuran at 23 °C. *Z* isomers are displayed in red, *E* isomers are displayed in blue.

66

Figure S40   Molar absorption coefficients ε of a) **13**, b) **14** in tetrahydrofuran at 23 °C. *Z* isomers are displayed in red, *E* isomers are displayed in blue.
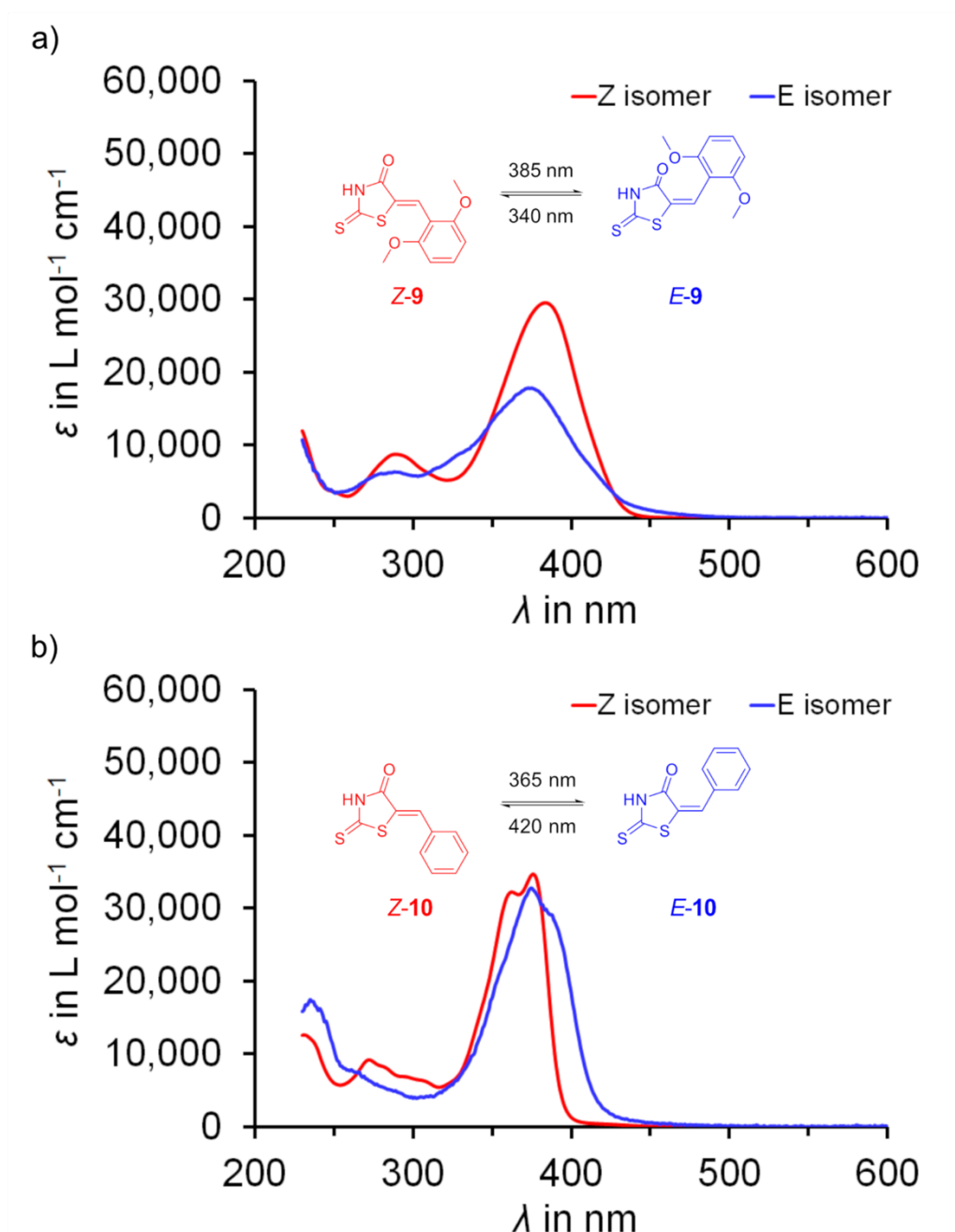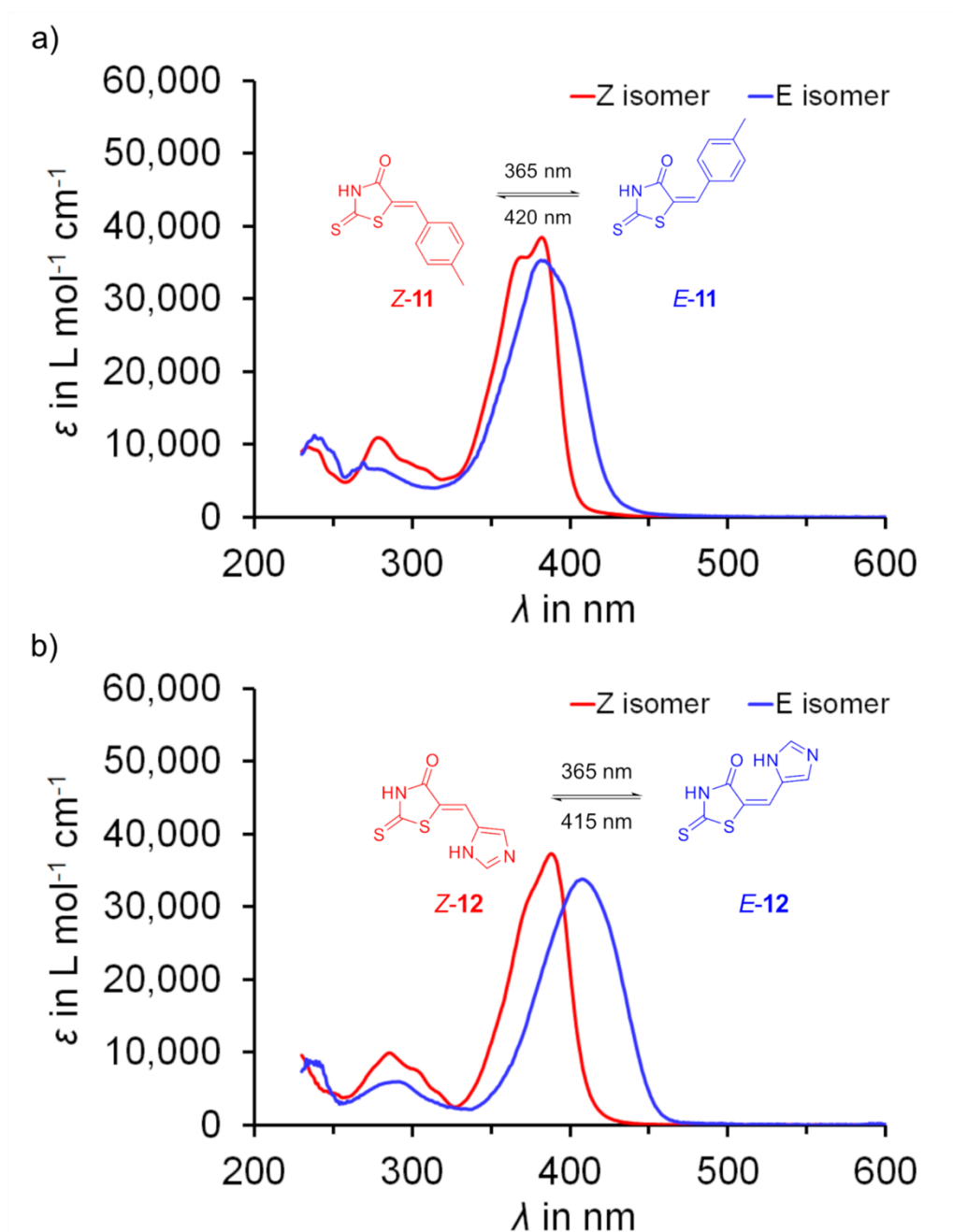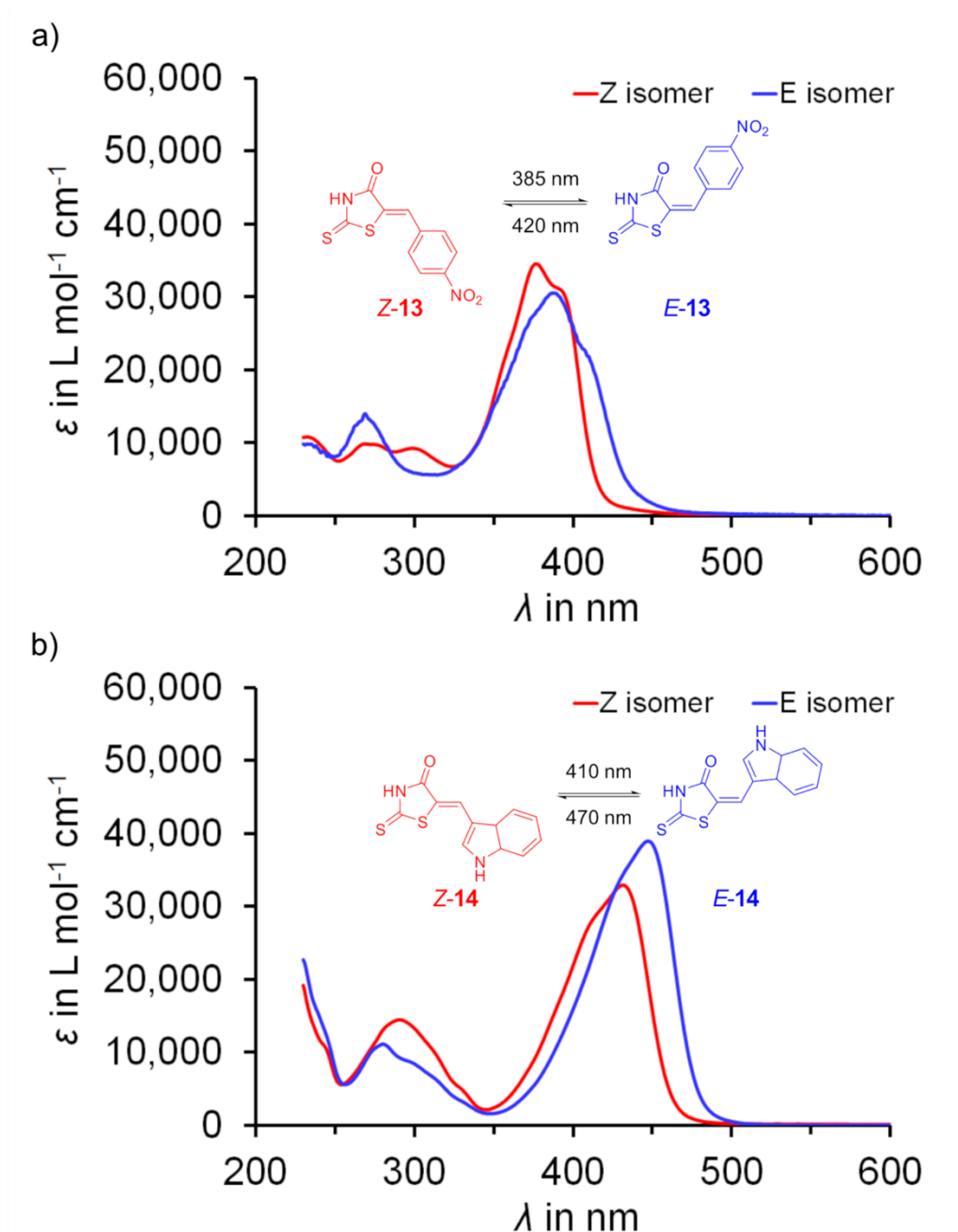
67

Quantum Yield Determination

The photochemical quantum yield of the *Z*/*E* photoisomerization $\Phi_{Z \to E}$ and the *E*/*Z* photoisomerization $\Phi_{E \to Z}$, respectively were determined by using the instrumental setup developed by the group of *E. Riedle*.[2] The photochemical quantum yield Φ of a particular wavelength is calculated from the ratio between the number of isomerized molecules and the number of absorbed photons, see equation 2:

$$\Phi = \frac{N(isomerized\ molecules)}{N(absorbed\ photons)} \qquad \text{eq. 2}$$

Therefore, a solution of each compound in THF (2.00 mL) was prepared in a cuvette. The sample was irradiated at the isosbestic point (IP) with a certain wavelength for distinct time intervals after which the power and the degree of isomerization by UV Vis were measured.

The determined values of the photochemical quantum yields $\Phi_{Z \to E}$ and $\Phi_{E \to Z}$ are shown in Table S5.

Table S5   Comparison of photochemical quantum yield of *Z*/*E* isomerization $\Phi_{Z \to E}$ and *E*/*Z* isomerization $\Phi_{E \to Z}$ of rhodanine based photoswitches **1 – 14** in tetrahydrofuran at 23 °C.

	$\Phi_{Z \to E}$	$\Phi_{E \to Z}$	λ_{LED}
1	36%	33%	365 nm
2	36%	34%	400 nm
3	28%	28%	400 nm
4	34%	11%	365 nm
5	36%	38%	400 nm
6	26%	27%	450 nm
7	37%	25%	425 nm
8	40%	21%	400 nm
9	39%	39%	340 nm
10	29%	37%	365 nm
11	32%	38%	365 nm
12	37%	36%	400 nm
13	22%	50%	425 nm
14	35%	19%	425 nm

Starting from a *Z/E* mixture the photochemical quantum yields $\Phi_{Z \to E}$ and $\Phi_{E \to Z}$ of **1** were measured by irradiating the sample ($c = 5 \cdot 10^{-5}$ mol L^{-1}) with 365 nm (3.24 V, 0.10 A). UV Vis spectra were taken immediately after irradiating for certain time intervals at 23 °C. The sample was irradiated for about 240 s in total. In Figure S41 the *Z/E* isomerization and the change of concentration of *Z* and *E* isomer over time is shown.

Figure S41   Determination of the photochemical quantum yield of **1** in THF at 23 °C. a) UV Vis spectra of *Z/E* isomerization and b) change of concentration of *Z* and *E* isomer of **1** after irradiating with 365 nm for over 240 s.

Starting from a *Z/E* mixture the photochemical quantum yields $\Phi_{Z \to E}$ and $\Phi_{E \to Z}$ of **2** were measured by irradiating the sample ($c = 3 \cdot 10^{-5}$ mol L^{-1}) with 400 nm (3.08 V, 0.08 A). UV Vis spectra were taken immediately after irradiating for certain time intervals at 23 °C. The sample was irradiated for about 330 s in total. In Figure S42 the *Z/E* isomerization and the change of concentration of *Z* and *E* isomer over time is shown.
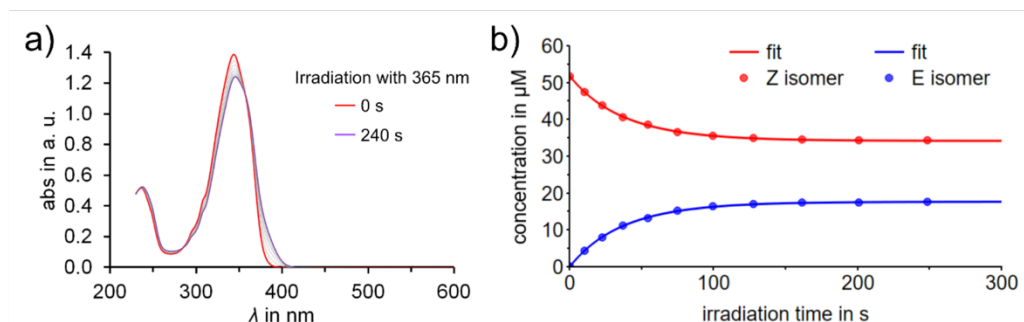

Figure S42   Determination of the photochemical quantum yield of **2** in THF at 23 °C. a) UV Vis spectra of *Z/E* isomerization and b) change of concentration of *Z* and *E* isomer of **2** after irradiating with 400 nm for over 330 s.

Starting from a *Z/E* mixture the photochemical quantum yields $\Phi_{Z \to E}$ and $\Phi_{E \to Z}$ of **3** were measured by irradiating the sample ($c = 8 \cdot 10^{-5}$ mol L^{-1}) with 400 nm (3.07 V, 0.08 A). UV Vis spectra were taken immediately after irradiating for certain time intervals at 23 °C. The sample was irradiated for about 660 s in total. In Figure S43 the *Z/E* isomerization and the change of concentration of *Z* and *E* isomer over time is shown.
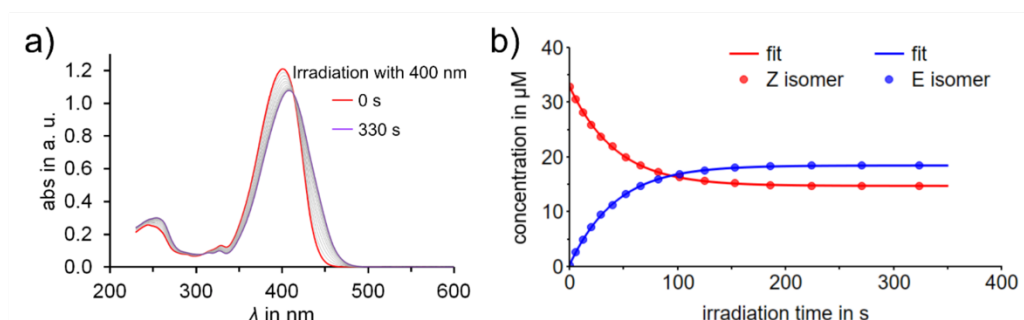
69

Figure S43   Determination of the photochemical quantum yield of **3** in THF at 23 °C. a) UV Vis spectra of *Z*/*E* isomerization and b) change of concentration of *Z* and *E* isomer of **3** after irradiating with 400 nm for over 660 s.

Starting from a *Z*/*E* mixture the photochemical quantum yields $\Phi_{Z\rightarrow E}$ and $\Phi_{E\rightarrow Z}$ of **4** were measured by irradiating the sample (c = 5·10⁻⁵ mol L⁻¹) with 365 nm (3.25 V, 0.10 A). UV Vis spectra were taken immediately after irradiating for certain time intervals at 23 °C. The sample was irradiated for about 360 s in total. In Figure S44 the *Z*/*E* isomerization and the change of concentration of *Z* and *E* isomer over time is shown.

Figure S44   Determination of the photochemical quantum yield of **4** in THF at 23 °C. a) UV Vis spectra of *Z*/*E* isomerization and b) change of concentration of *Z* and *E* isomer of **4** after irradiating with 365 nm for over 360 s.

Starting from a *Z*/*E* mixture the photochemical quantum yields $\Phi_{Z\rightarrow E}$ and $\Phi_{E\rightarrow Z}$ of **5** were measured by irradiating the sample (c = 3·10⁻⁵ mol L⁻¹) with 400 nm (3.08 V, 0.08 A). UV Vis spectra were taken immediately after irradiating for certain time intervals at 23 °C. The sample was irradiated for about 210 s in total. In Figure S45 the *Z*/*E* isomerization and the change of concentration of *Z* and *E* isomer over time is shown.
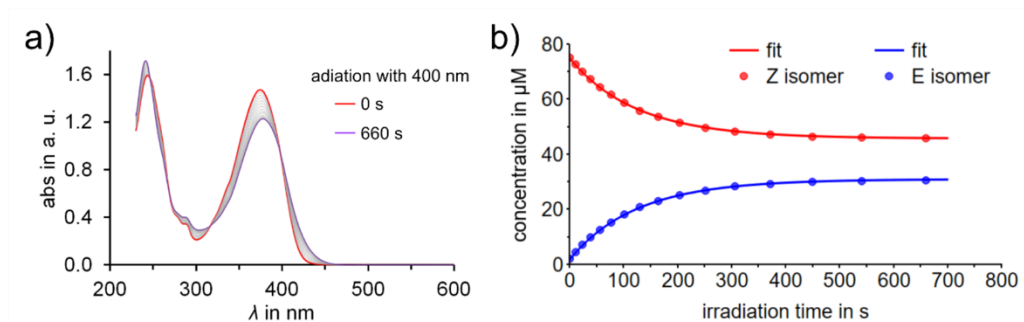
70

Figure S45   Determination of the photochemical quantum yield of **5** in THF at 23 °C. a) UV Vis spectra of *Z*/*E* isomerization and b) change of concentration of *Z* and *E* isomer of **5** after irradiating with 400 nm for over 210 s.

Starting from a *Z*/*E* mixture the photochemical quantum yields $\Phi_{Z \rightarrow E}$ and $\Phi_{E \rightarrow Z}$ of **6** were measured by irradiating the sample (c = 3·10^{-5} mol L^{-1}) with 450 nm (2.70 V, 0.05 A). UV Vis spectra were taken immediately after irradiating for certain time intervals at 23 °C. The sample was irradiated for 220 s in total. In Figure S46 the *Z*/*E* isomerization and the change of concentration of *Z* and *E* isomer over time is shown.
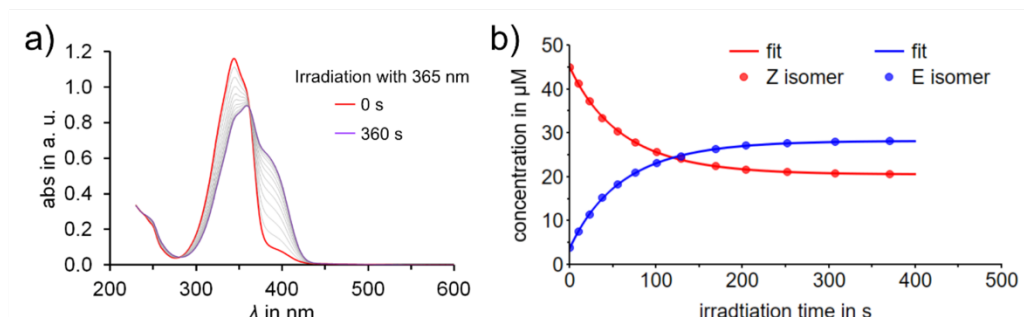

Figure S46   Determination of the photochemical quantum yield of **6** in THF at 23 °C. a) UV Vis spectra of *Z*/*E* isomerization and b) change of concentration of *Z* and *E* isomer of **6** after irradiating with 450 nm for over 220 s.

Starting from a *Z*/*E* mixture the photochemical quantum yields $\Phi_{Z \rightarrow E}$ and $\Phi_{E \rightarrow Z}$ of **7** were measured by irradiating the sample (c = 4·10^{-5} mol L^{-1}) with 425 nm (2.76 V, 0.05 A). UV Vis spectra were taken immediately after irradiating for certain time intervals at 23 °C. The sample was irradiated for 360 s in total. In Figure S47 the *Z*/*E* isomerization and the change of concentration of *Z* and *E* isomer over time is shown.
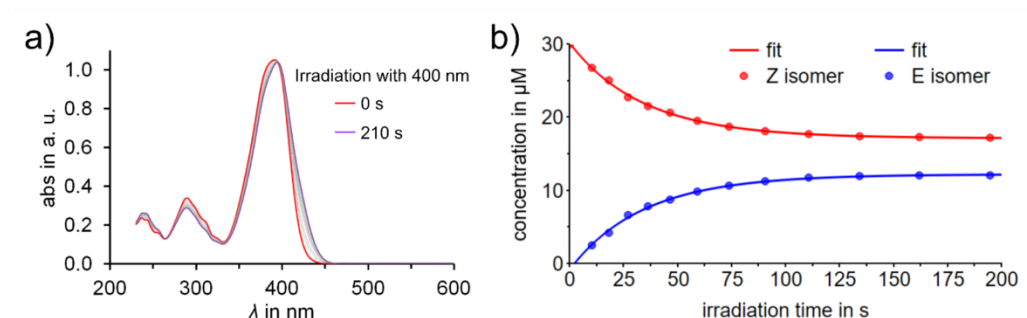
71

Figure S47   Determination of the photochemical quantum yield of **7** in THF at 23 °C. a) UV Vis spectra of *Z*/*E* isomerization and b) change of concentration of *Z* and *E* isomer of **7** after irradiating with 425 nm for over 360 s.

Starting from a *Z*/*E* mixture the photochemical quantum yields $\Phi_{Z \to E}$ and $\Phi_{E \to Z}$ of **8** were measured by irradiating the sample ($c = 6 \cdot 10^{-5}$ mol L^{-1}) with 400 nm (3.10 V, 0.10 A). UV Vis spectra were taken immediately after irradiating for certain time intervals at 23 °C. The sample was irradiated for about 550 s in total. In Figure S48 the *Z*/*E* isomerization and the change of concentration of *Z* and *E* isomer over time is shown.
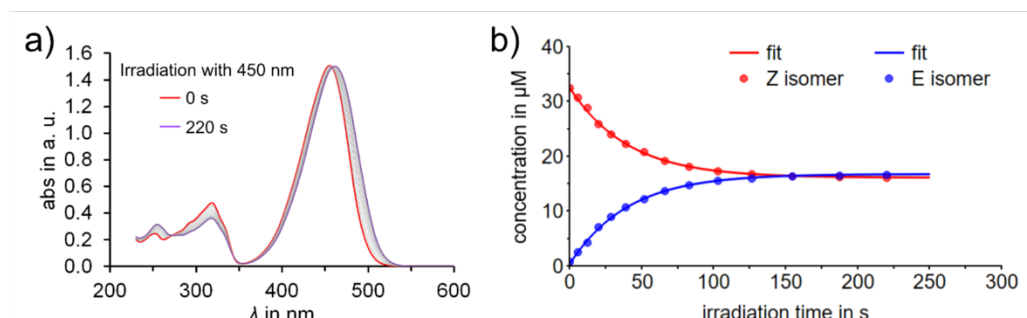

Figure S48   Determination of the photochemical quantum yield of **8** in THF at 23 °C. a) UV Vis spectra of *Z*/*E* isomerization and b) change of concentration of *Z* and *E* isomer of **8** after irradiating with 400 nm for over 550 s.

Starting from pure *Z* isomer the photochemical quantum yields $\Phi_{Z \to E}$ and $\Phi_{E \to Z}$ of **9** were measured by irradiating the sample ($c = 5 \cdot 10^{-5}$ mol L^{-1}) with 340 nm (4.83 V, 0.20 A). UV Vis spectra were taken immediately after irradiating for certain time intervals at 23 °C. The sample was irradiated for about 840 s in total. In Figure S49 the *Z*/*E* isomerization and the change of concentration of *Z* and *E* isomer over time is shown.
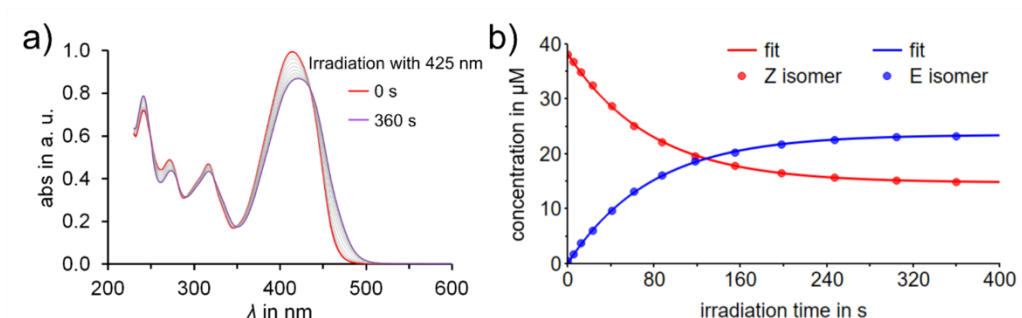
72

Figure S49   Determination of the photochemical quantum yield of **9** in THF at 23 °C. a) UV Vis spectra of *Z*/*E* isomerization and b) change of concentration of *Z* and *E* isomer of **9** after irradiating with 340 nm for over 840 s.

Starting from a *Z*/*E* mixture the photochemical quantum yields $\Phi_{Z\rightarrow E}$ and $\Phi_{E\rightarrow Z}$ of **10** were measured by irradiating the sample (c = 4·10⁻⁵ mol L⁻¹) with 365 nm (3.24 V, 0.10 A). UV Vis spectra were taken immediately after irradiating for certain time intervals at 23 °C. The sample was irradiated for 210 s in total. In Figure S50 the *Z*/*E* isomerization and the change of concentration of *Z* and *E* isomer over time is shown.

Figure S50   Determination of the photochemical quantum yield of **10** in THF at 23 °C. a) UV Vis spectra of *Z*/*E* isomerization and b) change of concentration of *Z* and *E* isomer of **10** after irradiating with 365 nm for over 210 s.

Starting from a *Z*/*E* mixture the photochemical quantum yields $\Phi_{Z\rightarrow E}$ and $\Phi_{E\rightarrow Z}$ of **11** were measured by irradiating the sample (c = 4·10⁻⁵ mol L⁻¹) with 365 nm (3.20 V, 0.07 A). UV Vis spectra were taken immediately after irradiating for certain time intervals at 23 °C. The sample was irradiated for about 240 s in total. In Figure S51 the *Z*/*E* isomerization and the change of concentration of *Z* and *E* isomer over time is shown.
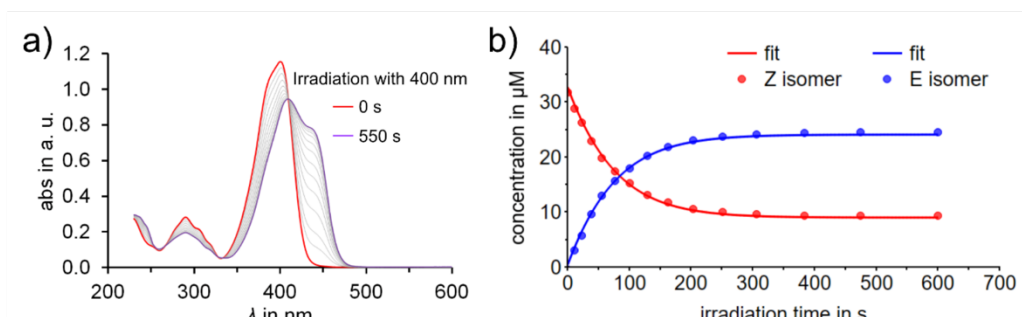
73

242

Figure S51   Determination of the photochemical quantum yield of **11** in THF at 23 °C. a) UV Vis spectra of *Z/E* isomerization and b) change of concentration of *Z* and *E* isomer of **11** after irradiating with 365 nm for over 240 s.

Starting from a *Z/E* mixture the photochemical quantum yields $\Phi_{Z \to E}$ and $\Phi_{E \to Z}$ of **12** were measured by irradiating the sample ($c = 5 \cdot 10^{-5}$ mol L^{-1}) with 400 nm (3.07 V, 0.08 A). UV Vis spectra were taken immediately after irradiating for certain time intervals at 23 °C. The sample was irradiated for about 270 s in total. In Figure S52 the *Z/E* isomerization and the change of concentration of *Z* and *E* isomer over time is shown.
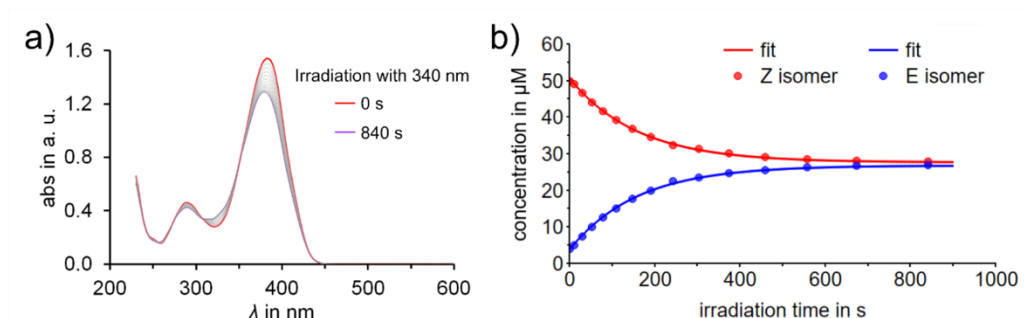

Figure S52   Determination of the photochemical quantum yield of **12** in THF at 23 °C. a) UV Vis spectra of *Z/E* isomerization and b) change of concentration of *Z* and *E* isomer of **12** after irradiating with 400 nm for over 270 s.

Starting from a *Z/E* mixture the photochemical quantum yields $\Phi_{Z \to E}$ and $\Phi_{E \to Z}$ of **13** were measured by irradiating the sample ($c = 5 \cdot 10^{-5}$ mol L^{-1}) with 400 nm (3.08 V, 0.08 A). UV Vis spectra were taken immediately after irradiating for certain time intervals at 23 °C. The sample was irradiated for 300 s in total. In Figure S53 the *Z/E* isomerization and the change of concentration of *Z* and *E* isomer over time is shown.
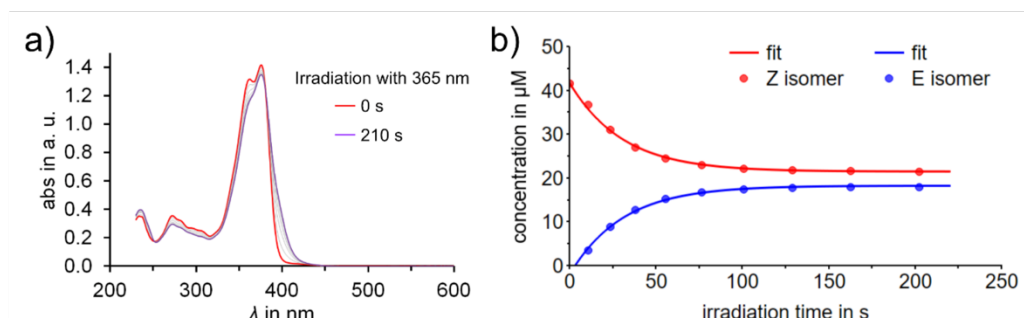
74
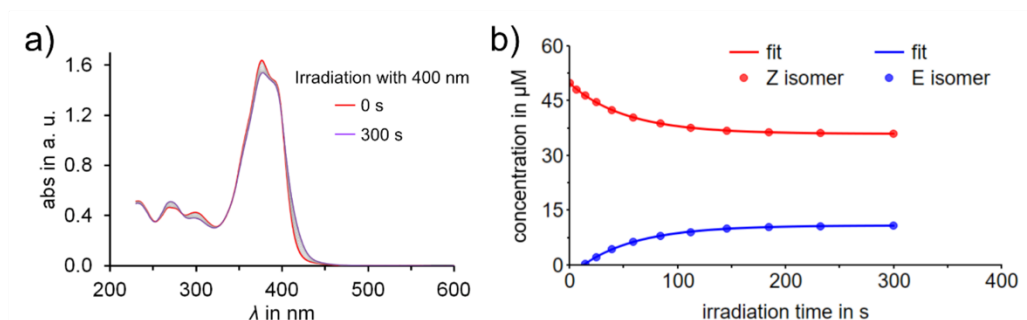
Figure S53   Determination of the photochemical quantum yield of **13** in THF at 23 °C. a) UV Vis spectra of *Z/E* isomerization and b) change of concentration of *Z* and *E* isomer of **13** after irradiating with 400 nm for over 300 s.

Starting from a *Z/E* mixture the photochemical quantum yields $\Phi_{Z\to E}$ and $\Phi_{E\to Z}$ of **14** were measured by irradiating the sample ($c = 5 \cdot 10^{-5}$ mol L^{-1}) with 425 nm (2.76 V, 0.05 A). UV Vis spectra were taken immediately after irradiating for certain time intervals at 23 °C. The sample was irradiated for about 600 s in total. In Figure S54 the *Z/E* isomerization and the change of concentration of *Z* and *E* isomer over time is shown.
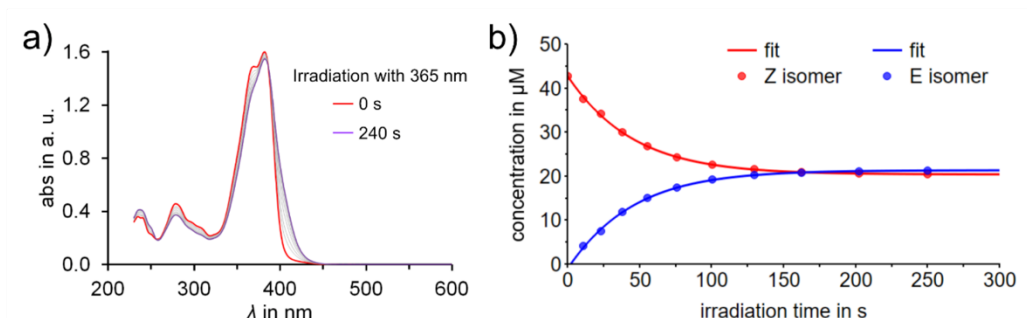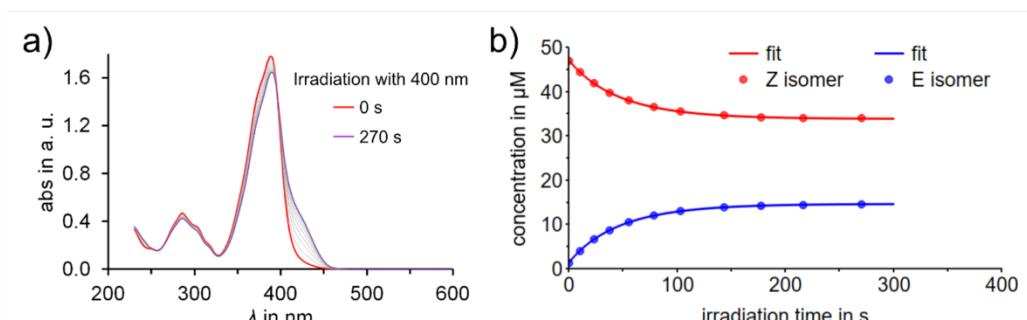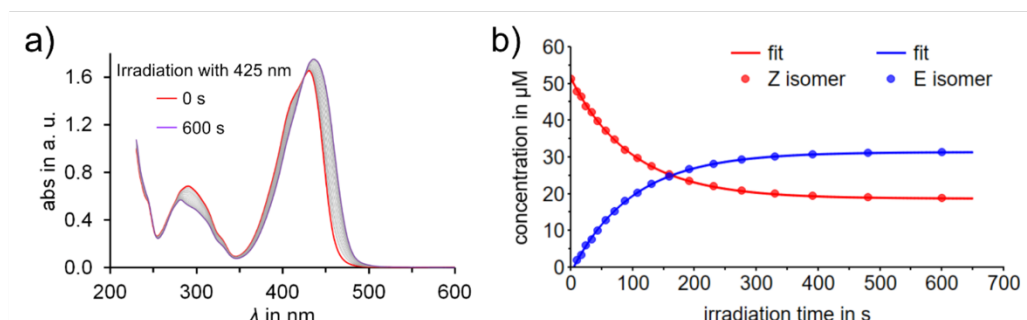

Figure S54   Determination of the photochemical quantum yield of **14** in THF at 23 °C. a) UV Vis spectra of *Z/E* isomerization and b) change of concentration of *Z* and *E* isomer of **14** after irradiating with 425 nm for over 600 s.

75

Conformational analysis in solution

To determine whether the *Z* or *E* isomer is present in solution, suitable proton signals in the corresponding ^{1}H NMR spectra can be analyzed. Therefore, the ^{1}H NMR spectra of the isomerically pure photoswitch (typically the thermodynamically most stable state) in tetrahydrofuran-d_8 was compared to the ^{1}H NMR spectra of an isomeric mixture. The difference between the chemical shifts $\Delta\delta$ of the protons **a** and the difference between the protons **b** were calculated for both isomers with the following eq. 5:

$$\Delta\delta(H_x) = \delta_Z - \delta_E \qquad \text{eq. 5}$$

x = a, b

Table S6   Difference of the chemical shifts $\Delta\delta$ of the proton signals **a** and **b** between the *Z* and *E* isomers of photoswitches **1** – **14** in the respective ^{1}H NMR spectra (400 MHz, THF-d_8, 25 °C).

	$\Delta\delta(H_a)$ [ppm]	$\Delta\delta(H_b)$ [ppm]
1	0.06	0.63
2	0.00	0.74
3	0.00	0.70
4	0.77	0.44
5	0.23	0.44
6	0.23	0.51
7	0.30	0.43
8	0.42	0.19
9	0.14	0.91
10	0.22	0.38
11	0.23	0.41
12	0.33	0.22
13	0.26	0.34
14	0.14	0.33

Z isomer   **E isomer**

downfield shift   upfield shift
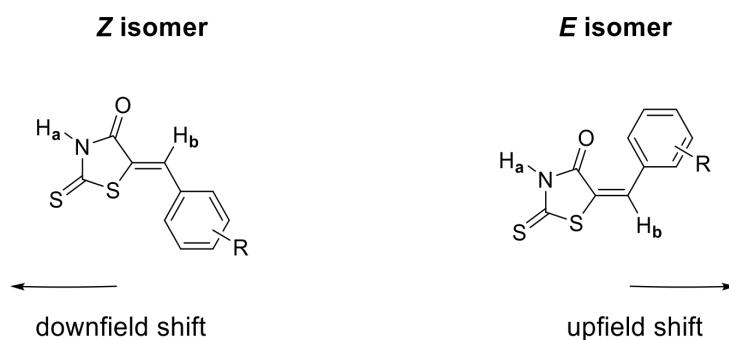
Figure S55   Chemical shifts in ^{1}H NMR spectra of *Z* and *E* isomers. Proton **a** of *Z* isomers show a downfield shift, whereas for *E* isomers an upfield shift of protons **a** occur. Interactions of the carbonyl group and proton **b** cause proton **b** of the *Z* isomers to shift downfield as well. Proton **b** of *E* isomers shift upfield.

As shown in Table S6 the protons **a** and **b** of the *Z* isomers are always downfield shifted and for the *E* isomers upfield shifted. Interactions of the carbonyl group and proton **b** causes proton **b** of the *Z* isomers to shift downfield as well.

Photophysical and thermal measurements for biological applications

Concept
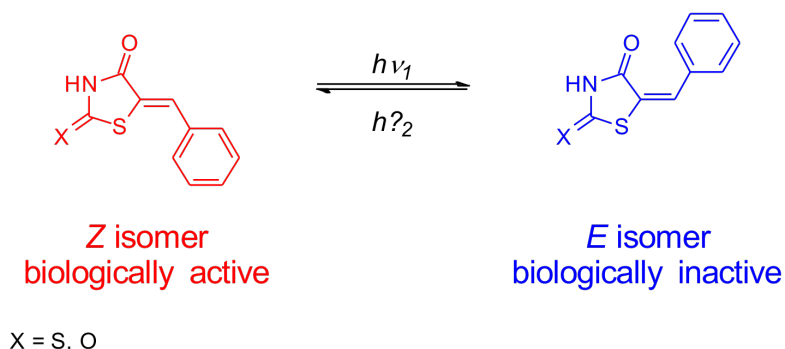
Figure S56   Schematic presentation of the concept. The *Z* isomer (red) is the biological active isomer and the *E* isomer (blue) is the biological inactive isomer.

Photoswitch **1** in its *Z* isomeric form is a known PIM-1 protein kinase inhibitor.[3–6] However, the *E* isomer was to the best of our knowledge not scrutinized for biological activity before. Photoswitches **5** and **8** were additionally investigated if biological activity is present. To get a deeper insight into the photochemical and thermal isomerization behavior of these four switches irradiation experiments in DMSO and 1% DMSO/ PBS buffer solution were conducted.

Separation of *E* isomers using HPLC

For the biological pre-experiments, the *E* isomers of **1**, **5** and **8** were isolated using HPLC. Therefore, the *Z* isomers were each solved in the mobile phase and irradiated with a certain wavelength to enrich the instable *E* isomer. Afterwards HPLC was performed to separate the *Z/E* mixture.

1: SiO_2, 95% *i*-hex, 3.75% EtOAc, 1.25% *i*-prop

5: SiO_2, 97% *i*-hex, 2.25% EtOAc, 0.75% *i*-prop

8: SiO_2, 50% *i*-hex, 37.5% EtOAc, 12.5% *i*-prop

78

Pss determination of photoswitches 1, 5, and 8 in DMSO and buffer using ^{1}H NMR spectroscopy

In Table S7 the isomeric ratio of photoswitches **1**, **5**, and **8** in the photostationary state (pss) at certain wavelengths of irradiation are shown. The isomeric ratios of Z and E isomers were obtained by ^{1}H NMR spectroscopy after reaching the pss in DMSO-d_6 at 23 °C. Therefore, pure Z isomer was irradiated with a certain wavelength to enrich the E isomer. After no further change of the isomeric ratio was observed, the E isomer enriched solution was irradiated with a second wavelength to accumulate the Z isomer.

Table S7   Isomer yields of photoswitches **1**, **5**, and **8** obtained after irradiation with different wavelengths until the respective pss was reached. Isomeric rations were determined in DMSO-d_6 solutions at 23 °C using ^{1}H NMR spectroscopy.

	$\lambda\,Z \rightarrow E$	$Z : E$	$\lambda\,E \rightarrow Z$	$Z : E$
1	340 nm	42 : 58	365 nm	97 : 3
5	395 nm	49 : 51	450 nm	91 : 9
8	385 nm	39 : 61	470 nm	98 :2

Figure S57 – Figure S59 show ^{1}H NMR spectra of rhodanine photoswitches **1**, **5**, and **8** measured at 25 °C before and after irradiation at 23 °C in DMSO-d_6 solution. Starting with 100% of the stable Z isomer, the metastable E isomer can be enriched by irradiating. Using a different wavelength the reverse E/Z photoisomerisation occurs.

79
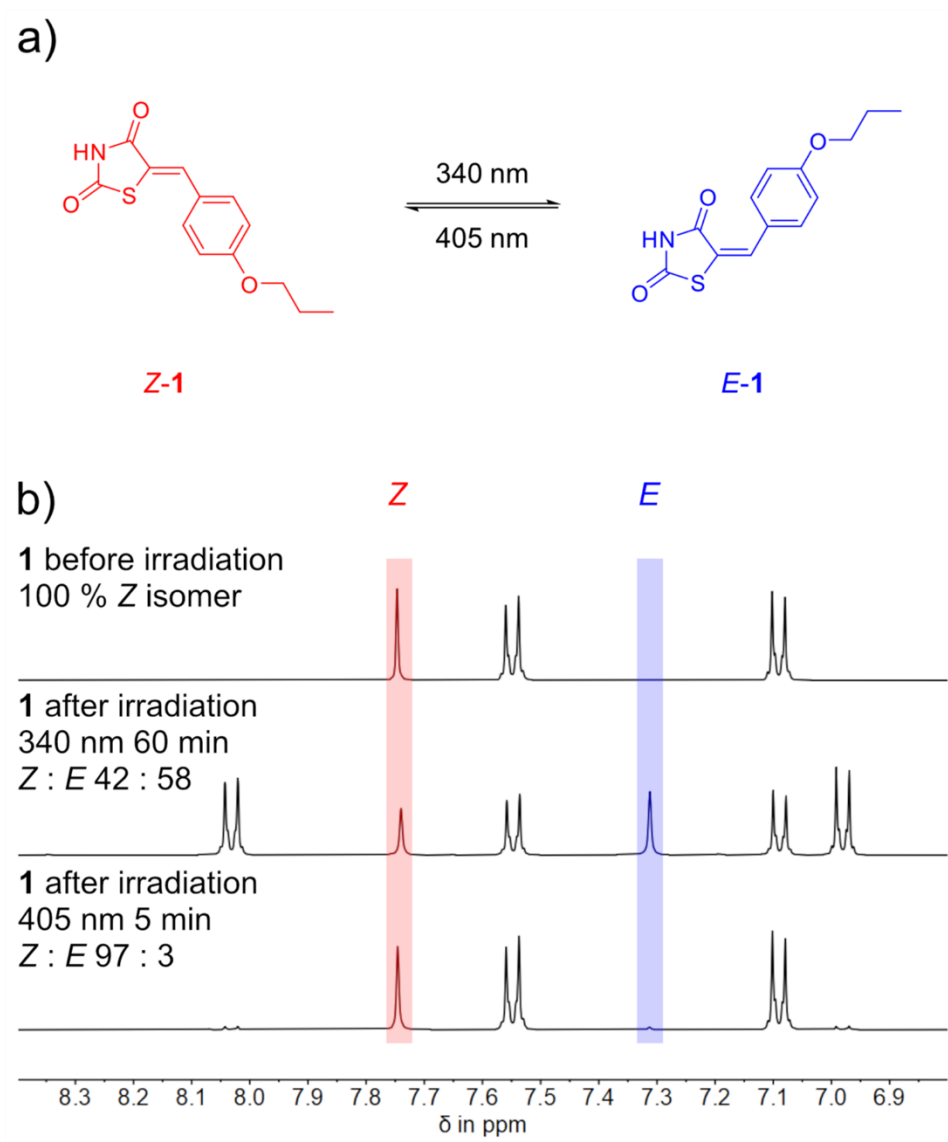
Figure S57   Determination of the *E* to *Z* isomeric ratio of **1** in the pss at different wavelengths of irradiation. a) Schematic representation of the photoisomerization. b) ^{1}H NMR spectra of photoisomerization in DMSO-d_6 at 23 °C. Starting form pure *Z* isomer irradiation with 340 nm for 60 min leads to *E* isomer (58%) enrichment. Irradiation of the resulting *Z/E* mixture with 405 nm for 5 min gives 97% of *Z* isomer.

80
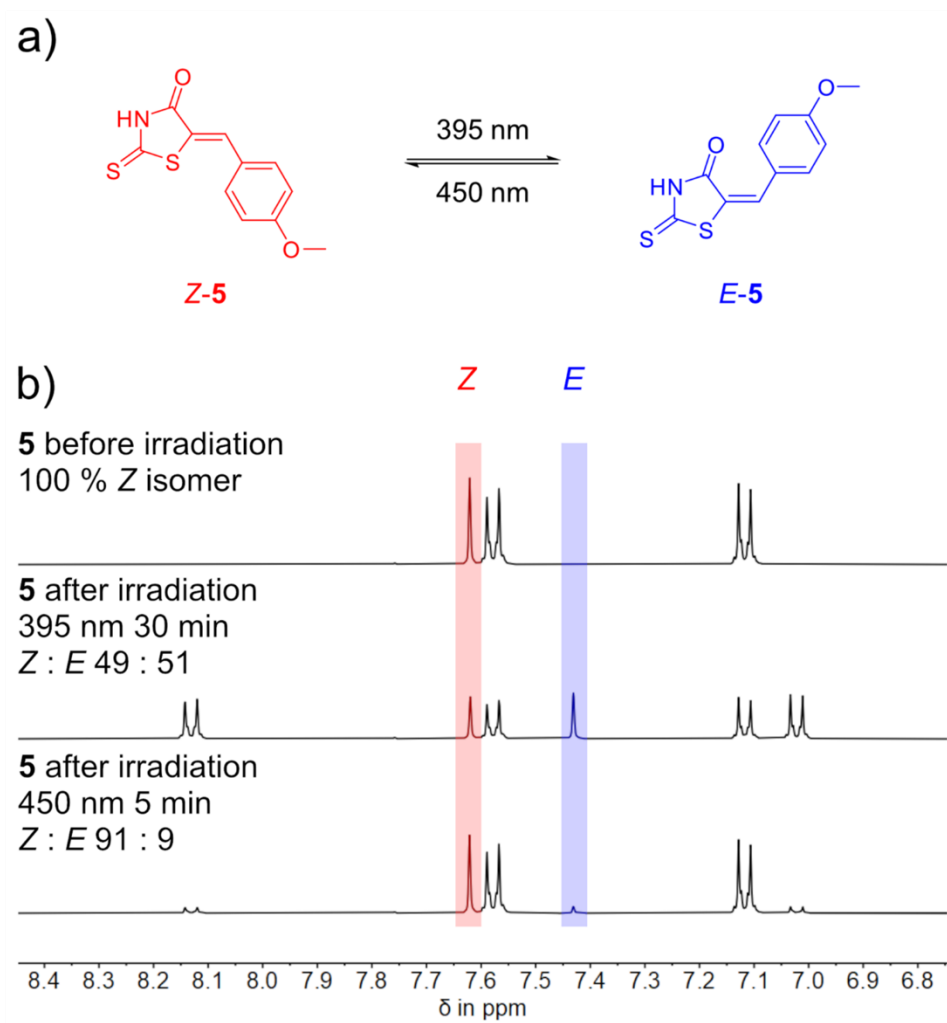
Figure S58   Determination of the *E* to *Z* isomeric ratio of **5** in the pss at different wavelengths of irradiation. a) Schematic representation of the photoisomerization. b) ^{1}H NMR spectra of the photoisomerization of **5** in DMSO-d_6 at 23 °C. Starting form pure *Z* isomer irradiation with 395 nm for 30 min leads to *E* isomer (51%) enrichment. Irradiation of the resulting *Z/E* mixture with 450 nm for 5 min gives 91% of *Z* isomer.

81
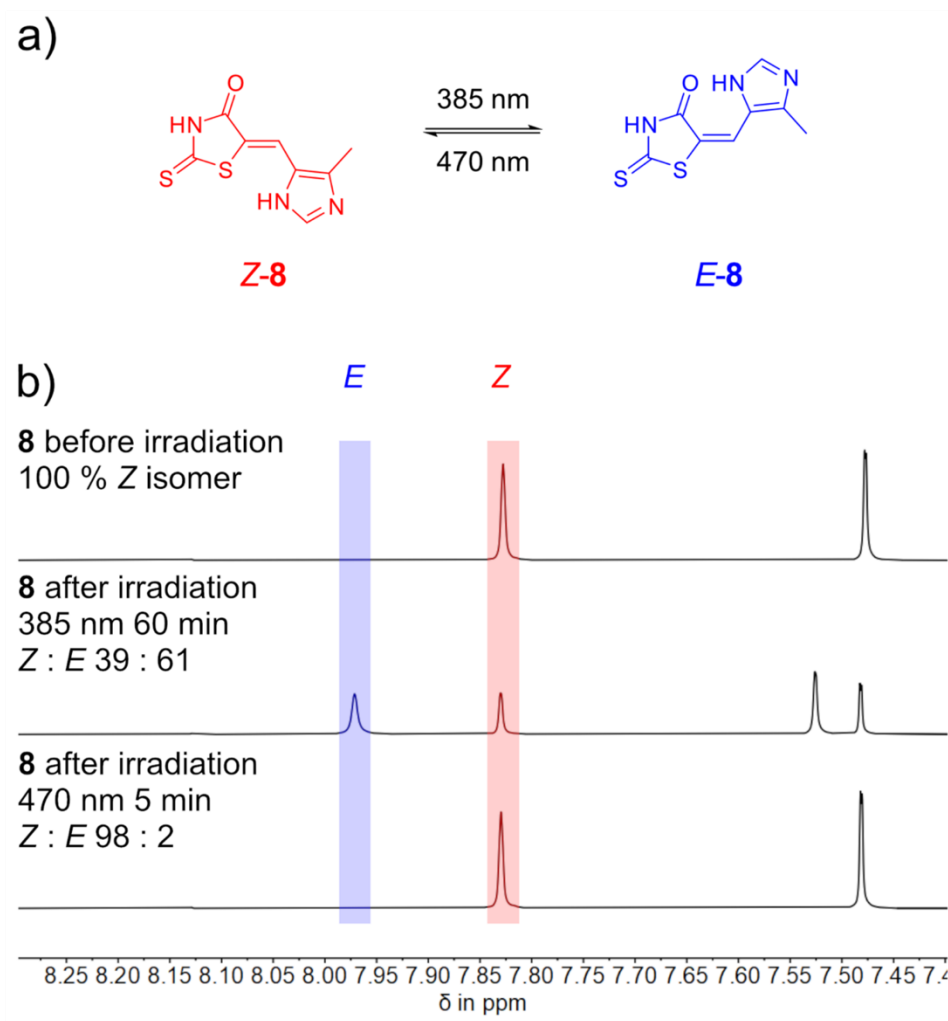
Figure S59 — Determination of the *E* to *Z* isomeric ratio of **8** in the pss at different wavelengths of irradiation. a) Schematic representation of the photoisomerization. b) ^{1}H NMR spectra of the photoisomerization of **8** in DMSO-d_6 at 23 °C. Starting form pure *Z* isomer irradiation with 385 nm for 60 min leads to *E* isomer (61%) enrichment. Irradiation of the resulting *Z/E* mixture with 470 nm for 5 min gives 98% of *Z* isomer.

82

251

Irradiation of 1, 5, and 8 in DMSO and buffer followed by UV/Vis spectroscopy

Figure S60 – Figure S62 show normalized UV/Vis spectra recorded before and after irradiation of photoswitches **1**, **5**, and **8** in 100% DMSO or in a mixture of 1% DMSO and PBS buffer at 23 °C. Starting with 100% of the stable *Z* isomer, the metastable *E* isomer can be enriched by irradiating with certain wavelengths. Irradiating with different wavelengths the reverse *E/Z* photoisomerisation is achieved.

A stock-solution (2 mM) of each pure *Z* isomer was prepared in DMSO. The respective photoswitch was then either diluted with pure DMSO or with PBS buffer to generate a 1% DMSO/PBS solution.
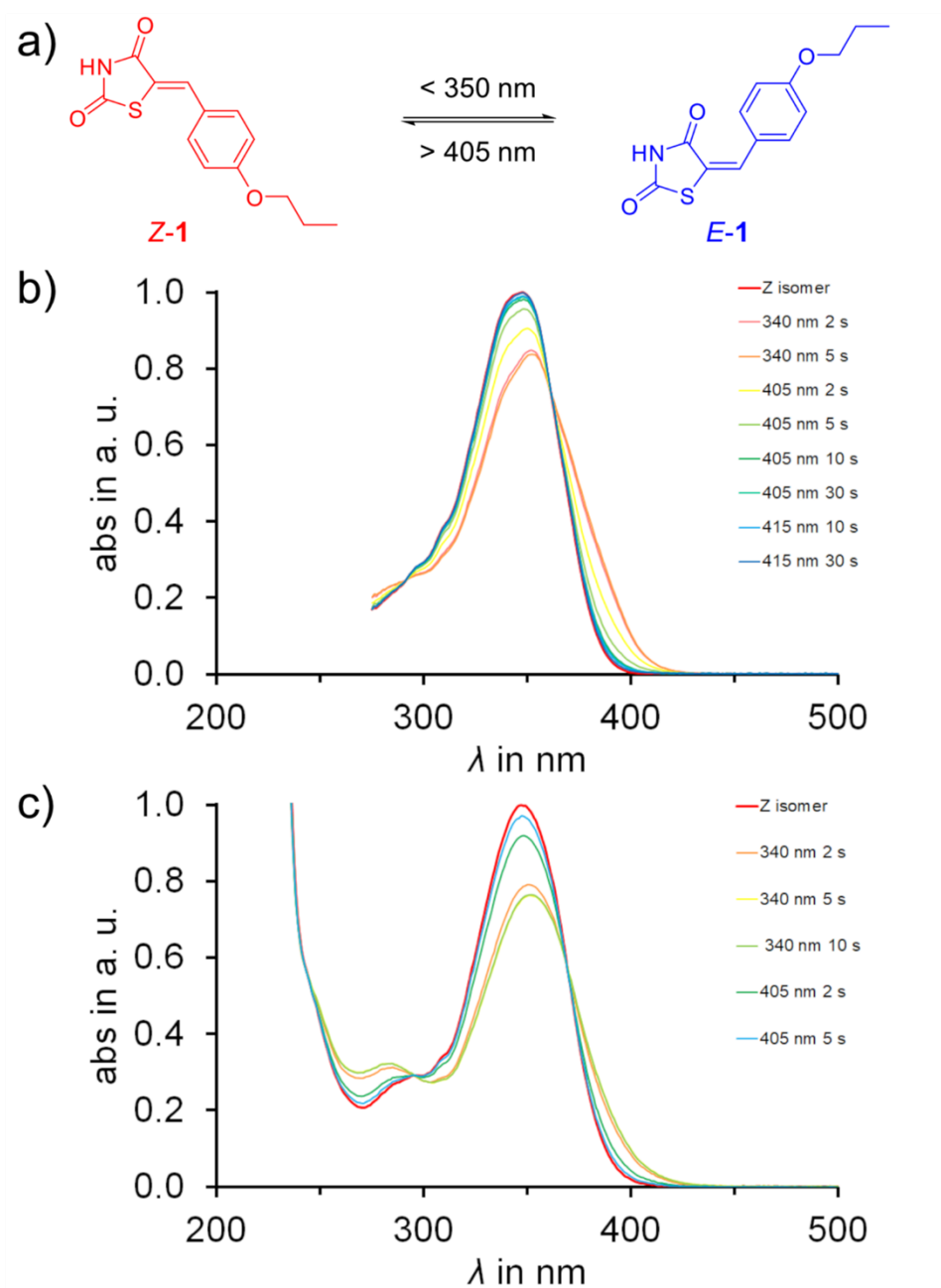
Figure S60   Photoisomerization of **1** monitored by UV/Vis spectroscopy at 23 °C. a) Schematic representation of photoisomerization. b) Photoisomerization in DMSO, normalized absorption spectra. c) Photoisomerization in 1% DMSO, PBS, normalized absorption spectra.

84

253
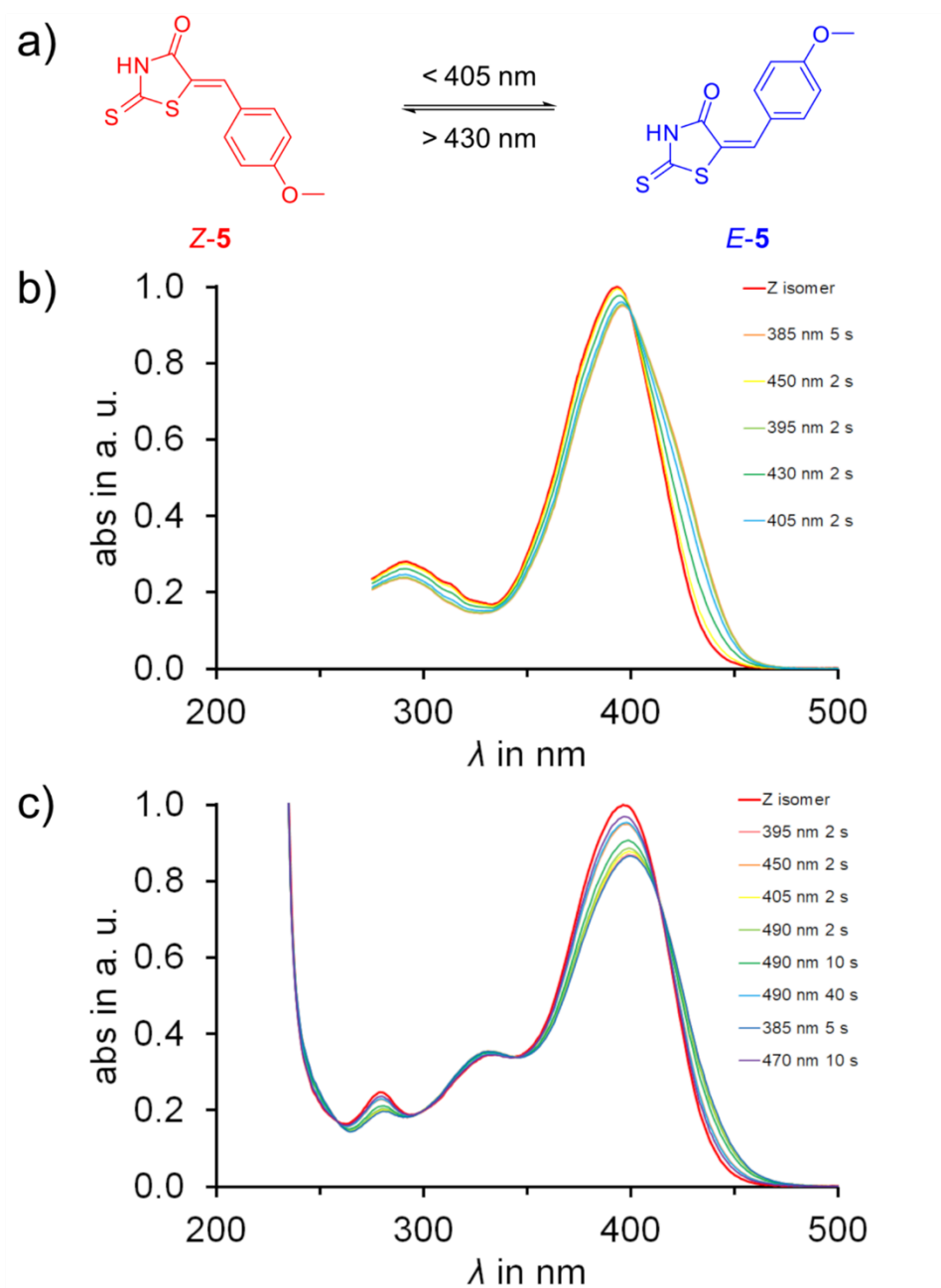
Figure S61   Photoisomerization of **5** monitored by UV/Vis spectroscopy at 23 °C. a) Schematic representation of photoisomerization. b) Photoisomerization in DMSO, normalized absorption spectra. c) Photoisomerization in 1% DMSO, PBS, normalized absorption spectra.

85
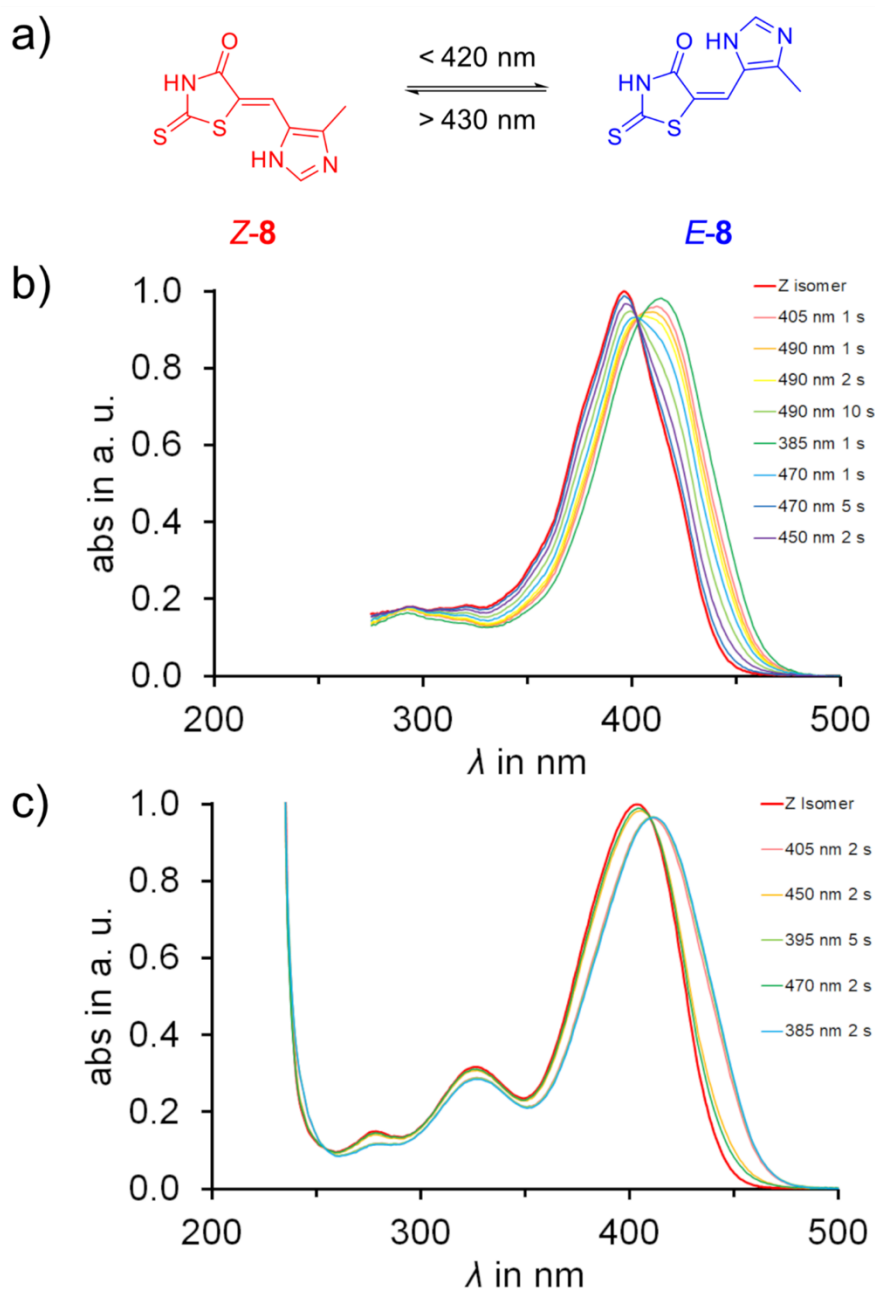
Figure S62   Photoisomerization of **8** monitored by UV/Vis spectroscopy at 23 °C. a) Schematic representation of photoisomerization. b) Photoisomerization in DMSO, normalized absorption spectra. Due to aggregation no defined isosbestic point. c) Photoisomerization in 1% DMSO, PBS, normalized absorption spectra.

86

In Table S8 the isomeric ratio of photoswitches **1**, **5**, and **8** in the photostationary state (pss) at certain wavelengths of irradiation are shown. The isomeric ratios of *Z* and *E* isomers were obtained by UV/Vis spectroscopy after reaching the pss in 1% DMSO/PBS buffer solution at 23 °C. Therefore, pure *Z* isomer was irradiated with a certain wavelength to enrich the *E* isomer. After no further change of the isomeric ratio was observed, the *E* isomer enriched solution was irradiated with a second wavelength to accumulate the *Z* isomer.

Table S8   Isomer yields of photoswitches **1**, **5**, and **8** obtained after irradiation with different wavelengths until the respective pss was reached. Isomeric rations were determined in 1% DMSO/ PBS buffer solutions at 23 °C using UV/ Vis spectroscopy.

	$\lambda\, Z \rightarrow E$	$Z : E$	$\lambda\, E \rightarrow Z$	$Z : E$
1	340 nm	39 : 61	405 nm	93 : 7
5	385 nm	35 : 65	470 nm	86 : 14
8	385 nm	25 : 75	470 nm	89 :11

Molar absorption coefficients of 1, 5, and 8 in DMSO and buffer solution

The molar absorption coefficients ε of Z isomers and E isomers were obtained directly from isomerically pure material (E isomers were isolated previously by HPLC or column chromatography) using the *Lambert-Beer* law. Table S9 summarizes the maximum wavelength and molar absorption coefficient of the most redshifted absorption in 100% DMSO or in a mixture of 1% DMSO and PBS at 23°C, as well as the difference of the maximum wavelength $\Delta\lambda_{max}$ of the most redshifted absorption band between the Z isomer and E isomer.

Table S9   Quantitative comparison of the maximum wavelength λ_{max} and molar absorption coefficients ε of most redshifted absorption of photoswitches **1**, **5**, and **8** in DMSO and buffer solution. Data were measured in DMSO or 1% DMSO and PBS buffer at 23°C.

	solvent	Z isomer		E isomer	
		λ_{max} [nm]	ε [L mol^{-1} cm^{-1}]	λ_{max} [nm]	ε [L mol^{-1} cm^{-1}]
1	DMSO	348	25,700	356	19,000
	1% DMSO, PBS	347	26,000	358	16,600
5	DMSO	393	35,800	397	33,600
	1% DMSO, PBS	396	33,900	404	27,500
8	DMSO	396	34,300	424	28,800
	1% DMSO, PBS	404	33,600	419	32,300

Figure S63 – Figure S65 show the molar absorption coefficients ε photoswitches **1**, **5** and **8** measured at 23 °C in DMSO and 1% DMSO/PBS buffer. Z isomers are shown in red, E isomers are displayed in blue.

88
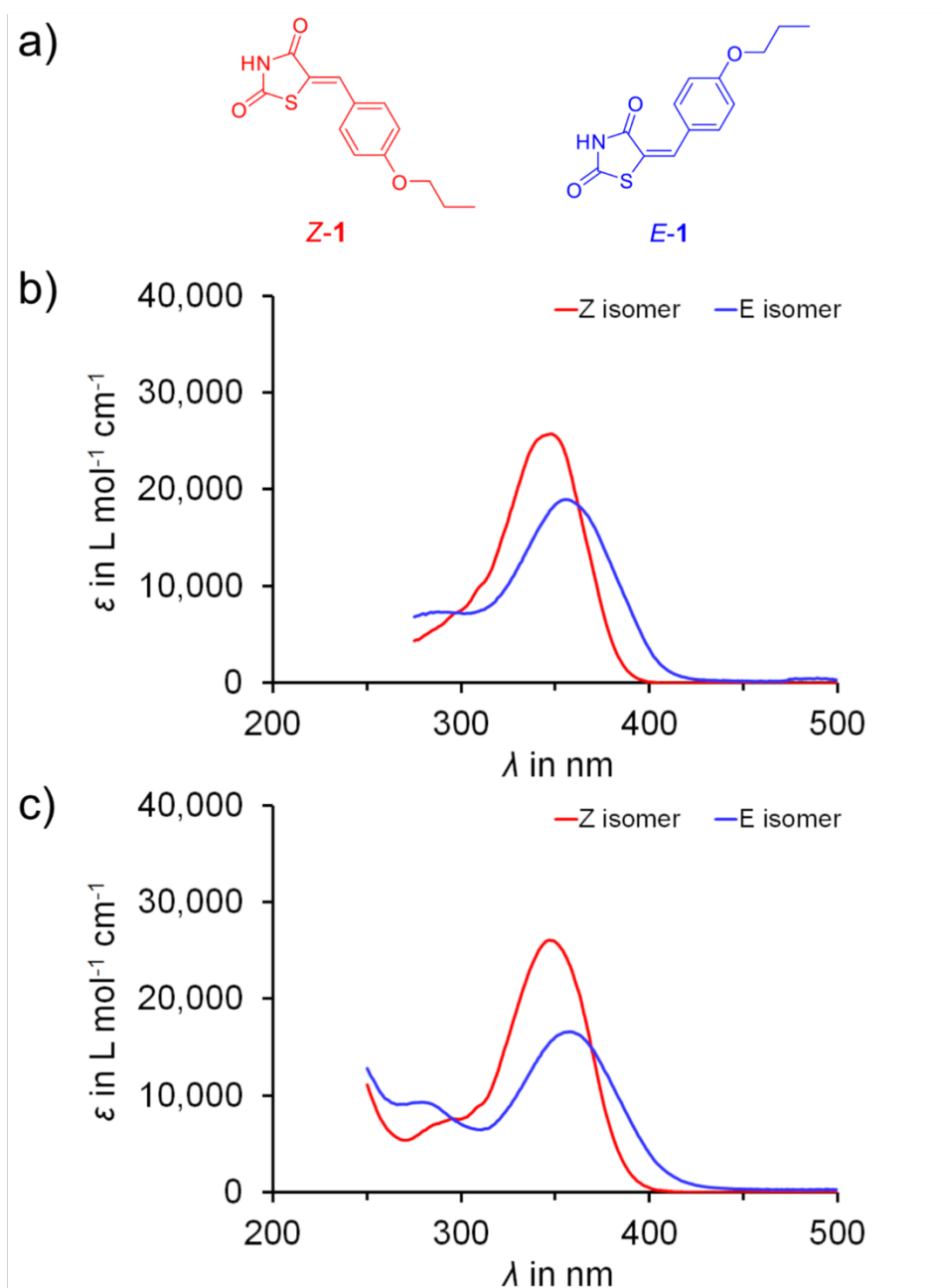
Figure S63   Molar absorption coefficients of **1** at 23 °C. a) Schematic representation of *Z* and *E* isomer. b) Molar absorption coefficients in DMSO. c) Molar Absorption coefficients in 1% DMSO/PBS.

89
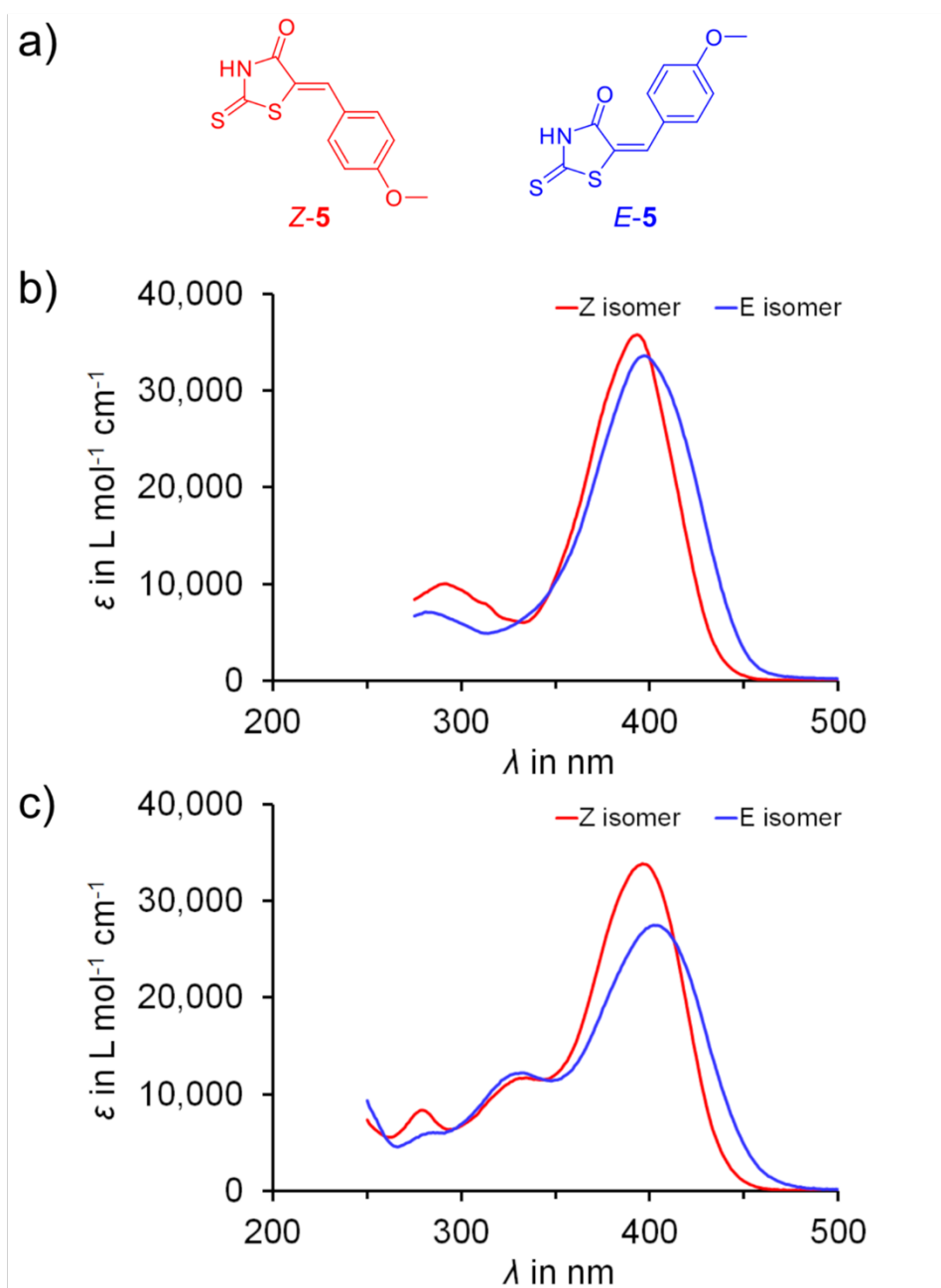
Figure S64   Molar absorption coefficients of **5** at 23 °C. a) Schematic representation of *Z* and *E* isomer. b) Molar absorption coefficients in DMSO. c) Molar extinction coefficients in 1% DMSO/PBS.

90
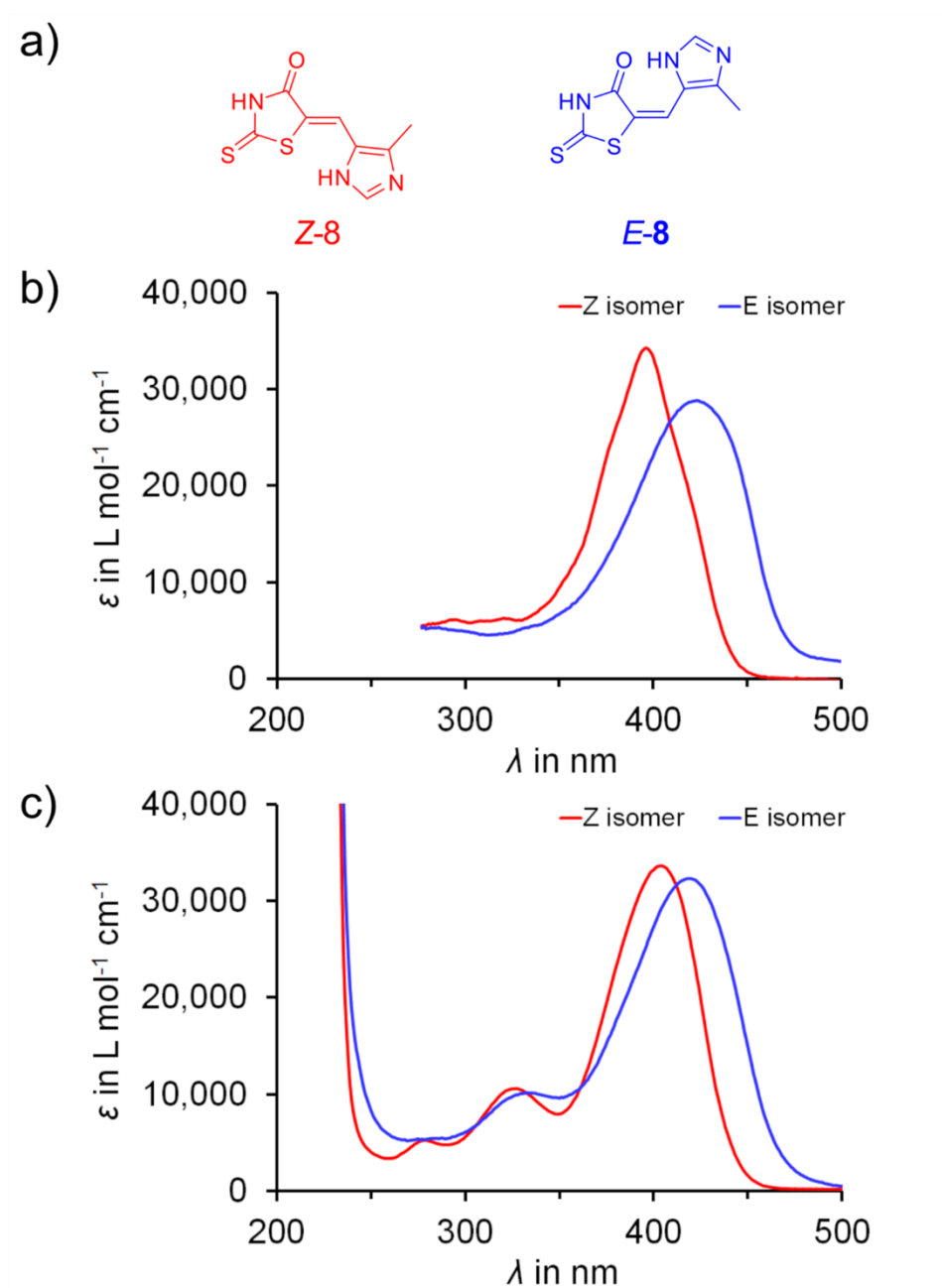
Figure S65   Molar absorption coefficients of **8** at 23 °C. a) Schematic representation of *Z* and *E* isomer. b) Molar absorption coefficients in DMSO. c) Molar extinction coefficients in 1% DMSO/PBS.

91

Thermal stability of 1, 5, and 8 in DMSO and buffer solution

Z isomers are the thermodynamically most stable forms of all (oxo)-rhodanine photoswitches. At elevated temperatures metastable *E* isomers are interconverting into *Z* isomers. Since the *E* isomer is biological inactive, it has to be stable for a longer time period in 1% DMSO/PBS buffer solution. Therefore, thermal *E* to *Z* isomerization was determined from the decay kinetics of the *E* isomers at 37 °C, respectively. A stock-solution of pure *E* isomer was prepared in DMSO. This was diluted with PBS buffer solution to achieve a final proportion of 1% DMSO. Spectra were taken immediately after placing the sample inside the UV/Vis spectrometer and after distinct time intervals at 37 °C.

Figure S66 – Figure S68 show conversion of metastable *E* isomers into stable *Z* isomers of (oxo)-rhodanine photoswitches **1**, **5** and **8** in 1% DMSO/PBS at 37 °C.

92
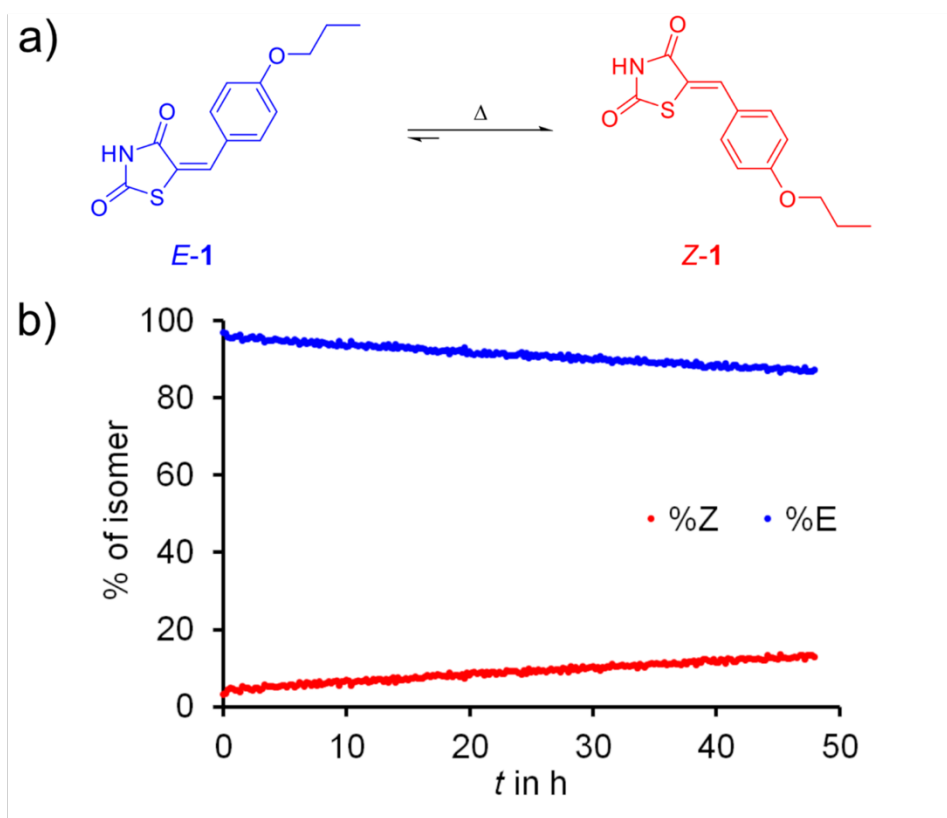
Figure S66 Thermal Stability of **1** in 1% DMSO/PBS buffer solution. a) Schematic representation of thermal isomerization from metastable *E* isomer to stable *Z* isomer. b) Conversion of isomers at 37°C.

93
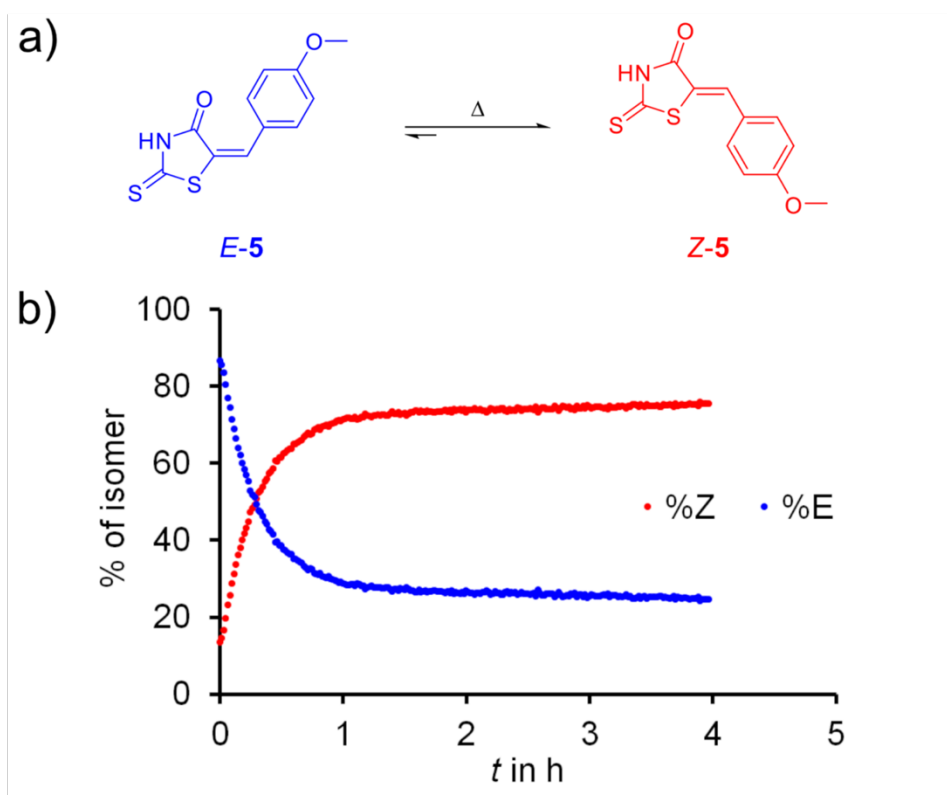
Figure S67   Thermal Stability of **5** in 1% DMSO/PBS buffer solution. a) Schematic representation of thermal isomerization from metastable *E* isomer to stable *Z* isomer. b) Conversion of isomers at 37°C.

94

263
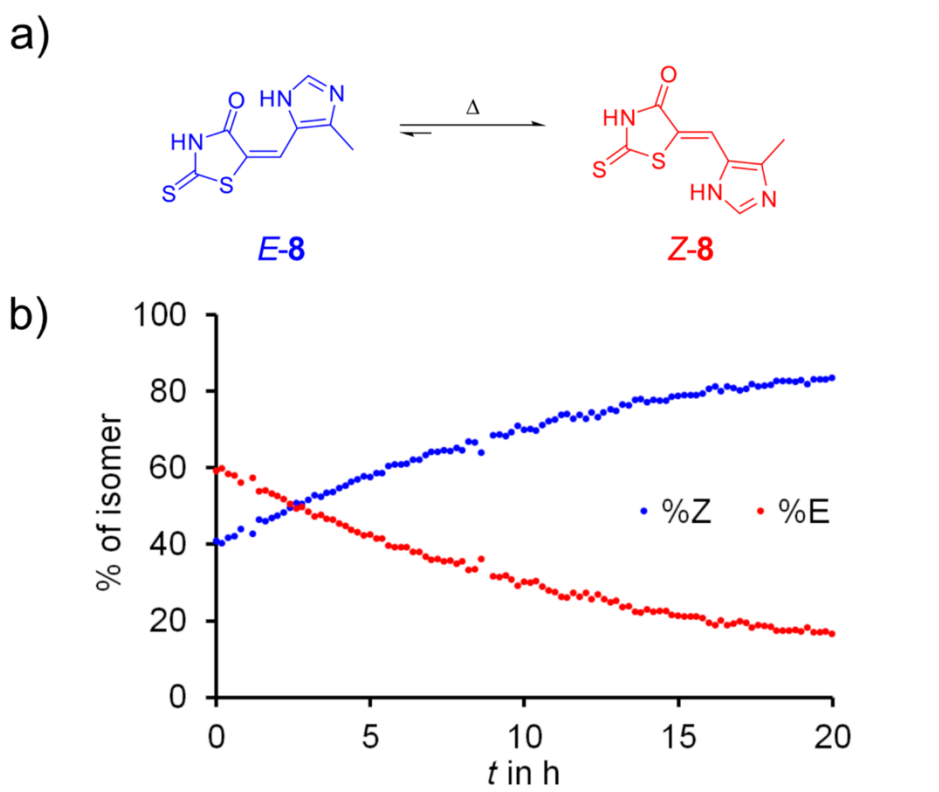
Figure S68   Thermal Stability of **8** in 1% DMSO/PBS buffer solution. a) Schematic representation of thermal isomerization from metastable *E* isomer to stable *Z* isomer. b) Conversion of isomers at 37°C.

Stability of 1, 5, and 8 against reduced glutathione (GSH)

The stability of rhodanine based photoswitches against reduced glutathione (GSH) was tested to ensure proper biocompatibility. A stock solution of GSH in DMSO/PBS buffer (1:1) with a GSH concentration of 16.3 mM and a second stock solution of a (oxo)-rhodanine based photoswitch in DMSO was prepared. To measure the stability of the photoswitches, a solution was prepared in a cuvette with a final GSH concentration of 10 mM and a final (oxo)-rhodanine photoswitch concentration of 50 µM in DMSO/PBS buffer (1:1). Spectra were taken immediately after placing the sample inside the UV Vis spectrometer and after certain time intervals at 23 °C. The experiment was performed according to a previously reported procedure.[7,8]

In Figure S69 the GSH stability of the pure Z isomer of oxo-rhodanine based photoswitch **1** is displayed. The indicative absorbance at λ = 353 nm was plotted against time.

Figure S69   Stability of pure Z isomer of oxo-rhodanine based photoswitch **1** (50 µM) against GSH (10 mM) in DMSO/PBS (1:1) at 23 °C over 600 min. The absorbance at λ = 353 nm was plotted against time.

In Figure S70 the GSH stability of enriched E isomer of oxo-rhodanine based photoswitch **1** is displayed. A solution of pure Z isomer of **1** was irradiated with 340 nm for 15 s to receive a mixture of Z and E isomer (pss ~ 50% : 50%). GSH solution was added and spectra were taken after certain time intervals for over 600 min at 23 °C. The absorbance at λ = 357 nm was plotted against time.

96

265

Figure S70   Stability of enriched *E* isomer of rhodanine based switch **1** (50 µM) against GSH (10 mM) in DMSO/PBS (1:1) at 23 °C over 600 min. The absorbance at λ = 357 nm was plotted against time.

In Figure S71 the GSH stability of the pure *Z* isomer of rhodanine based photoswitch **5** at 23 °C is displayed. The absorbance at λ = 395 nm was plotted against time.

97

Figure S71　　Stability of pure *Z* isomer of rhodanine based switch **5** (50 µM) against GSH (10 mM) in DMSO/PBS (1:1) at 23 °C over 600 min. The absorbance at λ = 395 nm was plotted against time.

In Figure S72 the GSH stability of the pure *Z* isomer of rhodanine based photoswitch **8** at 23 °C is displayed. The absorbance at λ = 408 nm was plotted against time.

Figure S72　　Stability of pure *Z* isomer of Rhodanine based switch **8** (50 µM) against GSH (10 mM) in DMSO/PBS (1:1) at 23 °C over 600 min. The absorbance at λ = 408 nm was plotted against time.

98

Further, the stability of rhodanine based photoswitches against reduced GSH was tested in MeOH/PBS. Due to low solubility of the (oxo)-rhodanines a larger amount of MeOH was needed and a 1:1 mixture of MeOH/PBS was ultimately used as solvent mixture. A stock solution of GSH in MeOH/PBS buffer (1:1) with a GSH concentration of 10.5 mM (32.5 mg in 5 mL MeOH and 5 mL PBS) and a second stock solution of a (oxo)-rhodanine based photoswitch with a concentration of 2 mM in MeOH was prepared. To measure the stability of the photoswitches, a solution was prepared in a cuvette with a final GSH concentration of 10 mM and a final (oxo)-rhodanine photoswitch concentration of 50 µM in MeOH/PBS buffer (1:1). Spectra were taken immediately after placing the sample inside the UV Vis spectrometer and after certain time intervals at 23 °C.

In Figure S73 the GSH stability of the pure Z isomer of oxo-rhodanine based photoswitch **1** in MeOH/PBS buffer is displayed. The indicative absorbance at λ = 353 nm was plotted against time.
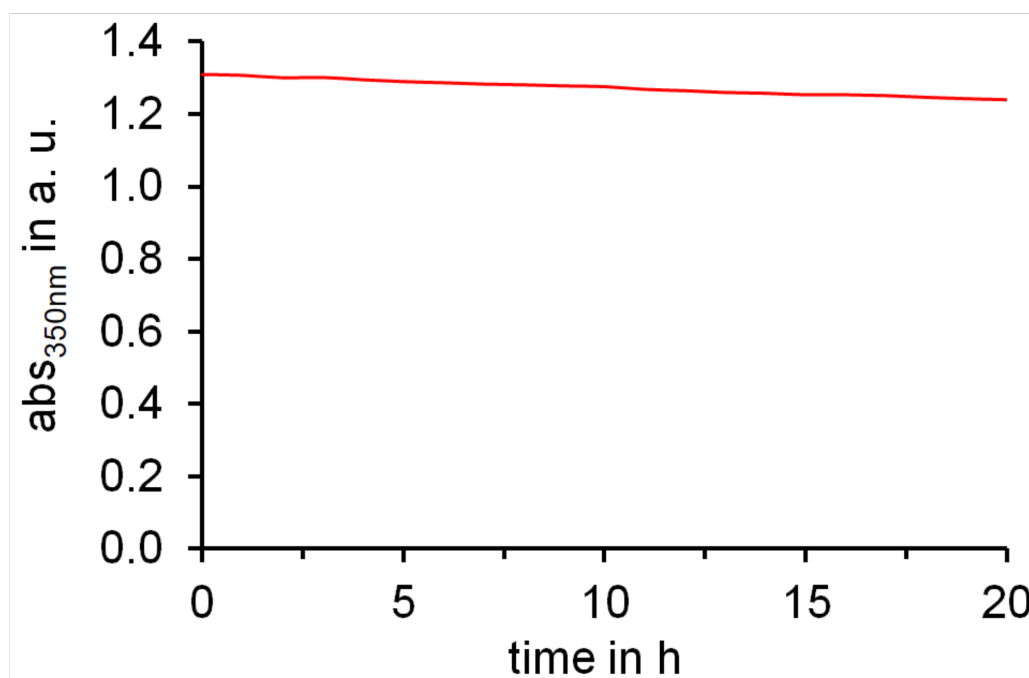
Figure S73　　Stability of pure Z isomer of Rhodanine based switch **1** (50 µM) against GSH (10 mM) in MeOH/PBS (1:1) at 23 °C over 20 h. The absorbance at λ = 350 nm was plotted against time. The concentration of the stock solution of **1** was 2.0 mM (1.00 mg in 1.90 mL MeOH).

In Figure S74 the GSH stability of the pure Z isomer of oxo-rhodanine based photoswitch **5** in MeOH/PBS buffer is displayed. The indicative absorbance at λ = 396 nm was plotted against time.

99
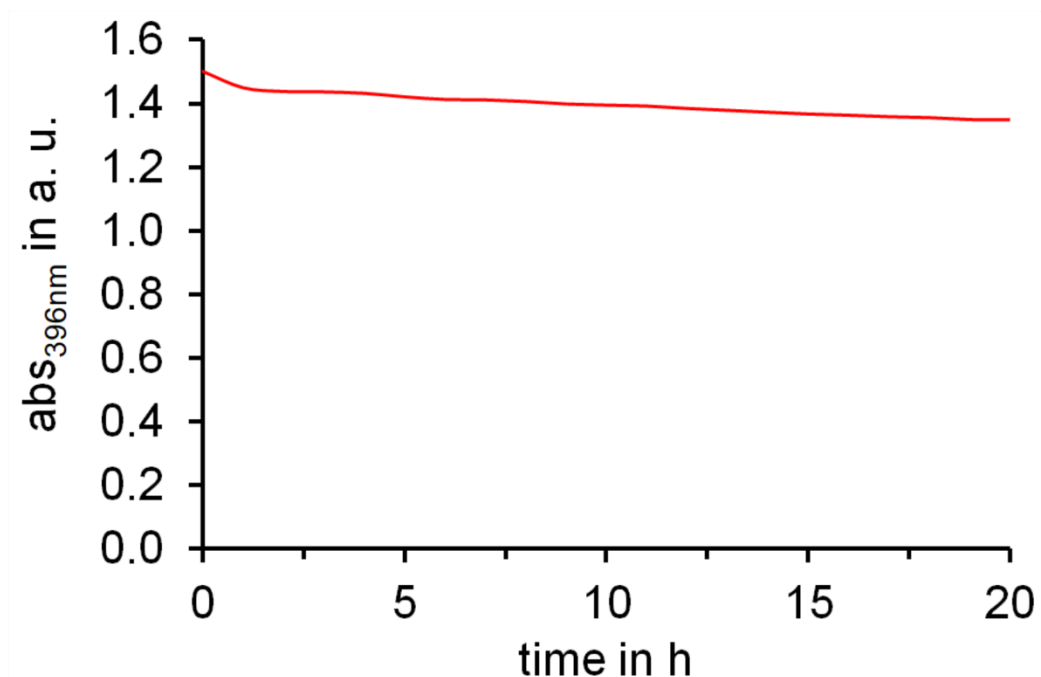
Figure S74　　　Stability of pure *Z* isomer of Rhodanine based switch **5** (50 μM) against GSH (10 mM) in MeOH/PBS (1:1) at 23 °C over 20 h. The absorbance at λ = 396 nm was plotted against time. The concentration of the stock solution of **5** was 2.0 mM (0.61 mg in 1.20 mL MeOH).

In Figure S75 the GSH stability of the pure *Z* isomer of oxo-rhodanine based photoswitch **8** in MeOH/PBS buffer is displayed. The indicative absorbance at λ = 394 nm was plotted against time.

100

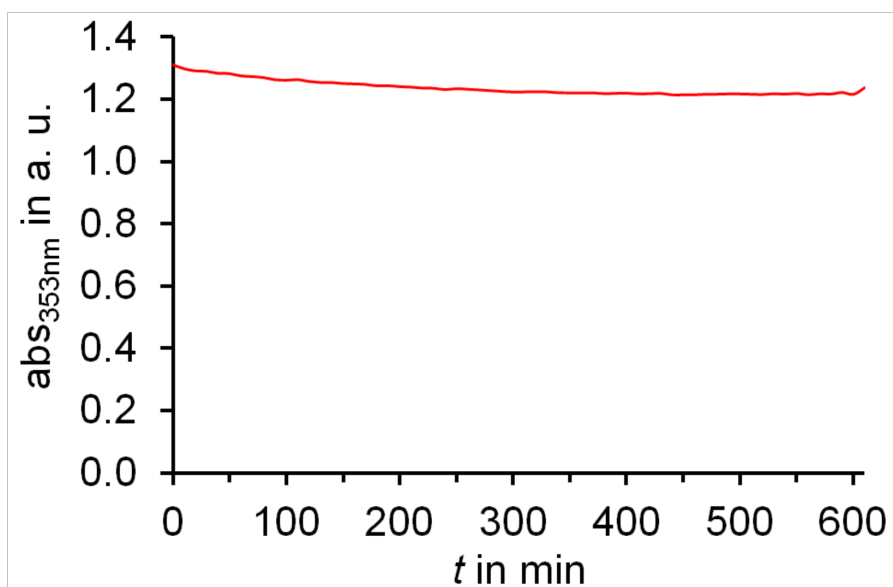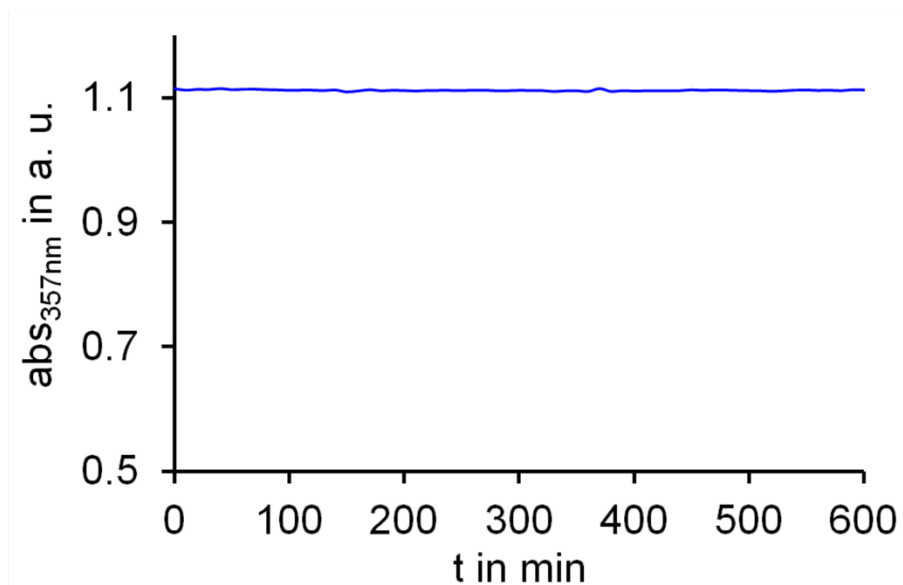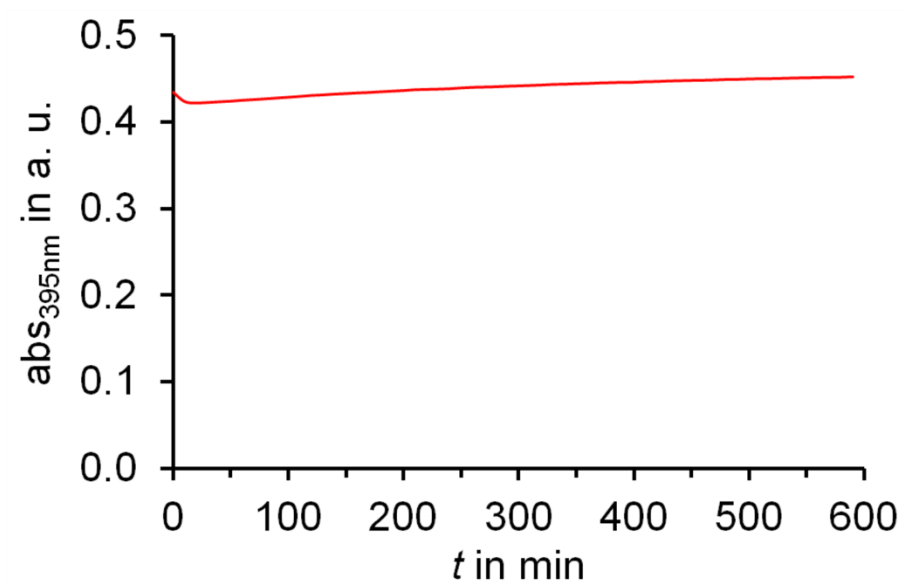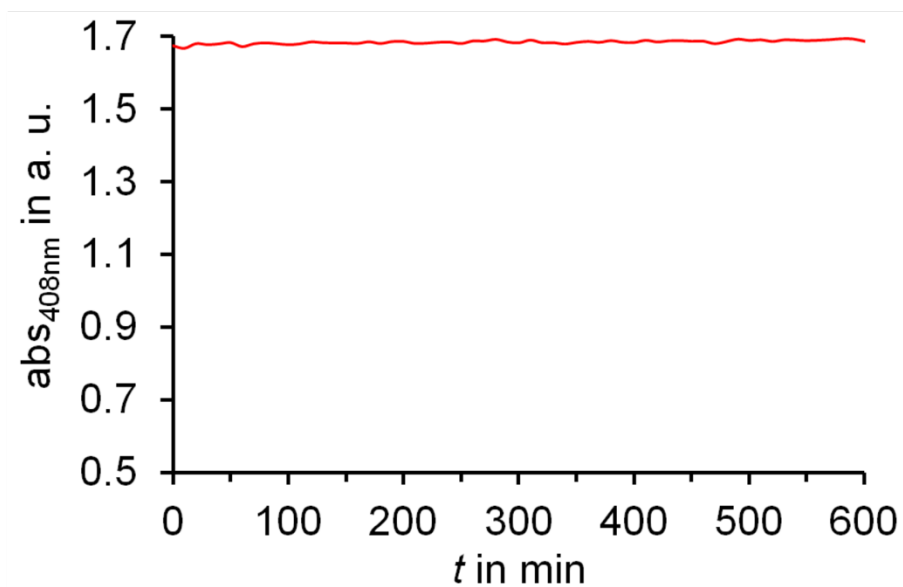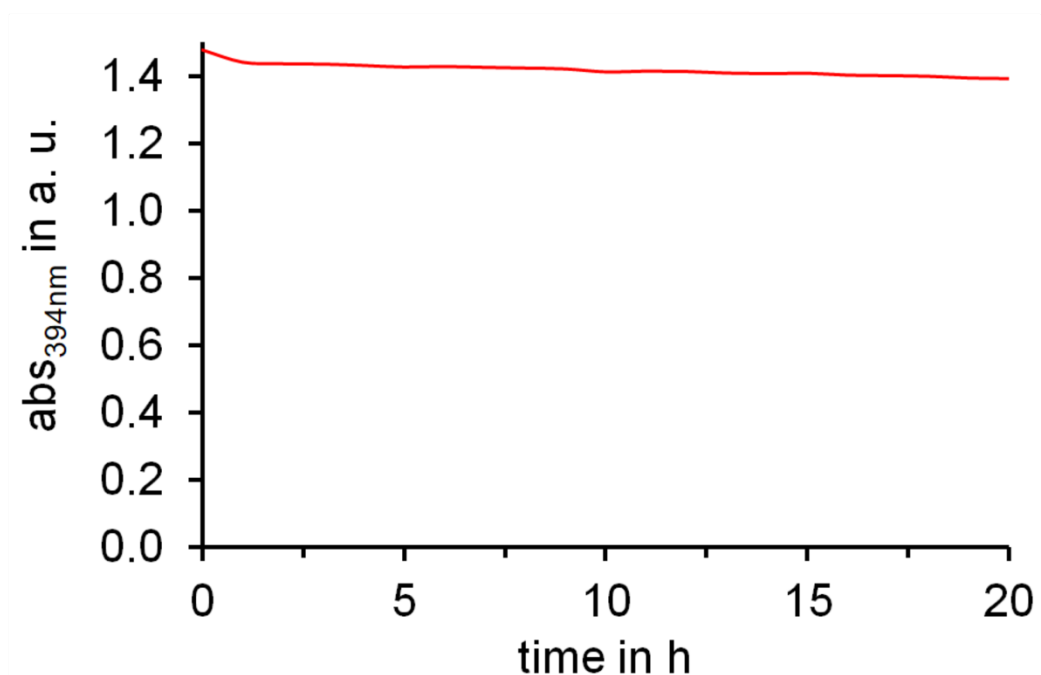Figure S75   Stability of pure *Z* isomer of Rhodanine based switch **8** (50 μM) against GSH (10 mM) in MeOH/PBS (1:1) at 23 °C over 20 h. The absorbance at λ = 394 nm was plotted against time. The concentration of the stock solution of **8** was 2.0 mM (0.60 mg in 1.30 mL MeOH).

Further irradiation experiments with photoswitch 1

To validate the activation of the biological inactive *E*-**1** isomer under biological-like conditions further experiments were performed.

First, the biological inactive isomer was *ex situ* irradiated with 415 nm for distinct time periods in 1% DMSO/PBS buffer at 23 °C. A similar experiment was performed with the biological active *Z*-**1** isomer, which can be deactivated by irradiating with 340 nm. A stock-solution of each *E*-**1** and *Z*-**1** in DMSO was prepared and then diluted with PBS to receive a solution of 1% DMSO/PBS buffer.

First the *Z* isomer was irradiated with 340 nm for 30 min. Since the rather hypsochromic *Z* isomer shows good absorption at 340 nm, full *Z*/*E* photoisomerization is expected. Figure S76 shows the absorption spectra of *Z*-**1** after certain time intervals (b)). Figure S76 c) shows the photodegradation at λ = 348 nm over 30 min. As seen in the figure, there is almost no photodegradation while irradiating with 340 nm for 30 min.

Next the *E* isomer was irradiated with 415 nm for 30 min, to affect the *Z*/*E* photoisomerization. In Figure S77 the corresponding absorption spectra of *E*-**1** measured after certain time intervals (b) and monitoring the photodegradation at λ = 348 nm over 30 min (c) are shown. As seen in the figure, there is almost no photodegradation while irradiating with 415 nm for 30 min.
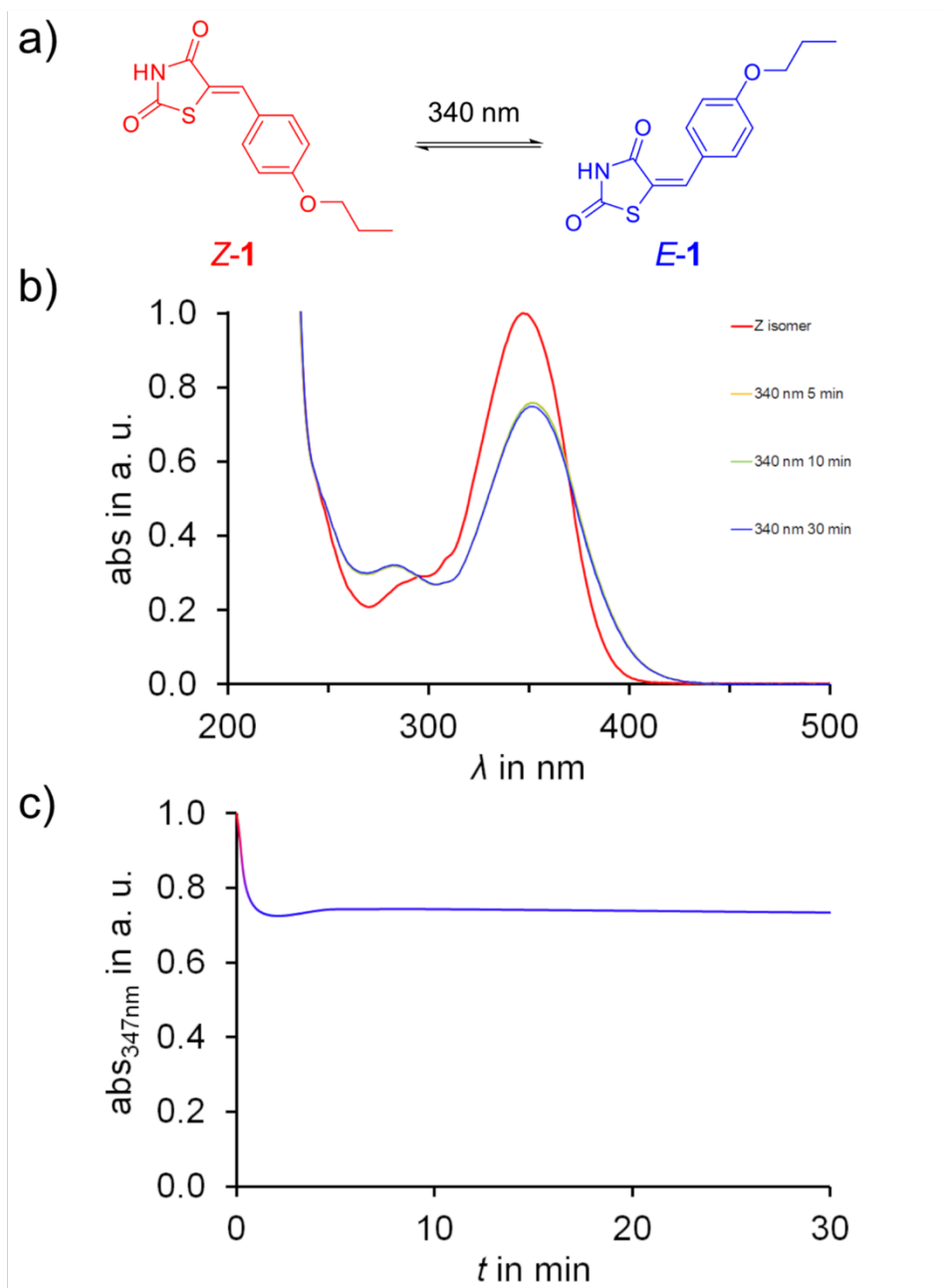
Figure S76   Permanent irradiation experiment of *Z*-**1** in 1% DMSO/PBS buffer solution at 23 °C. a) Schematic representation of the photoisomerization. b) Normalized absorption spectra recorded before and after irradiation with 340 nm. c) Photodegradation monitored at λ = 347 nm.
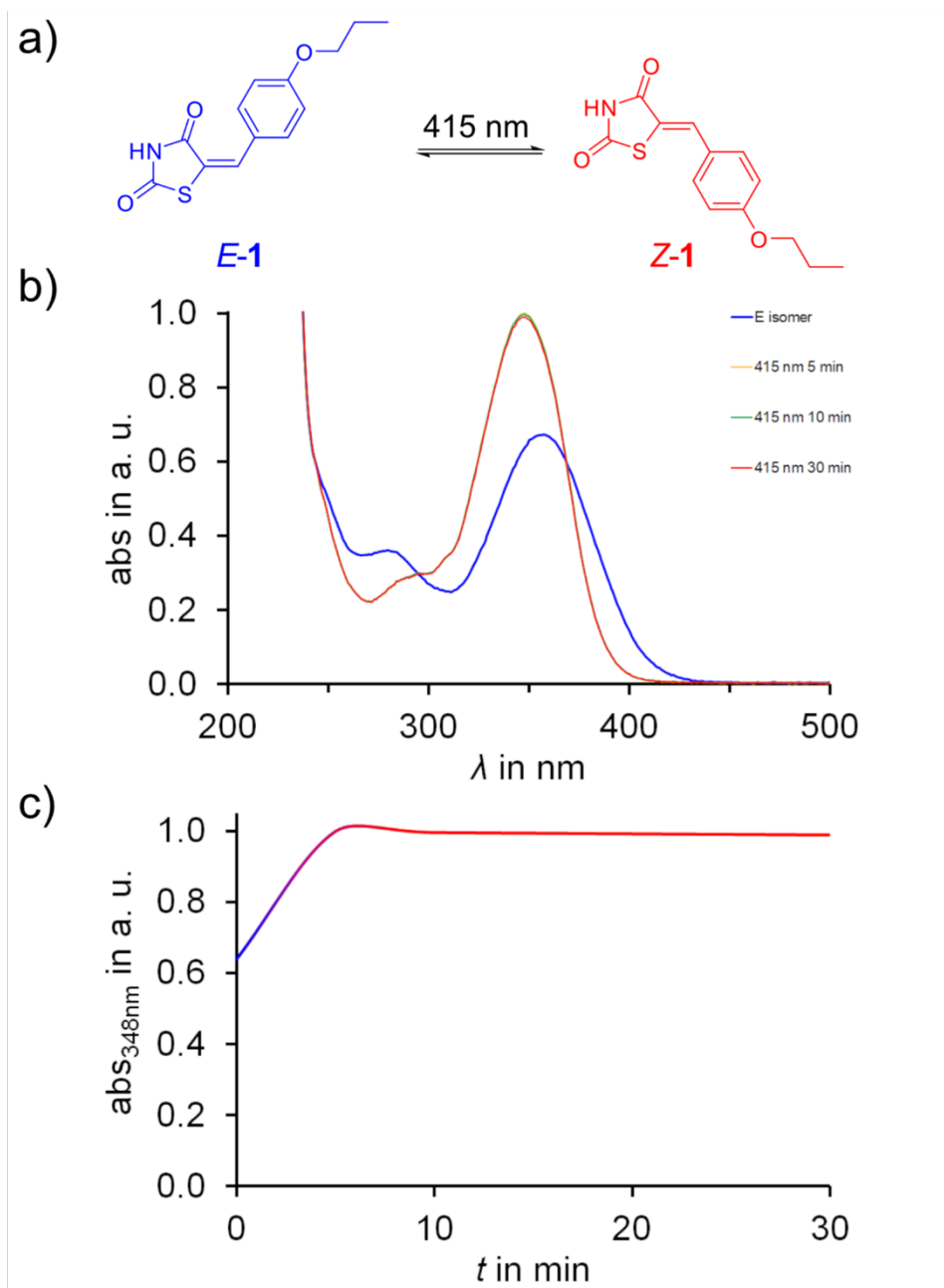
Figure S77   Permanent irradiation experiment of *E*-**1** in 1% DMSO/PBS buffer solution at 23 °C. a) Schematic representation of the photoisomerization. b) Normalized absorption spectra recorded before and after irradiation with 415 nm. c) Photodegradation monitored at λ = 348 nm.

To proof that irradiation of the cell culture after addition of the inhibitor leads to photoisomerization of **1**, irradiation experiments of **1** were performed in cell medium *ex situ*

104

273

with 340 nm and 415 nm using UV/Vis spectroscopy as analytical tool. Therefore, a stock-solution of *Z*-**1** in DMSO was diluted with the cell medium used for cell culture experiments to generate a 20 µM and a 150 µM solution of **1** in 1% DMSO, cell medium, see Figure S78 and Figure S79.
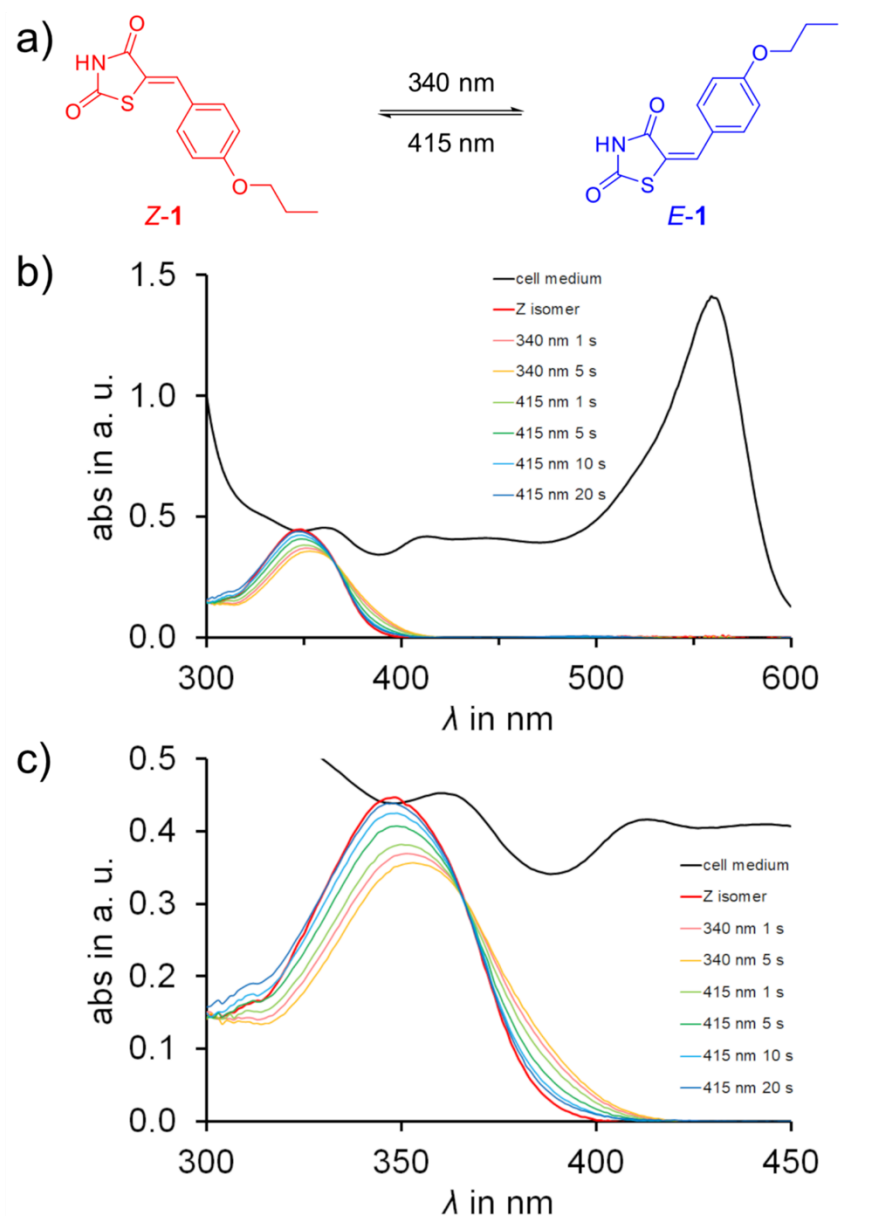
Figure S78   Irradiation of **1** in 1% DMSO/cell medium at 23 °C. Concentration c of **1** is 20 µM. a) Schematic representation of the photoisomerization. b) Absorption spectra of **1** before and after irradiation with 340 nm and 415 nm in. c) Enlarged spectra of **1** before and after irradiation.

105
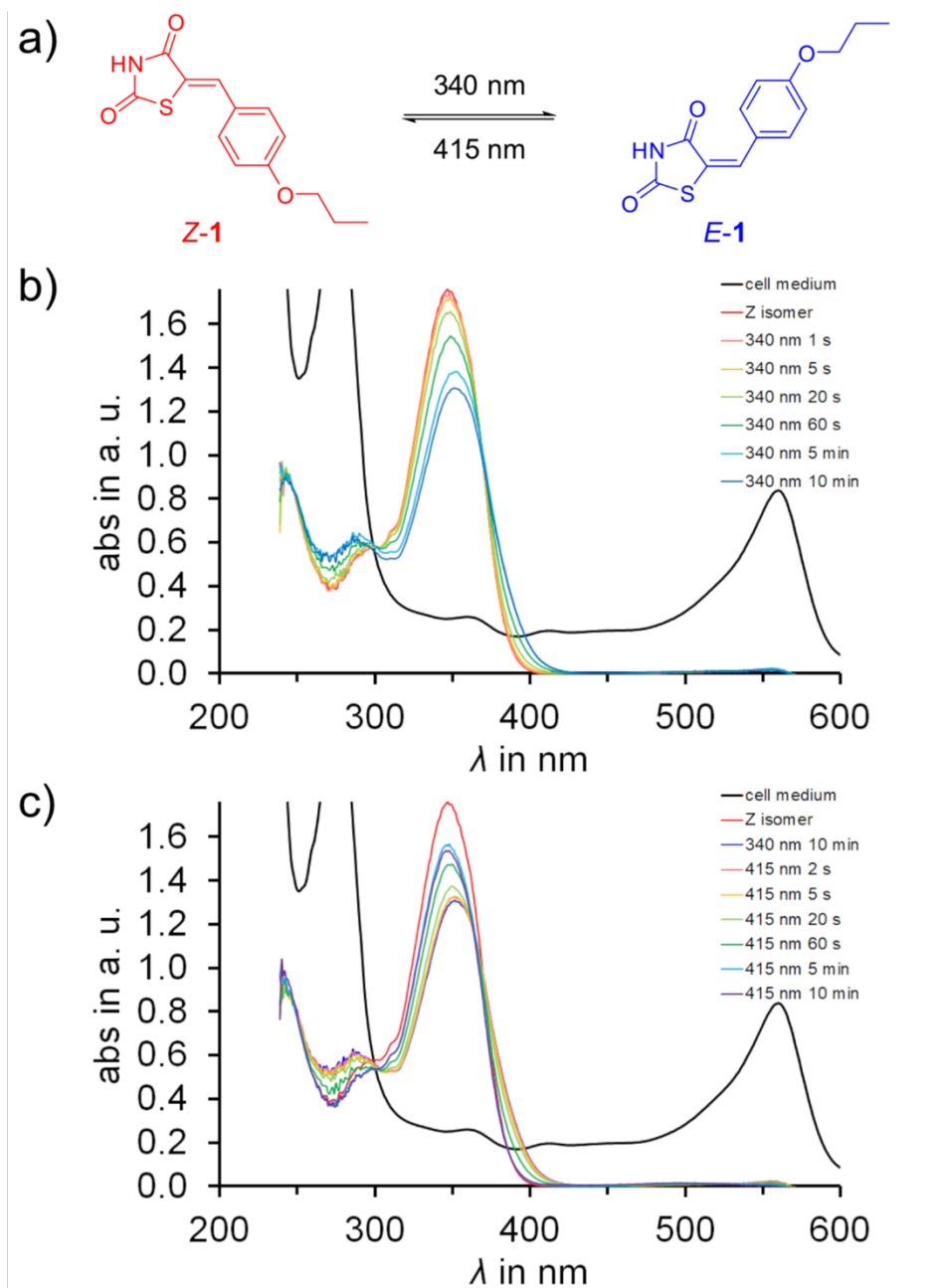
Figure S79   Irradiation of **1** in 1% DMSO/cell medium at 23 °C. Concentration c of **1** is 150 µM. a) Schematic representation of the photoisomerization. b) Absorption spectra of **1** before irradiation with 340 nm. c) Absorption spectra of **1** before and after irradiation with 340 nm and 415 nm.

NMR spectra
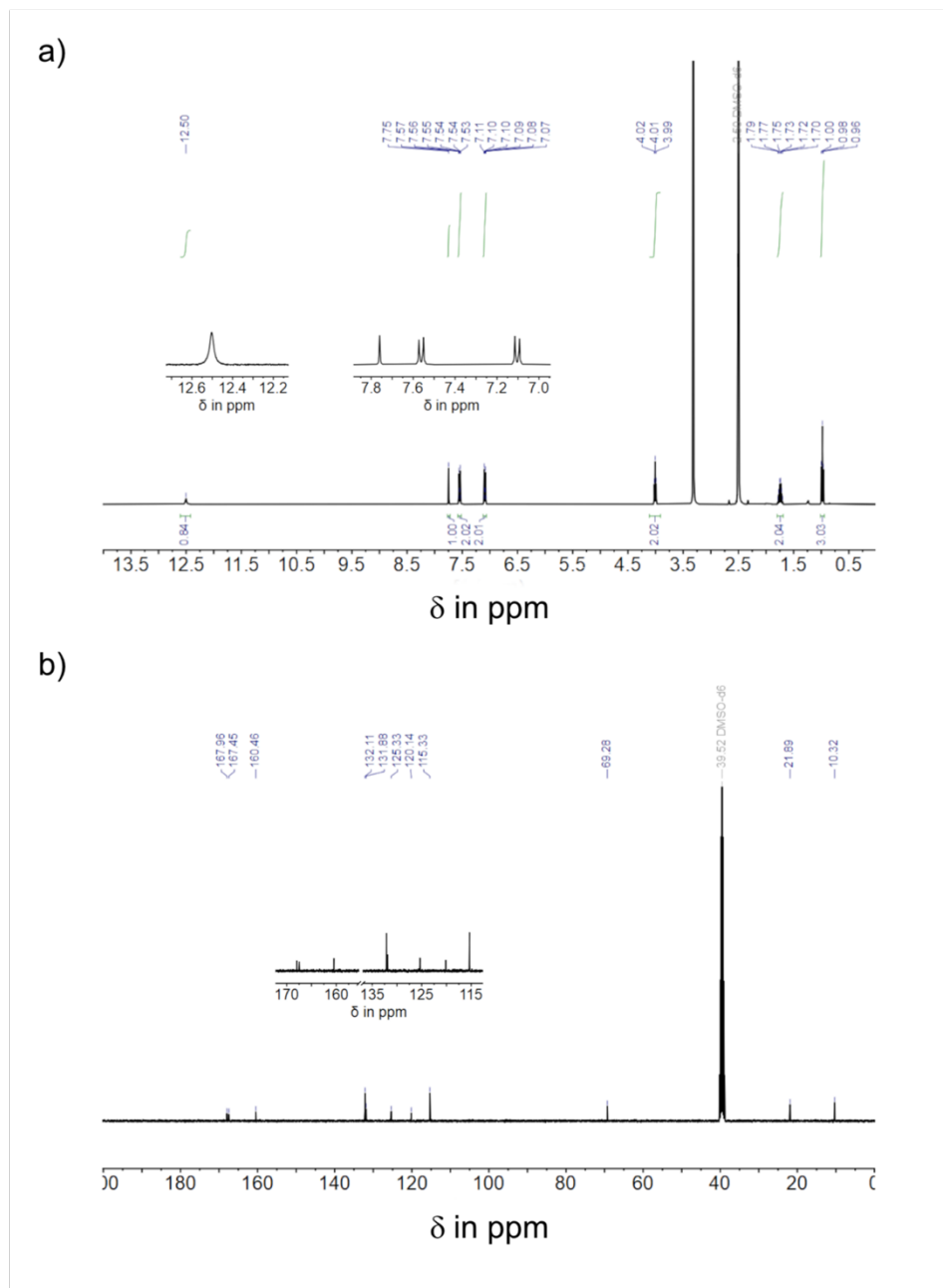
Figure S80   NMR spectra of **1** in DMSO-d_6 at 23 °C. a) ^{1}H NMR spectrum (400 MHz). b) ^{13}C NMR spectrum (101 MHz).
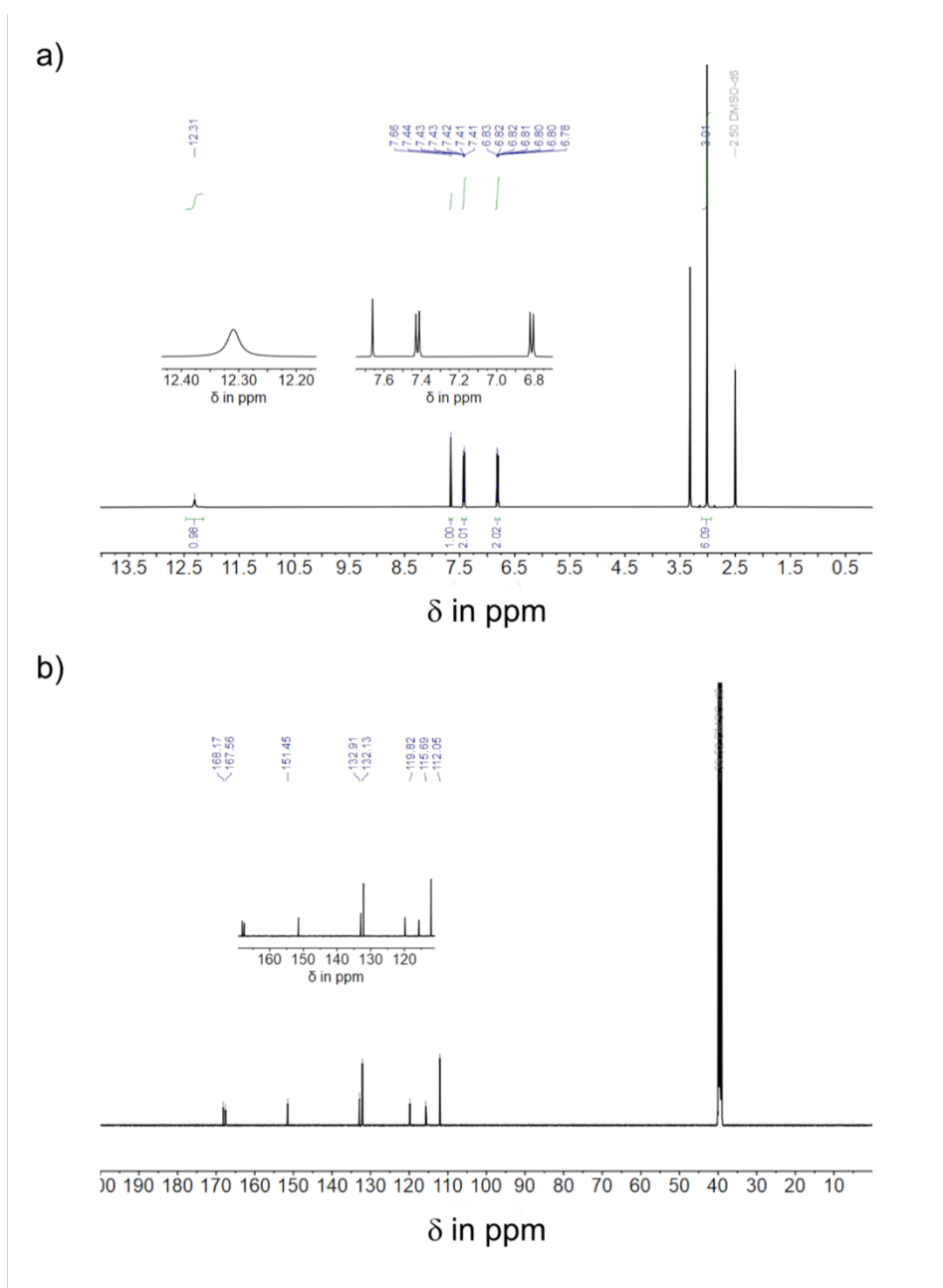
Figure S81   NMR spectra of **2** in DMSO-d_6 at 23 °C. a) ^{1}H NMR spectrum (500 MHz). b) ^{13}C NMR spectrum (126 MHz).
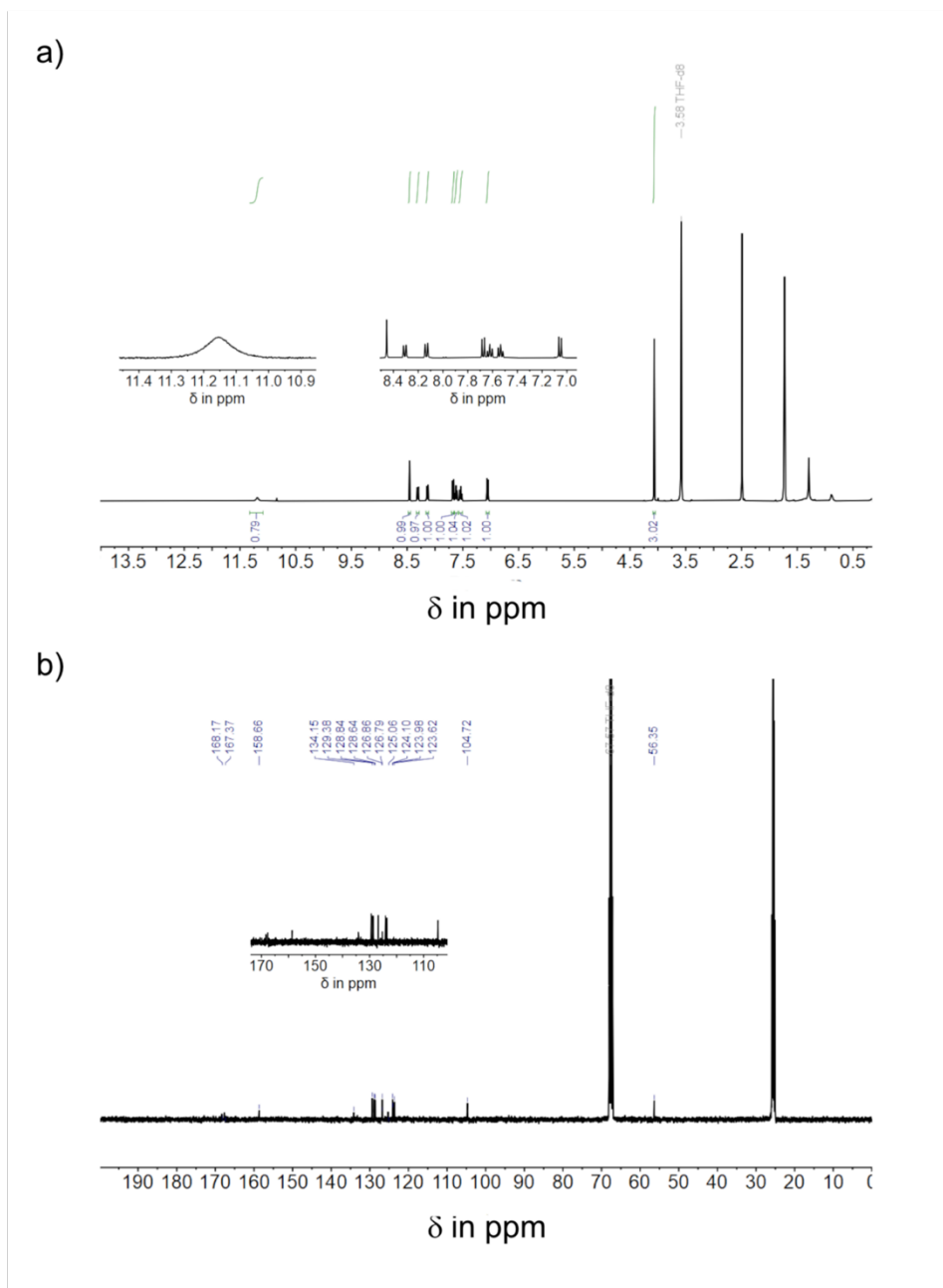
Figure S82   NMR spectra of **3** in tetrahydrofuran-d_8 at 23 °C. a) ^{1}H NMR spectrum (400 MHz). b) ^{13}C NMR spectrum (101 MHz).

109
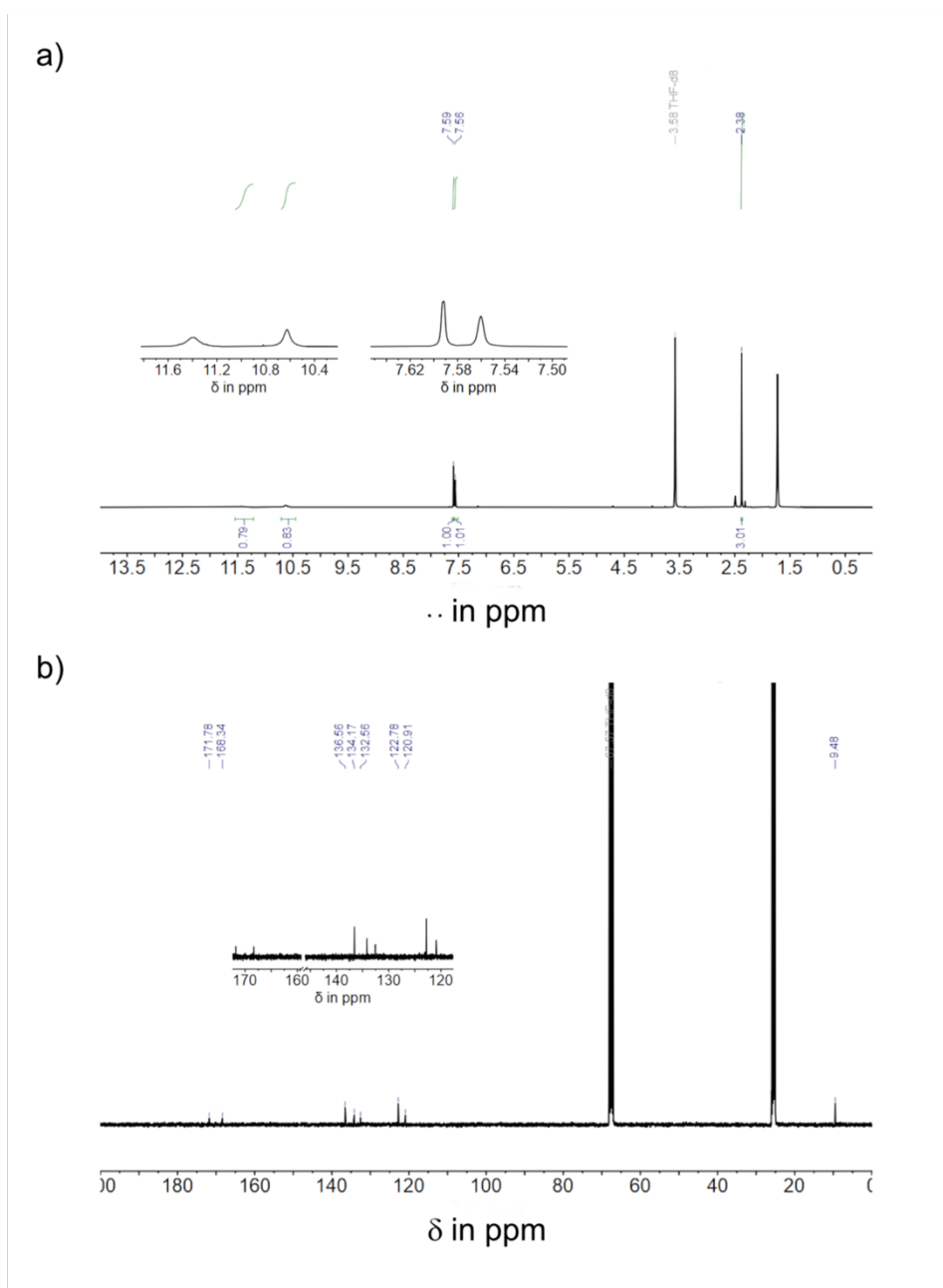
Figure S83   NMR spectra of **4** in tetrahydrofuran-d_8 at 23 °C. a) ^{1}H NMR spectrum (400 MHz). b) ^{13}C NMR spectrum (101 MHz).

110
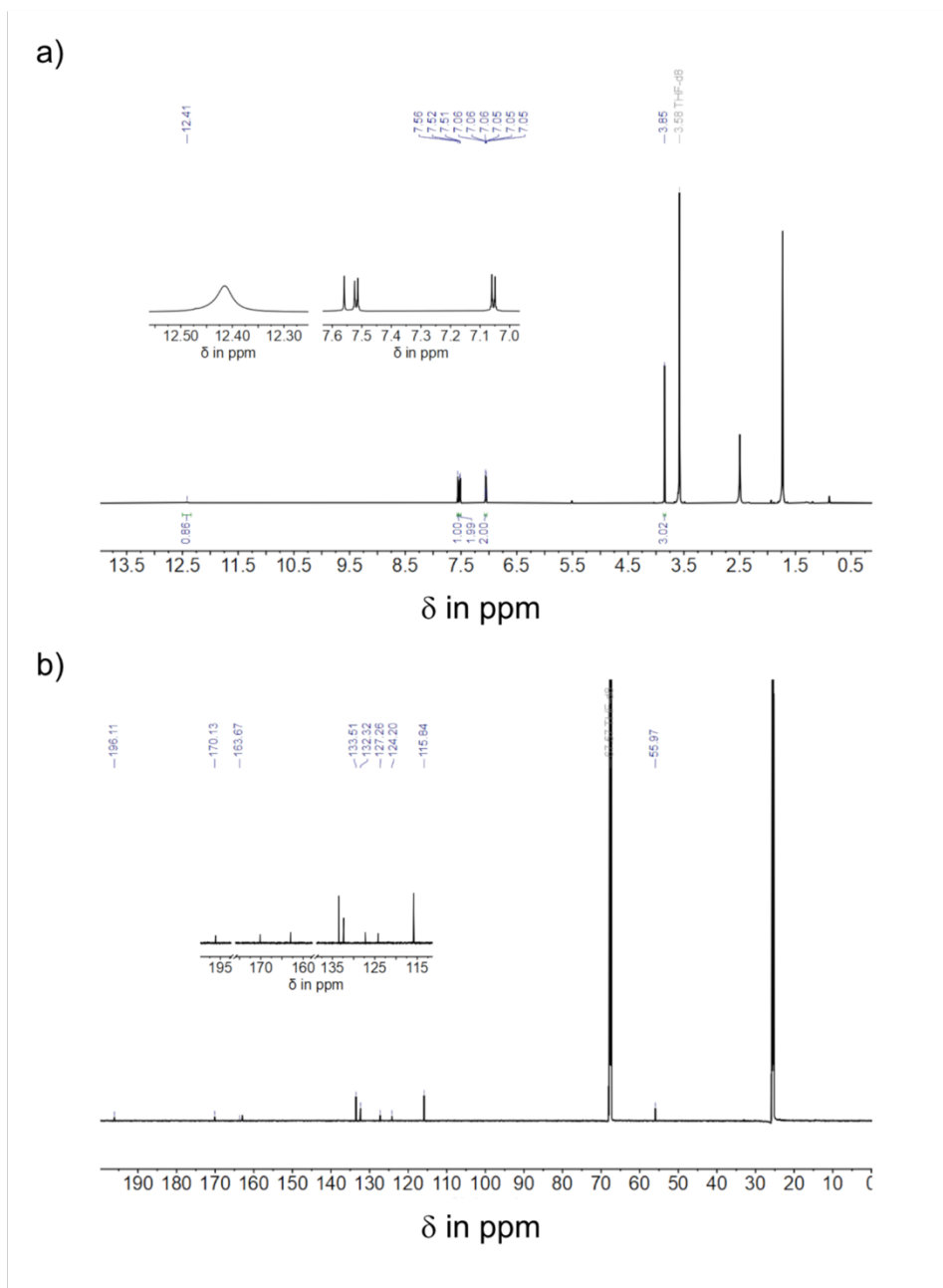
Figure S84   NMR spectra of **5** in tetrahydrofuran-d_8 at 23 °C. a) ^{1}H NMR spectrum (400 MHz). b) ^{13}C NMR spectrum (101 MHz).

111
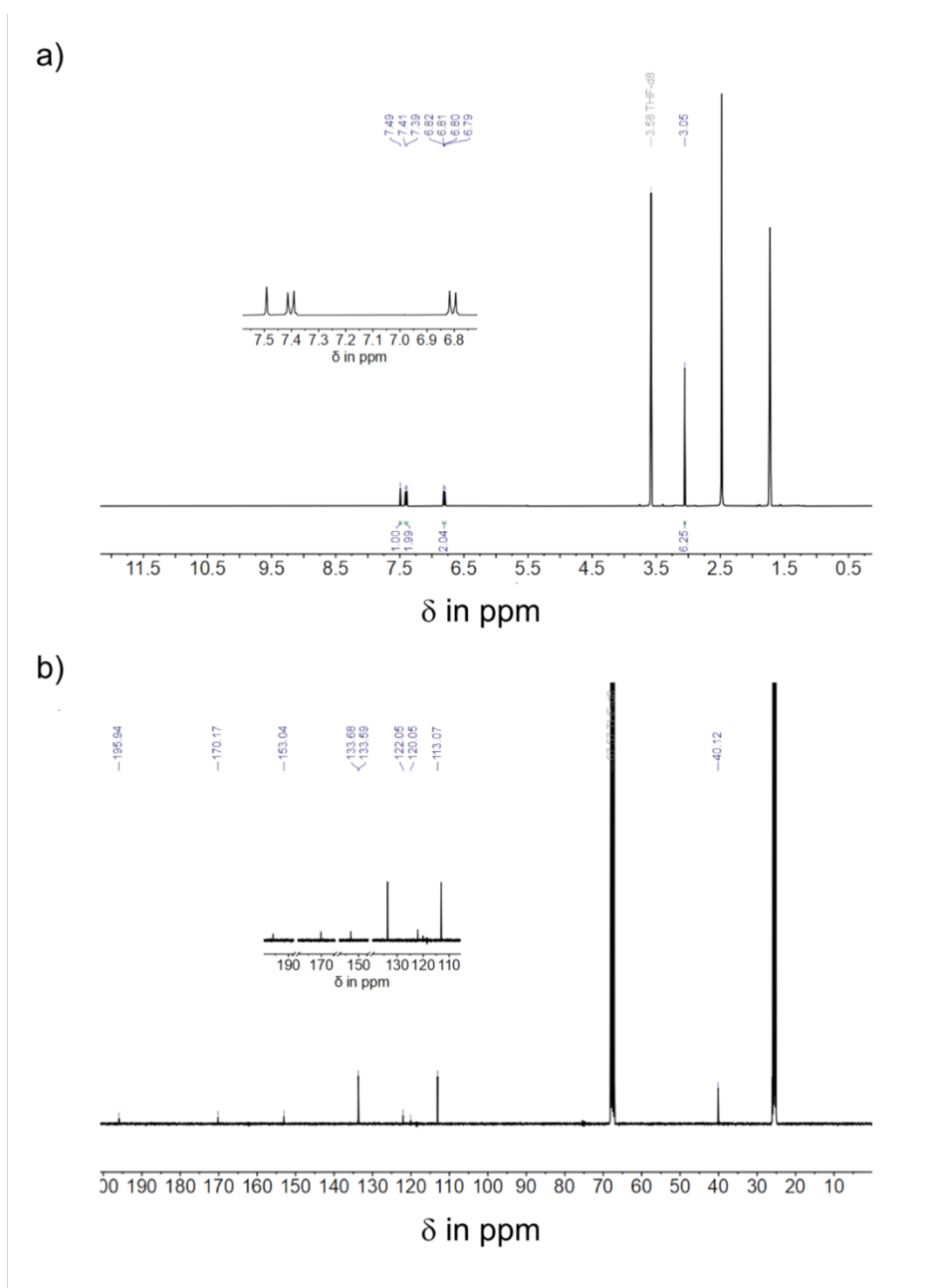
Figure S85   NMR spectra of **6** in tetrahydrofuran-d_8 at 23 °C. a) ^{1}H NMR spectrum (400 MHz). b) ^{13}C NMR spectrum (101 MHz).

112

Figure S86   NMR spectra of **7** in tetrahydrofuran-d_8 at 23 °C. a) ^{1}H NMR spectrum (800 MHz). b) ^{13}C NMR spectrum (201 MHz).

113
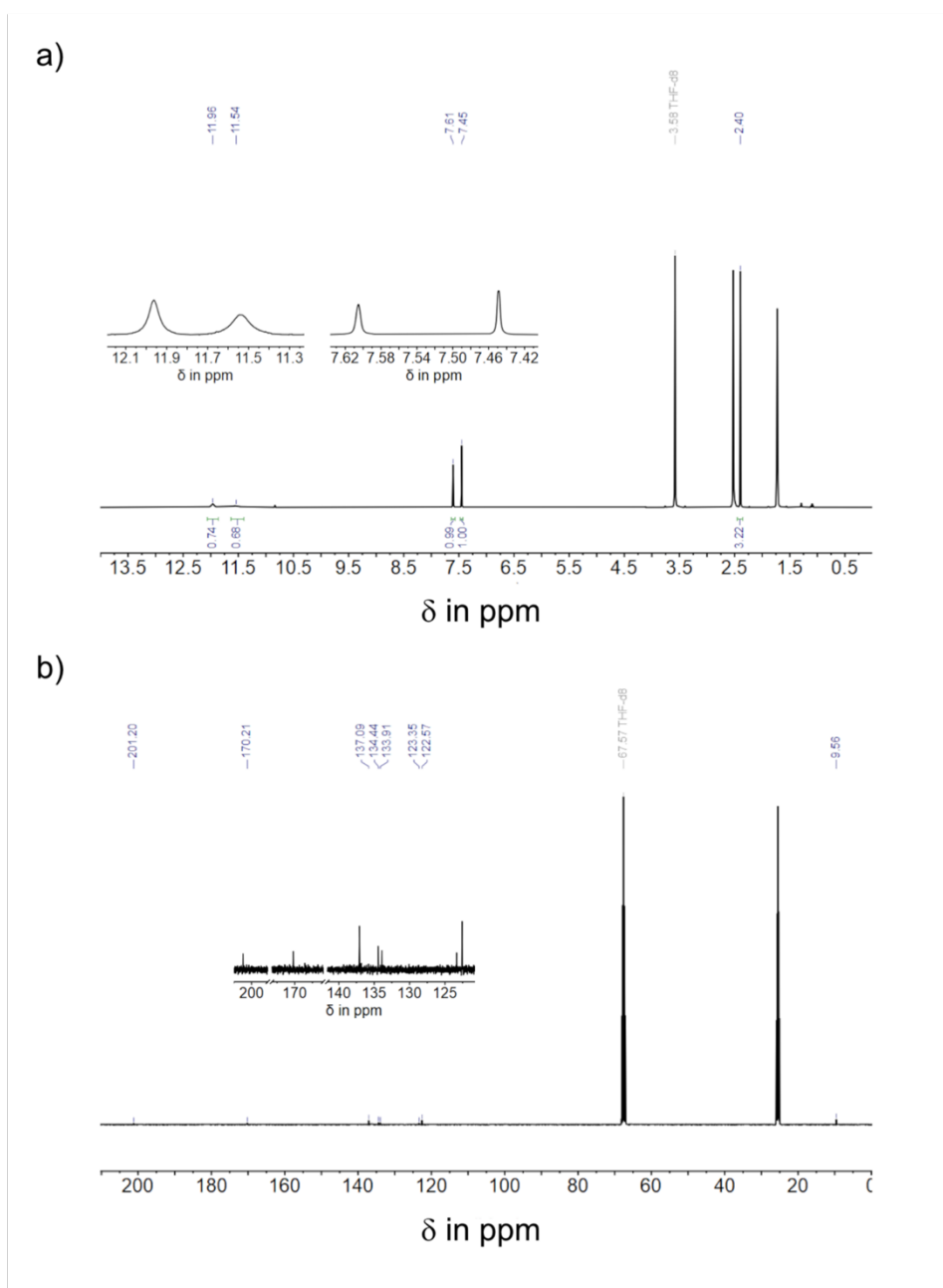
Figure S87   NMR spectra of **8** in tetrahydrofuran-d_8 at 23 °C. a) ^{1}H NMR spectrum (400 MHz). b) ^{13}C NMR spectrum (101 MHz).

114

Figure S88   NMR spectra of **9** in tetrahydrofuran-d_8 at 23 °C. a) ^{1}H NMR spectrum (400 MHz). b) ^{13}C NMR spectrum (101 MHz).

115
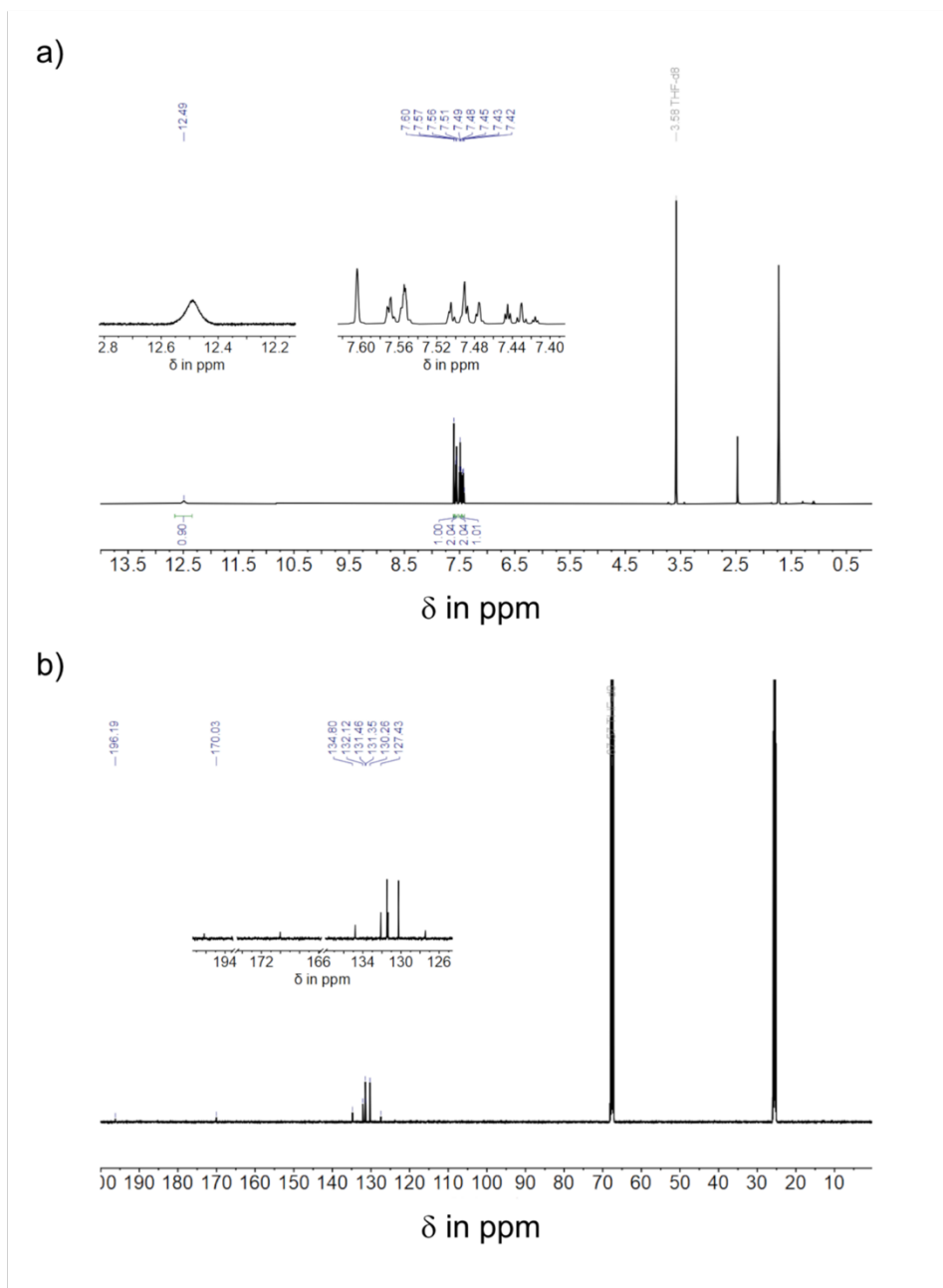
Figure S89   NMR spectra of **10** in tetrahydrofuran-d_8 at 23 °C. a) ^{1}H NMR spectrum (400 MHz). b) ^{13}C NMR spectrum (101 MHz).

116
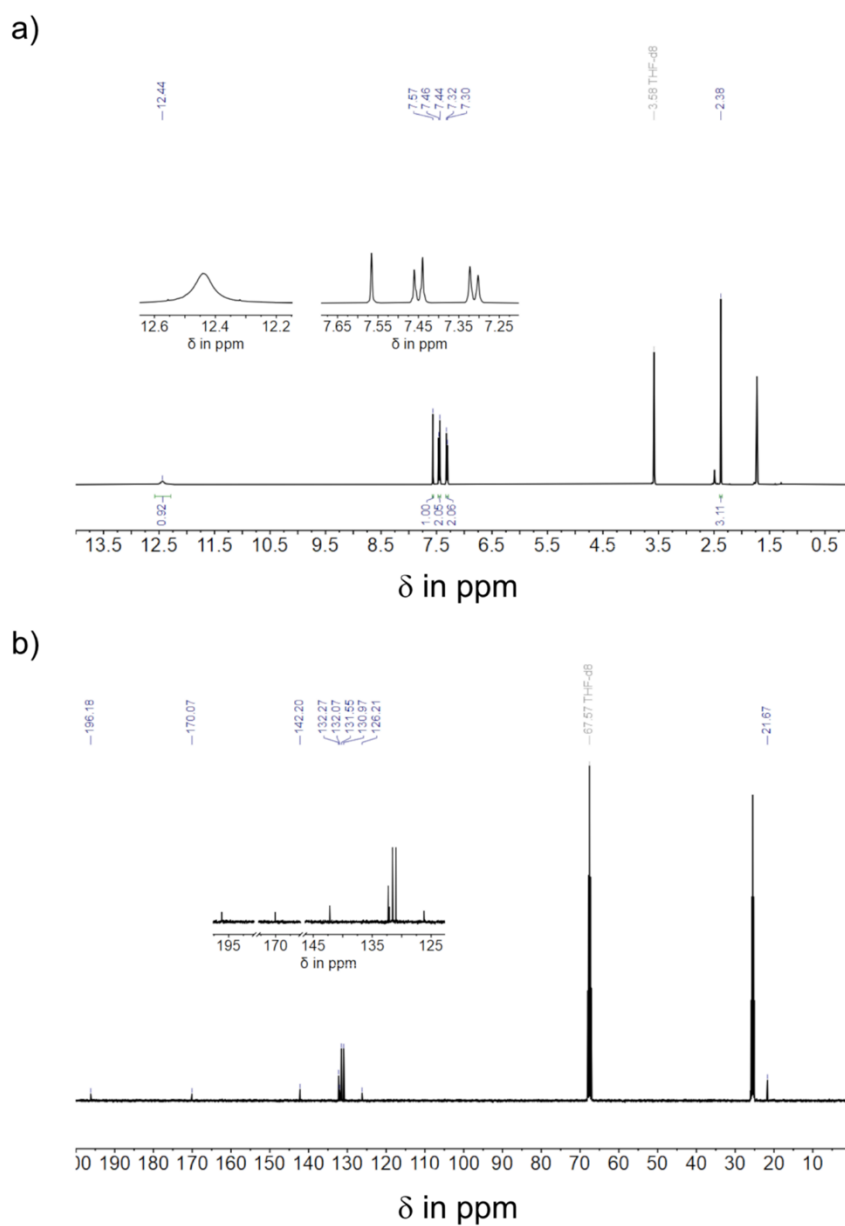
Figure S90   NMR spectra of **11** in tetrahydrofuran-d_8 at 23 °C. a) ^{1}H NMR spectrum (400 MHz). b) ^{13}C NMR spectrum (101 MHz).

117
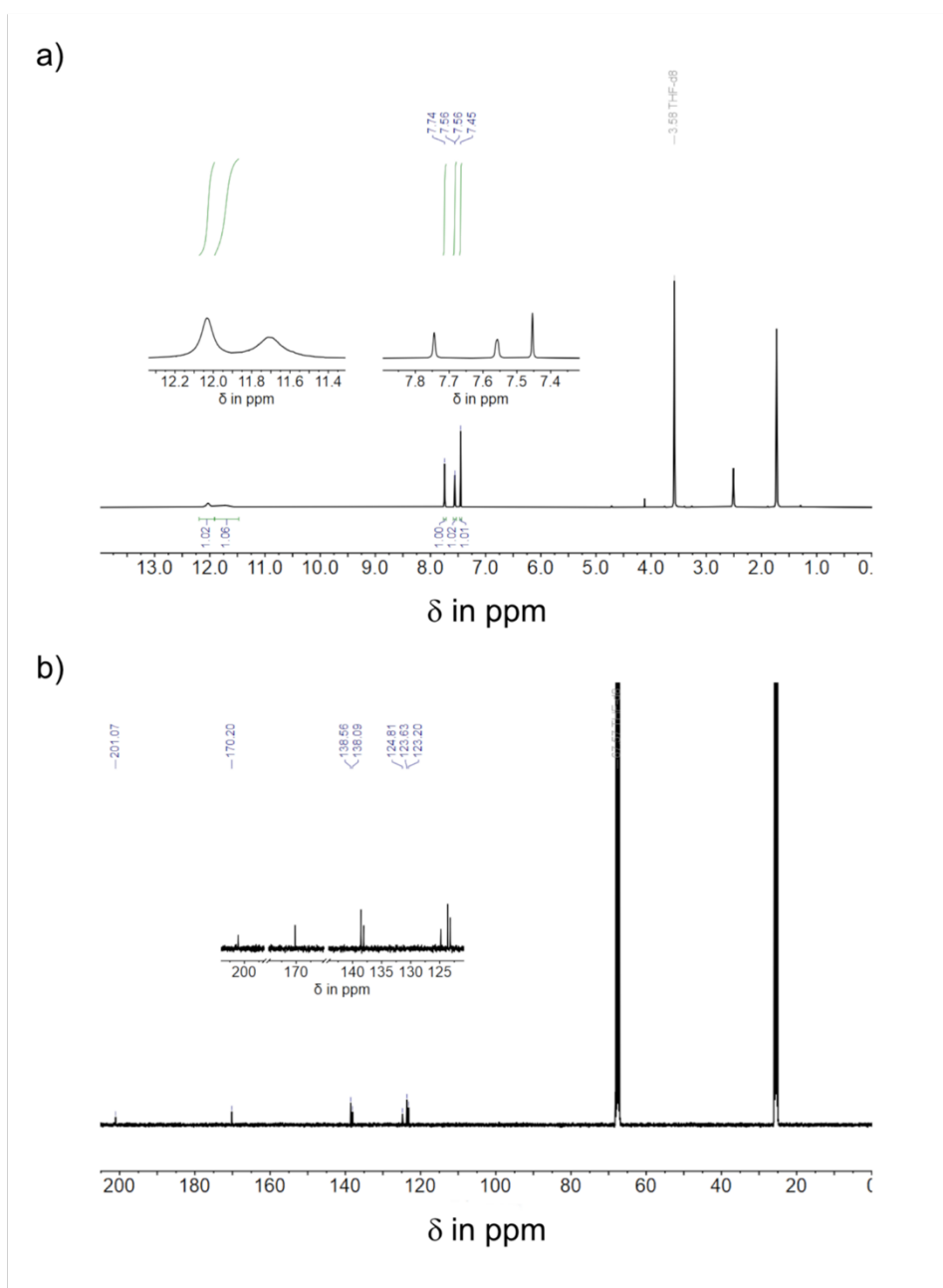
Figure S91   NMR spectra of **12** in tetrahydrofuran-d_8 at 23 °C. a) ^{1}H NMR spectrum (500 MHz). b) ^{13}C NMR spectrum (126 MHz).
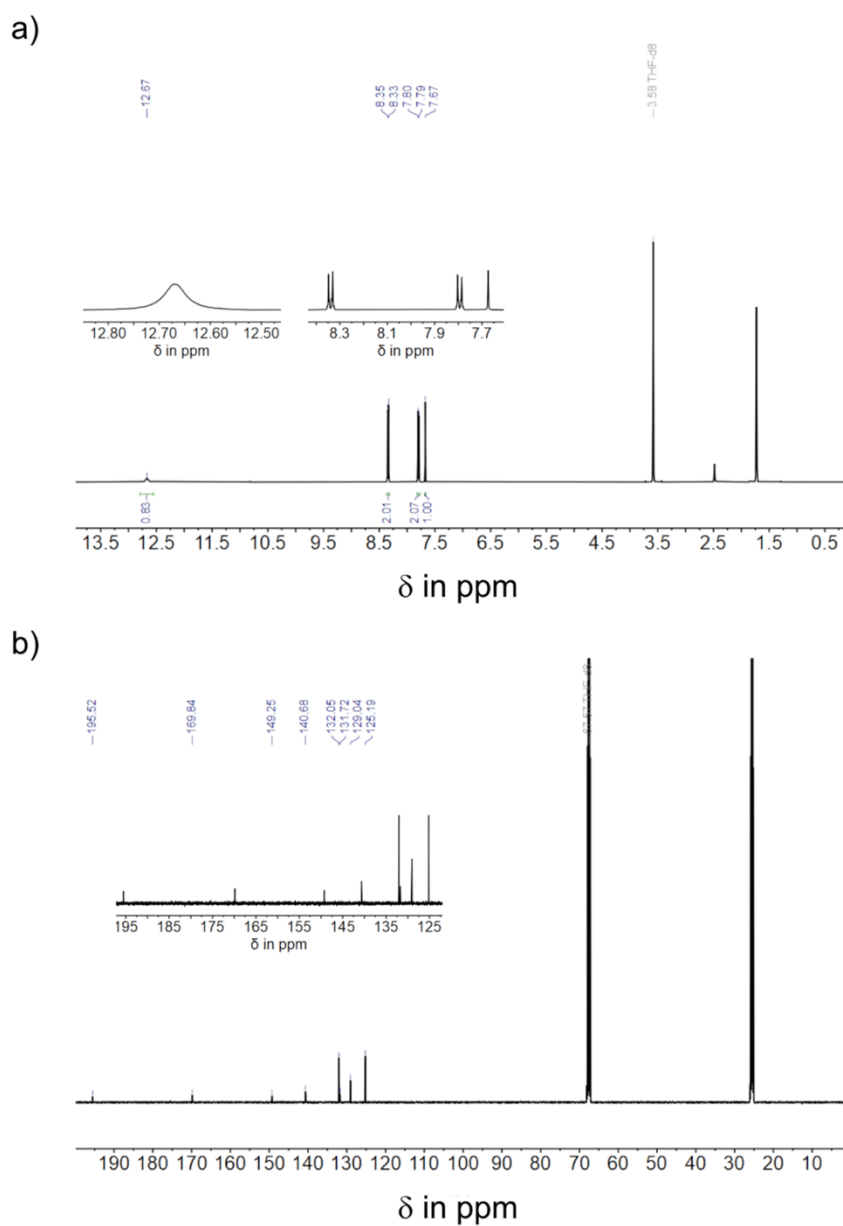
Figure S92   NMR spectra of **13** in tetrahydrofuran-d_8 at 23 °C. a) ^{1}H NMR spectrum (400 MHz). b) ^{13}C NMR spectrum (101 MHz).
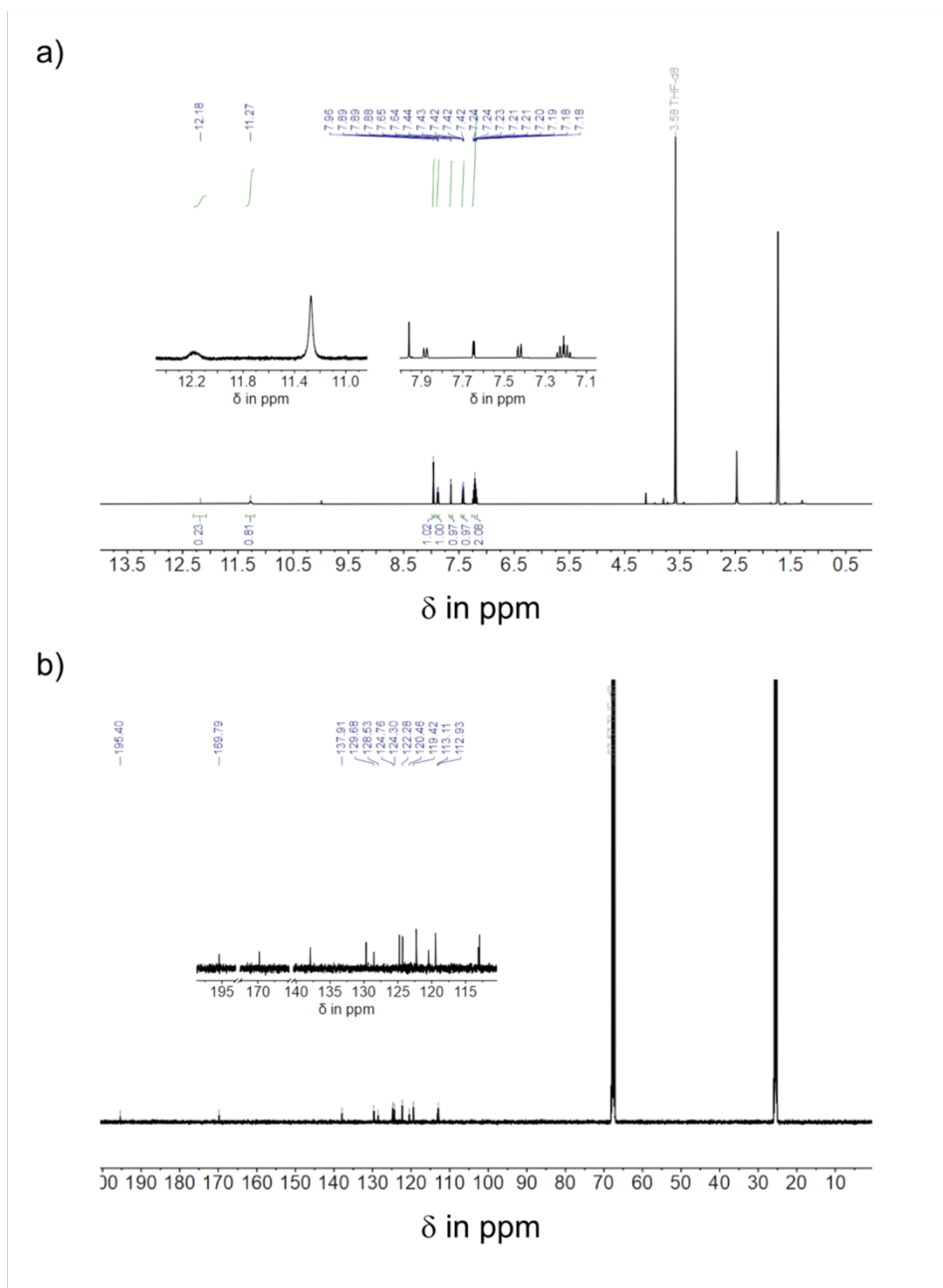
Figure S93 NMR spectra of **14** in tetrahydrofuran-d_8 at 23 °C. a) ^{1}H NMR spectrum (500 MHz). b) ^{13}C NMR spectrum (126 MHz).

120

Crystal Structural Data

In Figure S94 Structures of rhodanine based photoswitches **5**, **6**, **7** and **11** in the crystalline state were obtained in their most stable Z isomeric form.
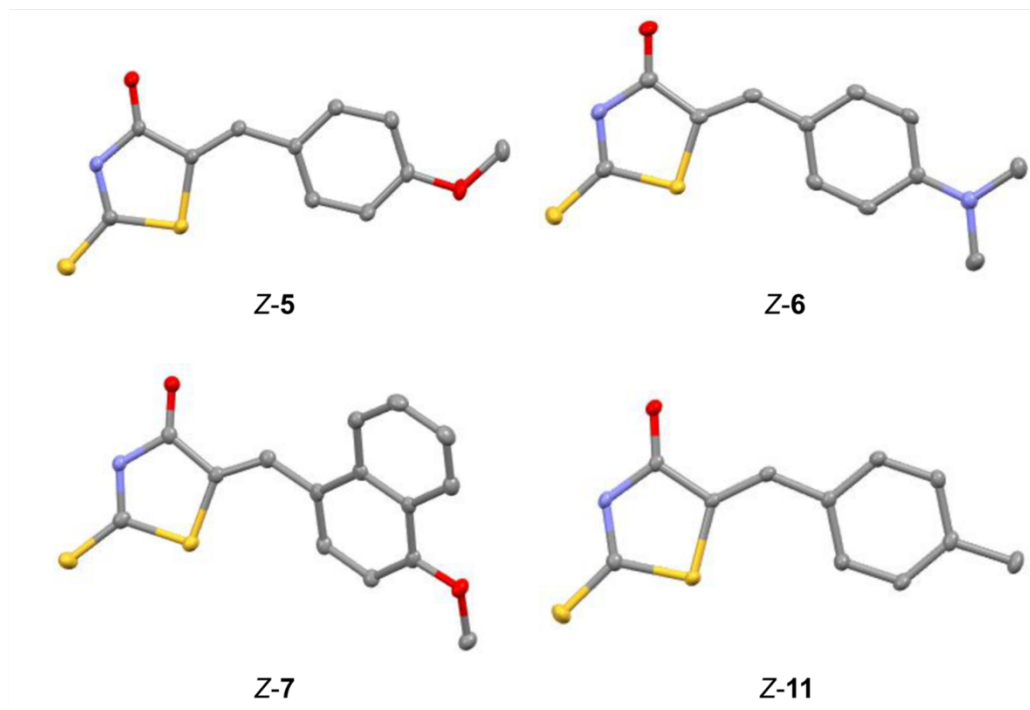
Figure S94   Crystal structures of rhodanine based photoswitches *Z*-**5**, *Z*-**6**, *Z*-**7** and *Z*-**11**. Colour coding: C grey, N blue, O red, S yellow.

121

Compound	Z-5 (xv773)	Z-6 (xv774)
	CCDC 223327 (Ref. [11])	CCDC 2233274 (Ref. [12])
net formula	$C_{11}H_9NO_2S_2$	$C_{12}H_{12}N_2OS_2$
M_r/g mol^{-1}	251.31	264.36
crystal size/mm	0.090 × 0.050 × 0.030	0.040 × 0.040 × 0.010
T/K	102.(2)	102.(2)
radiation	MoKα	MoKα
diffractometer	'Bruker D8 Venture TXS'	'Bruker D8 Venture TXS'
crystal system	monoclinic	monoclinic
space group	'P 1 21/c 1'	'P 1 21/c 1'
a/Å	5.1299(2)	3.9374(3)
b/Å	10.4630(5)	11.2442(8)
c/Å	20.5307(10)	26.7143(19)
$α$/°	90	90
$β$/°	91.715(2)	93.976(2)
$γ$/°	90	90
V/Å^3	1101.47(9)	1179.87(15)
Z	4	4
calc. density/g cm^{-3}	1.515	1.488
$μ$/mm^{-1}	0.465	0.434
absorption correction	Multi-Scan	Multi-Scan
transmission factor range	0.94–0.99	0.89–1.00
refls. measured	20498	16393
R_{int}	0.0287	0.0378
mean $σ(I)/I$	0.0203	0.0236
θ range	3.558–30.508	3.057–26.371
observed refls.	3024	2200
x, y (weighting scheme)	0.0387, 0.7539	0.0214, 1.8160
hydrogen refinement	H(C) constr, H(N) refall	H(C) constr, H(N) refall
refls in refinement	3359	2389
parameters	150	160
restraints	0	0
$R(F_{obs})$	0.0342	0.0432
$R_w(F^2)$	0.0921	0.0949
S	1.089	1.181
shift/error$_{max}$	0.001	0.001
max electron density/e Å^{-3}	0.462	0.520
min electron density/e Å^{-3}	−0.412	−0.271

122

Compound	Z-7 (xv777)	Z-11 (xv658)
	CCDC 2233276	CCDC 2233275 (Ref. [13])
net formula	$C_{15}H_{11}NO_2S_2$	$C_{11}H_9NOS_2$
M_r/g mol^{-1}	301.37	235.31
crystal size/mm	0.060 × 0.020 × 0.010	0.100 × 0.020 × 0.010
T/K	102.(2)	102.(2)
radiation	MoKα	MoKα
diffractometer	'Bruker D8 Venture TXS'	'Bruker D8 Venture TXS'
crystal system	monoclinic	monoclinic
space group	'P 1 21/n 1'	'P 1 21/c 1'
a/Å	21.0618(7)	4.9428(3)
b/Å	4.97740(10)	20.0454(11)
c/Å	25.8559(8)	10.7778(7)
α/°	90	90
β/°	97.2350(10)	90.803(2)
γ/°	90	90
V/Å^3	2688.97(13)	1067.76(11)
Z	8	4
calc. density/g cm^{-3}	1.489	1.464
μ/mm^{-1}	0.395	0.468
absorption correction	Multi-Scan	Multi-Scan
transmission factor range	0.97–1.00	0.93–0.99
refls. measured	44333	18838
R_{int}	0.0526	0.0382
mean $\sigma(I)/I$	0.0293	0.0239
θ range	2.685–26.369	3.588–27.877
observed refls.	4591	2259
x, y (weighting scheme)	0.0286, 3.5524	0.0293, 0.8703
hydrogen refinement	H(C) constr, H(N) refall	H(C) constr, H(N) refall
refls in refinement	5486	2552
parameters	371	141
restraints	0	0
$R(F_{obs})$	0.0409	0.0331
$R_w(F^2)$	0.0916	0.0791
S	1.066	1.075
shift/error$_{max}$	0.001	0.001
max electron density/e Å^{-3}	0.356	0.418
min electron density/e Å^{-3}	−0.409	−0.254

123

Material and Methods of biological characterization

Compound treatment, light exposure and immunostaining

Human cervix carcinoma HeLa Flp-In T-Rex, RPE1, DLD-1, and HCT116 cells were grown at 37°C with 5% CO_2 in DMEM (Dulbecco's growth medium, Thermo Scientific, 61965059) supplemented with 10% FCS (Thermo Scientific, 10270106), and 1% penicillin/streptomycin (PS, Merck, A2213). Prior to inhibitor treatment cells were seeded in a 12-well plate (Greiner, 665180) containing 18 mm poly-L-lysine (Y1251-100G, Sigma) coated glass coverslips with 1 ml supplemented DMEM medium and grown for 19-24 h. Inhibitor stock solutions were prepared in DMSO at ~10 mM for E (isolated by HPLC after irradiation of the Z isomer with 340 nm light) and Z isomer of oxo-rhodanine **1** (SMI16a, CAS 587852-28-6, *BLDpharm*) and 20 mM for rhodanine **5**. To this end ~1 mg of inhibitor was dissolved in ~0.40 mL DMSO and sonicated for 5 min. 1 ml of supplemented DMEM containing 1.5% DMSO or the compound was illuminated in a 12-well plate for 10 min with 415 nm or 340 nm LED lights (*Thorlabs* M340D3, 340 nm, 53 mW and *Thorlabs* M415D2, 415 nm, 1640 mW) placed at a distance of approximately 5 cm above the medium in a custom-~build box. After removing the growth media from the cells, 1 ml of the illuminated media containing 1.5% DMSO, 50 µM, or 150 µM rhodanine inhibitor was added to each well. For illumination on cells, 1 ml media (Gibco, FluoroBrite™ DMEM, A18967-01) containing the compound, 1.5% DMSO or no additive were added to the cells and illuminated for 10 min with 340 nm or for 20 min with 415 nm. For short time illuminations of 10 sec or 30 sec with 405 nm a high-power LED light (*Mightex* LCS-0405-65-22, 405nm, 65 W) was used.

After compound treatment cells were incubated at 37°C for 19 h in the dark and subsequently immunostained by fixing in 4% PFA/1x PBS (formaldehyde, 28908 Thermo Scientific) for 15 min on ice. Fixed cells were treated with blocking solution (4% BSA/1x PBS/0.1% TritonTM X-100) for 1 h at 4 °C and stained with Alexa FluorTM phalloidin 568 (1:500, Life Technologies, A12380) and Hoechst 33258 (1:1,000, Sigma-Aldrich, 86140) diluted in blocking solution for 1 h at 22 °C.[9] Coverslips were washed 3x with 0.1%TritonTM X-100/1xPBS for 5min and mounted on glass slides using 1x PBS/4% n-Propyl-Gallate, 90% Glycerol, sealed with nail polish and stored at −20 °C.

Immunofluorescence images were acquired either with a 40x plan-neofluoar objective (NA 0.75) on a Zeiss AxioImager.Z1 ApoTome1 microscope with an AxioCamMRm3 camera controlled by ZEN 2 pro software or with a Apo LWD 40x WI Lambda S DIC N2 objective on a Nikon Ti eclipse spinning disk confocal microscope equipped with an Andor DU-888 X-11056

124

camera. To analyze cell viability, the open-source software Fiji[10] was used and graphs were plotted with GraphPad Prism V8.0.1. Statistical analyses were performed using GraphPad Prism Data analysis tool.

Immunoblotting against PARP

Human cervix carcinoma HeLa Flp-In T-Rex cells were seeded in 6-well plates at 30% confluency and one day later 150 µM *E*-**1** or *Z*-**1** isomer, or 1.5% DMSO were added. Plates were irradiated for 10 min with 340 nm or 20 min with 415 nm, respectively, or maintained in the dark. After 10 h incubation, cells were collected in ice-cold 1x PBS and washed 3x with 1xPBS. For cell lysis, cells were incubated in RIPA buffer (50mM Tris-HCL pH7.5, 150mM NaCl, 0.5% Na-deoxycholate, 1% Triton-X 100, 1%SDS) rotating for 30 min at 4°C following addition of 4x Sample buffer (0.25M Tris, 8% SDS, 10% β-mercaptoethanol, 40% glycerol, 1% Bromphenol blue). Samples were sonicated in water bath for 20 min at 60°C, heated at 95°C for 5 min and resolved on a 10% SDS-page. As primary antibodies rabbit anti-PARP (1:1,000, #9542, Cell Signaling) and mouse anti-actin (1:10,000, #A5316, Sigma). Primary anti-PARP antibody was incubated over-night at 4°C, primary anti-actin antibody for 1 h at RT. As secondary antibodies HRP-conjugated anti-rabbit (1:3,000 for PARP, #170-6515, Bio-Rad) and anti-mouse (1:10,000 for actin, #170-6516, Bio-Rad) were used and incubated for 1 h at RT. Membranes were developed using ECL^{TM} Prime Western Blotting (Cytiva, RPN2236) and imaged on a Molecular Imager ChemiDoc^{TM} XRS+ (Bio-Rad). The percentage of uncleaved and cleaved PARP was analyzed using Image Lab software (Bio-Rad).

Resazurin-based cell viability assay

For cell viability assay, ~15,000 human cervix carcinoma HeLa Flp-In T-Rex cells were seeded into black 96-well plates (#655090, Greiner) and allowed to attach for several hours. On the same day, medium was removed and 100 µl medium containing 150 µM *Z*-**1** or *E*-**1** isomer, or 1.5% DMSO were added in triplicates. Additionally, medium was added to empty wells without cells, which were used to correct for background fluorescence intensity. Plates were either kept in the dark or irradiated with 340 nm for 10 min (*Z*-**1**) or 415 nm for 20 min (*E*-**1**). After 19 h of incubation at 37°C, 10 µl of CellTiter Blue® reagent containing resazurin (#G8080, Promega) was added to each well. Plates were shaken for 2 min and centrifuged at 1,000 rpm for 1 min. The fluorescence intensity (excitation 560 nm; emission 590 nm) was measured

125

every hour using a Tecan Infinite Pro2000 (bottom reading) until saturation of the signal. For each condition, the mean fluorescence intensity of the triplicate was calculated and the background intensity of empty wells without cells was substracted. All values were normalized to the mean fluorescence intensity of DMSO-treated cells maintained in the dark.

126

Comparison of cytotoxicity of *Z*-1 and *Z*-5

Supplemental Figure

a)

b)

c)

d)

e)
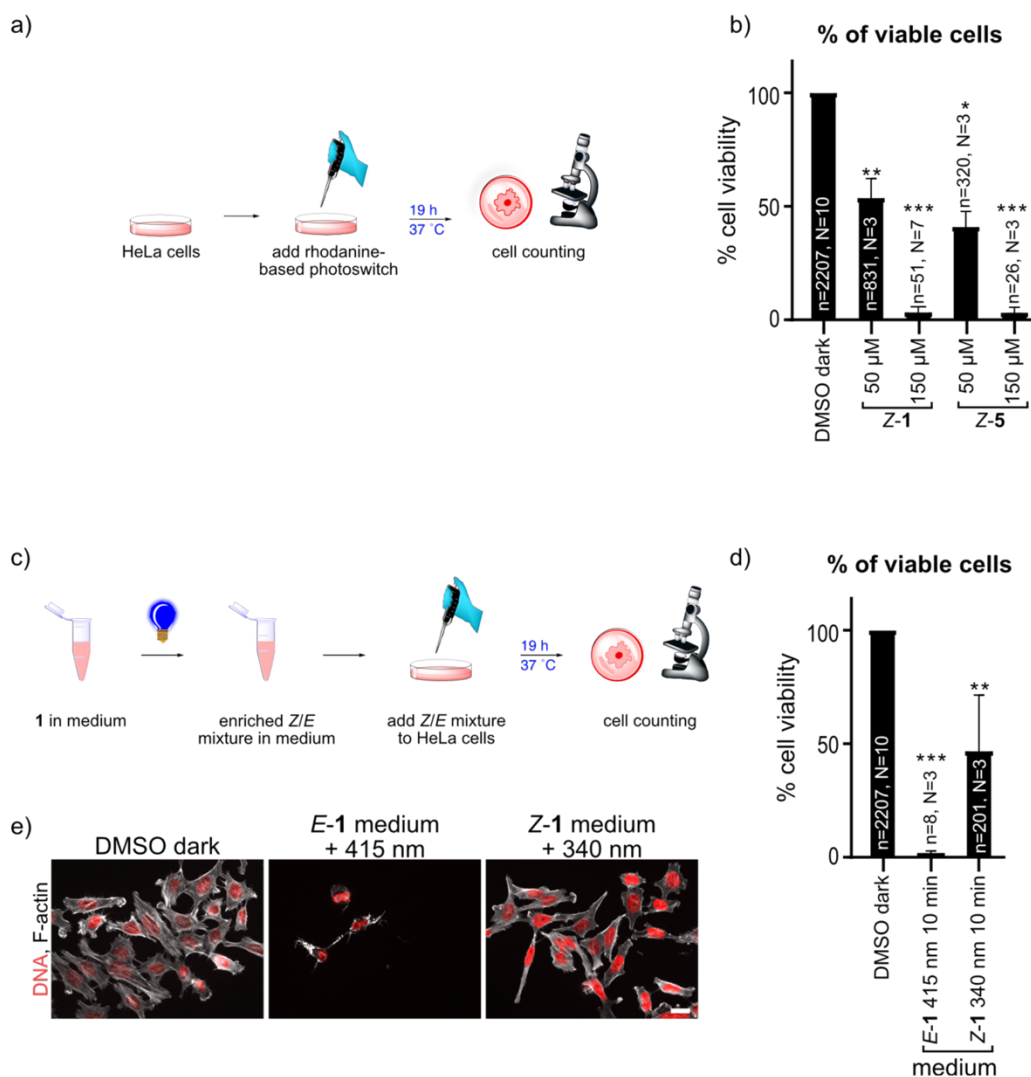
Figure S95   a, b) Human cervix carcinoma cells (HeLa) were treated with 1.5% DMSO or indicated concentrations of oxo-rhodanine **1** (*Z*-**1**), or oxo-rhodanine **5** (*Z*-**5**) in the dark for 19 h and subsequently the % of viable cells was determined by staining against F-actin and DNA. c) Cell culture medium containing 150 μM *Z*-**1** or *E*-**1** were irradiated with 340 nm or 415 nm for 10 min, respectively. Subsequently the irradiated medium was added to the cells and cells were incubated for 19 h. d) Quantification of the % of viable cells incubated with *Z*-**1** or *E*-**1** irradiated in medium. Error bars represent standard deviation (SD) and the total number of experiments (N) and cells (n) analyzed are indicated. e) Sample microscopy images of HeLa cells stained for DNA (red) and F-actin (white) for the indicated conditions. Scale bar is 20 μm. All p-values were calculated using either Student's t test or Kruskal Wallis multiple comparison and represent n.s. p>0.05, * p<0.05, ** p<0.01, *** p<0.001 in comparison to DMSO-treated cells (dark).

127

Light-induced cytotoxicity in different cell lines
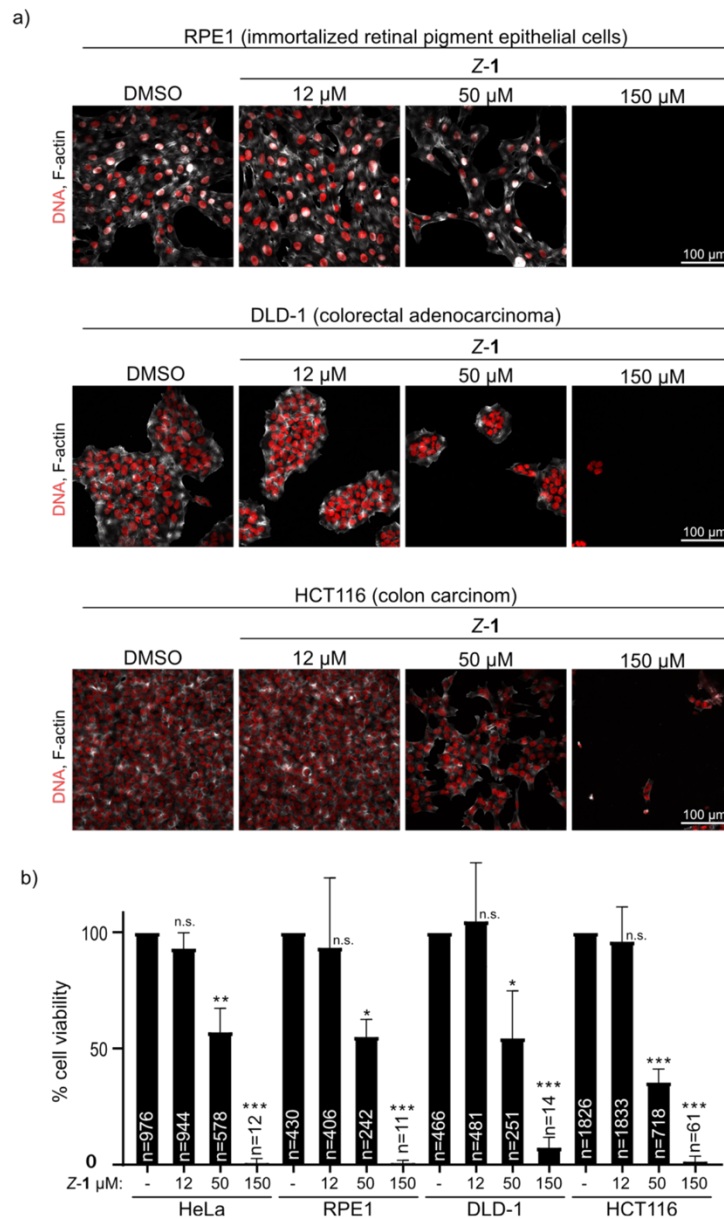
Figure S96   Cytotoxicity of Z-**1** (dark) is comparable across different cell lines. a) RPE1 (immortalized retinal pigment epithelial cells), DLD-1 (colorectal adenocarcinoma), or HCT116 (colon carcinom) or were incubated with 1.5% DMSO or indicated µM concentrations of Z-**1** in the dark for 19 h. After 19 h incubation cells were fixed and stained against F-actin (white) and DNA (Hoechst, red) and imaged with a confocal microscope. b) Mean number of viable cells for the indicated cell lines and µM concentrations of Z-**1** (dark) for three independent experiments are shown. The total number of cells (n) analysed are indicated. Error bars represent SD and all p-values were calculated using either Student's t test or Kruskal Wallis multiple comparison and represent n.s. p>0.05, * p<0.05, ** p<0.01, *** p<0.001 in comparison to DMSO-treated cells of the same cell type.

128

297

Light-induced cytotoxicity quantified with CellTiter® blue assay

CellTiter® blue assay
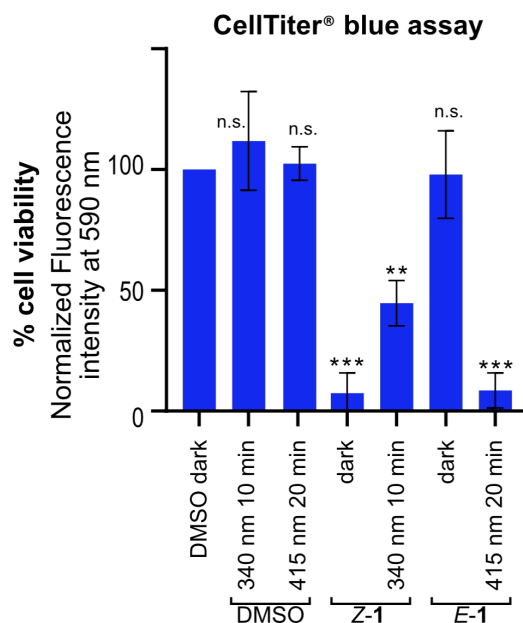
Figure S97   Light-induced *E/Z* isomerization of **1** results in a strong biological response. HeLa cells seeded in 96-well plates were treated with 1.5% DMSO, 150 µM *Z*-**1** or 150 µM *E*-**1** and either kept in the dark or exposed to 340 nm light for 10 min or 415 nm light for 20 min as indicated. After 19 h incubation CellTiter® blue was added and fluorescence intensity was measured with a plate reader at 590 nm. Oxidation of resazurin in the mitochondria results in high fluorescence signal at 590 nm and is an indicator of the quantity of healthy cells. Means of three independent experiments are shown and each condition was tested in triplicate. Error bars are SD and all p-values were calculated using either Student's t test or Kruskal Wallis multiple comparison and represent n.s. p>0.05, ** p<0.01, *** p<0.001 in comparison to DMSO-treated cells (dark).

129

Dose-dependent induction of cytotoxicity
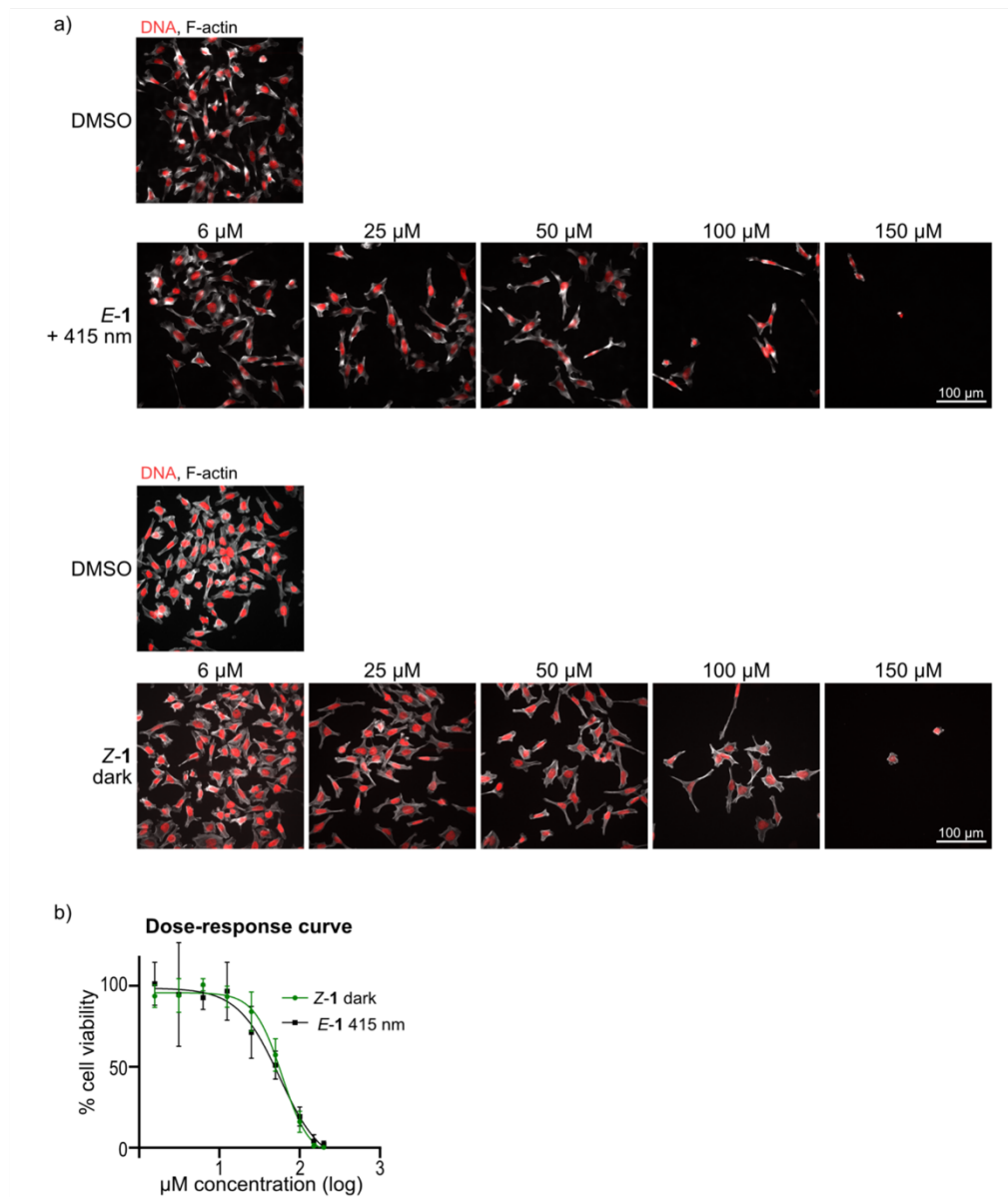
Figure S98   Dose-dependent induction of cytotoxicity has the same efficiency for *Z*-**1** and *E*-**1** (415 nm). a) HeLa cells were treated with 1.5% DMSO or the indicated concentrations of *Z*-**1** or *E*-**1** and either kept in the dark (*Z*-**1**) or illuminated with 415 nm light for 20 min (*E*-**1**). After 19 h incubation cells were fixed and stained against F-actin (white) and DNA (Hoechst, red) and imaged with a confocal microscope. b) Mean percent (%) cell viability for different concentrations of *Z*-**1** (dark) or *E*-**1** illuminated with 415 nm light for 20 min. Mean of 3 independent experiments is shown. Error bars represent SD and all p-values were calculated using either Student's t test or Kruskal Wallis multiple comparison and represent n.s. p> 0.05, ** p<0.01, *** p<0.001 in comparison to DMSO-treated cells (dark).

130

References

[1]   S. Shah, B. Singh, *Bioorg. Med. Chem. Lett.* **2012**, *22*, 5388–5391.

[2]   Henrieta Volfova, Qi Hu, Eberhard Riedle, *EPA Newsletter* **2019**, 51–69.

[3]   Z. Beharry, M. Zemskova, S. Mahajan, F. Zhang, J. Ma, Z. Xia, M. Lilly, C. D. Smith, A. S. Kraft, *Mol. Cancer Ther.* **2009**, *8*, 1473–1483.

[4]   Z. Xia, C. Knaak, J. Ma, Z. M. Beharry, C. McInnes, W. Wang, A. S. Kraft, C. D. Smith, *J. Med. Chem.* **2009**, *52*, 74–86.

[5]   S. C. Heo, J. C. You, S. Jung, Y. N. Kim, S.-H. Shin, J.-Y. Lee, H. J. Kim, *J. Cell. Physiol.* **2022**, *237*, 3381–3393.

[6]   S. Fujii, S. Nakamura, A. Oda, H. Miki, H. Tenshin, J. Teramachi, M. Hiasa, A. Bat-Erdene, Y. Maeda, M. Oura, M. Takahashi, M. Iwasa, I. Endo, S. Yoshida, K. Aihara, K. Kurahashi, T. Harada, K. Kagawa, M. Nakao, S. Sano, M. Abe, *Br. J. Haematol.* **2018**, *180*, 246–258.

[7]   J. E. Zweig, T. R. Newhouse, *J. Am. Chem. Soc.* **2017**, *139*, 10956–10959.

[8]   A. Sailer, J. C. M. Meiring, C. Heise, L. N. Pettersson, A. Akhmanova, J. Thorn-Seshold, O. Thorn-Seshold, *Angew. Chem. Int. Ed.* **2021**, *60*, 23695–23704.

[9]   S. Schneid, F. Wolff, K. Buchner, N. Bertram, S. Baygün, P. Barbosa, S. Mangal, E. Zanin, *Cell Reports* **2021**, *34*, 108805.

[10]   J. Schindelin, I. Arganda-Carreras, E. Frise, V. Kaynig, M. Longair, T. Pietzsch, S. Preibisch, C. Rueden, S. Saalfeld, B. Schmid, J.-Y. Tinevez, D. J. White, V. Hartenstein, K. Eliceiri, P. Tomancak, A. Cardona, *Nat. Methods* **2012**, *9*, 676–682.

[11]   M. Okazaki, N. Uchino, M.Ishihara, H. Fukunaga, H. *Bull. Chem. Soc. Jpn.* **1998,** *71*, 1713-1718.

[12]   A. Guerraoui, M. Goudjil, A. Direm, A. Guerraoui, İ. Y. Şengün, C. Parlak, A. Djedouani, L. Chelazzi, F. Monti, E. Lunedei, A. Boumaza, *J. Mol. Struct.* **2023,** *1280*, 135025.

[13]   P. Delgado, J. Quiroga, J. Cobo, J. N. Low, C. Glidewell, *Acta Crystallogr. C* **2005,** *61*, o477-82.

131

6 Discussion

6.1 The BRCT domains of Ect2 have distinct functions during cytokinesis

During cytokinesis, a contractile ring forms and constricts between the segregating chromosomes to physically split the mother cell into two daughter cells. The crucial step for the formation and subsequently needed contractile activity of this ring is the activation of the small GTPase RhoA. To ensure successful cell division it is important that RhoA is locally activated at the cell equator and that active RhoA is maintained in a narrow zone to avoid contractility at the cell poles. Even though it is known that the GEF Ect2 is activating RhoA, the principles behind this are still poorly understood since it is not clear how Ect2 itself is regulated. The current model predicts that Ect2 is autoinhibited due to the interaction of its three N-terminal BRCT domains with its catalytic DH-GEF domain (Chen et al., 2020; Kim et al., 2005; Saito et al., 2004; Tatsumoto et al., 1999). This autoinhibitions is released due to phosphorylation of the centralspindlin component RacGAP1 by Plk1 and its subsequent binding to the BRCT1 domain of Ect2 at the spindle midzone (Burkard et al., 2009; 2007; Petronczki et al., 2007; Su et al., 2011; Wolfe et al., 2009; Yüce et al., 2005). This interaction opens up the confirmation of Ect2 and releases its GEF activity. However, it is not clarified how the single BRCT domains contribute to its regulation and function. Therefore, this study (section 2 – Chapter I) examined the distinct functions of each BRCT domain of Ect2 for successful cell division by deleting entire domains or inserting specific point mutations. This was accomplished by using a genetic replacement system for Ect2 in human HeLa cells, which was established earlier in our laboratory (Thesis of Dr. Kristina Buchner, 2019). We were able to express different mutants of Ect2 after depletion of endogenous Ect2 via RNAi. Cell division dynamics and Ect2 expression as well as localisation were analyzed using live-cell confocal imaging. Pattern of active RhoA localisation was followed by immunofluorescence staining against anillin which binds active RhoA (Piekny & Glotzer, 2008). Using biochemical techniques, binding and phosphorylation partners of Ect2 were identified and analysed. In this study, it was revealed that each BRCT domain has distinct functions for Ect2 regulation, functioning and subsequently cell division. The following model of Ect2 regulation is proposed (Figure 10): During

301

metaphase, Ect2 GEF activity is inhibited due to binding of W307 of the BRCT2 domain to the catalytic DH-GEF domain (Chen et al., 2020). During anaphase onset, Plk1 is taking part in three main steps: First, it phosphorylates RacGAP1 at the forming spindle midzone, second, it binds to the BRCT domains of Ect2 via its PBD and third, it phosphorylates the BRCT0. Binding and phosphorylation of BRCT0 by Plk1 partially opens the autoinhibited confirmation of Ect2, which allows subsequent binding of RacGAP1. RacGAP1 binding to the BRCT1 domain, supported by binding to BRCT0 and BRCT2 as well, leads to unbinding of the BRCT2 domain from the DH-GEF domain what subsequently releases autoinhibition and activates Ect2 GEF activity. Furthermore, RacGAP1 binding anchors active Ect2 at the equatorial zone of the cell. This maintenance is additionally supported by the BRCT2 domain, which binds the DH-GEF domain in case Ect2 is escaping the equatorial zone and thereby shuts its activity off again. Including previous studies in this model, it is likely that at this point Ect2 is not fully active yet and still partially inhibited by binding of the PH domain to the DH-GEF domain. This binding is released upon plasma membrane association of Ect2, where PH-mediated inhibition is released due to binding of GTP-bound RhoA to the PH domain (Chen et al., 2020). This step leads to complete release of Ect2 autoinhibition and fully active Ect2 at the equatorial membrane during anaphase. The different findings for each BRCT domain are discussed in the following sections.
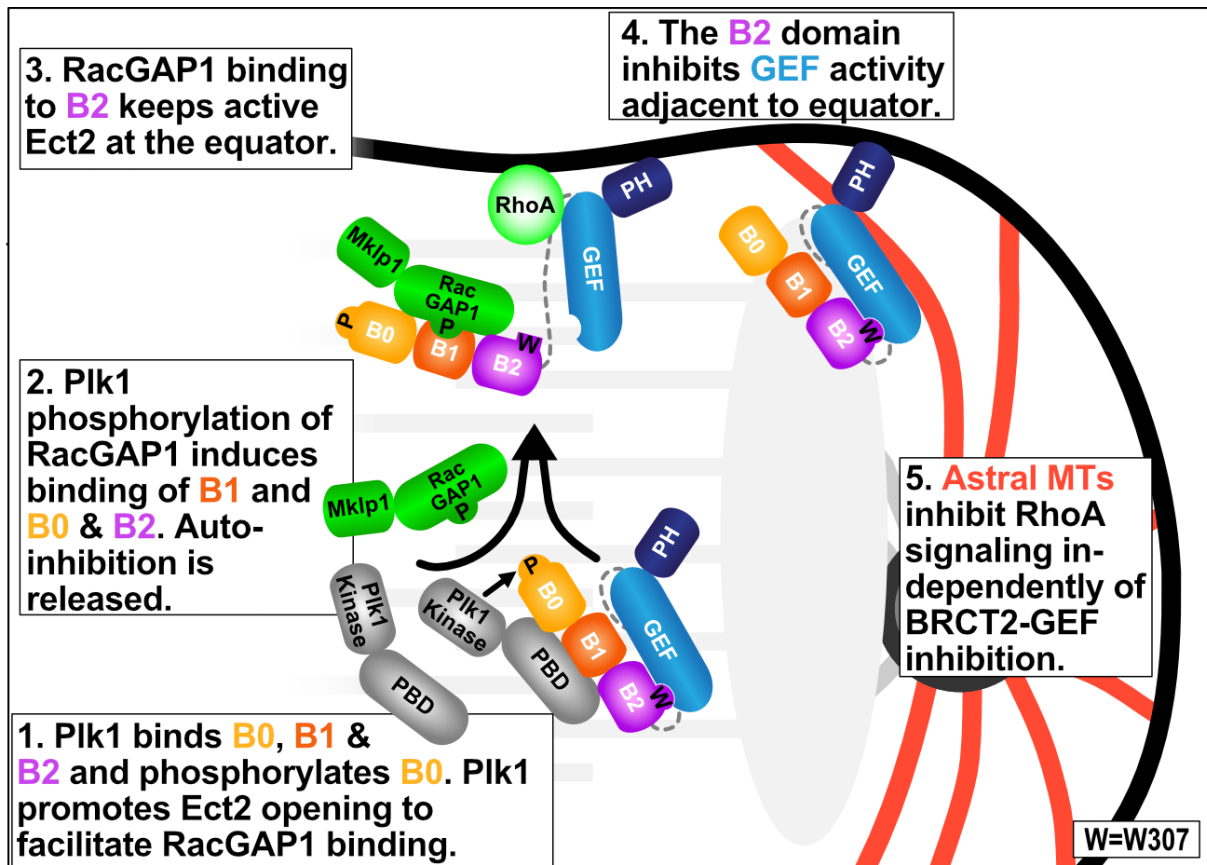
Figure 10: Schematic model of Ect2 regulation during cytokinesis in human cells.
1. Plk1 binds the BRCT domains at the spindle midzone and phosphorylates BRCT0, which favours an open confirmation of Ect2. 2. In addition, Plk1 phosphorylates RacGAP1, which induces binding of the BRCT1 domain to RacGAP1. RacGAP1 binds BRCT0 and BRCT2, and BRCT2 is released from the GEF domain. 3. Autoinhibition of Ect2 is released, RacGAP1 remains bound to Ect2 and tethers active Ect2 to the cell equator. 4. Active Ect2 that escapes from the cell equator is shut off by binding of the BRCT2 to the GEF domain. 5. Astral microtubules inhibit RhoA signaling independently of BRCT2-GEF. (Figure adapted from Schneid et al., 2021)

6.1.1 The BRCT1 domain activates Ect2 GEF activity by releasing its autoinhibition

It was assumed that Ect2 is activated by the release of its autoinhibition by binding of phosphorylated RacGAP1 to the BRCT1 domain at the spindle midzone (Burkard et al., 2009; Kamoji et al., 2006; Kim et al., 2014; Wolfe et al., 2009; Yüce et al., 2005; Zou et al., 2014). However, this hypothesis was contradicted by a study showing that

interrupting binding of RacGAP1 to the BRCT1 via two point mutations (T153A and K195M) did not result in cytokinesis failure (Kotýnková et al., 2016). Since Ect2 activity is essential for cytokinesis and its depletion via RNAi leads to >95% cytokinesis failure, this study implies that RacGAP1 interaction with the BRCT1 domain is dispensable for Ect2 activation. However, it is important to highlight that this conclusion is based on the assumption these two point mutations completely abolish RacGAP1 interaction. This was indeed counteracted by a study showing that interaction of RacGAP1 and Ect2 is not abolished in this mutant (Gomez-Cavazos et al., 2020). Due to these contradicting results, in this thesis two approaches were followed: First, an Ect2 mutant was expressed which was missing the entire BRCT1 domain, and second the before mentioned Ect2 mutant containing the two point mutations (T153A and K195M) was expressed – both after depletion of endogenous Ect2. Expression of Ect2 missing the BRCT1 domain showed high cytokinetic failure since cells were not able to form an ingressing furrow due to missing RhoA activity. Interestingly, deletion of BRCT1 domain completely abolished Ect2 midzone localization and led to a reduction in Ect2 equatorial localization. This indicates that missing activation of RhoA is not due to missing Ect2 localization but rather missing Ect2 activation since little midzone localization already supports cytokinesis (Figure 11).
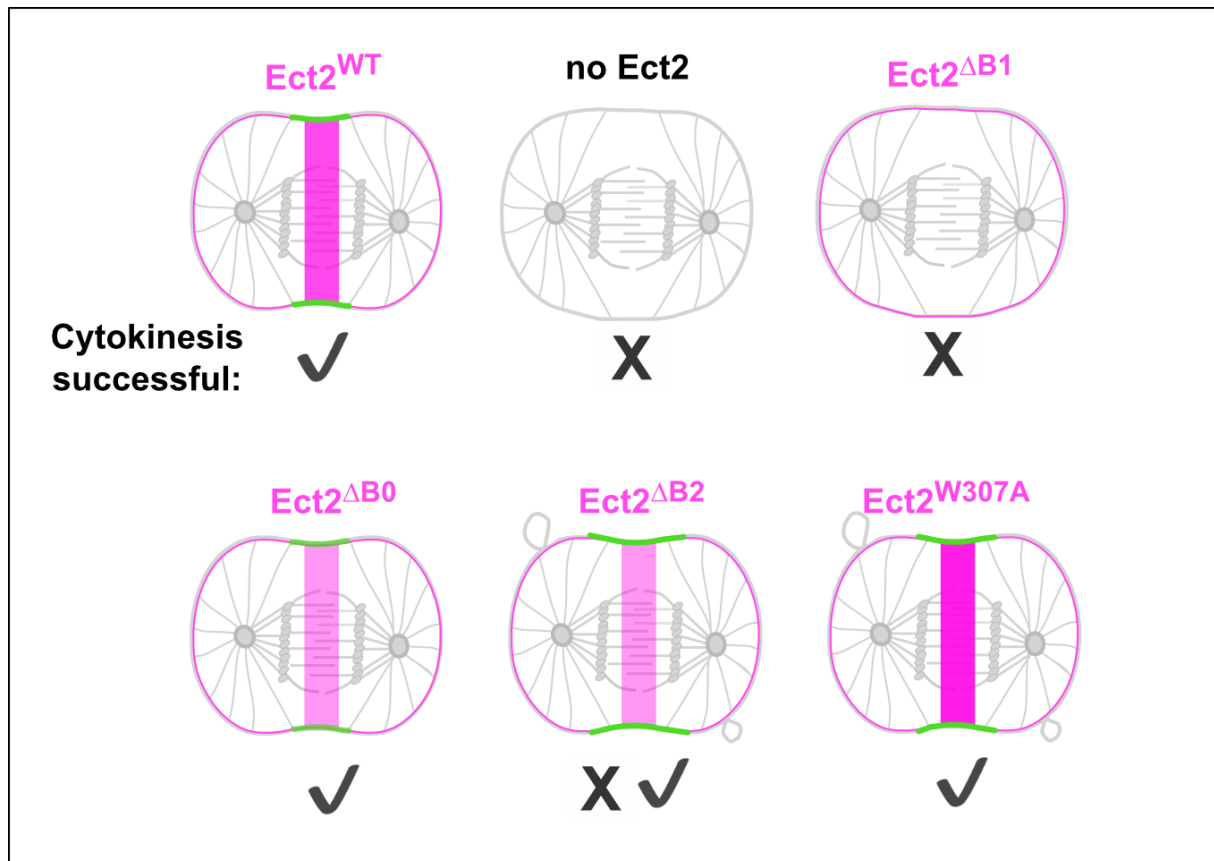
Figure 11: Schematic overview of Ect2 and RhoA localization of the different Ect2 mutant proteins.

In Ect2^{WT}, Ect2 is localizing at the spindle midzone and RhoA in a narrow zone at the cell equator. After depletion of Ect2 by RNAi (no Ect2), Ect2 as well as RhoA localization is lost. Deletion of BRCT1 domain (Ect2$^{\Delta B1}$), leads to loss of Ect2 at the spindle midzone and loss of RhoA at the cell equator. Deletion of BRCT0 domain (Ect2$^{\Delta B0}$), reduced both, Ect2 and RhoA, localization. Deletion of BRCT2 domain (Ect2$^{\Delta B2}$) reduced Ect2 localization to the spindle midzone and strongly broadened equatorial RhoA zone. Mutation of residue W307 in the BRCT2 domain (Ect2^{W307A}) increased Ect2 localization to the spindle midzone and broadened equatorial RhoA zone. (Figure adapted from Schneid et al., 2021)

The second approach showed that mutating T153 and K195 in the BRCT1 also led to a reduction of Ect2 midzone and membrane localization, but still higher as compared to complete domain deletion. Furthermore, only a slight increase in cytokinetic failure was observed in this mutant which fits to the finding of unperturbed RhoA activity. This strongly implies that there is a residual RacGAP interaction left in this mutant which is sufficient to support Ect2 and subsequent RhoA activation, confirming results by Gomez-Cavazos et al. (2020). Interestingly, via binding studies we found that

RacGAP1 was binding the BRCT1, but also the BRCT0 and BRCT2 domain, however to a lesser extent. Since Ect2 is not active in the absence of the BRCT1 domain, we assume that binding of RacGAP1 to BRCT0 and BRCT2 is not essential, but supports opening up the autoinhibited confirmation of Ect2. All together, we have shown that the BRCT1 domain of Ect2 is essential for its activation by releasing its autoinhibited confirmation via RacGAP1 binding.

6.1.2 The BRCT0 is not essential for but supports Ect2 function

The BRCT0 domain is the least conserved BRCT domain through the animal kingdom and since most BRCT domains occur in tandem repeats of two, it was very interesting to investigate this domain for Ect2 regulation. We found that expression of a Ect2 mutant missing the entire BRCT0 domain showed reduced Ect2 midzone localization and reduced RhoA levels at the equator (Figure 11). This is in correspondence with a previous study showing no increase of *in vitro* GEF activity after deletion of BRCT0 (Chen et al., 2020). These results indicate that Ect2 is less active if the BRCT0 domain is missing and therefore also less RhoA gets activated, however, both levels are sufficient to support cytokinesis. We further found that the BRCT0 gets heavily phosphorylated by Plk1 and binds to RacGAP1 *in vitro*. Therefore, our data suggest that even if the BRCT0 is dispensable for successful cytokinesis, its phosphorylation by Plk1 supports opening of Ect2 conformation which allows subsequent binding of RacGAP1 to the BRCT domains. BRCT0 then further assists the BRCT1 domain in releasing Ect2 activity upon binding to RacGAP1. Additionally, phosphorylation of BRCT0 by Plk1 might weaken the autoinhibitory binding of the BRCT2 to the DH-GEF by opening up confirmation of Ect2, which subsequently could allow binding of phosphorylated RacGAP1. Another possibility is that phosphorylation of BRCT0 keeps Plk1 in close proximity to RacGAP1, which might support the formation of Ect2-RacGAP1 complex. In summary, we suggest that the BRCT0 domain is dispensable for cytokinesis but assists in release of Ect2 autoinhibition and activation.

6.1.3 The BRCT2 plays a dual role in Ect2 regulation

During the course of this work, it was shown that the BRCT2 inhibits Ect2 GEF activity since deletion of this domain increases *in vitro* GEF activity (Chen et al., 2020). Furthermore, based on crystal structure analysis and *in vitro* GEF assays it was shown that a specific residue in the BRCT2 domain – W307 – is in direct contact with the DH-GEF domain and mutation of this residue to alanine also increased Ect2 GEF activity (Chen et al., 2020). This suggested that this specific residue is essential for inhibition of Ect2 GEF activity and thus its mutation to alanine leads to increased GEF activity. To test if the BRCT2 domain is inhibiting GEF activity during cytokinesis, Ect2 mutants either without the BRCT2 domain or a W307A mutation in the BRCT2 domain were analysed. Deletion of the BRCT2 domain or mutation of W307 in the BRCT2, but not BRCT0 or BRCT1 deletion, led to the formation of large blebs during metaphase and anaphase (Figure 11). To ensure a stable cell shape, cells are releasing internal pressure through the formation of small membrane blebs (Sedzinski, 2011). Increased activity of RhoA induces cellular tension and results in the formation of unusual large blebs (Zanin et al., 2013). Therefore, in this study formation of large blebs was used as a readout for increased Ect2 activity and hyperactive RhoA. Removal of BRCT2 and expression of W307A led to this phenotype, indicating hyperactive Ect2 and RhoA in these mutants. To further proof hyperactive RhoA in these mutants, the RhoA inhibitor C3 exoenzyme was added. This treatment indeed suppressed bleb formation, which strongly corroborates hyperactivity of RhoA in these mutants. Moreover, cells missing the BRCT2 domain showed a strong increase of cytokinesis failure and slightly reduced RhoA activity at the equator (Figure 11). This result seemed puzzling at first sight since an increase in RhoA activity was expected if the BRCT2-mediated inhibition of Ect2 GEF activity is absent. However, it was shown that the total amount of active RhoA is not different to control, it's rather distributed in a broader region at the equator. This indicates that there was not more RhoA activated, it just cannot be restricted to a narrow zone if the BRCT2 domain is missing. Interestingly, the mutation of the W307 residue in the BRCT2 domain did not induce cytokinetic failure, however showed strongly increased equatorial RhoA activity. The zone of RhoA was broadened in this mutant as well, but not to the same extend as full deletion of the BRCT2 domain. This points towards the fact that binding of the BRCT2 to the GEF domain is required to

form a narrow RhoA zone. It was shown that RacGAP1 is not only binding to the BRCT1 domain, but also to the BRCT2 domain. Therefore, a deletion of the BRCT2 domain affects both functions - binding to RacGAP1 and release of autoinhibition - indicating that RacGAP1-BRCT2 interaction anchors active Ect2 to the plasma membrane if autoinhibition is absent. The W307 allows RacGAP1 binding but lacks the BRCT2-mediated inhibition, therefore, it is just partially rescuing the narrow RhoA patterning at the equator. All together, the BRCT2 domain has a dual role for Ect2 regulation: it inhibits Ect2 GEF activity by binding to its DH-GEF domain and restricts Ect2 activity to a narrow zone to the equator via RacGAP1 binding.

6.1.4 RhoA patterning in cells expressing Ect2 missing all BRCT domains

Localization of active Ect2 to the midzone directs contractile ring formation at the cell equator. However, cells expressing an Ect2 construct lacking all three BRCT domains (Ect2$^{\Delta BRCT0-2}$) still formed an equatorial RhoA zone and cytokinesis was at least partially successful even though Ect2 was absent from the midzone and Ect2 autoinhibition was lost. This strongly indicates the existence of another spatial cue that restricts contractility to the equator. Since signals from the spindle midzone and the astral microtubules contribute to contractility at the cell equator (D'Avino et al., 2015; Green et al., 2012; Mishima, 2016, von Dassow, 2009), we hypothesized that signals from astral microtubules lead to formation of an equatorial RhoA zone even though all three BRCT domains are missing (Figure 12).
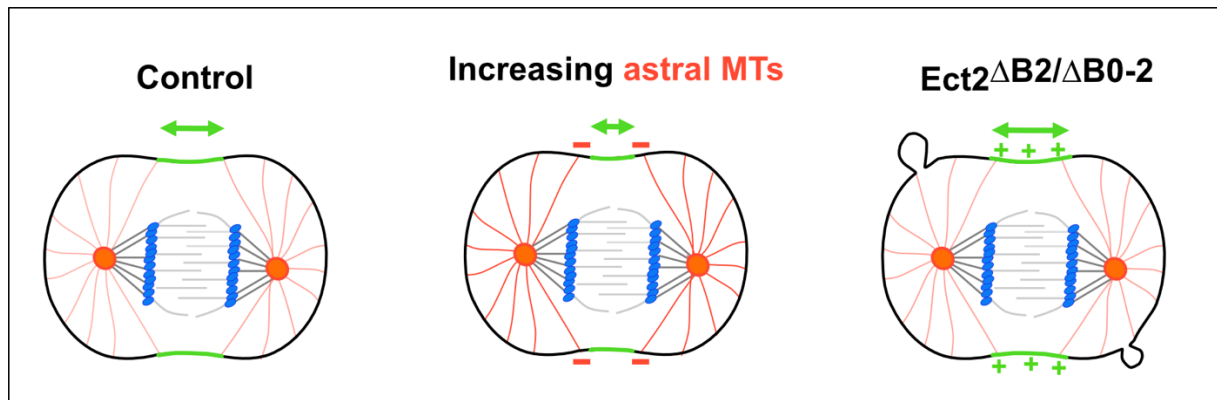
Figure 12: Schematic overview of RhoA zone width for different conditions.
In control cells, a narrow RhoA zone forms at the cell equator. Increasing length and number of astral microtubules narrows the width of RhoA zone. Cells expressing Ect2 lacking the BRCT2 or all BRCT domains show a broadened RhoA zone. (Figure adapted from Schneid et al., 2021)

To test this hypothesis, we increased the number of astral microtubules by depleting the microtubule depolymerizing kinesin MCAK via RNAi. It has been shown before that this treatment leads to an even more narrow RhoA zone in human cells (Desai et al., 1999; Hedrick et al., 2008; Rankin and Wordeman, 2010; van Oostende Triplet et al., 2014; Zanin et al., 2013), which we could also show for control and Ect2^{WT} cells. Interestingly, increasing astral microtubules length by depletion of MCAK in cells missing the BRCT2 domain (Ect2$^{\Delta BRCT2}$ and Ect2$^{\Delta BRCT0-2}$) results also in a reduction of the RhoA zone width. However, this phenotype was not found due to increased Ect2 enrichment at the cell equator since Ect2 levels were not elevated by this treatment meaning that elongated astral microtubules themself do not promote Ect2 enrichment. This rather indicates that astral microtubules inhibit RhoA signaling independently of BRCT2-mediated inhibition since otherwise we would not expect a decrease in the zone width in mutants missing the BRCT2 domain. In summary, we found more evidence for the existence of an aster-based model, in which astral microtubules pattern RhoA signaling even in the absence of stimulating signals from the spindle midzone and thereby represent an independent additional control mechanism of RhoA signaling besides Ect2 autoinhibition. However, it is important to mention that even if inhibiting signals from the astral microtubules were increased, they could not completely compensate the increased GEF activity of Ect2 when autoinhibition is absent, which is shown by the still broadened RhoA patterning in Ect2$^{\Delta BRCT2}$ and Ect2$^{\Delta BRCT0-2}$ cells after MCAK depletion.

6.1.5 Ect2 regulation by Plk1 kinase: Upstream or downstream?

It is assumed that Plk1 phosphorylates RacGAP1, which induces its binding to the BRCT domains of Ect2 and subsequent Ect2-RhoA signaling pathway (Burkard et al., 2009; Yüce et al., 2005). However, it was shown that Plk1 interacts with Ect2 via its PBD and phosphorylates Ect2 *in vitro*, which suggests a direct role of Plk1 in Ect2 regulation and functioning (Niiya et al., 2006; Suzuki et al., 2015; Wolfe et al., 2009). This was further collaborated by a study showing that a phosphomimetic RacGAP1 mutant rescues the interaction with the N-term of Ect2 *in vitro*, however these cells fail in cytokinesis in the absence of Plk1 activity. Additionally, phosphomimetic RacGAP1 was able to recruit the N-term, but not full length Ect2, to the spindle midzone (Wolfe et al., 2009). Therefore, a potential role of Plk1 in releasing Ect2 autoinhibited was hypothesized. To investigate if Plk1 assists in release of Ect2 autoinhibition, Plk1 was inhibited in cells which already lack the BRCT2-mediated inhibition: BRCT2 deletion or BRCT0-2 deletion (Figure 13).
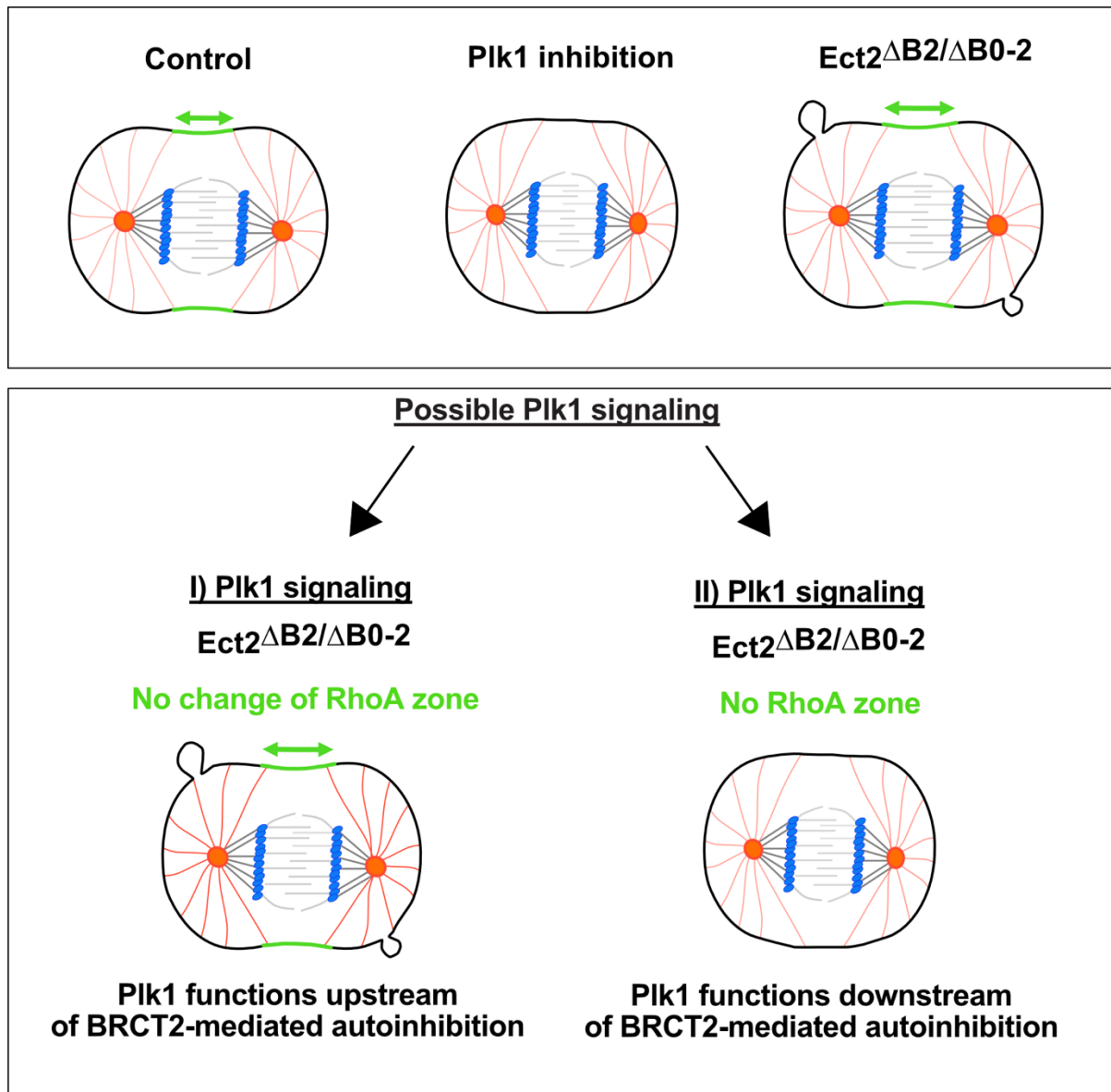
Figure 13: Schematic overview of possible signaling pathways of Plk1.
Plk1 could act upstream (I) of BRCT2-mediated inhibition (no change in RhoA zone expected) or downstream (II) of BRCT2-mediated inhibition of Ect2 (no formation of RhoA zone expected).

Interestingly, we found that inhibition of Plk1 in these cells did not change Ect2 activity. Neither the levels of active RhoA and its corresponding zone width nor formation of large blebs were affected. This means that requirement of Plk1 activity must occur upstream of releasing BRCT2-mediated inhibition. Via *in vitro* binding studies, we found that the PBD of Plk1 binds to all BRCT domains, but the strongest interaction was found with the BRCT0 domain. Furthermore, *in vitro* phosphorylation of BRCT0, but not BRCT1 and BRCT2, by Plk1 was shown. These findings put attention

especially on an interaction between Plk1 and the BRCT0 domain, that might regulate Ect2 activity. We hypothesize that Plk1 binding and subsequent phosphorylation of BRCT0 has two effects: first, it keeps Plk1 close to RacGAP1, which binds all BRCT domains and second, this interaction could assist in opening up the confirmation of Ect2, which allows access for RacGAP1 to the BRCT domains. This sequential model of Plk1 interaction with the BRCT0 might explain the found phenotypes of reduced Ect2 midzone localization and RhoA levels at the equator if the BRCT0 domain is missing.

6.1.6 Concluding remarks and outlook

This study investigates the role of the N-terminal structural domains of the GEF Ect2 on its function and regulation during cytokinesis. By examining the effects of structural modifications, it provides detailed insights into how Ect2 is regulated in time and space. The study shows that the N-terminal BRCT domains do not act as a single functional unit, as previously assumed, but rather have distinct roles. However, it was also shown that the BRCT domains cooperate with each other to fulfil their function. BRCT0 and BRCT1 cooperate to facilitate activation of Ect2 GEF activity, whereas BRCT2 inhibits GEF activity. Additionally, the essential role of RacGAP1 in releasing Ect2 autoinhibition was further underscored. Moreover, the hypothesis of a redundancy of two regulatory mechanism ensuring proper contractile ring formation and positioning was further strengthened: On the one hand, stimulatory signals based on Ect2 emanating from the spindle midzone, and on the other hand, inhibitory signals emanating from astral microtubules. Over the last few years, more evidence has emerged that has shaken the model of Ect2 regulation. Recent studies suggested a putative role for the membrane binding PH domain as well as the S-loop in GEF inhibition meaning the current model needs to be revisited to incorporate the latest findings (Chen et al., 2020, Su et al., 2011). Although this study has provided significant insights, further research is required to fully understand the precise mechanisms of cytokinetic regulation. The key question arising from this study is how RacGAP1 binding to the BRCT1 disrupts the BRCT2-GEF interaction. The binding site of RacGAP1 on BRCT1 have been shown (Gomez-Cavazos et al., 2020), however,

the binding interface on BRCT0 and BRCT2 are unknown. Therefore, the molecular mechanism of how RacGAP1 disrupts binding of the BRCT2 to the GEF domain is not fully understood yet. Additionally arising by this study is the question about involvement of the PH membrane and the S-loop in GEF inhibition. If there is a role of these two structural parts, where and when does it take place? Furthermore, is this role upstream or downstream of BRCT2-mediated GEF inhibition? To gain full understanding of how successful cytokinesis in human cells is guaranteed, future research also has to focus on the inhibitory signals. What are the molecular mechanisms behind the inhibitory signals emanating from the astral microtubules?

6.2 Spindle-pole enriched Aurora A kinase activates Mitotic-phase GAP to locally restrict RhoA signaling for successful cell division

During cytokinesis, a contractile ring consisting of actin and myosin assembles underneath the equatorial plasma membrane and divides the cell into two daughter cells. Formation and constriction of this ring is induced by active RhoA at the cell equator. However, how is RhoA activity restricted to the equator of the cell? Stimulatory signals deriving from the spindle midzone promote RhoA activity at the cell equator by releasing Ect2 autoinhibition (Burkard et al., 2009; Chen et al., 2019; Gomez-Cavazos et al., 2020; Schneid et al., 2021; Wolfe et al., 2009; Yüce et al., 2005). Even though, research over the last years gave meaningful insights how contractility is induced at the cell equator by RhoA activation, the question remains how RhoA activity is spatially confined. How is active RhoA kept at the equator and its activation blocked at the cell poles? Several studies proposed that astral microtubules could limit contractility to the cell equator and prevent it at polar regions (Bement et al., 2006; D'Avino et al., 2015; Green et al., 2012; Mishima, 2016; von Dassow, 2009). However, the molecular nature and mechanisms of these inhibitory were almost unknown. A study from the Zanin laboratory in 2018 showed for the first time that there is an active process which prevents contractility at the cell poles in *C. elegans.* This active process is depended on the kinase Aurora A and its aster-based activator TPXL-1 (Mangal et al., 2018). Nevertheless, it is not clarified if this process is also conserved in other species.

Therefore, this study (section 3 - Chapter II) examined the role of Aurora A kinase in spatially confining RhoA activity in human cells. This was accomplished by usage of a highly specific Aurora A kinase inhibitor in human cells. Cell division dynamics and RhoA activity patterning were analyzed using live-cell confocal imaging and immunofluorescence staining. Furthermore, usage of biochemical techniques allowed deeper understanding of the molecular basis underlying inhibitory signals in human cells. In this part of the thesis, it was revealed that Aurora A kinase spatially restricts RhoA activity to the cell equator by phosphorylating the GAP MP-GAP at three specific residues. Therefore, the following model of spatially limiting RhoA signaling in human cells is proposed (Figure 14):

Spindle-pole localized Aurora A kinase phosphorylates MP-GAP at the cell poles. Aurora A kinase phosphorylates MP-GAP at three amino acids in its hinge region, which opens up its confirmation, releases its autoinhibition and promotes its GAP activity. Thereby, MP-GAP shuts off RhoA activity at the cell poles and ensures its activity only at the cell equator.
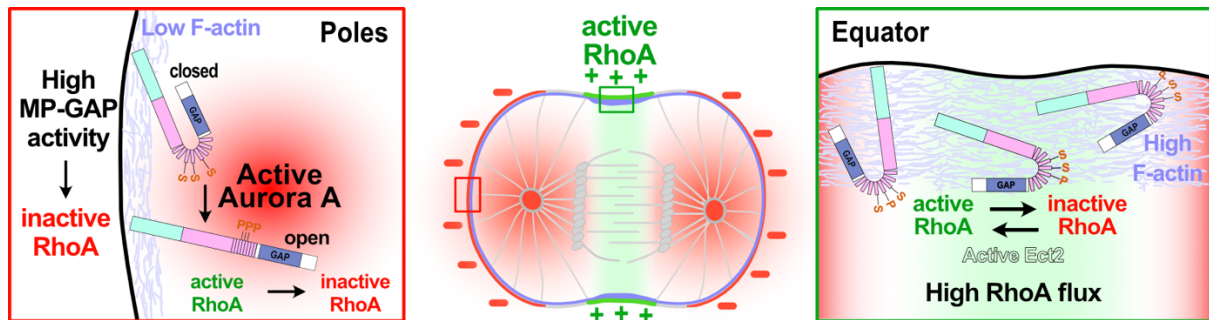
Figure 14: Schematic model of Aurora A signaling and MP-GAP regulation during cytokinesis in human cells.
MP-GAP activity is regulated by two spatially distinct inputs at the cell poles (left) and cell equator (right) during anaphase. At the cell poles, low F-actin levels (purple) coincide with high Aurora A kinase activity (red). Aurora A kinase phosphorylates the hinge region of MP-GAP, leading to conformational opening and activation of MP-GAP, which promotes RhoA inactivation (red) at the poles. At the cell equator, Ect2 autoinhibition is released, which promotes RhoA activation (green) and subsequent F-actin polymerization. Increased equatorial F-actin levels drive MP-GAP accumulation, which enhances RhoA GTP hydrolysis and RhoA turnover at the equator spatially confining active RhoA in a narrow equatorial zone.

6.2.1 Aurora A kinase inhibits RhoA activity at the cell poles

Aurora A kinase is a serine/threonine kinase, which has a crucial role in regulating cell cycle progression, especially during the transition from G2 to M-phase. Besides choreographing events during progression of the cell cycle, it is crucial for processes such as centrosome maturation and spindle assembly (Tavernier et al., 2021). Aurora A kinase is localized to the centrosomes and a rapid turnover rate was shown via FRAP experiments in the *C. elegans* embryo as well as human cells (Portier et al., 2007; Stenoien et al., 2003).

It was shown that that Aurora A promotes clearing of contractile ring proteins from the cell poles in *C. elegans* and the presented study could indeed show that this function is conserved in human cells. First of all, acute inhibition of Aurora A kinase at

anaphase onset reduced the spindle midzone length. This is in harmony with a former study showing that inhibition of Aurora A kinase perturbs assembly of the mitotic spindle and chromosome movement towards the poles in human cells (Reboutier et al., 2013). Furthermore, inhibition of Aurora A kinase indeed increased anillin levels at the poles and broadened the equatorial anillin zone in anaphase, however it did not increase the overall equatorial anillin levels. These findings suggest that Aurora A kinase has an inhibitory role conserved in human cells, which limits anillin accumulation outside of the equator of a cell. Several studies showed evidence for the existence of an aster-based model, in which the astral microtubules pattern RhoA signaling. Therefore, it's possible that inhibition of Aurora A kinase alters astral microtubules dynamics and thereby indirectly alters anillin patterning. We have shown that astral microtubules remained intact after inhibition treatment of Aurora A and can thereby exclude that the observed phenotypes originate from reduced astral microtubules.

It was shown that the cortical anillin levels were not only increased during anaphase, but also in metaphase after Aurora A inhibition. This is an important finding since elevated RhoA activity during metaphase leads to defects in spindle positioning and chromosome segregation and might be the driver of cancer development (Limzerwala et al., 2020). As mentioned before, RhoA activation is prevented in metaphase due to phosphorylation of Ect2 by CDK1 (Su et al., 2011). Our data suggests that Aurora A phosphorylation of MP-GAP represents an independent safeguard mechanism that limits RhoA activity in metaphase. Previous studies have shown the existence of an activity gradient of Aurora A kinase around the spindle poles in *Drosophila* S2 cells (Ye et al., 2015). Notably, in humans and *C. elegans* Aurora A is regulated by its activator TPX2/TPXL-1, which is not the case for *Drosophila* (Goshima, 2011). Therefore, an even stronger gradient could by formed by the assistance of TPX2/TPXL-1. It is assumed that these gradients are partially due to a high turnover rate of Aurora A kinase at the centrosomes in human HeLa cells and *C. elegans* embryos (Portier et al., 2007; Stenoien et al., 2003). And indeed, fluorescence recovery after photobleaching (FRAP) experiments have shown an extraordinarily high turnover rate for Aurora A kinase at the centrosomes (Stenoien et al., 2003). However, even though Aurora A kinase exist in a gradient with a high turnover rate at the centrosomes, how does it reach the adjacent polar cortex? The Nuclear Mitotic Apparatus protein (NuMA) localizes to the spindle poles during metaphase and

becomes highly enriched at the polar cortex during anaphase in human cells (Kiyomutsi &Cheeseman, 2013; Kotak & Gönzy, 2013). Interestingly, NuMA also has a high turnover rate, however, Aurora A kinase turns over much faster (Stenoien et al., 2003). Therefore, it is like that Aurora A kinase is also able to localize to the adjacent polar cortex and facilitates its inhibitory role by limiting anillin accumulation. And indeed, it has been shown that increasing Aurora A activity by inhibition of PP6 (Serine/threonine-protein phosphatase 6, limits Aurora A activity) in *C. elegans* embryos causes ectopic accumulation of Aurora A kinase on the cell cortex, which increases cortical stiffness (Afshar et al., 2010; Kotak et al., 2016). Therefore, it is likely that Aurora A kinase can also localize from the centrosomes to the polar cortex in human cells. However, it's still not clear how Aurora A localizes from the centrosomes to the cortex. It is well known that molecules can move along microtubules primarily facilitated though molecular motor proteins, which use hydrolysis of ATP to generate direct movement. The two main classes of motor proteins are kinesins and dyneins: while kinesisn typically move towards the plus ends of microtubules (directed towards cell periphery), dyneins move towards the minus ends of microtubules (directed towards the microtubule-organizing center) (Goldstein & Yang, 2000; Hirokawa, 1998; Verhey & Hammond, 2009). While association of Aurora B kinase with microtubules has been shown several times (Delacour-Lacrose et al., 2004; Gruneberg et al., 2004), there is no evidence that Aurora A kinase localization is dependent on microtubules. A previous study has even shown that association of Aurora A kinase with the centrosome is independent of microtubules in *Drosophila*, which suggests that microtubules are not required for Aurora A to reach the polar cortex (Giet et al., 2002). Therefore, it is assumed that Aurora A kinase diffuses from the centrosomes to the polar cortex, which allows its spatial organization without an active transport. During metaphase, the cell is rounded and the spindle poles are close together, which suggests a uniform distribution of active Aurora A throughout the cell. During anaphase, the cell elongates and the spindle poles move away from each other to the poles. Since Aurora A is localized at the centrosomes, Aurora A activity is expected to be high at the cell poles and low at the cell equator (Figure 15). This gradient and localization of Aurora A activity was corroborated in the presented study by showing that Aurora A preferentially interacts with MP-GAP at the polar cell periphery and not at the cell equator.
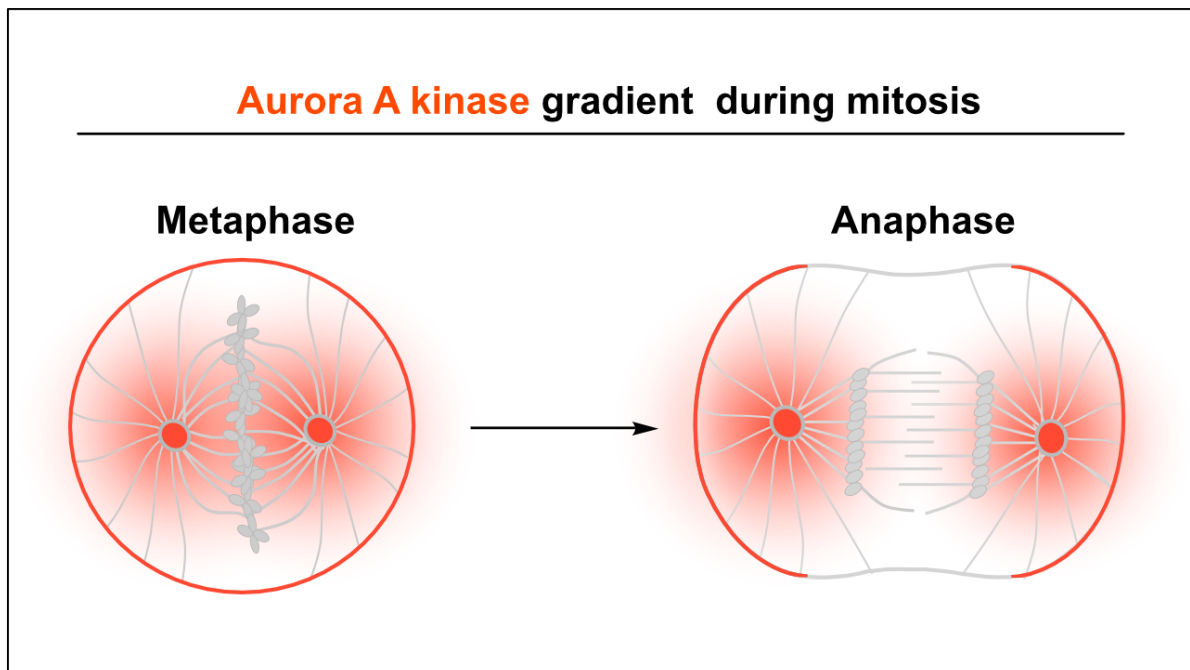
Figure 15: Schematic model of Aurora A kinase gradient during mitosis in human cells.
Aurora A is localized at the centrosomes and astral microtubules. During metaphase the cell has a round shape and spindle poles and centrosomes are close together, therefore active Aurora A is uniformly distributed throughout the cell. During metaphase to anaphase transition, the cell poles and centrosomes move away from each other due to cell elongation. Therefore, Aurora A activity is assumed to be high at the cell poles and low at the cell equator.

6.2.2 Aurora A kinase limits RhoA signaling by phosphorylating MP-GAP

From the above discussed findings about Aurora A limiting RhoA activity the question arises how Aurora A kinase blocks RhoA signaling at the cell poles in human cells. Since it was shown that Aurora A kinase phosphorylates substrates coming close to the spindle poles (Bayliss et al., 2003; Kinoshita et al., 2005), it was hypothesized that Aurora A activates the negative RhoA regulator MP-GAP by phosphorylation. Indeed, we showed phosphorylation of MP-GAP by Aurora A kinase *in vitro*, which could be even narrowed down to three specific amino acid residues in the first fragment of MP-GAP. The fact that Aurora A kinase phosphorylates MP-GAP, the negative regulator of RhoA, indicates that this is the underlying, long-searched molecular mechanism of

the inhibitory signaling. Indeed, depletion of MP-GAP or expression of a phosphodeficient mutant of MP-GAP mimics the Aurora A inhibition phenotype by showing increased polar anillin levels and a broadened equatorial anillin zone, which strongly suggests that Aurora A promotes MP-GAP activity and thereby restricts contractility from the cell poles (Figure 16).
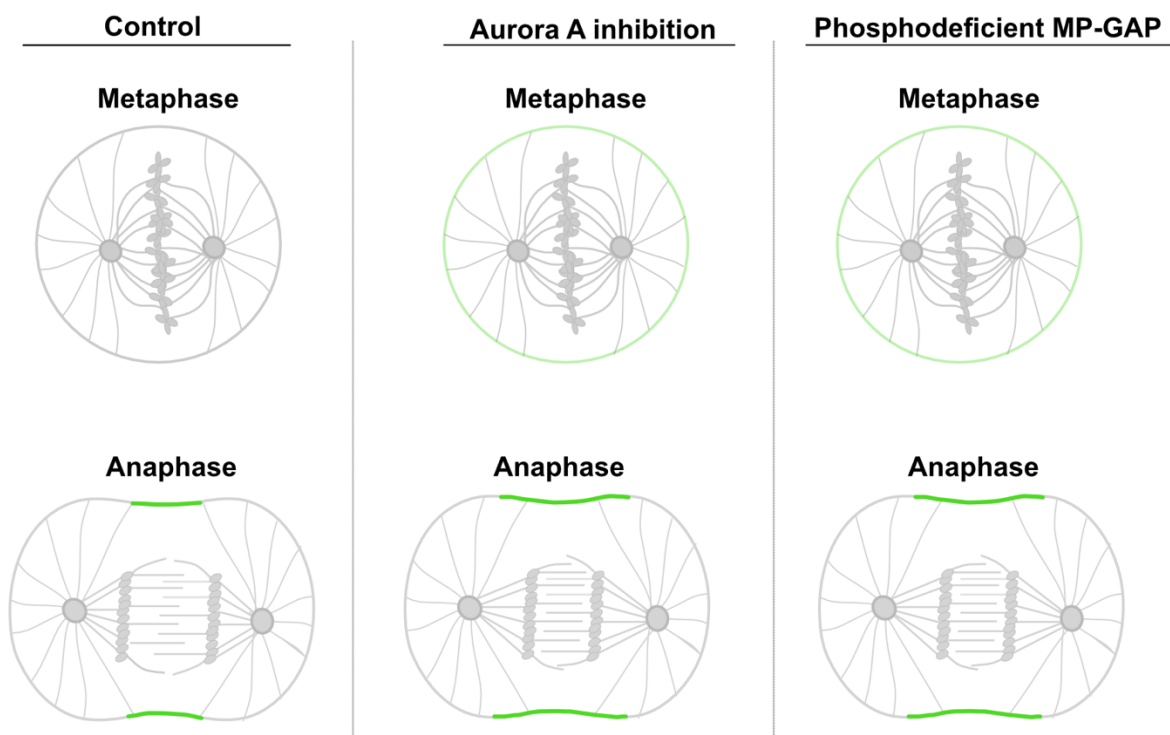
Figure 16: Summary of anillin localization for different conditions during cytokinesis in human cells.
During metaphase, anillin is absent from the cortex. In anaphase, anillin localizes to the equatorial region of the cell and enriches in a narrow zone. Inhibition of Aurora A kinase leads to increased anillin levels during metaphase and a broadened equatorial zone in anaphase. This anillin localization is mimicked by expression of phosphodeficient MP-GAP mutant and simultaneous depletion of endogenous MP-GAP.

However, Aurora A kinase and MP-GAP show different localization patterns within the cell. While Aurora A kinase is localized at the centrosomes and astral microtubules (Marumoto et al., 2005; Portier et al., 2007; Stenoien et al., 2003), MP-GAP localizes to the cell periphery (Zanin et al., 2013). Therefore, it is most likely that Aurora A

phosphorylates MP-GAP preferentially at the polar cell periphery and not at the spindle poles which was further corroborated by the finding that both are in close proximity at the cell poles. This hypothesis fits with the idea of an active Aurora A kinase gradient reaching the adjacent polar cortex. However, MP-GAP is enriched at the equatorial cortex of a cell, meaning it does not only restrict RhoA activity at the cell poles but also at the cell equator. If Aurora A activates MP-GAP at the poles, how does it fulfil its function at the cell equator? Active RhoA induces F-actin polymerization, and since RhoA activity is high at the cell equator, F-actin levels are high at the equator and low at the poles. Several studies have shown that RGA-3/4, the orthologue of MP-GAP, gets recruited by F-actin in echinoderm eggs and *C. elegans* (Bement et al., 2015; Michaeux et al., 2018). These findings raised the idea of an activation-inhibition mechanism: RhoA activity induces F-actin polymerization, which results in recruitment of the RhoA GAP MP-GAP to locations with high RhoA activity, which subsequently inactivates RhoA. Thereby, RhoA induces F-actin polymerization and simultaneously gets indirectly negatively regulated by F-actin. In the present study, we show that F-actin is required to recruit MP-GAP to the cell equator in human cells. We speculate that equatorial MP-GAP then takes its part in the before mentioned RhoA flux model, which is based on a simultaneous activation and inactivation of RhoA. This dynamic regulation of RhoA is leading to a flux of active RhoA at the equator. Recruitment of MP-GAP by F-actin to the cell equator is therefore essential to inactivate RhoA at the equator and to restrict RhoA activity to a narrow zone at the equator. At the same time, F-actin levels and subsequently also MP-GAP levels are low at the cell poles. We therefore hypothesize that phosphorylation of MP-GAP by Aurora A is needed to elevate MP-GAP activity and inactivate RhoA at the cell poles. Collectively, this means that MP-GAP function is regulated by two distinct spatial cues: localization and targeting of MP-GAP is dependent on F-actin and the required boost in activity is dependent on Aurora A phosphorylation.

6.2.3 Aurora A kinase activates MP-GAP

We suggest that Aurora A activates MP-GAP and thereby boosts its activity especially at the cell poles. The crucial question is: how? It has been shown for several GAPs

that they exist in an autoinhibited state (Dee et al., 2020; Fincham et al., 1999; Roof et al., 2000), similar to the GEF Ect2, which has to be released first to increase GEF activity (Chen et al., 2020; Kim et al., 2005; Saito et al., 2004; Schneid et al., 2021). A previous study has shown that the RhoA GAP GRAF3 (GTPase Regulatory Associated with FAK), which is expressed in smooth muscle cells in mice and humans, and controls blood pressure by inhibiting RhoA-mediated contractility, adapts an autoinhibitory confirmation which gets released upon phosphorylation at a specific amino acid in its linker region between the GAP domain and the N-terminus (Dee et al., 2020). Therefore, we hypothesized that human MP-GAP might adapt an inhibitory confirmation as well, which gets released upon phosphorylation by Aurora A kinase (Figure 17).
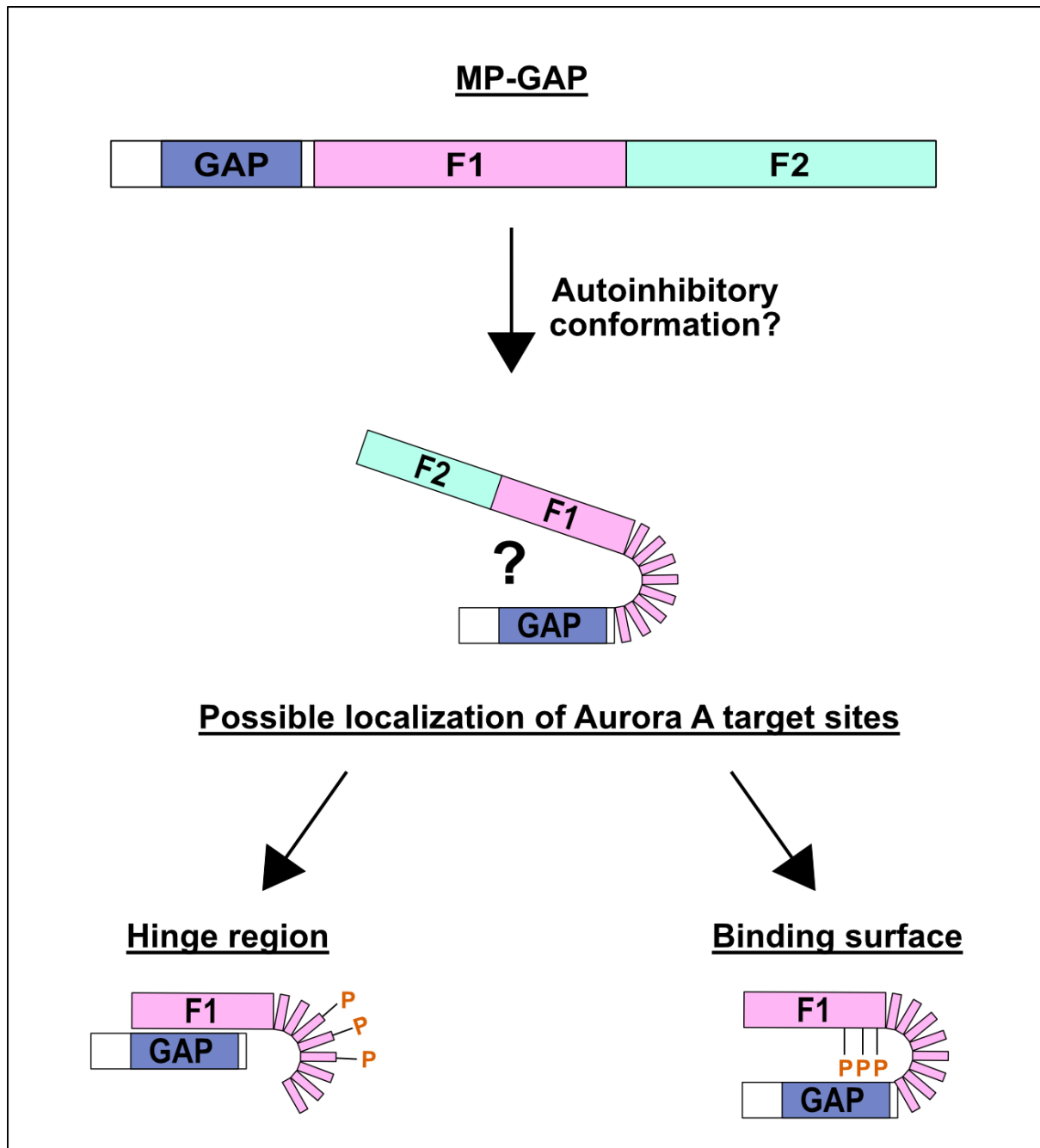
Figure 17: Schematic representation of the possible autoinhibitory confirmation of MP-GAP.
Aurora A target sites could be located in the hinge region of MP-GAP, which connects the GAP domain to the N-terminus, or in the binding surface of the F1 fragment to the GAP domain.

In this study it was shown that the F1 region of MP-GAP binds to it catalytic GAP domain, which made the possibility of MP-GAP adopting an autoinhibitory conformation highly likely. However, it was furthermore shown that the phosphorylation target sites for Aurora A are located in the hinge region of MP-GAP,

which connects its GAP domain with the N-terminus, since binding of the F1 region and GAP domain was not blocked after rendering target sites to phosphomimetic residues. Therefore, we speculate that phosphorylation of the hinge region by Aurora A promotes confirmational opening of MP-GAP and thereby increases its GAP activity.

6.2.4 Aurora A kinase and Ect2 together ensure successful cytokinesis

The successful development of multicellular organisms depends on their ability to adapt to perturbations. To achieve this, biological processes must exhibit robustness, enabling them to proceed effectively despite potential perturbations (Wagner & Wright, 2007). Since cell division is an enormous robust process, the existence of redundant mechanisms would not be surprising. There are several impressive examples for the robustness of cell division in different organisms, from plants where the very critical and correct orientation of the division plane is ensured by multiple redundant processes (Uyehara & Rasmussen, 2023) to *C. elegans* where the co-existence of centrosome-dependent and centrosome-independent pathways for spindle assembly ensure proper cell division and embryonic viability (Mullen & Wignall, 2017; Müller-Reichert et al., 2010). In the presented study we show another evidence for the robustness of cytokinesis in human cells by identifying Aurora A signaling and Ect2 autoinhibition as redundant mechanisms to ensure successful cell division. Inhibition of Aurora A kinase did not result in cytokinesis failure, despite a broadened equatorial zone of anillin and increased accumulation of anillin at the cell poles. A very similar phenotype regarding anillin pattern is observed after increased RhoA signaling by abolishing Ect2 autoinhibition and here again, the cells are still successful in cytokinesis (Schneid et al., 2021). This raised the idea that these both mechanisms – Aurora A signaling and Ect2 autoinhibition – protect the cell against cytokinesis failure and thereby contribute to the extreme robustness of cell division. We therefore asked whether the combined effects of Aurora A inhibition and loss of Ect2 autoinhibition lead to cytokinesis failure (Figure 18).
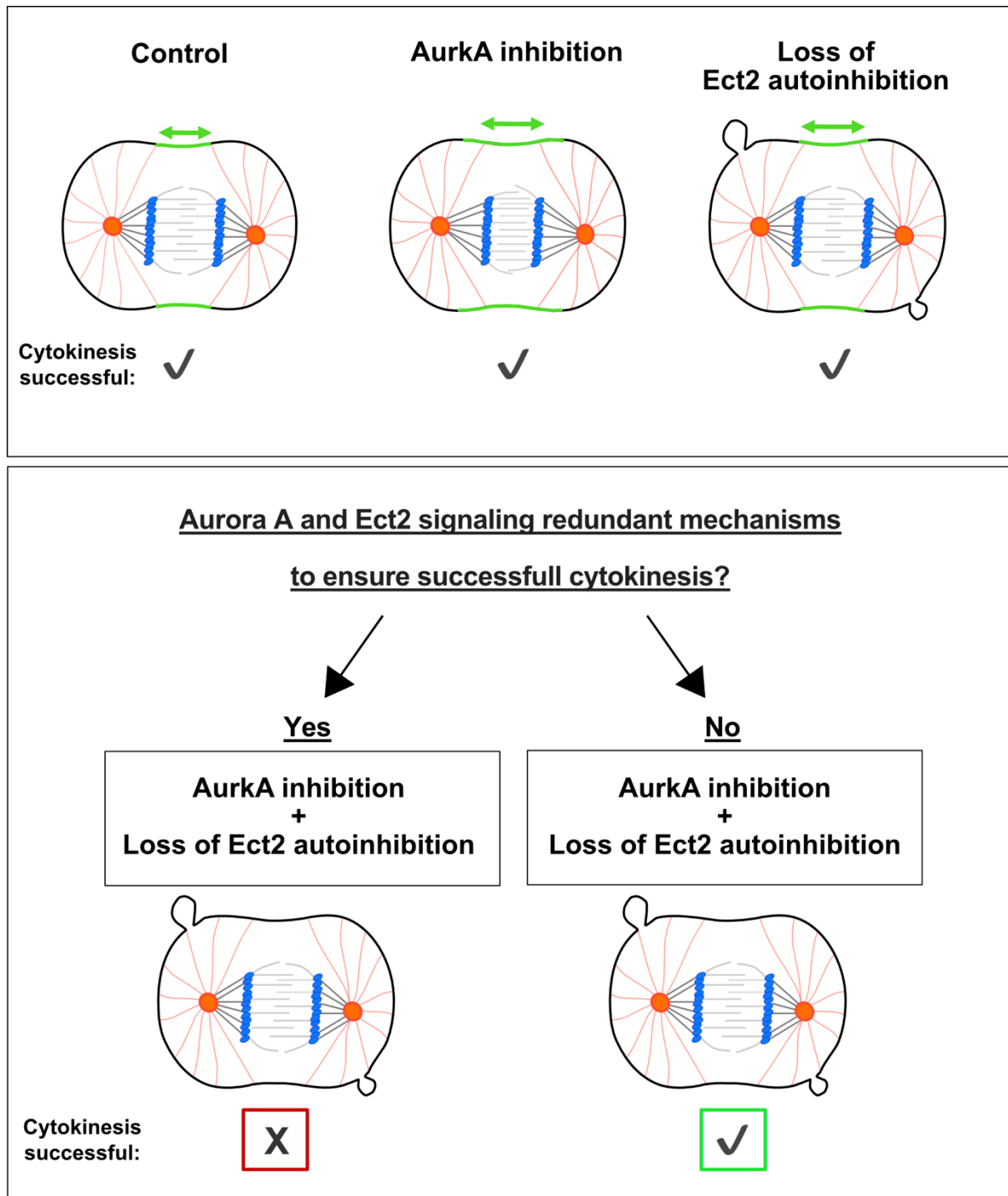
Figure 18: Schematic illustration of Aurora A signaling and Ect2 autoinhibition in the spatial regulation of RhoA activity during cytokinesis in human cells. Aurora A and Ect2 may function as parallel or redundant mechanisms to spatially pattern RhoA activity. If they act redundantly, simultaneous disruption of both pathways is expected to impair cytokinesis success (left). Conversely, if both pathways act independently, cytokinesis may proceed successfully (right).

Indeed, it was shown that loss of Aurora A kinase activity induced cytokinesis failure in cells which are lacking Ect2 autoinhibition. This means Aurora A signaling and autoinhibition of Ect2 are redundant mechanisms, which act singly in regulating RhoA activity, but act combined in protecting cells against cytokinesis failure. However, each of both mechanisms is sufficient to limit RhoA activity. This is most likely possible since both pathways act at different spatial positions within a cell. While Aurora A signaling is high at the spindle poles, Ect2 activity is concentrated at the equatorial region. Since they are independent from each other, inhibition or absence of one does not impact localization or activity of the other one. In case Aurora A signaling is abolished, Ect2 activity is still released at the spindle midzone and therefore RhoA is still activated at the cell equator although the activity zone is broadened. The other way around, Aurora A still restricts RhoA activity from the cell poles in case Ect2 and subsequently RhoA activity is not inhibited. The redundancy of these two regulatory mechanisms reflects the robustness of cytokinesis against perturbations to still ensure its overall success.

6.2.5 Concluding remarks and Outlook

This study uncovered a long-searched mechanism by which MP-GAP spatially restricts RhoA activity during cytokinesis through its dual-layered regulation by Aurora A kinase and F-actin. It is shown that the GAP MP-GAP is central to modulate RhoA activity at the cell equator, but also at the cell poles. Activity of MP-GAP is regulated by two distinct inputs: its localization is governed by F-actin and its activity is tuned via phosphorylation by Aurora A kinase. This mechanism of dual regulation ensures that RhoA is inactive at the poles and restricted to a narrow zone at the cell equator, where it is essential for formation and ingression of the contractile ring, which also underscores the robustness of preventing mislocalized and unrestricted RhoA activity during cytokinesis. The study provides first evidence that Aurora A kinase promotes MP-GAP activity at the polar cortex, thus enhancing its function in RhoA inactivation. MP-GAP accumulates at the cell periphery and the cell equator due to binding to F-actin, which ensures that RhoA activity is spatially confined and maintained to the equatorial region of the cell. Additionally, this study highlights the redundancy of Aurora A signaling and Ect2 autoinhibition in regulating RhoA activity. By elucidating

the functional connection between these two pathways, this work provides a more detailed picture of how RhoA activity is fine-tuned to ensure successful cell division. Even though the presented study gives meaningful insights, further research is required.

It is essential to gain deeper and more detailed insights of the interaction of Aurora A kinase and MP-GAP. Does Aurora A kinase indeed enhance MP-GAP GAP activity via phosphorylation? Even though the presented study hints to this possibility and the fact that this is known for several GAPs and GEFs, further structural and biochemical analyses are crucial to confirm that MP-GAP adapts a structural confirmation which inhibits its GAP activity. The subsequent question is if this closed MP-GAP conformation opens after phosphorylation by Aurora A kinase and if this structural change induces its GAP activity.

Additionally, a key point for future research is to identify other phosphorylation targets of Aurora A kinase. The shown interplay of Aurora A signaling and Ect2 autoinhibition in this study point towards a putative direct interaction of Aurora A kinase and the GEF Ect2. Previous studies already provided evidence that Aurora A kinase may phosphorylate Ect2 and thereby regulates its activity through various mechanisms. A study by Kapoor and Kotak (2019) in *C.* elegans has shown that depletion of AIR-1 (Aurora A kinase in *C. elegans*) induced increased contractility and led to multiple PAR-2 polarity axis. Since both observed phenotypes are traceable to perturbed ECT-2 (Ect2 in *C. elegans*) activation and localization, an interaction of AIR-1 and ECT-2 is highly likely. Furthermore, a recent study identified putative phosphorylation sites of AIR-1 in the PH-domain of ECT-2 in *C. elegans*. Even though no direct phosphorylation of ECT-2 by AIR-1 was shown, it strongly raises the idea of AIR-1 regulating ECT-2 dynamics (Longhini & Glotzer, 2022). It might be feasible that Aurora A is phosphorylating Ect2 and thereby governs its localization and/or its activity in human cells as well. Given that small GTPases play a fundamental role in several cellular processes, it is likely that more similar regulatory mechanisms dependent on Aurora A kinase exist.

Furthermore, it would be interesting to investigate a putative redundancy between RhoA inactivation by MP-GAP and different spindle-independent pathways involved in regulation of cortical contractility. Recent studies have presented alternative mechanisms which limit the accumulation of actomyosin at the poles, such as dynein-mediated removal of myosin II in *C. elegans* (Chapa-y-Lazo et al., 2020) and the

326

inhibition of formin in human cells (Chen et al., 2020). Are these redundant mechanisms, which work in parallel to restrict RhoA activity to the cell equator? Additional work should investigate how these pathways and also spindle-midzone derived signals as Aurora B kinase, integrate with Aurora A and MP-GAP signaling during cytokinesis.

This work focused on signaling of Aurora A, but it is also important to further investigate the role of Aurora B kinase. Even though it is likely that Aurora B plays a more direct role in F-actin regulation, we cannot rule out an additional role of Aurora B kinase in the regulation of contractile ring components.

Since Aurora A kinase is a known oncogene which is frequently overexpressed in various cancers (Du et al., 2021), the findings of this study also raise questions about how this pathway or its mis-regulation might contribute to aberrant cell division and tumor progression. Targeting Aurora A kinase might represent a potential novel therapeutic approach for malignancies in which cytokinetic defects lead to disease development and progression.

6.3 Light-controlled cell cycle arrest and apoptosis

It is a key goal in chemical biology to develop molecular tools that allow precise spatial and temporal control of biological activities. Modulating bioactive molecules in drugs using light, called photopharmacology, has emerged as a powerful approach to advance fundamental research. The side effects of common drugs are mostly due to their untamed reactivity in time and space, which still limits their usage in therapy. These side effects can be highly minimized by gaining control over the activity of drugs – by selectively activating and inactivating drugs, their activity can be purposefully deployed if needed. In the presented study (section 4 - Chapter III), a powerful photocaging strategy has been developed by Prof. Dr. H. Dube and Dr. E. Uhl. For this the proteasome inhibitor MG132 was rendered into an inactive caged form, with fully restored inhibitory function upon exposure to blue light. This was achieved by protecting the aldehyde group of MG132, which is essential for proteasome binding, using a 4,5-dimethoxy-2-nitrobenzyl (DMNB) cage. This protective cage prevents unwanted reactivity as well as toxicity of MG132 before activation by light. Thereby, full spatiotemporal control over MG132 activity was achieved and effectiveness was demonstrated through light-induced cell cycle arrest and apoptosis in human cells. Therefore, this study presents a novel tool to gain temporal control over proteasome inhibition and cell cycle arrest in human cells.

6.3.1 Development of photocaged analogs of MG132

The development of a caged version of MG132 relies on the protection of its aldehyde functionality with a photolabile group to inhibit its biological activity. Several photolabile groups have been developed during the last years of research and are used in photocaging applications (Becker et al., 2018; Bojtár et al., 2020; Olson et al., 2013; Peterson et al., 2018; Shrestha et al., 2020). However, all of these groups vary in their solubility and/or light absorption properties. Nitroveratryloxycarbonyl (NVOC) often finds usage I photocaging of amines (Wietor et al., 2005) while Pyrrolo [3,4-b]quinolin-1(2H)-yl groups are used in photocaging of nucleid acids and proteins (Medvedeva et al., 2022; Van et al., 2005). Additionally, caged Glutamate, e.g. MNI-glutamate, is used

to protect the release of neurotransmitters (Ellis-Davies et al., 2020; Schembekar et al., 2005). In this study the 4,5-dimethoxy-2-nitrobenzyl (DMNB) group was chosen to cage MG132, which is a widely used photolabile protecting group due to its blue light sensitivity and high photorelease efficiency. DMNB is a derivate of nitrobenzyl, which contains of a nitro group (NO_2) and two methoxy groups (OMe). Its photoreactive properties are attributed the nitro group, while the methoxy groups enhance the overall stability (Görner, 2005; Young & Deiters, 2007). While irradiation with UV or blue light, DMNB undergoes a hymolotic cleavage, which results in the breakage of the C-O bind, which is binding the protection group to the molecule (Görner, 2005). Thereby, the bioactive molecule gets released from the protective aldehyde group. In this study, caged versions of MG132 were synthesized through a peptide-coupling sequence, where DMNB was introduced to the peptide structure early in the synthesis and a final mixed acetal formation yielded the desired compound (Figure 19). Measurements of quantum yield confirmed that irradiation with 405nm induced effective uncaging.
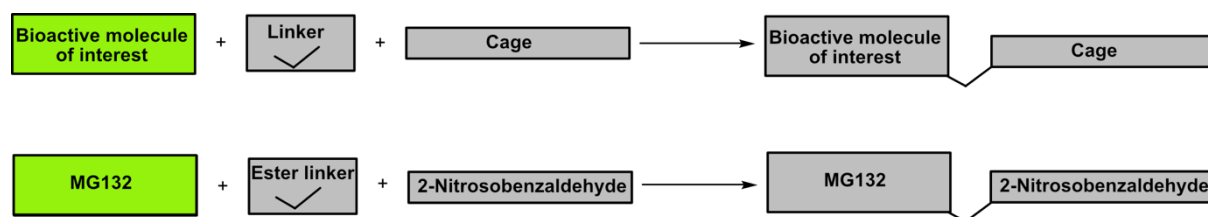
Figure 19: Schematic representation of synthesis of photocaged molecules.
Bioactivity of the molecule of interest (in this study MG132) is masked by a caging group (in this study 2-Nitrosobenzaldehyde), which is introduced via a linker (in this study an ester linker).

As mentioned in section 1.10.1, Bortezomib is the first clinical approved and used anti-cancer drug based on proteasome inhibition (Kane et al., 2003; 2007). Hansen et al. (2014) synthesized inhibitors which incorporate an azobenzene photoswitch, which allows the reversible isomerization between an active trans and less active cis configuration upon irradiation with light. Thereby, the researchers developed a photoswitchable analog of Bortezomib and assessed activity of proteasome inhibition in cell extracts, however, this may not reflect functionality in living cells and organisms. Even though the developed analogs of Bortezomib already showed promising results, they also contained disadvantages as incomplete isomerization efficiency and slow thermal revision to the active isomer. This motivated us to develop a photocaged

proteasome inhibitor with improved physical properties and biological efficiency.

6.3.2 Application of a photocaged MG132 in living human cells

After synthesis and demonstration of photochemical response of MG132-Cage, functionality was investigated in a biological context. To this end, light-induced control over the cell cycle was investigated in human HeLa cells using immunofluorescence imaging. It was shown that addition of caged version of MG132 in absence of light did not induce metaphase arrest, which highlight the functionality of the protective group inhibiting MG132 activity. After irradiation with light, cells arrested in metaphase which showed efficient uncaging of the photolabile group. Additionally, it was shown that the light-induced metaphase arrest was reversible. To confirm specificity of the compound- and light-induced metaphase arrest, it was also shown that the photoreleased byproduct, the nitrosobenzaldehyde, did not cause metaphase arrest, which rules out potential side effects of this product on the cell cycle. Additionally, it was proven that irradiation with light itself (no compound added) does not impair cell cycle progression. These results show that MG132 is the active component inducing metaphase arrest. In this study, metaphase arrest was achieved with high specificity meaning only upon irradiation with light and not due to any unspecific effects as light only or caged compound only. This strongly supports a potential of caged MG132 as a tool to study cell cycle progression and proteasome function but also the idea of caging active compounds in numerous biological research fields. Furthermore, this study highlights important consideration in drug uptake and activation. It was shown that exchanging MG132-containing medium with fresh medium just before irradiation does not reduce efficiency of metaphase arrest. This shows that caged MG132 is taken up by the cells before irradiation with light, ruling out that this is facilitated by light. These results ensure that the observed arrest in cell cycle progression is solely due to the efficient release of MG132 activity, rather than changes in ability of cells to internalize the compound. The fact that the metaphase arrest was reversible gives on the hand one meaningful insights for putative therapeutic application and on the other hand again highlights the dynamic regulation of cellular processes.

The next main objective of this study was the potential of caged MG132 as an anti-

cancer drug by investigating its ability to induce cell death via apoptosis. Inhibition of the proteasome induces apoptosis in various cell types, including cancer cells. Inducing apoptosis by proteasome inhibition relies on disruption of protein degradation pathways, which subsequently leads to accumulation of pro-apoptotic factors as p53 and caspases. This increase of pro-apoptotic factors triggers initiation of the apoptotic pathway (Hideshima et al., 2001; Kisselev et al., 2012; Tanaka, 2009). Treatment of patients with Bortezomib induces cell death through multiple converging pathways. Via proteasome inhibition, it stabilizes p53 -normally degraded by the proteasome via MDM2-mediated ubiquitination – inducing transcription of pro-apoptotic genes (as Bax and PUMA), which promotes permeabilization of the outer mitochondrial membrane and activates caspases. Furthermore, the nuclear factor kappa B (Nf-kB) – promotes survival and proliferation in cells – gets inactivated after proteasome inhibition since its inhibitor IkB is not degraded by the proteasome. This leads to suppression of anti-apoptotic genes and promotes apoptosis. Additionally, proteasome inhibition leads to an accumulation of misfolded proteins in the endoplasmatic reticulum, which is normally handled by the unfolded protein response (UPR), however, prolonged and excessive overload of these misfolded proteins can induce apoptosis (Piperdi et al., 2011; Ri, 2016). These numerous cellular pathways highlight the tightly controlled degradation system within cells, but also shows the potential of proteasome inhibition as a therapeutic target. Regarding cell death, it is crucial to differentiate between two types, which mainly differ in their causes and mechanisms: while apoptosis is a programmed and tightly regulated process of cell death, necrosis describes an uncontrolled form of cell death (D'arcy, 2019; Krysko et al., 2008). Programmed cell death is a response of the cell to intrinsic pathways as explained before. In contrast, necrosis is caused by insults as infection or toxins. Therefore, the molecular mechanisms behind necrosis highly differ to those during apoptosis. It involves osmotic imbalance, lysosomal enzyme release and the generation of reactive oxygen species (ROS). Both types of cell death also show characteristic morphological changes. Apoptosis is characterized by cell shrinkage, DNA fragmentation, membrane blebbing and formation of apoptotic bodies, which contain the cell contents. Morphological hallmarks of necrosis are cell swelling, loss of membrane integrity and subsequent release of intracellular content into the extracellular space (Berghe et al., 2014; Elmore, 2007; Galluzzi & Kroemer, 2008; Hotchkiss et al., 2009). Summarized, apoptosis is a beneficial process which is induced by the cell itself to prevent further

damage, while necrosis is non-beneficial and often leads to inflammatory responses e.g. due to cell rupture. Therefore, it is of major importance to differentiate if a drug is inducing apoptosis or necrosis to use it as a medical therapeutic agent. This study has shown that caged MG132 induced apoptosis over after irradiation with light. It was confirmed via two independent assays that the observed induced cell death was due to apoptosis and not necrosis, which strengthens the potential of caged MG132 in a therapeutic context. Furthermore, it was shown that this effect relies on activation of the compound by light and additionally shows stability of the compound, since no spontaneous uncaging was observed in the dark. Similar to the before reported results regarding metaphase arrest, it was shown that survival of cells could be rescued after removal of active compound. Additionally, it was shown the nitrosobenzaldehyde byproduct after uncaging did not negatively affect cellular growth and viability over time. To identify and optimize the therapeutic potential of a drug candidate, it is highly important to systematically evaluate the biological response to varying drug concentrations. This is reflected in a dose-response assessment, which allows to identify the minimum required drug dose for a maximal drug effect. This is also required to determine the range in which a drug is sufficiently effective without causing harmful side effects. Of course, specifically during development of new drugs it is also important to compare via dose-response analysis the efficiency between already existing treatments and newly invented ones to ensure most efficient patient treatment (Berenbaum, 1989; Chou, 2010; Tashijan & Armstrong, 2011). Dose-response analyses are crucial part of drug development and e.g. regulatory agencies as the Food and Drug Administration (FDA) demand these data before granting approval for a drug. Therefore, in this study various concentrations of caged MG132 were tested and it was shown that apoptosis was induced by caged MG132 upon light irradiation in a dose-dependent manner with similar results to previous studies about dose-response of MG132 (Han et al., 2009). This highlights that the synthesized caged MG132 shows same efficiency as commercially available MG132.

6.3.3 Concluding remarks and Outlook

In this study a novel approach was presented to control the cell cycle and apoptosis in human cells. This achievement relied on the development of a photocaging strategy, which protects the aldehyde group of the proteasome inhibitor MG132 and thereby inhibits its activity. In this caged form, the compound remained inactive and did not show any side effects on cell viability even when applied over longer periods. Upon irradiation with light on a minute scale, the photocage was cleaved and activity of MG132 was released. Activation of MG132 subsequently led to arrest of cells in metaphase and induced apoptosis over time. The effect of cell cycle arrest was reversible after removal of the active compound. Choosing live-cell imaging in this study was important to follow cellular events in real time, which provided detailed insights into cell cycle and apoptosis progression. Therefore, this technique was crucial for understanding the potential, but also the limitations of synthesized compounds. The presented concept of temporal control over the cell cycle and cell death is a versatile and innovative approach, which is a major advancement in the field of photopharmacology. However, in this study a photocage was used to protect the bioactive molecule, which gets cleaved from the molecule after irradiation. This cleavage results in an irreversible activation step meaning that once the cage is removed, the molecule and its activity is permanently released. This is ideal for one-time activation events, however it cannot be switched back to an inactive state. In contrast, a photoswitch is a molecule that can be reversibly switched between an active and inactive state and thereby allows reversibility (Fuchter, 2020; Lerch et al., 2018; Volaric et al., 2021). Therefore, photoswitches also present a very fascinating approach to control biological processes. Furthermore, the concept of achieving spatial control within a cell or even an organism is an exciting aspect, which was not further investigated in this study. Minor attempts to spatially induce metaphase arrest were not successful so far and need to be further addressed. One major limitation for the spatial control might be the aspect of diffusion. Putative challenging aspects are the high diffusibility of the used inhibitors as well as the required incubation times. Nevertheless, the presented study shows a sophisticated approach to gain control over bioactive compounds opening up new aspects for fundamental as well as pharmacological research fields.

6.4 Rhodanine-Based chromophores – Fast access to capable photoswitches and application in light induced apoptosis

In section 5 - Chapter IV a photocaging strategy was developed to gain control over the cell cycle with light. In this presented study a novel class of photoswitches was developed by Prod. Dr. H. Dube and Dr. L. Köttner with strong potential in biological applications. This time, rhodanine-based photoswitches were designed inspired by the commercially available PIM kinase inhibitor SMI-16a, which is an oxo-rhodanine. It was shown that the inhibitor SMI-16a inherently functions as a pharmacological tool since its activity could be reversibly controlled by light. In its active but not inactive state, SMI-16a induced apoptosis in different human cell lines such as HeLa, DLD-1, HCT116 and RPE1 cells. Light-induced activation of this compound was proofed by irradiation with light resulting in apoptosis of human cells. Furthermore, inactivation of the active compound with light was successfully performed with ~60% efficiency. Therefore, in this study a photoswitch based on PIM kinase inhibition was developed, whose activity can be turned on and off. This offers great advantage and highly improves a putative application of photoactive molecules compared to photocages in therapeutic treatments.

6.4.1 Development of light switchable chromophores

In this study the main objective was to design chemical photoswitches that can be used in biological applications. Photoswitches are a highly investigated field in chemical biology since switching biological activities on and off could present a highly desirable therapeutic tool. Photoswitches are often based on molecules as azobenzenes or diarylethenes and are already used in the optical control of receptor activity or enzyme functions (Beharry & Woolley, 2011, Zhu & Zhou, 2018). One well-known and widely used azobenzene-based photoswitch is for example Azo-AQ (AAQ), which is an azobenzene-derived potassium channel modulator. It is used in optogenetics and neuroscience to control neuronal activity allowing precise regulation of ion channel function. By irradiation with UV light it undergoes cis-isomerization, meaning it turns its activity off, and under visible light it switches back to its trans-

isomerization, which is restoring its activity. Furthermore, it shows high photochemical stability which enables prolonged usage in experimental set ups (Bandara & Burdette, 2012; Lima & Miesenböck, 2005; Szymanski et al., 2013).

Another class of light-switchable molecules are rhodanine-based chromophores. They represent a class of heterocyclic compounds consisting of a ring with a thiocarbonyl (C=S) and a carbonyl (C=O) functional group. They are structurally related to hemithioindigo (HTI) and indigoid, which are known for their light-inducible properties. Rhodanine derivates can undergo photoisomerization, which means that they can undergo a switch between their Z- (active) and E- (inactive) isomers after exposure to specific wavelengths of light. This switching from Z to E is reversible and the molecule can be chemically modified to affect thermal stability, absorption spectra and efficiency of switching. By adding substituents at different positions of the molecule, the isomerization wavelengths can be modulated. For example, rhodanine derivates substituted with sulfur at X-position often exhibit a red shift in absorption, while oxygen-substituted derivates (oxo-rhodanines) show a shift to visible light (Bartelmann & Dube, 2022; Huang et al., 2017). Thereby, rhodanine-based chromophores represent a promising candidate in photopharmacology since their reversible photoisomerization and especially also their tunability via substitutions make them ideal for light-controlled usage. For medical applications some substituted rhodanine derivates are already used for diabetes treatment (Ramirez & Borja, 2008; Odom et al., 2008). In the presented study, a new class of related but still distinct rhodanine-based photoswitches was synthesized. The switches were synthesized from commercially available starting compounds as oxo-rhodanine or rhodanine through a one-step condensation of (oxo-) rhodanine and different aldehydes, and obtained in their pure Z-isomer (active). Each compound was characterized for its photochemical properties, describing the switching efficiency from Z- to E-Isomer and E- to Z-isomer, and physical properties as thermal stability via NMR and UV/Vis spectroscopy. All synthesized chromophores showed light induced isomerization (Z/E, E/Z), however their absorption spectra and thermal stabilities differed. This relied on the before mentioned substitutions at the X-position and at the stilbene moiety. Consistent with previous studies, rhodanines showed a more redshifted absorption spectra than the rhodanines in which oxygen was substituted (oxo-rhodanines). Furthermore, substitution of oxygen to rhodanines increased their thermal half-time life. However, the isomerization efficiency from E- to Z-isomer did not differ between rhodanines and

oxo-rhodanines, and also comparable and sufficient quantum yields were achieved for both derivates and both isomeric forms. Preliminary tests if the photochemical and physical properties of the synthesized compounds can be maintained in living cells were successful – functionality of synthesized photoswitches in presence of reduced glutathione (GSH), which is present in living cells, was shown.

6.4.2 Application of rhodanine-based photoswitches in human cells

Next, the potential of the synthesized (oxo-) rhodanine-based photoswitches as a therapeutic tool was demonstrated in human cells. The active compound in its Z-isomeric form induced apoptosis in human HeLa, DLD-1, HCT116 and RPE1 cells in the dark, while the inactive, E-Isomeric form did not alter cell viability. This confirms that the E-isomer is inactive in the dark and presents an opportunity for light-controlled activation. Indeed, it was shown that the inactive E-isomer could be converted to its active Z-isomerization upon irradiation with blue light and significantly reduced cell viability. This activation by light was even possible with only ten seconds of irradiation by using a high-power light source. It was shown that activity of the (oxo-)rhodanine-based photoswitches could be switched on, but also switched off. The active Z-isomer was at least partially converted into its inactive E-isomeric state by irradiation with light. A full Z- to E-isomer conversion and inactivation was not expected, since chemical analyses have shown that that there is only a limited E-isomer enrichment in solution after irradiating the Z-isomer, therefore the biological results perfectly align with obtained chemical data. Previous studies have shown that for several molecules Z- to E- isomer conversion is more efficient than the other way around (Bharmoria et al., 2022; Goulet-Hanssens et al., 2017; Hansen et al., 2014). This is based on several reasons as chemical structure and steric factors, but also on the fact that Z- to E-isomer requires lower activation energy and less steric hindrance (Bortolus & Monti, 1979). The before mentioned azobenzene-based photoswitches for example show faster Z to E than E to Z conversion since irradiation leads to rotation around the N=N double bond, which is facilitated by less steric hindrance. In this case, E to Z conversion requires higher energy since steric hindrance is higher (Bandara & Burdette, 2012). Additionally, in the presented study dose-response assessment was

performed to evaluate the biological response to various compound dosages. The results demonstrate that light-activated E-isomer induced cell death with the same efficiency as the active Z-isomer, which highlights the excellent photoreversion from E- to Z-isomer and showcases its potential as a molecular tool. As discussed in section 6.3.2, it is essential to differentiate necrosis and apoptosis. Therefore, in this study PARP cleavage was used as a readout for apoptosis and results confirm that active Z-isomer and light-activated E-isomer reduced cell viability by inducing apoptosis in human cells.

6.4.3 Concluding remarks and Outlook

The presented study identifies (oxo-) rhodanines as highly effective photoswitches. The straightforward synthesis enables diversity of structural variants and fine tuning of chemical and physical properties. It was shown that minimal structural modifications as substitution of oxygen with sulfur change the photochemical properties as the absorption spectra, which offers a broad range of possibilities. Furthermore, this study incorporates the relevance and potential use of these photoswitches in biological systems. Rhodanine-based photoswitches successfully induced apoptosis in human cells and photomodulation of their biological activity was proven. Temporal control over Pim kinase inhibition was successfully achieved in this study, however, spatial control with the synthesized photsowitches was not investigated and presents an exciting aspect for future research. Furthermore, there are several aspects that need to be further addressed to improve usage of photoswitches in a therapeutic context. The effective application of photoswitchable molecules and drugs requires precise illumination with specific wavelengths of light. To overcome limitations regarding light penetration it would be desirable to shift required wavelengths to a red shifted absorption, which in addition reduces cytotoxic side effects. On the long-term, photoswitchable inhibitors require testing in animals to make them putative candidates for therapeutic treatment in humans. In summary, (oxo-)-rhodanines represent a valuable molecular tool with high potential for application in medicinal research.

Bibliography

Adams, J. (2003). The proteasome: structure, function, and role in the cell. *Cancer treatment reviews*, *29*, 3-9.

Afshar, K., Werner, M. E., Tse, Y. C., Glotzer, M., & Gönczy, P. (2010). Regulation of cortical contractility and spindle positioning by the protein phosphatase 6 PPH-6 in one-cell stage C. elegans embryos. *Development, 137*(2), 237-247.

Alberts, B., Johnson, A., Lewis, J., Raff, M., Roberts, K., & Walter, P. (2002). An overview of the cell cycle. In *Molecular Biology of the Cell* (4th ed.).

Alberts, B., Bray, D., Hopkin, K., Johnson, A. D., Lewis, J., Raff, M., & Walter, P. (2015). *Essential cell biology* (4th ed.). Garland Science.

Arlt, A., Bauer, I., Schafmayer, C., Tepel, J., Müerköster, S. S., Brosch, M., ... & Schäfer, H. (2009). Increased proteasome subunit protein expression and proteasome activity in colon cancer relate to an enhanced activation of nuclear factor E2-related factor 2 (Nrf2). *Oncogene*, *28*(45), 3983-3996.

Arrigo, A. P., Tanaka, K., Goldberg, A. L., & Welch, W. J. (1988). Identity of the 19S'prosome'particle with the large multifunctional protease complex of mammalian cells (the proteasome). *Nature*, *331*(6152), 192-194.

Bagge, J., Oestergaard, V. H., & Lisby, M. (2021). Functions of TopBP1 in preserving genome integrity during mitosis. *Semin Cell Dev Biol, 113*, 57-64.

Bandara, H. D., & Burdette, S. C. (2012). Photoisomerization in different classes of azobenzene. *Chemical Society Reviews, 41*(5), 1809-1825.

Barnum, K. J., & O'Connell, M. J. (2014). Cell cycle regulation by checkpoints. *Cell cycle control: mechanisms and protocols*, 29-40.

Barr, A. R., & Gergely, F. (2007). Aurora-A: the maker and breaker of spindle poles. *Journal of cell science*, *120*(17), 2987-2996.

Bartelmann, T., & Dube, H. (2022). Indigoid Photoswitches. *Molecular Photoswitches: Chemistry, Properties, and Applications*, 2 Volume Set, 283-302.

Basant, A., & Glotzer, M. (2018). Spatiotemporal regulation of RhoA during cytokinesis. *Current Biology*, 28(11), R570–R580.

Bastos, R. N., Penate, X., Bates, M., Hammond, D., & Barr, F. A. (2012). CYK4 inhibits

Rac1-dependent PAK1 and ARHGEF7 effector pathways during cytokinesis. *Journal of cell biology, 198*(5), 865-880.

Bayliss, R., Sardon, T., Vernos, I., & Conti, E. (2003). Structural basis of Aurora-A activation by TPX2 at the mitotic spindle. *Molecular Cell, 12*(4), 851-862.

Becker, Y., Unger, E., Fichte, M. A., Gacek, D. A., Dreuw, A., Wachtveitl, J., ... & Heckel, A. (2018). A red-shifted two-photon-only caging group for three-dimensional photorelease. *Chemical science*, *9*(10), 2797-2802.

Bedford, L., Paine, S., Sheppard, P. W., Mayer, R. J., & Roelofs, J. (2010). Assembly, structure, and function of the 26S proteasome. *Trends in cell biology*, *20*(7), 391-401.

Beharry, A. A., & Woolley, G. A. (2011). Azobenzene photoswitches for biomolecules. *Chemical Society Reviews, 40*(8), 4422-4437.

Bement, W. M., Benink, H. A., & von Dassow, G. (2005). A microtubule-dependent zone of active RhoA during cleavage plane specification. *J Cell Biol, 170*(1), 91-101.

Bement, W. M., Miller, A. L., & von Dassow, G. (2006). Rho GTPase activity zones and transient contractile arrays. *BioEssays, 28*, 983-993.

Bement, W. M., Leda, M., Moe, A. M., Kita, A. M., Larson, M. E., Golding, A. E., ... & von Dassow, G. (2015). Activator–inhibitor coupling between Rho signalling and actin assembly makes the cell cortex an excitable medium. *Nature Cell Biology, 17*(11), 1471-1483.

Berenbaum, M. C. (1989). What is synergy?. *Pharmacological Reviews, 41*(2), 93-141.

Berghe, T. V., Linkermann, A., Jouan-Lanhouet, S., Walczak, H., & Vandenabeele, P. (2014). Regulated necrosis: the expanding network of non-apoptotic cell death pathways. *Nature Reviews Molecular Cell Biology, 15*(2), 135-147.

Bharmoria, P., Ghasemi, S., Edhborg, F., Losantos, R., Wang, Z., Mårtensson, A., ... & Moth-Poulsen, K. (2022). Far-red triplet sensitized Z-to-E photoswitching of azobenzene in bioplastics. *Chemical science*, *13*(40), 11904-11911.

Biron, D., Moses, E., Borukhov, I., & Safran, S. A. (2005). Inter-filament attractions narrow the length distribution of actin filaments. *Europhysics Letters*, *73*(3), 464.

Bojtár, M., Németh, K., Domahidy, F., Knorr, G., Verkman, A., Kállay, M., & Kele, P. (2020). Conditionally activatable visible-light photocages. *Journal of the*

American Chemical Society, *142*(35), 15164-15171.

Borowiak, M., Nahaboo, W., Reynders, M., Nekolla, K., Jalinot, P., Hasserodt, J., ... & Thorn-Seshold, O. (2015). Photoswitchable inhibitors of microtubule dynamics optically control mitosis and cell death. *Cell, 162*(2), 403-411.

Bortolus, P., & Monti, S. (1979). Cis-trans photoisomerization of azobenzene. Solvent and triplet donors effects. *Journal of Physical Chemistry, 83*(6), 648-652.

Bringmann, H., & Hyman, A. A. (2005). A cytokinesis furrow is positioned by two consecutive signals. *Nature, 436*(7051), 731-734.

Burkard, M. E., Maciejowski, J., Rodriguez-Bravo, V., Repka, M., Lowery, D. M., Clauser, K. R., Zhang, C., Shokat, K. M., Carr, S. A., Yaffe, M. B., & Jallepalli, P. V. (2009). Plk1 self-organization and priming phosphorylation of HsCYK-4 at the spindle midzone regulate the onset of division in human cells. *PLoS Biology, 7*(5), e1000111.

Burkard, M. E., Randall, C. L., Larochelle, S., Zhang, C., Shokat, K. M., Fisher, R. P., & Jallepalli, P. V. (2007). Chemical genetics reveals the requirement for Polo-like kinase 1 activity in positioning RhoA and triggering cytokinesis in human cells. *Proc Natl Acad Sci U S A, 104*(11), 4383-4388.

Canman, J. C., Lewellyn, L., Laband, K., Smerdon, S. J., Desai, A., Bowerman, B., & Oegema, K. (2008). Inhibition of Rac by the GAP activity of centralspindlin is essential for cytokinesis. *Science, 322*(5907), 1543-1546.

Carmena, M., & Earnshaw, W. C. (2003). The cellular geography of aurora kinases. *Nature reviews Molecular cell biology, 4*(11), 842-854.

Carmena, M., Wheelock, M., Funabiki, H., & Earnshaw, W. C. (2012). The chromosomal passenger complex (CPC): From easy rider to the godfather of mitosis. *Nature Reviews Molecular Cell Biology*, 13(12), 789–803.

Carvalho, A., Desai, A., & Oegema, K. (2009). Structural memory in the contractile ring makes the duration of cytokinesis independent of cell size. *Cell, 137*(5), 926-937.

Castrillon, D. H., & Wasserman, S. A. (1994). Diaphanous is required for cytokinesis in Drosophila and shares domains of similarity with the products of the limb deformity gene. *Development, 120*(12), 3367-3377.

Chan, E., & Nance, J. (2013). Mechanisms of CDC-42 activation during contact-induced cell polarization. *J Cell Sci, 126*(Pt 7), 1692-1702.

Chapa-y-Lazo, B., Hamanaka, M., Wray, A., Balasubramanian, M. K., & Mishima, M. (2020). Polar relaxation by dynein-mediated removal of cortical myosin II. *The Journal of Cell Biology, 219*(1250), 1225.

Chaugule, V. K., & Walden, H. (2016). Specificity and disease in the ubiquitin system. *Biochemical Society Transactions*, *44*(1), 212-227.

Chen, W., Foss, M., Tseng, K. F., & Zhang, D. (2008). Redundant mechanisms recruit actin into the contractile ring in silkworm spermatocytes. *PLoS Biology*, 6(9), e209.

Chen, D., Frezza, M., Schmitt, S., Kanwar, J., & P Dou, Q. (2011). Bortezomib as the first proteasome inhibitor anticancer drug: current status and future perspectives. *Current cancer drug targets*, *11*(3), 239-253.

Chen, M., H. Pan, L. Sun, P. Shi, Y. Zhang, L. Li, Y. Huang, J. Chen, P. Jiang, X. Fang, C. Wu, and Z. Chen. (2019). Structure and regulation of human epithelial cell transforming 2 protein. *Proceedings of the National Academy of Sciences of the United States of America*. 16:201913054.

Chen, M., Pan, H., Sun, L., Shi, P., Zhang, Y., Li, L., Huang, Y., Chen, J., Jiang, P., Fang, X., Wu, C., & Chen, Z. (2020). Structure and regulation of human epithelial cell transforming 2 protein. *Proceedings of the National Academy of Sciences of the United States of America, 117*(2), 1027-1035.

Chen, A., Ulloa Severino, L., Panagiotou, T. C., Moraes, T. F., Yuen, D. A., Lavoie, B. D., & Wilde, A. (2021). Inhibition of polar actin assembly by astral microtubules is required for cytokinesis. *Nat Commun, 12*(1), 2409.

Chihara, K., Amano, M., Nakamura, N., Yano, T., Shibata, M., Tokui, T., ... & Kaibuchi, K. (1997). Cytoskeletal rearrangements and transcriptional activation of c-fos serum response element by Rho-kinase. *Journal of Biological Chemistry*, *272*(40), 25121-25127.

Chou, T. C. (2010). Drug combination studies and their synergy quantification using the Chou-Talalay method. *Cancer Research, 70*(2), 440-446.

Clute, P., & Pines, J. (1999). Temporal and spatial control of cyclin B1 destruction in metaphase. *Nature cell biology*, *1*(2), 82-87.

Combes, G., Alharbi, I., Braga, L. G., & Elowe, S. (2017). Playing polo during mitosis: PLK1 takes the lead. *Oncogene, 36*(34), 4819-4827.

D'arcy, M. S. (2019). Cell death: a review of the major forms of apoptosis, necrosis and autophagy. *Cell biology international*, *43*(6), 582-592.

D'Avino, P. P., Giansanti, M. G., & Petronczki, M. (2015). Cytokinesis in animal cells. *Cold Spring Harb Perspect Biol, 7*(4), a015834.

De Smedt, R., Morscio, J., Reunes, L., Roels, J., Bardelli, V., Lintermans, B., ... & Van Vlierberghe, P. (2020). Targeting cytokine-and therapy-induced PIM1 activation in preclinical models of T-cell acute lymphoblastic leukemia and lymphoma. *Blood, The Journal of the American Society of Hematology*, *135*(19), 1685-1695.

Dee, R. A., Bai, X., Mack, C. P., & Taylor, J. M. (2020). Molecular regulation of the RhoGAP GRAF3 and its capacity to limit blood pressure in vivo. *Cells, 9*(4), 1042.

Delacour-Larose, M., Molla, A., Skoufias, D. A., Margolis, R. L., & Dimitrov, S. (2004). Distinct dynamics of Aurora B and Survivin during mitosis. *Cell Cycle*, *3*(11), 1418-1426.

Delic, J., Masdehors, P., Ömura, S., Cosset, J. M., Dumont, J., Binet, J. L., & Magdelenat, H. (1998). The proteasome inhibitor lactacystin induces apoptosis and sensitizes chemo-and radioresistant human chronic lymphocytic leukaemia lymphocytes to TNF-α-initiated apoptosis. *British journal of cancer*, *77*(7), 1103-1107.

DeLuca, K. F., Meppelink, A., Broad, A. J., Mick, J. E., Peersen, O. B., Pektas, S., ... & DeLuca, J. G. (2018). Aurora A kinase phosphorylates Hec1 to regulate metaphase kinetochore–microtubule dynamics. *Journal of Cell Biology*, 217(1), 163–177.

DeMartino, G. N., & Gillette, T. G. (2007). Proteasomes: machines for all reasons. *Cell*, *129*(4), 659-662.

Desai, A., Verma, S., Mitchison, T. J., & Walczak, C. E. (1999). Kin I kinesins are microtubule-destabilizing enzymes. *Cell, 96*(1), 69-78.

do Patrocinio, A. B., Rodrigues, V., & Guidi Magalhães, L. (2022). P53: stability from the ubiquitin–proteasome system and specific 26S proteasome inhibitors. *ACS omega*, *7*(5), 3836-3843.

Du, R., Huang, C., Liu, K., Li, X., & Dong, Z. (2021). Targeting AURKA in cancer: Molecular mechanisms and opportunities for cancer therapy. *Molecular Cancer, 20*, 15.

Dutertre, S., Descamps, S., & Prigent, C. (2002). On the role of aurora-A in centrosome function. *Oncogene*, 21(40), 6175–6183.

Elia, A. E., Cantley, L. C., & Yaffe, M. B. (2003). Proteomic screen finds pSer/pThr-

binding domain localizing Plk1 to mitotic substrates. *Science, 299*(5610), 1228-1231.

Elia, A. E., Rellos, P., Haire, L. F., Chao, J. W., Ivins, F. J., Hoepker, K., Mohammad, D., Cantley, L. C., Smerdon, S. J., & Yaffe, M. B. (2003). The molecular basis for phosphodependent substrate targeting and regulation of Plks by the Polo-box domain. *Cell, 115*(1), 83-95.

Elia, N., Sougrat, R., Spurlin, T. A., Hurley, J. H., & Lippincott-Schwartz, J. (2011). Dynamics of endosomal sorting complex required for transport (ESCRT) machinery during cytokinesis and its role in abscission. *Proceedings of the National Academy of Sciences*, 108(12), 4846–4851.

Ellis-Davies, G. C., Matsuzaki, M., Paukert, M., Kasai, H., & Bergles, D. E. (2007). 4-Carboxymethoxy-5, 7-dinitroindolinyl-Glu: An improved caged glutamate for expeditious ultraviolet and two-photon photolysis in brain slices. *Journal of Neuroscience, 27*(25), 6601-6604.

Elmore, S. (2007). Apoptosis: A review of programmed cell death. *Toxicologic Pathology, 35*(4), 495-516.

Evangelista, M., Pruyne, D., Amberg, D. C., Boone, C., & Bretscher, A. (2002). Formins direct Arp2/3-independent actin filament assembly to polarize cell growth in yeast. *Nat Cell Biol, 4*(3), 260-269.

Eyers, P. A., Erikson, E., Chen, L. G., & Maller, J. L. (2003). A novel mechanism for activation of the protein kinase Aurora A. *Current Biology*, *13*(8), 691-697.

Fededa, J. P., & Gerlich, D. W. (2012). Molecular control of animal cell cytokinesis. *Nature Cell Biology*, 14(5), 440–447.

Fhu, C. W., & Ali, A. (2021). Dysregulation of the ubiquitin proteasome system in human malignancies: a window for therapeutic intervention. *Cancers*, *13*(7), 1513.

Field, C. M., Coughlin, M., Doberstein, S., Marty, T., & Sullivan, W. (2005). Characterization of anillin mutants reveals essential roles in septin localization and plasma membrane integrity. *Development, 132*(12), 2849-2860.

Fincham, V. J., Chudleigh, A., & Frame, M. C. (1999). Regulation of p190 Rho-GAP by v-Src is linked to cytoskeletal disruption during transformation. *Journal of cell science*, *112*(6), 947-956.

Finn, R. S., Martin, M., Rugo, H. S., Jones, S., Im, S. A., Gelmon, K., ... & Slamon, D. J. (2016). Palbociclib and letrozole in advanced breast cancer. *New England*

Journal of Medicine, 375(20), 1925–1936.

Foe, V. E., & von Dassow, G. (2008). Stable and dynamic microtubules coordinately shape the myosin activation zone during cytokinetic furrow formation. *Journal of Cell Biology*, 183(3), 457–470.

Frenette, P., Haines, E., Loloyan, M., Kinal, M., Pakarian, P., & Piekny, A. (2012). An anillin-Ect2 complex stabilizes central spindle microtubules at the cortex during cytokinesis. *PLoS One, 7*(4), e34888.

Fuchter, M. J. (2020). On the promise of photopharmacology using photoswitches: A medicinal chemist's perspective. *Journal of Medicinal Chemistry, 63*(20), 11436-11447.

Gadde, S., & Heald, R. (2004). Mechanisms and molecules of the mitotic spindle. *Curr Biol, 14*(18), R797-805.

Gai, M., Camera, P., Dema, A., Bianchi, F., Berto, G., Scarpa, E., Germena, G., & Di Cunto, F. (2011). Citron kinase controls abscission through RhoA and anillin. *Mol Biol Cell, 22*(20), 3768-3778.

Galluzzi, L., & Kroemer, G. (2008). Necroptosis: A specialized pathway of programmed necrosis. *Cell, 135*(7), 1161-1163.

Garcia-Mata, R., Boulter, E., & Burridge, K. (2011). The'invisible hand': regulation of RHO GTPases by RHOGDIs. *Nature reviews Molecular cell biology*, *12*(8), 493-504.

Genschik, P., Criqui, M. C., Parmentier, Y., Derevier, A., & Fleck, J. (1998). Cell cycle–dependent proteolysis in plants: Identification of the destruction box pathway and metaphase arrest produced by the proteasome inhibitor MG132. *The Plant Cell*, 10(12), 2063–2075.

Gerloff, D. L., Woods, N. T., Farago, A. A., & Monteiro, A. N. (2012). BRCT domains: A little more than kin, and less than kind. *FEBS letters*, *586*(17), 2711-2716.

Giet, R., McLean, D., Descamps, S., Lee, M. J., Raff, J. W., Prigent, C., & Glover, D. M. (2002). Drosophila Aurora A kinase is required to localize D-TACC to centrosomes and to regulate astral microtubules. *The Journal of cell biology*, *156*(3), 437–451.

Glickman, M. H., Rubin, D. M., Fried, V. A., & Finley, D. (1998). The regulatory particle of the Saccharomyces cerevisiae proteasome. *Molecular and cellular biology*, *18*(6), 3149-3162.

Glotzer, M. (2009). The 3Ms of central spindle assembly: microtubules, motors and MAPs. *Nat Rev Mol Cell Biol, 10*(1), 9-20.

Glotzer, M., Murray, A. W., & Kirschner, M. W. (1991). Cyclin is degraded by the ubiquitin pathway. *Nature*, *349*(6305), 132-138.

Goldstein, L. S., & Yang, Z. (2000). Microtubule-based transport systems in neurons: the roles of kinesins and dyneins. *Annual review of neuroscience*, *23*(1), 39-71.

Gomez-Cavazos, J. S., Lee, K. Y., Lara-Gonzalez, P., Li, Y., Desai, A., Shiau, A. K., & Oegema, K. (2020). A non-canonical BRCT-phosphopeptide recognition mechanism underlies RhoA activation in cytokinesis. *Current Biology, 30*(16), 3101-3115.e3111.

Görner, H. (2005). Effects of 4, 5-dimethoxy groups on the time-resolved photoconversion of 2-nitrobenzyl alcohols and 2-nitrobenzaldehyde into nitroso derivatives. *Photochemical & Photobiological Sciences, 4*, 822-828.

Goshima, G. (2011). Identification of a TPX2-like microtubule-associated protein in Drosophila. *PloS one*, *6*(11), e28120.

Goulet-Hanssens, A., Utecht, M., Mutruc, D., Titov, E., Schwarz, J., Grubert, L., ... & Hecht, S. (2017). Electrocatalytic Z→ E isomerization of azobenzenes. *Journal of the American Chemical Society*, *139*(1), 335-341.

Green, R. A., Paluch, E., & Oegema, K. (2012). Cytokinesis in animal cells. *Annu Rev Cell Dev Biol, 28*, 29-58.

Groll, M., Ditzel, L., Löwe, J., Stock, D., Bochtler, M., Bartunik, H. D., & Huber, R. (1997). Structure of 20S proteasome from yeast at 2.4 Å resolution. *Nature*, *386*(6624), 463-471.

Gruneberg, U., Neef, R., Honda, R., Nigg, E. A., & Barr, F. A. (2004). Relocation of Aurora B from centromeres to the central spindle at the metaphase to anaphase transition requires MKlp2. *The Journal of cell biology*, *166*(2), 167-172.

Hanahan, D., & Weinberg, R. A. (2011). Hallmarks of cancer: the next generation. *cell*, *144*(5), 646-674.

Hansen, M. J., Velema, W. A., de Bruin, G., Overkleeft, H. S., Szymanski, W., & Feringa, B. L. (2014). Proteasome inhibitors with photocontrolled activity. *ChemBioChem, 15*(14), 2053-2057.

Hänzelmann, P., Schäfer, A., Völler, D., & Schindelin, H. (2012). Structural insights into functional modes of proteins involved in ubiquitin family pathways. *Ubiquitin*

Family Modifiers and the Proteasome: Reviews and Protocols, 547-576.

Hartwell, L. H., & Weinert, T. A. (1989). Checkpoints: controls that ensure the order of cell cycle events. *Science*, *246*(4930), 629-634.

Hateboer, G., Kerkhoven, R. M., Shvarts, A., Bernards, R., & Beijersbergen, R. L. (1996). Degradation of E2F by the ubiquitin-proteasome pathway: regulation by retinoblastoma family proteins and adenovirus transforming proteins. *Genes & development*, *10*(23), 2960-2970.

He, J., Abdel-Wahab, O., Nahas, M. K., Wang, K., Rampal, R. K., Intlekofer, A. M., ... & Levine, R. L. (2016). Integrated genomic DNA/RNA profiling of hematologic malignancies in the clinical setting. *Blood, The Journal of the American Society of Hematology*, *127*(24), 3004-3014.

Hedrick, D. G., Stout, J. R., & Walczak, C. E. (2008). Effects of anti-microtubule agents on microtubule organization in cells lacking the kinesin-13 MCAK. *Cell Cycle, 7*(14), 2146-2156.

Hentzen, N. B., Mogaki, R., Otake, S., Okuro, K., & Aida, T. (2020). Intracellular photoactivation of caspase-3 by molecular glues for spatiotemporal apoptosis induction. *Journal of the American Chemical Society*, *142*(18), 8080-8084.

Hershko, A., & Ciechanover, A. (1998). The ubiquitin system. *Annual review of biochemistry*, *67*(1), 425-479.

Hideshima, T., Richardson, P., Chauhan, D., Palombella, V. J., Elliott, P. J., Adams, J., & Anderson, K. C. (2001). The proteasome inhibitor PS-341 inhibits growth, induces apoptosis, and overcomes drug resistance in human multiple myeloma cells. *Cancer Research, 61*(7), 3071-3076.

Hirokawa, N. (1998). Kinesin and dynein superfamily proteins and the mechanism of organelle transport. *Science*, *279*(5350), 519-526.

Hortobagyi, G. N., Stemmer, S. M., Burris, H. A., Yap, Y. S., Sonke, G. S., Paluch-Shimon, S., ... & Slamon, D. J. (2018). Ribociclib as first-line therapy for HR-positive, advanced breast cancer. *New England Journal of Medicine*, 379(26), 2582–2592.

Hotchkiss, R. S., Strasser, A., McDunn, J. E., & Swanson, P. E. (2009). Cell death. *New England Journal of Medicine, 361*(16), 1570-1583.

Hu, C. K., Coughlin, M., & Mitchison, T. J. (2012). Midbody assembly and its regulation during cytokinesis. *Mol Biol Cell, 23*(6), 1024-1034.

Huang, C. Y., Bonasera, A., Hristov, L., Garmshausen, Y., Schmidt, B. M., Jacquemin, D., & Hecht, S. (2017). N,N′-disubstituted indigos as readily available red-light photoswitches with tunable thermal half-lives. *Journal of the American Chemical Society, 139*(42), 15205-15211.

Hull, K., Morstein, J., & Trauner, D. (2018). In vivo photopharmacology. *Chemical reviews, 118*(21), 10710-10747.

Jaffe, A. B., & Hall, A. (2005). Rho GTPases: biochemistry and biology. *Annu. Rev. Cell Dev. Biol., 21*(1), 247-269.

Jantsch-Plunger, V., Gönczy, P., Romano, A., Schnabel, H., Hamill, D., Schnabel, R., ... & Glotzer, M. (2000). Cyk-4A Rho Family Gtpase Activating Protein (Gap) Required for Central Spindle Formation and Cytokinesis. *Journal of Cell Biology, 149*(7), 1391-1404.

Jenkins, N., Saam, J. R., & Mango, S. E. (2006). CYK-4/GAP provides a localized cue to initiate anteroposterior polarity upon fertilization. *Science, 313*(5791), 1298-1301.

Jordan, S. N., & Canman, J. C. (2012). Rho GTPases in animal cell cytokinesis: an occupation by the one percent. *Cytoskeleton (Hoboken), 69*(11), 919-930.

Kamijo, K., Ohara, N., Abe, M., Uchimura, T., Hosoya, H., Lee, J. S., & Miki, T. (2006). Dissecting the role of Rho-mediated signaling in contractile ring formation. *Molecular Biology of the Cell, 17*(1), 43-55.

Kane, R. C., Bross, P. F., Farrell, A. T., & Pazdur, R. (2003). Velcade®: US FDA approval for the treatment of multiple myeloma progressing on prior therapy. *The Oncologist, 8*(6), 508-513.

Kane, R. C., Dagher, R., Farrell, A., Ko, C. W., Sridhara, R., Justice, R., & Pazdur, R. (2007). Bortezomib for the treatment of mantle cell lymphoma. *Clinical Cancer Research, 13*(18), 5291-5294.

Kapoor, S., & Kotak, S. (2019). Centrosome Aurora A regulates RhoGEF ECT-2 localisation and ensures a single PAR-2 polarity axis in C. elegans embryos. *Development, 146*(22).

Kechad, A., Jananji, S., Ruella, Y., & Hickson, G. R. (2012). Anillin acts as a bifunctional linker coordinating midbody ring biogenesis during cytokinesis. *Curr Biol, 22*(3), 197-203.

Khaliullin, R. N., Green, R. A., Shi, L. Z., Gomez-Cavazos, J. S., Berns, M. W., Desai, A., & Oegema, K. (2018). A positive-feedback-based mechanism for constriction

rate acceleration during cytokinesis in Caenorhabditis elegans. *Elife*, 7, e36073.

Kim, J.-E., Billadeau, D. D., & Chen, J. (2005). The tandem BRCT domains of Ect2 are required for both negative and positive regulation of Ect2 in cytokinesis. *Journal of Biological Chemistry, 280*, 5733-5739.

Kim, H., Guo, F., Brahma, S., Xing, Y., & Burkard, M. E. (2014). Centralspindlin assembly and two phosphorylations on MgcRacGAP by Polo-like kinase 1 initiate Ect2 binding in early cytokinesis. *Cell Cycle, 13*(18), 2952-2961.

Kimura, K., Ito, M., Amano, M., Chihara, K., Fukata, Y., Nakafuku, M., ... & Kaibuchi, K. (1996). Regulation of myosin phosphatase by Rho and Rho-associated kinase (Rho-kinase). *Science*, *273*(5272), 245-248.

Kimura, K., Tsuji, T., Takada, Y., Miki, T., & Narumiya, S. (2000). Accumulation of GTP-bound RhoA during cytokinesis and a critical role of ECT2 in this accumulation. *J Biol Chem, 275*(23), 17233-17236.

Kinoshita, K., Noetzel, T. L., Pelletier, L., Mechtler, K., Drechsel, D. N., Schwager, A., ... & Hyman, A. A. (2005). Aurora A phosphorylation of TACC3/maskin is required for centrosome-dependent microtubule assembly in mitosis. *Journal of Cell Biology, 170*(7), 1047-1055.

Kirschner, A. N., Wang, J., Van Der Meer, R., Anderson, P. D., Franco-Coronel, O. E., Kushner, M. H., ... & Abdulkadir, S. A. (2015). PIM kinase inhibitor AZD1208 for treatment of MYC-driven prostate cancer. *Journal of the National Cancer Institute*, *107*(2), dju407.

Kisselev, A. F., van der Linden, W. A., & Overkleeft, H. S. (2012). Proteasome inhibitors: An expanding army attacking a unique target. *Chemistry & Biology, 19*(1), 99-115.

Kiyomitsu, T., & Cheeseman, I. M. (2013). Cortical dynein and asymmetric membrane elongation coordinately position the spindle in anaphase. *Cell, 154*, 391-402.

Kotak, S., & Gönczy, P. (2013). Mechanisms of spindle positioning: Cortical force generators in the limelight. *Current Opinion in Cell Biology, 25*(6), 741-748.

Kotak, S., Afshar, K., Busso, C., & Gönczy, P. (2016). Aurora A kinase regulates proper spindle positioning in *C. elegans* and in human cells. *Journal of Cell Science, 129*(15), 3015-3025.

Kotýnková, K., Su, K.-C., West, S. C., & Petronczki, M. (2016). Plasma membrane association but not midzone recruitment of RhoGEF ECT2 is essential for cytokinesis. *Cell Reports, 17*(10), 2672-2686.

Krysko, D. V., Berghe, T. V., D'Herde, K., & Vandenabeele, P. (2008). Apoptosis and necrosis: detection, discrimination and phagocytosis. *Methods*, *44*(3), 205-221.

Kumar, J. K., Ping, R. Y. S., Teong, H. F., Goh, S., & Clément, M. V. (2011). Activation of a non-genomic Pim-1/Bad-Pser75 module is required for an efficient pro-survival effect of Bcl-xL induced by androgen in LNCaP cells. *The International Journal of Biochemistry & Cell Biology*, *43*(4), 594-603.

Lacroix, B., & Maddox, A. S. (2012). Cytokinesis, ploidy and aneuploidy. *J Pathol, 226*(2), 338- 351.

Lane, H. A., & Nigg, E. A. (1997). Cell-cycle control: POLO-like kinases join the outer circle. *Trends in cell biology*, *7*(2), 63-68.

LeBlanc, R., Catley, L. P., Hideshima, T., Lentzsch, S., Mitsiades, C. S., Mitsiades, N., ... & Anderson, K. C. (2002). Proteasome inhibitor PS-341 inhibits human myeloma cell growth in vivo and prolongs survival in a murine model. *Cancer research*, *62*(17), 4996-5000.

Leite, J., Osorio, D. S., Sobral, A. F., Silva, A. M., & Carvalho, A. X. (2019). Network contractility during cytokinesis—from molecular to global views. *Biomolecules*, *9*(5), 194.

Lemmon, M. A. (2007). Pleckstrin homology (PH) domains and phosphoinositides. *Biochem Soc Symp*(74), 81-93.

Lemmon, M. A. (2008). Membrane recognition by phospholipid-binding domains. *Nat Rev Mol Cell Biol, 9*(2), 99-111.

Lenoir, M., Kufareva, I., Abagyan, R., & Overduin, M. (2015). Membrane and Protein Interactions of the Pleckstrin Homology Domain Superfamily. *Membranes (Basel), 5*(4), 646-663.

Lens, S., Voest, E. E., & Medema, R. H. (2010). Shared and separate functions of polo-like kinases and aurora kinases in cancer. *Nature Reviews Cancer*, *10*(12), 825-841.

Lens, S. M. A., & Medema, R. H. (2019). Cytokinesis defects and cancer. *Nat Rev Cancer, 19*(1), 32-45.

Lerch, M. M., Szymański, W., & Feringa, B. L. (2018). The (photo)chemistry of Stenhouse photoswitches: Guiding principles and system design. *Chemical Society Reviews, 47*(6), 1910-1937.

Leung, C. C., & Glover, J. N. (2011). BRCT domains: easy as one, two, three. *Cell*

Cycle, 10(15), 2461-2470.

Li, Y., Li, S., & Wu, H. (2022). Ubiquitination-proteasome system (UPS) and autophagy two main protein degradation machineries in response to cell stress. *Cells*, *11*(5), 851.

Lima, S. Q., & Miesenböck, G. (2005). Remote control of behavior through genetically targeted photostimulation of neurons. *Cell, 121*(1), 141-152.

Limzerwala, J. F., Jeganathan, K. B., Kloeber, J. A., Davies, B. A., Zhang, C., Sturmlechner, I., Zhong, J., Velasco, R. F., Fields, A. P., Yuan, Y., Baker, D. J., Zhou, D., Li, H., Katzmann, D. J., & van Deursen, J. M. (2020). FoxM1 insufficiency hyperactivates Ect2–RhoA–mDia1 signaling to drive cancer. *Nature Cancer*, 1-34.

Liot, C., Seguin, L., Siret, A., Crouin, C., Schmidt, S., & Bertoglio, J. (2011). APC(cdh1) mediates degradation of the oncogenic Rho-GEF Ect2 after mitosis. *PLoS One, 6*(8), e23676.

Lodish, H. F. (2000). *Molecular cell biology* (4th ed.). W.H. Freeman.

Longhini, K. M., & Glotzer, M. (2022). Aurora A and cortical flows promote polarization and cytokinesis by inducing asymmetric ECT-2 accumulation. *Elife*, *11*, e83992.

Löwe, J., Stock, D., Jap, B., Zwickl, P., Baumeister, W., & Huber, R. (1995). Crystal structure of the 20 S proteasome from the archaeon T. acidophilum at 3.4 Å resolution. *Science*, *268*(5210), 533-539.

Machiels, B. M., Henfling, M. E., Gerards, W. L., Broers, J. L., Bloemendal, H., Ramaekers, F. C., & Schutte, B. (1997). Detailed analysis of cell cycle kinetics upon proteasome inhibition. *Cytometry*, 28(3), 243–252.

Mailhes, J. B., Hilliard, C., Lowery, M., & London, S. N. (2002). MG-132, an inhibitor of proteasomes and calpains, induced inhibition of oocyte maturation and aneuploidy in mouse oocytes. *Cell & Chromosome*, 1, 1–7.

Magnaghi-Jaulin, L., Eot-Houllier, G., Gallaud, E., & Giet, R. (2019). Aurora A protein kinase: To the centrosome and beyond. *Biomolecules*, 9(1), 28.

Mangal, S., Sacher, J., Kim, T., Osório, D. S., Motegi, F., Carvalho, A. X., Oegema, K., & Zanin, E. (2018). TPXL-1 activates Aurora A to clear contractile ring components from the polar cortex during cytokinesis. *The Journal of Cell Biology, 217*, 837-848.

Marumoto, T., Zhang, D., & Saya, H. (2005). Aurora-A—a guardian of poles. *Nature*

Reviews Cancer, 5(1), 42-50.

Matthews, Helen K., Delabre, U., Rohn, Jennifer L., Guck, J., Kunda, P., & Baum, B. (2012). Changes in Ect2 Localization Couple Actomyosin-Dependent Cell Shape Changes to Mitotic Progression. *Developmental Cell, 23*(2), 371-383.

Maupin, P., & Pollard, T. D. (1986). Arrangement of actin filaments and myosin-like filaments in the contractile ring and of actin-like filaments in the mitotic spindle of dividing HeLa cells. *Journal of ultrastructure and molecular structure research*, *94*(1), 92-103.

Mavrakis, M., Azou-Gros, Y., Tsai, F. C., Alvarado, J., Bertin, A., Iv, F., ... & Lecuit, T. (2014). Septins promote F-actin ring formation by crosslinking actin filaments into curved bundles. *Nature cell biology*, *16*(4), 322-334.

Medvedeva, S. M., Movchan, A. V., Sidorenko, O. E., Shestakov, A. S., Ledenyova, I. V., Zavarzin, I. V., & Shikhaliev, K. S. (2022). Synthesis of substituted 1, 3-oxazino[5, 4, 3-ij]quinolin-1, 3-diones by the oxidation of various pyrrolo[3, 2, 1-ij]quinoline-1, 2-diones with m-chloroperbenzoic acid. *ARKIVOC: Online Journal of Organic Chemistry*, 2022.

Menon, M. B., Sawada, A., Chaturvedi, A., Mishra, P., Schuster-Gossler, K., Galla, M., ... & Gaestel, M. (2014). Genetic deletion of SEPT7 reveals a cell type-specific role of septins in microtubule destabilization for the completion of cytokinesis. *PLoS Genetics*, 10(8), e1004558.

Michaelson, D., Silletti, J., Murphy, G., D'Eustachio, P., Rush, M., & Philips, M. R. (2001). Differential localization of Rho GTPases in live cells: regulation by hypervariable regions and RhoGDI binding. *J Cell Biol, 152*(1), 111-126.

Michaux, J. B., Robin, F. B., McFadden, W. M., & Munro, E. M. (2018). Excitable RhoA dynamics drive pulsed contractions in the early *C. elegans* embryo. *Journal of Cell Biology*, 217(12), 4230-4252.

Mikhael, J. R., Belch, A. R., Prince, H. M., Lucio, M. N., Maiolino, A., Corso, A., ... & Stewart, A. K. (2009). High response rate to bortezomib with or without dexamethasone in patients with relapsed or refractory multiple myeloma: results of a global phase 3b expanded access program. *British journal of haematology*, *144*(2), 169-175.

Miki, T., Fleming, T. P., Bottaro, D. P., Rubin, J. S., Ron, D., & Aaronson, S. A. (1991). Expression cDNA cloning of the KGF receptor by creation of a transforming autocrine loop. *Science, 251*(4989), 72-75.

Miller, A. L., & Bement, W. M. (2009). Regulation of cytokinesis by Rho GTPase flux.

Nat Cell Biol, 11(1), 71-77.

Mishima, M. (2016). Centralspindlin in Rappaport's cleavage signaling. *Semin Cell Dev Biol, 53*, 45-56.

Mishima, M., Kaitna, S., & Glotzer, M. (2002). Central spindle assembly and cytokinesis require a kinesin-like protein/RhoGAP complex with microtubule bundling activity. *Dev Cell, 2*(1), 41-54.

Morgan, D. (2006). *The cell cycle : principles of control*. Oxford: Oxford University Press.

Motegi, F., Velarde, N. V., Piano, F., & Sugimoto, A. (2006). Two phases of astral microtubule activity during cytokinesis in C. elegans embryos.

Mou, S., Wang, G., Ding, D., Yu, D., Pei, Y., Teng, S., & Fu, Q. (2016). Expression and function of PIM kinases in osteosarcoma. *International Journal of Oncology, 49*(5), 2116-2126.

Mullen, T. J., & Wignall, S. M. (2017). Interplay between microtubule bundling and sorting factors ensures acentriolar spindle stability during *C. elegans* oocyte meiosis. *PLoS Genetics, 13*(9), e1006986.

Murthy, K., & Wadsworth, P. (2008). Dual role for microtubules in regulating cortical contractility during cytokinesis. *Journal of Cell Science*, 121(14), 2350–2359.

Musacchio, A., & Salmon, E. D. (2007). The spindle-assembly checkpoint in space and time. *Nature reviews Molecular cell biology*, *8*(5), 379-393.

Musacchio, A. (2015). The molecular biology of spindle assembly checkpoint signaling dynamics. *Current biology*, *25*(20), R1002-R1018.

Müller-Reichert, T., Greenan, G., O'Toole, E., & Srayko, M. (2010). The elegans of spindle assembly. *Cellular and Molecular Life Sciences*, 67, 2195-2213.

Nihira, K., Ando, Y., Yamaguchi, T., Kagami, Y., Miki, Y., & Yoshida, K. (2010). Pim-1 controls NF-κB signalling by stabilizing RelA/p65. *Cell Death & Differentiation*, *17*(4), 689-698.

Nikonova, A. S., Astsaturov, I., Serebriiskii, I. G., Dunbrack, R. L., & Golemis, E. A. (2013). Aurora A kinase (AURKA) in normal and pathological cell division. *Cellular and Molecular Life Sciences*, 70, 661–687.

Niiya, F., Tatsumoto, T., Lee, K. S., & Miki, T. (2006). Phosphorylation of the cytokinesis regulator ECT2 at G2/M phase stimulates association of the mitotic

kinase Plk1 and accumulation of GTP-bound RhoA. *Oncogene*, 25(6), 827-837.

Niiya, F., Xie, X., Lee, K. S., Inoue, H., & Miki, T. (2005). Inhibition of cyclin-dependent kinase 1 induces cytokinesis without chromosome segregation in an ECT2 and MgcRacGAP- dependent manner. *J Biol Chem, 280*(43), 36502-36509.

Nishimura, Y., & Yonemura, S. (2006). Centralspindlin regulates ECT2 and RhoA accumulation at the equatorial cortex during cytokinesis. *J Cell Sci, 119*(Pt 1), 104-114.

Odom, J., Williamson, B., & Carter, L. (2008). Rosiglitazone and pioglitazone in the treatment of diabetes mellitus. *American Journal of Health-System Pharmacy*, 65(19), 1846-1850.

Oegema, K., Savoian, M. S., Mitchison, T. J., & Field, C. M. (2000). Functional analysis of a human homologue of the Drosophila actin-binding protein anillin suggests a role in cytokinesis. *Journal of Cell Biology*, 150(3), 539–552.

Olson, J. P., Banghart, M. R., Sabatini, B. L., & Ellis-Davies, G. C. (2013). Spectral evolution of a photochemical protecting group for orthogonal two-color uncaging with visible light. *Journal of the American Chemical Society*, *135*(42), 15948-15954.

Ong, J. Y., Bradley, M. C., & Torres, J. Z. (2020). Phospho-regulation of mitotic spindle assembly. *Cytoskeleton*, 77(12), 558–578.

Osório, D. S., Chan, F. Y., Saramago, J., Leite, J., Silva, A. M., Sobral, A. F., ... & Carvalho, A. X. (2019). Crosslinking activity of non-muscle myosin II is not sufficient for embryonic cytokinesis in *C. elegans*. *Development*, 146(21), dev179150.uh

Pavin, N., & Tolic, I. M. (2021). Mechanobiology of the Mitotic Spindle. *Dev Cell, 56*(2), 192- 201.

Peltola, K., Hollmen, M., Maula, S. M., Rainio, E., Ristamäki, R., Luukkaa, M., ... & Jalkanen, S. (2009). Pim-1 kinase expression predicts radiation response in squamocellular carcinoma of head and neck and is under the control of epidermal growth factor receptor. *Neoplasia*, *11*(7), 629-IN1.

Peters, J. M. (1994). Proteasomes: protein degradation machines of the cell. *Trends in biochemical sciences, 19*(9), 377-382.

Peterson, J. A., Wijesooriya, C., Gehrmann, E. J., Mahoney, K. M., Goswami, P. P., Albright, T. R., ... & Winter, A. H. (2018). Family of BODIPY photocages cleaved by single photons of visible/near-infrared light. *Journal of the American Chemical*

Society, *140*(23), 7343-7346.

Petronczki, M., Glotzer, M., Kraut, N., & Peters, J. M. (2007). Polo-like kinase 1 triggers the initiation of cytokinesis in human cells by promoting recruitment of the RhoGEF Ect2 to the central spindle. *Dev Cell, 12*(5), 713-725.

Petronczki, M., Lénárt, P., & Peters, J. M. (2008). Polo on the rise—From mitotic entry to cytokinesis with Plk1. *Developmental Cell*, 14(5), 646–659.

Piekny, A., Werner, M., & Glotzer, M. (2005). Cytokinesis: welcome to the Rho zone. *Trends Cell Biol, 15*(12), 651-658.

Piekny, A. J., & Glotzer, M. (2008). Anillin is a scaffold protein that links RhoA, actin, and myosin during cytokinesis. *Curr Biol, 18*(1), 30-36.

Pines, J. (2011). Cubism and the cell cycle: the many faces of the APC/C. *Nature reviews Molecular cell biology*, *12*(7), 427-438.

Pinto, I. M., Rubinstein, B., Kucharavy, A., Unruh, J. R., & Li, R. (2012). Actin depolymerization drives actomyosin ring contraction during budding yeast cytokinesis. *Developmental Cell*, 22(6), 1247–1260.

Piperdi, B., Ling, Y. H., Liebes, L., Muggia, F., & Perez-Soler, R. (2011). Bortezomib: understanding the mechanism of action. *Molecular Cancer Therapeutics*, 10(11), 2029-2030.

Portier, N., Audhya, A., Maddox, P. S., Green, R. A., Dammermann, A., Desai, A., & Oegema, K. (2007). A microtubule-independent role for centrosomes and Aurora A in nuclear envelope breakdown. *Developmental Cell*, 12, 515-529.

Prokopenko, S. N., Brumby, A., O'Keefe, L., Prior, L., He, Y., Saint, R., & Bellen, H. J. (1999). A putative exchange factor for Rho1 GTPase is required for initiation of cytokinesis in Drosophila. *Genes Dev, 13*(17), 2301-2314.

Prosser, S. L., & Pelletier, L. (2017). Mitotic spindle assembly in animal cells: a fine balancing act. *Nature Reviews Molecular Cell Biology*, *18*(3), 187-201.

Ramirez, M. A., & Borja, N. L. (2008). Epalrestat: an aldose reductase inhibitor for the treatment of diabetic neuropathy. *Pharmacotherapy: The Journal of Human Pharmacology and Drug Therapy*, 28(5), 646-655.

Ramkumar, N., Patel, J. V., Anstatt, J., & Baum, B. (2021). Aurora B-dependent polarization of the cortical actomyosin network during mitotic exit. *EMBO Rep, 22*(10), e52387.

Rankin, K. E., & Wordeman, L. (2010). Long astral microtubules uncouple mitotic spindles from the cytokinetic furrow. *Journal of Cell Biology*, 190(1), 35-43.

Rappaport, R. (1961). Experiments concerning the cleavage stimulus in sand dollar eggs. *Journal of Experimental Zoology*, 148(1), 81-89.

Rappaport, R. (1985). Repeated furrow formation from a single mitotic apparatus in cylindrical sand dollar eggs. *J Exp Zool, 234*(1), 167-171.

Reboutier, D., Troadec, M.-B., Cremet, J.-Y., Chauvin, L., Guen, V., Salaun, P., & Prigent, C. (2013). Aurora A is involved in central spindle assembly through phosphorylation of Ser 19 in P150Glued. *The Journal of Cell Biology*, 201, 65-79.

Reiß, B., Hu, Q., Riedle, E., & Wagenknecht, H. A. (2021). The dependence of chemical quantum yields of visible light photoredox catalysis on the irradiation power. *ChemPhotoChem*, 5(11), 1009-1019.

Rhind, N., & Russell, P. (2012). Signaling pathways that regulate cell division. *Cold Spring Harb Perspect Biol, 4*(10).

Ri, M. (2016). Endoplasmic-reticulum stress pathway-associated mechanisms of action of proteasome inhibitors in multiple myeloma. *International Journal of Hematology*, 104(3), 273-280.

Rieder, C. L., Khodjakov, A., Paliulis, L. V., Fortier, T. M., Cole, R. W., & Sluder, G. (1997). Mitosis in vertebrate somatic cells with two spindles: implications for the metaphase/anaphase transition checkpoint and cleavage. *Proceedings of the National Academy of Sciences*, 94, 5107–5112.

Roof, R. W., Dukes, B. D., Chang, J. H., & Parsons, S. J. (2000). Phosphorylation of the p190 RhoGAP N-terminal domain by c-Src results in a loss of GTP binding activity. *FEBS letters*, 472(1), 117-121.

Rossman, K. L., Der, C. J., & Sondek, J. (2005). GEF means go: turning on RHO GTPases with guanine nucleotide-exchange factors. *Nat Rev Mol Cell Biol, 6*(2), 167-180.

Saito, S., Liu, X.-F., Kamijo, K., Raziuddin, R., Tatsumoto, T., Okamoto, I., Chen, X., Lee, C.-C., Lorenzi, M.V., Ohara, N., & Miki, T. (2004). Deregulation and mislocalization of the cytokinesis regulator ECT2 activate the Rho signaling pathways leading to malignant transformation. *Journal of Biological Chemistry*, 279, 7169–7179.

Saurabh, K., Scherzer, M. T., Shah, P. P., Mims, A. S., Lockwood, W. W., Kraft, A. S.,

& Beverly, L. J. (2014). The PIM family of oncoproteins: small kinases with huge implications in myeloid leukemogenesis and as therapeutic targets. *Oncotarget*, *5*(18), 8503.

Schmidt, O., & Teis, D. (2012). The ESCRT machinery. *Current Biology*, *22*(4), R116-R120.

Schneid, S., Wolff, F., Buchner, K., Bertram, N., Baygün, S., Barbosa, P., Mangal, S., & Zanin, E. (2021). The BRCT domains of ECT2 have distinct functions during cytokinesis. *Cell Reports*, 34, 108805.

Schroeder, T. E. (1968). Cytokinesis: Filaments in the cleavage furrow. *Experimental Cell Research*, 53(1), 272–276.

Schroeder, T. E. (1972). The contractile ring. II. Determining its brief existence, volumetric changes, and vital role in cleaving Arbacia eggs. *Journal of Cell Biology*, 53(2), 419–434.

Sedzinski, J., Biro, M., Oswald, A., Tinevez, J. Y., Salbreux, G., & Paluch, E. (2011). Polar actomyosin contractility destabilizes the position of the cytokinetic furrow. *Nature*, 476(7361), 462-466.

Seeger, M., Hartmann-Petersen, R., Wilkinson, C. R., Wallace, M., Samejima, I., Taylor, M. S., & Gordon, C. (2003). Interaction of the anaphase-promoting complex/cyclosome and proteasome protein complexes with multiubiquitin chain-binding proteins. *Journal of Biological Chemistry*, *278*(19), 16791-16796.

Seguin, L., Liot, C., Mzali, R., Harada, R., Siret, A., Nepveu, A., & Bertoglio, J. (2009). CUX1 and E2F1 regulate coordinated expression of the mitotic complex genes Ect2, MgcRacGAP, and MKLP1 in S phase. *Mol Cell Biol, 29*(2), 570-581.

Severson, A. F., Baillie, D. L., & Bowerman, B. (2002). A Formin Homology protein and a profilin are required for cytokinesis and Arp2/3-independent assembly of cortical microfilaments in C. elegans. *Current Biology*, *12*(24), 2066-2075.

Shembekar, V. R., Chen, Y., Carpenter, B. K., & Hess, G. P. (2005). A protecting group for carboxylic acids that can be photolyzed by visible light. *Biochemistry*, 44(19), 7107-7114.

Shrestha, P., Dissanayake, K. C., Gehrmann, E. J., Wijesooriya, C. S., Mukhopadhyay, A., Smith, E. A., & Winter, A. H. (2020). Efficient far-red/near-IR absorbing BODIPY photocages by blocking unproductive conical intersections. *Journal of the American Chemical Society*, *142*(36), 15505-15512.

Sledge, G. W., Toi, M., Neven, P., Sohn, J., Inoue, K., Pivot, X., ... & Goetz, M. P.

(2017). MONARCH 2: Abemaciclib in combination with fulvestrant in women with HR+/HER2– advanced breast cancer who had progressed while receiving endocrine therapy. *Journal of Clinical Oncology*, 35(25), 2875–2884.

Soave, C. L., Guerin, T., Liu, J., & Dou, Q. P. (2017). Targeting the ubiquitin-proteasome system for cancer treatment: discovering novel inhibitors from nature and drug repurposing. *Cancer and Metastasis Reviews*, *36*, 717-736.

Somers, W. G., & Saint, R. (2003). A RhoGEF and Rho family GTPase-activating protein complex links the contractile ring to cortical microtubules at the onset of cytokinesis. *Developmental Cell*, 4(1), 29–39.

Spring, L. M., Zangardi, M., Moy, B., & Bardia, A. (2017). Clinical management of potential toxicities and drug interactions related to CDK4/6 inhibitors in breast cancer: practical considerations and recommendations. *The Oncologist, 22(9), 1039–1048.*

Stenoien, D. L., Sen, S., Mancini, M. A., & Brinkley, B. R. (2003). Dynamic association of a tumor amplified kinase, Aurora-A, with the centrosome and mitotic spindle. *Cell Motility and the Cytoskeleton*, 55, 134-146.

Straight, A. F., Field, C. M., & Mitchison, T. J. (2005). Anillin binds nonmuscle myosin II and regulates the contractile ring. *Molecular Biology of the Cell*, 16(1), 193–201.

Su, K.-C., Takaki, T., & Petronczki, M. (2011). Targeting of the RhoGEF Ect2 to the equatorial membrane controls cleavage furrow formation during cytokinesis. *Developmental Cell*, 21, 1104-1115.

Sullivan, M., & Morgan, D. O. (2007). Finishing mitosis, one step at a time. *Nature reviews Molecular cell biology*, *8*(11), 894-903.

Sun, L., Guan, R., Lee, I. J., Liu, Y., Chen, M., Wang, J., ... & Chen, Z. (2015). Mechanistic insights into the anchorage of the contractile ring by anillin and Mid1. *Developmental cell*, *33*(4), 413-426.

Suzuki, K., Sako, K., Akiyama, K., Isoda, M., Senoo, C., Nakajo, N., & Sagata, N. (2015). Identification of non-Ser/Thr-Pro consensus motifs for Cdk1 and their roles in mitotic regulation of C2H2 zinc finger proteins and Ect2. *Scientific Reports*, 5, 7929.

Szymanski, W., Beierle, J. M., Kistemaker, H. A., Velema, W. A., & Feringa, B. L. (2013). Reversible photocontrol of biological systems by the incorporation of molecular photoswitches. *Chemical Reviews*, 113(8), 6114-6178.

Tanaka, K. (2009). The proteasome: overview of structure and functions. *Proceedings of the Japan Academy, Series B*, 85(1), 12-36.

Tashjian, A. H., & Armstrong, E. J. (2011). Principles of pharmacology: the pathophysiologic basis of drug therapy. *Lippincott Williams & Wilkins*.

Tatsumoto, T., Xie, X., Blumenthal, R., Okamoto, I., & Miki, T. (1999). Human ECT2 is an exchange factor for Rho GTPases, phosphorylated in G2/M phases, and involved in cytokinesis. *J Cell Biol, 147*(5), 921-928.

Tavernier, N., Sicheri, F., & Pintard, L. (2021). Aurora A kinase activation: Different means to different ends. *The Journal of Cell Biology*, 220.

Thapaliya, E. R., Mony, L., Sanchez, R., Serraz, B., Paoletti, P., & Ellis-Davies, G. C. (2021). Photochemical control of drug efficacy: a comparison of uncaging and photoswitching ifenprodil on NMDA receptors. *ChemPhotoChem*, *5*(5), 445-454.

Tomko Jr, R. J., & Hochstrasser, M. (2013). Molecular architecture and assembly of the eukaryotic proteasome. *Annual review of biochemistry*, *82*(1), 415-445.

Uyehara, A. N., & Rasmussen, C. G. (2023). Redundant mechanisms in division plane positioning. *European Journal of Cell Biology*, 102(2), 151308.

van Oostende Triplet, C., Jaramillo Garcia, M., Haji Bik, H., Beaudet, D., & Piekny, A. (2014). Anillin interacts with microtubules and is part of the astral pathway that defines cortical domains. *Journal of Cell Science*, 127(17), 3699-3710.

Van Es, T., Staskun, B., & Van Vuuren, S. (2005). Sulphur-substituted Pyrrolo [3, 4-b] quinolines: synthesis, chemistry and antimicrobial activity. *South African Journal of Chemistry*, 58(1), 74-81.

von Dassow, G., Verbrugghe, K. J., Miller, A. L., Sider, J. R., & Bement, W. M. (2009). Action at a distance during cytokinesis. *Journal of Cell Biology*, 187(6), 831-845.

Verhey, K. J., & Hammond, J. W. (2009). Traffic control: regulation of kinesin motors. *Nature reviews Molecular cell biology*, *10*(11), 765-777.

Verma, V., & Maresca, T. J. (2019). Microtubule plus-ends act as physical signaling hubs to activate RhoA during cytokinesis. *eLife*, 8, 309.

Vietri, M., Radulovic, M., & Stenmark, H. (2020). The many functions of ESCRTs. *Nature Reviews Molecular Cell Biology*, 21(1), 25–42.

Volarić, J., Szymanski, W., Simeth, N. A., & Feringa, B. L. (2021). Molecular photoswitches in aqueous environments. *Chemical Society Reviews*, 50(22),

12377-12449.

Wagner, A., & Wright, J. (2007). Alternative routes and mutational robustness in complex regulatory networks. *Biosystems*, 88, 163–172.

Walczak, C. E., & Heald, R. (2008). Mechanisms of mitotic spindle assembly and function. *International review of cytology*, *265*, 111-158.

Wang, K., Deng, X., Shen, Z., Jia, Y., Ding, R., Li, R., ... & Jie, W. (2017). High glucose promotes vascular smooth muscle cell proliferation by upregulating proto-oncogene serine/threonine-protein kinase Pim-1 expression. *Oncotarget*, *8*(51), 88320.

Wang, Q., Bode, A. M., & Zhang, T. (2023). Targeting CDK1 in cancer: mechanisms and implications. *NPJ precision oncology*, *7*(1), 58.

Wardle, B. (2009). Principles and applications of photochemistry. *John Wiley & Sons*.

Werner, M., Munro, E., & Glotzer, M. (2007). Astral signals spatially bias cortical myosin recruitment to break symmetry and promote cytokinesis. *Current Biology*, 17(15), 1286–1297.

White, E. A., & Glotzer, M. (2012). Centralspindlin: at the heart of cytokinesis. *Cytoskeleton*, *69*(11), 882-892.

Wolfe, B. A., Takaki, T., Petronczki, M., & Glotzer, M. (2009). Polo-like kinase 1 directs assembly of the HsCyk-4 RhoGAP/Ect2 RhoGEF complex to initiate cleavage furrow formation. *PLoS Biology*, 7(5), e1000110.

Ye, A. A., Deretic, J., Hoel, C. M., Hinman, A. W., Cimini, D., Welburn, J. P., & Maresca, T. J. (2015). Aurora A kinase contributes to a pole-based error correction pathway. *Current Biology*, 25, 1842-1851.

Young, D. D., & Deiters, A. (2007). Photochemical control of biological processes. *Organic & Biomolecular Chemistry*, 5(7), 999-1005.

Yüce, Ö., Piekny, A., & Glotzer, M. (2005). An ECT2–centralspindlin complex regulates the localization and function of RhoA. *The Journal of Cell Biology*, 170(4), 571-582.

Zanin, E., Desai, A., Poser, I., Toyoda, Y., Andree, C., Moebius, C., Bickle, M., Conradt, B., Piekny, A., & Oegema, K. (2013). A conserved RhoGAP limits M phase contractility and coordinates with microtubule asters to confine RhoA during cytokinesis. *Developmental Cell*, 26(5), 496-510.

Zeng, X., Sigoillot, F., Gaur, S., Choi, S., Pfaff, K. L., Oh, D. C., ... & King, R. W. (2010). Pharmacologic inhibition of the anaphase-promoting complex induces a spindle checkpoint-dependent mitotic arrest in the absence of spindle damage. *Cancer Cell*, 18(4), 382–395.

Zhang, Y., & Glotzer, M. (2015). The RhoGEF Ect2 coordinates actomyosin and microtubule dynamics to control polarized cell shape. *Developmental Cell*, 33(3), 332–343.

Zhao, W. M., Fang, G. (2005). MgcRacGAP controls the assembly of the contractile ring and the initiation of cytokinesis. *Proceedings of the National Academy of Sciences*, 102(39), 13158–13163.

Zheng, Y. (2001). Dbl family guanine nucleotide exchange factors. *Trends Biochem Sci, 26*(12), 724-732.

Zhu, X., Xu, J. J., Hu, S. S., Feng, J. G., Jiang, L. H., Hou, X. X., ... & Ge, M. H. (2014). Pim-1 acts as an oncogene in human salivary gland adenoid cystic carcinoma. *Journal of Experimental & Clinical Cancer Research*, *33*, 1-12.

Zhu, M., & Zhou, H. (2018). Azobenzene-based small molecular photoswitches for protein modulation. *Organic & Biomolecular Chemistry*, 16(44), 8434-8445.

Zou, Y., Shao, Z., Peng, J., Li, F., Gong, D., Wang, C., Zuo, X., Zhang, Z., Wu, J., Shi, Y., & Gong, Q. (2014). Crystal structure of triple-BRCT-domain of ECT2 and insights into the binding characteristics to CYK-4. *FEBS Letters*, 588(17), 2911-2920.

Zumdieck, A., Kruse, K., Bringmann, H., Hyman, A. A., & Jülicher, F. (2007). Stress generation and filament turnover during actin ring constriction. *PloS one*, *2*(8), e696.

Curriculum Vitae

Personal details

Name   Friederike Eleonore Wolff

Nationality   German

Education

05/2019 – 12/2023   PhD Candidate (Biology)
                    Ludwig-Maximilians-University Munich, Germany

04/2017 – 04/2019   Master of Science (Molecular Ecology)
                    University of Bayreuth, Germany

04/2012 – 04/2017   Bachelor of Science (Biology)
                    University of Bayreuth, Germany

Working Experience

01/2024 – current   Project Manager GMP Intercompany Business
                    Eurofins Biopharma Product Testing GmbH, Germany

05/2019 – 12/2023   Graduate Researcher with Prof. Dr. Esther Zanin
                    Ludwig-Maximilians-University Munich, Germany

Awards

2022   ASCB/EMBO Cell Bio 2022 Travel Grant Award

2021   Inside Cover Angewandte Chemie International Edition:
                    Volume 60, Issue 3

2019   Heinrich Kutter Price of Central European IUSSI, 2nd Best
                    Student Poster

Publications

Wolff F., Srinivasan S., Nöcker M., Mangal S., Mikeladze-Dvali T., Zanin E. (2023). Spatially distinct inputs modulate the amount of active Mitotic-phase GAP to locally restrict RhoA signaling for successful cell division. *bioRxiv* Preprint.

Schneid, S.*, **Wolff, F.***, Buchner, K., Bertram, N., Baygün, S., Barbosa, P., Mangal, S., & Zanin, E. (2021). The BRCT domains of ECT2 have distinct functions during cytokinesis. *Cell reports*, *34*(9), 108805.

Uhl, E.*, **Wolff, F.***, Mangal, S., Dube, H., & Zanin, E. (2021). Light-Controlled Cell-Cycle Arrest and Apoptosis. *Angewandte Chemie (International ed. in English)*, *60*(3), 1187–1196

Köttner, L.*, **Wolff, F.***, Mayer, P., Zanin, E., & Dube, H. (2024). Rhodanine-Based Chromophores: Fast Access to Capable Photoswitches and Application in Light-Induced Apoptosis. *Journal of the American Chemical Society*, *146*(3), 1894-1903.

Schreiner, A., Heim, A., **Wolff, F**., Zanin, E., Mikeladze-Dvali, T. (2024). PCMD-1 stabilizes the PCM scaffold and facilitates centriole separation. bioRxiv Preprint.

* contributed equally